

# Inter- and intramolecular interactions of purified (and modified) mucin glycoproteins with other molecules, cells, and artificial materials

Theresa Monika Lutz

Vollständiger Abdruck der von der TUM School of Engineering and Design der Technischen  
Universität München zur Erlangung einer  
Doktorin der Naturwissenschaften (Dr. rer. nat.)  
genehmigten Dissertation.

Vorsitz: Prof. Dr. rer. nat. Rudolf Neu

Prüfer\*innen der Dissertation:

1. Prof. Dr. rer. nat. Oliver Lieleg
2. Prof. Dr. ir. Mireille M.A.E. Claessens
3. .....

Die Dissertation wurde am 20.04.2023 bei der Technischen Universität München eingereicht  
und durch die TUM School of Engineering and Design am 21.08.2023 angenommen.



## Summary

The glycoprotein mucin with its multiple properties, such as the formation of a mechanical protective layer on wet epithelia or the selective filtering of molecules (e.g., of pathogens), has gained importance in medical research. Not only because these proteins have endogenously important tasks and their physiological function is important for the maintenance of human health, but also since structural changes, for example caused by degradation of certain structure motifs through (bacterial) enzymes, can offer crucial information about mucin-based disease development and therapy.

In this thesis, first, several structural motifs on mucin are removed and the interaction change with molecules whose surfaces have different physicochemical properties are investigated in more detail. The resulting absence of repulsion leads to structural changes within the glycoprotein and thus to reduced interaction behavior between mucin and other molecules. Such fundamental research emphasizes the importance of intact mucin molecules. However, those findings highlight the potential of the functional groups in mucin as well. Furthermore, it is shown in the thesis that individual structural motifs such as thiols are modified with DNA strands or amines and hydroxyl groups are altered by methacrylates to create stable mucin-based drug delivery systems by hybridization of short palindromic DNA sequences or a free radical-based reaction with UV light. Due to those structural changes within the glycoprotein, stable globular frameworks are formed that are able to transport drugs and release them under certain conditions such as binding of a mRNA strand serving as a 'key' to the protein transport system, or enzymatic degradation of the mucin carrier. Moreover, such structural motifs on mucins are also applicable to enable anchoring of glycoproteins on surfaces such as catheters and stents by a dopamine-based strategy. The results impressively demonstrated how such coatings reduce eukaryotic cell attachment and tribological stress. This is particularly desirable if biomedical products are inserted into the body and predominantly remain in the body permanently.

The different functionalizations of naturally occurring mucin molecules shown herein aim at creating modified biomacromolecules for novel applications in medicine. Owing to their excellent biocompatibility, biodegradability and mechanical stability, mucins are attractive candidates as carriers for pharmaceuticals or for coatings of medical products to improve human health.

## Zusammenfassung

Das Glykoprotein Muzin mit seinen vielfältigen Eigenschaften, wie die Bildung einer mechanischen Schutzschicht auf feuchtem Epithelgewebe oder die selektive Filterung von Molekülen (z. B. von Pathogenen), ist von der medizinischen Forschung nicht mehr wegzudenken. Nicht nur weil diese Proteine endogen wichtige Aufgaben haben und ihre physiologische Funktion für die Aufrechterhaltung der menschlichen Gesundheit wichtig ist, sondern auch weil Strukturveränderungen, beispielsweise bedingt durch den Abbau bestimmter Strukturmodule durch (bakterielle) Enzyme, wichtige Aufschlüsse über Muzin-basierte Krankheitsentwicklung und -therapie bieten können.

In dieser Dissertation werden zunächst verschiedene Strukturmodule an Muzin entfernt und die Interaktionsveränderung mit Molekülen, deren Oberflächen verschiedene physikochemische Eigenschaften haben, genauer untersucht. Durch daraus resultierende, fehlende Repulsion kommt es innerhalb des Glykoproteins zu Strukturveränderungen und somit zu einem reduzierten Interaktionsverhalten zwischen Muzin und anderen Molekülen. Solche grundlegenden Forschungen zeigen wie wichtig intakte Muzinmoleküle sind. Diese Ergebnisse verdeutlichen aber auch welches Potential diese funktionellen Gruppen an Muzin haben. Ferner wird gezeigt, dass einzelne Strukturmodule wie etwa Thiole mit DNA-Strängen modifiziert, oder Amino- und Hydroxylgruppen durch Methacrylate verändert werden, um durch Hybridisierung von palindromischen DNA-Sequenzbereichen oder eine freie radikal-basierte Reaktion mit UV-Licht stabile Trägermaterialien aus Muzin entstehen zu lassen. Bedingt durch die Strukturveränderung innerhalb des Glykoproteins entstehen so stabile, globuläre Gerüste, die Medikamente transportieren und diese unter bestimmten Voraussetzungen, wie etwa durch Binden eines mRNA-Strangs, der als ‚Schlüssel‘ für das Proteingerüst dient, oder durch enzymatischen Abbau der Mucine wieder freigeben. Des Weiteren sind in dieser Dissertation solche Strukturmodule an Muzinen auch verwendet worden, um eine Verankerung der Glykoproteine auf Oberflächen wie Kathetern und Stents durch eine Dopamin-basierte Strategie zu ermöglichen. Es kann eindrucksvoll gezeigt werden, wie solche Beschichtungen die Anlagerung von eukaryotischen Zellen und tribologischen Stress reduzieren. Dies ist besonders dann erstrebenswert, wenn biomedizinische Produkte in den Körper eingeführt werden und mitunter auch dauerhaft im Körper verbleiben.

Die hier vorgestellten unterschiedlichen Funktionalisierungen der natürlich vorkommenden Muzinmoleküle zielen darauf ab, modifizierte Biomakromoleküle für neuartige Anwendungen in der Medizin zu schaffen. Aufgrund ihrer hervorragenden Biokompatibilität, biologischen Abbaubarkeit und mechanischen Stabilität sind Mucine attraktive Kandidaten als Träger für Arzneimittel oder für Beschichtungen von Medizinprodukten zur Verbesserung der menschlichen Gesundheit.



## Contents

1. Introduction.....	10
2. Materials and Methods.....	13
2.1 Mucin macromolecules.....	13
2.2 Purification of porcine gastric mucin .....	13
2.4 Chemical modification of mucins.....	14
2.4.1 Production of UV-cross-linkable mucins .....	14
2.5 Preparation of mucin-based (nano)particles.....	14
2.5.1 Ionically crosslinked mucin particles .....	14
2.5.2 Covalently crosslinked mucin particles .....	15
2.5.3 DNA crosslinked mucin particles.....	15
2.6 Enzymatic modification of mucins .....	18
2.6.1 Enzymatic treatment of mucins .....	18
2.6.1.1 DNase treatment of mucins.....	18
2.6.1.2 Enzymatic treatment of mucins with sulfatase .....	18
2.6.1.3 Trypsin and pepsin treatment of mucin particles .....	19
2.7 Detection of molecules by fluorescence labeling or polymerization.....	19
2.7.1 Coupling of mucin molecules with an ATTO dye .....	19
2.7.2 Mucin labeling with fluorescein <i>o</i> -acrylate.....	19
2.8 Mucin binding with molecules, ions, and oxidation agents.....	20
2.8.1 Detectable binding partners.....	20
2.8.1.1 Dextrans and lectins .....	20
2.8.1.2 Antibodies .....	21
2.8.2 Drug loading and degradation of particles .....	22
2.8.3 Ferric reducing antioxidant power (FRAP) assay .....	24
2.8.4 (Ionic) crosslinkers.....	25
2.8.5 Dopamine-based coating process.....	25
2.9 Biocompatibility of mucin molecules and mucin particles.....	27
2.9.1 Cell cultivation.....	27
2.9.2 Water-soluble tetrazolium (WST-1) assay .....	27

2.9.3 Flow Cytometry .....	27
2.9.4 Fluorescence microscopy – cellular uptake of mucin particles.....	29
2.10 Techniques for the evaluation of mucin particle sizes .....	30
2.10.1 Dynamic light scattering (DLS) measurements [39] .....	30
2.10.2 Electrophoretic light scattering (ELS) measurements [40] .....	32
2.10.3 Atomic force microscopy (AFM) [43] .....	34
2.11 Technique to determine the gelation behavior of mucin molecules with oscillatory shear rheology [44].....	35
2.12 Statistics .....	36
3. Summaries of publications .....	38
3.1 Bio-based and bio-inspired adhesives from animals and plants for biomedical applications.....	38
3.2 Repulsive backbone-backbone interactions modulate access to specific and unspecific binding sites on surface-bound mucins .....	40
3.3 Bioinspired dopamine/mucin coatings provide lubricity, wear protection, and cell-repellent properties for medical applications .....	42
3.4 DNA strands trigger the intracellular release of drugs from mucin-based nanocarriers...	45
3.5 A stable mucin based nanoparticle system for the co-delivery of hydrophobic and hydrophilic drugs .....	48
4. Discussion .....	51
5. Outlook .....	58
Appendix.....	60
A. Crosslinking strategy modulates the mechanical properties of mucin nanoparticles and the governing cellular uptake mechanisms.....	60
A.1 Mucin particle characterization .....	61
A.2 Biocompatibility of mucin particles .....	64
A.3 Cellular uptake of different types of mucin particles .....	65
A.4 Endosomal escape of mucin-based particles with Pearson’s correlation .....	67
B. Full text of publications presented in this thesis.....	70
B.1 Bio-based and bio-inspired adhesives from animals and plants for biomedical applications.....	70

B.2 Repulsive backbone-backbone interactions modulate access to specific and unspecific binding sites on surface-bound mucins .....	91
B.2.1 Supplementary information for: Repulsive backbone-backbone interactions modulate access to specific and unspecific binding sites on surface-bound mucins .....	101
B.3 Bioinspired dopamine/mucin coatings provide lubricity, wear protection, and cell-repellent properties for medical applications .....	124
B.3.1 Supplementary information for: Bioinspired dopamine/mucin coatings provide lubricity, wear protection, and cell-repellent properties for medical applications .....	135
B.4 DNA strands trigger the intracellular release of drugs from mucin-based nanocarriers	143
B.4.1 Supplementary information for: DNA strands trigger the intracellular release of drugs from mucin-based nanocarriers .....	156
B.5 A stable mucin based nanoparticle system for the co-delivery of hydrophobic and hydrophilic drugs .....	178
B.5.1 Supplementary information for: A stable mucin based nanoparticle system for the co-delivery of hydrophobic and hydrophilic drugs .....	189
C. Licences for publications .....	203
C.1 Bio-based and bio-inspired adhesives from animals and plants for biomedical applications.....	203
C.2 Repulsive backbone-backbone interactions modulate access to specific and unspecific binding sites on surface-bound mucins .....	205
C.3 Bioinspired dopamine/mucin coatings provide lubricity, wear protection, and cell-repellent properties for medical applications .....	206
C.4 DNA strands trigger the intracellular release of drugs from mucin-based nanocarriers	212
C.5 A stable mucin based nanoparticle system for the co-delivery of hydrophobic and hydrophilic drugs .....	213
D. Full list of publications .....	215
D.1 Peer-reviewed.....	215
D.2 Not peer-reviewed yet .....	216
E. Bibliography .....	217
F. Acknowledgements.....	224





## 1. Introduction\*

Biomaterials composed of biomacromolecules are promising candidates in the field of medical applications since those compounds possess excellent biocompatibility, biodegradability, and (possibly) bioabsorption characteristics. Chemical modifications, especially bioconjugation or the integration of new functional groups, can result in multiple additional or novel properties of the biomolecule such as improved mechanical stability, adhesion or deformability of the molecule and the material formed thereof. The sensible approach is to selectively apply modifications to the molecule that avoid interfering with its native properties and allow it to function properly for medical applications. One negative example from the literature is acrylated epoxidized soybean oil (AESO) tissue adhesive, wherein residues and DOPA-based groups (that can be activated by UV light) are covalently linked to the biomolecule. Indeed, a stronger crosslinked biomaterial network is supposed to be formed by those modifications *via* a free radical reaction (by UV irradiation) and ionic interactions with trivalent cations (*via*  $\text{Fe}^{3+}$ ); however, the binding strength within the system was decreased instead [1]. To circumvent such risks, it is advisable to select a biomolecule offering already relevant functional groups for the desired medical application. Often, those functional groups are also involved in forming crosslinked networks thus allowing for the production of scaffolds for tissue engineering, films and wound adhesives to replace sutures and staples, as well as drug release depots.

Nature provides an immense array of macromolecules, which humans have purified, possibly recombinantly produced, analyzed, modified, and harnessed for medical purposes. Numerous animal- and plant-based biomolecules exist, such as polypeptides, polysaccharides, lipids, and molecular combinations thereof (*e.g.*, glycoproteins and proteoglycans). However, one molecule that is particularly attractive for therapeutic purposes is the glycoprotein mucin, known from aquatic animals such as hagfish. Mucins offer natively a variety of diverse functional groups that allows them to interact with each other (gel forming) or to form specific and unspecific interactions with other molecules. Such interactions can be both, attractive and repulsive and thus, the mucin possesses anti-bacterial as well as anti-biofouling properties [2]. The endogenously occurring glycoprotein is characterized by its superior biocompatibility and the ability to provide hydration properties in different body tissues such as nose and gastrointestinal tract. Moreover, mucin molecules show excellent tribological performance and thus, decrease friction between tissue surfaces of the body [3]. Owing to the complexity and high molecular weight of the biomacromolecule mucin, it is difficult to produce those glycoproteins synthetically or to obtain them recombinantly. To date, its purification requires the isolation of mucin from natural animal sources [4]. This method, in turn, may create a health problem associated with its use as a medical product, particularly since such biomaterials could

---

\* This section follows in part the publication Lutz *et al.*, *Materials Today Bio* (2022)

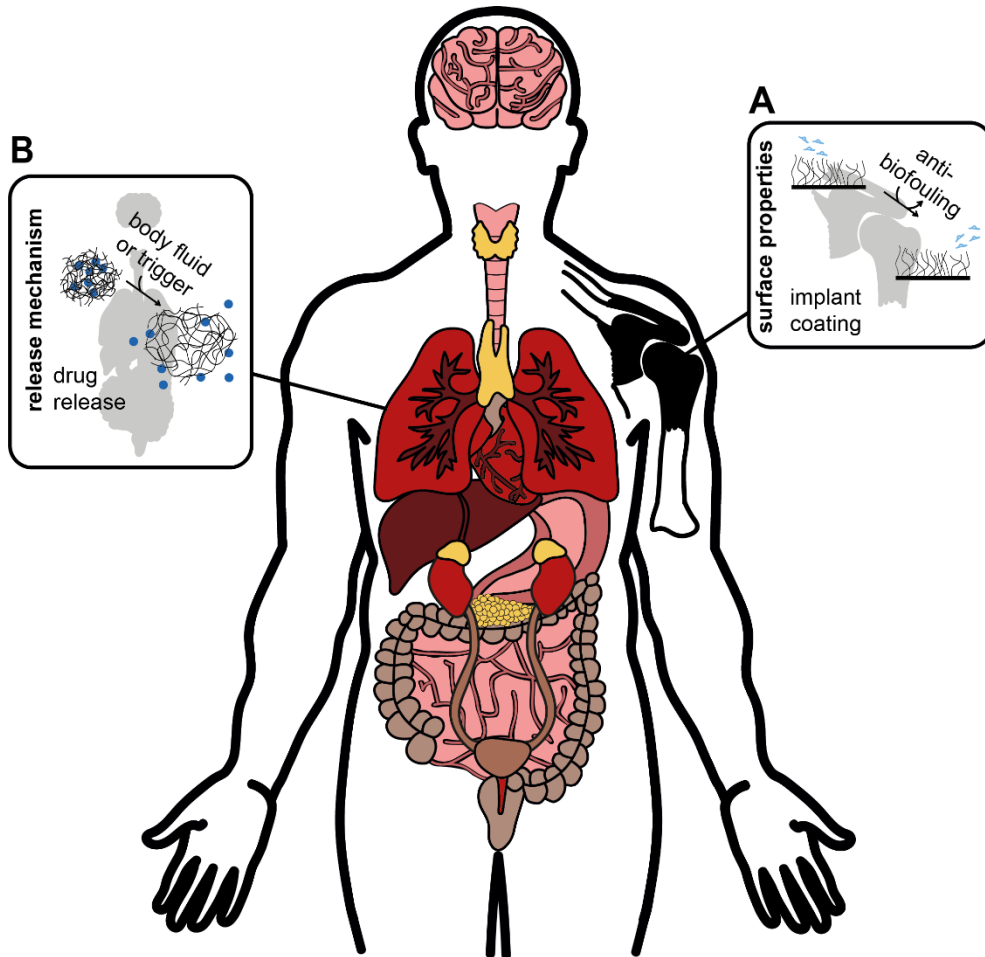
conceivably be contaminated and therefore cause allergic reactions or infections in the human body [5]. Whereas many nature-based macromolecules are unable to resist a crude sterilization process and thus lose their functionality [6, 7], mucin is highly resistant and the accessibility of the mucin-bound groups is preserved [8]. However, there are other challenges that mucin needs to overcome on the way to its application as a medical product. *In vivo*, unique challenges during the application occur which may cause mucin-based systems to degrade prematurely, before fulfilling their function, or complicate their proper, intended application. Factors such as shear force, fluid flow, altered pH/temperature conditions, and enzymatic degradation [9] can result in new complications such as – in the worst case – poor integrity of mucin-based materials in the body or complete loss of functionality.

For this reason, synthetic or semi-synthetic based materials, in particular, are currently mainly on the market. Of course, those alternatives can be explicitly adapted and produced specifically to the individual application and the desired body area [10]. However, one thing that remains uncontrolled with this type of (semi-)synthetic option is an associated biological response. Since the material is exogenous for the human body, it may induce encapsulation of the material (fibrous capsule formation), which, in turn, may result in chronic inflammatory reactions [11]. Possibly, further surgery is required to remove the material [12] with excess formed tissue and the administration of medication to control the infection [13].

Scientists continue to work at full speed to find new, creative solutions for exploiting the existing challenges in the body and turning these challenges into advantages. For instance, the mucin-based systems may be designed to be triggered selectively by specific endogenous mechanisms that cause changes in the bio-hybrid material, *e.g.*, the controlled detachment of the material from the tissue surface following an external stimulus. Such smart mucin-based materials could, for example, serve next-generation medical applications targeting complicated physiological scenarios and they might be obtainable by simply modifying some functional groups, adding more specific groups, or inducing controlled structural alterations in the glycoprotein.

Such modifications of mucins suitable for various medical applications are addressed in this thesis: Two mucin-based systems potentially applicable to the human body in the future are discussed in more detail. Firstly, mucins may serve as a coating on medical devices (**Fig. 1A**) fulfilling some tasks, which they otherwise also perform in the body: In particular, this includes establishing the anti-biofouling properties and thus ensuring the optimal integrity of the implant. Moreover, mucins can act as stable drug carrier particles to transport different molecules independently of charge, hydrophobicity/hydrophilicity, and those particles are stable in various simulated body fluids surrounding them (**Fig. 1B**). In this context, the various functional groups of mucins play an important role, both in the formation of the particles and the transport of

cargo molecules. These examples offer an exciting insight into the modification and application of mucin-based systems for medical applications. Moreover, this thesis focuses on molecules of plant and animal origin possessing mucilaginous, sticky properties and the effect of their chemical composition on adhesion and cohesion. Those or other biomolecules could be (semi-)synthetically engineered or recombinantly produced and modified, and could offer similar potential for medical applications as mucin molecules.

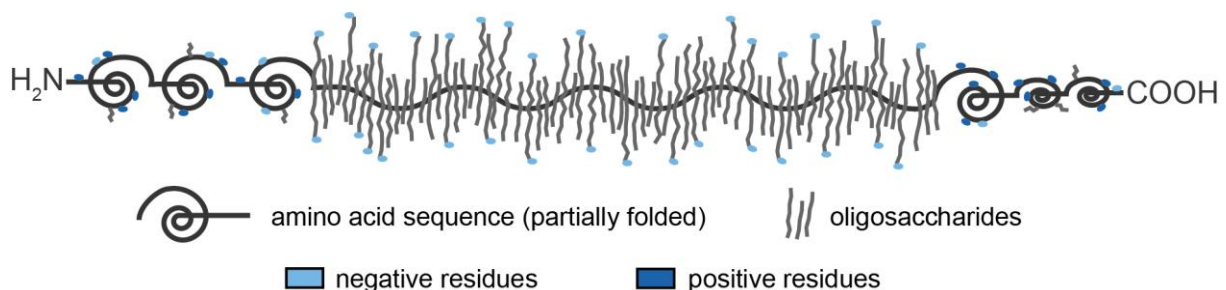


**Figure 1: Illustration of the versatility of mucin in the human body as a biomedical application.** Mucin offers application potential as a coating for implant materials (A), as well as a drug carrier material (B).

## 2. Materials and Methods

### 2.1 Mucin macromolecules\*

The differences between terrestrial mammals (e.g., pigs) and human mucin are comparably low. However, the latter show more considerable structural heterogeneity, and it is not easy to artificially produce mucins from biotechnological sources. The polysaccharide content in mucins varies between individuals and also within the same person. The long glycan chains in the core domain (up to ~80 % of the molecular weight) of the 3 MDa mucin consist of mannose, fucose, N-acetyl-galactosamine, N-acetyl-glucosamine, galactose, anionic sialic acid and glycans-carrying sulfate groups, for example (**Fig. 2**). Typically, the carbohydrates are linked *via* O-glycosylation of highly conserved serines and threonines in the core domain of the protein sequence, thus conferring a negative net charge and a hydrophilic character to the molecule in this domain. Different from the protein core, the termini are almost glycan-free, hydrophobic, contain positively and negatively charged amino acid side chains, and are partially folded: three von Willebrand factor-like D domains are located in the N-terminus and one in the C-terminus, and two von Willebrand factor-like C domains in the C-terminus. Those folded domains facilitate here the supramolecular assembly of more mucin molecules [14]. Repulsive (steric) forces originating from the carbohydrates are absent. Moreover, the content of cysteines in both termini is very high, which allows for the oligomerization of mucin molecules into large networks.



**Figure 2: Schematic depiction of common structural motifs in mucin molecules.** The protein sequence is flanked by partially folded regions in the N- and C-termini, which contain both anionically and cationically charged amino acid side chains. In contrast to the termini, which hardly have glycosylation, the core domain is surrounded by many long-chain glycans, which carry predominantly negatively charged functional groups.

### 2.2 Purification of porcine gastric mucin

Meticulous purification of mucins was the first step to obtain an intact, highly functional material to investigate and modify mucins in a controlled manner. The mucin purification from pig stomachs followed a standardized protocol described in Schömig *et al.* [15] and Marczynski *et al.* [16] First, fresh pig stomachs were picked up from a slaughterhouse and processed directly

\* This section follows in part the publications Lutz *et al.*, *Langmuir* (2020) and Lutz *et al.*, *Materials Today Bio* (2022)

as follows: The individual pig stomachs were first cut in half at the median plane, briefly cleaned under running tap water, and finally the mucus was scrapped off. This crude mucus was carefully stirred at 4°C overnight. To do so, the mucus was mixed in a ratio of 1:5 with 10 mM sodium phosphate-buffered saline containing an additional 170 mM NaCl and 0.04% (w/v) NaN<sub>3</sub> (pH 7.0; Carl Roth, Karlsruhe, Germany). To separate the larger components from the mucin proteins (e.g., food or cellular debris), either two consecutive centrifugation steps were conducted (the first was performed for 30 min at 17,590 x g and the second for 1 h at 158,306 x g (Beckmann Optima L-70 equipped with the Type 45 Ti rotor; Beckman Coulter, Brea, CA, USA)) or a cascade filtering procedure (grid mesh sizes: 1 mm, 500 µm, 200 µm, and 125 µm) was applied. To remove the smaller impurities from mucin, the centrifugate was further purified in an ÄKTA purifier system (GE Healthcare, Munich, Germany). The system included a size exclusion chromatography (SEC) column (volume: ~1.6 L) filled with Sepharose 6FF resin, equilibrated with 10 mM PBS buffer, and then used to separate molecular impurities from the mucin molecules. Finally, most mucin-bound salt ions were removed by cross-flow filtration (Xampler Ultrafiltration Cartridge equipped with a filter hollow fiber cartridge, MWCO: 100 kDa; GE Healthcare) with ddH<sub>2</sub>O. After a lyophilization step (Alpha 1-2 LDplus, -54°C, 0.057 mbar; Christ, Osterode, Germany) of the concentrate, the mucin molecules were stable enough to be stored at -80°C until further use.

## 2.4 Chemical modification of mucins

### 2.4.1 Production of UV-cross-linkable mucins

Lab-purified mucins (see **2.2**) were functionalized with methacrylic anhydride (MA, 94% solution; Sigma Aldrich) according to Duffy *et al.* [17] and Olăreţ *et al.* [18], albeit with minor modifications. The mucin molecules (**Fig. 3A**) were dissolved in ddH<sub>2</sub>O at 10 mg mL<sup>-1</sup> (w/v) concentration and cooled on ice. After titration of the mucin solution to a pH value of 8.0, the MA was added (8.47x10<sup>-4</sup> mL methacrylic anhydride per mg mucin), and the pH was maintained at 8.0 for 24 h with 5 M NaOH (Carl Roth) on ice to obtain optimal conditions for the formation of methacryloyl mucins. To separate unbound MA from the reacted product, the mucin was further purified by a centrifugation step (4,300 x g for 10 min at 4°C; Eppendorf centrifuge 5430) and SEC (see **2.2**, column equilibrated with ddH<sub>2</sub>O). The collected fractions from the SEC were lyophilized again and the product was stored at -80°C (**see 2.2**).

## 2.5 Preparation of mucin-based (nano)particles

### 2.5.1 Ionically crosslinked mucin particles

The formation of ionically crosslinked mucin particles with CaCl<sub>2</sub> (Carl Roth) or MgCl<sub>2</sub> (Carl Roth) was conducted by mixing 500 µL of 38% glycerol (Ca<sup>2+</sup> particles; Carl Roth; project: crosslinking strategy modulates the mechanical properties of mucin nanoparticles and the governing cellular uptake mechanisms) or 25% glycerol (Mg<sup>2+</sup> particles) and 250 µL of a 1%

mucin solution dissolved in ddH<sub>2</sub>O. Both components together were vortexed for 1 min. Afterward, 500  $\mu$ L of 38% (crosslinking strategy modulates the mechanical properties of mucin nanoparticles and the governing cellular uptake mechanisms) glycerol containing 25 mM CaCl<sub>2</sub> (final concentration: 10 mM CaCl<sub>2</sub>) or 500  $\mu$ L of 25% glycerol containing 125 mM MgCl<sub>2</sub> (final concentration: 50 mM MgCl<sub>2</sub>) were added to the corresponding mucin-glycerol solution and vortexed (30 sec) again (**Fig. 3B**). Afterward, the glycerol was removed by a dialysis step against ddH<sub>2</sub>O (dialysis tubes from Spectrum™ Spectra/Por™ Float-A-Lyzer™, Roth, Germany MWCO: 100 kDa) at 4°C for 2 d under stirring. Then, the formed particles were used directly for measurements.

### 2.5.2 Covalently crosslinked mucin particles

To form particles from the MA-modified mucin molecules, first, a 1% methacryloyl mucin solution was prepared in ddH<sub>2</sub>O. One part of this solution was mixed with 4 parts of 100% (project: stable mucin based nanoparticle system for the co-delivery of hydrophobic and hydrophilic drugs) or 75% (project: crosslinking strategy modulates the mechanical properties of mucin nanoparticles and the governing cellular uptake mechanisms) glycerol for 1 min under vortexing. Then, the photoinitiator 2-hydroxy-4'-(2-hydroxyethoxy)-2-methylpropiophenone (Irgacure 2959; Sigma Aldrich) dissolved in 70% (v/v) ethanol (VWR, Radnor, PA, USA) at a final concentration of 200 mg mL<sup>-1</sup> was added to the condensed mucin particles (10  $\mu$ L photoinitiator per 1 mL of mucin-glycerol mixture). After vortexing for 30 sec, the particles were stabilized by forming covalent bonds between the acrylic groups using a radical reaction triggered by UV (365 nm, ~10 mW cm<sup>-2</sup>; M365L2, Thorlabs GmbH, Lübeck, Germany) exposure for 15 min. To separate the glycerol from the particles, the particles in 100% or 75% glycerol were centrifuged at 20,817 x g (Eppendorf) for 10 min (**Fig. 3C**). The glycerol was discarded, and the particles were dissolved in the appropriate amount of water, buffer or, cell culture medium. The particles prepared in 75% glycerol were dialyzed against ddH<sub>2</sub>O (dialysis tubes from Spectrum™ Spectra/Por™ Float-A-Lyzer™, Roth, Germany MWCO: 100 kDa) at 4°C for 1 d with stirring.

### 2.5.3 DNA crosslinked mucin particles

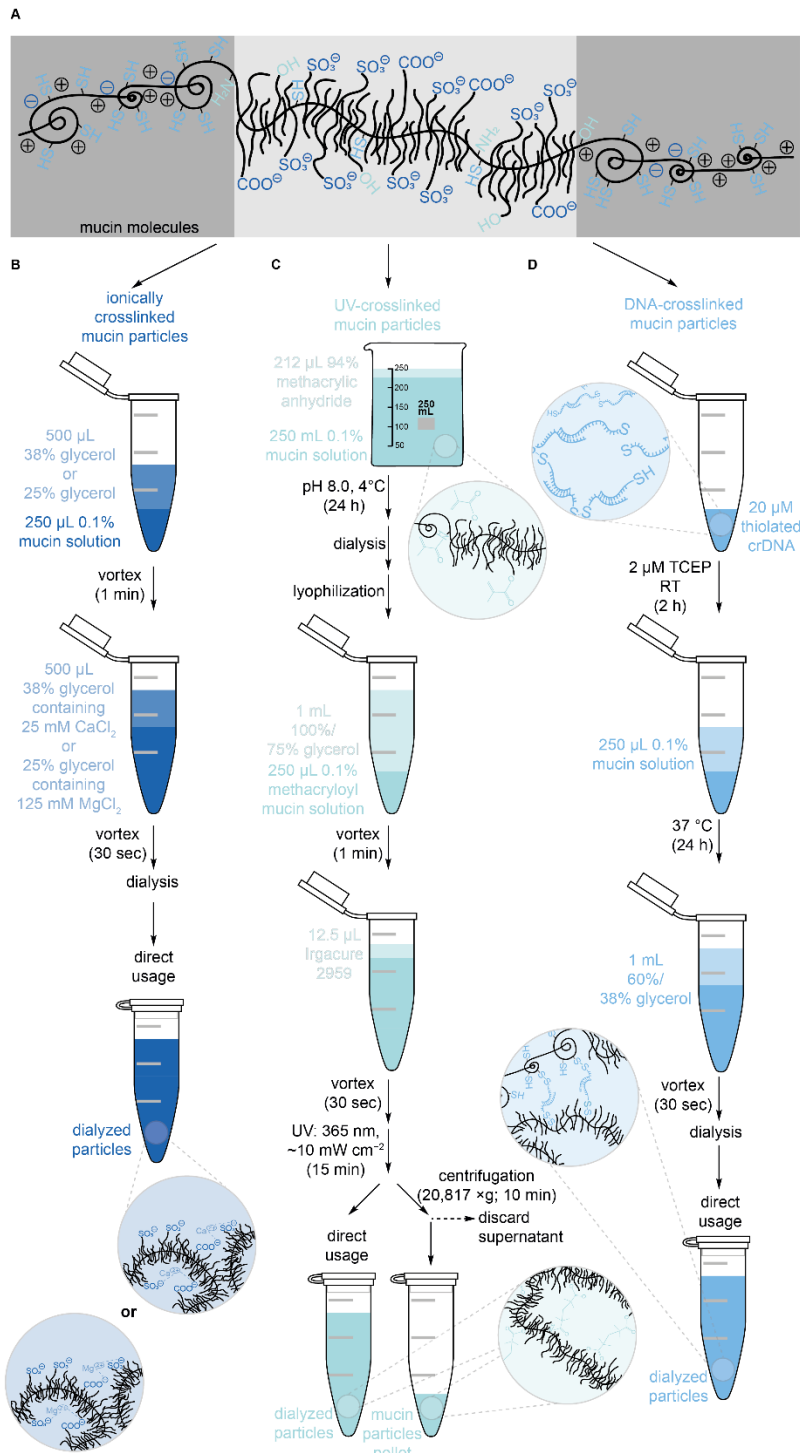
The third possibility to form mucin particles is the DNA-based crosslinking procedure (**Fig. 3D**). Similar to Kimna *et al.* [19], 20  $\mu$ M (1  $\mu$ L) of synthetic DNA sequences containing a thiol functionalization (**Tab. 1**; IDT, Munich, Germany) were mixed with 2  $\mu$ M (20  $\mu$ L of a 200  $\mu$ M stock solution) tris(2-carboxyethyl)phosphine hydrochloride (TCEP; Carl Roth) and incubated for 2 h at room temperature. Then, the thiol groups can interact with the mucins' cysteine side chains by mixing the prepared DNA and mucin solution (10 mg mL<sup>-1</sup> in ddH<sub>2</sub>O). After incubation at 37°C overnight, DNA-crosslinked mucin particles were obtained by mixing 250  $\mu$ L of the DNA-mucin solution with 1 mL of a 38% (project: crosslinking strategy modulates the

mechanical properties of mucin nanoparticles and the governing cellular uptake mechanisms) or 60% (project: DNA strands trigger the intracellular release of drugs from mucin-based nanocarriers) glycerol solution for 30 sec. Glycerol was separated from the particles by dialysis (Pur-A-Lyzer™ Maxi Dialysis Kit, MWCO = 12 kDa; Sigma Aldrich) overnight.

**Table 1: Applied DNA sequence for the formation of DNA crosslinked mucin particles.** The overview shows the details of the sequence, such as the dimerization energy, melting temperature and hybridizable base pairs.

sequence type	sequence (5'→3')	dimerization energy, $\Delta G$ (kcal/mol)	melting temperature (°C)	base pair hybridization
crosslinker DNA (crDNA)	5'-/5 ThioIMC6-D/AAA AGA AGC AAA GAC AAC CCG GGT AA 3'	-18.57	60.6	8
displacement DNA (dDNA)	5' TTA CCC GGG TTG TCT TTG CTT C 3'	-43.99	75.3	22





**Figure 3: Illustration of three different methods to obtain mucin particles.** Mucins possess multiple functional groups, e.g., anionic glycans, thiol, hydroxyl, and amine groups (A), which could be modified to obtain stable, crosslinked protein particles. One common feature that negatively charged sulfated glycans and sialic acids share is the ability to interact with cations, especially divalent cations such as calcium and magnesium, to form mucin-mucin crosslinks (B). The following system is based on a two-step method: First, the hydroxyl and amine groups of the mucins are modified with methacrylate groups; second, particles are formed by a radical-based reaction, which crosslinks the methylene groups (C). The highly conserved cysteines in the mucin molecule are used to modify them with DNA strands. Partially palindromic sequence sections of the DNA hybridize and can thus cross-link the mucin particles (D).

## 2.6 Enzymatic modification of mucins

### 2.6.1 Enzymatic treatment of mucins

Treating mucins with enzymes allows for the removal of the DNA contained in lab-purified mucins or for the cleavage of specific structural motifs, such as the negatively charged sulfate groups on the glycans in the core domain, for example. Such controlled alterations make it possible to study changes in the interaction properties of mucins with other molecules. In addition, trypsin (cleaves after basic amino acids, e.g., lysines and arginines [20]) or pepsin (cleaves after aromatic amino acids, e.g., phenylalanine [21]), as found in the intestine or stomach, are specific enzymes for the degradation of proteins. By employing them, the enzymatic degradation of mucins was assessed to evaluate the suitability of mucin nanoparticles as a carrier material for drugs.

#### 2.6.1.1 DNase treatment of mucins

To remove the mucin-bound DNA, the lyophilized mucin molecules were initially disinfected in a UV irradiation chamber (254 nm, 5 x 8 W; BLX-254, Vilber Lourmat GmbH, Eberhardzell, Germany) on ice for 1 h. Then, the mucin was dissolved in sterile 50 mM Tris-HCl buffer (pH 7.5; AppliChem, Darmstadt, Germany) supplemented with 10 mM MgCl<sub>2</sub> (Carl Roth) at a final concentration of 1 mg mL<sup>-1</sup>. Afterward, 1 mL of the 0.1% (w/v) mucin solution was mixed with 50 µL bovine pancreas deoxyribonuclease I solution (0.1% (w/v) dissolved in the aforementioned TRIS buffer; AppliChem) and incubated at 37°C overnight under continuous shaking (250 rpm; Heidolph Instruments GmbH & Co. KG, Schwabach, Germany). Further steps include, as already mentioned in the section on lab-purified mucin (see 2.2), SEC, cross-flow filtration, lyophilization, and storage at -80°C.

#### 2.6.1.2 Enzymatic treatment of mucins with sulfatase

The DNA-treated mucin was further treated with sulfatase as follows. After UV treatment (see 2.6.1.1) for 1 h on ice, the mucin molecules were dissolved in sterile 200 mM sodium acetate buffer (pH 5.0; Carl Roth) at a final concentration of 1 mg mL<sup>-1</sup>. Afterward, 1 mL of the 0.1% (w/v) mucin solution was added to 1 U of lyophilized sulfatase powder (*Helix pomatia* type H-1; Sigma Aldrich). The mixture was incubated overnight at 37°C under constant shaking (Heidolph 1000, Heidolph) at 250 rpm. Subsequently, the sulfatase-treated mucin was purified as outlined above to separate the enzyme and the cleaved groups from the mucin molecules and to render it fit for storage.

As stated in the manufacturer's manual, the accessible sulfate groups were detected using the QuantiChrom™ Sulfate Assay kit (BioAssay Systems, Hayward, CA, USA).

### 2.6.1.3 Trypsin and pepsin treatment of mucin particles

Mucin particles were enzymatically challenged by trypsin and pepsin to simulate physical conditions in the intestine and stomach. For this purpose, particles were resuspended either in 10 mM sodium phosphate buffer supplemented with 170 mM NaCl (pH 8.0; Carl Roth) and trypsin (Sigma Aldrich) in a ratio of 1:20 (mucin: trypsin) or with 10 mM HCl containing 1 mg mL<sup>-1</sup> pepsin (pH 3.0; Sigma Aldrich).

## 2.7 Detection of molecules by fluorescence labeling or polymerization

### 2.7.1 Coupling of mucin molecules with an ATTO dye

Unmodified, DNase and DNase/sulfatase-treated mucin variants were labeled with the carboxy-modified fluorescent dye ATTO488 (ATTO-TEC, Siegen, Germany). For this purpose, 5 mM 1-ethyl-3(3-dimethyl-aminopropyl)-carbodiimide (Carl Roth) and 10 mM sulfo-N-hydroxysuccinimide (sulfo-NHS; abcr chemicals, Karlsruhe, Germany) were dissolved together with the fluorescent dye (final concentration of 1 mg mL<sup>-1</sup>) in 10 mM 2-(N-morpholino)-ethanesulfonic acid buffer (pH 5.0, Carl Roth) and incubated for 3 h at room temperature while shaking (Heidolph 1000, Heidolph) at 250 rpm. Then, 0.2% (w/v) modified and unmodified mucin solutions were prepared in Dulbecco's phosphate-buffered saline (D-PBS; Lonza, Verviers, Belgium), and each was mixed with 100 µL of the activated, carboxy-modified ATTO488 molecule solution. After 3 h incubation time at room temperature, the mucins were coupled to the fluorescent dye *via* amine groups. The unbound ATTO488 molecules were separated by dialysis (Spectrum™ Spectra/Por®7 Pre-treated RC Tubing, Roth, Germany MWCO: 50 kDa) against ddH<sub>2</sub>O; the labeled mucins were lyophilized and stored at -80°C.

To obtain fluorescent mucins for particle preparation, (methacrylated) mucin was linked to fluorescein (Sigma Aldrich) *via* EDC/sulfo-NHS coupling. The reaction was performed as described above. However, 30 mg of fluorescein was used per 300 mg of mucin. Unbound fluorescent dye was separated by dialysis against ddH<sub>2</sub>O for 5 days.

### 2.7.2 Mucin labeling with fluorescein *o*-acrylate

First, mucin-MA and mucin molecules were mixed with fluorescein *o*-acrylate in a 1:1 ratio and dissolved in water (final concentrations: 1 mg mL<sup>-1</sup>). After adding the photoinitiator (10 µL of a 200 mg mL<sup>-1</sup> solution per mL mucin solution) and UV irradiation, the modified mucins interact with the dye *via* acrylate groups. The unbound dye was separated by dialysis (Spectrum™ Spectra/Por®7 Pre-treated RC Tubing, Roth, Germany MWCO: 50 kDa) against ddH<sub>2</sub>O for 5 d under constant stirring. After lyophilization, the fluorescein bound to the mucin molecules was measured with a scanning multi-well spectrophotometer (Ex/Em = 485/538 nm; Fluoroskan Ascent L, Thermo Fisher Scientific, Waltham, MA, USA). For this purpose, a 0.1% (w/v) solution of the fluorescein-labeled mucin was prepared, and a standard curve of fluorescein *o*-acrylate was obtained to calculate the amount of mucin-bound fluorescent dye.

Similarly, fluorescein mucin particles were prepared with 1 mg mL<sup>-1</sup> fluorescein *o*-acrylate per 10 mg mL<sup>-1</sup> mucin solution. The further steps of particle formation were performed as described in 2.5.2.

## 2.8 Mucin binding with molecules, ions, and oxidation agents

### 2.8.1 Detectable binding partners

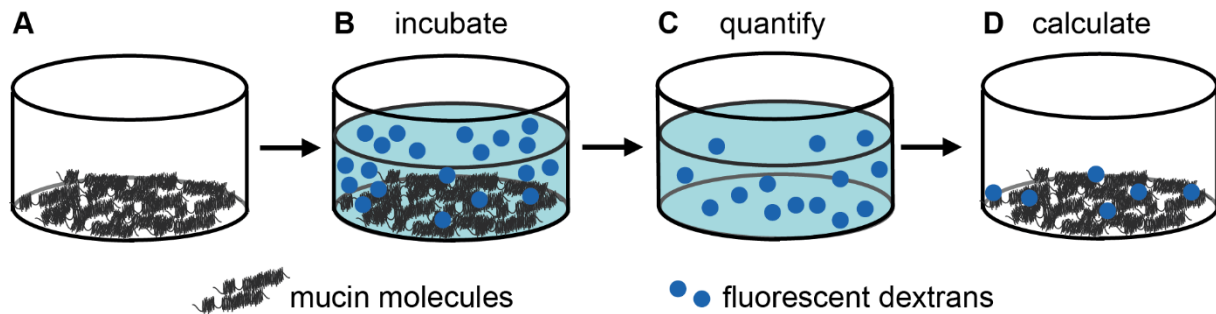
#### 2.8.1.1 Dextran and lectins

The polysaccharide dextran comprises glucose monomers covalently linked *via*  $\alpha$ -1,6 (and, less frequently, *via*  $\alpha$ -1,3 glycosidic bonds). The six-membered sugar rings are the primary energy source for the body and are stored in the human liver as glycogen (branched variant). Dextran is known for its high biocompatibility and ability to resist enzymatic degradation [22]. They are commercially available in different molecular weights (e.g., 4 kDa and 150 kDa) and with various modifications (e.g., fluorescein isothiocyanate (FITC) labeling and/or as electrostatically neutral, cationic (diethylaminoethyl (DEAE) variant) or anionic (carboxymethyl (CM) variant)), and different ones were acquired by Sigma Aldrich and applied for binding studies with mucin variants.

Lectins are small proteins produced by animals [23], plants [24] or microorganisms [25] and serve to initiate biochemical processes. Wheat germ agglutinin (WGA) is a specific lectin with a molecular weight of 33.7 kDa in the dimeric state [26]. Unique binding sites within the molecule enable specific binding to sialic acid [27]; thus, WGA serves as a probe for detecting these accessible carbohydrate groups in glycoproteins (e.g., in mucin molecules). Similarly to the dextran molecules, fluorescently modified WGA (e.g., FITC-conjugated WGA) can also be obtained from the manufacturer (Sigma Aldrich). Thus, determining interactions of this lectin with mucin molecules is possible in binding studies using fluorescence detection methods.

The binding interaction of dextran or lectins to mucin molecules was investigated by a depletion assay (**Fig. 4**). First, a 0.1% (w/v) mucin solution was prepared in 20 mM 4-(2-hydroxyethyl)-1-piperazineethanesulfonic acid (HEPES) buffer (pH 7.0;). Five wells of a 96-well microtiter plate were incubated with 200  $\mu$ L each of the mucin solution at 4°C overnight. After washing the wells with HEPES buffer, 200  $\mu$ L of dextran (4 kDa: 0.02% (w/v), 150 kDa: 0.00125% (w/v)) or WGA (10  $\mu$ g mL<sup>-1</sup>) dissolved in HEPES buffer was added and incubated at room temperature for 1 h in the dark. Then, 100  $\mu$ L of the unbound interaction molecules were transferred into a fresh 96-well microtiter plate, and the fluorescence signal was measured (Ex/Em = 485/538; Fluoroskan Ascent). Using the corresponding standard curve of the test molecule, the concentration of mucin-bound dextran and lectin was calculated from the fluorescence signal of unbound test molecules.

For studies using reduced mucins, 10 mM tris(2-carboxyethyl)phosphine (TCEP) was added to the HEPES buffer.



**Figure 4: Schematic representation of the depletion assay.** In the first step, the mucins adsorb to non-polar surfaces *via* their hydrophobic motifs interact with non-polar surfaces (A). Then, the glycoproteins interact with the added fluorescent dextran molecules (B), and after an incubation time that depends on the experimental settings, the supernatant is separated and characterized (C). From the obtained values, the mucin-bound dextrans are calculable (D).

#### 2.8.1.2 Antibodies

Y-shaped antibodies or immunoglobulins (Ig) represent the majority of proteins involved in the immune system. These molecules are composed of two heavy and light chains each with variable and constant domains. The latter differ in number (three to four), depending on which naturally occurring antibody is present (IgG, IgA, IgM, IgE, IgD) [28]. Commercially available antibodies such as the anti-MUC5AC antibody are suitable for detecting biomacromolecules (*e.g.*, mucins) in immunochemistry. The anti-MUC5AC antibodies are specific binding partners and tag a short (91 amino acids [29]) sequence in the C-termini of mucin molecules. To increase the specificity of antibodies in experiments (*i.e.*, to minimize background binding), indirect methods are often applied by using secondary antibodies, which bind to the first antibody. If this secondary antibody is additionally conjugated to an enzyme (*e.g.*, horseradish peroxidase (HRP)) that cleaves an added chromogen substrate, a photometrically detectable dye is generated, which then is used for quantification [30].

Here, the specific binding of the anti-MUC5AC antibody to mucin molecules was verified by an indirect enzyme-linked immunosorbent assay (ELISA). For this purpose, five wells of a 96-well plate were incubated with 200  $\mu$ L each of a 0.01% (w/v) mucin solution in PBS for 2 h at room temperature. Unbound mucins were removed by washing with PBS. Then, the wells were blocked (blocking buffer: 0.1% Tween 20 (v/v), Carl Roth, pH 7.4, supplemented with 5% (w/v) milk powder) at 4°C overnight to prevent non-specific binding of the primary antibodies. After a further washing step, the primary antibody (ABIN966608, antibodies-online GmbH, Aachen, Germany; 1:400 dissolved in blocking buffer) was added and incubated with the mucin at room temperature for 1 h, washed again, and incubated with the secondary antibody (ABIN237501,

antibodies-online GmbH; 1:5000 dissolved in blocking buffer) at room temperature for 2 h. After a final washing step with PBS, 100  $\mu$ L substrate (50 parts QuantaRed Enhancer Solution, 50 parts QuantaRed Stable Peroxide, and one part QuantaRed ADHP Concentrate; QuantaRed Working solution; QuantaRed Enhanced Chemifluorescent HRP Substrate Kit, Thermo Fisher Scientific, Waltham, MA, USA) was added per well. The substrate was converted by HRP conjugated to the secondary antibody, and after 30 min incubation at room temperature, the reaction was stopped by adding 20  $\mu$ L QuantaRed Stop Solution per well. The color change of the sample solutions was detected photometrically at a wavelength of 570 nm (SpectraMax ABS Plus, Molecular Devices, San Jose, CA, USA).

### 2.8.2 Drug loading and degradation of particles

To incorporate antibiotics, dyes, antioxidants, or other drugs into covalently/ionically crosslinked mucin particles, the initially prepared 1% mucin solution was directly mixed with the appropriate drug concentration (see **Tab. 2**). Then, the particles were prepared as described in **2.5**.

**Table 2: Detailed overview of the cargo molecules used for mucin particles and their properties.** The table lists the specifications of the drug molecules, such as the particle type used for those drugs, the name, manufacturer, molecular weight, net charge at physiological pH, pK<sub>a</sub> value, and partition coefficient of the drug molecule. N.A. = not applicable. N.D. = not determined/information not available.

Particle type	Molecule	Manufacturer	Molecular weight (g mol <sup>-1</sup> )	Net charge @ pH = 7.4	pK <sub>a</sub>	Partition coefficient (logP)
UV	$\beta$ -carotene	Sigma Aldrich (C9750)	537	neutral	N.A.	15
UV	hesperidin	Sigma Aldrich (H5254)	611	neutral	pK = 7.15	-0.26
UV	ascorbic acid	Carl Roth (3525.1)	176	anionic	pK <sub>1</sub> = 4.1 pK <sub>2</sub> = 11.6	-1.64
UV	ATTO 495 carboxy	ATTO-TEC (AD 495-21)	452	cationic	N.D.	-0.81
UV	ATTO 594 carboxy	ATTO-TEC (AD 594-21)	1137	anionic	N.D.	N.D.

**Table A2: Detailed overview of the cargo molecules used for mucin particles and their properties.** The table lists the specifications of the drug molecules, such as the particle type used for those drugs, the name, manufacturer, molecular weight, net charge at physiological pH, pK<sub>a</sub> value, and partition coefficient of the drug molecule. N.A. = not applicable. N.D. = not determined/information not available (continued).

Particle type	Molecule	Manufacturer	Molecular weight (g mol <sup>-1</sup> )	Net charge @ pH = 7.4	pK <sub>a</sub>	Partition coefficient (logP)
UV	fluorescein	Sigma Aldrich (F6377)	376	anionic	pK <sub>1</sub> = 3.14 pK <sub>2</sub> = 4.04 pK <sub>3</sub> = 6.28	0.61
UV	ATTO 532 amine	ATTO-TEC (AD 532-91)	916	cationic	N.D.	-6.48

For release studies, 100 µL of cargo-loaded mucin particles were filled into a transwell insert (suitable for 24-well microtiter plates; cellQART PET translucent, MWCO: 0.4 µm; Sabeu GmbH, Northeim, Germany; **Fig. 5**). The 500 µL acceptor buffer in the reservoir was either chosen as simulated gastric fluid (SGF; 80 µM sodium taurocholate (Carl Roth), 20 µM lecithin (Carl Roth), and 34.2 mM NaCl (Carl Roth); pH 1.6) or simulated intestinal fluid (SIF; 3 mM sodium taurocholate (Carl Roth), 0.2 mM lecithin (Carl Roth), 19.12 mM maleic acid (Carl Roth), 68.62 mM NaCl (Carl Roth), and 34.8 mM NaOH (Carl Roth); pH 6.5). Cargo released from the particles that passed by diffusion through the membrane accumulated in this acceptor buffer over time. The samples were incubated at 37°C; after different time points, 200 µL from the reservoir was replaced with fresh buffer. By photometrically measuring the collected supernatant and the respective standard curves, the cumulative release of the cargo was calculated with the following formula (**Eq. 1**):

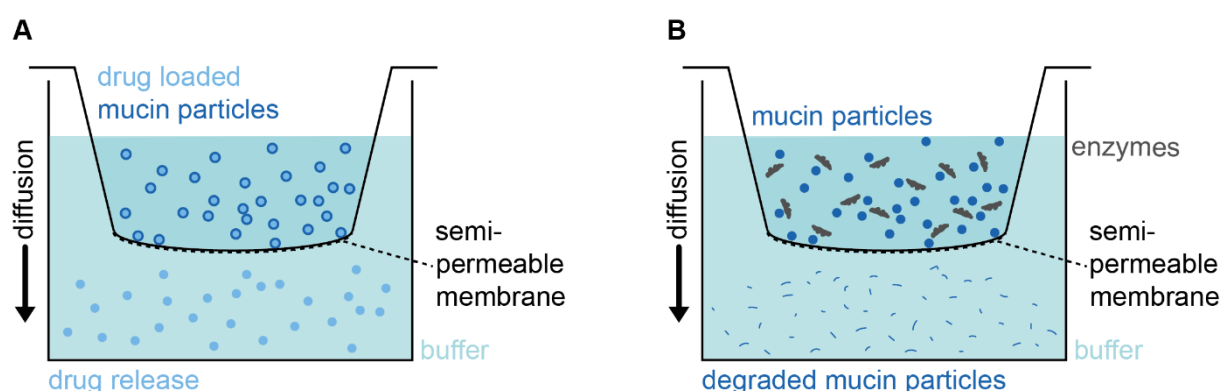
$$\text{Cumulative Release (\%)} = \frac{\text{mass of released cargo molecules}}{\text{mass of cargo molecules in the carriers}} \times 100 \quad (\text{Equation 1})$$

The following equations (**Eq. 2** and **Eq. 3**) were applied for the calculation of the encapsulation efficiency (EE) and drug loading capacity (DL) of the mucin carriers:

$$EE (\%) = \frac{\text{mass of cargo molecules in the particles}}{\text{mass of cargo molecules in the feed solution}} \times 100 \quad (\text{Equation 2})$$

$$DL = \frac{\text{mass of cargo molecules in the particles}}{\text{mass of mucin particles}} \quad (\text{Equation 3})$$

This permeation assay was not only used for the measurement of cumulative drug release, but also to detect the enzymatic degradation of the mucin particles (**Fig. 5**). For this purpose, fluorescent mucin particles (preparation, as described in **2.7.2** for fluorescein *o*-acrylate labeled mucin particles) were dissolved in 10 mM sodium phosphate buffer supplemented with 170 mM NaCl (Carl Roth; pH 8.0) and trypsin (Sigma Aldrich) in a mucin to trypsin ratio of 1:20 or in 10 mM HCl (Carl Roth; pH 3.0) containing 1 mg mL<sup>-1</sup> pepsin (Sigma Aldrich). As in the release studies, 100  $\mu$ L of each prepared sample was added to the transwell inserts and incubated at 37°C. After different time points, the buffer in the reservoir (200  $\mu$ L) was exchanged, and the increase in fluorescence (Ex/Em = 485/538; Fluoroskan Ascent) in the collected buffer samples was measured to determine the cumulative degradation of the mucin particles over time.



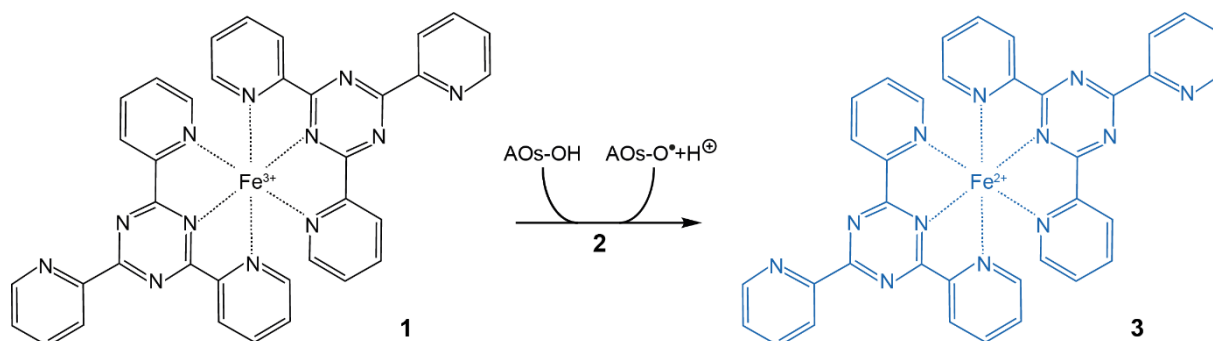
**Figure 5: Illustration of the versatility of transwell inserts.** In the first example, the inserts are used to test for the release of drugs from the particles. These smaller drug molecules can diffuse into the reservoir and thus be determined with further detection methods (**A**). In the second example, the inserts are applied to detect the enzymatic degradation of particles. The degradation products can diffuse through the semi-permeable membrane into the reservoir, whereas the larger enzymes and particle parts remain in the insert (**B**).

### 2.8.3 Ferric reducing antioxidant power (FRAP) assay

Antioxidants released from mucin particles (see **2.8.2**), such as  $\beta$ -carotene and hesperidin, were detected by a FRAP assay according to Müller *et al.* [31], but with minor modifications. The FRAP reagent consisted of 10 parts 300 mM acetate buffer (Carl Roth; pH 3.6), one part 20 mM FeCl<sub>3</sub> (Carl Roth), and one part 10 mM 2,4,6-tripyridyl-s-triazine (dissolved in HCl; Sigma Aldrich). Reservoir buffer from the transwell setup was mixed with the FRAP reagent in a 1:6 ratio (v/v). Afterward, the samples were shaken at room temperature for 6 min and centrifuged (106  $\times$  g for 30 sec). The released antioxidants then acted in a redox reaction: At acidic pH values, the initially formed ferric-tripyridyltriazine complex [Fe<sup>III</sup>(TPTZ)]<sup>3+</sup> was



reduced into the ferrous-tripyridyltriazine complex  $[\text{Fe}^{\text{II}}(\text{TPTZ})]^{2+}$  (whereas the antioxidant itself was oxidized). This resulted in a photometrically measurable color change from yellow to blue (**Fig. 6**), which was detected at an excitation wavelength of 595 nm (SpectraMax ABS Plus). The concentration of released  $\beta$ -carotene and hesperidin was determined by measuring a standard curve of both antioxidants using different antioxidant concentrations.



**Figure 6: Reduction of the ferric-tripyridyltriazine complex to the ferrous-tripyridyltriazine complex by antioxidants.** In this redox reaction, the yellow  $[\text{Fe}^{\text{III}}(\text{TPTZ})]^{3+}$  complex (1) formed interacts with antioxidants (2) to the blue  $[\text{Fe}^{\text{II}}(\text{TPTZ})]^{2+}$  complex (3).

#### 2.8.4 (Ionic) crosslinkers

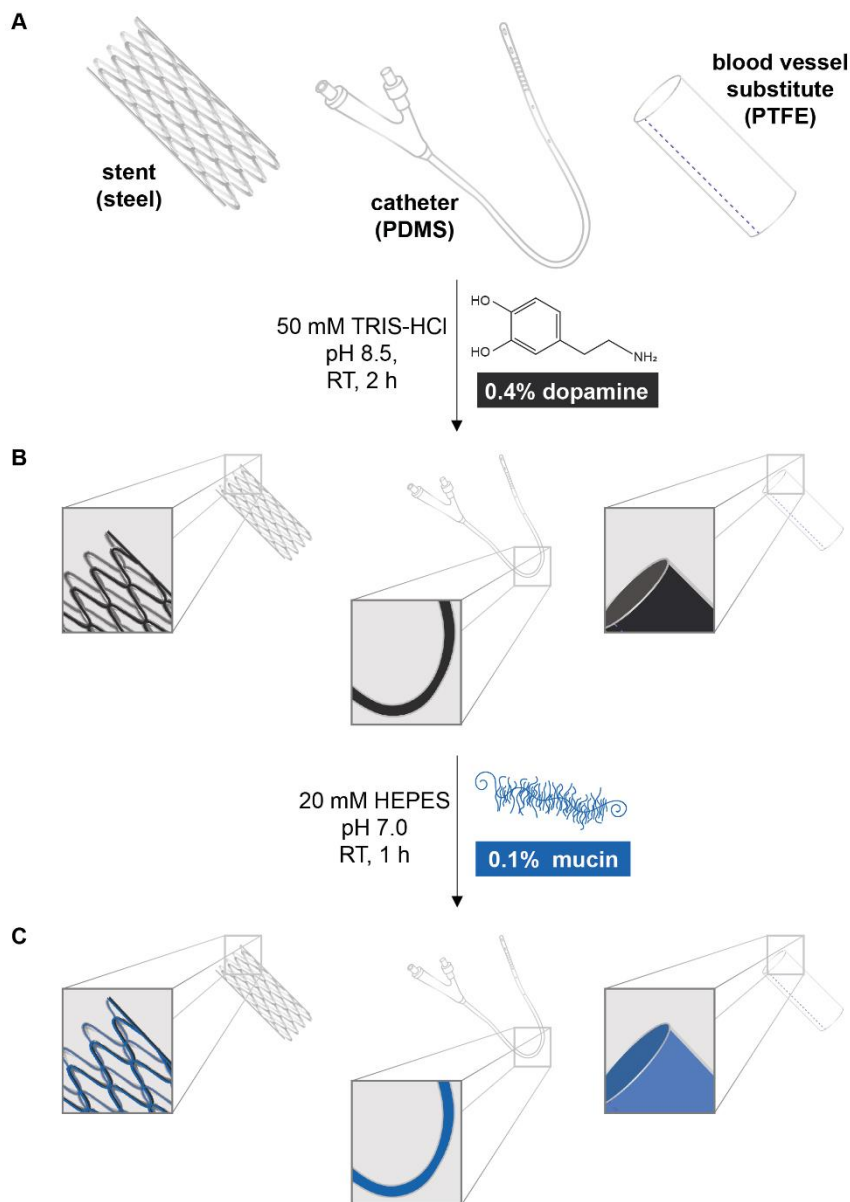
Calcium and magnesium can be applied to interact with biomaterials to obtain a mechanically stiffer composite and to design suitable materials for medical applications. Calcium is known for its binding affinity to alginates: the formation of gel-like structures is enabled by the ionic crosslinking of alginate polymers in the coordination of an egg-box geometry [32, 33]. The mechanical properties like the compressive strength, of the formed biomaterial is improved and allow for its application as scaffolds, films, and sponges for tissue engineering approaches [34] or membranes for wound dressing [35]. Similar to the ionic crosslinking abilities of calcium, the gel-forming effect of magnesium on polyhedral oligomeric silsesquioxane is described in the literature. The coordination of thiol groups of polyhedral oligomeric silsesquioxane by  $\text{Mg}^{2+}$  leads to the formation of a hydrogel-based scaffold which helps to promote bone cell growth and proliferation.

These divalent cations can also form inter- and intramolecular interactions with mucins [36, 37] leading to the formation of stable particles that can carry and transport drugs.

#### 2.8.5 Dopamine-based coating process

Dopamine-mediated coatings of mucins were generated on different substrates. Commercial PTFE-based blood vessel substitutes (Steris, OH, USA), steel-based stents (AS-21XXL, Andramed, Reutlingen, Germany), and PDMS-based catheters (U400, Medi1one Medical, Fellbech, Germany) were dip coated according to the following technique (**Fig. 7**):

In brief, before the adsorption of dopamine and mucin was initiated, the carrier material was cleaned with 80% ethanol (Carl Roth, Karlsruhe, Germany) and ultrapure water. Afterwards, the samples were incubated in a 0.4% (w/v) dopamine hydrochloride (Sigma Aldrich, St. Louis, MO, USA) solution prepared in 50 mM tris(hydroxymethyl)aminomethane buffer (Tris-HCl; pH 8.5; Carl Roth) at room temperature for 2 h. To remove unbound dopamine, a rinsing step with ultrapure water was conducted. Then, the dopamine-coated samples were inserted into a 0.1% (w/v) mucin solution, which was prepared in 20 mM 4-(2-hydroxyethyl)-1-piperazineethanesulfonic acid buffer (HEPES; pH 7.0; Carl Roth). After an incubation time of 1 h, the samples were washed again with ultrapure water.



**Figure 7: Schematic representation of the two-step dip-coating process using dopamine as a molecular adhesive.** First, the medical devices consisting of different substrates (steel, PDMS, PTFE) are incubated in a dopamine solution for 2 h (**A**). The adsorbed dopamine molecules form a sticky layer allowing for the immobilization of the second, macromolecular

layer (**B**). This second layer is generated by incubating the pre-coated substrates in a mucin solution for 1 h (**C**).

## 2.9 Biocompatibility of mucin molecules and mucin particles

### 2.9.1 Cell cultivation

HeLa cells were cultivated in Minimum Essential Medium Eagle (MEM; Sigma Aldrich) containing 10% (v/v) fetal bovine serum (FBS; Sigma Aldrich), 2 mM L-glutamine solution (Sigma Aldrich), 1% (v/v) non-essential amino acid solution (NEAA; Sigma Aldrich), and 1% penicillin/streptomycin (25 U mL<sup>-1</sup> penicillin, 25 µg mL<sup>-1</sup> streptomycin; Sigma Aldrich). In contrast, NIH 3T3 cells were incubated in Dulbecco's Eagle's high glucose Medium (DMEM, Sigma Aldrich) containing 10% FBS and 1% penicillin/streptomycin. Optimal growth conditions for both cell lines are 37°C, 5% CO<sub>2</sub>, and a humidified atmosphere. Cells were cultivated subconfluently in T75 cell culture flasks.

### 2.9.2 Water-soluble tetrazolium (WST-1) assay

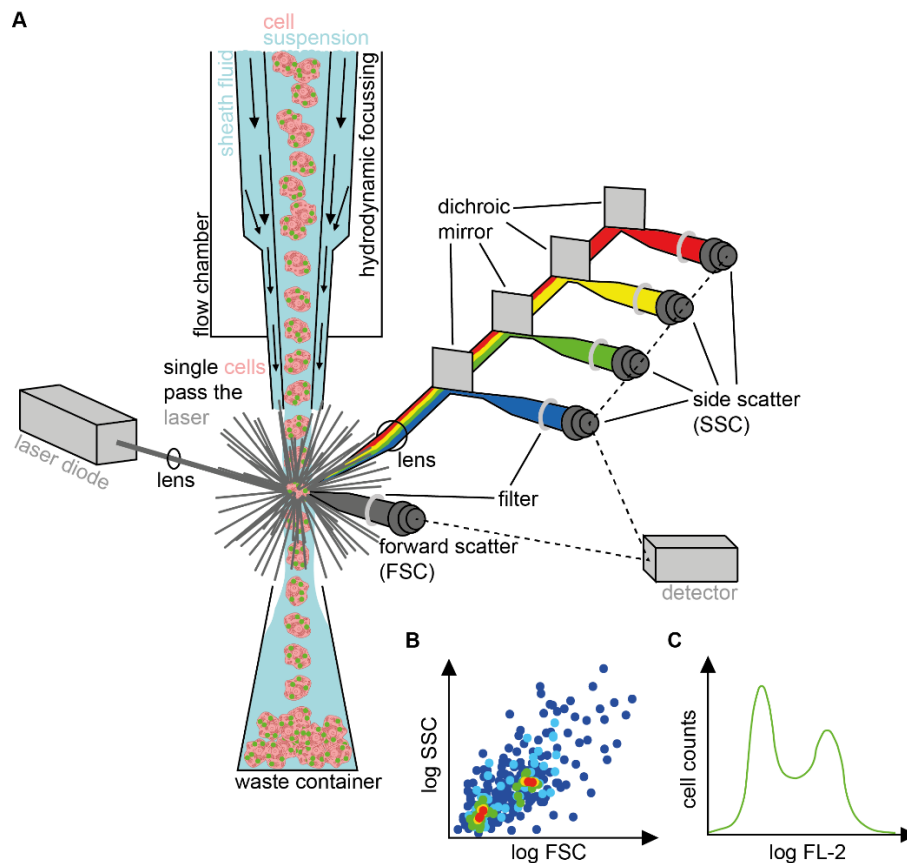
The biocompatibility of the different mucin particles was studied for five mucin particle amounts each (180000, 90000, 45000, 22500, 11250 particles/well). Cultivated cells were harvested from cell culture flasks using 0.25% (w/v) trypsin/EDTA (Sigma Aldrich) and seeded into a 96-well microtiter well plate (5,000 cells per well). After 24 h of cell growth, the cell medium of 15 wells of the microtiter plate was replaced by fresh medium (100 µL per well, negative control). In addition, each one of the 15 wells each was replaced with the medium incubated with the mucin particles (100 µL per well). Afterwards, 5 wells of each sample were always incubated for 24 h, 48 h, and 72 h. The experiments were conducted with human epithelial cells (HeLa).

After different incubation times, cell viability was assessed with a WST-1 assay. For this purpose, the medium was replaced with one containing 2% (v/v) WST-1 solution and incubated on the cells for 1 h. The absorbance of the medium was measured photometrically at an excitation wavelength of 450 nm (SpectraMax ABS Plus). The absorbance values of the cells treated with the particle-containing medium were normalized to the negative control cells. The experiment was conducted in biological triplicates.

### 2.9.3 Flow Cytometry

One common technique for the quantitative analysis of cells is flow cytometry [38] (**Fig. 8A**). Examples vary from analyzing the cell morphology/complexity of the cell architecture (by forward and sideward scattering; **Fig. 8B**), the investigation of the cell cycle stage (e.g., apoptosis), accumulation of fluorescent particles over time inside the cells (**Fig. 8C**), and attachment of antibodies to specific cell surface receptors. A flow cytometer is designed to use two flows (sheath flow; sample fluid = cell suspension) to detect the cells individually by increasing the pressure in the sample fluid (compared to lower pressure in the sheath flow).

Both flows together allow for a constant flow of cells in laser direction and reduce the amount of cell suspension flowing through the laser; this results in individually measurable cells (= hydrodynamic focusing). Afterward, a monochromatic laser (e.g., argon at a wavelength of 488 nm) encounters the cells unidirectionally (focused through a lens), whose fluorescent labels absorb the photons and emit light. Additional detection can be performed *via* forward and sideward scattering with adequate multiple photomultiplier tubes. With forward scattering, the signal of the entering laser beam is measured at 0° – the laser itself cannot pass through the cell sample and only the photons around the cell are detectable, which reflects the size and surface area of the cell. On the other hand, with sideward scattering, the light deflected/emitted by the organelles and/or fluorescent labeling is recorded *via* filters for specific wavelengths (band/long pass filters and dichroic mirrors enable the transmission of light with longer wavelengths) at an angle of 90° and shows the complexity inside the cell and/or the fluorescence signal intensity. In this process, the light signal is converted into electric signals (proportional to each other) by light (*i.e.*, photons) reaching a photocathode, passing through several diodes, striking the anode, and the output is an electrical signal. The resulting amplitudes are analyzed by a computer software (e.g., Cell Quest) and converted into plots.



**Figure 8: Schematic representation of the flow cytometry technique.** First, the cells are separated and focused on the laser beam by two streams (sheath flow and cell suspension). Forward scattering detects the cell size and surface, whereas sideward scattering addresses the organelles inside and/or fluorescent markers (A). Depending on the detection, different

graphs are created: *e.g.*, the size (log FSC; increasing from left to right) and the complexity (log SSC; increasing from bottom to top) of the cells is displayed (**B**), and the fluorescence distribution within a cell colony (**C**), respectively.

In this thesis, flow cytometer measurements were performed to investigate the cellular uptake of fluorescently labeled mucin particles (for the preparation of the particles, see **2.5** and **2.7.1**). For this purpose, HeLa cells were seeded into 12-well microtiter plates (100,000 cells per well) and, after an incubation time of 24 h, three different experiments were conducted. For all the experiments, mucin particles with a concentration of 180000 particles/well were used. For the first experiment, the cytosolic accumulation of (fluorescently labeled) mucin particles was tested over time (1 h, 4 h, 24 h; control without mucin particles). Furthermore, experiments were carried out with cells incubated at different temperatures (37°C or 4°C for 4 h) to investigate if the cellular uptake pathway for particles is driven by thermal energy. The last two tests focus on the cellular uptake over time, and the detailed cellular uptake mechanism (*e.g.*, caveolae or clathrin-mediated endocytosis, micropinocytosis) of the mucin particles. To do so, cells were incubated with specific uptake pathway blockers (*i.e.*, 7 µg mL<sup>-1</sup> chlorpromazine, Sigma Aldrich; 1 µg mL<sup>-1</sup> filipin, Sigma Aldrich; or 50 µM amiloride, Sigma Aldrich), and incubated for 1 h at 37°C. Then, the cells were washed with D-PBS and incubated with the mucin particles for 4 h.

To perform flow cytometer experiments, the cells were washed with 1 mL of D-PBS, followed by the addition of 200 µL (per well) of a 0.25% (w/v) trypsin/EDTA solution to detach them from the well bottoms. After 3 min, 1 mL of medium per well was added to stop the enzyme treatment, and the cells were centrifuged at 600 x *g* for 5 min. The medium was discarded, and the cell pellet was dissolved in 500 µL of D-PBS (to remove all medium, a second centrifugation step was conducted). Internalization of mucin particles was measured using a FACS device (BD FACS Calibur OS X, BD Biosciences, San Jose, CA, USA) equipped with an Ex/Em = 488/530 nm argon-ion laser (15 mW) to obtain the fluorescence signal of each cell population (10,000 events per sample) at medium or high detection rate. The detected signals were evaluated using the Cell Quest software (BD Biosciences).

#### 2.9.4 Fluorescence microscopy – cellular uptake of mucin particles

The internalization of different fluorescent mucin particles (Ca<sup>2+</sup>, Mg<sup>2+</sup>, UV, and DNA stabilized) was visualized by confocal laser scanning microscopy (STELLARIS 8 FALCON, Leica Microsystems, Wetzlar, Germany) equipped with an HC PL FLUOTAR 10x/0.30 objective (Leica) and an HC PL APO CS2 63x/1.40 OIL objective (Leica). For this purpose, the wells of a µ-slide 8-well ibidiTreat plate (ibidi GmbH, Gräfelfing, Germany) were seeded with HeLa cells (5,000 cells/well, suspended in 200 µL each) and incubated for 24 h. The endosomal uptake (after 1h, 4h, and 24h) was conducted, and in addition to the particles, 2 µL of endosome marker FM 4-64™ (Invitrogen T13320; stock solution: 10 µg/mL in ultrapure water) was added

per well. After each incubation, the cells were fixed with 4% (v/v) formalin dissolved in D-PBS (pH 7.3) for 30 min. Then, the fixing solution was replaced with 300 nM 4,6-diamino-2-phenylindole (DAPI (Sigma Aldrich) in D-PBS). After an incubation of 10 min, the staining solution was discarded, and 200  $\mu$ L D-PBS was added per well. The settings of the microscope were as follows: Images of cell nuclei (405 laser diode; Ex: 405 nm/Em: 420 – 600 nm), endosomes (tunable white light laser (WLL); Ex: 557 nm/Em: 565 – 680 nm), and particles (WLL; Ex: 488 nm/Em: 500 – 600 nm) were acquired at a laser intensity of 2% (10x objective) or 4% (63x objective) and a pinhole of 1 Airy unit. Image analysis was conducted using the software ImageJ (Fiji) and the Coloc2 plugin.

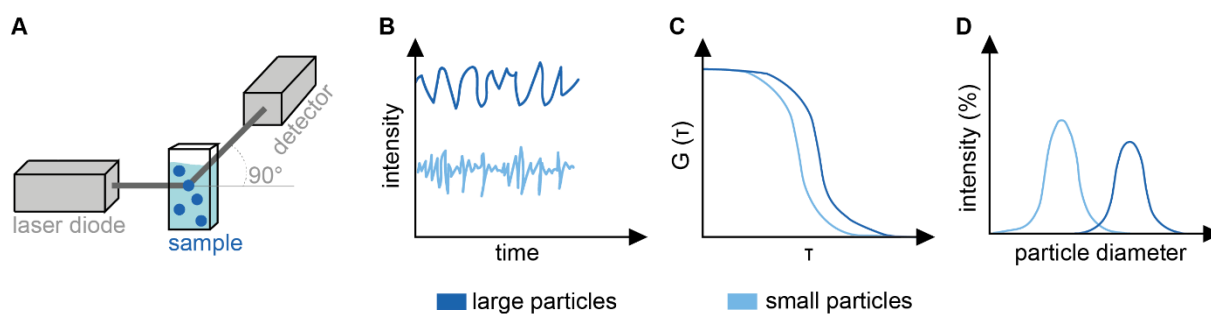
To study the transport of ATTO dyes as test cargo molecules, UV-crosslinked mucin particles (mucin concentration: 0.125 mg mL<sup>-1</sup>) were loaded with two carboxy-modified ATTO dyes (ATTO dye concentration: 5x10<sup>-4</sup> mg mL<sup>-1</sup> of ATTO495 and ATTO532, respectively) and ATTO dyes without particles served as control. Cells were incubated with free/encapsulated ATTO samples and observed at different time points (1 h, 4 h, 24 h). Fixation of the cells and DAPI staining were performed as described above, although the lysozyme tracker was not applied. Images were obtained using a Leica DMI8 microscope (Leica, Wetzlar, Germany; objective: Leica, HC PL FLUOTAR, 63x/0.70 CORR PH2) equipped with a digital camera (Orca Flash 4.0 C11440- 274 22C, Hamamatsu, Japan) and further analyzed with the software Fiji ImageJ (public 275 domain, version 1.53c, June 2020) to calculate the corrected total cell fluorescence (CTCF) for each channel (**Eq. 4**). Nine cells (from  $n \geq 3$  images) each were evaluated for the CTCF calculation.

$$\text{CTCF} = \text{integrated density} - (\text{area}_{\text{cell}} \times \text{mean fluorescence of background}) \quad \text{(Equation 4)}$$

## 2.10 Techniques for the evaluation of mucin particle sizes

### 2.10.1 Dynamic light scattering (DLS) measurements [39]

Dynamic light scattering is a common technique to characterize formed particles in the nano- and micrometer sizes. During the measuring procedure, a single frequency laser passes through the particle-containing sample and the light – when it encounters particles – is scattered in all directions, although the detection of the light occurs at a specific angle (e.g., 90°; **Fig. 9A**).



**Figure 9: Illustration of the dynamic light scattering technique.** A laser encounters the particle sample and the intensity of the laser beams scattered by the sample is recorded at 90° (A). Applying a mathematical correlation combined with a cumulative algorithm provides the translational diffusion coefficient *via* a fitting curve (C). This determined value, in turn, allows for calculating the hydrodynamic diameter of the particles (D).

The measuring strategy takes advantage of the Brownian motion of the particles: Collisions of the particles with molecules in the surrounding solvent lead to an energy transfer and, thus, to a random, unidirectional movement of the particles. The energy transfer affects larger particles less since those are more inert and move at a slower speed than smaller ones. Therefore, the intensity of the scattered light has higher amplitudes for the larger particles and lower oscillation times for the smaller particles (Fig. 9B).

Some calculations are required to estimate the speed of the moving particles (translational diffusion coefficient): the measured fluctuations show the deviations from the baseline (baseline = particles staying at the same position). They are fitted into a mathematical correlation function. A cumulant algorithm – the recorded fluctuations are shifted by  $\tau_1, \tau_2, \dots, \tau_\infty$ , and the initial intensity at time  $t_0$  together (overlay) with each single delay time curve ( $\tau_x$ ) correspond to the curve fittings from  $G(\tau)$  (Fig. 9C). Afterward, the determination of the hydrodynamic diameter occurs *via* the Stokes-Einstein equation (Eq. 5), whereby other parameters such as the Boltzmann constant, the temperature, and the viscosity of the solvent are required as well (Fig. 9D).

$$D = \frac{k_B * T}{6\pi\eta R_H} \quad \text{(Equation 5)}$$

D = translational diffusion coefficient (m<sup>2</sup>/s)

k<sub>B</sub> = Boltzmann constant (m<sup>2</sup>kg/KS<sup>2</sup>)

T = temperature (K)

η = viscosity (Pa s)

R<sub>H</sub> = hydrodynamic radius (m)

For the stability and aggregation experiments, the particles were characterized with a Litesizer 500 (35 mW laser diode;  $\lambda = 658$  nm; Anton Paar, Graz, Austria) in automatic mode at  $(25.0 \pm 0.1)$  °C. Then, the particles were characterized either by their hydrodynamic diameter or by their number-weighted size distribution over time. Buffers and liquids used for the measurements: SGF (pH 1.6), SIF (pH 6.5), D-PBS containing 10% FBS, and ddH<sub>2</sub>O (storage conditions).

### 2.10.2 Electrophoretic light scattering (ELS) measurements [40]

Dispersed nano- or microparticles interact with the surrounding ions of the solvent – functional groups such as sulfate groups of the mucin particles strongly accumulate cations (=Stern layer), which in turn interact with a few individual ions as well (lower interaction) – and the electrochemical double-layer formed around the particles allows for the determination of the particle surface charge (= zeta potential; **Fig. 10A**). To measure the zeta potential, the particles move in the electric field to the anode (particles with cationic charge) or cathode (particles with anionic charge). The speed of the moving particles (=electrical mobility) is calculated by comparing the frequency of a reference laser beam with the frequency shift (=Doppler shift) of the laser beam encountering the sample (this determination of the deviation is necessary since the direct measurement without a reference frequency determination is insufficient to calculate the sign of the zeta potential; **Fig. 10B**). The Doppler shift is proportional to the speed of the particles and is used for the zeta potential calculation *via* the Henry equation (**Eq. 6**) [41].

$$U_E = \frac{2\varepsilon\xi f(\kappa a)}{3\eta} \quad \text{(Equation 6)}$$

$U_E$  = electrophoretic mobility ( $\text{m}^2/\text{V s}$ )

$\varepsilon$  = dielectric constant (F/m)

$\xi$  = zeta potential (V)

$f(\kappa a)$  = Henry's function ( $a$  = particle radius;  $\kappa^{-1}$  = Debye length for the extent of the electrochemical double-layer across the particle radius)

$\eta$  = viscosity of the solution (Pa s)

In case the hydrodynamic radius of the particles is much larger than the electrochemical double-layer formed around the particles (e.g., for mucin particles), Smoluchowki's equation (**Eq. 7**; **Fig. 10C**) is additionally considered (together with the Henry equation) to obtain a more accurate zeta potential result [42]:



$$\xi = \frac{\eta U_E}{\epsilon_r \epsilon_0} \quad \text{(Equation 7)}$$

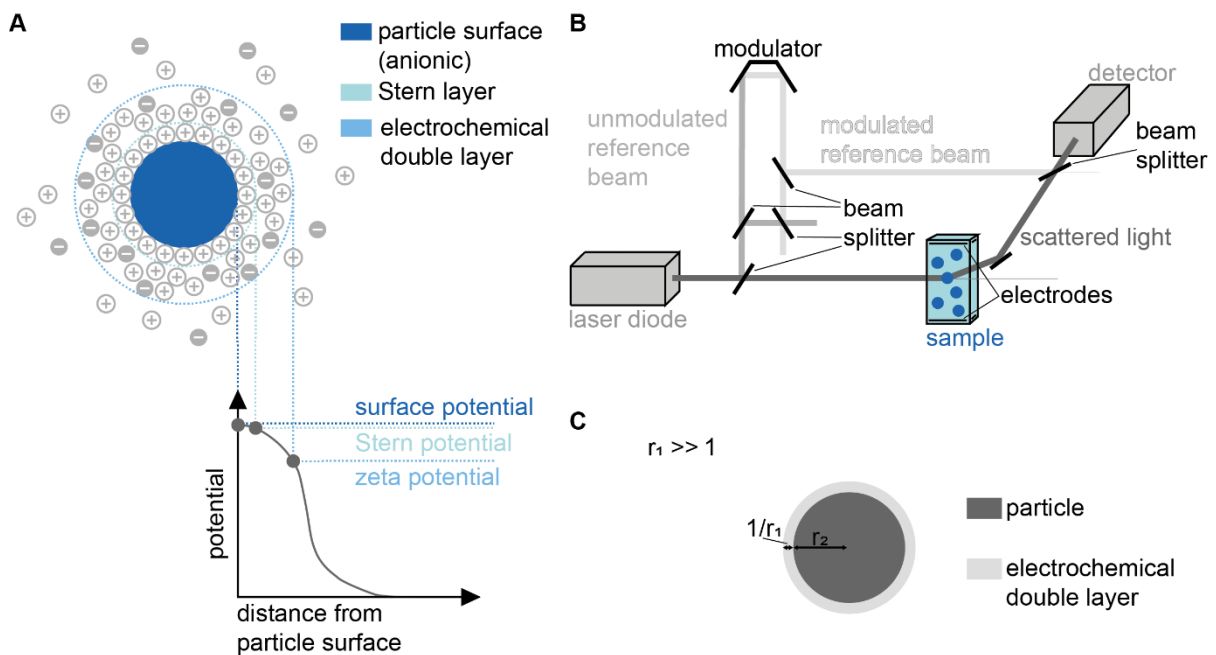
$\eta$  = viscosity of the solution (Pa s)

$U_E$  = electrophoretic mobility ( $\text{m}^2/\text{V s}$ )

$\epsilon_r$  = dielectric constant of the solvent (F/m)

$\epsilon_0$  = vacuum permittivity (F/m)

$\xi$  = zeta potential (V)



**Figure 10: Schematic representation of electrophoretic light scattering.** The anionic particle surface interacts with ions of the solvent, which form further layers such as the Stern layer and the electrochemical double layer. The resulting potentials of the particle and the individual layers are also represented (A). To determine the zeta potential, first, a laser encounters the samples to measure the frequency shift in comparison to the reference frequency (B). The zeta potential is determined (C) by including Henry's equation and, in the case of particles with a larger hydrodynamic radius relative to the electrochemical double-layer, considering Smoluchowki's function.

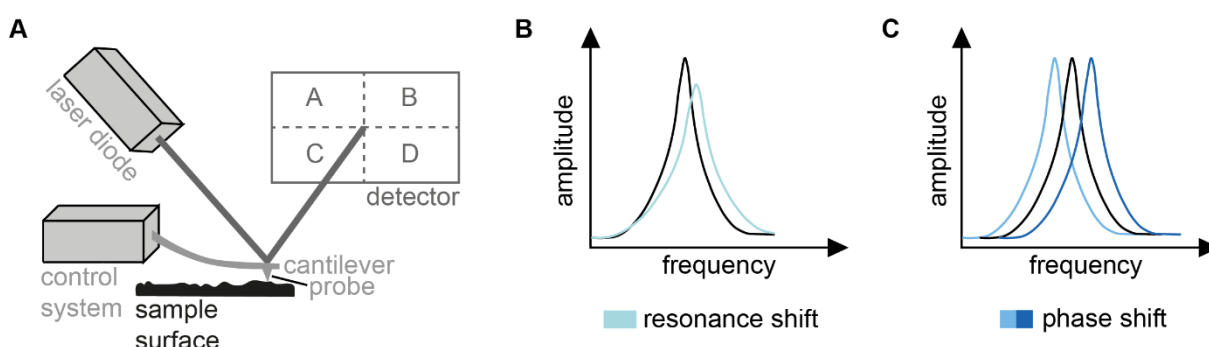
The interaction of particles with the solvent and the corresponding zeta potential provide information about the particle behavior *in-vivo* (e.g., aggregation and stability). Especially different pH values in the body (e.g., acidic in the stomach or basic in the intestine) influence the zeta potential since functional groups on the surface of the particles such as sialic acids in mucin particles are protonated at acidic pH values and deprotonated at basic pH values. This

changes ion accumulation (e.g., more anions bind), and consequently, the zeta potential is altered.

The zeta potential of the mucin particles was analyzed with the Litesizer 500 (Anton Paar) equipped with a 35 mW laser diode ( $\lambda = 658 \text{ nm}$ ). For this purpose, the different particles (up to  $12.5 \mu\text{g mL}^{-1}$ ) were measured in ddH<sub>2</sub>O, various buffers, and at different pH conditions (NaOH or HCl used for pH adjustment), respectively, in a capillary cuvette (Omega cuvette, Anton Paar) at  $(25.0 \pm 0.1)^\circ\text{C}$  in automatic mode (equilibration time of 1 min).

### 2.10.3 Atomic force microscopy (AFM) [43]

AFM is applied to determine the morphology of nanoparticles (**Fig. 11A**). This method uses a cantilever fixed to a control system on one side and the cantilever is modified with an oscillating probe (e.g., V-shaped) on the other side to scan the samples (z-axis) at the probe-surface (solid-air) interface. During this continuous raster scanning process, a laser beam is targeted at the cantilever, and the deflected light is detected. Lateral and torsional bending (acting forces, e.g., van der Waals interactions or Coulomb repulsion) of the cantilever (depending on the topography of the sample) results in deviations of the set point, i.e., the detected light is absorbed in the A, B, C or, D quadrants of a photodetector, thus representing the height profile of the sample. There are three different modes in which the cantilever can operate: contact mode (i.e., continuous measurement of probe-sample interactions), intermittent contact mode (i.e., deviations in the cantilever resonance frequency are measurable by limiting the amplitude oscillation; **Fig. 11B**) or non-contact mode (i.e., variations in the cantilever resonance frequency can be calculated by phase shifts; **Fig. 11C**).



**Figure 11: Schematic representation of atomic force microscopy.** To image the sample topography, a cantilever scans the sample surface while a laser beam hits the cantilever and the deflected laser is detected. Depending on the selected mode (e.g., tapping mode) cantilever deflections (**A**), resonance shifts (light blue; **B**) or, phase shifts are obtained, e.g., in the non-contact manner to observe the attractive forces (medium blue), the repulsive forces (dark blue) and the normal resonance frequency (black; **C**).

In this thesis, AFM measurements were conducted for different mucin particles in the dry state. For this purpose, images were recorded with the software NanoWizard II AFM (JPK

Instruments, Berlin, Germany) in contact mode using a cantilever (OMCL-AC160TS-R3, Olympus, Tokyo, Japan) with a tetrahedral probe. To do so, 10  $\mu\text{L}$  of a mucin particle dispersion was placed onto a glass surface and dried at room temperature for 5 d. Afterward, height images were acquired at a line rate of 1 Hz and the obtained data were analyzed using image processing software SPM (v.3.3.20, JPK).

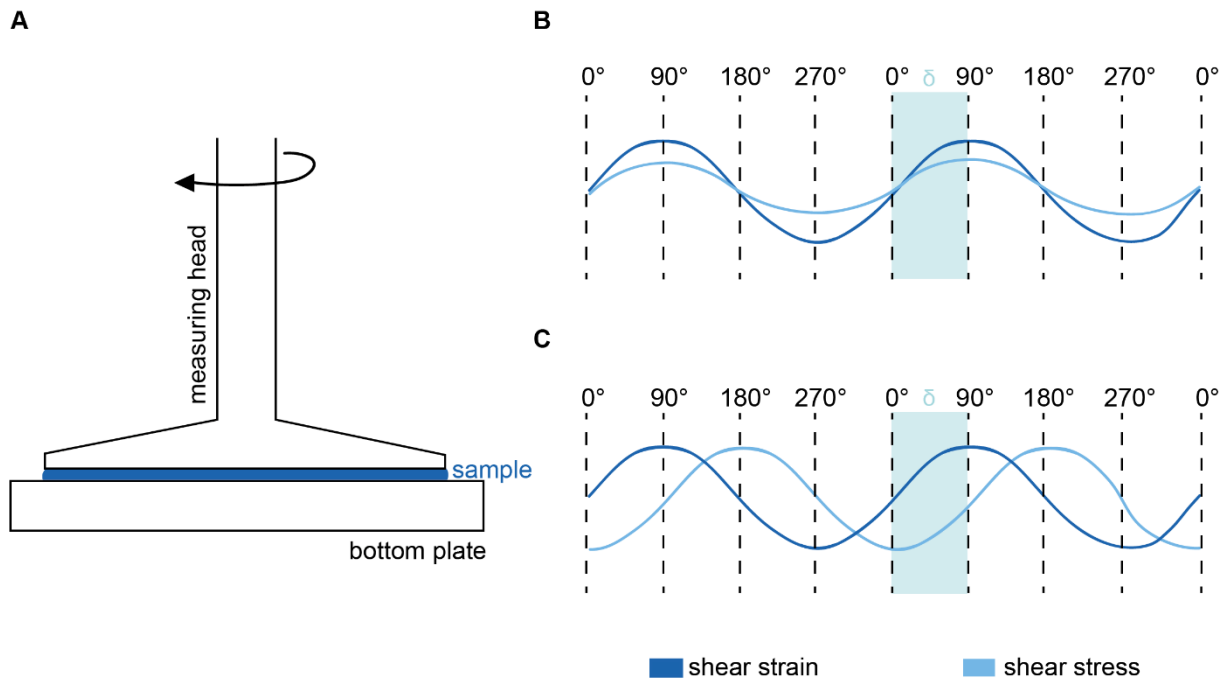
## 2.11 Technique to determine the gelation behavior of mucin molecules with oscillatory shear rheology [44]

Biological substances, *e.g.*, mucilaginous secretions of animals, show viscoelastic properties. This means that, from a physical point of view, the materials as a whole are never merely viscous or elastic but combines both aspects. In both cases, the material deforms but only elastic materials fully return to their original state. The detailed behavior of the material is determined with oscillatory rheology. In this technique, the material is inserted in the gap between a bottom plate and a measuring head, and the latter exerts an oscillating force on the material (**Fig. 12A**). As already mentioned, mixed behaviors are dominant in biological samples: if the viscous part prevails the material is called a viscous liquid; in contrast, if the elastic part dominates the material is called a elastic solid. This distinction is based on the phase shift ( $\delta$ ) between the oscillating force (shear stress) which is initially applied to the material (by sinusoidal waves) and the resulting deformation (shear strain). In the absence of a phase shift ( $0^\circ$ ) the material is purely elastically dominated (**Fig. 12B**); for purely viscously dominated materials, the phase shift is  $90^\circ$  (**Fig. 12C**). From those parameters (shear strain:  $\gamma_A$ ; shear stress:  $\tau_A$ ; phase shift:  $\delta$ ) the storage ( $G'$ ) and loss ( $G''$ ) modulus is determined by the following formulas (**Eq. 8** and **Eq. 9**).

$$G' = \frac{\tau_A}{\gamma_A} * \cos(\delta) \quad \text{(Equation 8)}$$

$$G'' = \frac{\tau_A}{\gamma_A} * \sin(\delta) \quad \text{(Equation 9)}$$

Accordingly, a material is either elastically (storage modulus > loss modulus:  $G'' > G'$ ) or viscously dominated ( $G' > G''$ ).



**Figure 12: Schematic representation of oscillatory shear rheology.** The sample is placed in the gap between the bottom plate and the measuring head. Afterward, an oscillatory shear force is applied and the viscoelastic properties are measured (**A**). Rheological parameters such as shear stress and shear strain are recorded, and the resulting phase shift angle ( $\delta$ ) describes whether the measured sample is elastically dominated ( $\delta = 0^\circ$ ; **B**) or viscously dominated ( $\delta = 90^\circ$ ; **C**).

To assess the viscoelastic properties of biopolymer samples (e.g., mucin-MA, mucin solutions or gels) rheometer measurements were conducted using a research grade shear rheometer (MCR 302, Anton Paar GmbH, Graz, Austria). For this purpose, a plate-plate geometry (25 mm; P-PTD200/GL, Anton Paar) with a gap of 300  $\mu\text{m}$  was selected and 150  $\mu\text{L}$  of a sample was used. Gelation was followed at a frequency of 1 Hz using a torque-controlled protocol ( $M = 5 \mu\text{Nm}$ ). Moreover, the storage ( $G'$ ) and loss moduli ( $G''$ ) of the samples were acquired at a sampling rate of 2  $\text{min}^{-1}$  at 20°C. For the measurements performed with the MA-mucin, the measurements were performed for 25 min, and 5 min after measurement initiation, the sample was exposed to UV light (365 nm; control: unmodified mucin) by using an illumination through a transparent bottom plate.

Moreover, the logarithmic frequency spectrum was measured (a frequency ramp from  $f = 10$  to 0.1 Hz; torque-control of  $M = 5 \mu\text{Nm}$ ) to characterize the linear viscoelastic response of the (modified) mucin materials. To do so, the storage ( $G'$ ) and loss moduli ( $G''$ ) of 150  $\mu\text{L}$  per sample were measured in a plate-plate geometry at 20°C.

## 2.12 Statistics

First, normal distribution and (un-)equal variances of the experimental data were examined using the Shapiro-Wilk and Levene tests. A paired Student's t-test (comparison of two data

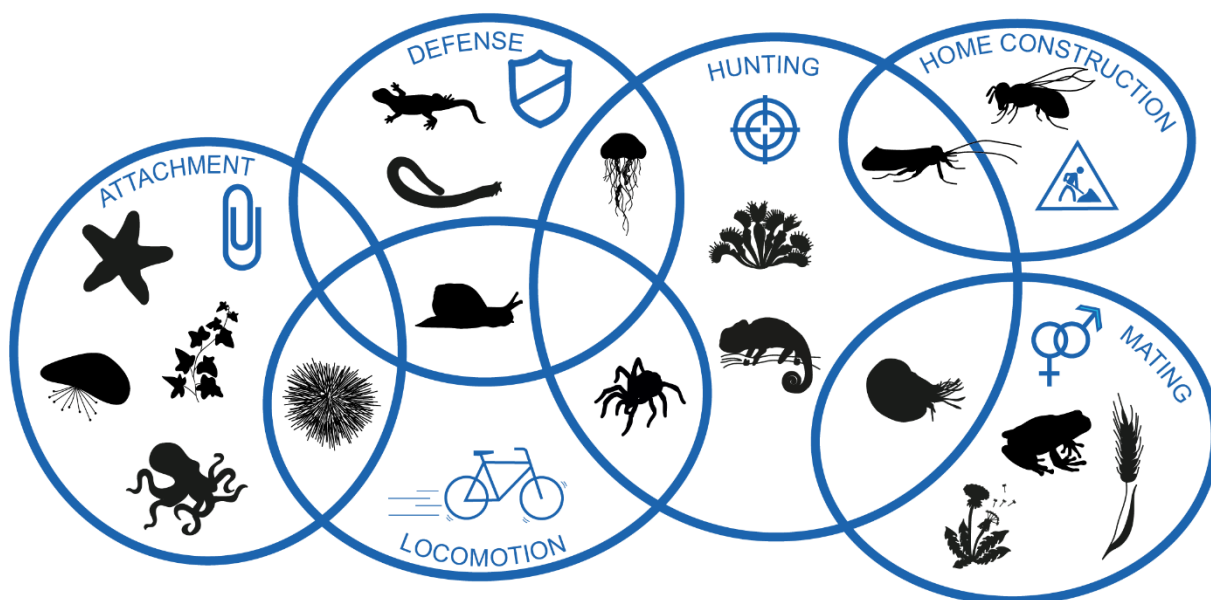
sets) or a one-way ANOVA/Tukey post-hoc test (comparison of multiple data groups) was conducted for normal distribution and equal variances. For unequal variances, the unpaired Welch's t-test was applied. In the case of a non-normal distribution and unequal variances, the Dunnett's T3 multiple comparisons test was performed. However, the threshold for significance was set to a  $p$ -value of  $p \leq 0.05$  for all statistical tests with the software GraphPad Prism (Prism 8, San Diego, CA, USA).

### 3. Summaries of publications

#### 3.1 Bio-based and bio-inspired adhesives from animals and plants for biomedical applications

Theresa M. Lutz, Ceren Kimna, Angela Casini, and Oliver Lieleg [45]

Evolution has allowed plants, animals, and humans to develop a broad range of slimy biocompounds called mucilage or mucus. These secretions can combine different characteristics to achieve multiple functions simultaneously: For example, the jellyfish uses its slimy secretions for defense and prey capture whereas English ivy needs mucilaginous substances for attachment purposes. In addition to their distinct functionality in nature, the complex hierarchical structure and chemical composition of biological secretions differs a lot. Most plant mucilage consists of polysaccharides or polymeric carbohydrates, forming long chains of linear or branched biological macromolecules. In contrast, mucins that are commonly present in the animal kingdom are glycoproteins. The complex molecular architecture of these molecules connects carbohydrates *via* amino acids with the protein backbone and provides functions such as anti-bacterial and anti-viral properties, lubricity, and tissue moistening.



**Figure 13: Schematic depiction of slimy compounds made by plants and animals for various tasks.** Those substances produced from different terrestrial and aqueous animals/plants assist in attachment, locomotion, defense, hunting, house construction, and mating.

This review article summarizes our current understanding of how such slimy molecules or rather their sticky structure motifs (*e.g.*, DOPA, phosphoserine) of natural origin interact with artificial and organic surfaces. In addition to the adhesion properties, intramolecular interactions to strengthen the crosslinked network are addressed and explained at the chemical level since the formation of both mechanisms is based on hydrogen bonds,

electrostatic interactions, metal chelation, hydrophobic interactions and polymerization reaction or mixtures thereof. Individual examples of carbohydrates – mostly based on plants containing sticky molecules or mixtures such as fucoidan, acacia gum, sundew mucilage, propolis and pollenkit (viscin) – and of adhesive (glyco-)proteins namely zein, egg albumin, ivy arabinogalactan proteins, qniumucin, secretions from the sandcastle worm, frog, salamander, silkworm, starfish, velvet worm, glowworm, mussel, spider, snail and hagfish are considered in more detail.

The characteristics, *i.e.*, the stickiness of animal and plant secretions and their additional attributes have the potential be used as components of medical products, such as tissue adhesives. Such compounds can either be directly isolated from nature, recombinantly produced and biotechnologically purified, or completely (semi-)synthetically generated using the natural biocompound as a template. Semi-synthetic or synthetic alternatives are often chosen for fast and pristine production. This constitutes an advantage over natural sources, because the latter need to withstand a sterilization process to allow for their application as a medical product. However, the biocompounds tend to denature or degrade under those harsh conditions and are deprived of their former function. On the contrary, (semi-)synthetic analogues not only retain the original function, but also allow novel/additional binding motifs or molecule parts to be inserted. As a result, materials with multiple functions are created. Such materials provide not only adhesion, they also allow for improved conductivity, exhibit resistance to pH fluctuations and enzymes, self-healing properties or are particularly stretchable. Indeed, these are only a few examples of how naturally occurring molecules or special structure motifs inspire scientists and exploit the availability of biologically based or biologically inspired materials. There are still many unknown slimy substances/compositions in the fauna and flora that need to be investigated and may have a benefit for medical research.

Individual contributions of the candidate: I contributed to the conception of this review and to the writing of the article.

## 3.2 Repulsive backbone-backbone interactions modulate access to specific and unspecific binding sites on surface-bound mucins

Theresa M. Lutz, Matthias Marczynski, Maximillian J. Grill, Wolfgang A. Wall, and Oliver Lieleg [46]

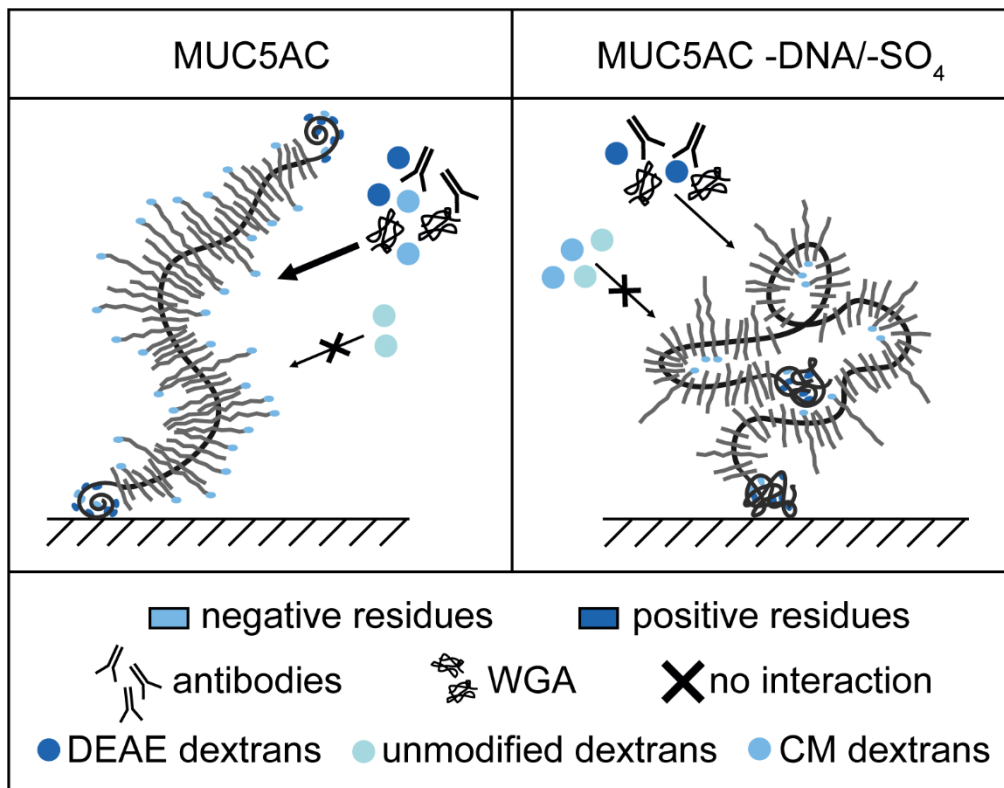
Mucins are ubiquitous molecules in the human body and fulfill surface-bound fundamental functions such as protecting the underlying epithelial cell layer in organs and tissues against microorganisms and noxious molecules [47]. Our knowledge of how mucin interacts with surfaces in natural environments grows continuously [3, 48, 49] – the mucin termini predominantly interact with hydrophobic surfaces, whereas the core domain can attach to hydrophilic surfaces. However, several unsolved questions still remain: Which structure motifs of those mucin molecules interact with particles? How is the particle-mucin interaction affected when external factors change the mucin structure through enzymatic attack (e.g., by bacteria)? A detailed understanding of the interaction mechanisms responsible for mucin function and the identification of the crucial individual structure motifs would allow researchers to design tailored medical-grade materials to e.g., combat diseases. To address all of those mucosal questions systematically, mucins must be reconstituted in such a way that they mimic the layer of the *in vivo* environment – but in a laboratory-controllable *in vitro* model system. It is reasonable to assume that the partially folded mucin termini bind to uncharged, hydrophobic surfaces such as polystyrene *via* hydrophobic interactions, resulting in accessible interacting functional groups within the glycoprotein – the charged glycans in the core domain and the anionic/cationic amino acid side chains in the protein backbone.

In this project, such a biomimetic mucin surface system was used to study mucin interactions with specific and non-specific binding partners. Alterations in the binding interactions of (modified) mucin molecules – removal of sulfate groups located at the glycans of the protein's core-domain and mucin-associated DNA, whose phosphate backbone is likely to interact with the mucin termini – is considered as a very promising strategy to reveal information about the binding properties of damaged mucins in their physiological environment (*i.e.*, after the bacterial or enzymatic attack).

The formed mucin layers, whether composed of unmodified mucin or sulfatase- and DNase-treated mucin molecules, interact strongly with cationic, slightly with anionic dextrans, and weakly with neutral ones. Intriguingly, the anionic dextrans show lower binding affinities to mucin-DNA/sulfate groups. This appears contradictory at first glance since the enzyme treatment should reduce the electrostatic repulsion between the anionic mucin molecule and the anionic dextran; thus, the binding of anionic dextrans should be higher or in a similar range as for the unmodified mucin variant. However, repulsive electrostatic forces within the



unmodified mucin convey an elongated, stretched protein structure, whereas the absence of anionic charges may entail (partially) folded, compacted mucin structures (**Fig. 14**). Thus, certain structure motifs are now likely to be concealed inside the mucin architecture and are less accessible to binding interactions with dextrans and other molecules such as antibodies and lectins.



**Figure 14: Schematic visualizing how a removal of anionic motifs from mucin could lead to conformational rearrangements and an alteration in binding interactions.** Native mucins can interact with anti-MUC5AC antibody, WGA, and charged dextrans, however not with neutral dextrans. Those binding interactions are reduced with the enzymatically treated mucin variant and, in addition, the anionic dextrans fail to interact electrostatically.

Numerical simulations of mucins agree with this picture and suggest that the mucin architecture is affected by the loss of ionic (repulsive) interactions, which may create new target sites for further compaction of the macromolecule. Such altered mucin structures may also show an overall changed interaction with drugs, viruses or, other harmful substances *in vivo*.

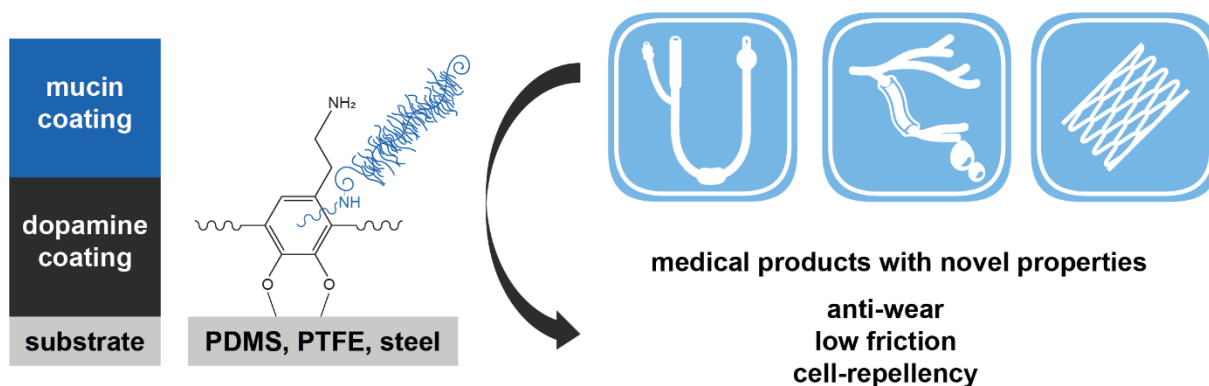
Individual contributions of the candidate: I contributed to the conception of the study, the design and performance of the experiments, the data analysis, and the writing of the article.

### 3.3 Bioinspired dopamine/mucin coatings provide lubricity, wear protection, and cell-repellent properties for medical applications

Jian Song, Theresa M. Lutz, Nora Lang, and Oliver Lieleg [2]

Mucus is mainly composed of the protein mucin and provides protection of moist body surfaces from pathogens. In addition to their anti-biofouling properties, mucins ensure lubrication in the body which helps to transport food through the gastrointestinal tract of the organism. This lubricating characteristic is caused by the structural motifs of mucins [48, 50]: The high density of carbohydrates (approximately 70-85%; [51-55]) in the core domain of mucin allows for the binding and the exchange of water molecules during tribological stress (= hydration lubrication) [56]. In addition to this hydration process, the cyclic adhesion and detachment of the hydrophobic mucin termini onto (body-) surfaces plays an important role in lubrication (= sacrificial layer formation). Hydration lubrication makes mucin coatings interesting for medical devices which are exposed to shear stress, e.g., created from the blood stream and by insertion into the body (e.g., catheter intubation). The challenge is: How can these mucin molecules be coated onto a medical device while remaining functional? When mucin molecules should be immobilized onto a surface, commercially available mucins are undesirable since, here, certain structure motifs (e.g., the hydrophobic termini and some carbohydrates) are damaged during their extraction [57]. Therefore, purifying intact mucins by a careful separation process [15, 16] is essential to minimize these limitations. Moreover, obtaining biological materials from humans is challenging, but animal mucins (e.g., from pigs) are accessible in high amounts. Of course, the mucin molecules' carbohydrate composition and protein backbone vary a bit between species. However, animal/porcine mucins are very similar to human mucins and thus can engage a variety of interactions with other molecules and surfaces [3, 48].

This article shows, how dopamine molecules can serve as molecular linkers between different synthetic materials (e.g., the surfaces of stents, blood vessel substitutes, and catheters) and the biomolecule mucin. This strategy uses a two-step dip-coating procedure to generate the macromolecular coating: first, a stable layer of polydopamine is formed on the material surface; second, the biomacromolecule binds to the dopamine layer, e.g., *via* hydrogen bonds and  $\pi$ - $\pi$  electron interactions (**Fig. 15**).



**Figure 15: Schematic depiction how modification of different medical products with macromolecular coating alters the surface properties.** Dip-coated dopamine (black)/ mucin (dark blue) surfaces are generated on medical product surfaces, *e.g.*, a catheter (PDMS material), blood vessel substitute (PTFE material) and stent (steel). First, dopamine self-polymerizes under alkaline conditions on the substrate surface and in the second step, the formed layer interacts with individual mucin molecules, *e.g.*, *via* the catechol of dopamine and the amino groups of amino acid side chains present in mucin. Those formed double-layer coatings provide the medical products with new properties such as wear resistance, friction reduction, and cell-repellence.

In detail, the catechol hydroxyl groups of dopamine oxidize under alkaline conditions to form ortho-quinones, which self-polymerize into a single-component network and cover the substrate. Since the poly-dopamine completely coats the surface and possesses excellent biocompatibility, the question arises: Why is the second layer of mucins necessary? Dopamine is known for its cell colonization ability based on its multiple interaction properties. It could promote undesired *in vivo* reactions such as inflammation (caused by macrophages) and neointima hyperplasia (ingrowth of smooth muscle cells into the substitute material) followed by restenosis (clogging of the interior of the substrate material). And indeed for epithelial cells and fibroblasts, the cell counts determined on the dopamine layers are similar to those on the cell-binding surface (control) of tissue culture plates.

This example illustrates that the dopamine layers alone are inefficient for reducing biofouling processes *in vitro*. However, with a second modification of the surface of catheters (PDMS material), blood vessel substitutes (PTFE material), and stents (steel) – the passive adsorption of a mucin layer – cells are strongly repelled (~90-100% reduced cell colonization) compared to the control. Since only a few round-shaped cells colonize these surfaces, the formed double-layer coatings are biocompatible and are shown to be suitable for anti-biofouling applications *in vitro*. In contrast, the cell-binding surface and dopamine coating promote cell adhesion, *i.e.*, well-spread morphology of cells, possibly leading to unwanted side reactions (*e.g.*, neointima hyperplasia) *in vivo*.

In addition, the dopamine-assisted mucin coating provides a reduced coefficient of friction (COF) in the boundary lubrication (by a factor of ~10) compared to the bare

polydimethylsiloxane (PDMS) material. Moreover, it is observed that the wear formation of coated and uncoated surfaces after tribological testing shows a significant increase in sample roughness for the uncoated control (by a factor of ~10). In other words, the dopamine/mucin coating leads to reduced wear generation. Similarly, the COF and surface topography of double-layer coating on other materials such as steel and polytetrafluorethylene (PTFE) indicates that the formed dopamine/mucin is stably immobilized on the different substrates tested and reduces friction and wear.

Mucin was already described in the literature as an excellent lubricant, so the result of an intact substrate surface after tribological stress seems realistic. However, it has not yet been investigated which mechanisms or structure motifs of mucin molecules are responsible for the cytological results suggesting strong repulsion effects between surface-bound mucins and eukaryotic cells. Based on the complex mucin structure and the results from the dextran-mucin interaction experiments, it could be speculated that anionic carbohydrates (*e.g.*, sialic acids, sulfated groups of glycans) in the core-domain or anionic amino acids in the protein backbone (*e.g.*, glutamic acid, aspartic acid) are responsible. Furthermore, mucin-associated DNA entangled in the brush-like structure and bound *via* hydrogen bonds – the binding sites of the DNA to mucin are unknown as well – can add further negative charges (*via* phosphate groups in the DNA backbone) to the mucins. Then, mucin likely interacts with the eukaryotic anionic cell membrane proteins *via* electrostatic repulsion. However, more detailed fundamental research on mucin molecules is needed to clarify this issue.

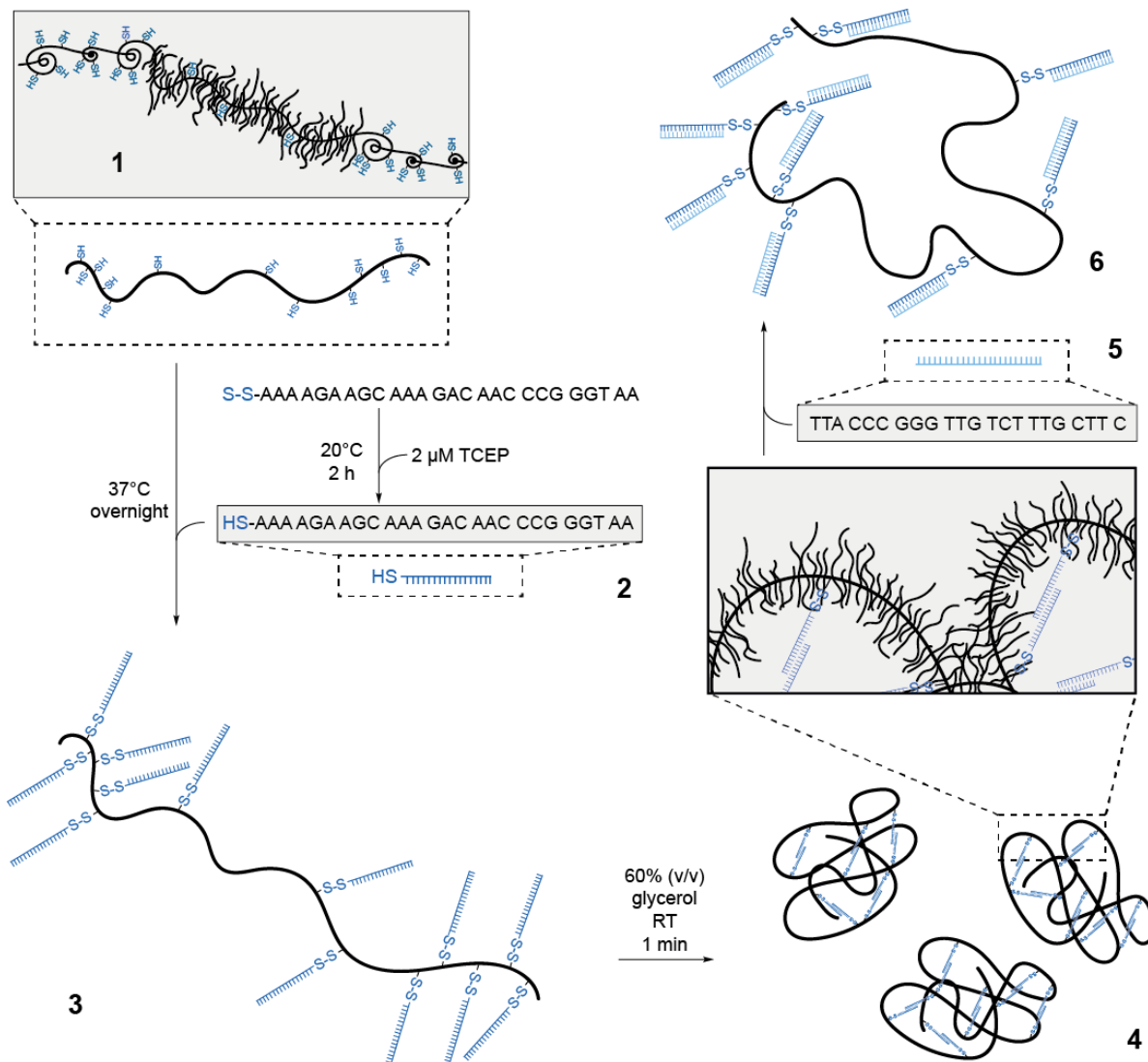
Individual contributions of the candidate: I contributed to the conception and performance of the eukaryotic cell experiments, the data analysis, and the writing of the article.

### 3.4 DNA strands trigger the intracellular release of drugs from mucin-based nanocarriers

Ceren Kimna, Theresa M. Lutz, Hongji Yan, Jian Song, Thomas Crouzier, and Oliver Lieleg [19]

In nature, mucins are secreted by goblet cells located in the submucosal glands of the epithelium [58]; here, the mucins are already arranged in fibers which can form a branched network after release into the lumen [59]. A compaction of single mucin molecules prior to release is caused by enzymatic treatment. Yan *et al.* [60] were inspired by those compaction processes and proposed a mechanism for mucin particle formation without eliminating charged motifs. In detail, the compaction mechanism relies on the low solubility of mucin in glycerol, resulting in the repulsion of the glycoproteins from the solvent which induces the formation of condensed mucin particles. Intermolecular interactions occur between the mucins at the glycerol/glycoprotein interface, enabling the formation of a globular macromolecule structure. In addition, glycerol inhibits the hydrophobic interaction between the termini (intermolecular interactions) of the formed mucin particles and thus prevents aggregation processes. From a biomedical perspective, in fact, such compacted mucins could be very interesting representatives of drug carriers. To keep the mucins in this globular state, the focus is now on stabilizing the obtained mucin architecture with DNA, for example.

To form DNA-stabilized mucin nanoparticles, the amino acid side chains of the cysteines located in the cysteine knots of the mucin backbone (especially in the hydrophobic termini) are targeted. Those cysteines spontaneously form covalent cystine bonds with other thiolated molecules, *e.g.*, by exposing them to synthetic DNA single strands (crDNA) carrying thiol residues on the termini. And indeed, after condensing such modified mucins in glycerol, the self-complementary palindromic sequences of the synthesized oligonucleotide strands hybridize with each other (*via* 8 base pairs) and maintain a compact, globular state of the mucin nanoparticles when removing the condensing agent by dialysis. The addition of displacement DNA (dDNA) opens the mucin particles on demand. This disassembly strategy is based on the better fit of the dDNA sequence, which interacts with the crDNA *via* 22 base pairs (the crDNAs hybridize only with 8 base pairs; **Fig. 16**).



**Figure 16: Shown is the process for preparing DNA-crosslinked mucin particles.** The cysteines of the mucin backbone (1) are targeted by synthesized single crosslinker DNA strands, which are reduced at the 5'-cystine bonds by TCEP (2). The newly formed cysteine bonds between mucin and the DNA (3) provide the basis for the mucin particles. After adding glycerol, the glycoproteins are condensed, and the DNA sequences form Watson-Crick base pairs through palindromic sequence segments (4). The stable particles can be opened by specific displacement DNA (5) and can release their cargo on demand (6).

This mucin particle stabilization strategy offers high potential for targeting specific cell types by using appropriate DNA sequences such that cellular miRNA 21, for example, can be used to open the particles in the cytoplasm. This particular RNA is predominantly overproduced by some cancer cells [61], and the selective opening mechanism is mimicked here in an *in vitro* study using HeLa cells. Mouse fibroblasts (NIH 3T3) serve as a negative control since those cells have a regulated miRNA 21 transcription. To demonstrate successful particle opening, an anticancer drug (doxorubicin) is incorporated into the particles, which, in appropriate concentration, leads to cell death (in case the particle is successfully opened). This occurs in HeLa cells, whereas fibroblasts remain unaffected. Moreover, *in vitro* experiments with

antibiotics such as neutral chloramphenicol, anionic tetracycline and cationic vancomycin show high encapsulation efficiency and drug release overtime.

By tailoring the specific particle opening process according to the different transcribed RNA sequences, DNA-crosslinked mucin particles offer further opportunities and potentials in medical research. Ensuring their opening in selected cell tissues and compartments entails that surrounding cells or tissue areas are no longer exposed to unwanted side effects which is, for example, the case with irradiation treatment during cancer therapy. Furthermore, drug doses could be reduced since the particles' content is only released in the targeted cells. This, ultimately, saves costs and the body has no unnecessary burden from increased drug doses.

Individual contributions of the candidate: I contributed to the conception and performance of the eukaryotic cell experiments, the data analysis, and the writing of the article.

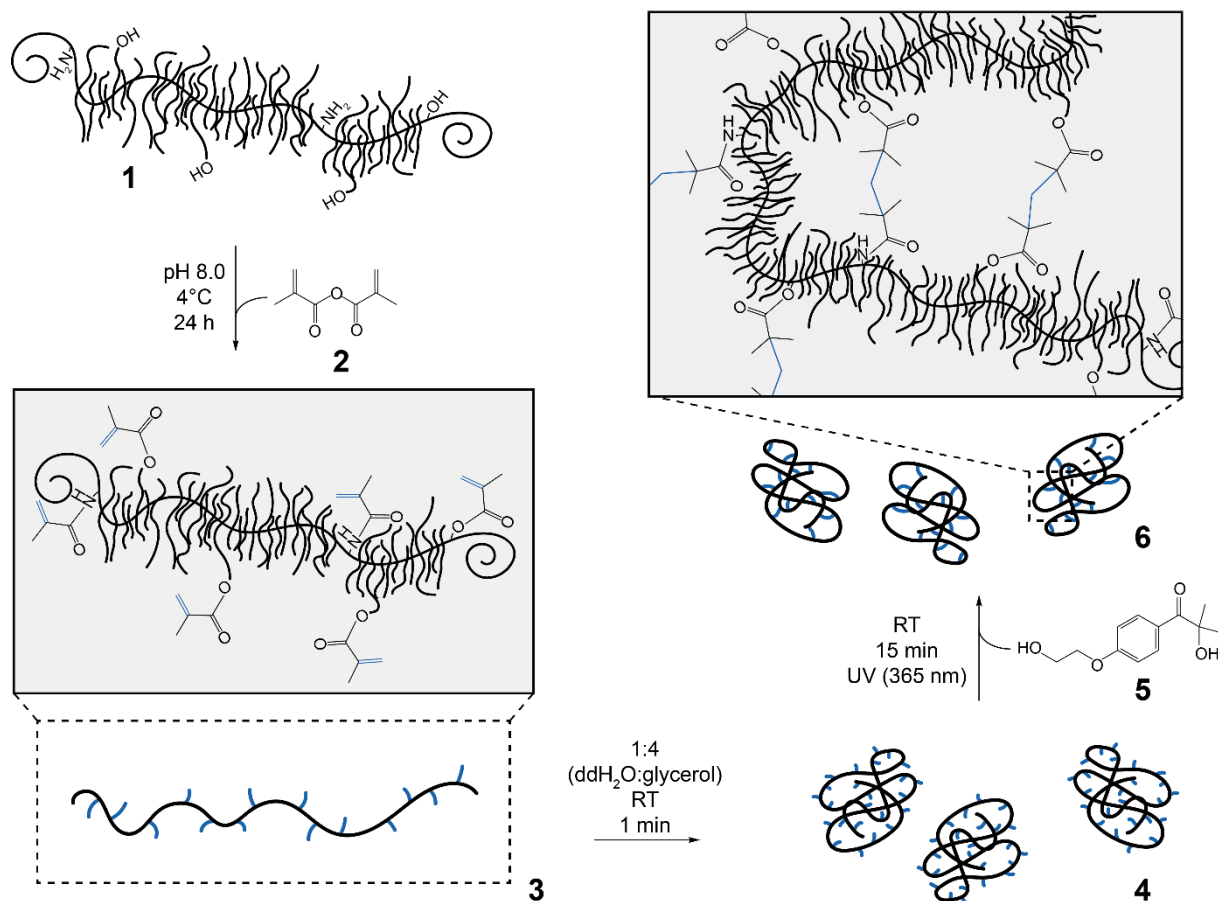
### 3.5 A stable mucin based nanoparticle system for the co-delivery of hydrophobic and hydrophilic drugs

Theresa M. Lutz, Ceren Kimna, and Oliver Lieleg [62]

Mucins have been recently suggested to be promising macromolecules for building blocks to be used for drug delivery applications not only due to the amphiphilic character but also to other structural and functional motifs allowing for particular advances to control the encapsulation or release of drugs [63]. Owing to the biochemical complexity of mucin glycoproteins, a wide variety of specific and unspecific binding interactions between mucin-based materials and drugs are possible. Non-covalent interactions – such as electrostatic interactions between mucin and anionic and cationic drug molecules – are likely to contribute to an efficient cargo encapsulation. According to their physicochemical properties, some drug molecules bind strongly (*e.g.*, cationic, hydrophilic) to the mucin carrier material, whereas others (*e.g.*, anionic, hydrophobic) exhibit low binding efficiencies. Although appearing contradictory at first glance, both examples can benefit from being carried by mucin-based nanoparticles. Overall, balancing the loading/release requirements of various drug molecules in a mucin-based drug delivery system is a challenge but at the same time an opportunity to improve the transport and co-loading of particles.

In contrast to the mucin particles stabilized by the DNA-crosslinking procedure [19], here, the particles are not directly generated from mucins in their naturally occurring state. Instead, this strategy is based on a two-step process (**Fig. 17**): First, the amino- and hydroxyl groups in the protein backbone and glycosylated core domain of the mucin molecule are functionalized with methacrylic anhydride (MA). Those methacryloyl mucins are mixed with glycerol to obtain condensed particles; then, covalent crosslinks between the formed methylene groups of the mucins are created by UV irradiation and a free radical-based reaction (*via* a photoinitiator). Unlike DNA crosslinked particles, the stable covalent bonds of the methacrylated mucin particles are irreversibly linked. Hence, specific particle opening is not possible here, and those particles release their cargo in a sustained manner.





**Figure 17: Mucin functionalization with methacrylic anhydride to form UV-crosslinked mucin particles.** The mucin molecules (1) are modified with methacrylic anhydride (2) to form methacryloyl mucins (3), which is the second step to form particles as a result of exposure to glycerol (4). Finally, after adding the photoinitiator Irgacure 2959 (5), these particles are covalently crosslinked by UV irradiation and consequently stabilized (6).

The stability of the formed particles is investigated in more detail. In *in vitro* studies, the mucin particles are exposed to simulated body fluids, enzymes, or cell medium (using *in vitro* assays). Such challenging scenarios may provide an overview of the cargo transport differences, drug release, and degradation properties of the nanoparticles. On the other hand, particle uptake into cells can adversely be affected by different factors such as the size and surface charge of the formed mucin particles. Those factors significantly impact *in vitro* studies and may differ between mucin particle species. All those influencing factors are explored in more detail with several characterization techniques, such as AFM imaging, dynamic light scattering, and electrophoretic light scattering. Based on these measurements, mucin particles within the diameter range of 0.09 to 0.3  $\mu\text{m}$  are produced with this cross-linking method (on average, most particles are 0.18  $\mu\text{m}$  in diameter according to AFM measurements).

Another important aspect for biocompatibility is the surface charge of the individual particle types: Positively charged particles would intercalate with the cell membranes, which can lead to cell death. Neutral particles cannot pass through the membrane; however, negatively charged particles are taken up by endosomes [64]. Therefore, mucin-based particles should have a negative  $\zeta$ -potential, which they indeed do (-30 mV). In these studies, fluorescent hydrophobic and hydrophilic dyes (chosen as model molecules due to their ease of detection) are observed to be encapsulated into mucin nanoparticles, and then released into the cytosols of cells over time. Further cytometric examinations show that clathrin-mediated endocytosis and micropinocytosis are the governing uptake pathways for mucin nanoparticle internalization.

Overall, covalently crosslinked mucin particles offer great potential for further applications in the body. It is feasible to transport either hydrophilic or hydrophobic drugs, as well as both at the same time *in vitro*. In addition, those particles are very stable in an acidic environment and possess the potential to be stably transported from the stomach to the intestine, where they release most drugs. Thus, pathological scenarios where hydrophilic and hydrophobic medications need to be co-delivered, can be a promising application for the particles developed in this study.

Individual contributions of the candidate: I contributed to the conception of the study, the design and performance of the experiments, the data analysis, and the writing of the article.

## 4. Discussion

Mucilaginous/sticky biomolecules have numerous functions (*e.g.*, attachment, locomotion, hunting, and mating) as described in **3.1**. One of the most prominent examples is the glycoprotein mucin, which is used in the animal world by jellyfish [65] and hagfish [66, 67] for macroscopic defense against predators. In the human body, mucin plays a protective role on a microscopic scale as well as it helps repelling bacteria and trapping viruses [55]. Infections and yearly influenza epidemics reveal that humans are still sensitive to bacterial and viral attacks [68]. Although mucin glycoproteins provide some protection against the invasion of epithelial tissue by pathogens, they are often attacked by mucin-degrading enzymes [69, 70]. This type of mucin degradation process weakens the mucus barrier and renders us humans more prone to viral and bacterial infection. Therefore, understanding the behavior of mucins on surfaces is important to gain fundamental knowledge about those defense and interaction processes – especially how an altered mucin architecture results in changed interactions of specific mucin binding motifs with other molecules (or noxious particles). This aspect is investigated in **3.2** by treating the manually purified gastric mucin MUC5AC with, for example, the enzyme sulfatase to mimic the initial steps of the mucin degradation process and to study the changes in mucin binding properties with other molecules (*e.g.*, dextrans with different physicochemical properties). It is observed, that, in addition to a reduced binding affinity towards cationic and anionic dextrans, the binding of specific antibodies and lectins to mucin is also reduced. Based on a numerical model, it is shown that the removal of negative binding motifs from mucin (*e.g.*, sulfate groups) eliminates intramolecular repulsive forces and, a more compact mucin molecule is formed. In this mucin conformation, certain binding sites are less accessible to specific and unspecific binding partners than in the native, elongated mucin state.

Since intact mucin molecules can repel both, prokaryotic and eukaryotic cells, one idea pursued here is to apply mucins to surfaces where biofouling processes require inhibition. Medical devices such as catheters, stents and blood vessel substitutes are typical examples where undesirable cell adhesion limits their use. Attachment and proliferation of smooth muscle cells, as well as the formation of an extracellular matrix on the materials (*e.g.*, during neointimal proliferation) can cause life-threatening risks [71, 72]. The devices can then become clogged by thrombus formation leading to myocardial infarction [73]. Another example are prostheses, where a cell repellent effect is also advantageous to suppress biofouling processes and related inflammations which otherwise can entail rejection of the implant [74, 75]. In **3.3**, a solution to this problem is presented based on the adhesion strategy of mussels. Simple dopamine/mucin double-layer coating (using a two-step dip coating process) produces stable mucin layers on the surfaces of commercially available medical devices through non-covalent bonds. The use of mucin on those materials has impressively demonstrated the cell-

repulsive characteristics of mucins. Yet, the physico-chemical nature of those repulsive interactions between mucins and eukaryotic cells are not identified.

It is conceivable that specific mucin motifs cause the cell-repellent properties. One candidate is the negatively charged structural elements in the core domain of mucin. This anionic charge could lead to the prevention of a further attachment of eukaryotic/prokaryotic cells due to the negatively charged cell membranes [76, 77]. This raises the question of why the mucin-underlying epithelial cell layer is not affected. One explanation for this, could be that the cells under the mucin layer are already present in associated, interconnected networks, *i.e.*, already firmly established on the surface and have formed strong cell-cell contacts. However, this is not the case for new soft muscle cells (*e.g.*, passing through stents or blood vessel substitutes) that want to attach to the manually mucin-coated surface. Those cells must first form cell-cell interactions on the existing mucin layer, but owing to the cell-repelling properties of mucin, they do not even have the possibility to attach on the surface, nor to establish cell network formations. The influence of the negative charge in the core domain of mucin, mostly established by sialic acids and sulfated carbohydrates [3], could be just one possible explanation for the glycoproteins' cell-repellence. Moreover, the hydrophobic terminal mucin domains could also influence the attachment of eukaryotic cells [51]. Indeed, the cell membrane is hydrophilic on the side facing the extracellular space [78, 79] and could therefore also be rejected by the terminal mucin domains, since hydrophobic interactions cannot occur and thus cannot support a binding interaction. However, this repulsion scenario could also be conceivable together with the anionic motifs. To test all these possibilities, specific mucin motifs have to be removed and the altered mucins need to be tested in an *in vitro* model. For this purpose, individual binding motifs, such as the sulfate groups (by enzymatic treatment with sulfatase) and the sialic acids (by the enzymatic treatment with neuraminidase) in the core domain or the hydrophobic termini (by enzymatic treatment with trypsin), should be removed and the individual enzymatically treated mucins should be immobilized onto surfaces and investigated with regard to their cell-repellent properties. In a second step, combinations of differently treated mucin domains can be used to see whether specific treatments have stronger effects on cell repulsion and whether several binding motifs exhibit anti-biofouling characteristics.

It must also be noted that the enzymatic treatment of mucins affects structural rearrangements within the mucin molecules (see **3.2**). It is possible that the elongated structure of mucin is also important for the cell-repellent function of mucin. Structural alteration (*e.g.*, after enzymatic treatment) of the mucin may either result in hidden functional groups that are now no longer available for repulsion or in the accessibility of functional groups that establish repulsion. A corresponding *in vitro* model is very challenging to implement since, here, ions (*e.g.*, in cell

medium) and proteins (e.g., albumin in FBS) are involved and may complicate the interpretation of the results: They may lead to additional interactions with mucin, alter the structure of the mucin molecule or change the repulsion of cells (e.g., by binding to the anionic structural motifs in the core domain of mucin and thus possibly reduce the repulsion of the negatively charged cell membranes). It is an interesting as well as challenging question to answer by using an *in vitro* setup together with (modified) mucins. In the future, this needs to be addressed in more detail using a suitable technique to analyze and fundamentally explain motif interactions with cells and consequently biofouling activities of the glycoprotein mucin.

However, the modification of the various structural motifs on the glycoprotein using different techniques is already possible. For example, methacrylation of hydroxyl- and amine- groups of individual mucin molecules is one way to achieve this. The use of methacrylated mucin to fabricate drug carriers (see 3.5) is an option but one is not limited to this application. An aspect that is overlooked at this point is that this modified mucin material itself forms a stable gel layer over time by a free radical based reaction activated with UV. Thus, methacryloyl mucin molecules also offer potential in modern pancreatic cancer surgery, for example. Here, pancreaticogastrostomy, anastomosis from the duct to the gastric mucosa, is the common method to connect the surviving, remaining enzyme-secreting pancreatic stump to the stomach [80]. This operation is hardly associated with risks; however, various types of secondary complications may occur such as inflammatory reactions, suture injuries or, in the worst case, reopening of the anastomosis. The latter leads to leakage of acidic digestive products that destroy the surrounding tissue and cause uncontrolled bleeding and eventually death [81]. In the future, these difficulties could be avoided by using smart UV-crosslinked mucin hydrogels embedding the surgical anastomosis to close the wound. Another advantage of using mucins is that they are stable at acidic pH values [82], impedes the diffusion of gastric acid [83], and that they can even form additional interactions (oligomerization *via* cysteines) with other mucins [51], which could enhance the cohesive stability of such mucin gels. This could prevent leakage of the acidic products into the abdomen. Questions that remain open here are whether not only the cohesive but also the adhesive properties of the UV mucin gel are sufficient to bind to tissues. Maybe it is necessary to either introduce a second system – e.g., molecules with better adhesion to cell surfaces that can be incorporated into those mucin gels and do not interfere with the crosslinking of single mucins – or to pursue a completely different strategy – such as the conjugation of sticky dopamine motifs to the glycoprotein to provide both, adhesive and cohesive properties.

Mucins have already demonstrated their enormous potential for applications on medical devices or tissue surfaces. However, mucin could also increase its relevance at the therapeutic and drug carrier level. Countless drug carrier systems based on (semi-)synthetic carrier

materials exist to transport drugs to site-specific tissues [84-86] and/or to release them at specific time points [87, 88]. The working principle of these techniques is based on the prevailing physical and chemical environment of the diseased area (e.g., changes in pH [89] or temperature [90]) and the release of the transported therapeutics is often initiated by a selective trigger mechanism. However, it is very difficult to find a trigger to specifically target a defined disease and thus to treat only affected cells with drugs (as is required in the case of metastases in the advanced stage of cancer). Here, the inability of healthy cells to open the particles would protect these cells from unnecessary exposure to drugs and/or from dying. In **3.4**, a solution to such a problem is introduced in form of a DNA-stabilized, mucin-based drug delivery system. With this strategy, therapeutics are transported across the cellular membrane and only in the presence of the correct trigger – namely a corresponding miRNA overexpressed in cancer cells – the particles are opened according to the 'lock-and-key' principle. This leads to a conformational change of the mucin particle from a compact (nanoparticle state) to an elongated shape (open state) and thus to the release of the therapeutics. In contrast to existing systems that prefer to build the entire carrier from DNA (=DNA origami [91]) to achieve controlled drug transport, the mucin-DNA strategy requires less of the expensive DNA material and, similarly to the DNA carriers, is able to deliver diverse therapeutics (e.g., antibiotics and cytostatics) in a site-specific manner. Thus, smart systems such as the mucin-DNA particles can pave the way to the new generation of personalized medication strategies.

Moreover, it is even possible to produce particularly robust mucin-based particles that remain closed. The advantage of these particles is that they allow for a simultaneous transport of multiple drugs. Packaging hydrophobic drugs is often a major challenge [92], and further difficulty is associated with incorporating hydrophobic and hydrophilic drugs into a single carrier system. As described in **3.5**, this can be achieved with methacryloyl mucin and a UV-stabilizing method. Such minimal chemical modification of the glycoprotein with methacrylate anhydride allows for the production of covalently crosslinked nanoparticles that release their cargo *via* swelling. The advantage over other biomolecule-based systems, such as those composed of albumin, is that the mucin is resistant to acidic conditions (e.g., in the stomach); in the compacted particle state, mucin survives even enzymatic degradation by pepsin. Those findings suggests that, when taken orally, mucin NPs may be able to deliver drugs through the stomach to the intestine in a nearly unaffected manner and can there target diseases such as Crohn's disease.

Another persistent disease often developed by post-menopausal women is osteoporosis. Here, estrogen deficiency promotes osteoporosis, since the hormone normally promotes osteoblast formation (=bone formation) and suppresses osteoclast formation (=bone resorption) [93]. In this case, calcium is increasingly dissolved from the bones and excreted

from the body (=renal calcium excretion); however, intake of calcium together with vitamin D tablets could increase intestinal calcium absorption to maintain the current state of bone health [94]. Since both calcium and vitamin D are needed, administering two tablets or using a drug carrier system that combines both in one step would be convenient. In **A** (see appendix), the formation of mucin particles is described using divalent cations, such as calcium and magnesium, which electrostatically stabilize the particles. Returning to osteoporosis, the calcium could have two essential roles (double effect): it would act as a stabilizer in the carrier structure and could be absorbed by the body when the carrier material is degraded. In addition, another drug can be delivered inside the carrier, such as vitamin D.

There are numerous possibilities of stabilizing mucin particles and their applications in medicine could be broad. It will be beneficial if these particles can be adapted to transport a wide variety of molecules, ranging from ACE inhibitors to Z-drugs, to address different diseases. For this purpose, however, the mucin molecules or their binding motifs need to be investigated in more detail. Could all drugs with different physicochemical properties (*e.g.*, hydrophilic/hydrophobic, anionic/cationic charge or uncharged, etc.) be transported and released equally efficiently by these mucin particle systems? A prediction is difficult here because the detailed folding of the mucin during particle formation is not known. Are the mucins always folded in the same way, so that the same binding motifs are always oriented toward the drug? In other words, do always identical interactions between mucins and drugs occur to transport the latter in the carrier matrix? Associated with this question: Which glycoprotein binding motifs are required to obtain a sufficient loading capacity and release profile of the cargo molecules? Again, many questions remain about the particular binding sites of mucins. Thus, drug loading into the mucin matrices should be systematically assessed. The data obtained could help to create a machine learning-assisted analysis that enables pharmacologists to identify which structural motifs of the carrier material and drugs represent the best combination for a specific medical application. In detail, this requires the identification of the structural motifs of mucin that interact with the relevant drugs and the investigation of the physicochemical properties of the cargo molecules responsible for efficient loading (and release out of those particles as well).

Once these binding motifs, the encapsulation, and the controlled release behavior of the mucin-drug interaction partners are identified, next-generation drug carrier materials (enabled by artificial intelligence) could be obtained, and it should be possible to transport a broader range of drugs into the body and thus solve complicated pathological scenarios. This includes, for example, the transport of hydrophobic drugs into the human organism, since the body is predominantly composed of water and the poor solubility of such drugs restricts their *in vivo* application. Accordingly, formulation scientists could produce (semi-)synthetic molecules with

the appropriate structural motifs to enable or enhance the transport of specific drugs. This provides the pharmacological field with a wide variety of molecules or countless opportunities to synthesize new materials to construct innovative drug carriers. Advantages of such novel materials are that they can sometimes be more efficient in drug loading and release, thus requiring lower drug concentrations. This has two particular advantages, firstly the body is exposed to less stress due to the lower drug levels and secondly, manufacturing costs can be reduced.

However, not only the transport of the cargo but also its release profile should be carefully considered. The different particle types can be opened by different stimuli in order to release the contents of the particles with a time delay (when required) or if conditions change (*e.g.*, inflammatory reactions) in the body. Most of the mucin-based particles can be degraded by trypsin, but to trigger a release cascade using enzymes is too uncontrolled; The drugs could be released too early or too late due to a lack of a defined trigger mechanism. Furthermore, if the drugs are released in the same way (*e.g.*, by enzymatic degradation or swelling), they are liberated at the identical time. Therefore, the particles should be modified and adjusted accordingly. First, other 'key-and-lock' principles, such as those that are the basis of DNA-stabilized particles, could be established. Another possibility is that, for example, ionically stabilized (*via* magnesium or calcium crosslinks) particles are adapted such that they can open in the environment of a physiological salt concentration (sodium competing with calcium and magnesium), thus releasing the cargo and another 'key' for the next particle opening event (=cascade). A pH-dependent system could also be implemented. Mucins are known to form covalent bonds in acidic environments (cystine bonds). Moreover, additional groups could be introduced into the mucin molecule to trigger the release of the cargo at an increased (alkaline) pH value, as it occurs in the intestine.

Another possibility for more efficient cargo transport is to introduce special binding motifs (*e.g.*, growth factors) onto the surface of the particles, which allow attachment to specific surface receptors of cells such as myocardial cells through the covalent linkage of oleic acid to the particle surface [95]. This could be used to accelerate internalization into this cell type and create a site-specific application. However, the shape of the particles could also be adapted so that they form more complex structures [96]. One example is to mimic the 'hedgehog' geometry of some viruses, such as SARS-CoV-2 [97]. The resulting spikes serve to penetrate more easily into the cells to be infected and enable their multiplication and distribution.

On the other hand, it must also be noted that the scope of *in vivo* applications needs to be chosen thoughtfully. It is known that mucin can interact with molecules such as integrin  $\beta 4$  [98], activating signal transduction cascades that could sometimes lead to cancer. MUC5AC is occasionally a biomarker for cancer in the stomach [99, 100] and lung [101]. This means



that increased expression [100] of MUC5AC is often associated with cancer. Of course, it is also known that the different mucin types can be upregulated in cancer in general and are therefore considered as biomarkers in almost all cases [102].

Thus, it should be clear that it is important to learn more about mucin and especially about the behavior of mucin at interfaces – how it interacts with body surfaces and molecules, which binding motifs are responsible for those interactions, what level of mucin is beneficial or detrimental. Applications of mucin can be positive on the one hand because it is an endogenous product and reduced inflammation is expected, but on the other hand, too much mucin in the body can be harmful.

## 5. Outlook

Biomedicine aims at developing new bio-inspired, yet smart and multifunctional materials for different applications such as tissue adhesives, scaffolds, and wound healing, to possess additional functions such as biodegradability, triggered detachment, transparency or, injectability. By means of the recombinant processing of molecules (e.g., repetition of special molecule-structures) or bioconjugation, molecules with multifunctional properties can be formed. Owing especially to bioconjugation, (bio-)molecules with different characteristics can be combined *via* covalent crosslinking and, in the best case, the newly created molecule shows advanced functional behavior (e.g., pH stability or reduced sensitivity to shear stress). One very common method of imparting 'stickiness' to biomolecules, for example, is to link molecules with the amino acid L-3,4-dihydroxyphenylalanine (L-DOPA), which is inspired by mussels in the sea. There are versatile reactions to connect carbohydrates such as chitosan [103] and hyaluronic acid [104] or proteins such as gelatin [105] and silk fibroin [106] to dopamine; they are based on N-(3-Dimethylaminopropyl)-N'-ethylcarbodiimide hydrochloride (EDC)/N-hydroxysuccinimide (NHS) coupling [107], Schiff base reaction of aldehyde-modified carbohydrate variants [108], and synthesis [109]. Such engineered materials can be excellent tissue adhesives with a tensile strength of up to 1 MPa [103, 110]. Once a mucin-based adhesive can be produced and achieve similar or better mechanical strengths, additional properties such as pH stability and prevention of acid diffusion through the material might provide a benefit for tissue adhesives.

In the future, however, mucin could find other medical applications beyond its use as a tissue adhesive. Cartilage and bone substitutes composed of mucin or mucin and (glyco-)protein/carbohydrate mixtures are also conceivable, since those mucin molecules are already present in natural joint fluids and could promote the ingrowth of autologous or endogenous tissue. An important requirement for a suitable material is the pore size [111] – too large pores result in the cells being flushed out of the scaffold again before possible attachment, and too small pores do not allow cells to grow into the bio-inspired material. In addition, the surface, both outside and inside the scaffold, should be rough enough for cells to adhere [112]. Furthermore, other influencing factors should be considered, such as the hardness of the matrix. Bone cells prefer scaffolds with a stiffness gradient similar to the natural template, and show accelerated proliferation rates on those materials [113]. For this reason, it is probably necessary to find a suitable interaction partner for mucin. Examples could be the carbohydrate chitosan or the protein collagen, which might form a suitable scaffold together with mucin. For this purpose, appropriate modifications and reaction conditions are required to obtain a crosslinked and mechanically stable 3D matrix. Mucin and chitosan [114] or collagen proteins [115] could be crosslinked by EDC/NHS coupling to provide a scaffold for tissue engineering. The stability of the matrix could be improved by nanoclay/hydroxyethyl methacrylate [114] or

methacrylated polyethylene glycol [115], which then forms a second network within the crosslinked collagen/mucin material by UV irradiation.

Moreover, mucins could also provide a significant advantage in wound healing. In these medical applications, it is important for the material used to be capable of stopping bleeding, have an anti-inflammatory effect, control cell attachment and proliferation, and thus enable the injured tissue to grow together [116]. There are already some interesting approaches, such as a mucin-honey hybrid material [117] or the use of transfersomes [118] from glycerol/mucin mixtures, which have a positive effect on wound healing.

In the future, mucin-based products could pave the way to a new medical standard and introduce further needed properties into medical products, such as antibacterial properties and resistance to acidic pH values. The potential of mucin might be exploited by adding it to composite materials and thus harnessing the positive properties of mucin.

## Appendix

### A. Crosslinking strategy modulates the mechanical properties of mucin nanoparticles and the governing cellular uptake mechanisms

Unpublished data

From the microscopic to the nanoscopic scale, the cellular absorption of particles is affected, for example, by their chemical composition [119], morphology [120, 121], stiffness [122-124], and cellular uptake mechanism [125]. Appropriate synthetic materials (e.g., PLGA) for particle preparation are known and characterized by biocompatibility, biodegradability, optimal drug release kinetics, and specific cell interactions [126]. However, *in vivo* applications, they show less stability in aqueous environments, and large amounts of the drug are required owing to rapid degradation in the liver *via* uptake in the blood stream [127]. Here, biological alternatives or combinations of synthetic/biological composites could remedy those problems. The shape of the particles is mostly spherical (micelles, liposomes, gold nanoparticles, niosomes [128]), but other structures are imaginable (carbon nanotubes, dendrimers [128]) when specific production techniques allow for them [129]. Studies comparing the different shapes *in vivo* would be useful but are – to date – scarce. It is known, for example, that for the transport of drug-loaded particles into the lungs, round particles with a size below 4  $\mu\text{m}$  are advantageous [130]. However, it is also discussed that particle sizes between 50 and 500 nm can be preferred, since bigger particles accumulate in organs such as the liver, whereas smaller particles (< 5 nm) are eliminated by the kidneys. Compared to size investigations, there are more studies available on how the stiffness of the particles affects their uptake by cells. Based on the results and simulations of different studies, it is speculated that stiffness/softness of the formed particles might alter the interaction/penetration with/through cell membranes [123, 124]. For the intravenous delivery of particles, it is known that stiff ones are more easily internalized by macrophages (low energy demand), whereas soft particles pass the extracellular matrix of tumor cells more efficiently. In comparison, semisoft alternatives are proven to enhance the oral uptake of drugs *via* mucosal and epithelial barriers [124]. Simulations show that amphiphilic materials penetrate membranes independent of the particle rigidity and are less deformed in this process. Hence, physical surface properties might also influence the particle transport process across membranes [123].

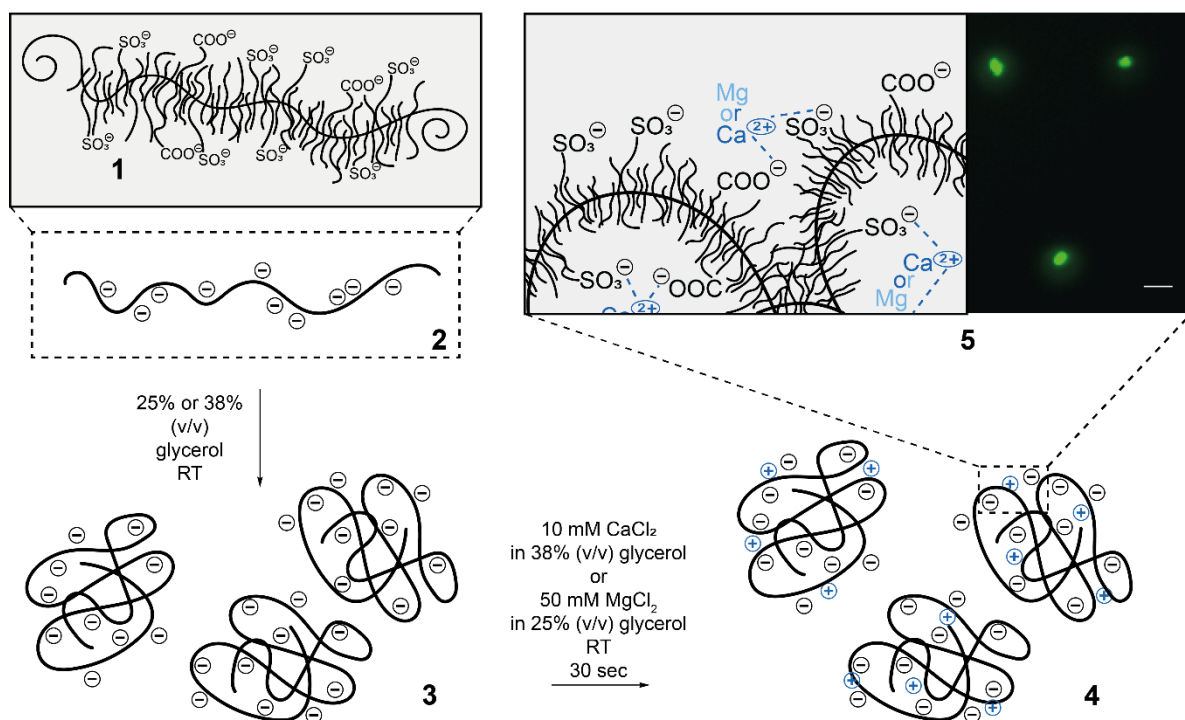
For all those issues and demands, the biomacromolecule mucin could provide a promising alternative. Example for the application of mucin as a particle is scarce in the literature. Mucosomes [131], DNA-crosslinked [19], and UV crosslinked [62] mucin particles are mentioned. All those studies show that a mixture of different (synthetic) molecules is not necessary for creating functional drug carriers, since mucin offers various binding motifs. With this wide range of functional groups on mucin, there are many possibilities to stabilize the

globular structure of mucin after a condensation step (which is needed for the formation of particles). Owing to the endogenous occurrence of the mucin carrier material compared to synthetic alternatives, the formed particles are biodegradable. In addition, nearly spherical particles are formed, which can be taken up by the cells *via* various mechanisms.

Here, different mucin particle variants – mucin-based carriers crosslinked by DNA, UV light or divalent ions – are compared to investigate in detail their stability/aggregation properties in body-related aqueous conditions. For those experiments, dynamic and electrophoretic light scattering measurements are conducted. The focus of the study is the physiological uptake mechanisms into the cells with flow cytometer experiments and, in a later step, to relate differences in the particle uptake pathways to the physical properties (stiffness) of the different mucin-based carrier materials.

### **A.1 Mucin particle characterization**

Previously, in the papers Kimna *et al.* [19] and Lutz *et al.* [62], it has been shown that mucin particles can be produced using different crosslinking principles. The most straightforward strategy to obtain stabilized mucin particles can be described by forming ionic crosslinks with divalent cations such as  $Mg^{2+}$  and  $Ca^{2+}$ . To form stable, ionically crosslinked mucin nanoparticles, one can make use of the polyanionic nature of mucins: those glycoproteins carry numerous negatively charged sialic acid groups and sulfated glycans in their core domain and some anionic amino acid side chains in their termini (**Fig. A18**). Thus, ionic cross linking of those mucins by exposing them to divalent cations should be easily possible. And indeed, fluorescence images obtained with ATTO488 labeled mucins show that, after condensing the mucins with glycerol and removing the condensing agent (as done previously in Yan *et al.* [60] and Kimna *et al.* [19]), the initially elongated glycoproteins are stabilized in their globular state when  $Ca^{2+}$  ions are present during the compaction step (**Fig. A18**).



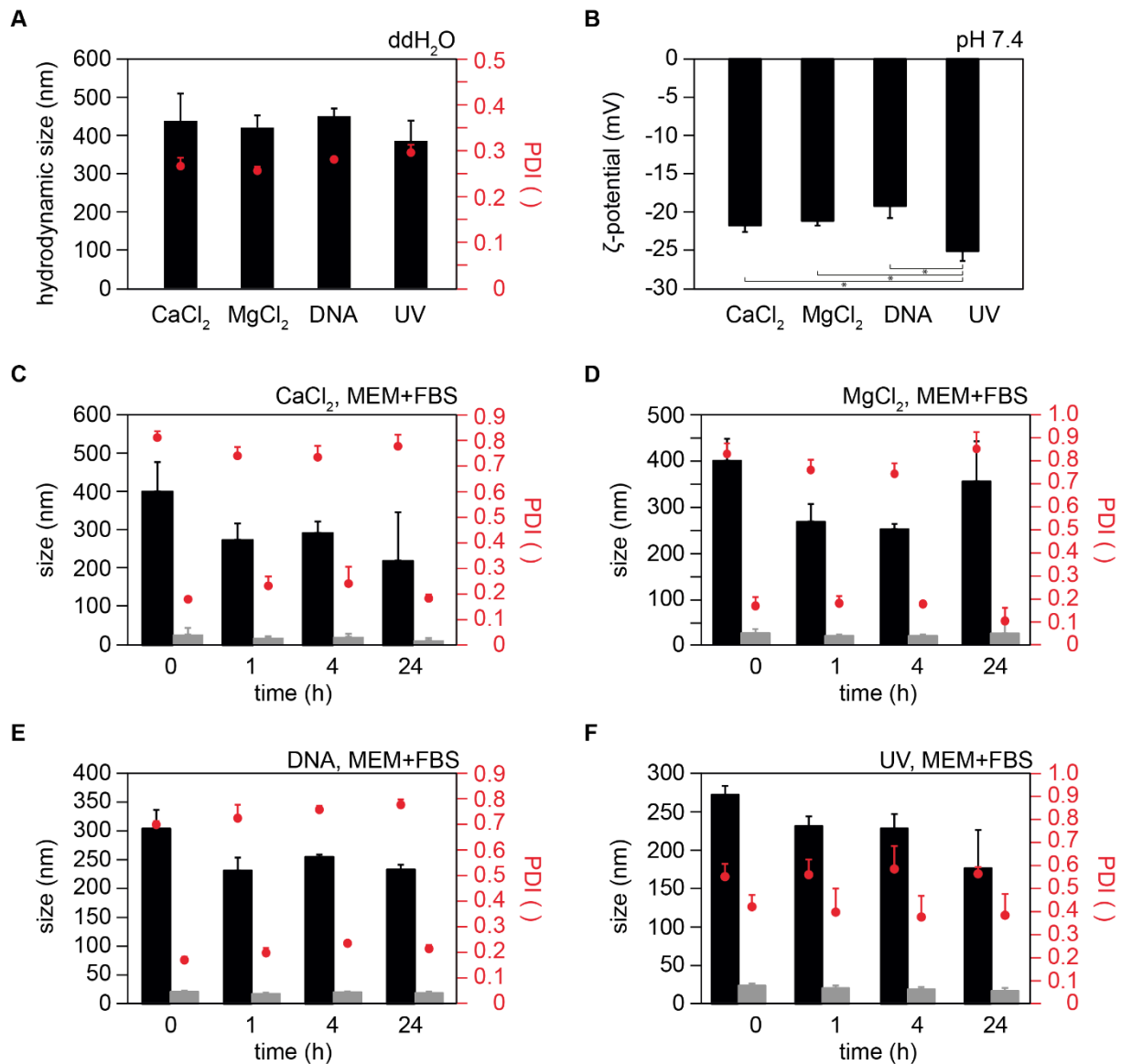
**Figure A18: Formation of ionically crosslinked mucin particles.** Mucin molecules with polyanionic character (**1**; schematic mucin glycoprotein: **2**) are condensed in glycerol (**3**) to obtain particles. Finally, the negatively charged amino acid side chains, sialic acids, and sulfate groups are electrostatically crosslinked with the help of divalent cations, such as  $Mg^{2+}$  or  $Ca^{2+}$  (**4**). After the dialysis process, stable particles are formed (**5**; on the left side: example of how such a crosslinking scenario between calcium/magnesium and different anionic motifs may face). The scale bar denotes  $20\ \mu m$ .

Next, the idea is to generate differently crosslinked mucin particles with similar size and surface parameters (e.g., surface charge) and search for differences in the cellular uptake. First, the size distribution of the different types of mucin particles ( $CaCl_2$ ,  $MgCl_2$ , DNA, and UV) is controlled by using different glycerol concentrations, as mentioned in the study of Yan *et al.* [60]. For all mucin particle types, a hydrodynamic radius of  $\sim 400\ nm$  ( $PDI = \sim 0.3$  for the whole mucin NP population) can be measured after adding 25% glycerol ( $MgCl_2$ ), 38% glycerol ( $CaCl_2$  and DNA), 75% glycerol (UV; **Fig. A19A**). Thus, one parameter is already controlled to be the same for all particles, so that the factor “size” will not influence the cellular uptake.

Another important parameter, which needs to be kept constant during the experimental study, is the charge of the particles. Based on the literature, it is known that positively charged particles could damage the cellular membrane and induce cell death. In comparison, uncharged particles are less efficiently absorbed by cells. Negatively charged particles are preferentially internalized compared to uncharged ones [64]. Since the mucin-based particles have a moderate negative zeta potential between  $-20\ mV$  and  $-25\ mV$  (**Fig. A19B**), it is assumed that those particles will not aggregate owing to the electrostatic repulsion forces between the NPs; additionally, they should be internalized by cells. Furthermore, the absolute

values for all mucin particle types are approximately the same, suggesting that this parameter should also be negligible for evoking differences in the cellular uptake mechanisms.

However, before the uptake of mucin particles is tested under *in vitro* conditions, they need to be assessed for stability [132] and aggregation [133], especially in interaction with other proteins. Such interactions or degradation processes can either change the size of the particles or result in unwanted side reactions. For this purpose, the nanoparticles are tested under biologically relevant conditions by placing the nanoparticles in a cell culture medium supplemented with 10% (v/v) FBS. Nanoparticle dispersions are then kept under sterile conditions and placed in a temperature-controlled shaking incubator (400 rpm) operating at 37°C. When the hydrodynamic size of the nanoparticles is assessed, a bimodal size distribution is observed for all the tested conditions (**Fig. A19C-F**). The first peak (which corresponds to the majority of the dispersion population) is obtained at the range of the previously determined nanoparticle size distribution, whereas the second peak is obtained at 15 nm – 20 nm. This second size distribution is attributed to the presence of serum proteins (mostly serum albumin), which are previously shown to be at this size range [134].



**Figure A19: Characterization of the different formed mucin particles.** After glycerol removal by dialysis, stable mucin particles with a size of ~400 nm are formed (A). Zeta potential measurements show the overall negative charge of the mucin particles (B) at pH 7.4. In addition, no aggregation and interaction propensity of particles with serum albumin is observed for ionically crosslinked (Ca<sup>2+</sup>, C; Mg<sup>2+</sup>, D), DNA stabilized (E), and covalently crosslinked (F) mucin particles, since only two peaks (peak 1=NPs; peak 2=FBS) are measured during incubation in a cell culture medium supplemented with 10 (v/v) % FBS at 37 °C for 24 hours. Data displayed in A-F are mean values, and error bars denote the standard deviation as obtained from three independent samples. Asterisks mark the statistical difference of the samples compared to the corresponding control (Student's t-test; significance threshold of  $p \leq 0.05$ ).

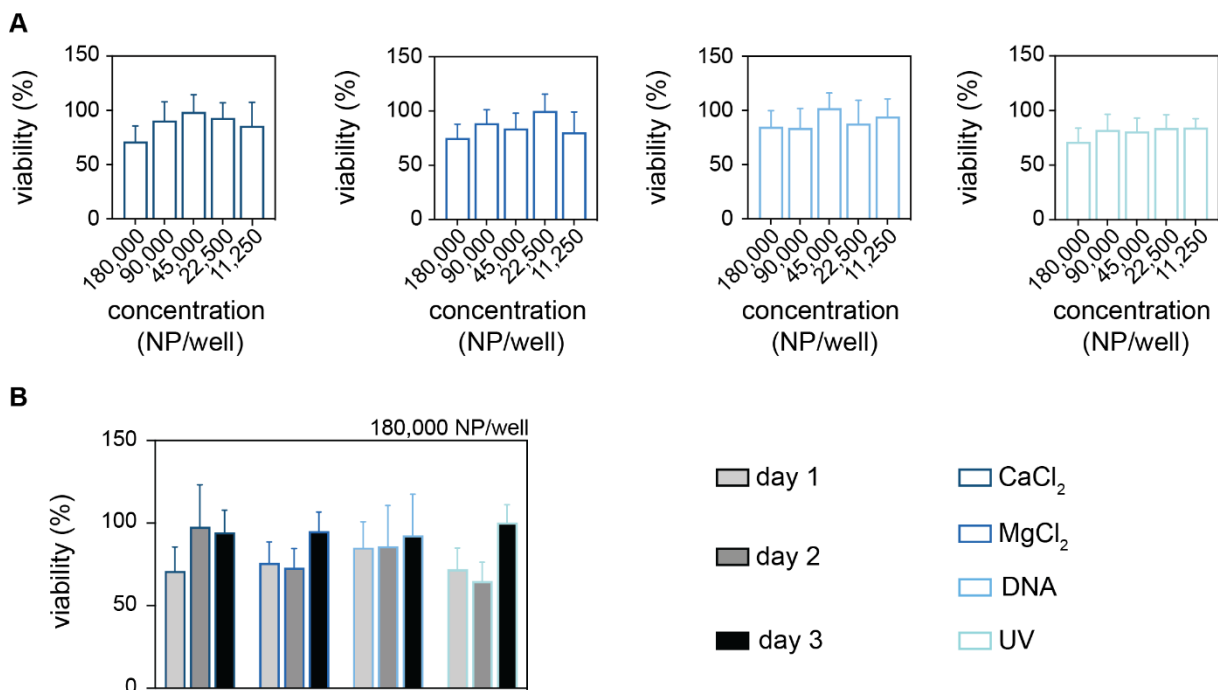
## A.2 Biocompatibility of mucin particles

Having shown that different crosslinking strategies have the potential to create stable mucin-based carrier materials (with approximately the same charge and size distribution), their absorption into human cells is studied in more detail using an *in vitro* model with HeLa cells. First, it is necessary to investigate whether the particles have a cell-toxic effect or not. For this



purpose, different particle concentrations are analyzed for two reasons: On the one hand, it needs to be assessed if high concentrations cause a loss of biocompatibility. On the other hand, a concentration has to be found that is optimal for a sufficient fluorescence signal to measure the uptake of the particles in cells *via* flow cytometer measurements.

Biocompatibility tests with HeLa cells reveal that the different types of mucin particles have hardly any inhibitory effect on cellular viability (**Fig. A20A**). All values are  $\geq 70\%$  which exceeds the limit set in the ISO standard for biocompatibility of tested medical devices and materials. Indeed, there is only a slightly lower viability of HeLa cells (which is still 70%) when exposed to the highest mucin particle concentrations. In this case, nutrient transport to the cells is expected to be limited by a gel-like layer of mucin particles that coat the cell surface. However, to show that these high mucin particle concentrations are acceptable for the cells and useable for further experiments, the 180000 particles/well (highest concentration) are tested for three days (**Fig. A20B**). Owing to the constant biocompatibility results ( $\geq 70\%$ ) after 24h, 48h, and 72h, the different mucin particle types are deemed suitable for the cellular uptake experiments.



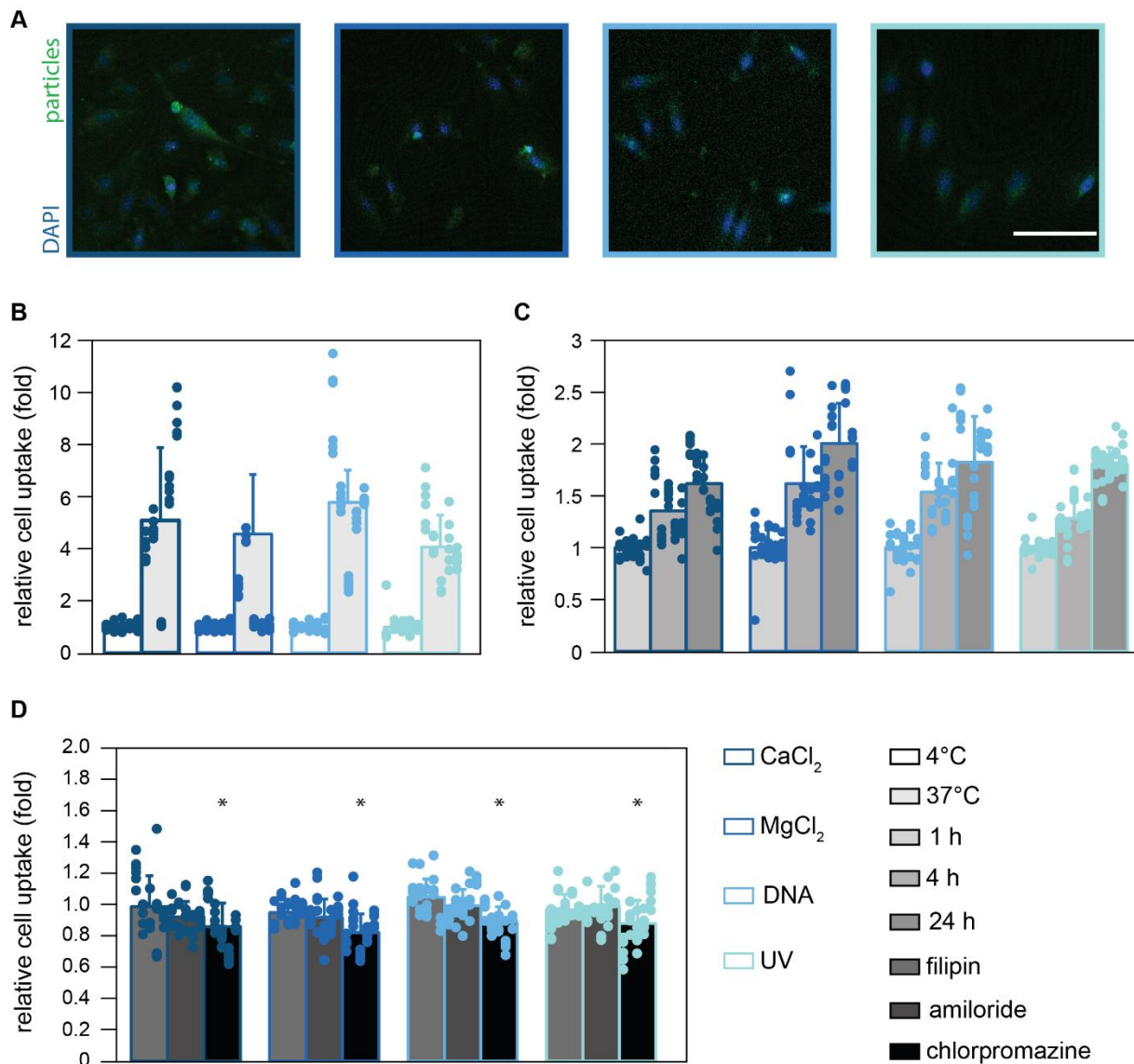
**Figure A20: Different types of mucin-based particles show biocompatible characteristics.** The formed mucin-based particles are tested regarding biocompatibility in HeLa cells. The Ca<sup>2+</sup>, Mg<sup>2+</sup>, DNA, and UV crosslinked particles are tolerated in different NP concentrations (**A**) and over a three-day period (**B**). The error bars display average values and the standard deviation determined from fifteen biological samples with five samples per condition (**A-B**).

### A.3 Cellular uptake of different types of mucin particles

Initially, the particles are used intracellularly to investigate the cellular uptake pathways of the particles. Increasing green fluorescence intensity in cells indicates internalization of the mucin

particles (**Fig. A21A**), but further investigations are needed to determine the uptake mechanism. Accordingly, the accumulation of particles under different conditions, such as changing temperature conditions, is studied by fluorescence intensity quantification through flow cytometer measurements. Specifically, it has been found that the internalization of the particles is strongly dependent on the temperature [135, 136]. At optimal body temperature conditions (37 °C), values that are up to 6-fold higher than at 4°C (**Fig. A21B**) are reached. The fact that particles are (not efficiently) taken up at low temperature can be explained as follows: the particles bind to the surface of the cells but can hardly be absorbed [137]. However, these surface-bound particles can be taken up into the cell when the temperature is increased, for example during trypsinization of the cells (sample preparation for FACS measurements). For this reason, weak absorption of particles and thus some detected fluorescence is also present at 4°C (**Fig. A21B**). The next step is to quantitatively measure the accumulation of the different mucin particle types over time (1h, 4h, 24h). The relative particle uptake increases constantly over time, which demonstrates that the particles are taken up into the HeLa cells (**Fig. A21C**).

Of interest now is whether a more detailed understanding of the microscopic mechanisms responsible for particle uptake can be obtained. For this purpose, HeLa cells are pre-incubated with different inhibitors that block either clathrin-mediated endocytosis (*via* chlorpromazine inhibitor), actin activity through macropinocytosis (*via* amiloride inhibitor) or caveolae-mediated endocytosis (*via* filipin inhibitor) [138]. According to the literature, negatively charged polyethylene glycol (PEG) particles, for example, are taken up *via* caveolae- and/or clathrin-mediated endocytosis [139]. This is consistent with our results, since all mucin particles are taken up *via* the clathrin-mediated endocytosis (**Fig. A21D**), although appearing contradictory at first glance owing to the hydrodynamic sizes from the DLS measurements (~400 nm per mucin particle type). Particles with those sizes could not normally be internalized by those mechanisms (clathrin: sizes of ~200 nm [140, 141]; caveolae: hydrodynamic sizes up to 100 nm [142]). However, the assumption that mucin particles of this size are taken up *via* macropinocytosis (particle sizes: 1-5 µm [143]) is not supported here (more data are still needed to definitely exclude this). At this point, maybe AFM measurements can help: these measurements would not only address the particle parameter stiffness, but could also provide a more precise insight into the sizes of individual particles since the resolution of AFM measurements would be much better than that of the DLS measurements.

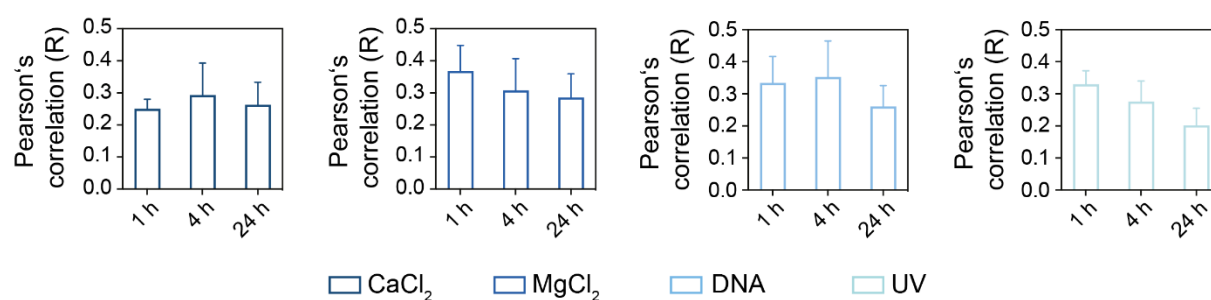


**Figure A21: Cellular internalization of different types of fluorescein-labeled mucin particles analyzed by microscope images and flow cytometer measurements.** HeLa cells (cell nuclei stained with DAPI; blue) internalize different mucin particles (green) visualized by microscope images. The scale bar displays 100  $\mu\text{m}$  and applies to all four images. The uptake of all the particle variants in HeLa cells is temperature-based (**B**), increase over time (**C**), and depends on a specific uptake pathway (**D**). The bar charts represent average values ( $\geq 27$  samples per condition) and the error bars represent the standard error of the mean. Asterisks in **D** mark the statistical difference of the samples compared to the corresponding control (Student's t-test; significance threshold of  $p \leq 0.05$ ).

#### A.4 Endosomal escape of mucin-based particles with Pearson's correlation

Since the successful internalization of particles by cells has already been proven, the focus is now on the particle release into the cytosol after uptake. This is particularly important since particles remaining in the endosomes are degraded by enzymes when the endosomes fuse with lysosomes [144]. If this happens, the drugs transported by the mucin particles cannot achieve their function. To determine the fraction of particles contained in endosomes, a

Pearson's correlation is performed [145]. In this method, the endosomes are labeled with a (red) fluorescent marker and the colocalization of (green fluorescent) particles is analyzed. Complete encapsulation of the particles into the endosomes (without any release) would be described with a Pearson's correlation coefficient of 1. Conversely, total endosomal escape of the particles would be described with a Pearson's correlation coefficient of 0. First, it is interesting to highlight that the calcium-linked particles show a Pearson's correlation coefficient of 0.2; compared with the other particles, especially at 1 h incubation time, this is somewhat lower (the other particle types: 0.3; **Fig. A22**). One reason for this could be that calcium promotes endosome rupture and thus a quick release of NPs [146]. All mucin particle types show a slight decrease in the Pearson's correlation coefficient at 4 h (or after 24 h at the latest), which indicates an endosomal escape of the particles into the cytosol.



**Figure A22: Endosomal escape of mucin-based particles from cell endosomes is presented.** The endosomal escape of the particles into the cytosol over time is assessed by the Pearson's correlation. The error bars display average values and the standard deviation determined from  $\geq$  seven analyzed cells.

Finally, after clarifying that the mucin-based particles can be internalized into cells and resist trapping in lysosomes, we failed in observing distinctive differences in the uptake mechanism between the individual mucin particle types. Basically, both endosomal escape and cellular uptake mechanisms could be influenced by differently linked mucin-based particles if, for example, parameters such as the size and stiffness vary or ions are present. Once the size (DLS measurements) and zeta potential (ELS measurements) are adjusted to an equivalent level for all mucin particle types, only the prevailing parameters such as stiffness could differ between the individual particles. It is conceivable either that all particle types have identical stiffness parameters or that other effects (e.g., other parameters not addressed here) accumulate and lead to those results.

Both, stiffness and final particle size, need to be determined by AFM measurements (more precise for size measurements than DLS) and included in the study. What is conceivable in this context is that the magnesium and/or calcium-linked mucins could lead to stiffer particles, since calcium, for example, is also used as a crosslinker in other particles and improved the elasticity [147]. Therefore, a detailed analysis of the different mucin-based particles with focus

on further parameters (*e.g.*, surface roughness) is important to determine the relevant factors influencing the cell uptake kinetics, which differ from the literature, and the endosomal escape data.

## B. Full text of publications presented in this thesis

### B.1 Bio-based and bio-inspired adhesives from animals and plants for biomedical applications

Materials Today Bio 13 (2022) 100203



Contents lists available at ScienceDirect

Materials Today Bio

journal homepage: [www.journals.elsevier.com/materials-today-bio](http://www.journals.elsevier.com/materials-today-bio)



## Bio-based and bio-inspired adhesives from animals and plants for biomedical applications



Theresa M. Lutz<sup>a,b</sup>, Ceren Kimna<sup>a,b</sup>, Angela Casini<sup>c, \*\*</sup>, Oliver Lieleg<sup>a, b, \*</sup>

<sup>a</sup> School of Engineering and Design, Department of Materials Engineering, Technical University of Munich, Boltzmannstraße 15, Garching, 85748, Germany

<sup>b</sup> Center for Protein Assemblies, Technical University of Munich, Ernst-Otto-Fischer Str. 8, Garching, 85748, Germany

<sup>c</sup> Chair of Medicinal and Bioinorganic Chemistry, Department of Chemistry, Technical University of Munich, Lichtenbergstraße 4, Garching, 85748, Germany

#### ARTICLE INFO

**Keywords:**  
Biogel  
Slime  
Adhesive  
Carbohydrate  
Protein  
Glycoprotein

#### ABSTRACT

With the “many-headed” slime mold *Physarum polycephalum* having been voted the unicellular organism of the year 2021 by the German Society of Protozoology, we are reminded that a large part of nature’s huge variety of life forms is easily overlooked – both by the general public and researchers alike. Indeed, whereas several animals such as mussels or spiders have already inspired many scientists to create novel materials with glue-like properties, there is much more to discover in the flora and fauna. Here, we provide an overview of naturally occurring slimy substances with adhesive properties and categorize them in terms of the main chemical motifs that convey their stickiness, i.e., carbohydrate-, protein-, and glycoprotein-based biological glues. Furthermore, we highlight selected recent developments in the area of material design and functionalization that aim at making use of such biological compounds for novel applications in medicine – either by conjugating adhesive motifs found in nature to biological or synthetic macromolecules or by synthetically creating (multi-)functional materials, which combine adhesive properties with additional, problem-specific (and sometimes tunable) features.

#### 1. Introduction

Nature offers an enormous range of materials that mankind has learned to analyze and use for its own benefit. For instance, the use of adhesives derived from natural sources can be traced back to the late 4th millennium BC, when hunter-gatherer tribes employed leftovers of collagenous meat to fabricate hunting weapons [1]. Since then, natural compounds with adhesive properties have played an important role in the development of societies, and typical applications range from home construction [2] to animal trapping [3].

In today’s world, many fields including the cosmetic industry [4,5], agriculture [6] and the furniture industry [7,8] make use of both, unmodified and purified bioadhesives; in addition – although being a newer addition to the spectrum of applications – modern medicine has started to employ them as well: for instance, a glue made from autologous [9] or heterologous [10] human fibrin has been developed in the 20th century, and this biomaterial typically serves as an additive to (or replacement of) sutures and staples [11,12]. Moreover, polypeptide mixtures containing

serum albumin [13], collagen [14] or gelatin [15] have been introduced and are commercially available in the form of adhesive patches or injectable hydrogels to be used in wound healing [16].

In contrast, unmodified natural glues on their own are often not suitable as a material for human usage: although they can exhibit adhesive properties when applied to tissue surfaces, their long curing time and the risk of them being contaminated with allergenic/infectious impurities can be problematic [17]. Synthetic alternatives such as cyanoacrylate glues, on the other hand, offer high mechanical strength [18]; however, their degradation products are often toxic [19]. Hence, an ideal tissue adhesive that fully satisfies both, medical and mechanical requirements, remains an important yet still unmet demand.

Even though our understanding of the main components in natural glues, conveying adhesive behavior, is continuously improving, a number of unsolved questions still holds – especially for the less-studied variants of such bio-adhesives – including: how do those different materials interact with different (natural or artificial) surfaces? How is the life time of the adhesive function determined by the chemical properties

\* Corresponding author. Technical University of Munich, School of Engineering and Design Department of Materials Engineering and Center for Protein Assemblies (CPA), Ernst-Otto-Fischer Straße 8, Garching, 85748, Germany.

\*\* Corresponding author. Technical University of Munich, Chair of Medicinal and Bioinorganic Chemistry – Department of Chemistry, Lichtenbergstraße 4, Garching, 85748, Germany.

E-mail addresses: [angela.casini@tum.de](mailto:angela.casini@tum.de) (A. Casini), [oliver.lieleg@tum.de](mailto:oliver.lieleg@tum.de) (O. Lieleg).

<https://doi.org/10.1016/j.mtbio.2022.100203>

Received 8 November 2021; Received in revised form 8 January 2022; Accepted 8 January 2022

Available online 12 January 2022

2590-0064/© 2022 The Authors. Published by Elsevier Ltd. This is an open access article under the CC BY-NC-ND license (<http://creativecommons.org/licenses/by-nc-nd/4.0/>).

of the glue/material interface and external influences such as changes in moisture content, temperature, or ionic milieu? Some species of the plant/animal kingdom even produce materials that, depending on their state of hydration, either act as an adhesive or as a lubricant [20], and the ability to recreate a material with such switchable properties for medical or technical applications would be highly desirable. In combination with ongoing advances in materials science, a more detailed understanding of the mechanisms responsible for the function of biological adhesives has recently allowed researchers to develop tailored, multifunctional glues with various properties. It is likely that biomedical applications will soon benefit from such innovations in the field of bio-derived glues. In this review, we highlight a range of natural glues/adhesives (we use those two phrases synonymously here) employed by animals and plants, and we discuss the biochemical composition of those substances as well as the chemical mechanisms and motifs conveying stickiness in the context of biomedical applications. Furthermore, we highlight selected examples of engineered, bio-derived glues that combine multiple functionalities useful for biomedical applications. Overall, the selected examples in this review article belong to one of the following three categories: materials derived directly from nature (biological adhesives), bio-based adhesives (conjugates of sticky structural motifs from bioglues with other molecules), and bio-inspired adhesives (fully synthetically produced materials that follow, at least in part, the principles of a biological template).

## 2. Naturally occurring 'sticky' compounds originating from animal and plant sources

For millions of years, evolution has allowed life to develop a broad variety of slime, gooey substances that provide animals and plants with the ability to survive, adapt, and reproduce. Sometimes, those bio-compounds serve multiple functions at the same time, *i.e.*, they can provide additional properties beyond stickiness. For instance, the secretion of the glowworm not only helps to capture prey and supports the housing-making of the larvae to the roof of the rocky cave, but also conducts light to attract prey [21]. Despite the large variations of those biological materials in terms of appearance and function, several species sometimes use such substances for similar reasons (see Fig. 1 and Table 1 for an overview). In the following, we highlight some interesting examples from the flora and fauna.

Many animals produce sticky substances to secure survival. For example, ecribellate spiders (such as *Araneus diadematus* [22]) fabricate a fine network of silk-like fibers that are coated with protein-based droplets, and this coating is paramount to capture prey [23–25]. Velvet

worms [26,27] and chameleons [28,29] produce sticky fibers or pads as weapons to bombard their victims, and sea cucumbers (*Holothuria doffeinii*) eject protein-based adhesive fibers (Cuveirian tubules) as an active defense response to attacks [30]. Similarly, certain hagfishes [31, 32] and salamanders [33] exude a sticky slime to discourage predators. Of course, slimy secretions are not only used to fight other animals: Northern spadefoot toad couples secrete a proteinous glue during mating, and this slime can bind to a wide range of materials including glass, plastics, and even Polytetrafluoroethylene (PTFE); interestingly, this glue has good sticky properties that are robust towards alterations of its hydration state or changes in the ambient temperature [34]. In addition to those survival and reproduction tasks, other biological slime such as mucus can aid locomotion processes. For instance, although appearing contradictory at first glance, snail slime combines lubricating and adhesive functions, both of which are needed for snails to move up a wall. A microscopic analysis of snail slimes reveals how this is possible: Glycoprotein-based microspheres in the slime act as a lubricant during forward movement while stiff, viscous and adhesive fibers assembled from those microspheres allow the snails to move vertically without sliding back down [35,36].

Importantly, slimy secretions are not limited to the animal kingdom; plants produce sticky substances as well and use them to adapt to difficult conditions and to increase their chance of survival. Similar to the locomotion strategy used by snails, mucopolysaccharide-based microspheres can also be found in the bio-glue used by climbing plants such as ivy (*Hedera helix*). This adhesive allows the plants to stably grow in the vertical direction while facing the sunlight as needed for efficient photosynthesis [37,38]. The carnivorous cape sundew (*Drosera capensis*) secretes an adhesive to trap and digest prey. Upon physical contact between the prey and the hairy leaves located on the plant surface, a two-step response mechanism is triggered: first, the polysaccharide-based secretions located at the tips of those hairs immobilize the prey, then, the plant closes its leaves and traps the prey to enhance the upcoming digestion phase [39]. Importantly, digestive enzymes are only produced once the aforementioned steps are concluded [40,41]. This minimizes the metabolic cost of the feeding process enabling the plant to grow in the relatively harsh environmental conditions of its natural habitat [42]. Furthermore, *Aloe vera* (*Aloe barbadensis* Miller) plants adapted to their environment with the help of slimy mucilage, producing a gel with very high water-binding capacity to protect themselves from dehydration during long drought periods [43]. Additionally, some plant species such as the hemiparasite *Phtheirospermum japonicum* secrete adhesives to attach themselves to a host

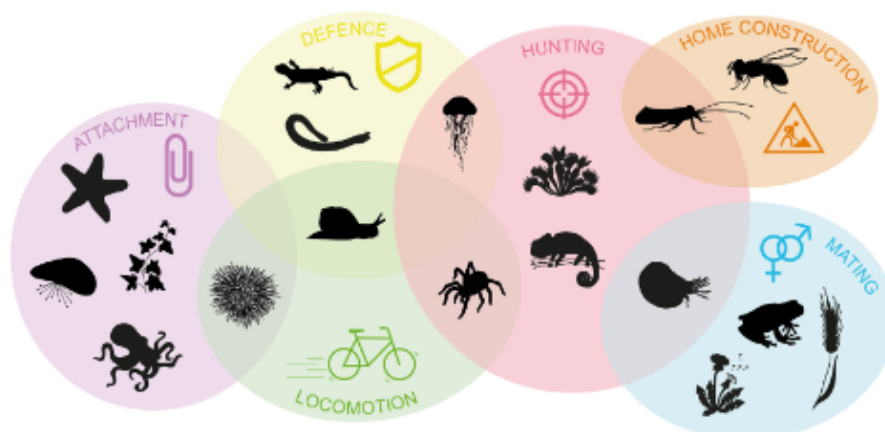


Fig. 1. Schematic representation of how slimy substances produced by animals and plants are used for attachment (purple), locomotion (green), defence (yellow), hunting (pink), home construction (orange), and mating (blue).

**Table 1**  
Specific functions fulfilled by bio-components of terrestrial (orange) or aquatic (grey) animals and plants, respectively.

common name	species	family	glue function	Ref.
burley	<i>hordium vulgare</i>	poaceae	attachment with hulls	[47]
chia	<i>savia hispanica</i>	lamiaceae	protection of germ	[48]
orchid	<i>phalaenopsis aphrodite</i>	orchidaceae	pollen spreading	[49]
philodendron	<i>syngonium podophyllum</i>	araceae	attachment	[50]
arabidopsis	<i>arabidopsis thaliana</i>	brassicales	germination	[51]
tropical milkweed	<i>asclepias curassavica</i>	apocynaceae	pollen spreading	[52]
dandelion	<i>taraxacum officinale</i>	asteraceae	pollen spreading	[53]
fly bush	<i>ruridula gorgonius</i>	ruridulaceae	prey capture	[54,55]
sundew	<i>drosera capensis</i>	droseraceae	prey capture	[42,56,57]
	<i>drosera glandulifera</i>	droseraceae		
	<i>droserophyllum lusitanicum</i>			
ivy	<i>hedera helix</i>	araliaceae	attachment	[37,38]
	<i>parthenocissus tricuspidate</i>	vitaceae		
aloe vera	<i>aloe barbadensis</i> Miller	asphodelaceae	storage, protection from desiccation	[43]
bee	<i>apis mellifera</i>	apidae	constructing nests	[58]
digger wasp	<i>anoplecter compressa</i>	anoplecteridae	egg attachment	[59]
spider	<i>latrodectus bennettii</i>	therididae	prey capture, locomotion	[60]
silkworm	<i>bombyx mori</i>	bombycidae	cocoon construction	[61–63]
velvet worm	<i>euperipatoides rowelli</i>	peripatopsidae	prey capture, defense	[64]
flatworm	<i>othelosoma impensum</i>	geoplanidae	prey capture	[65]
salamander	<i>plethodon shermani</i>	plethodontidae	defense	[33]
chameleon	<i>chamaeleo calyptratus</i>	chamaeleonidae	prey capture	[28]
snail	<i>limax maximus</i>	limacidae	locomotion	[35,36,66]
	<i>achatina fulica</i>	achatinaidae	defense	
	<i>helix aspersa</i>	helicidae		
	<i>arion subfuscus</i>	arionidae		
glowworm	<i>arachnocampa luminosa</i>	keroplatidae	prey capture	[67,68]
	<i>arachnocampa tasmaniensis</i>			
frog	<i>notaden bennettii</i>	lymnodynastidae	defense	[69]
caddisfly	<i>stenopsyche marmorata</i>	stenopsychidae	constructing nests, food capture	[70]
algae	<i>enteromorpha linza</i>	ulvaceae	attachment	[71]
fish	<i>sparus aurata</i>	sparidae	defense	[72,73]
	<i>scorpaena plumeri</i>	scorpaenidae	lubrication, osmoregulation, locomotion, recognition of individuals	
hagfish	<i>epatretus stoutii</i>	myxiniidae	defense	[31,74]
	<i>myxine glutinosa</i>			
squid	<i>sepioloides lineolata</i>	sepioidae	defense	[75,76]
	<i>sepioidarion austrinum</i>			
octopus	<i>octopus vulgaris</i>	octopodidae	lubrication, attachment	[77]
nautilus	<i>nautilus pompilius</i>	nautilidae	prey capture, mating	[78]
jellyfish	<i>aurelia coerulea</i>	ulmaridae	defense, prey capture	[79]
flatworm	<i>minona ileanae</i>	monocelididae	attachment, locomotion, feeding, defense	[80]
barnacles	<i>balanus amphitrite</i>	balanidae	attachment	[81,82]
mussel	<i>mytilus edulis</i>	mytilidae	attachment	[83,84]
starfish	<i>asterius rubens</i>	asteriidae	attachment	[85,86]
	<i>asterina gibbosa</i>	asterinidae		
sea urchin	<i>paracentrotus lividus</i>	parechinidae	attachment, locomotion	[87,88]
			food capture	
sandcastle worm	<i>sabellaria alveolata</i>	sabellariidae	attachment	[89–92]
	<i>phragmatopoma californica</i>		protection	
	<i>phragmatopoma caudata</i>		constructing tubular homes/sand reefs	
	<i>phragmatopoma californica</i>			

plant, from which they extract water and nutrients [44]. Similarly, mistletoe (*Phoradendron californicum*) plants produce seeds that are coated with the carbohydrate-based adhesive viscin [45], which solidifies on tree branches and thus anchors the mistletoe plant on the host to ensure nutrient supply [46].

This brief overview of selected examples already indicates that animal and plant-based secretions can serve different purposes and can even combine multiple functions at the same time. Therefore, it is not surprising that their composition and microstructure can be quite complex. In the following section, we attempt a categorization of the different biological adhesives used by animals and plants in terms of the chemical motifs that convey adhesive properties.

### 3. Chemistry of biological adhesives and their biomedical applications

Animal and plant adhesives are ubiquitously composed of few fundamental components, i.e., polypeptides, polysaccharides, polyphenols, lipids, and molecular combinations thereof (such as

glycoproteins, phenolic polysaccharides, and proteoglycans). Indeed, the multi-component nature of these biological adhesives seems to be responsible for both, their specificity and their ability to interact with a diverse range of surfaces. Specifically, certain functional groups of amino acids or sugar motifs and their chemical complementarity to the addressed surfaces play an important role. Interestingly, although covalent interactions can easily establish strong binding affinity and high surface-specificity, it is typically a combination of supramolecular non-covalent interactions, i.e., electrostatic interactions, hydrogen bonds, hydrophobic interactions, and van der Waals forces, that govern adhesive mechanisms in nature. In addition, there are other non-covalent interactions such as cation- $\pi$  complexation, metal coordination, and  $\pi$ - $\pi$  interactions, which act synergistically with the covalent and non-covalent interactions mentioned above. A prominent example for such a synergistic effect of different interaction types is the wet adhesion process of mussels [93]. Here, self-polymerization (by means of covalent interactions) of the catechol-containing amino acid 3,4-dihydroxy phenylalanine (DOPA) allows for the formation of stiff fibers, and hydrogen bonds established by the hydroxyl groups of DOPA are



responsible for the reversible, yet strong underwater adhesion of those fibers to surfaces. Furthermore, divalent and trivalent ions (such as  $Zn^{2+}$  or  $Fe^{3+}$ ) from the aqueous environment offer improved cohesion of the bio-adhesive by creating a coordination metal-chelate complex with the catechol groups of DOPA [94].

From the microscopic to the nanoscopic scale, biological adhesives typically exhibit complex hierarchical structures, which are relevant for the function of the adhesive as well as for its chemical composition. Specifically, the architecture of bio-glues influences the spatial distribution of adhesive moieties and how they get in contact with a surface; therefore, having an important impact on the adhesion forces that can be developed. For instance, by altering the loading angle on fibrillar arrays on their footpads, Geckos can maximize the interfacial adhesion to vertical surfaces via van der Waals forces, which allows them to easily climb vertical and inverted surfaces [95]. Another interesting example is the rock hyrax, a small mammal living in the rocky landscapes of southern Africa [96]. This animal employs a combination of capillary forces forming at the footpad/surface interface and a carbohydrate-based glue secreted from its pads to walk up walls [97]. In general, the mechanisms of bioadhesion may be classified into four main categories, including intermolecular bonding (between the chemical structures at the interface), electrostatic forces, chain entanglement, and mechanical interlocking [98]. The overall adhesive effect is often the result of more than one of these mechanisms. Chain entanglement occurs at the interface between the bioadhesive and the surface, where sticky macromolecules bind and form an interpenetrated layer of about 1–100 nm. In contrast, mechanical interlocking arises from an infiltration of the adhesive into surface defects and orifices.

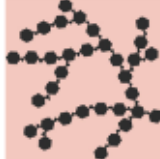

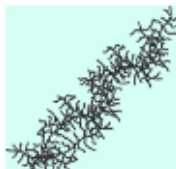
From a biochemical perspective, proteins and starch (a polymeric carbohydrate comprising lots of glucose units joined by glycosidic bonds) are very prominent representatives of natural adhesives – yet there are numerous other examples as well. On the basis of their chemical structure, adhesive substances can be categorized into eight major families: nucleic acids, polyesters, polyisoprenoids, polyoxoesters, polythioesters, polyphenols, polysaccharides, and polypeptides/proteins [99]. In this chapter, we will mostly focus on the chemical principles governing the adhesive properties of carbohydrate-based (e.g., starch, alginate, cellulose derivatives, and gums), protein-based (e.g., collagen, blood, and vegetable proteins), and glycoprotein-based bio-glues. In this context, selected examples of how these substances have been used to design materials for medical applications are introduced and discussed (Table 2).

### 3.1. Carbohydrate-based natural adhesives

Polysaccharides or polymeric carbohydrates are among the most common components of natural adhesives. They are composed of long chains of linear and branched monosaccharide units bound together by different glycosidic bonds (Fig. 2a and b). Owing to the numerous structural variants possible, polysaccharides constitute a highly diverse class of biological macromolecules. Their ability to act as an adhesive originates from two properties: first, the high density of polar functional groups on the polysaccharide chain and, second, the high molecular weight of the biomacromolecules. Indeed, the former is crucial for good adhesion to substrates with a high surface energy such as wood or metals, where a well-matching polarity of the adhesive molecule is required. The latter allows the biopolymer to assume specific secondary structures (helical, sheet, or spiral conformation) which are stabilized by non-covalent interactions (Fig. 2c), and such secondary structures improve the mechanical strength of carbohydrate-based adhesives by boosting their cohesive properties.

Accordingly, the adhesion and cohesion behavior of carbohydrates can be modulated by their architecture, and both properties can be further enhanced by further chemical modifications that either increase the density of functional groups (such as hydroxyl groups) or introduce additional moieties (e.g., carboxylate residues). Importantly, this strategy

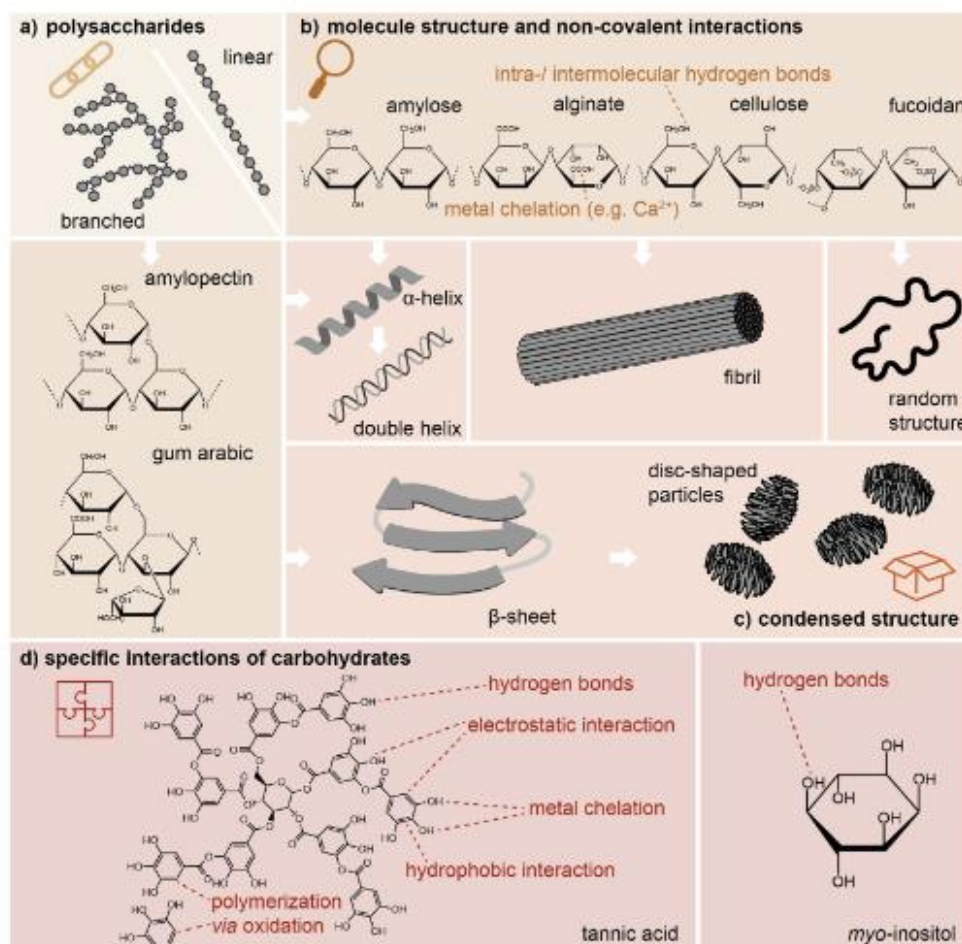
**Table 2**  
Overview of the three classes of biomolecular adhesives discussed in more detail in this review.

molecular classes	examples from nature	adhesives created via a modification of biomolecules	Ref.
carbohydrates 	starch, alginate, cellulose, fucoidan, tannic acid, acacia gum, sundew mucilage (myo-inositol), pollenkit (viscin), propolis	propionylated amylose	[100]
		boronic acid conjugated alginate	[101]
		cellulose-phenylboronic acid conjugate	[102]
		alginate crosslinked by organosilane	[103]
		tannic acid as crosslinker for chitosan	[104]
proteins 	egg albumen, zein, fibrin, various proteins from mussel, sandcastle worm, frog, salamander, silkworm, starfish, velvet worm, glowworm	cross-linking by functionalization with methacrylate groups	[105]
		phenols conjugated with zein	[106]
		composite of fibrin and hydroxyapatite	[107, 108]
		complex formation of DOPA with cations	[94]
		synthesized structure motifs of sandcastle adhesives	[109]
Glycoproteins 	from ivy, snail, spider, hagfish, jellyfish	Nb-IR proteins enzymatically cross-linked (frog)	[110]
		adhesive composed of sericin, gelatine and, carboxymethyl-chitosan	[111]
		adhesive Sfp1f proteins (starfish)	[112]
		collagen-derived scaffold with ivy nanoparticles	[113]
		snail slime-coated gold nanoparticles	[114]
		mucin/keratin scaffolds (hagfish) electrospun (glyco-) protein scaffold of jellyfish mucin	[115, 116]

can not only enhance non-covalent inter- and intra-chain interactions, but may also create new target sites for further chemical functionalization and cross-linking that, in turn, can improve the adhesive properties (Fig. 2d). In this section, we discuss a number of carbohydrate-based adhesives more in detail.

Starch is a polysaccharide produced by plants (e.g., cereals, potatoes, fruits, and others) and used to store the chemical energy produced during photosynthesis. Starch is a mix of amylose (a linear  $\alpha$ -(1,4)-D-glucan) and amylopectin (an  $\alpha$ -(1,4)-D-glucan that is highly branched via  $\alpha$ -(1-6) linkages [117]). Inter- and intramolecular hydrogen bonds between the hydroxyl groups of amylose molecules enable the formation of double-helices (Fig. 2c) and create a stably packed hydrophobic construct.

A similar double-helix structure can be observed for amylopectin; however, the branched structure of this polysaccharide entails a less structured packing of the helices leading to crystalline/amorphous constructions [118]. Owing to the multiple possibilities to interact with water molecules via hydrogen bonds, starch-rich compositions exhibit gel-like consistency. As a pharmacological excipient, starch is used as a



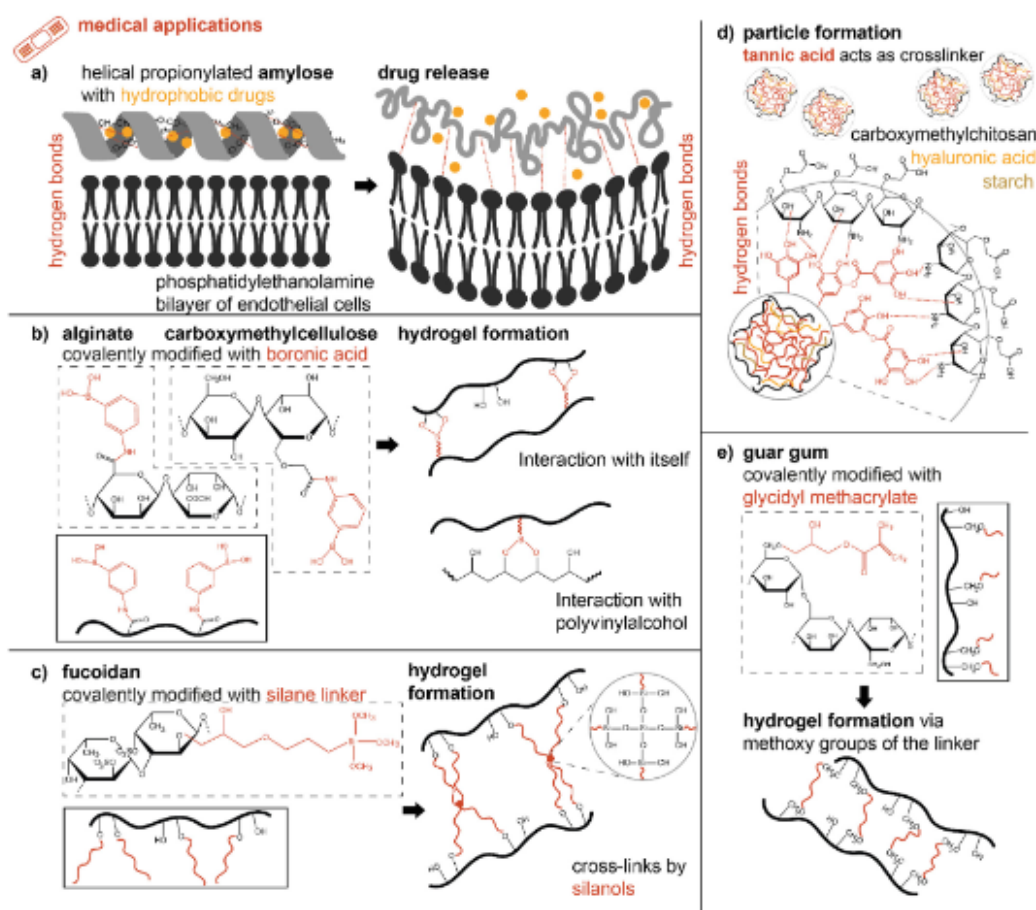
**Fig. 2.** Schematic overview of different molecular structures found in carbohydrate-based adhesives; the drawings visualize how different carbohydrate monomers are linked into polysaccharides (a, b) and how they can adopt specific (supramolecular) conformations (c). In addition, selected motifs are depicted that allow for a plethora of covalent and non-covalent interactions (d), which are relevant for the adhesion and cohesion behavior of this type of biological glues.

binder and disintegrant in solid dosage formulations. For instance, tablets containing starch as a disintegrating agent can release their active ingredients (e.g., ibuprofen) once in contact with the stomach fluid [119, 120]. In addition, starch-including films and 3D scaffolds have shown promising properties for applications in wound healing [121] and bone tissue engineering [122–124].

Interestingly, corn-derived amylose has been used as a smart carrier matrix for the delivery of hydrophobic drugs across the blood-brain barrier [100]. In detail, the amylose macromolecules were propionylated to maintain the typical helical structure, enabling efficient drug (propofol) loading into amylose nanoclusters (diameter  $\sim 55$  nm). Once the propofol-loaded amylose clusters reached the blood-brain barrier, competitive binding of amino groups of phospholipids located in the cellular membrane induced unfold of the carrier into a random coil structure, triggering drug release (Fig. 3a).

The second example we discuss here is alginate (or alginic acid), a polysaccharide found in marine brown algae (*phaeophyceae*) and soil bacteria [125]. This polysaccharide is composed of  $\alpha$ -L-guluronic and  $\beta$ -D-mannuronic acid monomers that are covalently linked via 1, 4'-glycosidic bonds (Fig. 2b) [126]. Two properties are responsible for the rigid structure of alginates: the six-membered sugar rings and the

limited ability to rotate around the glycosidic bonds [127]. Due to electrostatic repulsion acting between the individual monosaccharides, the polysaccharide chain is linear in shape. There are different variants of alginates in which the links between the two sugar subunits differ – and they can also comprise blocks of multiple repetitions of guluronic and mannuronic acid. Alginates are known for their high water-binding capacity (which can be up to  $\sim 300$  times of their molecular weight [126]) and their ability to form gel-like structures in the presence of divalent cations (such as  $\text{Ca}^{2+}$ ) establishing coordination bonds with flexible guluronic acid units [127]. In the latter case, two alginate strands can dimerize by forming a so-called egg-box geometry through coordination of four carboxyl groups [127,128]. Instead, alginate sequence segments with highly conserved mannuronic acid regions predominantly interact via hydrogen bonds [128]. Due to their biocompatibility and ease of processing, alginates are widely used to fabricate biomaterials with different functionalities including adhesive materials [129]. For instance, Hong et al. [101] developed a boronic acid conjugated alginate hydrogel (alginate-BA) (Fig. 3b) with high stretchability and self-healing as well as adhesive properties. Here, owing to the presence of alginate *cis*-diol and boronic acid hydroxyl groups, intra- and interpolymeric interactions could be established leading to the formation of a viscoelastic hydrogel.



**Fig. 3.** Selected examples of modified carbohydrates used for drug storage and release (a, d) as well as hydrogel formation (b, c, e). The underlying molecular forces are based on a combination of covalent and non-covalent interactions between the carbohydrates, which occur either directly between the polysaccharides or are mediated via linker motifs that are grafted to the biomacromolecules. Adapted from Ref. [100] (a) [101,102], (b) [103], (c) [104], (d).

Importantly, such alginate-BA hydrogels showed better mucosal adhesion performance *in vivo* compared to an unmodified alginate solution.

At variance with alginate, the other main macromolecular component of brown algae, cellulose, is composed of D-glucose units only, whereby the monosaccharides are connected by 1,4'- $\beta$ -glycosidic bonds (Fig. 2b) to form long, linear polysaccharide chains of up to  $\sim 1000$  monomers [130]. The functional hydroxyl groups of the glucose molecules establish inter- and intramolecular hydrogen bonds which allow individual cellulose strands to self-assemble: first, into fibrils, then into microfibrils and finally into parallel-packed crystal structures. The most common crystal structures found in algae are Ia (one-chain triclinic structure) and Ib (two-chain monoclinic structure), respectively [131]. To be applicable in medical applications, cellulose has to be chemically modified – otherwise, the charge profile and orientation of the cellulose fibrils limits their biocompatibility [132]. For example, carboxylated cellulose nanofibers in combination with the antibacterial macromolecule chitosan were shown to be suitable for wound tissue applications *in vivo* [133]. Moreover, cellulose has been used as a nanofiller in adhesive material formulations to enhance their mechanical properties [134]; however, it rarely serves as a base material in adhesive hydrogels. Recently, An et al. [102] developed such a cellulose-based adhesive hydrogel with self-healing properties. To this aim, a cellulose-phenylboronic acid

conjugate was synthesized through a condensation reaction and fabricated hydrogels via dynamic boronic ester cross-linking (Fig. 3b). In detail, the hydrogel was formed by mixing phenylboronic acid-derivatized cellulose and polyvinyl alcohol (PVA) at room temperature. In addition to showing a good adhesion behavior to skin tissue, these hydrogels were biocompatible, and could release a loaded drug in a sustained manner. Interestingly, since large amount of carboxyl groups were ionized at neutral pH, the resulting ionic hydrogel also showed electrical conductivity, which could be beneficial for different applications.

In addition to producing carbohydrate-based natural compounds (such as alginate and cellulose), multicellular algae also use sticky (fucose-based) polysaccharides in their cell walls [135]. These so-called fucoidans are based on linearly linked  $\alpha$ -L-fucans, featuring sulfate moieties on the C2 or C4 position (Fig. 2b) [136] and form randomly structured motifs in nature [137]. However, with certain modifications (e.g., functionalized with methacrylic anhydride residues), the fucoidans can bind to each other through covalent interactions leading to the formation of stable particles with excellent biocompatibility [138] as well as other advantages including antiviral [139,140] and antibacterial [141, 142] effects. These properties were suggested to originate from molecular interactions of fucoidans with viral enzymes (such as

neuraminidase), an inhibition of the viral replication process, or with bacterial membrane proteins [139–142].

When fucoidan-containing hydrogels are desired, combinations with other carbohydrates such as alginate are typically reported in the literature [143]. However, fucoidans were also proposed to be useable in their unmodified form as a single-component network [144]. Ferreira et al. [103] described a fucoidan gel that makes use of an organosilane precursor: first, the silane linker covalently binds to the hydroxyl groups of the carbohydrates and, in a second step, the hydrolyzed groups on the silanol moiety act as a cross-linker boosting the cohesive properties of the gel (Fig. 3c). Importantly, with this type of chemical modification, the negatively charged sulfate groups on the fucoidans are still accessible and allow for the biosorption or sensing of cations such as  $\text{Cu}^{2+}$  or  $\text{Zn}^{2+}$  [103].

Carbohydrates represent the majority of metabolic products produced by plants, also phytochemicals such as carotenoids and polyphenols are created as primary and secondary metabolites. Selected polyphenols play an important role in the function of carbohydrate-based glue as they can act as mediators responsible for surface anchoring and/or allow carbohydrates to interact with each other to form dense macromolecular complexes. Among these mediators, tannic acid (TA) is an important example. This high molecular weight polyphenolic substance contains a central carbohydrate core that is esterified by phenolic acids (Fig. 2c) [145]. In nature, tannins are abundantly found in fruits and seeds of vascular plants. Due to their high antioxidant activity and ability to interact with other biological macromolecules, tannins have been widely used as cross-linkers in biomaterial applications. Owing to the numerous phenolic hydroxyl groups acting as hydrogen-bond donors, TA can readily connect macromolecular chains in polymer matrices – especially in those containing carboxyl groups that can serve as hydrogen-bond acceptors. In addition, its polyphenolic structure renders TA prone to hydrophobic interactions with other aromatic rings through  $\pi$ - $\pi$  stacking (Fig. 2c). Finally, TA can also act as a multidentate ligand to coordinate metal ions (e.g.,  $\text{Fe}^{3+}$ ) to form pentagonal ring chelates [146]. Owing to their broad range of attractive properties, polyphenols are very interesting building blocks for the development of biomaterials: they are abundant in nature, biocompatible, biodegradable, can self-assemble into polymeric constructs and cross-link other (macro)molecules. Indeed, in recent years, a variety of TA-based biomaterials with different physical/chemical properties were produced, including hydrogels [146, 147]. For instance, cross-linking of carboxymethylated chitosan with TA enabled the fabrication of gel-like particles into which hyaluronic acid molecules, promoting wound-healing processes, were integrated (Fig. 3d) [104]. Through synergistic effect of these biomaterials, the process of wound healing could be precisely regulated. When applied to a tissue, the obtained microparticles interact with the tissue surface via their hydroxyl groups, providing a 3D network structure for the proliferation and migration of the cells. Over time, due to water adsorption, the microparticles disintegrate releasing their components and forming a protective macromolecular barrier towards the external environment. For example, the incorporated TA interacts with blood components and improves the blood clotting process [104]. Relying on a similar strategy using TA as a ‘molecular glue’ to promote hydrogel formation, Deng et al. [148] developed an agarose-TA hydrogel for the treatment of skin wounds. Here, the TA-cross-linked agarose network was further stabilized by the coordination with  $\text{Fe}^{3+}$  ions between the hydroxyl groups of the TA molecules. The resulting gel showed excellent biocompatibility, outstanding photothermal effect, as well as anti-bacterial and wound healing properties *in vivo* [148].

Some plants secrete complex mixtures of polysaccharides and glycoproteins (so-called gums) as a defensive protection mechanism against insects and molds. One well-known example from this class of biogluers is the acacia gum (gum Arabic; carbohydrates: 90 wt%, glycoproteins: 10 wt%) [149]; whereby, the carbohydrate monomers (i.e., galactose, arabinose, rhamnose, and glucuronic acid) form branched polysaccharides. The main core of the construct is established by

galactopyranosyl units connected via  $\beta$ -1,3-linkages, and 1,6-linkages add more galactopyranosyl units as well as  $\alpha$ -L-arabinofuranosyl,  $\alpha$ -L-rhamnopyranosyl,  $\beta$ -D-glucuronopyranosyl and 4-O-methyl- $\beta$ -D-glucopyranosyl groups (Fig. 2b) to the macromolecule. These carbohydrate-based constructs exhibit  $\beta$ -sheets and  $\beta$ -turns generated via hydrogen bonds between the functional groups on the sugar residues and tend to form disk-shaped particles with diameters of 20 nm and thicknesses up to 2 nm [150]. Gums have already been widely applied in medicine – mostly as films [151] or as a hydrogel matrix to deliver enzymes or active pharmaceutical ingredients [105,152,153]. However, in their unmodified form, gum-based gels are water-soluble. Therefore, gums are typically either functionalized (e.g., with methacrylate groups [105]; Fig. 3e) and/or cross-linked (e.g., chemically or via UV radiation [154]) to create stable networks.

As an example of aggressively used biogluers, secretions of carnivorous plants (such as *Drosera* spp.), typically exhibiting a chemical composition rich in carbohydrates or resins, are worth mentioning. Among those plants, Cape sundew (*Drosera capensis*) and its viscoelastic mucilaginous secretions have been investigated in detail. A chemical analysis showed that this mucilage mainly contains large molecular weight polysaccharides (around 65%), digestive enzymes, mineral salts, and secondary metabolites (that exhibit antimicrobial activity). The polysaccharide mixture is mainly composed of L-arabinose, D-xylose, D-galactose, D-mannose, and D-glucuronic acid [155]. In addition, the carbohydrate myo-inositol (Fig. 2c), which carries multiple hydroxyl groups, is present in the adhesive in high amounts (at a myo-inositol:carbohydrate monomer ratio of 1:2) and acts as a cross-linker likely by establishing hydrogen bonds that enable the formation of a gel-like network [42].

Huang et al. [156] revealed that carboxyl groups of glucuronic acid molecules can be electrostatically cross-linked with divalent cations – a mechanism, which is similar to the chelate formation of alginate. The resulting particles form gel-like nano-networks with high water binding capacity and are thought to confer adhesiveness to the polysaccharide network [156]. Initial experiments proved the mucilage of sundew to be biocompatible, and successfully support the adhesion and differentiation of neural cells *in vitro* [157].

Another area from biology where stickiness is highly important is the pollination process of plants. Here, the adhesive coating ‘pollenkit’ allows pollen grains to bind to the stigma of flowers via capillary bridges and van der Waals forces [158]. In addition (as required for successful cross-pollination), the pollens also stick to hydrophobic locations of the insect body which enables their transportation between plants. The coat of those pollen grains contains viscin, a glue substance that comprises triterpenes, fatty acids, and carbohydrates. Viscin fibers connect distinct grains to each other and facilitate their adhesion to the insect body. Moreover, viscin plays an important role in the survival of semi-parasitic plants as it facilitates their attachment to host plants [159]. In 2019, Horbelt et al. reported that a hydrogel-like viscin-based substance secreted by the European mistletoe *Viscum album* contains self-assembled, stiff cellulosic fibers which are generated in response to mechanical load; here, viscin forms reversible cross-links during the drying process of the crystalline cellulose fibers (which can be rehydrated again by humidity) [160]. It was shown that viscin mainly contains neutral sugars (such as xylose and arabinose) as well as substantial amounts of uronic acid and proteins [45,161]. However, the main component responsible for the adhesive properties of viscin has not been identified yet, and medical applications of this biological adhesive have not been developed either.

To conclude the section on carbohydrate-based adhesive, we discuss a second example from the world of insects, namely propolis. This multi-component glue produced by bees contains a range of different plant secretions including mucilage, gums, and resins and is mixed with salivary and enzymatic secretions of the bee. Propolis comprises more than 300 different components including flavonoids, phenolic acids, terpenoids, esters, phenolic aldehydes, and ketones, and its particular

composition depends on the collection time and region [162,163]. This variable composition of propolis makes it very difficult to identify the key molecular components conveying stickiness and to elucidate the distinct physicochemical interactions between the different molecules. Owing to the presence of aromatic compounds (mainly aromatic acids such as cinnamic acid) and flavonoids, propolis exhibits anti-inflammatory [164] and strong anti-bacterial activity against both, gram-positive and gram-negative bacteria [165]. The latter property makes propolis an interesting component for applications in medicine. For instance, it has been used as a film to heal recurrent oral aphthous ulcers [166], as a coating on dentin to prevent caries [167], and as an active anti-bacterial component in wound healing scaffolds [168,169]. Moreover, its polyphenol-rich composition provides propolis with antioxidant, anti-fungal, and antiseptic properties [170]. Interestingly, other molecular components extracted from propolis (such as combinations of biochanin A, formononetin, and liquiritigenin [171]) or isolated prenylated components, which are further modified to obtain specific molecules (e.g., artemillin C and baccharin modified with amino acids) have shown anti-proliferative effects against breast cancer cells *in vitro* [172]. Finally, propolis components/extracts were suggested to be beneficial in combating other diseases such as diabetes [173] and obesity [174,175].

### 3.2. Protein-based natural adhesives

The second main class of biological adhesives belongs to the group of proteins, whereby amino acid side chains patterned with different functional groups are responsible for establishing various intrinsic properties of the adhesive material and enable specific interactions with different surfaces. For instance, carboxylic acids, amines, and thiol groups can create both strong electrostatic interactions and disulfide bridges, thus, generating electrostatic and covalent linkages, respectively. Moreover, most polypeptides make use of secondary or tertiary structures, and the corresponding spatial arrangements of the amino acid chains can also be relevant for the adhesive properties of a protein-based glue to different substrates.

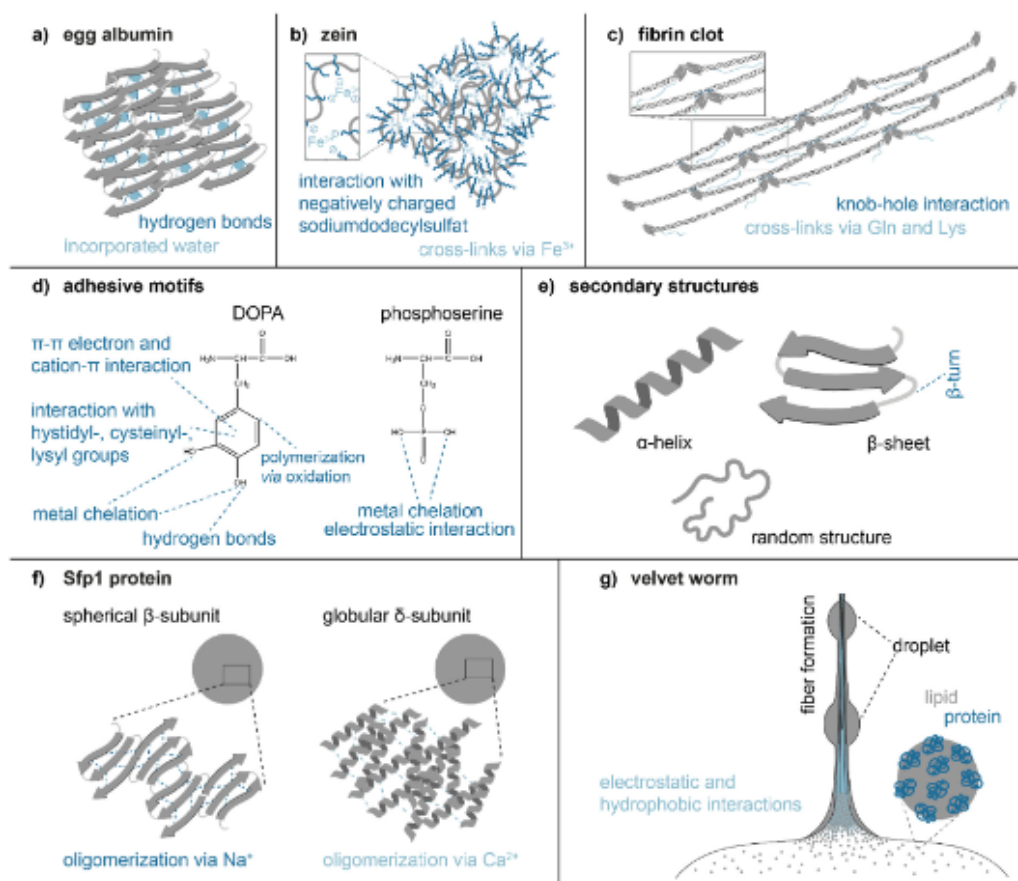
A good example for this dual concept of combined chemical and structural contributions to stickiness is found in egg albumen. The latter has a protein content of approximately 10% (ovalbumin, conalbumin, ovomucoid, and globulins). It should be noted that, while egg albumin sticky properties are not part of the natural function of this substance, they can serve as a biocompatible and mechanically strong alternative to synthetic medical adhesives. For example, its main component, egg albumin, was shown to be a promising component for materials in soft tissue regeneration [176] and wound closure processes [177]. In terms of mechanistic principles contributing to the adhesive properties of albumin, Xu et al. [178] demonstrated that egg albumin can aggregate via hydrogen bonds during air-drying [178]. When the secondary structures of such dried albumins were analyzed, it was found that the fraction of  $\beta$ -sheets and  $\beta$ -turns increased dramatically during the drying process, which confirmed the high degree of inter-/intramolecular hydrogen bonds present in this material (Fig. 4a). Indeed, such a modulation of the cohesive/adhesive properties driven by conformational changes of polypeptide chains may very well be a more general trend for protein-based adhesives. Furthermore, there are also disulfide bonds in egg albumin that – once activated with reducing agents – can react with free thiol groups of binding partners. Importantly, due to its advantages such as ease in processing, biocompatibility, and low cost, egg albumin can be considered as a very promising material for future medical glue formulations.

Similar to egg albumin, also the adhesive properties of the maize protein zein are driven by structural rearrangements. Zein is the major storage protein of maize and accounts for 50–70% of the total seed protein content [181]. The protein sequence of zein is dominated by nonpolar, neutral amino acids including proline, leucine, alanine, and glutamine; this particular chemical composition indicates that binding of zein to other objects strongly relies – at least in part – on hydrophobic

interactions. This feature makes zein a very interesting compound for eco-friendly, water-resistant adhesive formulations. However, when denaturing molecules carrying negative charges (e.g., sodium dodecyl sulfate) are added to a zein solution, they trigger a conformational change in the zein structure; as a consequence, polar groups become accessible and can engage in hydrogen bonds – a mechanism that boosts the adhesion behavior of zein (Fig. 4b) [179]. Up to now, studies leveraging the sticky properties of zein-based formulations were mostly limited to industrial applications such as glass and wood binding [182, 183]. For example, when zein solutions (dissolved in organic solvents) were applied to wood surfaces, they could strongly bind woodblocks during the tested time interval, i.e., for 24 h [184]. Although their potential use in drug delivery [185] and tissue engineering [186] has been tested recently, employing zein-based formulations as an inexpensive, antibacterial, and biocompatible medical adhesive is an underexplored area. Yet, recent studies make use of phenolic components [106], chelating ions [179], and nanocomposite formulations [187] to improve the bonding strength of zein-based materials. A zein modification conducted by Schmidt et al. [106] could open up new fields of application: by conjugating different plant phenolics to zein proteins, a material with improved underwater adhesion capacity was obtained, and this might pave the way for the development of novel wet-adhesive materials [106].

One of the most established biological adhesives used in healthcare is the fibrin sealant, a material which is often derived from animals [10] or humans [188]. Physiologically, the sticky properties of this polypeptide are required during the last part of the coagulation cascade: as soon as the enzyme thrombin cleaves selected subunits of the (inactive) precursor protein fibrinogen, active fibrin monomers are generated. These monomers assemble laterally and/or longitudinally via specific sequences and form protofibrils by weak knob-hole interactions (acting between Gly-Pro-Arg sequences and Trp-Trp, Trp-Asn and Phe-Tyr combinations) [180]. This first self-assembly step creates a “soft fibrin clot”, which is modified during an additional cross-linking step conducted by a transglutaminase (factor XIII). This enzyme catalyzes the covalent cross-linking of lysine and glutamate side chains and thus, stabilizes the fibrin network (Fig. 4c) [189]. For most medical applications, a hybrid material is used where the fibrin sealant and the converting enzyme stem from different organisms. A prominent example of such a hybrid sealant combines buffalo-based (*Bubalus bubalis*) fibrinogen with a serine protease purified from snake venom (*Crotalus durissus terrificus*); the latter taking over the role of thrombin [10]. Such heterologous fibrin adhesives are used for sealing damaged tissues [190,191] as well as for peripheral nerve repair [192]. Furthermore, in combination with hydroxyapatite, they can be employed as bone scaffolds to support fracture healing processes [107,108].

Another famous example of a biological, peptide-based adhesive can be found at the tips of threads mussels use to stick to stones, wood, or ships: here, three ‘foot proteins’ named Mfp-3 (up to 7 kDa), Mfp-5 (8.9 kDa) [94] and Mfp-6 (~11.6 kDa) [193] are located, and the key amino acid present in those proteins is L-3,4-dihydroxyphenylalanine (L-DOPA; Fig. 4d), obtained by post-translational hydroxylation of tyrosine [94]. L-DOPA can engage in a variety of interactions with other molecules and surfaces, and those include covalent and non-covalent bonds. It has been postulated that the hydroxyl groups of DOPA can chemisorb to polar surfaces via hydrogen bonds. Under oxidizing or alkaline conditions, DOPA promotes a cross-linking reaction of the adhesive mussel proteins through the oxidation of catechol hydroxyl groups to ortho-quinone, and this is important for the cohesive and bulk elastic properties of the adhesive. DOPA is also able to form coordination bonds with metal ions from the marine environment, and it can establish cation- $\pi$  complexation and  $\pi$ - $\pi$  electron stacking interactions, as well as covalent bonds with the nucleophilic amino acid side chains of, e.g., cysteine, lysine, or tyrosine [94]. The strong adhesion of the mussel proteins to a broad range of surfaces (even under wet conditions) has inspired many researchers to mimic this unique strategy. Owing to the high versatility, good biocompatibility, and broad adhesion behavior DOPA-functionalization



**Fig. 4.** Selected examples of natural modified polypeptides with adhesive properties. In addition, examples of typical molecular motifs responsible for the adhesion of egg albumin (a), zein (b), fibrin (c), starfish (f), and velvet worm (g) proteins are depicted together with relevant adhesive motifs (d) and secondary structures (e) that are typical for polypeptide-based biogluers. Adapted from Ref. [178] (a) [179], (b) [180], (c) [64], (g).

of polymers has become the gold standard for improving their adhesion properties. Indeed, numerous studies on  $\iota$ -DOPA-modified polymers (and smaller molecules) are available in the literature [194–197]. In most cases, this DOPA-modification conveys adhesive properties to the conjugate without interfering with other molecular characteristics of the target molecule. Applications of such  $\iota$ -DOPA-conjugated polymers can be found in a wide range of medical scenarios such as wound healing [198,199], drug delivery for cancer therapy [200–202], bone regeneration [203], and coatings on stents for cardiovascular-related diseases [204,205]. Additionally, many DOPA-based adhesives take advantage of the self-polymerization propensity of DOPA [206] and its ability to form complexes with divalent and trivalent cations – both of which enhances the mechanical properties of the adhesive [94].

Similar to mussels, also sandcastle worms (e.g. *Sabellaria alveolata*) make use of an adhesive that contains  $\iota$ -DOPA [207]. However, the sandcastle worm is a marine species, which forms its shell by gluing together silica-based sand grains in an environment saturated with calcium [91]. In addition to the intrinsically sticky molecule  $\iota$ -DOPA, a chromatographic analysis of this glue revealed the presence of another class of important biomolecules, namely phosphoserines (Fig. 4d) [208]. In detail, the proteins identified to be responsible for adhesion are Sa-1, Sa-2, Sa-3A, Sa-3B (each <22 kDa), and those polypeptides differ in terms of their amino acid composition. The first two proteins are cationic

at pH 8.2, and the most abundant amino acids are Gly, Ala, Tyr (functionalized via a hydroxylation) and Lys; in contrast, the other two proteins exhibit an anionic character and comprise mostly (~75%) serines (functionalized via phosphorylation) [207]. Moreover, enzymes such as tyrosinase and peroxidase are detected in the glue of sandcastle worms and are thought to link several  $\iota$ -DOPA containing proteins with each other to increase the cohesive and adhesive properties of the glue [91]. In addition to this enzyme-dependent process, phosphoserine side chains are also able to bind to each other through electrostatic interactions mediated by divalent cations such as  $Ca^{2+}$  and  $Mg^{2+}$  [207]. To understand the molecular interactions of the different components of ‘sandcastle glue’ in more detail and to explore its potential as a medical adhesive for bone fractures, Shao et al. [109] synthesized polyacrylate glue protein analogs of the natural glue featuring phosphate (to mimic phosphoserine), primary amine, and catechol (to resemble the  $\iota$ -DOPA structure) sidechains with molar ratios similar to the native proteins. Importantly, this sandcastle worm-inspired adhesive system formed liquid polymer coacervates [209] and responded to changes in pH [109]. Specifically, at acidic pH, the generated molecular complexes were found to be condensed, whereas, at pH values around 8, the negatively charged molecules were subjected to repulsive forces which entailed more extended structures. In this state, binding of divalent cations (such as  $Ca^{2+}$ ) could facilitate the formation of adhesive structures. Based on

these results, the authors suggested that the two-component adhesive could be very promising for applications in bone regeneration, where calcium ions are physiologically present at sufficiently high concentrations.

Different from the adhesion mechanism employed by mussels and sandcastle worms, the stickiness of frog secretions cannot be rationalized by specific (modified) amino acids. For instance, the secretion of *Notaden bennetti* frogs is best described as a cocktail of proteins, and the two best studied and most abundant proteins in this secretion are Nb-1R (350–500 kDa) and Nb-3 (up to 250 kDa). The most frequent amino acids in this protein mix are Gly (15.8 mol%), Pro (8.8 mol%), Glu/Gln (14.1 mol%) and, Hyp (4.6 mol%); however, its carbohydrate content is negligibly small (<1%). Based on current understanding, the self-assembly process of this frog slime is mainly governed by hydrophobic protein-protein interactions. In addition, Nb-1R contains cysteines that allow these molecules to oligomerize via the formation of covalent disulfide bonds, and electrostatic interactions are thought to occur in the protein mixture as well. Interestingly, in-depth investigations performed with purified frog adhesives revealed that those frog slime proteins contain 36%  $\beta$ -sheets and 64% random coils (Fig. 4e) [210]. Moreover, the same study revealed that the naturally occurring frog glue features a mixture of nanoparticles (diameters: 12.5–25 nm), microspheres (diameters: 150–200 nm), and bundled filaments. The different structures are all likely to contribute to the mechanical properties of the adhesive by providing a tensile strength of ~78 kPa and a mean adhesion force of 1.9 nN. In an *ex vivo* study, the frog adhesive was applied to a tendon-bone-suture interface to facilitate rotator cuff repair [211]. The obtained results showed that, in contrast to conventional sutures, the application of the frog glue to this tissue interface improved the stability of the latter towards fracture [211]. Also purified frog slime components, i.e., Nb-1R proteins, can be converted into an adhesive material – yet this requires a suitable chemical modification, e.g., via enzymatic cross-linking by horseradish peroxidase. Afterward, a soft hydrogel with satisfactory biocompatibility *in vivo* is obtained [110].

Two other examples of sticky protein cocktails found in nature are the slime of salamanders (*Plethodon shermani*) and the glue-coated cocoons of *Bombyx mori*. In the first mixture, proteins (with molecular weights of up to 170 kDa) comprise 77% of the total dry weight, and the carbohydrate content was reported to be 0.4% only [33]. As polar and non-polar amino acids are present in very similar amounts, this secretion has an amphiphilic character. Chromatographic analyses showed that positively charged amino acids are almost twice as frequent than anionic ones, which is why this salamander secretion is overall positively charged. Intriguingly, *L-DOPA* is present in this mixture as well; however, it only accounts for 0.1% of the total protein content [33]. From a structural point of view, the salamander bioglue is almost completely constituted by  $\alpha$ -helices,  $\beta$ -sheets, and  $\beta$ -turns (Fig. 4e), which seem to be relevant to the self-assembly process of this protein mixture into hydrogels (by providing intra- and intermolecular hydrogen bonds). Glue cohesion as well as adhesion to hydrophobic surfaces (such as fat tissue) is thought to be facilitated via hydrophobic interactions between certain amino acids from the slime and the tissue constituents. However, other interactions such as cation- $\pi$  interactions with the amino acid benzene rings (of tyrosine and phenylalanine) and the substrate scaffold are likely to contribute as well. In a medical setting, salamander slime demonstrated excellent biocompatibility and could promote wound closure as well as re-epithelization [212].

The second protein mixture we discuss here is found in the cocoons of *Bombyx mori* and is composed of the fiber protein fibroin and the glue-like protein sericin. Fibroin is a hydrophobic, high molecular weight glycoprotein comprising a heavy chain (~390 kDa), light chains (~26 kDa), and fibrohexamers [213]. Sericin, on the other hand, is a globular protein that is soluble in hot water, contains several polypeptides that self-assemble into  $\beta$ -sheets (Fig. 4e) and holds the fibroin fibers together [214]. Owing to its cytocompatibility, anti-inflammatory, antibacterial and antioxidant activity, sericin has found its way into the field of skin

and neural tissue engineering [215,216]. However, to meet the mechanical demands of those applications, sericin has to be combined with other macromolecules. For instance, Liang et al. proposed an adhesive comprising a mixture of gelatin, sericin, and carboxymethyl chitosan for medical applications: and indeed, this bio-derived adhesive showed a slightly higher bond strength (2.5 N) compared to commercially used alpha-cyanoacrylate glues (2.3 N) [111].

Starfish use a similar strategy for attachment as other echinoderms such as sea urchins [217], i.e., a set of two secretions, where the first one helps the podia glue to the substrate whereas the second one is used to detach the podia by denaturing the glue. Here, the glue is protein-based (20.6%) with a moderate content of lipids (5.6%) and carbohydrates (8%) [218]. Here, the most abundant amino acids are Asp/Asn, Glu/Gln, and Gly, and there are also low amounts of cysteines [218]. In the starfish exudate, Hennebert et al. [219] detected a total of 34 proteins with adhesive characteristics. Among those 34 proteins, the best-characterized one with sticky properties is Sfp1 (MW: 426 kDa) [219]. This protein possesses four subunits ( $\alpha$ ,  $\beta$ ,  $\gamma$  and  $\delta$ ) and certain binding sites for interactions with other proteins (e.g., a trypsin inhibitor-like, cysteine rich domain), carbohydrates (e.g., a galactose-binding, lectin domain), and metals (e.g., via a calcium-binding, EGF-like domain) [220]. Lefevre et al. [220] generated recombinantly the  $\delta$ -subunit and sections of the  $\beta$ -subunit to investigate the assembly process of the starfish proteins. The results showed that the  $\beta$ -subunit predominantly forms  $\beta$ -sheets and builds spherical nanostructures in the presence of  $\text{Na}^+$  ions (which are abundantly present in sea water). In contrast, the  $\delta$ -subunit mainly comprises  $\alpha$ -helices, and interacts predominantly with  $\text{Ca}^{2+}$  ions to form globular structures (Fig. 4f). Here, ionic interactions are not only responsible for the formation of particles with sizes up to 250 nm, but also promote adhesion to different surfaces such as glass and polystyrene. One common feature both subunits share is their ability to oligomerize, and this process is partially supported by disulfide bridges [220]. Moreover, Hennebert et al. [221] observed that proteoglycans and a very small amount of glycoproteins (carrying oligosaccharides assembled from, e.g., N-acetylgalactosamine, fucose, sialic acid and mannose), such as Sfp-290 and Sfp-210 contribute to the adhesion to surfaces as well, i.e., via hydrogen bonds and electrostatic interactions [221]. Due to their strong adhesion behavior and favorable mechanical properties, starfish proteins were already considered as adhesives for (medical) applications. Lefevre et al. [112] investigated the adhesion properties of recombinant Sfp1  $\delta$ - and  $\beta$ -subunits to glass surfaces in the presence of different salt concentrations. For the  $\beta$ -subunit, an adhesion strength ranging from ~90 pN (without salt) to ~200 pN (with 450 mM NaCl) was reported with the corresponding elastic moduli of ~300 MPa and ~500 MPa, respectively. Interestingly, mixing both subunits gave rise to a material with both lower adhesion strength and weaker elastic moduli (~70 pN and ~10 MPa, respectively) [112].

Lastly, we present here two additional bioglue examples that, although showing promising properties, have not yet been tested in a medical setting. The first system, the slime secreted by velvet worms (*Euperipatoides rowelli*), contains globular particles consisting of lipid droplets and folded proteins. During mechanical loading, these small particles (<100 nm) self-assemble into fibrils – a process that is facilitated by electrostatic and hydrophobic interactions (Fig. 4g). On a molecular level, those binding events are mostly brought about by amino acids; the slime proteins comprise high amounts of charged amino acids (aspartate, histidine and glutamic acid) and prolines. Moreover, post-translational modifications (phosphorylations) of amino acids and divalent cations (e.g.,  $\text{Ca}^{2+}$ ,  $\text{Mg}^{2+}$ ) boost the cohesion of the fibrils. However, as those stabilizing forces are non-covalent, the fibers degrade easily, and new fibers or particles can be produced from old, disintegrated ones. Once dehydrated, the fibers form a material with a stiffness of 4–5 GPa that interacts strongly with anionic surfaces (e.g., glass); in contrast, positively charged polymer surfaces prevent binding interactions, and neutral surfaces allow for moderate attractive forces only [26,64].

The second slime system yet to be exploited in medical applications is

the adhesive used by glowworms. Most species of the genus *Arachnocampa* secrete slimy substances that contain urea, ethanol and high amounts of the modified amino acid 1-methylhistidine [21]. However, although the composition of glowworm slime has been deciphered, it is poorly understood how the adhesion and cohesion characteristics of the adhesive are established by the different components. Byern et al. [222] proposed that urea could be relevant for the adhesive properties of the secretion. In fact, the silk-like filaments found in the glowworm secretion are composed of  $\beta$ -sheets, which are covered with ellipsoidal droplets. An X-ray Photoelectron Spectroscopy (XPS) analysis showed that these droplets contain urea, which might cohesively coordinate peptides into an adhesive material [222]. Moreover, those droplets interact with hydrophobic substrates, and upon drying they rearrange into parallel fibers and crystals. In addition, Wolff et al. [21] suggested that the interactions between glowworm adhesive and various substrates are regulated by the amino acid composition of the peptides and rely on van der Waals interactions, hydrogen bonds and, putatively, also covalent interactions [21]. Probably, more detailed research is required to clarify the mode of action by which the glowworm adhesive sticks to different objects. Nevertheless, this example nicely illustrates that there are even more biological examples of sticky protein secretions to discover in the flora and fauna.

### 3.3. Glycoprotein-based natural adhesives

As a third class of bioglues, adhesives comprising glycoproteins are discussed in this section. As already indicated by the name, those macromolecules combine chemical structural motifs of carbohydrates and proteins, which leads to even more complex molecular interactions.

Plants such as the English ivy (*Hedera helix*) make use of glycoproteins for attachment purposes. The yellowish ivy mucilage contains spherical nanoparticles, which are mainly composed of pectic polysaccharides and arabinogalactan proteins, i.e., a superfamily of hydroxyproline-rich glycoproteins localized in the extracellular matrix. In a study by Huang et al. [38], the adhesion of ivy roots to surfaces was rationalized by calcium-aided electrostatic interactions between carboxyl groups of uronic acid residues on the pectic substances within the proteinaceous matrix, which favors hardening of the adhesive and the formation of a film. Furthermore, the submicron size of the mucilage particles facilitates attachment to irregular surfaces (Fig. 5a) [38]. Recent studies showed that collagen-derived scaffolds enriched with ivy nanoparticles support the regeneration of smooth muscle cells *in vitro* [113]. Moreover, the negatively charged ivy nanoparticles themselves were proposed as carriers to deliver cationic drugs [113]. Indeed, electrostatic and hydrophobic interactions between the carrier matrix and the active pharmaceutical ingredient (i.e., doxorubicin hydrochloride) facilitated drug loading and enhanced the intracellular delivery efficiency compared to freely administered drugs.

Another interesting example from this class of bioglues is given by the glycoprotein-based microspheres secreted by snails, which combine hydrophobic and hydrophilic domains. In the presence of calcium carbonate, glycan motifs stabilize the structure of the microspheres via electrostatic interactions: upon binding of calcium carbonate to the microspheres, the sticky network forms elastic fibers with  $\alpha$ -helix structural motifs at their termini. Amazingly, these fibrous structures allow snails to stick and move simultaneously; here, rapidly formed, small microspheres help during horizontal crawling (Fig. 5b) [36].

From a physical point of view, this mechanism is based on the complex viscoelastic behavior of the snail slime, which acts as a viscoelastic liquid at high shear stresses (occurring during locomotion), but returns into a viscoelastic solid/adhesive once the shear stress level is reduced [224]. Owing to its sticky, gel-like properties, it is not surprising that snail slime (in combination with gelatine) can be well manufactured into adhesive patches (for potential skin applications) that allow for embedding drugs with, e.g., antifungal properties [225]. Similarly, improved closure capabilities of damaged cell layers and anti-inflammatory effects

of gold nanoparticles coated with snail slime were observed *in vitro* and indicate the high potential of snail slime for tissue regeneration [114].

As the first species of insects making use of the family of bioglues, we highlight spiders (especially the family *Araneidae*), which produce seven different silk fibers [226], whose main components are spidroin proteins with molecular weights of up to 350 kDa [227]. The most important type of adhesive silk is the flagelliform, which is coated with glue droplets after the spinning process. The termini of the silk fiber protein contains up to  $\sim$ 130 amino acids with anionic (C-terminus) and cationic (N-terminus) properties [226]; the core domain (up to 200 amino acids) exhibits Gly-rich and/or Ala-rich sections [227]. The structure of those terminal motifs changes from  $\alpha$ -helical (at acidic pH) to  $\beta$ -sheets (at alkaline pH); in contrast, the core domain forms  $\beta$ -sheets,  $\beta$ -turns and helical structures independent of pH. By means of electrostatic interactions with each other, the termini stabilize the fiber structure, and silk fibers show high toughness (up to  $280 \text{ MJ m}^{-3}$ ) and strength (up to 1.3 GPa) [226]. The adhesive droplets covering the flagelliform silk fibers contain two key molecules: the glycoproteins ASG1 and ASG2. The elastic ASG2 protein provides linkages between the silk fiber and the adhesive protein ASG1. ASG1, in turn, exhibits specific binding motifs such as a chitin-binding domain, and thus, enables efficient insect attachment [25]. The binding domain of ASG1 consists of a  $\beta$ -sheet structure stabilized by cysteines, and aromatic amino acids such as Phe and Trp provide additional interactions with the insect bodies. Moreover, polar amino acids such as Ser, Gln, Glu, Thr and Pro are frequently found as well and form a mucin-like domain. The presence of prolines is responsible for the  $\beta$ -turns in the structure and ensures accessibility of Thr and Ser for glycosylation. ASG2 contains glycosylated domains as well and forms  $\beta$ -sheets,  $\beta$ -turns, and random coils. The most common amino acids in ASG2 are Ser, Gly and Val; in addition, Cys is highly conserved and enables these molecules to oligomerize via disulfide bridges (Fig. 5c) [228]. Opell et al. [229] investigated the mechanical properties of the spider glue droplets and determined toughness values of  $1\text{--}5 \text{ MJ m}^{-3}$  and Young's moduli of  $0.02\text{--}2 \text{ MPa}$  [229]. For medical applications, recombinant silk fibers have shown to be better suitable than glue droplets and were used to form biocompatible membranes for tissue engineering, e.g., for the treatment of epidermal wound defects [230].

The last set of glycoprotein-based glues we discuss here is taken from the world of marine animals. The adhesion strategy used by hagfishes (*Myxine glutinosa*) is based on cross-linked networks made from mucin-like glycoproteins and protein filaments. Mucins are large glycoproteins that are ubiquitous in the animal kingdom, where they are involved in a broad range of functions such as providing anti-bacterial/anti-viral barriers, lubricity and tissue hydration [231,232]. The chemical structure of the mucin glycoproteins can be simply described as the protein core domain where serine and threonine residues are connected to branched oligosaccharides through O-glycosidic bonds [233]. Hagfish mucins are composed of 80% protein and 20% carbohydrates; they can oligomerize via the formation of disulfide bridges, and sulfonated structures in the mucin carbohydrates convey an overall negative charge to this glycoprotein [234]. In the concentrated exudate of the hagfish, disc-shaped vesicles with sizes of a few microns are present (Fig. 5d) [234]. Here, the protein keratin can be found in small quantities, forming filaments with lengths of up to 30  $\mu\text{m}$  and which, after secretion, undergoes a structural transformation from  $\alpha$ -helical into  $\beta$ -sheet-like structures [32,235]. The latter motifs form interconnected networks, which are stabilized by divalent calcium ions and attract large amounts of water – eventually leading to hydrogel formation [223]. On a molecular scale, it was observed that specific Leu-Asp-Val-sequences in the keratin threads can interact with cellular integrins to promote cell adhesion and proliferation, whereas the carbohydrate motifs of the mucin glycoproteins can support cell attachment by interacting with cell adhesion molecules such as selectins and lectins [115]. Indeed, mucin/keratin scaffolds promote the attachment, growth and formation of organoids and tissues *in vitro* [115]. Thus, the hagfish exudate was put forward as a potential substance for tissue engineering.



Our final example of a natural adhesive from the animal world is the jellyfish sticky-material. Jellyfish species such as *Rhopilema esculentum* contain two adhesive components: the protein collagen (predominantly collagen I) and a mucilaginous slime containing the glycoprotein qniumucin. The structure of jellyfish collagen is best described as helical fibres composed of three elongated  $\alpha$ -chains. Here, the most abundant amino acids are glycine and (4-hydroxy)prolin, and the individual collagen chains are stabilized into a triple-helix via hydrogen bonds [236]. There are many examples of how jellyfish collagens can be used in medical applications – either in their pristine form (e.g., as a scaffolding material) or in combination with other molecules such as agarose or alginate (to promote the regeneration of bone [237,238] or cartilage [239] tissue). Furthermore, jellyfish collagens were used as a sensor for thrombin detection [240] and to create microparticles to transport therapeutics [241]. The second highly conserved macromolecule of jellyfish secretions is the glycoprotein qniumucin, whose function is still poorly understood. The protein structure includes monomers (with molecular weights up to 150 kDa) to which a range of carbohydrates (mostly N-acetyl-D-galactosamines, arabinose and galactose [242]) are attached; overall, glycans contribute a third of the molecular weight of qniumucin.

Owing to repulsive forces originating from the long glycan chains, qniumucins assume a stretched, linear configuration [233]. The individual qniumucins can then oligomerize and form a network. Differently from mammalian mucins, where oligomerization is established via cysteines [231], the content of cysteines in qniumucin is comparably low [242]. Based on NMR investigations, Uzawa et al. [233] suggested that, in qniumucins, oligomerization might occur as a result of N-acetyl-D-galactosamines interacting with threonine residues (Fig. 5e) [233]. Owing to the difficulty of artificially reproducing mucins by biotechnological methods or chemical synthesis, so far, only mucins extracted from natural sources are available for commercial purposes [243]. Typically, mucins are known for their structural heterogeneity; however, qniumucins are more homogeneous, and the level of purity achieved during their isolation is high. Thus, this marine-based molecule could help in the production of customized mucins for biomedical applications. In recent years, the jellyfish adhesive compounds (both qniumucin and collagen) started to set foot in the field of healthcare applications as they were tested as components of materials for wound healing. *In vivo* experiments have demonstrated that electrospun (glyco-)protein scaffolds made from jellyfish mucins promote cardiac cell proliferation without causing any

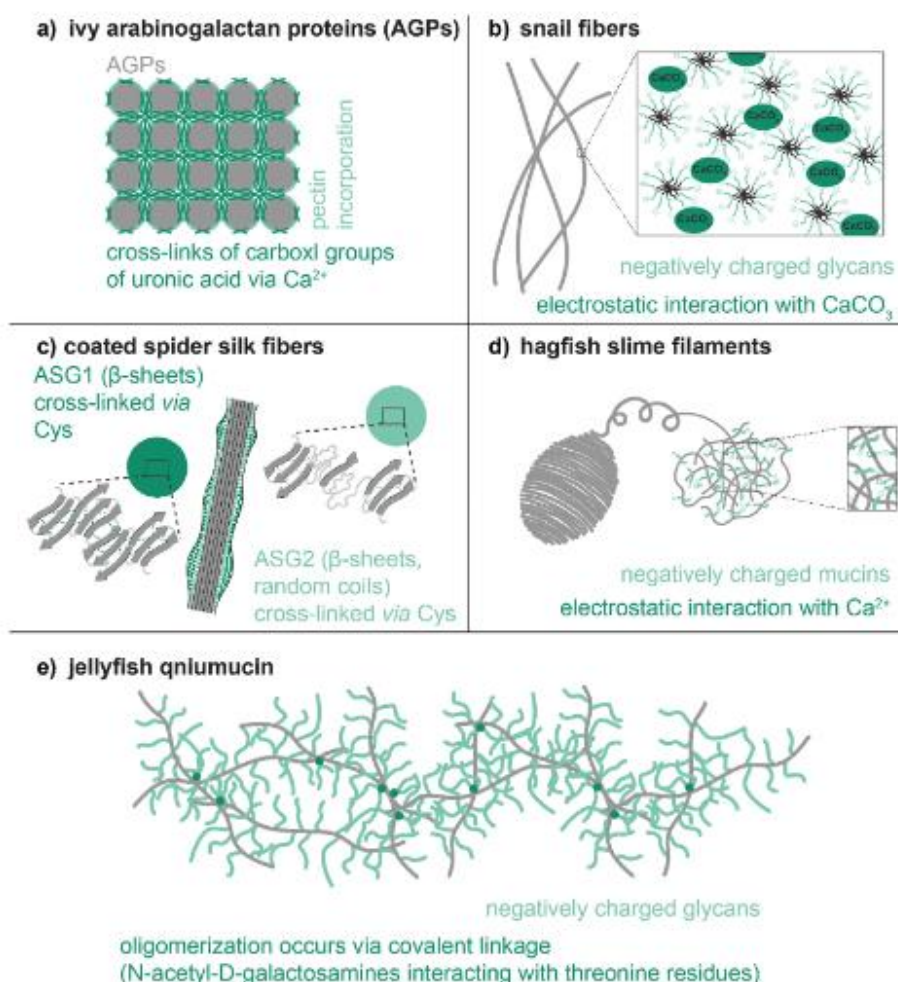


Fig. 5. Selected examples of glycoprotein-based adhesives are those produced by ivy (a), snails (b), spiders (c), hagfish (d), and jellyfish (e). Owing to the biochemical complexity of this class of bioglues, a broad variety of different structures and a range of physicochemical interactions between the glue components and target objects are possible. Adapted from Ref. [38] (a) [36], (b) [223], (d).

cytotoxic effects [116].

#### 4. Bio-inspired and smart, multifunctional adhesives

Owing to their good biocompatibility, biodegradability and (possibly) bioabsorption properties, bio-derived materials are very interesting candidates for medical purposes. However, to obtain an ideal medical adhesive (Fig. 6), numerous additional requirements such as good mechanical stability, proper adhesion, and a sufficiently short curing time must be met simultaneously without adversely affecting other material's physicochemical or biological functions. In addition, the final material needs to undergo a sterilization process, whose harsh conditions are not tolerated by most biological macromolecules [244,245]. Finally, even when all those criteria are fulfilled, the material must be able to deal with the challenges of the *in vivo* environment, including shear forces, liquid flux, pH and temperature changes, as well as enzymatic attack. Of course, the detailed conditions the adhesive material must withstand vary with both the medical condition and the place of material application. In a nutshell, it is unlikely that a given biological material can provide all of those properties at the same time, which is why synthetic alternatives using naturally occurring molecular motifs can be a better solution for this multifaceted optimization problem.

Thanks to recent advances in the field of material science, it is now possible to exert an advanced level of control over the structure and composition of a bio-hybrid material; this control allows scientists not only to tune and adjust selected material characteristics and functionalities, but also to trigger desired "on-demand" actions/properties that the material only activates when pre-defined scenarios occur. In this final section of the review article, we discuss selected examples of both, (semi-)synthetic as well as smart/multifunctional, '3rd generation adhesives', the latter of which can have a broad range of properties in addition to being sticky (Table 3).

##### 4.1. Adhesives using recombinant molecules

Compared to purely synthetic adhesives, recombinantly produced adhesion motifs represent an intermediate stage in the development of novel, bio-inspired glues [263]. In such an approach, the relevant amino acid sequences (e.g., sticky peptide segments or sequence fragments involved in the formation of a specific structure important for the function of an adhesive) are partially recreated. This strategy comes with the advantage of reducing biological variability while preserving the important natural characteristics of the bio-adhesive. The examples we discuss in the following subsection contain such recombinantly produced

molecules and hold the potential to be used in a medical application. However, as these studies are very novel, the behavior of the developed materials has not been tested in a physiological setting yet.

Li et al. [264] developed spider glue-like droplets made from recombinant AgSp1 spidroins. In detail, three different proteins (1RP: 11.5 kDa; 1RC: 24.7 kDa; 3RP: 30.2 kDa) were generated from the amino acid sequence of AgSp1 and were characterized. Both RP variants showed random coil structures that, during a spinning process with polar hexafluoroisopropanol (HFIP), could be transformed into helical structures; conversely, the RC variant assumed an  $\alpha$ -helix configuration by itself. All three protein variants could be assembled into fibers with different mechanical properties: 3RP-HFIP-methanol fibers showed tensile strength values up to 38 MPa (and toughness values around  $0.8 \text{ MJ m}^{-3}$ ), whereas 1RC-water-ethanol fibers were slightly less stable (tensile strength: 21 MPa; toughness  $0.5 \text{ MJ m}^{-3}$ ). However, the breaking strains for all three fibers were rather low (4.5–6.0%). Thus, before creating an adhesive material, the mechanical properties of the fibers need to be improved; moreover, their biocompatibility needs to be assessed to evaluate their suitability for biomedical purposes. In similar studies, the recombinant expression of mussel-glue proteins responding to a pH-based cohesion trigger [265], elastin peptides assembling into hydrogels with self-healing properties [266], and silkworm egg glue proteins creating hydrogels with promising adhesive properties [267] was successfully demonstrated. However, also in those cases, more detailed characterization of the developed materials is required before they can be considered for medical applications.

Ma et al. [268] were inspired by elastin, a protein of the extracellular matrix found in most vertebrates. Recombinant protein was produced with tandem repeats comprising sequence units with Val-Pro-Gly-Lys-Gly motifs, and polypeptides with lengths of up to 144 repeats (K18, K36, K72, K108 and K144) were generated. Those cationic molecules could interact with negatively charged sodium dodecylbenzene sulfonate (SDBS) micelles, and the resulting complexes were shown to strongly adhere to dry surfaces such as glass and metals [268]. Here, the fracture strengths determined from lap shear tests were on the order of 14 MPa. In addition, also wet adhesion to those materials (glass: fracture strength of 490 kPa; steel: fracture strength of 330 kPa) was found to be promising. One possible explanation for this good adhesion behavior could be the presence of lysine residues in the construct, which can engage in electrostatic interactions and cation- $\pi$  interactions (e.g., with the phenyl rings of SDBS thus, boosting the cohesive properties of the adhesive). *Ex vivo* studies with muscle, liver, and skin tissues confirmed the promising adhesion properties (interfacial toughness up to  $80 \text{ J m}^{-2}$ ) of this material. Moreover, this bio-inspired glue showed anti-inflammatory



Fig. 6. Overview of the different requirements an ideal adhesive for medical applications should meet. In addition to the general material properties of such an adhesive, also physiological challenges imposed by the human physiology need to be considered. In addition, further properties can be integrated into synthetic adhesives to achieve multifunctional behavior tailored to specific areas of application.

**Table 3**  
Examples of microscopic mechanisms that give rise to multifunctional properties in bio-derived and bio-inspired adhesive materials.

property	material	responsible mechanism	Ref.
controlled attachment/ detachment	- poly(6-(4-(p-tolyldiazonyl)phenoxy)hexyl acrylate)	photo-activation	[246–248]
	- arylazides-azoles - nematic liquid crystal elastomers - chitosan-grafted-dihydrocaffeic acid (CS-DA) and oxidized pullulan (OP) - dopamine methacrylamide (DMA) and 3-acrylamido phenylboronic acid - poly( <i>N</i> -isopropylacrylamide <sub>100</sub> -co- <i>n</i> -butyl acrylate <sub>5</sub> )-poly(ethylene glycol)-poly( <i>N</i> -isopropylacrylamide <sub>100</sub> -co- <i>n</i> -butyl acrylate <sub>5</sub> ) copolymer - poly(dopamine methacrylamide-co-methoxyethyl-acrylate-co- <i>N</i> -isopropyl acrylamide) copolymer - recombinant protein V40K72	pH control thermal activation	[249,250] [251–253]
on-demand adhesiveness	PVA/PAA - alginate and Poly(glycerol sebacate) acrylate - salmine sulfate and sodium inositol hexaphosphate poly(glycerol sebacate acrylate)	cleavage of crosslinks electrostatic interactions	[254] [255,256]
	self-healing	uran-end functionalized POSS and bismaleimide oligo(ethylene glycol) methacrylate and methacrylic acid  tannic acid coated cellulose nanocrystals in poly(vinyl alcohol) borax network  catechol conjugated chitosan and aldehyde-modified cellulose nanocrystals Polyethylene glycol based hydrogel and organogel	photo-activation Diels-Alder reaction reversible bonding (hydrogen bonds) reversible bonding (borate-diol bonds and hydrogen bonds) dynamic Schiff-base linkages reversible bonding (acylhydrazone bonds)

properties, hemostatic effects, and accelerated wound healing *in vivo*, which renders this recombinant adhesive a highly interesting candidate for surgical use [268]. There are also promising examples of recombinant materials reproducing segments of adhesive mussel proteins, and those have shown good biocompatibility *in vivo* as well [269].

#### 4.2. Multifunctional materials

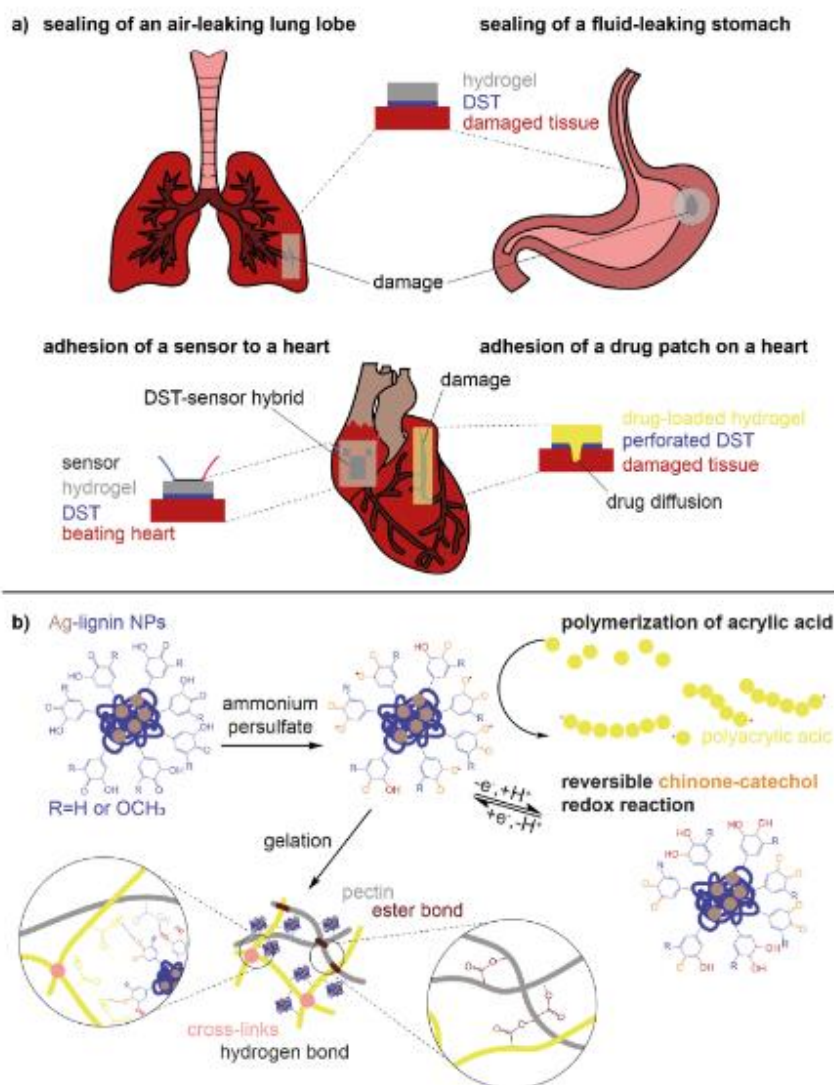
So far, we have focused on (semi-)synthetic materials where the adhesive behavior was the main focus during the material development process. However, for certain applications, further properties are desired in addition to stickiness. As a first example of a multifunctional glue material we highlight the dry adhesive developed by Yuk et al. for wound closure applications [270]. This material quickly adheres to wet tissues, connects two tissue surfaces with each other, exhibits high mechanical stability and flexibility, and can be stored for two weeks without loss of functionality. To attain those properties, a dry double-sided tape (DST) was designed consisting of a combination of a biopolymer (gelatin or chitosan) and cross-linked poly(acrylic acid) (PAA) grafted with *N*-hydroxysuccinimide ester. This combination is endowed with sticky properties via an ensemble of hydrogen bonds, electrostatic, and covalent interactions. Methacrylated gelatin molecules embedded into the PAA-material serve as cross-linkers and strengthen the polymeric network such that an interfacial toughness of  $\sim 1 \text{ kJ m}^{-2}$  is obtained. Once placed *in vivo*, however, the material can be degraded within two to four weeks, and this is made possible by the integrated gelatine and chitosan molecules (which also provide good biocompatibility), respectively [270]. This multi-component material was used as a wound patch to cover tissue ruptures (Fig. 7a) and – at least *ex vivo* – could prevent leakage of fluids (such as gastric juice). Moreover, this adhesive was employed to attach a sensor to the heart, which allowed for investigating the cardiac function *ex vivo* [24]. On the basis of their findings, authors claim that the DST offers several advantages over existing tissue adhesives and sealants, including fast adhesion formation, robust adhesion performance, flexibility, as well as ease of storage and application. In addition, the material could be enriched with drug depots to release pharmaceuticals to accelerate the wound healing process.

In the example discussed above, multi-functionality was achieved by combining different (macro)molecular components, and each component had its specific tasks. However, such an approach is not necessarily straightforward as one (or several) of the components may interfere with

the function of others. To illustrate this problem, we mention an example from the literature where the goal was to obtain a strong network by combining chelate-based and UV-based cross-linking strategies into the same material [271]. Here, an acrylated epoxidized soybean oil (AESO) was employed, which combines UV-activatable residues and DOPA groups. The first modification allows the polymer to be covalently cross-linked via UV light whereas the DOPA-functionalization can covalently autoxidize, or form chelate complexes with added  $\text{Fe}^{3+}$  ions. However, when making use of both cross-linking strategies at the same time, the authors obtained a lower bonding strength of 1.1 MPa than when they used one of those cross-linking strategies only. Probably, the different active groups inhibit each other and thus prevent optimal cross-linking.

To circumvent such issues, two-component adhesives can be created. In the example herewith highlight, one component was a four-armed polyethylene glycol-poly(lactic-co-glycolic acid)-*N*-hydroxysuccinimide (PEG<sub>4</sub>-PLGA-NHS) molecule and the second one was a four-armed polyethylene glycol-NH<sub>2</sub> (PEG<sub>4</sub>-NH<sub>2</sub>) construct. When mixed with each other at room temperature, these two polymers started to interact with each other and with a tissue sample they were placed onto, and the initially viscosity-dominated solution was converted into an elasticity-dominated adhesive (with an elastic modulus of up to 15 kPa) within 2 min. Here, the PEG<sub>4</sub>-PLGA-NHS interacts via NHS ester groups with amine groups from the tissue surface (providing adhesion) and with PEG<sub>4</sub>-NH<sub>2</sub> (providing cohesion), and the PLGA motifs render the sealant degradable by presenting hydrolysable esters. Importantly, even when exposed to high blood pressures (which can be as high as 120 mm Hg<sup>-1</sup>), sealants created from 9:1 mixtures of PEG<sub>4</sub>-PLGA-NHS/PEG<sub>4</sub>-NH<sub>2</sub> showed acceptable stability and good biocompatibility *in vitro* and *in vivo* [272].

Another example of a successfully engineered multi-component glue draws inspiration from plants. Here, an adhesive hydrogel was developed by Gan et al. [273] using Ag-lignin core-shell nanoparticles to trigger a dynamic catechol-based redox system in poly(acrylic acid)/pectin hydrogels (Fig. 7b). This strategy made use of two effects: first, a continuous formation of free radicals and, second, maintaining the quinone-catechol redox balance in the network. As a consequence, a continuous reductive/oxidative environment was created that not only enabled self-gelation of the polymeric system at ambient conditions, but endows the hydrogel with long-term and repeatable adhesiveness. The adhesion mechanism of the hydrogel is attributable to the hydrogen



**Fig. 7.** Schematic representation of *ex vivo* experiments with porcine lung, stomach, and heart tissue, where a prevention of air-/fluid leakage was achieved by applying a multi-functional (drug-loaded) adhesive (DST; a). Moreover, the same adhesive system could be used to attach a sensor to the heart muscle. Dry double-sided tape (DST) is a combination of a biopolymer (gelatin or chitosan) and cross-linked poly(acrylic acid) (PAA) grafted with *N*-hydroxysuccinimide ester. Figure adapted from Ref. [270]. Multi-component adhesion system comprising pectin and polyacrylic acid macromolecules combined with plant-inspired, DOPA-modified Ag-lignin nanoparticles (NPs; b). These particles trigger the gelation process of the mixture based on the redox reaction of quinones. Adapted from Ref. [273].

bonding or hydrophobic interaction between the material and different surfaces. The successful formation of an adhesive substance was verified by adhesion and stripping tests on skin tissue. Intriguingly, the hydrogel showed high antibacterial activity due to the catechol groups and bactericidal ability of Ag-Lignin NPs [273].

In certain cases, some specific functions of an adhesive materials are only needed at selected time points. For instance, Chen et al. [254] presented a wet-adhesive material that can be detached on demand by adding a biocompatible trigger solution. Inspired by mussels employing the amino acid *L*-DOPA, also this material sticks to a wet tissue surface via physical and covalent bonds; however, different from how mussels achieve this combination of attractive interactions, here, a combination of highly abundant carboxylic groups present on poly(acrylic acid) (PAA) and cleavable *N*-hydroxysuccinimide (NHS) ester groups grafted onto PAA, respectively, provides this combination of covalent and non-covalent interactions. Once applied to its target, the material forms a highly stretchable and tough hydrogel with a fracture toughness over  $1 \text{ kJ m}^{-2}$ . Upon contact with the trigger solution, the physical and covalent

bonds to the surface are cleaved by two trigger molecules: sodium carbonate (which weakens hydrogen bonds) and *L*-glutathione (which reduces cysteine bonds). Furthermore, this material as well as the trigger solution enabling its controlled detachment process were found to be biocompatible *in vivo*, which enables its use for temporary organ sealing, or for attaching medical devices such as drains and drug depots to a tissue. Related strategies that convey 'switchable' attachment/detachment properties to adhesive materials make use of polymers with photo-responsive [246–248], pH responsive [249,250,274], and temperature responsive properties [251,275].

The ability to precisely trigger adhesive properties on-demand is highly desirable in the context of minimally invasive surgeries; here, very narrow tubes are used to deposit a tissue adhesive at the point of need. To overcome problems arising from tube clogging, a biomimetic system using the granule-mediated adhesive strategy of sandcastle worms was introduced [255]. In this material, glue droplets made from hydrophobic poly(glycerol sebacate)-acrylate were stabilized with negatively charged alginate biopolymers to reduce the viscosity of the material and thus to

optimize its injectability. After injection, contact with a positively charged trigger polymer (i.e., protamine, which is applied after the polymeric mixture has reached its target site) converted the nanoparticle dispersion into a viscoelastic adhesive. With this trick, it was easily possible to control the dose and timing of the glue application with high precision. Similarly, other bioinspired materials with on-demand adhesion properties were successfully employed for medical purposes such as bone fracture healing [276], endovascular embolization [256], and hemostatic sealing [257].

Of course, applications of bio-inspired glues do not have to be limited to the medical sector. Especially when combined with another highly desired material property – autonomous damage management (also known as ‘self-healing’) – adhesives with an increased lifetime and constant mechanical characteristics can be created which are very interesting for many fields of materials science. Indeed, self-healing materials were developed on the basis of different mechanistic principles, and examples include the application of an external stimulus (such as pH change, UV irradiation, or temperature change) [258,277], non-covalent interactions [259,278,279], or dynamic covalent bonds [280–282]. In this context, owing to their dynamic behavior and the simplicity of the required chemical reactions, synergistic interactions between borate-diol bonds have been put forward as a promising strategy for the formulations of bioadhesives [283]. For instance, Ge et al. [284] developed poly(vinyl alcohol)/borax hybrid hydrogels containing functional cellulose nanofibrils and tannic acid molecules. Here, the formation of dynamic ester complexes between borate groups and *cis*-diols of PVA, cellulose, and tannic acid introduced (and maintained) chemical cross-links into the hydrogel, whereas the dispersed cellulose nanofibrils reinforced the material. As evidenced by cutting/healing and rheological recovery tests, the high reversibility of borate-ester bonds allowed this material to successfully restore its properties within 10 s after mechanical damage was applied. Initial tests with *ex vivo* skin samples verified the adhesive behavior of this formulation, which indicates that several medical applications will benefit from it. Other areas where recent advances in the design and modification of bio-based glues opened new avenues for their application include the development of wood adhesives [285,286] and general sealants [287]. This demonstrates the broad versatility of such bio-based and bio-inspired materials.

## 5. Conclusion and outlook

As the examples we discuss here nicely illustrate, nature has developed a broad range of glues that often serve additional purposes other than ‘just’ being adhesive. Of course, we humans are often interested in applying such biological or bio-based adhesives in a different context, e.g., in contact with human tissue. Whether protein-based, carbohydrate-based or glycoprotein-based adhesives are most suitable in a particular biomedical setting is *a priori* not clear, though. Here, studies that systematically conduct a direct comparison of different bio-based adhesives on the same tissue substrate (using the same methodology and testing conditions) would be useful but are – to date – scarce. Of course, there is already a large body of literature available where different experiments with bio-based and bio-derived adhesives are described. In this context, a machine learning-assisted analysis of the existing data might help pinpointing selection criteria that enable material scientists to rapidly identify a bio-driven solution for a particular medical scenario.

For the development of biomedical adhesives, it is equally important to meet various biological demands and to achieve the required mechanical properties. Thus, considering the biological limitations of sensitive tissues, hazardous chemicals and very robust, non-degradable formulations are rarely suitable for medical applications. Instead, bio-inspired adhesives combining biological motifs with (semi-)synthetic polymer backbones may provide the best of both worlds, i.e., tunable material properties and biological compatibility/degradability. Having revealed a range of smart adhesives with controllable behavior, researchers now have access to a large toolbox of molecular motifs they can

use to develop multi-functional adhesives. With those next-generation bio-adhesives, it should be possible to address complicated pathological scenarios in the future where currently established adhesives are insufficient. Examples of such difficult scenarios requiring next-generation adhesives are the closure of fetal membranes or the treatment of diabetic wounds. Here, rationally designed materials with tailored adhesion/detachment (or degradation) properties in combination with controlled drug release abilities would constitute an important milestone.

Further deepening our understanding of biological adhesion mechanisms and reproducing the relevant biochemical motifs in semi-synthetic constructs will therefore, not only advance our control over medical problems such as wound healing. Progress in this area is also likely to trigger the development of novel materials for other medical purposes such as drug monitoring or bioelectronics as well as other fields where adhesives with well-controlled and tunable properties are required. Whether purified bio-compounds or bio-inspired, (semi-)synthetic materials are better suited for this purpose will not only depend on the level of desired multi-functionality, the durability/life time, and the amount of adhesive required for a particular application, but also on the purity of the used components and the ensuing biocompatibility of the created adhesive. Regarding the latter two aspects, biomedical applications certainly come with the most complex demands.

## Statement of ethics approval

Approval of ethics is not required for the experiments conducted in this manuscript.

## Declaration of competing interest

The authors declare that they have no known competing financial interests or personal relationships that could have appeared to influence the work reported in this paper.

## Acknowledgments

This project has received funding from the European Union's Horizon 2020 research and innovation program under grant agreement No 863183. This publication represents the views of the author(s) only. The European Commission is not responsible for any use that may be made of the information it contains. In addition, support from TUM's Innovation Network ARTEMIS is acknowledged as well.

## References

- [1] N. Bleicher, et al., Molecular evidence of use of hide glue in 4th millennium BC Europe, *J. Archaeol. Sci.* 63 (2015) 65–71.
- [2] Y. Xiao, et al., Properties, characterization, and decay of sticky rice–lime mortars from the Wuyang Ming dynasty city wall (China), *Mater. Char.* 90 (2014) 164–172.
- [3] P.R. Kozowyk, G.H. Langrjans, J.A. Poullis, Lap shear and impact testing of ochre and beeswax in experimental Middle Stone Age compound adhesives, *PLoS One* 11 (3) (2016) e0150436.
- [4] P. Jong-Sung, W. Kun-Suk, The usage and composition of propolis added cosmetics in Korea, in: *Bee Products*, Springer, 1997, pp. 121–124.
- [5] Y. Dror, Y. Cohen, R. Yerushalmi-Rozen, Structure of gum Arabic in aqueous solution, *J. Polym. Sci. B Polym. Phys.* 44 (22) (2006) 3265–3271.
- [6] P.K. Bhagwat, P.B. Dandge, Isolation, characterization and valorizable applications of fish scale collagen in food and agriculture industries, *Biocatal. Agric. Biotechnol.* 7 (2016) 234–240.
- [7] Y. Zhang, et al., Preparation and properties of a starch-based wood adhesive with high bonding strength and water resistance, *Carbohydr. Polym.* 115 (2015) 32–37.
- [8] Y.H. Song, et al., Mussel adhesive protein as an environmentally friendly harmless wood furniture adhesive, *Int. J. Adhesion Adhes.* 70 (2016) 260–264.
- [9] C. Moser, et al., Autologous fibrin sealant reduces the incidence of prolonged air leak and duration of chest tube drainage after lung volume reduction surgery: a prospective randomized blinded study, *J. Thorac. Cardiovasc. Surg.* 136 (4) (2008) 843–849.
- [10] L.P. Abbade, et al., Treatment of chronic venous ulcers with heterologous fibrin sealant: a phase I/II clinical trial, *Front. Immunol.* 12 (2021) 83.

- [11] A.P.S. Leite, et al., Heterologous fibrin sealant potentiates axonal regeneration after peripheral nerve injury with reduction in the number of suture points, *Injury* 50 (4) (2019) 834–847.
- [12] U. Wirth, et al., Long-term outcome and chronic pain in traumatic fibrin glue versus staple fixation of extra light titanized meshes in laparoscopic inguinal hernia repair (TAPP): a single-center experience, *Surg. Endosc.* 34 (5) (2020) 1929–1938.
- [13] I. Kim, et al., In situ facile-forming PEG cross linked albumin hydrogels loaded with an apoptotic TRAIL protein, *J. Contr. Release* 214 (2015) 30–39.
- [14] C. Pines, et al., In vivo evaluation of hybrid patches composed of PLA based copolymers and collagen/chondroitin sulfate for ligament tissue regeneration, *J. Biomed. Mater. Res. B Appl. Biomater.* 105 (7) (2017) 1778–1788.
- [15] L. Fan, et al., Preparation and characterization of chitosan/gelatin/PVA hydrogel for wound dressings, *Carbohydr. Polym.* 146 (2016) 427–434.
- [16] L. Ge, S. Chen, Recent advances in tissue adhesives for clinical medicine, *Polymers* 12 (4) (2020) 930.
- [17] A. Assmann, et al., A highly adhesive and naturally derived sealant, *Biomaterials* 140 (2017) 115–127.
- [18] B. Mizrahi, et al., Elasticity and safety of alkoxymethyl cyanoacrylate tissue adhesives, *Acta Biomater.* 7 (8) (2011) 3150–3157.
- [19] P.A. Leggat, D.R. Smith, U. Kedjarame, Surgical applications of cyanoacrylate adhesives: a review of toxicity, *ANZ J. Surg.* 77 (4) (2007) 209–213.
- [20] A. Kreitschitz, A. Kovalev, S.N. Gorb, Slipping vs sticking: water-dependent adhesive and frictional properties of *Linum usitatissimum* L. seed mucilaginous envelope and its biological significance, *Acta Biomater.* 17 (2015) 152–159.
- [21] J.O. Wolff, et al., Adhesive droplets of glowworm snares (Keroplatidae: *Arachnocampa* spp.) are a complex mix of organic compounds, *Front. Mech. Eng.* 7 (2021) 27.
- [22] F. Vollrath, et al., Compounds in the droplets of the orb spider's viscid spiral, *Nature* 345 (6275) (1990) 526–528.
- [23] S.J. Blamires, S. Zhang, I.-M. Tso, *Web: Diversity, Structure and Function, in Behaviour and Ecology of Spiders*, Springer, 2017, pp. 137–164.
- [24] N. Kono, et al., Spideoin profiling of cribellate spiders provides insight into the evolution of spider prey capture strategies, *Sci. Rep.* 10 (1) (2020) 1–11.
- [25] G. Amarputi, et al., Ubiquitous distribution of salts and proteins in spider glue enhances spider silk adhesion, *Sci. Rep.* 5 (1) (2015) 1–7.
- [26] A. Baer, et al., Reversible supramolecular assembly of velvet worm adhesive fibers via electrostatic interactions of charged phosphoproteins, *Biomacromolecules* 19 (10) (2018) 4034–4043.
- [27] A. Concha, et al., Oscillation of the velvet worm slime jet by passive hydrodynamic instability, *Nat. Commun.* 6 (1) (2015) 1–6.
- [28] F. Brau, et al., Dynamics of prey rejection by chameleons through viscous adhesion, *Nat. Phys.* 12 (10) (2016) 931–935.
- [29] M. Houze, P. Dammann, Predation with the tongue through viscous adhesion, a scaling approach, *Soft Matter* 13 (10) (2017) 2120–2124.
- [30] Y.Y. Peng, et al., Identification of proteins associated with adhesive prints from *Holothuria duffleyi* *Carverian* tubules, *Mar. Biotechnol.* 16 (6) (2014) 695–706.
- [31] G. Chaudhary, et al., Concentration independent mechanics and structure of hagfish slime, *Acta Biomater.* 79 (2018) 123–134.
- [32] L. Böni, et al., Hagfish slime and mucin flow properties and their implications for defense, *Sci. Rep.* 6 (1) (2016) 1–8.
- [33] J. von Byern, et al., Chemical characterization of the adhesive secretions of the salamander *Plethodon shermani* (Caudata, Plethodontidae), *Sci. Rep.* 7 (1) (2017) 1–13.
- [34] M.J. Tyler, J.A. Ramshaw, An adhesive derived from amphibian skin secretions. PCT/AU2001/001172(WO2002/022756), 1–29, 2002 Australia, 2002.
- [35] R.H. Ewaldt, A.E. Hossel, G.H. McKinley, Nonlinear viscoelastic biomaterials: meaningful characterization and engineering inspiration, *Integr. Comp. Biol.* 49 (1) (2009) 40–50.
- [36] T. Zhong, et al., Controlled self-assembly of glycoprotein complex in snail mucus from lubricating liquid to elastic fiber, *RSC Adv.* 8 (25) (2018) 13806–13812.
- [37] C. Lee, et al., Boston ivy disk-inspired pressure-mediated adhesive film patches, *Small* 16 (9) (2020) 1904282.
- [38] Y. Huang, et al., Nanospherical arabinogalactan proteins are a key component of the high strength adhesive secreted by English ivy, *Proc. Natl. Acad. Sci. Unit. States Am.* 113 (23) (2016) E3193–E3202.
- [39] Y. Naidoo, S. Hemeidah, Morphological investigation of glandular hairs on *Drosera capensis* leaves with an ultrastructural study of the sessile glands, *Botany* 91 (4) (2013) 234–241.
- [40] M. Krausko, et al., The role of electrical and jasmonate signalling in the recognition of captured prey in the carnivorous sundew plant *Drosera capensis*, *New Phytol.* 213 (4) (2017) 1818–1835.
- [41] G. Pallavi, et al., Genomes of the Venus flytrap and close relatives unveil the roots of plant carnivory, *Curr. Biol.* 30 (12) (2020) 2312–2320, e5.
- [42] T. Kokubun, Occurrence of myo inositol and alkyl substituted polysaccharide in the prey-trapping mucilage of *Drosera capensis*, *Sci. Nat.* 104 (9) (2017) 1–12.
- [43] R. Minjares-Fuentes, et al., Influence of water deficit on the main polysaccharides and the rheological properties of Aloe vera (*Aloe barbadensis* Miller) mucilage, *Ind. Crop. Prod.* 109 (2017) 644–653.
- [44] A. Kokla, C.W. Mehryk, Developing a thief: haustoria formation in parasitic plants, *Dev. Biol.* 442 (1) (2018) 53–59.
- [45] E. Gedalovich, J. Kujit, N. Carpita, Chemical composition of viscin, an adhesive involved in dispersal of the parasite *Phoradendron californicum* (Viscaceae), *Physiol. Mol. Plant Pathol.* 32 (1) (1988) 61–76.
- [46] J.E. Aukema, Vectors, viscin, and Viscaceae: mistletoes as parasites, mutualists, and resources, *Front. Ecol. Environ.* 1 (4) (2003) 212–219.
- [47] S. Yu, et al., A single nucleotide polymorphism of *Nud* converts the caryopsis type of barley (*Hordeum vulgare* L.), *Plant Mol. Biol. Rep.* 34 (1) (2016) 242–248.
- [48] L. Muñoz, et al., Chia seeds: microstructure, mucilage extraction and hydration, *J. Food Eng.* 108 (1) (2012) 216–224.
- [49] Y. Zhang, et al., Caudicles in vandoid orchids: a carotenoid based soft material with unique properties, *Acta Biomater.* 113 (2020) 478–487.
- [50] X. Yang, W. Deng, Morphological and structural characterization of the attachment system in aerial roots of *Syngonium podophyllum*, *Planta* 245 (3) (2017) 507–521.
- [51] M.-C. Rulet, et al., Xylans provide the structural driving force for mucilage adhesion to the Arabidopsis seed coat, *Plant Physiol.* 171 (1) (2016) 165–178.
- [52] M.L. Warren, K.E. Kram, K.E. Theiss, Characterizing the nectar microbiome of the non-native tropical milkweed, *Asclepias curassavica*, in an urban environment, *PLoS One* 15 (9) (2020) e0237561.
- [53] D. Shin, et al., Humidity tolerant rate-dependent capillary viscous adhesion of bee-collected pollen fluids, *Nat. Commun.* 10 (1) (2019) 1–9.
- [54] D. Voigt, W. Konrad, S. Gorb, A universal glue: underwater adhesion of the secretion of the carnivorous flypaper plant *Roridula gorgonias*, *Interface focus* 5 (1) (2015) 20140053.
- [55] L. Frenzke, et al., Plant pressure sensitive adhesives: similar chemical properties in distantly related plant lineages, *Planta* 244 (1) (2016) 145–154.
- [56] N. Bertel, M. Paniw, F. Ojeda, Effective prey attraction in the rare *Drosophyllum lusitanicum*, a flypaper-trap carnivorous plant, *Am. J. Bot.* 102 (5) (2015) 689–694.
- [57] S. Poppinga, et al., Catapulting tentacles in a sticky carnivorous plant, *PLOS ONE* 7 (2) (2012) e45735.
- [58] R.S. Borbas, M. Spivak, Propolis envelope in *Apis mellifera* colonies supports honey bees against the pathogen, *Paenibacillus larvae*, *Sci. Rep.* 7 (1) (2017) 1–6.
- [59] W. Gnatzy, W. Volkmandt, A. Drwonek, Egg-laying behavior and morphological and chemical characterization of egg surface and egg attachment glue of the digger wasp *Ampulex compressa* (Hymenoptera, Ampulicidae), *Arthropod Struct. Dev.* 47 (1) (2018) 74–81.
- [60] K. Vasanthavada, et al., Spider glue proteins have distinct architectures compared with traditional spiderin family members, *J. Biol. Chem.* 287 (43) (2012) 35986–35999.
- [61] C. Schaefer, et al., Silk protein solution: a natural example of sticky reptation, *Macromolecules* 53 (7) (2020) 2669–2676.
- [62] Z. Dong, et al., Identification of Bombyx mori sericin 4 protein as a new biological adhesive, *Int. J. Biol. Macromol.* 132 (2019) 1121–1130.
- [63] F. Chen, D. Porter, F. Vollrath, Morphology and structure of silkworm cocoons, *Mater. Sci. Eng. C* 32 (4) (2012) 772–778.
- [64] A. Baer, et al., Mechanoresponsive lipid-protein nanoglobules facilitate reversible fibre formation in velvet worm slime, *Nat. Commun.* 8 (1) (2017) 1–7.
- [65] M. Thielicke, R. Sluys, Prey capture and feeding behaviour in an endemic land flatworm from São Tomé Island, *J. Nat. Hist.* 53 (23–24) (2019) 1385–1393.
- [66] J. Pawlicki, et al., The effect of molluscan glue proteins on gel mechanics, *J. Exp. Biol.* 207 (7) (2004) 1127–1135.
- [67] J. von Byern, et al., Biomechanical properties of fishing lines of the glowworm *Arachnocampa luminosa* (Diptera: Keroplatidae), *Sci. Rep.* 9 (1) (2019) 1–14.
- [68] D. Firkowski, et al., Humidity-dependent mechanical and adhesive properties of *Arachnocampa tasmaniensis* capture threads, *J. Zool.* 305 (4) (2018) 256–266.
- [69] L.D. Graham, et al., An adhesive secreted by Australian frogs of the genus *Notaden*, in biological adhesives, Springer (2016) 223–243.
- [70] T. Hatano, T. Nagashima, The secretion process of liquid silk with nanopillar structures from *Stenopsyche marmorata* (Trichoptera: Stenopsychidae), *Sci. Rep.* 5 (1) (2015) 1–8.
- [71] J. Callow, et al., The application of atomic force microscopy to topographical studies and force measurements on the secreted adhesive of the green alga *Enteromorpha*, *Planta* 211 (5) (2000) 641–647.
- [72] F.A. Guardiola, et al., Comparative skin mucus and serum humoral defence mechanisms in the teleost gilthead seabream (*Sparus aurata*), *Fish Shellfish Immunol.* 36 (2) (2014) 545–551.
- [73] M.H. Borges, et al., Combined proteomic and functional analysis reveals rich sources of protein diversity in skin mucus and venom from the *Scorpaena plumieri* fish, *J. Proteonomics* 187 (2018) 200–211.
- [74] R.H. Ewaldt, T.M. Winegard, D.S. Fudge, Non-linear viscoelasticity of hagfish slime, *Int. J. Non Lin. Mech.* 46 (4) (2011) 627–636.
- [75] N.J. Caruana, et al., Quantitative proteomic analysis of the slime and Ventral Mantle glands of the striped Pyjama squid (*Sepioides lineolata*), *J. Proteome Res.* 19 (4) (2020) 1491–1501.
- [76] N.J. Caruana, et al., A combined proteomic and transcriptomic analysis of slime secreted by the southern bottletail squid, *Sepioides lineolata* (Cephalopoda), *J. Proteonomics* 148 (2016) 170–182.
- [77] A. González-Costa, et al., Mucus characterisation in the Octopus vulgaris skin throughout its life cycle, *Anat. Histol. Embryol.* 49 (4) (2020) 502–510.
- [78] J. von Byern, et al., Old and sticky—adhesive mechanisms in the living fossil *Nautilus pompilius* (Mollusca, Cephalopoda), *Zoology* 115 (1) (2012) 1–11.
- [79] W. Liu, et al., Stress-induced mucus secretion and its composition by a combination of proteomics and metabolomics of the jellyfish *Aurelia coerulea*, *Mar. Drugs* 16 (9) (2018) 341.
- [80] R. Fjeta, et al., Temporary adhesion of the proseriate flatworm *Minoma ileanae*, *Philosophical Trans. Royal Soc. B* 374 (1784) (2019) 20190194.
- [81] N. Aldred, et al., Chitin is a functional component of the larval adhesive of barnacles, *Commun. Biol.* 3 (1) (2020) 1–8.
- [82] K.P. Feurs, et al., Acorn barnacles secrete phase separating fluid to clear surfaces ahead of cement deposition, *Adv. Sci.* 5 (6) (2018) 1700762.

- [83] J. Monahan, J.J. Wilker, Specificity of metal ion cross linking in marine mussel adhesives, *Chem. Commun.* 14 (2003) 1672–1673.
- [84] K. Green, *Mussel adhesive protein*. Surgical adhesives and sealants, *Curr. Technol. Appl.* (2020) 19–27.
- [85] E. Henebert, et al., Micro and nanostructure of the adhesive material secreted by the tube feet of the sea star *Asterias rubens*, *J. Struct. Biol.* 164 (1) (2008) 108–118.
- [86] B. Lengerer, et al., The structural and chemical basis of temporary adhesion in the sea star *Asterina gibbosa*, *Beilstein J. Nanotechnol.* 9 (1) (2018) 2071–2086.
- [87] M. Simão, et al., Characterization of the glycans involved in sea urchin *Paracentrotus lividus* reversible adhesion, *Mar. Biol.* 167 (9) (2020) 1–15.
- [88] N. Lebesgue, et al., Deciphering the molecular mechanisms underlying sea urchin reversible adhesion: a quantitative proteomics approach, *J. Proteomics* 138 (2016) 61–71.
- [89] R. Sanfilippo, et al., *Sabellaria alveolata* sandcastle worm from the Mediterranean Sea: new insights on tube architecture and bioinspiration, *J. Morphol.* 280 (12) (2019) 1839–1849.
- [90] A. Li, et al., Humid bonding with a water soluble adhesive inspired by mussels and sandcastle worms, *Macromol. Chem. Phys.* 216 (4) (2015) 450–459.
- [91] J.-P. Buffet, et al., Adhesive gland transcriptomics uncovers a diversity of genes involved in glue formation in marine tube building polychaetes, *Acta Biomater.* 72 (2018) 316–328.
- [92] L. Zhang, V. Lipik, A. Miserez, Complex coacervates of oppositely charged copolypeptides inspired by the sandcastle worm glue, *J. Mater. Chem. B* 4 (8) (2016) 1544–1556.
- [93] Q. Guo, et al., Recent progress in synthesis and application of mussel-inspired adhesives, *Nanoscale* 12 (3) (2020) 1307–1324.
- [94] P. Kord Poroshahi, B.P. Lee, Recent approaches in designing bioadhesive materials inspired by mussel adhesive proteins, *J. Polym. Sci. Polym. Chem.* 55 (1) (2017) 9–33.
- [95] C.T. Mitchell, et al., The effect of substrate wettability and modulus on gecko and gecko-inspired synthetic adhesion in variable temperature and humidity, *Sci. Rep.* 10 (1) (2020) 1–9.
- [96] K.A. Maswanganye, et al., Life on the rocks: Multilocus phylogeography of rock hyrax (*Procavia capensis*) from southern Africa, *Mol. Phylogenet. Evol.* 114 (2017) 49–62.
- [97] P. Stumpf, U. Welsch, Cutaneous eccrine glands of the foot pads of the rock hyrax (*Procavia capensis*, Hyracoidea, Mammalia), *Cells Tissues Organs* 171 (2–3) (2002) 215–226.
- [98] N. Pandey, et al., Mussel-inspired bioadhesives in healthcare: design parameters, current trends, and future perspectives, *Biomater. Sci.* 8 (5) (2020) 1240–1255.
- [99] A.K. Patel, J.-D. Mathias, P. Michaud, Polysaccharides as adhesives, *Rev. Adhesion Adhesives* 1 (3) (2013) 312–345.
- [100] W. Gao, et al., Rapid and efficient crossing blood-brain barrier: hydrophobic drug delivery system based on propionylated amylose helix nanoclusters, *Biomaterials* 113 (2017) 133–144.
- [101] S.H. Hong, et al., Dynamic bonds between boronic acid and alginate: hydrogels with stretchable, self-healing, stimuli responsive, remoldable, and adhesive properties, *Biomacromolecules* 19 (6) (2018) 2053–2061.
- [102] H. An, et al., Cellulose-based self-healing hydrogel through boronic ester bonds with excellent biocompatibility and conductivity, *RSC Adv.* 10 (19) (2020) 11300–11310.
- [103] V.R. Ferreira, et al., Metal cation sorption ability of immobilized and reticulated chondroitin sulfate or fucoidan through a sol-gel crosslinking scheme, *Mater. Today Commun.* 8 (2016) 172–182.
- [104] N. Li, et al., Tannic acid cross-linked polysaccharide-based multifunctional hemostatic microparticles for the regulation of rapid wound healing, *Macromol. Biosci.* 18 (11) (2018) 1800209.
- [105] B.H. Viltinski, et al., Photophysics and drug delivery behavior of methylene blue into Arabic-gum based hydrogel matrices, *Mater. Today Commun.* 26 (2021) 101889.
- [106] G. Schmidt, B.R. Hamaker, J.J. Wilker, High strength adhesives from catechol cross-linking of zeta protein and plant phenolics, *Adv. Sustain. Syst.* 2 (3) (2018) 1700159.
- [107] M.R.d. Cunha, et al., Hydroxyapatite and a new fibrin sealant derived from snake venom as scaffold to treatment of cranial defects in rats, *Mater. Res.* 18 (1) (2015) 196–203.
- [108] J.B. de Oliveira Gonçalves, et al., Effects of low-level laser therapy on autogenous bone graft stabilized with a new heterologous fibrin sealant, *J. Photochem. Photobiol. B Biol.* 162 (2016) 663–668.
- [109] H. Shao, K.N. Bachus, R.J. Stewart, A water-borne adhesive modeled after the sandcastle glue of *P. californica*, *Macromol. Biosci.* 9 (5) (2009) 464–471.
- [110] L.D. Graham, et al., Biocompatibility and modification of the protein-based adhesive secreted by the Australian frog *Notaden bennetti*, *J. Biomed. Mater. Res. A: Off. J. Soc. Biomater. Japan. Soc. Biomater. Australian Soc. Biomater. Korean Soc. Biomater.* 93 (2) (2010) 429–441.
- [111] M. Liang, et al., Preparation and characterization of gelatin/sericin/carboxymethyl chitosan medical tissue glue, *J. Appl. Biomater. Punct. Mater.* 16 (2) (2018) 97–106.
- [112] M. Lefevre, et al., On the nanomechanical and viscoelastic properties of coatings made of recombinant sea star adhesive proteins, *Front. Mech. Eng.* 7 (2021) 43.
- [113] Y. Huang, et al., Exploring naturally occurring ivy nanoparticles as an alternative biomaterial, *Acta Biomater.* 25 (2015) 268–283.
- [114] J. Gubitosa, et al., Biomolecules from snail mucus (*Helix aspersa*) conjugated gold nanoparticles, exhibiting potential wound healing and anti-inflammatory activity, *Soft Matter* 16 (48) (2020) 10876–10888.
- [115] M.B. Dastjerdi, et al., Novel versatile 3D bio scaffold made of natural biocompatible hagfish exudate for tissue growth and organoid modeling, *Int. J. Biol. Macromol.* 158 (2020) 894–902.
- [116] R. Nudelman, et al., Jellyfish-based smart wound dressing devices containing in situ synthesized antibacterial nanoparticles, *Adv. Funct. Mater.* 29 (38) (2019) 1902783.
- [117] O.O. Kumble, Starch source and its impact on pharmaceutical applications, *Chem. Properties Starch* (2019) 35.
- [118] F. Spinozzi, C. Ferrero, S. Perez, The architecture of starch blocklets follows phyllotactic rules, *Sci. Rep.* 10 (1) (2020) 1–16.
- [119] L. Pachuan, et al., Physicochemical and disintegrant properties of glutinous rice starch of Mizoram, India, *Int. J. Biol. Macromol.* 95 (2017) 1298–1304.
- [120] A. Nokhodchi, et al., Crystal engineering of ibuprofen using starch derivatives in crystallization medium to produce promising ibuprofen with improved pharmaceutical performance, *RSC Adv.* 5 (57) (2015) 46119–46131.
- [121] F.G. Torres, S. Commaux, O.P. Troncoso, Starch-based biomaterials for wound-dressing applications, *Starch-Stärke* 65 (7–8) (2013) 543–551.
- [122] C. Koski, et al., Starch hydroxyapatite composite bone scaffold fabrication utilizing a slurry extrusion-based solid freeform fabricator, *Additive manufacturing* 24 (2018) 47–59.
- [123] A. Martins, et al., Hierarchical starch-based fibrous scaffold for bone tissue engineering applications, *J. Tissue Eng. Regen. Med.* 3 (1) (2009) 37–42.
- [124] A. Salgado, O.P. Coutinho, R.L. Reis, Novel starch-based scaffolds for bone tissue engineering: cytotoxicity, cell culture, and protein expression, *Tissue Eng.* 10 (3–4) (2004) 465–474.
- [125] K.I. Draget, O. Smidsrud, G. Skjåk-Bræk, Alginates from algae, *Polysaccharides Polyamides Food Industry: Properties, Production Patents* (2005) 1–30.
- [126] Y. Liang, et al., Algal biorefineries, in: *Industrial Biorefineries & White Biotechnology*, Elsevier, 2015, pp. 35–90.
- [127] H. Hecht, S. Srebnik, Structural characterization of sodium alginate and calcium alginate, *Biomacromolecules* 17 (6) (2016) 2160–2167.
- [128] J. Brus, et al., Structure and dynamics of alginate gels cross-linked by polyvalent ions probed via solid state NMR spectroscopy, *Biomacromolecules* 18 (8) (2017) 2478–2488.
- [129] K.Y. Lee, D.J. Mooney, Alginate: properties and biomedical applications, *Prog. Polym. Sci.* 37 (1) (2012) 106–126.
- [130] P.K. Gupta, et al., An update on overview of cellulose, its structure and applications, *Cellulose* (2019) 846–1297.
- [131] Z. Ling, et al., Unraveling variations of crystalline cellulose induced by ionic liquid and their effects on enzymatic hydrolysis, *Sci. Rep.* 7 (1) (2017) 1–11.
- [132] K. Ilna, et al., Translational study between structure and biological response of nanocellulose from wood and green algae, *RSC Adv.* 4 (6) (2014) 2892–2903.
- [133] H. Gao, et al., Construction of cellulose nanofibers/quaternized chitin/organic rectorite composites and their application as wound dressing materials, *Biomater. Sci.* 7 (6) (2019) 2571–2581.
- [134] C. Shao, et al., Mussel-inspired cellulose nanocomposite tough hydrogels with synergistic self-healing, adhesive, and strain-sensitive properties, *Chem. Mater.* 30 (9) (2018) 3110–3121.
- [135] S. Palanisamy, et al., Isolation of fucoidan from *Sargassum polycystum* brown algae: structural characterization, in vitro antioxidant and anticancer activity, *Int. J. Biol. Macromol.* 102 (2017) 405–412.
- [136] R.V. Usoltseva, et al., Fucoidans from brown algae *Laminaria longipes* and *Saccharina echinoides*: structural characteristics, anticancer and radiosensitizing activity in vitro, *Carbohydr. Polym.* 221 (2019) 157–165.
- [137] G. Kopplin, et al., Structural characterization of fucoidan from *Laminaria Hyperborea*: assessment of coagulation and inflammatory properties and their structure-function relationship, *ACS Appl. Bio Mater.* 1 (6) (2018) 1880–1892.
- [138] L.L. Reys, et al., Fucoidan hydrogels photo cross-linked with visible radiation as matrices for cell culture, *ACS Biomater. Sci. Eng.* 2 (7) (2016) 1151–1161.
- [139] W. Wang, et al., Inhibition of influenza A virus infection by fucoidan targeting viral neuraminidase and cellular EGFR pathway, *Sci. Rep.* 7 (1) (2017) 1–14.
- [140] H. Li, et al., Fucoidan from *Pucus vesiculosus* suppresses hepatitis B virus replication by enhancing extracellular signal-regulated Kinase activation, *Viro. J.* 14 (1) (2017) 1–8.
- [141] S. Palanisamy, et al., Antibacterial efficacy of a fucoidan fraction (Fu F2) extracted from *Sargassum polycystum*, *Int. J. Biol. Macromol.* 125 (2019) 485–495.
- [142] M. Liu, et al., Antibacterial activity and mechanisms of depolymerized fucoidans isolated from *Laminaria japonica*, *Carbohydr. Polym.* 172 (2017) 294–305.
- [143] P. Karunanithi, et al., Three dimensional alginate-fucoidan composite hydrogel augments the chondrogenic differentiation of mesenchymal stromal cells, *Carbohydr. Polym.* 147 (2016) 294–303.
- [144] Q. Liu, et al., Zeln/fucoidan-based composite nanoparticles for the encapsulation of pterostilbene: Preparation, characterization, physicochemical stability, and formation mechanism, *Int. J. Biol. Macromol.* 158 (2020) 461–470.
- [145] M. Božić, S. Gorgieva, V. Kokol, Homogeneous and heterogeneous methods for lysozyme-mediated functionalization of chitosan by tannic acid and quercetin, *Carbohydr. Polym.* 89 (3) (2012) 854–864.
- [146] J. Guo, et al., Modular assembly of biomaterials using polyphenols as building blocks, *ACS Biomater. Sci. Eng.* 5 (11) (2019) 5578–5596.
- [147] M. Shin, et al., DNA/tannic acid hybrid gel exhibiting biodegradability, extensibility, tissue adhesiveness, and hemostatic ability, *Adv. Funct. Mater.* 25 (8) (2015) 1270–1278.
- [148] H. Deng, et al., Facile and eco-friendly fabrication of polysaccharides-based nanocomposite hydrogel for photothermal treatment of wound infection, *Carbohydr. Polym.* 230 (2020) 115565.

- [149] N. Isobe, et al., Primary structure of gum Arabic and its dynamics at oil/water interface, *Carbohydr. Polym.* 249 (2020) 116843.
- [150] C. Sanchez, et al., Acacia gum: History of the future, *Food Hydrocolloids* 78 (2018) 140–160.
- [151] B.R. Moreira, et al., A bioactive film based on cashew gum polysaccharide for wound dressing applications, *Carbohydr. Polym.* 122 (2015) 69–76.
- [152] P. Jana, et al., Preparation of guar gum scaffold film grafted with ethylenediamine and fish scale collagen, cross-linked with ceftazidime for wound healing application, *Carbohydr. Polym.* 153 (2016) 573–581.
- [153] R.R. Palem, K.M. Rao, T.J. Kang, Self-healable and dual-functional guar gum-grafted polyacrylamidoglycolic acid based hydrogels with nano silver for wound dressings, *Carbohydr. Polym.* 223 (2019) 115074.
- [154] C. Talodthaisong, et al., Composite guar gum-silver nanoparticle hydrogels as self-healing, injectable, and antibacterial biomaterials, *Mater. Today Commun.* 24 (2020) 100992.
- [155] D.C. Gowda, G. Resuter, R. Schauer, Structural studies of an acidic polysaccharide from the mucin secreted by *Drosera capensis*, *Carbohydr. Res.* 113 (1) (1983) 113–124.
- [156] Y. Huang, et al., Sundew adhesive: a naturally occurring hydrogel, *J. R. Soc. Interface* 12 (107) (2015) 20150226.
- [157] S. Lenaghan, et al., A naturally occurring nanomaterial from the Sundew (*Drosera*) for tissue engineering, *Bioinspiration Biomimetics* 6 (4) (2011) 46009.
- [158] H. Liu, I. Gomez, J.C. Meredith, Pollenkitt wetting mechanism enables species-specific tunable pollen adhesion, *Langmuir* 29 (9) (2013) 3012–3023.
- [159] K. Urech, et al., Apoptosis inducing activity of viscain, a lipophilic extract from *Viscum album L.*, *J. Pharm. Pharmacol.* 57 (1) (2005) 101–109.
- [160] N. Horbelt, et al., Unraveling the rapid assembly process of stiff cellulose fibers from mistletoe berries, *Biomacromolecules* 20 (8) (2019) 3094–3103.
- [161] E. Gedalovich-Shedletsky, D.P. Delmer, J. Kujir, Chemical composition of viscain macilage from three mistletoe species—a comparison, *Ann. Bot.* 64 (3) (1989) 249–252.
- [162] N. Drescher, et al., A clue on bee glue: New insight into the sources and factors driving resin intake in honeybees (*Apis mellifera*), *PLoS One* 14 (2) (2019) e0210594.
- [163] V. Bankova, M. Popova, B. Trusheva, Propolis volatile compounds: chemical diversity and biological activity: a review, *Chem. Cent. J.* 8 (1) (2014) 1–8.
- [164] S.I. Falcão, et al., In vitro interactions of moroccan propolis phytochemicals on human tumor cell lines and anti-inflammatory properties, *Biomolecules* 9 (8) (2019) 315.
- [165] I. Przybyłek, T.M. Karpiński, Antibacterial properties of propolis, *Molecules* 24 (11) (2019) 2047.
- [166] M.G. Arafa, et al., Propolis-based niosomes as oromuco-adhesive films: a randomized clinical trial of a therapeutic drug delivery platform for the treatment of oral recurrent aphthous ulcers, *Sci. Rep.* 8 (1) (2018) 1–14.
- [167] M. Roelianto, et al., In vivo study of sealing capability of raw propolis extract and calcium hydroxide on dentin surface, *Clinical, Cosmetic Investig. Dentist.* 12 (2020) 335.
- [168] A. Ekandarinia, et al., A propolis enriched polyurethane hyaluronic acid nanofibrous wound dressing with remarkable antibacterial and wound healing activities, *Int. J. Biol. Macromol.* 149 (2020) 467–476.
- [169] A. Piccolotto, et al., Bacterial cellulose membrane associated with red propolis as phytonutrient: improved healing effects in experimental models of diabetes mellitus, *Bioméd. Pharmacother.* 112 (2019) 108640.
- [170] S. Ezzat, et al., Cytotoxicity, antioxidant, anti-inflammatory activity, and GC-MS analysis of Egyptian propolis, *Comp. Clin. Pathol.* 28 (6) (2019) 1589–1598.
- [171] C.O. da Silva Froza, et al., Antitumor activity of Brazilian red propolis fractions against Hep-2 cancer cell line, *Bioméd. Pharmacother.* 91 (2017) 951–963.
- [172] D.M. Rodrigues, et al., Synthesis, antitumor activity and in silico analyses of amino acid derivatives of artemisinin C, drupanin and baecharin from green propolis, *Bioorg. Med. Chem.* (2021) 116372.
- [173] M. Zakerkish, et al., The effect of Iranian propolis on glucose metabolism, lipid profile, insulin resistance, renal function and inflammatory biomarkers in patients with type 2 diabetes mellitus: a randomized double-blind clinical trial, *Sci. Rep.* 9 (1) (2019) 1–11.
- [174] Y. Zheng, et al., Chinese propolis prevents obesity and metabolism Syndromes induced by a high fat diet and accompanied by an altered gut Microbiota structure in mice, *Nutrients* 12 (4) (2020) 959.
- [175] N. Cardinault, et al., Poplar propolis ethanolic extract reduces body weight gain and glucose metabolism disruption in high-fat diet-fed mice, *Mol. Nutr. Food Res.* 64 (18) (2020) 2000275.
- [176] A.M. Gharbousseau, J.M. Kinsella, S.D. Tran, 3D Cultures of salivary gland Cells in Native or gelled egg yolk Plasma, Combined with egg White and 3D-Printing of gelled egg yolk Plasma, *Materials* 12 (21) (2019) 3480.
- [177] Z. Rafati, et al., Honey-loaded egg white/poly (vinyl alcohol)/clay bionanocomposite hydrogel wound dressings: in vitro and in vivo evaluations, *J. Polym. Environ.* 28 (1) (2020) 32–46.
- [178] K. Xu, et al., Egg albumen as a fast and strong medical adhesive glue, *Adv. Healthcare Mater.* 6 (19) (2017) 1700132.
- [179] Y. Wei, et al., Water-resistant zein-based adhesives, *ACS Sustain. Chem. Eng.* 8 (20) (2020) 7668–7679.
- [180] J.W. Weisel, R.I. Litvinov, Fibrin formation, structure and properties, *Fibrous proteins: structures and mechanisms* (2017) 405–456.
- [181] J. Browns, et al., The structure and function of zein genes of maize, *Biochem. Physiol. Pflanz.* (BPP) 183 (2–3) (1988) 99–106.
- [182] N. Parris, L.C. Dickey, Adhesive properties of corn zein formulations on glass surfaces, *J. Agric. Food Chem.* 51 (13) (2003) 3892–3894.
- [183] H. Simonds, A. Weith, M. Bigelow, *Manufacture of Zein Plastic*. Handbook of Plastics, second ed., Van Nostrand, New York, 1949, pp. 754–756.
- [184] W.C. Uy, *Dry Spinning Process for Producing Zein Fibers*, Google Patents, 1998.
- [185] C. Kimsa, S. Tamburaci, P. Tihminlioglu, Novel zein-based multilayer wound dressing membranes with controlled release of gentamicin, *J. Biomed. Mater. Res. B Appl. Biomater.* 107 (6) (2019) 2057–2070.
- [186] M. Demir, et al., Zein-based composites in biomedical applications, *J. Biomed. Mater. Res.* 105 (6) (2017) 1656–1665.
- [187] M. Oh, et al., Comparative study of zein-and gluten-based wood adhesives containing cellulose nanofibers and crosslinking agent for improved bond strength, *Int. J. Adhesion Adhes.* 92 (2019) 44–57.
- [188] W.D. Spontitz, *Fibrin sealant: past, present, and future: a brief review*, *World J. Surg.* 34 (4) (2010) 632–634.
- [189] V. Bhagat, M.L. Becker, Degradable adhesives for surgery and tissue engineering, *Biomacromolecules* 18 (10) (2017) 3009–3039.
- [190] S. Rahal, et al., Effect of fibrin glue derived from snake venom on the viability of autogenous split-thickness skin graft, *J. Venom. Anim. Toxins Incl. Trop. Dis.* 10 (2004) 161–172.
- [191] M.D. Barbosa, et al., Fibrin adhesive derived from snake venom in periodontal surgery: histological analysis, *J. Appl. Oral Sci.* 16 (2008) 310–315.
- [192] R.L. Buchain, et al., Effect of low-level laser therapy (LLL) on peripheral nerve regeneration using fibrin glue derived from snake venom, *Injury* 46 (4) (2015) 655–660.
- [193] J. Yu, et al., Mussel protein adhesion depends on interprotein thiol-mediated redox modulation, *Nat. Chem. Biol.* 7 (9) (2011) 588–590.
- [194] T.-N. Pham, et al., Biomimetic hydrogels based on L-Dopa conjugated gelatin as pH-responsive drug carriers and antimicrobial agents, *Colloids Surf. B Biointerfaces* 196 (2020) 111316.
- [195] I. Kotvasalo, et al., Tissue adhesive hyaluronic acid hydrogels for sutureless stem cell delivery and regeneration of corneal epithelium and stroma, *Biomaterials* 225 (2019) 119516.
- [196] Y. Shou, et al., Thermoresponsive chitosan/DOPA-based hydrogel as an injectable therapy approach for tissue-adhesion and hemostasis, *ACS Biomater. Sci. Eng.* 6 (6) (2020) 3619–3629.
- [197] D. Giuri, P. Ravarino, C. Tomasini, L-Dopa in small peptides: an amazing functionality to form supramolecular materials, *Org. Biomol. Chem.* 19 (21) (2021) 4622–4636.
- [198] A.H. Gowda, et al., Design of tunable gelatin dopamine based bioadhesives, *Int. J. Biol. Macromol.* 164 (2020) 1384–1391.
- [199] B. Peng, et al., Scarless wound closure by a mussel-inspired poly (amideamine) tissue adhesive with tunable degradability, *ACS Omega* 2 (9) (2017) 6053–6062.
- [200] E. Masoudipour, S. Kashanian, N. Maleki, A targeted drug delivery system based on dopamine functionalized nano graphene oxide, *Chem. Phys. Lett.* 668 (2017) 56–63.
- [201] R. Yu, et al., Surface modification of pH sensitive honokiol nanoparticles based on dopamine coating for targeted therapy of breast cancer, *Colloids Surf. B Biointerfaces* 177 (2019) 1–10.
- [202] D. Zhu, et al., Enzyme/redox responsive mesoporous silica nanoparticles based on functionalized dopamine as nanocarriers for cancer therapy, *ACS Omega* 4 (4) (2019) 6097–6105.
- [203] Z. Lu, et al., Electrospun highly porous poly (L-lactic acid)-dopamine-SiO<sub>2</sub> fibrous membrane for bone regeneration, *Mater. Sci. Eng. C* 117 (2020) 111359.
- [204] Z. Yang, et al., Mussel-inspired catalytic scienocystamine-dopamine coatings for long-term generation of therapeutic gas on cardiovascular stents, *Biomaterials* 178 (2018) 1–10.
- [205] J. Song, et al., Bioinspired dopamine/mucin coatings provide lubricity, wear protection, and cell-repellent Properties for medical applications, *Adv. Healthcare Mater.* 10 (4) (2021) 2000831.
- [206] B.D.B. Tiu, et al., Enhanced adhesion and cohesion of bioinspired dry/wet pressure-sensitive adhesives, *ACS Appl. Mater. Interfaces* 11 (31) (2019) 28296–28306.
- [207] P.T. Becker, et al., Identification, characterization, and expression levels of putative adhesive proteins from the tube-dwelling polychaete *Sabellaria alveolata*, *Biol. Bull.* 223 (2) (2012) 217–225.
- [208] R.J. Stewart, et al., The tube cement of *Phragmatopoma californica*: a solid foam, *J. Exp. Biol.* 207 (26) (2004) 4727–4734.
- [209] C.G. De Kruij, F. Weinbreck, R. de Vries, Complex coacervation of proteins and anionic polysaccharides, *Curr. Opin. Colloid Interface Sci.* 9 (5) (2004) 340–349.
- [210] L.D. Graham, et al., Characterization of a protein-based adhesive elastomer secreted by the Australian frog *Notaden bennetti*, *Biomacromolecules* 6 (6) (2005) 3300–3312.
- [211] N.I. Millar, et al., Frog glue enhances rotator cuff repair in a laboratory cadaveric model, *J. Shoulder Elbow Surg.* 18 (4) (2009) 639–645.
- [212] J. Deng, et al., A bioinspired medical adhesive derived from skin secretion of *Andrias davidianus* for wound healing, *Adv. Funct. Mater.* 29 (31) (2019) 1809110.
- [213] P. Dubey, et al., Effect of macromolecular crowders on the self-assembly process of silk fibroin, *Macromol. Chem. Phys.* 221 (16) (2020) 2000113.
- [214] S.C. Kunda, et al., Natural protective glue protein, sericin bioengineered by silkworms: potential for biomedical and biotechnological applications, *Prog. Polym. Sci.* 33 (10) (2008) 998–1012.
- [215] F. Seyedghamiri, et al., Sericin modulates learning and memory behaviors by tuning of antioxidant, inflammatory, and apoptotic markers in the hippocampus of aged mice, *Mol. Biol. Rep.* 48 (2) (2021) 1371–1382.



- [216] J.P. Kumar, B.B. Mandal, Antioxidant potential of mulberry and non mulberry silk sericin and its implications in biomedicine, *Free Radic. Biol. Med.* 108 (2017) 803–818.
- [217] R. Santos, et al., First insights into the biochemistry of tube foot adhesive from the sea urchin *Paracentrotus lividus* (Echinoida, Echinodermata), *Mar. Biotechnol.* 11 (6) (2009) 686–698.
- [218] P. Flammang, et al., A study of the temporary adhesion of the podia in the sea star *Asterias rubens* (Echinodermata, Asteroidea) through their footprints, *J. Exp. Biol.* 201 (16) (1998) 2383–2395.
- [219] E. Hennebert, et al., An integrated transcriptomic and proteomic analysis of sea star epidermal secretions identifies proteins involved in defense and adhesion, *J. Proteomics* 128 (2015) 83–91.
- [220] M. Lefevre, et al., Sea star-inspired recombinant adhesive proteins self-assemble and adsorb on surfaces in aqueous environments to form cytocompatible coatings, *Acta Biomater.* 112 (2020) 62–74.
- [221] E. Hennebert, R. Watriez, P. Flammang, Characterisation of the carbohydrate fraction of the temporary adhesive secreted by the tube feet of the sea star *Asterias rubens*, *Mar. Biotechnol.* 13 (3) (2011) 484–495.
- [222] J. Von Byern, et al., Characterization of the fishing lines in *Tiriwai* (= *Arachnocampa luminosa* Skuse, 1890) from New Zealand and Australia, *PLoS One* 11 (12) (2016) e0162687.
- [223] L.J. Böni, et al., Effect of ionic strength and seawater cations on hagfish slime formation, *Sci. Rep.* 8 (1) (2018) 1–12.
- [224] R.L.I. Ewaldt, et al., Rheological fingerprinting of gastropod pedal mucus and synthetic complex fluids for biomimicking adhesive locomotion, *Soft Matter* 3 (5) (2007) 634–643.
- [225] M.F. Di Filippo, et al., Novel drug-loaded film forming patch based on gelatin and snail slime, *Int. J. Pharm.* 598 (2021) 120408.
- [226] A. Rising, J. Johanson, Toward spinning artificial spider silk, *Nat. Chem. Biol.* 11 (5) (2015) 309–315.
- [227] N.A. Ayoub, et al., Blueprint for a high-performance biomaterial: full-length spider dragline silk genes, *PLoS One* 2 (6) (2007) e514.
- [228] M.A. Collin, et al., Evidence from multiple species that spider silk glue component ASG2 is a spidroin, *Sci. Rep.* 6 (1) (2016) 1–12.
- [229] B.D. Opell, S.D. Stellwagen, Properties of orb weaving spider glycoprotein glue change during *Argiope trifasciata* web construction, *Sci. Rep.* 9 (1) (2019) 1–11.
- [230] L. Gustafsson, et al., Recombinant spider silk forms tough and elastic nanomembranes that are protein permeable and support cell attachment and growth, *Adv. Funct. Mater.* 30 (40) (2020) 2002982.
- [231] M. Marczynski, B. Winkelmann, O. Lieleg, Advances in mucin biopolymer research: Purification, characterization, and applications, *Biopolym. Biomed. Biotechnol. Appl.* (2021) 181–208.
- [232] A.R. Cerullo, et al., Comparative animal mucinomics: inspiration for functional materials from ubiquitous and understudied biopolymers, *ACS Biomater. Sci. Eng.* 6 (10) (2020) 5377–5398.
- [233] J. Uzawa, et al., NMR study on a novel mucin from jellyfish in natural abundance, *gnamuc* from *Aurelia aurita*, *J. Nat. Prod.* 72 (5) (2009) 818–823.
- [234] K. Rementzi, et al., Structure and dynamics of hagfish mucin in different saline environments, *Soft Matter* 15 (42) (2019) 8627–8637.
- [235] J. Fu, P.A. Guerette, A. Miserez, Self-assembly of recombinant hagfish thread keratin amenable to a strain-induced  $\alpha$ -helix to  $\beta$ -sheet transition, *Biomacromolecules* 16 (8) (2015) 2327–2339.
- [236] X. Cheng, et al., Isolation, characterization and evaluation of collagen from jellyfish *Rhopilema esculentum* Kishinouye for use in hemostatic applications, *PLoS One* 12 (1) (2017) e0169731.
- [237] Z. Rustian, et al., Type I collagens from jellyfish *Cyanea lamarckii* for biomaterial applications, *ACS Biomater. Sci. Eng.* 4 (6) (2018) 2115–2125.
- [238] I. Flaig, et al., In vivo analysis of the biocompatibility and immune response of jellyfish collagen scaffolds and its suitability for bone regeneration, *Int. J. Mol. Sci.* 21 (12) (2020) 4518.
- [239] W. Pastlank, et al., Jellyfish collagen and alginate: combined marine materials for superior chondrogenesis of hMSC, *Mater. Sci. Eng. C* 64 (2016) 190–198.
- [240] B. Derkus, et al., Development of a novel aptasensor using jellyfish collagen as matrix and thrombin detection in blood samples obtained from patients with various neurodegeneration, *Sens. Actuators B Chem.* 228 (2016) 725–736.
- [241] M.T. Galejo, A.J. Almeida, A.I. Fernandes, Exploring a new jellyfish collagen in the production of microparticles for protein delivery, *J. Microencapsul.* 29 (6) (2012) 520–531.
- [242] A. Masuda, et al., Mucin (gnamuc), a glycoprotein from jellyfish, and determination of its main chain structure, *J. Nat. Prod.* 70 (7) (2007) 1089–1092.
- [243] K. Ushida, T. Murata, Materials science and engineering of mucin: a new aspect of mucin chemistry, *Stud. Nat. Prod. Chem.* 39 (2013) 115–159.
- [244] A. Yaman, Alternative methods of terminal sterilization for biologically active macromolecules, *Curr. Opin. Drug Discov. Dev.* 4 (6) (2001) 760–763.
- [245] K. Punatsa, et al., Impact of ethylene oxide sterilization of polymer based prefilled syringes on chemical degradation of a model therapeutic protein during storage, *J. Pharmaceut. Sci.* 108 (1) (2019) 770–774.
- [246] Y. Zhou, et al., Light-switchable polymer adhesive based on photoinduced reversible solid-to-liquid transitions, *ACS Macro Lett.* 8 (8) (2019) 968–972.
- [247] I. Kortekaas, et al., Rapid Photoswitching of low molecular weight Arylazoxazole adhesives, *ACS Appl. Mater. Interfaces* 12 (28) (2020) 32054–32060.
- [248] T. Ohtsuno, et al., Light-driven dynamic adhesion on photosensitized nematic liquid crystalline elastomers, *ACS Appl. Mater. Interfaces* 12 (28) (2020) 31992–31997.
- [249] Y. Liang, et al., pH responsive injectable hydrogels with mucosal adhesiveness based on chitosan-grafted-dihydrocaffeic acid and oxidized pullulan for localized drug delivery, *J. Colloid Interface Sci.* 536 (2019) 224–234.
- [250] A.R. Narkar, et al., pH responsive and oxidation resistant wet adhesive based on reversible catechol–boronate complexation, *Chem. Mater.* 28 (15) (2016) 5432–5439.
- [251] X. Yan, et al., Thermoresponsive in situ forming hydrogel with sol–gel irreversibility for effective methicillin resistant *Staphylococcus aureus* infected wound healing, *ACS Nano* 13 (9) (2019) 10074–10084.
- [252] Y. Ma, et al., Remote control over underwater dynamic attachment/detachment and locomotion, *Adv. Mater.* 30 (30) (2018) 1801595.
- [253] L. Xiao, et al., An artificial phase transitional underwater biogel with robust and switchable adhesion performance, *Angew. Chem. Int. Ed.* 60 (21) (2021) 12082–12089.
- [254] X. Chen, et al., Instant tough bioadhesive with triggerable benign detachment, *Proc. Natl. Acad. Sci. United States Am.* 117 (27) (2020) 15497–15503.
- [255] Y. Lee, et al., Bioinspired nanoparticulate medical glues for minimally invasive tissue repair, *Adv. Healthcare Mater.* 4 (16) (2015) 2587–2596.
- [256] J.P. Jones, et al., Water-borne endovascular embolics inspired by the underside adhesive of marine sandcastle worms, *Adv. Healthcare Mater.* 5 (7) (2016) 795–801.
- [257] N. Lang, et al., A blood-resistant surgical glue for minimally invasive repair of vessels and heart defects, *Sci. Transl. Med.* 6 (218) (2014), 218ra6–218ra6.
- [258] Z. Xu, et al., A thermally healable polyhedral oligomeric silsesquioxane (POSS) nanocomposite based on Diels–Alder chemistry, *Chem. Commun.* 49 (60) (2013) 6755–6757.
- [259] L. Teng, et al., Weak hydrogen bonds lead to self-healable and bioadhesive hybrid polymeric hydrogels with mineralization active functions, *Biomacromolecules* 19 (6) (2018) 1939–1949.
- [260] C. Shao, et al., Mimicking dynamic adhesiveness and strain-stiffening behavior of biological tissues in tough and self-healable cellulose nanocomposite hydrogels, *ACS Appl. Mater. Interfaces* 11 (6) (2019) 5885–5895.
- [261] W. Huang, et al., Noncompressible hemostasis and bone regeneration induced by an absorbable bioadhesive self-healing hydrogel, *Adv. Funct. Mater.* 31 (22) (2021) 2009189.
- [262] G. Deng, et al., Macroscopic organohydrogel hybrid from rapid adhesion between dynamic covalent hydrogel and organogel, *ACS Macro Lett.* 4 (4) (2015) 467–471.
- [263] K. Liu, et al., Bioengineered protein based adhesives for biomedical applications, *Chem. A Eur. J.* 28 (2021) e202102902.
- [264] X. Li, et al., Wet-spinning synthetic fibers from aggregate glue: aggregate spidroin 1 (AgSp1), *ACS Appl. Bio Mater.* 3 (9) (2020) 5957–5965.
- [265] S. Arias, et al., Toward artificial mussel-glu proteins: differentiating sequence Modules for Adhesion and switchable cohesion, *Angew. Chem. Int. Ed.* 59 (42) (2020) 18495–18499.
- [266] M.A. Gonzalez, et al., Strong, tough, stretchable, and self adhesive hydrogels from intrinsically unstructured proteins, *Adv. Mater.* 29 (10) (2017) 1604743.
- [267] Y. Lei, et al., Adhesive property and mechanism of silkworm egg glue protein, *Acta Biomater.* 134 (2021) 499–512.
- [268] C. Ma, et al., Ultra-strong bio-gel from genetically engineered polypeptides, *Nat. Commun.* 12 (1) (2021) 1–14.
- [269] I.L.J. Kim, et al., Sandcastle worm-inspired blood-resistant bone graft binder Using a sticky mussel Protein for augmented in vivo bone regeneration, *Adv. Healthcare Mater.* 5 (24) (2016) 3191–3202.
- [270] H. Yuk, et al., Dry double-sided tape for adhesion of wet tissues and devices, *Nature* 575 (7781) (2019) 169–174.
- [271] G. Xiong, et al., Fast-curing mussel-inspired adhesive Derived from vegetable oil, *ACS Appl. Bio Mater.* 4 (2) (2021) 1360–1368.
- [272] N. Shimony, et al., Liquid copolymers as biodegradable surgical sealant, *Adv. Healthcare Mater.* (2021) 2100803.
- [273] D. Gan, et al., Plant-inspired adhesive and tough hydrogel based on Ag-Lignin nanoparticles-triggered dynamic redox catechol chemistry, *Nat. Commun.* 10 (1) (2019) 1–10.
- [274] J. Yang, R. Bai, Z. Suo, Topological adhesion of wet materials, *Adv. Mater.* 30 (25) (2018) 1800671.
- [275] L. Zhou, et al., Injectable self healing natural biopolymer based hydrogel Adhesive with Thermoresponsive reversible Adhesion for minimally invasive surgery, *Adv. Funct. Mater.* 31 (14) (2021) 2007457.
- [276] A. Kirillova, et al., Bioinspired mineral-organic bioresorbable bone adhesive, *Adv. Healthcare Mater.* 7 (17) (2018) 1800467.
- [277] M. Krogsgaard, M.R. Hansen, H. Birkedal, Metals & polymers in the mix: fine-tuning the mechanical properties & color of self-healing mussel-inspired hydrogels, *J. Mater. Chem. B* 2 (47) (2014) 8292–8297.
- [278] A.H. Pandit, et al., Injectable, self-healing, and biocompatible N, O-carboxymethyl chitosan/Multialdehyde guar gum Hydrogels for sustained anticancer drug delivery, *Biomacromolecules* 22 (9) (2021) 3731–3745.
- [279] Q. Chang, et al., Hydrogels from natural egg white with extraordinary stretchability, direct-writing 3D printability and self-healing for fabrication of electronic sensors and actuators, *J. Mater. Chem.* 7 (42) (2019) 24626–24640.
- [280] C. Shao, et al., A self-healing cellulose nanocrystal-poly (ethylene glycol) nanocomposite hydrogel via Diels–Alder click reaction, *ACS Sustain. Chem. Eng.* 5 (7) (2017) 6167–6174.
- [281] Y. Chen, et al., Multiphase design of autonomic self-healing thermoplastic elastomers, *Nat. Chem.* 4 (6) (2012) 467–472.
- [282] C.S. Lee, et al., Inspired by nature: facile design of Nanoclay-organic hydrogel bone sealant with multifunctional properties for robust bone regeneration, *Adv. Funct. Mater.* 30 (43) (2020) 2003717.

- [283] M. Shin, et al., Rheological criteria for distinguishing self healing and non self healing hydrogels, *Polymer* 229 (2021) 123969.
- [284] W. Ge, et al., Rapid self-healing, stretchable, moldable, antioxidant and antibacterial tannic acid-cellulose nanofibril composite hydrogels, *Carbohydr. Polym.* 224 (2019) 115147.
- [285] Z. He, *Bio based Wood Adhesives: Preparation, Characterization, and Testing*, CRC Press, 2017.
- [286] Y. Liu, K. Li, Chemical modification of soy protein for wood adhesives, *Macromol. Rapid Commun.* 23 (13) (2002) 739-742.
- [287] S. Magalhães, et al., Brief overview on bio based adhesives and sealants, *Polymers* 11 (10) (2019) 1685.

## B.2 Repulsive backbone-backbone interactions modulate access to specific and unspecific binding sites on surface-bound mucins

# LANGMUIR

pubs.acs.org/langmuir

Article

## Repulsive Backbone–Backbone Interactions Modulate Access to Specific and Unspecific Binding Sites on Surface-Bound Mucins

Theresa M. Lutz, Matthias Marczyński, Maximilian J. Grill, Wolfgang A. Wall, and Oliver Lieleg\*

Cite This: <https://dx.doi.org/10.1021/acs.langmuir.0c02256>

Read Online

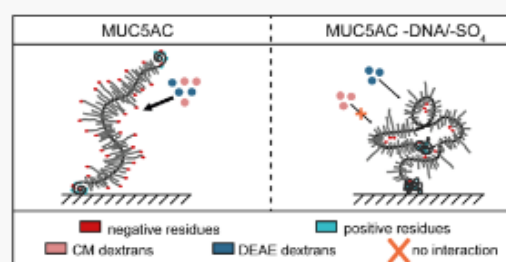
ACCESS |

Metrics & More

Article Recommendations

Supporting Information

**ABSTRACT:** Mucin glycoproteins are the matrix-forming key components of mucus, the innate protective barrier protecting us from pathogenic attack. However, this barrier is constantly challenged by mucin-degrading enzymes, which tend to target anionic glycan chains such as sulfate groups and sialic acid residues. Here, we demonstrate that the efficiency of both unspecific and specific binding of small molecules to mucins is reduced when sulfate groups are enzymatically removed from mucins; this is unexpected because neither of the specific mucin-binding partners tested here targets these sulfate motifs on the mucin glycoprotein. Based on simulation results obtained from a numerical model of the mucin macromolecule, we propose that anionic motifs along the mucin chain establish intramolecular repulsion forces which maintain an elongated mucin conformation. In the absence of these repulsive forces, the mucin seems to adopt a more compacted structure, in which the accessibility of several binding sites is restricted. Our results contribute to a better understanding on how different glycans contribute to the broad spectrum of functions mucin glycoproteins have.



### INTRODUCTION

With the current corona pandemic forcing most of the world's population to self-isolate, we are reminded that our innate immune system cannot fully protect us from all the pathogens the human body is exposed to. In healthy individuals, the first physical barrier invading pathogens encounter is the mucus layer that covers all wet epithelial tissues of the human body.<sup>1–5</sup> This hydrogel lining can retain microscopic objects such as dust particles<sup>6,7</sup> or bacteria<sup>8,9</sup> due to its mere size constraints. Additionally, mucin glycoproteins, which are the key component of mucus, can also immobilize small viruses—either *via* unspecific (hydrophobic or electrostatic) binding interactions or *via* specific binding to certain motifs of the mucin molecule such as sialic acid residues.<sup>10–12</sup>

This versatility of mucin-binding properties is based on the complex structure of the glycoprotein. Mucins are organized in three distinct sections: an elongated, hydrophilic, and highly glycosylated protein core is terminated by two hydrophobic, partially folded, and almost glycan-free termini. Despite their overall hydrophobic character, the mucin termini contain a large number of (both positively and negatively) charged amino acid side chains. The oligoglycan chains attached to the core of the polypeptide contain a large amount of sialic acid and sulfate groups, which convey an overall negative net charge to mucins—at least at neutral pH levels.<sup>13–17</sup>

*In vivo*, mucins are constantly challenged by enzymes, and those enzymes either originate from the mucin-secreting organisms<sup>18,19</sup> or from pathogens<sup>20,21</sup> which try to weaken

the mucosal barrier. Indeed, anionic glycan motifs are a typical starting point for bacterial or viral degradation of mucins.<sup>22</sup> Previous work has already indicated how important the molecular integrity of mucins is for mucin functionality,<sup>23,24</sup> and also anionic mucin glycans have been put forward to be critical in this context<sup>15</sup> since the repulsive electrostatic forces acting between these anionic groups contribute to maintaining an elongated conformation. The weakening of intramolecular electrostatic repulsion is thought to result in a conformational change of this elongated bottle brush-like mucin structure into a rather globular state.<sup>25–28</sup> Such a severe conformational change can be expected to also affect the interaction of mucins with other particles, molecules,<sup>29</sup> or microorganisms<sup>30</sup> and thus the permeability of a mucin network toward these objects.

In this article, we show that the removal of anionic residues from porcine gastric mucin reduces the binding capability of mucin toward both cationic and anionic molecules as well as specific-binding partners, which do not directly target the anionic residues. By combining experimental data obtained from a molecular depletion assay, ELISA, and adsorption

Received: July 31, 2020

Revised: October 8, 2020

ACS Publications

© XXXX American Chemical Society

A

<https://dx.doi.org/10.1021/acs.langmuir.0c02256>  
Langmuir XXXX, XXX, XXX–XXX

Downloaded via CENTRAL MICHIGAN UNIV on November 2, 2020 at 09:48:01 (UTC).  
See <https://pubs.acs.org/sharingguidelines> for options on how to legitimately share published articles.

experiments with numerical simulations of mucins with different charge profiles, we propose that the mucin glycoprotein undergoes a conformational change when anionic glycans are removed. In turn, our results suggest that anionic residues along the mucin chain establish intramolecular repulsion forces that maintain the “natural”, elongated conformation of an intact mucin.

## MATERIALS AND METHODS

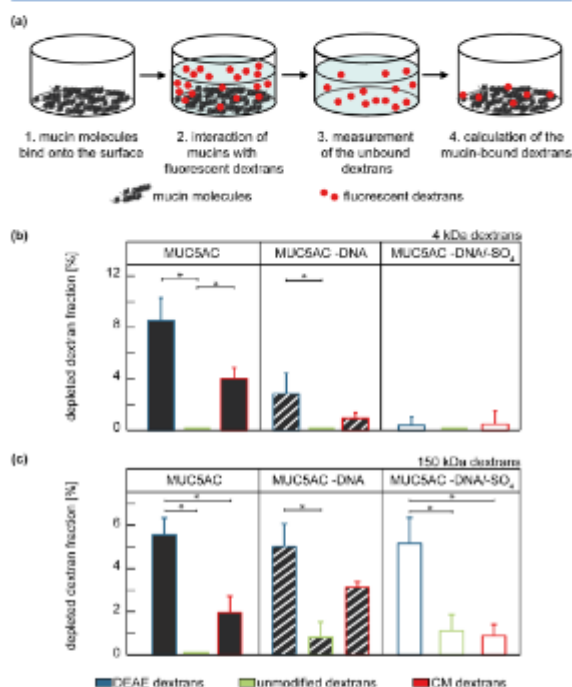
**Mucin Purification and Reconstitution.** Porcine gastric mucin was purified as previously described.<sup>31</sup> In brief, pig stomachs were gently rinsed with tap water, and mucus was harvested by manually scraping the gastric mucosa with spoons. The collected mucus was diluted 5-fold in 10 mM sodium phosphate buffer (pH 7.0) containing 170 mM NaCl and 0.04% (w/v) Na<sub>2</sub>S<sub>2</sub>O<sub>3</sub>. After homogenization at 4 °C overnight, cellular debris was removed via two centrifugation steps (first at 8300g and 4 °C for 30 min, second at 15,000g and 4 °C for 45 min) and a final ultracentrifugation step (150,000g and 4 °C for 1 h). Subsequently, the mucins were isolated by means of size exclusion chromatography using an ÄKTA purifier system (GE Healthcare, Chicago, IL, USA) and an XK50/100 column packed with Sepharose 6FF. The obtained mucin fractions were pooled, dialyzed against ultrapure water, and concentrated by cross-flow filtration using a membrane with a molecular weight cut-off of 100 kDa (GE Healthcare). The concentrate was then lyophilized and stored at -80 °C until further usage. To reconstitute mucin solutions, the lyophilized mucin powder was dissolved in ultrapure water while shaking at 4 °C for 1 h. Since we do not add any reducing agent to the harvested mucus, we expect our lab-purified mucin to contain both monomeric mucin molecules and mucin oligomers. We have demonstrated previously that—in either state—our lab-purified mucin is of superior quality compared to commercial porcine gastric mucin.<sup>15</sup> Moreover, a mass spectrometer analysis of our lab-purified mucin solution has shown that, whereas molecular contaminants are still present, MUC5AC is (in terms of identified matches with the generated fragments) the most frequent protein in the purified product.

**Enzymatic Treatment of Mucins.** Mucin that is purified from gastric mucus is always associated with DNA, and this might be the physiological state gastric mucins occur in. This DNA, however, can be removed efficiently by an enzymatic treatment as indicated by a gel electrophoresis with subsequent DNA staining (Figure S1a). For enzymatic removal of mucin-associated DNA, lyophilized MUC5AC powder was first exposed to UV radiation for 1 h and then dissolved in sterile 50 mM Tris-HCl (AppliChem, Darmstadt, Germany and Carl Roth, Karlsruhe, Germany) buffer (pH 7.5) supplemented with 10 mM MgCl<sub>2</sub> (Carl Roth) at a concentration of 1 mg mL<sup>-1</sup>. Per 1 mg mucin, 50 μL of a 0.1% (w/v) bovine pancreas deoxyribonuclease I (DNase I) solution (Sigma-Aldrich, St. Louis, USA) was mixed with the mucin solution and incubated at 37 °C overnight while shaking at 250 rpm (Promax 1020, Heidolph Instruments GmbH & Co. KG, Schwabach; Germany). This DNase-treated mucin was then further purified as described above.

Afterward, some of the DNase-treated mucin was further treated with sulfatase (which we checked for proteinase-activity as shown in Figure S1b): again, the DNA-reduced mucin was exposed to UV light for 1 h and then dissolved in sterile 200 mM sodium acetate buffer (pH 5.0). Per 1 mg of mucin, 1 U sulfatase from *Helix pomatia* (type H-1, Sigma-Aldrich, St. Louis, MO, USA) was added. The reaction was allowed to take place at 37 °C overnight while shaking at 250 rpm (Heidolph Instruments GmbH & Co. KG). Also here, the modified mucin was further purified as described above. Using a commercial kit for quantification of the released sulfate groups (QuantiChrom Sulfate Assay; BioAssay Systems, Hayward, CA, USA), we have determined previously that the removed sulfate motifs account to ~1.35% of the mucin dry weight.<sup>15</sup> For another batch of lab-purified gastric mucin, we found that, with the same enzymatic treatment, ~0.9 ± 0.1% of the mucin dry weight was removed; this agrees well with both literature values<sup>32,33</sup> and our previous experimental results.<sup>15</sup> We note

that the sulfatase used in this study is an arylsulfatase. Mucins, however, do not carry aryl sulfate groups but a significant amount of *N*-acetylglucosamine-6-sulfate (GlcNAc-6-SO<sub>3</sub>) groups.<sup>34,35</sup> We verified the activity of the arylsulfatase against this specific motif by repeating the sulfate assay using heparin as a substrate, which also carries such GlcNAc-6-SO<sub>3</sub> groups. The sulfate groups removed by this treatment account to ~0.56 ± 0.02% of the heparin dry weight. Given that each disaccharide unit of heparin, on average, carries 2–2.5 sulfate groups,<sup>36</sup> this suggests that the activity of the enzyme used here against GlcNAc-6-SO<sub>3</sub> groups is rather low.

**Depletion Assay.** To determine relative binding affinities of molecules toward different mucin variants, a depletion assay was conducted as recently described (Figure 1a).<sup>37</sup> As unspecific binding



**Figure 1.** Depletion assay to assess the binding interaction of native and enzymatically treated mucins with different dextrans. (a) Schematic representation of the experimental setup used for the depletion assay. Mucins are passively adsorbed onto the bottom and lateral wall of wells of a well plate. Then, a solution of fluorescently labeled dextrans is added, from which dextrans are depleted by binding to the adsorbed mucin layer. Finally, the fluorescence intensity of the supernatant (which contains the remaining, i.e., unbound dextrans) is determined, from which the amount of depleted (=mucin bound) dextrans can be derived. (b,c) Binding of cationic (blue), neutral (green), and anionic (red) dextrans to adsorbed mucin layers is compared for dextrans with a molecular weight of 4 (b) and 150 kDa (c). The error bars represent the standard error of the mean as obtained from five individual samples. Asterisks mark significant differences between the dextran groups ( $p \leq 0.05$ ) determined by one-way ANOVA combined with a Tukey post-hoc test for pairwise comparison.

partners for mucins, we selected dextrans since these polysaccharides are easy to handle and available as different variants, for example, with different functionalizations but similar molecular weights. In addition to six different dextran species (MW: 4 and 150 kDa, respectively; three variants per MW: diethylaminoethyl-modified, unmodified, and carboxymethyl-(CM-) modified; each conjugated with fluorescein isothiocyanate (FITC); Sigma-Aldrich), also the FITC-conjugated

lectin wheat germ agglutinin (WGA, which binds to sialic acid motifs) was tested. Dextrans with a molecular weight of 4 kDa were dissolved in 20 mM HEPES buffer (pH 7.0) at a concentration of 0.02% (w/v), dextrans with a molecular weight of 150 kDa at a concentration of 0.00125% (w/v) in the same buffer. The WGA was dissolved at a concentration of 10  $\mu\text{g mL}^{-1}$  in 20 mM HEPES buffer (pH 7.0).

Then, wells of a 96-well microtiter plate (Corning, Inc., Corning, NY, USA) were coated with mucin molecules by means of passive adsorption. For this purpose, 0.1% (w/v) mucin was dissolved in 20 mM HEPES buffer (pH 7.0), and 200  $\mu\text{L}$  of this mucin solution was added to each well; then, incubation was conducted at 4 °C overnight. Afterward, the wells were rinsed with 200  $\mu\text{L}$  of 20 mM HEPES buffer twice, and each well was incubated with 200  $\mu\text{L}$  of a test molecule solution at RT for 1 h. After incubation, 100  $\mu\text{L}$  of the test molecule solution was transferred from each well into a fresh well of an uncoated 96-well microtiter plate, and the fluorescence intensity of each sample was measured with a multi-label plate reader (Viktor3, PerkinElmer, Inc., MA, USA) at a wavelength of 535 nm using a data acquisition time of 0.1 s. Normalization of these measured fluorescence values was then conducted as follows: for each ligand molecule tested here (*i.e.*, either a dextran variant or WGA), both mucin-coated and uncoated wells were filled with equal amounts of the respective ligand solution and incubated as described above. Then, average values were determined for the fluorescence signal measured for samples from coated and uncoated wells, and the ratio of those values was calculated.

**Fluorescence Labeling of Mucins.** The three mucin variants were each labeled with the green fluorescent dye ATTO488 (carboxy-modified, ATTO-TEC GmbH, Siegen, Germany). 5 mM 1-ethyl-3-(3-dimethylaminopropyl)-carbodiimide and 10 mM sulfo-*N*-hydroxysuccinimide (sulfo-NHS) were mixed with the fluorescent dye at a concentration of 1 mg  $\text{mL}^{-1}$  in 10 mM 2-(*N*-morpholino)ethanesulfonic acid buffer (pH 5.0). After an incubation time of 3 h at room temperature, 100  $\mu\text{L}$  of this mixture was added to a 0.2% (w/v) solution of mucins (dissolved in Dulbecco's phosphate-buffered saline solution = DPBS; Lonza, Verviers, Belgium). The activated, carboxy-modified fluorophore is covalently coupled to the amine groups of the mucin molecule by incubation at room temperature for 3 h. The ATTO488-labeled mucins were then further purified as described above for native mucin. Solutions of the fluorescently labeled mucin variants were prepared in 20 mM HEPES buffer (pH 7.0) and incubated in the wells of a 96-well plate in a concentration series ranging from 0.001 to 0.1% (w/v) at 4 °C overnight. The fluorescence intensity of each mucin solution was determined with a multi-label plate reader (Viktor3) at a wavelength of 535 nm using a data acquisition time of 0.1 s.

**Indirect Enzyme-Linked Immunosorbent Assay.** For ELISA experiments, first, five wells of a 96-well microtiter plate (Corning, Inc., Corning, NY, USA) were incubated with a solution containing a particular mucin variant [0.01% (w/v) mucin in PBS] each. After an incubation step conducted at room temperature for 2 h, the wells were washed three times with PBS and then blocked with PBS-Tween [0.1% Tween 20, Carl Roth, pH 7.4, supplemented with 5% (w/v) milk powder] at 4 °C overnight. After washing the wells with PBS-Tween, the primary antibody (ABIN966608, antibodies-online GmbH, Aachen, Germany, diluted 1:400 in blocking buffer) was added to each well. After incubating the samples at room temperature for 1 h while shaking at 100 rpm (Heidolph), the wells were washed with PBS-Tween again. Then, the secondary antibody [horse radish peroxidase (HRP) conjugated goat anti-mouse IgG antibody, ABIN237501, antibodies-online GmbH; diluted 1:5000 in blocking buffer] was added to the wells. The samples were incubated at room temperature for 2 h while shaking at 100 rpm and washed with PBS. Since the secondary antibody is conjugated to a HRP enzyme, 100  $\mu\text{L}$  of the corresponding substrate (QuantaRed Working solution; QuantaRed Enhanced Chemifluorescent HRP Substrate Kit, Thermo Fisher Scientific, Waltham, MA, USA) comprising 50 parts QuantaRed Enhancer Solution, 50 parts QuantaRed Stable Peroxide, and one part QuantaRed ADHP Concentrate, was added to each well. Then, the samples were incubated at room temperature for 30 min

while shaking at 100 rpm, and the peroxidase reaction was stopped by adding 20  $\mu\text{L}$  QuantaRed Stop Solution to each well. Finally, the absorbance properties of the samples were determined photometrically with a multi-label plate reader (Viktor3) at an excitation wavelength of 570 nm.

**Statistics.** Statistical analyses were conducted using software R together with the user interface RStudio (version 3.4.2, September 2017). Normal distribution of data was verified by *Q-Q* plots and a Shapiro–Wilk test, and variance homogeneity was confirmed using a Levene test. To detect statistically significant differences in the examined groups, *t*-tests were performed in pairwise comparisons. As a threshold for significance, a *p*-value of  $p \leq 0.05$  was used.

**Numerical Model and Methods.** The numerical investigations conducted here aimed at investigating qualitative differences in the conformation of a mucin filament due to different effective line charge distributions. The simulations thus considered a single, initially straight mucin filament, which is modeled by a 3D beam theory and discretized in space by means of finite elements. Specifically, the geometrically exact Hermitian Simo–Reissner element formulation was applied here.<sup>38</sup> Thermal excitation and viscous damping of the filament due to the implicitly modeled surrounding fluid were incorporated via the micromechanical continuum approach to Brownian dynamics.<sup>39</sup> The electrostatic (self-)interaction of the mucin filament was modeled by the so-called section–section interaction potential (SSIP) approach.<sup>40</sup> Steric repulsive forces due to (self-)contact of the filament were accounted for by means of the penalty beam contact formulation<sup>41</sup> and precluded any mutual penetration. The challenging combination of this beam contact formulation with the possibly attractive electrostatic forces from the SSIP approach has been verified in previous work.<sup>40,42</sup> The software package used for the simulations is the in-house research code BACL.<sup>43</sup> Further details on the models and the simulation setup including all parameter values can be found in Section S3.3 of Supporting Information.

## RESULTS AND DISCUSSION

**Binding Capability of Small Charged Molecules toward Mucins is Modulated by the Mucin Charge Density.** Previously, we could show that binding interactions between native mucins and charged dextran molecules are dominated by attractive electrostatic forces: charged dextrans with a molecular weight of 4 kDa bind to mucins, whereas uncharged dextrans do not.<sup>37</sup> Here, we repeat this adsorption-based affinity assay using the same three 4 kDa dextran variants and confirm the result from our previous study (Figures 1 and S2). Both cationic and anionic dextrans bind to surface-bound mucin layers in a concentration-dependent manner; in contrast, we do not find such a concentration dependency for neutral dextrans, which show low binding at all the concentrations tested (Figure S3). In addition, cationic dextrans tend to show a slightly higher (but not statistically significant;  $p = 0.09$  for Figure 1 and  $p = 0.07$  for Figure S2) MUC5AC binding capability than anionic ones. Determining  $K_D$  values for the binding of the different dextran variants to our lab-purified mucins is, however, challenging for conceptual and technical reasons: First, the binding of dextrans to binding sites of the mucin molecule can be strongly influenced by previous binding events. For instance, binding of dextrans to the mucin molecule can alter the (local) charge state of the mucin molecule; this, in turn, can result in conformational changes of certain domains of the mucin molecule. Second, we find that binding data obtained at high ligand concentrations comes with larger experimental errors, which renders a fitting procedure of those curves unreliably. This increased experimental variability may—at least in part—reflect the complex consequences multiple binding events can have on the

C

<https://doi.org/10.1021/acs.langmuir.0c02256>  
Langmuir XXXX, XXX, XXX–XXX

mucin molecule. Thus, to avoid such complications, we here compare the binding of dextrans to different mucin variants at a low dextran concentration of 0.02% (w/v), where our molecular depletion test returns data with high accuracy.

In the next step, we ask if an enzymatic removal of anionic motifs from the mucin glycoprotein were to affect their adsorption efficiency onto hydrophobic surfaces and their dextran binding abilities. Thus, to clarify the first issue, we try to estimate the amount of surface-adsorbed mucin molecules based on an optical method. In brief, all three mucin variants are covalently labeled with a fluorophore targeting free amine residues on the mucin polypeptide backbone; then, these fluorescently labeled mucins are allowed to passively adsorb onto polystyrene surfaces, and the fluorescence intensity values of the adsorbed mucin surface layers are determined. Interestingly, we obtain differences in the labeling efficiencies of those three mucin variants which are already visible by eye (Figure S4a). The fluorescence signals of mucin solutions of the enzymatically modified mucins are similar, whereas the native mucin differs significantly with  $\sim 4$  fold higher fluorescence intensities (Figure S4b). Afterward, we investigate the relative adsorption efficiency of the three mucin variants by quantifying fluorescence microscope images (see Figure S4c). After correcting for differences in the fluorophore labeling efficiency, we find that the MUC5AC -DNA/-SO<sub>4</sub> variant shows the strongest surface adsorption among all mucin variants. In addition, QCM-D measurements (Figure S4d) show that the presence of a fluorescent dye on the mucin does not significantly influence the adsorption of mucin molecules onto hydrophobic surfaces.

With this mucin adsorption data in mind, the interaction of surface-bound mucins with solubilized dextrans could be affected by three aspects: differences in the amount of surface-bound mucin molecules, structural motifs on the mucin glycoprotein, and mucin-bound DNA. For instance, mucin-bound DNA may interact with the predominantly positively charged termini of the mucin protein backbone and thus influence its interaction with dextran molecules. We here compare the influence of two enzymatic mucin modifications: First, we test mucins from which associated DNA was removed; second, we analyze mucins, where—in addition to DNA removal—also sulfate residues were cleaved.

When we compare the binding behavior of the three dextran variants to DNA-free mucins, a qualitatively similar result is obtained as for untreated mucins; however, now, we only find slightly better binding of charged dextrans than for uncharged dextrans (Figure 1). This is interesting since the removal of anionic DNA strands from the mucin glycoprotein should have decreased intermolecular repulsion forces acting between the mucin backbone and the anionic dextrans, which—in turn—should have facilitated binding of anionic dextrans rather than weakening it. If sulfate groups are removed from mucins as well, the picture is further modified: now, both charged dextrans show negligible binding at levels as low as for uncharged dextrans (Figure 1). For cationic dextrans, this result can be rationalized as anionic motifs such as sulfate residues constitute a very likely target for the unspecific binding of cationic molecules. For the anionic dextrans, however, this outcome—albeit reproducible (Figure S2)—requires further investigation.

Thus, the same assay is repeated with a similar set of dextrans carrying the same chemical modifications (thus, representing the same set of charge species) but having larger

molecular weights of 150 kDa. With these larger dextrans, the results obtained after enzymatic treatment are very similar to what we described above for binding of small 4 kDa dextrans: also here, CM-dextrans do not show significant binding to mucins anymore once the mucin-associated DNA and sulfate groups are removed. However, we would like to mention that this experimental outcome of molecular binding tests can depend on the mucin purification batch.<sup>37</sup> For a complex biological macromolecule as mucin, this is not surprising as the glycosylation pattern of mucin glycoproteins is subject to a certain degree of biological variability: the glycosylation of MUC5AC molecules can vary not only between individual pigs<sup>44</sup> (from whose stomachs we purify our mucins) but also within one and the same animal depending on its health state and diet.<sup>45</sup> As a consequence, we also find slight variations in the dextran binding patterns when different purification batches of our lab-purified mucin are compared (Figure S2).

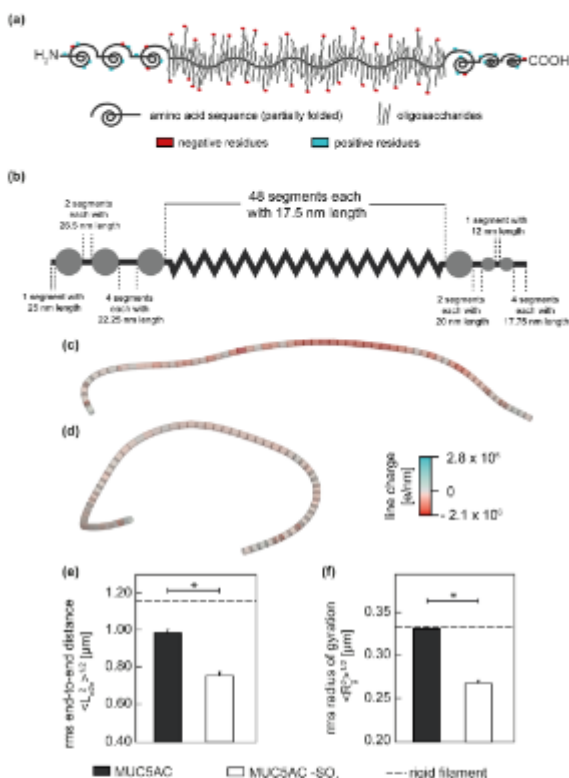
Considering the counterintuitive outcome of the mucin binding tests conducted with CM-dextrans in the depletion assay, we next try to verify this result with other quantitative experimental techniques. We choose two adsorption-based assays to test dextran binding to the different mucin variants, that is, QCM-D measurements (Figure S5) and polydimethylsiloxane (PDMS)-based capillary filter systems (Figure S6).<sup>46</sup> In both cases, the surfaces are functionalized with mucin molecules and, in the second step, the dextrans are selectively depleted from the solution by the surface-bound mucins. Also with those two techniques, we find that the binding of positively charged dextrans to native mucin molecules is very pronounced, whereas the anionic and neutral dextrans are depleted to a much lower extent (Figures S5 and S6). Moreover, also as shown in Figure S5, those additional experiments confirm that glycan-reduced mucins do not bind anionic dextrans anymore.

Taken together, all these experiments indicate that—in addition to removing binding sites for cationic molecules—an enzymatic cleavage of anionic residues from mucin glycoproteins also affects the binding capability of mucins toward anionic molecules. At this point, it is important to recall that the most likely target motifs on mucins, which could allow for the binding of those anionic molecules, are located in the termini of the mucin glycoprotein, that is, in the unglycosylated areas of the peptide backbone. If the conformation of the (largely unfolded) mucin is well elongated, that is, if those termini are accessible, then binding to those terminal groups should be easily possible. In turn, conformational changes as, for example, brought about by weakened intramolecular repulsion forces (as we expect them for sulfate-reduced mucins), could reduce the accessibility of these termini—thus lowering the efficiency of anionic CM-dextran binding. In fact, previous experiments on the adsorption properties of native and enzymatically modified mucins had already motivated that the mucin macromolecule might undergo such a conformational change upon removal of negatively charged residues from the backbone.<sup>15</sup>

**Anionic Groups on the Mucin Backbone Modulate the Conformation of the Mucin Glycoprotein.** To test the idea that mucin macromolecules adopt a different, more contracted conformation upon removal of anionic charges from the backbone, we employ numerical simulations of the mucin molecule. Our goal is to compare structural parameters of thermally fluctuating mucins that describe the configuration

of the macromolecule—both in the presence and absence of negative charges within the mucin backbone.

To set up a numerical model of the complex mucin glycoprotein, we first segment the macromolecule into different subunits. This approach is motivated by the presence of different structural motifs in the porcine gastric mucin (Figure 2a): MUC5AC comprises a strongly glycosylated core-



**Figure 2.** Schematic representation of a mucin macromolecule and numerical simulation results obtained for native and enzymatically treated mucin. (a) Schematic structure of the mucin glycoprotein and its charge distribution. (b) The segmentation of the mucin molecule conducted for modeling results in 48 units for the glycosylated region, whereas each terminus is represented by three units modeling the VWF-like, folded domains and seven connecting segments. Representative examples of the modeled conformation of native and sulfate-reduced (MUC5AC-SO<sub>4</sub>) mucin are shown in (c,d), respectively. The corresponding structural parameters, that is, the end-to-end distance and the radius of gyration as calculated from the simulated mucins are shown in (e,f). The error bars depict the standard error of the mean as obtained from five independent simulation runs. Asterisks mark significant differences ( $p \leq 0.05$ ).

domain which is flanked by partially folded termini. These termini contain three von-Willebrand-factor (VWF)-like D domains in the N-terminus and one VWF-like D domain as well as two VWF-like C domains in the C-terminus. We here simplify this structure and model these spherical VWF-like domains as cylinders (Figure 2b), which are connected by other cylindrical segments corresponding to the respective protein strands (see Supporting Information, Section S3.1 for details). The central, glycosylated region of the mucin is broken down into 48 segments of 50 amino acids each, and

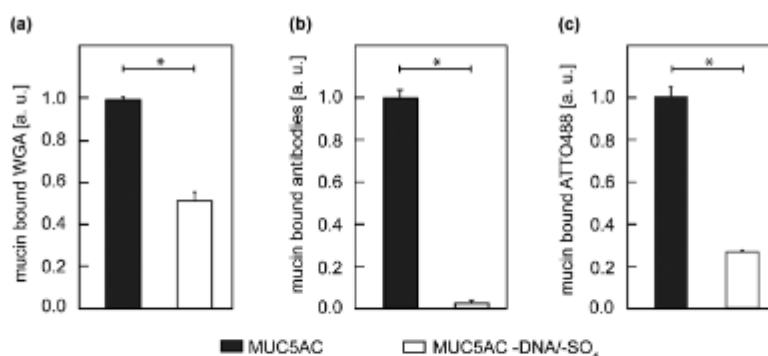
each of these segments was treated as a beam element with a persistence length of 50 nm.<sup>27,47</sup> Then, a longitudinal charge profile was applied onto the segmented mucin glycoprotein as described in Section S3.2 of Supporting Information. Of course, this is still a simplified model of the mucin glycoprotein, which is why the absolute numbers of the quantities we determine from the simulated mucin molecules below should be considered to be estimates.

Interestingly, for simulated mucin at neutral pH, we obtain average end-to-end distances and radii of gyration that are close to values one would obtain for a rigid, well-elongated molecule. This finding indicates that the high density of negatively charged groups in the central area of the mucin macromolecule establishes rather strong (intramolecular) repulsive forces, which keep the polypeptide in a stretched conformation (Figure 2c). We then challenge the validity of the numerical mucin model by comparing the conformation of an enzymatically untreated mucin (neglecting any mucin-associated DNA) at neutral and acidic pH. This step is motivated by experimental results from the literature, which have reported a clear compaction of the mucin glycoprotein when the pH level of the solvent was decreased from 7.0 to 2.0.<sup>28,48</sup> Indeed, this behaviour is reproduced here (Figure S7): when mucin charge profiles corresponding to neutral and acidic buffer conditions are applied in our model, we find a reduction of both the end-to-end distance and the radius of gyration of simulated mucins by a factor of ~4.5 and ~2, respectively.

Having confirmed that our model can successfully reproduce charge-driven conformational changes (induced by alterations in the pH) reported in the literature, we next ask if the same model would predict a conformational change of the mucin macromolecule when anionic residues are removed. In these simulations, we can test the influence of two modifications, that is, removal of either sulfate residues (Figure 2) or sialic acid groups (Figure S8). However, mucin-associated DNA cannot be simulated since it is unclear which part of the mucin molecule DNA binds to. Thus, the MUC5AC-DNA molecule serves as a reference here. The conformational change depicted in the simulated mucins might thus underestimate the structural alteration native mucins undergo upon removal of both DNA and anionic glycans.

Indeed, when anionic sulfate groups are removed from the charge profile used for modeling, we obtain a compacted mucin conformation (Figure 2d) as demonstrated by both a significant reduction of the end-to-end distance (Figure 2e) and the radius of gyration (Figure 2f). We conclude that a loss of repulsive forces between the glycan chains forces the mucin to adopt a compacted conformation. For simulated mucins, where the anionic motifs originating from sialic acid groups were removed, we find the same outcome—albeit more weakly pronounced (Figure S8c,d). This reflects the lower density of sialic acid groups on the mucin glycoproteins compared to sulfate residues.<sup>15</sup>

At this point, we would like to emphasize again that the numerical model we chose to describe the mucin conformation reflects a simplified scenario. It allows for making statements on the conformational changes of monomeric mucins only; yet, physiologically, gastric mucins typically occur in an oligomeric state. Such a simplification, however, is still reasonable, given that our lab-purified mucins return a similar interaction pattern with dextrans in their reduced, monomeric state as in their oligomerized state (Figure S9). Indeed, the



**Figure 3.** ELISA test, depletion assay, and ATTO488 labeling efficiency to assess the interaction of native and enzymatically treated mucins with specific binding partners. WGA (a), anti-MUC5AC antibodies (b) and fluorescent dye molecules (c) show a higher binding capability toward native mucin (MUC5AC) than toward the enzymatically modified mucin variants. The error bars represent the standard error of mean obtained from five (ELISA and depletion assay) and three (ATTO488 labeling) technical replicates. Asterisks mark significant differences between samples ( $p \leq 0.05$ ).

conformational changes we propose here for monomeric mucins upon removal of charges from the mucin backbone might be even more pronounced in mucin oligomers: here, conformational changes occurring for individual mucin molecules might add-up, thus resulting in a more strongly decreased accessibility of the mucin termini than what we estimate with our mucin model.

**Removal of Anionic Mucin Motifs Affects the Accessibility of Specific Mucin-Binding Sites.** Having demonstrated that the removal of sulfate groups should indeed be sufficient to induce a significant change in the mucin conformation, we now, in the last step, ask if specific binding interactions with mucins are also affected by the enzymatic cleavage of those anionic mucin residues and the ensuing mucin compaction. At this point, it is crucial to recall that our enzymatic treatment targets DNA strands and sulfate groups only. Thus, cleaving those chemical motifs is unlikely to chemically remove target groups on mucins required for binding of the WGA, a molecule that binds specifically to sialic acid groups.

Interestingly, when we repeat the depletion assay described above using this specific lectin variant as a binding partner for mucin, we find that the amount of WGA that is depleted by MUC5AC from a WGA solution exceeds the amount of WGA that is depleted by MUC5AC -DNA/-SO<sub>4</sub> by a factor of ~2 (or ~5, respectively), and this difference is statistically significant (Figure 3a; Figure S10). Thus, this finding indicates lower WGA binding to the sulfate-reduced mucin.

We obtain a qualitatively similar result as for the WGA binding test described above when we perform an ELISA test, that is, another specific mucin binding assay which is based on an anti-MUC5AC antibody, which targets the C-terminus of the mucin molecule.<sup>49</sup> Whereas the antibody returns a strong fluorescence signal for native mucin, a ~20-fold weaker signal is detected for the enzymatically modified mucin (Figures 3b and S10).

At this point, it is important to recall that these adsorption-based binding tests—as well as the depletion assay that we have discussed above—come with the complication that native MUC5AC and MUC5AC -DNA/-SO<sub>4</sub> differ in terms of adsorption efficiency. As mentioned above, first, we analyzed the labeling efficiency of native MUC5AC and enzymatically treated MUC5AC -DNA/-SO<sub>4</sub>. The fluorescence intensities of

aqueous solutions generated with these two labeled mucins differ significantly: we obtain a ~4 fold weaker fluorescence signal for the enzymatically treated mucin variant (Figures 3c and S4b). In full agreement with the results obtained with the anti-MUC5AC antibody and WGA, this underscores that specific binding sites on glycan-depleted mucins are less accessible. Moreover, the relative ratio of surface-bound native and enzymatically modified mucins is determined by fluorescence microscopy. The data shows stronger adsorption for MUC5AC -DNA/-SO<sub>4</sub> than for the untreated mucin (Figure S4c). With this in mind, the relative binding differences shown in Figure 3 represent an underestimation; in other words, the reduction in accessibility of specific binding sites can be expected to be stronger than what the data shown in Figure 3 suggests.

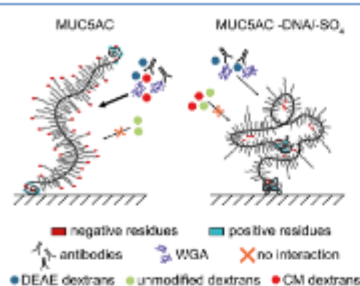
Together, this data suggests that also binding of specific binding partners to mucin is rendered more difficult when a sufficient number of anionic groups are removed from the glycoprotein. Also, this finding is consistent with the idea that a loss of intramolecular repulsion forces in the glycosylated domain induces conformational changes of the mucin structure such that certain mucin motifs (including the cationic C-terminus of the macromolecule) are hidden in the coiled-up mucin and thus become less accessible for binding partners.

In summary, both our numerical model and the experimental data imply that the native MUC5AC exhibits a stretched and elongated conformation, whereas the enzymatic modifications studied here yield mucins with a more compacted, globular structure, in which the mucin termini are (partially) shielded from the surrounding fluid. Of course, our numerical model comes with limitations: for instance, DNA-associated mucin cannot be simulated, and thickness variations along the backbone of the mucin glycoprotein (*i.e.*, between glycosylated and unglycosylated regions) are not considered. Thus, the visualization of the mucin molecules in Figure 2c,d does not necessarily indicate the full effect of how binding sites on the modified mucin become inaccessible for other small molecules.

Yet, the idea put forward here is in agreement with our previous result where we found that an enzymatic removal of mucin-associated DNA and sulfate groups from the mucin glycan chains impairs the functionality of mucins in terms of lubricity and adsorption efficiency.<sup>15</sup> Here, we show that the



same mucin modifications lead to an altered binding capability of mucins toward charged molecules—both cationic and anionic ones—and proteins, which specifically bind to certain motifs of the mucin molecule (Figure 4).



**Figure 4.** Schematic representation of how removal of anionic residues could affect the conformation of MUC5AC and thus the accessibility of mucin binding sites. Native gastric mucin can bind the anti-MUC5AC antibody, WGA, and charged dextran but not electrostatically neutral dextran. In contrast, enzymatically treated (charge-reduced) MUC5AC shows less efficient binding to antibodies and WGA and does not bind anionic dextran anymore.

In this study, we use surface-bound mucins for all experimental and numerical tests. Indeed, in their physiological state, mucins can occur in the surface bound form; yet, they are also secreted and form solutions or gels. For interpreting the binding results presented here, using surface-bound mucins helps us avoiding certain technical complications: for instance, as dextran molecules carry multiple charges (~5 charges for the 4 kDa dextran and ~185 charges for the 150 kDa dextran), the polyanionic/polycationic character of those macromolecules could lead to intermolecular interactions of mucin molecules with each other (e.g., triggered via cross-linking by the dextran) and thus to the formation of agglomerates.<sup>50</sup>

**Possible Physiological Role of MUC5AC-Associated DNA.** We here study porcine gastric MUC5AC, which we purify manually in the lab. Interestingly, this lab-purified MUC5AC is always associated with DNA, and we could show previously that this mucin-associated DNA reduces the accessibility of sialic acids and sulfate groups on the mucin backbone towards enzyme.<sup>15</sup> Thus, before treating mucin with sulfatase, we first perform an enzymatic removal of DNA. In contrast to MUC5AC, lab-purified salivary mucin MUC5B hardly contains any DNA.<sup>15</sup> The content of sialic acid and sulfate groups in MUC5B, however, strongly exceeds that of MUC5AC: sialic acid and sulfate groups each account for ~6% of the mass of MUC5B but only for <2% of the mass of MUC5AC.<sup>15,32,51,52</sup> If we assume that the decoration of MUC5AC with DNA might not just be the result of the (relatively harsh) harvesting method used for collecting gastric mucus (which is collected by manual scraping of the gastric mucosa) but rather represents the physiological state of MUC5AC, the question arises if mucin-associated DNA might provide MUC5AC with additional or improved properties.

Based on the results we obtained in this study, we speculate that MUC5AC-associated DNA might compensate for the relatively low amount of sialic acid and sulfate residues present in this mucin variant compared to MUC5B. Thus, by its association with gastric mucin, DNA might help keeping the mucin glycoprotein in an extended state so that all of its

(specific and unspecific) interaction sites are accessible. Whereas at neutral pH levels, as we study them here, the mucin can maintain an extended configuration on its own, at acidic pH levels, this is more difficult, which represent the physiological environment the gastric MUC5AC occurs in. With our model, we can predict that, at an acidic pH of 4.0, protonation of anionic residues on the polypeptide chain induces a compaction of the mucin molecule (Figure S7). Here, the phosphate groups from mucin-associated DNA strands, however, might still be deprotonated (given that the  $pK_a$  value of phosphate groups in phosphodiester bonds is close to 1),<sup>53</sup> thus adding negatively charged groups and, consequently, intramolecular repulsion forces to the mucin glycoprotein. However, as neither the detailed amount of DNA bound per mucin nor the position on the mucin glycoprotein where DNA strands bind to are known, it is—at this point of research—very difficult to include this aspect into our numerical mucin model.

It is reasonable to assume that DNA strands are likely to bind via electrostatic forces to positively charged amino acid side chains that are located in the mucin termini. The high density of anionic glycan chains might render binding of polyanionic DNA molecules to the central region difficult. Other DNA binding mechanisms, for example, *via* physical entanglement with glycan side chains or *via* hydrogen bonds, are, of course, also possible.<sup>54</sup> When attached to mucin, DNA strands might not only help stretching the mucin molecule but also act as a protective barrier against enzymatic attack from pathogens: indeed, several bacteria or viruses have developed strategies to enzymatically target mucin motifs.<sup>55,56</sup> For instance, sialic acid residues are known as binding sites for influenza viruses<sup>57,58</sup> and are thus targeted by viral neuraminidases to set immobilized viruses free again.<sup>59</sup> Moreover, some bacteria residing in airway or gastrointestinal mucus secrete sulfatases,<sup>21,32,60</sup>—and, as we show here, the removal of sulfate residues alters the mucin conformation and affects mucin functionality. How the protective barrier function of mucus-containing such charge-reduced, collapsed mucins might be corrupted due to the inaccessibility of certain mucin-binding sites will have to be clarified in future experiments.

## CONCLUSIONS

The biochemical structure of mucin glycoproteins is highly complex, and the particular role of the different glycans present in mucins remains to date poorly understood. Electrostatically neutral carbohydrates such as mannose, fucose, *N*-acetyl-galactosamine, *N*-acetyl-glucosamine, or galactose comprise the main components of the mucin glycan pattern and have been shown to constitute a protective barrier against proteolytic degradation of the polypeptide backbone.<sup>61–63</sup> Here, we suggest that anionic glycan residues contribute to the conformational stability of mucins by establishing intramolecular repulsion, and these repulsion forces seem to be required to maintain the broad binding properties of mucins toward other molecules. Future research will show if and how other mucin glycans contribute to similar or other properties of the complex mucin glycoprotein, including selective binding, surface adsorption, or bacterial/eukaryotic repulsion.

## ASSOCIATED CONTENT

### Supporting Information

The Supporting Information is available free of charge at <https://pubs.acs.org/doi/10.1021/acs.langmuir.0c02256>.

SDS-PAGE to show the successful enzymatic modification of mucin molecules; experimental repetitions of the depletion assay with dextrans, WGA, and anti-MUC5AC antibodies; analysis of the mucin–dextran interaction with different assays: depletion assay with increasing dextran concentrations, QCM-D measurements, and selective PDMS filters; quantification of the relative amount of surface-bound mucin (ATTO-labeled mucins); details of the numerical model; and conformational change of the simulated natural mucin at different pH levels and of the enzymatically treated mucins at physiological pH (PDF)

## AUTHOR INFORMATION

### Corresponding Author

Oliver Lielég – Department of Mechanical Engineering and Munich School of Bioengineering, Technical University of Munich, 85748 Garching, Germany; [orcid.org/0000-0002-6874-7456](https://orcid.org/0000-0002-6874-7456); Email: [oliver.lieleg@tum.de](mailto:oliver.lieleg@tum.de)

### Authors

Theresa M. Lutz – Department of Mechanical Engineering and Munich School of Bioengineering, Technical University of Munich, 85748 Garching, Germany

Matthias Marczynski – Department of Mechanical Engineering and Munich School of Bioengineering, Technical University of Munich, 85748 Garching, Germany

Maximilian J. Grill – Department of Mechanical Engineering and Institute for Computational Mechanics, Technical University of Munich, 85748 Garching, Germany

Wolfgang A. Wall – Department of Mechanical Engineering and Institute for Computational Mechanics, Technical University of Munich, 85748 Garching, Germany

Complete contact information is available at:

<https://pubs.acs.org/10.1021/acs.langmuir.0c02256>

### Author Contributions

The experiments were designed by T.M.L., M.M., and O.L. T.M.L. and M.M. performed the experiments and analyzed the data. M.J.G. and W.A.W. developed the numerical model, ran the simulations, and analyzed the data. The manuscript was written by contributions of all authors.

### Notes

The authors declare no competing financial interest.

## ACKNOWLEDGMENTS

The authors thank Tobias Fuhrmann for assistance with mucin purification. This project was supported by the Deutsche Forschungsgemeinschaft (DFG) through grant I.I 1902/9-1 awarded to O.L.

## REFERENCES

- (1) Khanvilkar, K.; Donovan, M. D.; Flanagan, D. R. Drug transfer through mucus. *Adv. Drug Delivery Rev.* **2001**, *48*, 173–193.
- (2) Lai, S. K.; Wang, Y.-Y.; Hanes, J. Mucus-penetrating nanoparticles for drug and gene delivery to mucosal tissues. *Adv. Drug Delivery Rev.* **2009**, *61*, 158–171.
- (3) Yakubov, G. E.; McColl, J.; Bongaerts, J. H. H.; Ramsden, J. J. Viscous boundary lubrication of hydrophobic surfaces by mucin. *Langmuir* **2009**, *25*, 2313–2321.
- (4) Hoffmann, W. Regeneration of the gastric mucosa and its glands from stem cells. *Curr. Med. Chem.* **2008**, *15*, 3133–3144.
- (5) Yildiz, H. M.; Carlson, T. L.; Goldstein, A. M.; Carrier, R. L. Mucus barriers to microparticles and microbes are altered in Hirschsprung's disease. *Macromol. Biosci.* **2015**, *15*, 712–718.
- (6) Peatfield, A. C.; Richardson, P. S. The action of dust in the airways on secretion into the trachea of the cat. *J. Physiol.* **1983**, *342*, 327–334.
- (7) Lo-Guidice, J.-M.; Péroni, J.-M.; Lafitte, J.-J.; Ducourouble, M.-P.; Roussel, P.; Lamblin, G. Characterization of a sulfotransferase from human airways responsible for the 3-O-sulfation of terminal galactose in N-acetyllactosamine-containing mucin carbohydrate chains. *J. Biol. Chem.* **1995**, *270*, 27544–27550.
- (8) Parsons, C. L.; Mulholland, S. G. Bladder surface mucin. Its antibacterial effect against various bacterial species. *Am. J. Pathol.* **1978**, *93*, 423.
- (9) Belley, A.; Göttke, M.; Keller, K.; Chadee, K.; Göttke, M. Intestinal mucins in colonization and host defense against pathogens. *Am. J. Trop. Med. Hyg.* **1999**, *60*, 10–15.
- (10) Scharfman, A.; Lamblin, G.; Roussel, P. Interactions between human respiratory mucins and pathogens. *Biochem. Soc. Trans.* **1995**, *23*, 836–839.
- (11) Yolken, R. H.; Peterson, J. A.; Vonderfecht, S. L.; Fouts, E. T.; Midthun, K.; Newburg, D. S. Human milk mucin inhibits rotavirus replication and prevents experimental gastroenteritis. *J. Clin. Invest.* **1992**, *90*, 1984–1991.
- (12) Altgård, N.; Eriksson, C.; Peerboom, N.; Phan-Xuan, T.; Moeller, S.; Schnabelrauch, M.; Svedhem, S.; Trybala, E.; Bergström, T.; Bally, M. Mucin-like region of herpes simplex virus type 1 attachment protein glycoprotein C (gC) modulates the virus-glycosaminoglycan interaction. *J. Biol. Chem.* **2015**, *290*, 21473–21485.
- (13) Bansil, R.; Turner, B. S. Mucin structure, aggregation, physiological functions and biomedical applications. *Curr. Opin. Colloid Interface Sci.* **2006**, *11*, 164–170.
- (14) Käs Dorf, B. T.; Weber, F.; Petrou, G.; Srivastava, V.; Crouzier, T.; Lielég, O. Mucin-inspired lubrication on hydrophobic surfaces. *Biomacromolecules* **2017**, *18*, 2454–2462.
- (15) Marczynski, M.; Balzer, B. N.; Jiang, K.; Lutz, T. M.; Crouzier, T.; Lielég, O. Charged glycan residues critically contribute to the adsorption and lubricity of mucins. *Colloids Surf., B* **2020**, *187*, 110614.
- (16) Yakubov, G. E.; Papagiannopoulos, A.; Rat, E.; Easton, R. L.; Waigh, T. A. Molecular structure and rheological properties of short-side-chain heavily glycosylated porcine stomach mucin. *Biomacromolecules* **2007**, *8*, 3467–3477.
- (17) McColl, J.; Yakubov, G. E.; Ramsden, J. J. Complex desorption of mucin from silica. *Langmuir* **2007**, *23*, 7096–7100.
- (18) Copeman, M.; Matuz, J.; Leonard, A. J.; Pearson, J. P.; Dettmar, P. W.; Allen, A. The gastroduodenal mucus barrier and its role in protection against luminal pepsins: The effect of 16, 16 dimethyl prostaglandin E<sub>2</sub>, carbopol-polyacrylate, sucralfate and bismuth subsalicylate. *J. Gastroenterol. Hepatol.* **1994**, *9*, S55–S59.
- (19) Chang, M.; Alsaigh, T.; Kistler, E. B.; Schmid-Schönbein, G. W. Breakdown of Mucin as Barrier to Digestive Enzymes in the Ischemic Rat Small Intestine. *PLoS One* **2012**, *7*, No. e40087.
- (20) Hoskins, L. C.; Boulding, E. T. Mucin degradation in human colon ecosystems: evidence for the existence and role of bacterial subpopulations producing glycosidases as extracellular enzymes. *J. Clin. Invest.* **1981**, *67*, 163–172.
- (21) Wright, D. P.; Rosendale, D. I.; Robertson, A. M. Prevotella enzymes involved in mucin oligosaccharide degradation and evidence for a small operon of genes expressed during growth on mucin. *FEMS Microbiol. Lett.* **2000**, *190*, 73–79.
- (22) Robertson, A. M.; Corfield, A. P. Mucin Degradation and Its Significance in Inflammatory Conditions of the Gastrointestinal Tract. In *Medical Importance of the Normal Microflora*; Springer, 1999; pp 222–261.
- (23) Crouzier, T.; Boettcher, K.; Geonnotti, A. R.; Kavanaugh, N. L.; Hirsch, J. B.; Ribbeck, K.; Lielég, O. Modulating mucin hydration and

- lubrication by deglycosylation and polyethylene glycol binding. *Adv. Mater. Interfaces* **2015**, *2*, 1500308.
- (24) Zappone, B.; Patil, N. J.; Madsen, J. B.; Pakkanen, K. I.; Lee, S. Molecular structure and equilibrium forces of bovine submaxillary mucin adsorbed at a solid–liquid interface. *Langmuir* **2015**, *31*, 4524–4533.
- (25) Rose, M. C.; Voter, W. A.; Sage, H.; Brown, C. F.; Kaufman, B. Effects of deglycosylation on the architecture of ovine submaxillary mucin glycoprotein. *J. Biol. Chem.* **1984**, *259*, 3167–3172.
- (26) Kramer, J. R.; Onoa, B.; Bustamante, C.; Bertozzi, C. R. Chemically tunable mucin chimeras assembled on living cells. *Proc. Natl. Acad. Sci. U.S.A.* **2015**, *112*, 12574–12579.
- (27) Shogren, R.; Gerken, T. A.; Jentoft, N. Role of glycosylation on the conformation and chain dimensions of O-linked glycoproteins: light-scattering studies of ovine submaxillary mucin. *Biochemistry* **1989**, *28*, 5525–5536.
- (28) Hong, Z.; Chasan, B.; Bansil, R.; Turner, B. S.; Bhaskar, K. R.; Afzal, N. H. Atomic force microscopy reveals aggregation of gastric mucin at low pH. *Biomacromolecules* **2005**, *6*, 3458–3466.
- (29) Menchicchi, B.; Fuenzalida, J. P.; Hensel, A.; Swamy, M. J.; David, L.; Rochas, C.; Goycoolea, F. M. Biophysical analysis of the molecular interactions between polysaccharides and mucin. *Biomacromolecules* **2015**, *16*, 924–935.
- (30) Co, J. Y.; Crouzier, T.; Ribbeck, K. Probing the Role of Mucin-Bound Glycans in Bacterial Repulsion by Mucin Coatings. *Adv. Mater. Interfaces* **2015**, *2*, 1500179.
- (31) Schömig, V. J.; Käschorf, B. T.; Scholz, C.; Bidmon, K.; Liele, O.; Berensmeier, S. An optimized purification process for porcine gastric mucin with preservation of its native functional properties. *RSC Adv.* **2016**, *6*, 44932–44943.
- (32) Robinson, C. V.; Elkins, M. R.; Bialkowski, K. M.; Thornton, D. J.; Kertesz, M. A. Desulfurization of mucin by *Pseudomonas aeruginosa*: influence of sulfate in the lungs of cystic fibrosis patients. *J. Med. Microbiol.* **2012**, *61*, 1644–1653.
- (33) Bhaskar, K. R.; Gong, D. H.; Bansil, R.; Pajevic, S.; Hamilton, J. A.; Turner, B. S.; LaMont, J. T. Profound increase in viscosity and aggregation of pig gastric mucin at low pH. *Am. J. Physiol.* **1991**, *261*, G827–G832.
- (34) Xia, B.; Royall, J. A.; Damera, G.; Sachdev, G. P.; Cummings, R. D. Altered O-glycosylation and sulfation of airway mucins associated with cystic fibrosis. *Glycobiology* **2005**, *15*, 747–775.
- (35) Amerongen, A. V. N.; Bolscher, J. G.; Bloemena, E.; Veerman, E. C. Sulfomucins in the human body. *Biol. Chem.* **1998**, *379*, 1–18.
- (36) Shriver, Z.; Capila, I.; Venkataraman, G.; Sasisekharan, R. Heparin and Heparan Sulfate: Analyzing Structure and Microheterogeneity. In *Heparin—A Century of Progress*; Springer, 2012; pp 159–716.
- (37) Marczyński, M.; Käschorf, B. T.; Altaner, B.; Wenzler, A.; Gerland, U.; Liele, O. Transient binding promotes molecule penetration into mucin hydrogels by enhancing molecular partitioning. *Biomater. Sci.* **2018**, *6*, 3373–3387.
- (38) Meier, C.; Grill, M. J.; Wall, W. A.; Popp, A. Geometrically exact beam elements and smooth contact schemes for the modeling of fiber-based materials and structures. *Int. J. Solids Struct.* **2018**, *154*, 124–146.
- (39) Cyron, C. J.; Wall, W. A. Numerical method for the simulation of the Brownian dynamics of rod-like microstructures with three-dimensional nonlinear beam elements. *Int. J. Numer. Methods Eng.* **2012**, *90*, 955–987.
- (40) Grill, M. J.; Wall, W. A.; Meier, C. A Computational Model for Molecular Interactions Between Curved Slender Fibers Undergoing Large 3D Deformations With a Focus on Electrostatic, van der Waals and Repulsive Steric Forces. *Int. J. Numer. Methods Eng.* **2020**, *121*, 2285–2330.
- (41) Meier, C.; Popp, A.; Wall, W. A. A finite element approach for the line-to-line contact interaction of thin beams with arbitrary orientation. *Comput. Methods Appl. Mech. Eng.* **2016**, *308*, 377–413.
- (42) Grill, M. J.; Meier, C.; Wall, W. A. Investigation of the peeling and pull-off behavior of adhesive elastic fibers via a novel computational beam interaction model. *J. Adhes.* **2019**, *95*, 1–30.
- (43) Institute for Computational Mechanics BACI: A Multiphysics Simulation Environment; Institute for Computational Mechanics: Technical University of Munich, 2020.
- (44) Karlsson, N. G.; Nordman, H.; Karlsson, H.; Carlstedt, L.; Hansson, G. C. Glycosylation differences between pig gastric mucin populations: a comparative study of the neutral oligosaccharides using mass spectrometry. *Biochem. J.* **1997**, *326*, 911–917.
- (45) Padra, M.; Adamczyk, B.; Flahou, B.; Erhardsson, M.; Chahal, G.; Smet, A.; Jin, C.; Thorell, A.; Ducatelle, R.; Haesebrouck, F.; Karlsson, N. G.; Lindén, S. K. *Helicobacter suis* infection alters glycosylation and decreases the pathogen growth inhibiting effect and binding avidity of gastric mucins. *Mucosal Immunol.* **2019**, *12*, 784–794.
- (46) Winkeljann, B.; Käschorf, B. T.; Boekhoven, J.; Liele, O. Macromolecular Coating Enables Tunable Selectivity in a Porous PDMS Matrix. *Macromol. Biosci.* **2018**, *18*, 1700311.
- (47) Round, A. N.; Berry, M.; McMaster, T. J.; Stoll, S.; Gowers, D.; Corfield, A. P.; Miles, M. J. Heterogeneity and Persistence Length in Human Ocular Mucins. *Biophys. J.* **2002**, *83*, 1661–1670.
- (48) Maleki, A.; Lafitte, G.; Kjøniksen, A.-L.; Thuresson, K.; Nyström, B. Effect of pH on the association behavior in aqueous solutions of pig gastric mucin. *Carbohydr. Res.* **2008**, *343*, 328–340.
- (49) Bara, J.; Chastre, E.; Mahiou, J.; Singh, R. L.; Fougere-Lafitte, M. E.; Hollande, E.; Godeau, F. Gastric M1 mucin, an early oncofetal marker of colon carcinogenesis, is encoded by the MUC5AC gene. *Int. J. Cancer* **1998**, *75*, 767–773.
- (50) Marczyński, M.; Rickert, C. A.; Semerdzhiev, S. A.; Van Dijk, W. R.; Segers-Nolten, I. M. J.; Claessens, M. M. A. E.; Liele, O.  $\alpha$ -Synuclein Penetrates Mucin Hydrogels Despite Its Mucoadhesive Properties. *Biomacromolecules* **2019**, *20*, 4332–4344.
- (51) Loomis, R. E.; Prakobphol, A.; Levine, M. J.; Reddy, M. S.; Jones, P. C. Biochemical and biophysical comparison of two mucins from human submandibular-sublingual saliva. *Arch. Biochem. Biophys.* **1987**, *258*, 452–464.
- (52) Henke, M. O.; John, G.; Germann, M.; Lindemann, H.; Rubin, B. K. MUC5AC and MUC5B mucins increase in cystic fibrosis airway secretions during pulmonary exacerbation. *Am. J. Respir. Crit. Care Med.* **2007**, *175*, 816–821.
- (53) Thapalyal, P.; Bevilacqua, P. C. Experimental Approaches for Measuring  $pK_a$ 's in RNA and DNA. *Methods in Enzymology*; Elsevier, 2014; Vol. 549, pp 189–219.
- (54) Wenz, C.; Jeltsch, A.; Pingoud, A. Probing the indirect readout of the restriction enzyme EcoRV mutational analysis of contacts to the DNA backbone. *J. Biol. Chem.* **1996**, *271*, 5565–5573.
- (55) Corfield, A. P.; Wagner, S. A.; O'Donnell, L. J. D.; Durley, P.; Mountford, R. A.; Clamp, J. R. The roles of enteric bacterial sialidase, sialate O-acetyl esterase and glycosulfatase in the degradation of human colonic mucin. *Glycoconjugate J.* **1993**, *10*, 72–81.
- (56) Flynn, J. M.; Niccum, D.; Dunitz, J. M.; Hunter, R. C. Evidence and Role for Bacterial Mucin Degradation in Cystic Fibrosis Airway Disease. *PLoS Pathog.* **2016**, *12*, No. e1005846.
- (57) Weis, W.; Brown, J. H.; Cusack, S.; Paulson, J. C.; Skehel, J. J.; Wiley, D. C. Structure of the influenza virus haemagglutinin complexed with its receptor, sialic acid. *Nature* **1988**, *333*, 426–431.
- (58) Suzuki, Y.; Ito, T.; Suzuki, T.; Holland, R. E.; Chambers, T. M.; Kiso, M.; Ishida, H.; Kawaoka, Y. Sialic acid species as a determinant of the host range of influenza A viruses. *J. Virol.* **2000**, *74*, 11825–11831.
- (59) Gubareva, L. V.; Kaiser, L.; Hayden, F. G. Influenza virus neuraminidase inhibitors. *Lancet* **2000**, *355*, 827–835.
- (60) Rho, J.-h.; Wright, D. P.; Christie, D. L.; Clinch, K.; Furneaux, R. H.; Robertson, A. M. A novel mechanism for desulfation of mucin: identification and cloning of a mucin-desulfating glycosidase (sulfoglycosidase) from *Prevotella* strain RS2. *J. Bacteriol.* **2005**, *187*, 1543–1551.

(61) Lottspeich, F.; Engels, J. W.; Solodkoff, Z. L. *Bioanalytik*; Spektrum Akademischer Verlag, 2012; pp 617–661.

(62) Chillappagari, S.; Preuss, J.; Licht, S.; Müller, C.; Mahavadi, P.; Sarode, G.; Vogelmeier, C.; Guenther, A.; Nahrlich, L.; Rubin, B. K. Altered protease and antiprotease balance during a COPD exacerbation contributes to mucus obstruction. *Respir. Res.* **2015**, *16*, 85.

(63) Hedstrom, L. Serine protease mechanism and specificity. *Chem. Rev.* **2002**, *102*, 4501–4524.

**B.2.1 Supplementary information for: Repulsive backbone-backbone interactions modulate access to specific and unspecific binding sites on surface-bound mucins**

**Supplementary Material**

for

**Repulsive backbone-backbone interactions  
modulate access to specific and unspecific binding  
sites on surface-bound mucins**

Theresa M. Lutz<sup>a</sup>, Matthias Marczynski<sup>a</sup>, Maximilian J. Grill<sup>b</sup>,  
Wolfgang A. Wall<sup>b</sup>, and Oliver Lieleg<sup>#a</sup>

<sup>a</sup>Department of Mechanical Engineering and Munich School of Bioengineering,  
Technical University of Munich, Boltzmannstr. 11, 85748, Garching, Germany

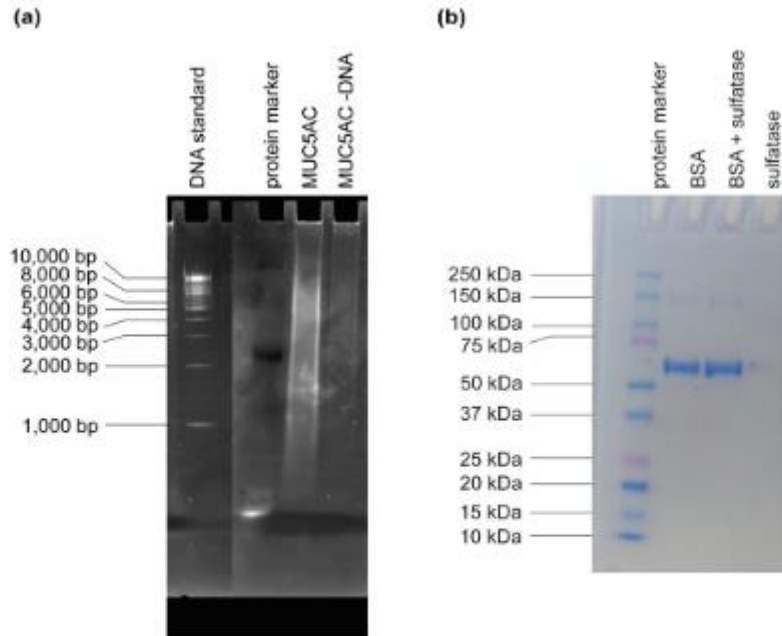
<sup>b</sup>Department of Mechanical Engineering and Institute for Computational Mechanics,  
Technical University of Munich, Boltzmannstr. 15, 85748, Garching, Germany

<sup>#</sup>: correspondence: [oliver.lieleg@tum.de](mailto:oliver.lieleg@tum.de)

## 1. SDS-PAGE to prove the successful removal of mucin-associated DNA

For sodium dodecyl sulfate polyacrylamide gel electrophoresis (SDS-PAGE), MUC5AC (both, native and DNase-treated) was rehydrated in ultrapure water at a concentration of 0.1 % (w/v) during shaking at 4 °C for 30 min. Similarly, 1 mg mL<sup>-1</sup> bovine serum albumin (BSA) and 0.5 mg mL<sup>-1</sup> sulfatase were dissolved in 200 mM sodium acetate buffer (pH 5.0). The enzymatically modified BSA was treated as described in the main paper. Per protein solution, 20 µL were mixed with 2x sample buffer (120 mM TRIS-HCl, pH 6.8, 4 % (w/v) SDS, 20 % glycerol, 0.02 % bromophenol blue) in a ratio of 1:1. After sample denaturation at 95 °C for 5 min, 20 µL of this mixture were loaded onto a pre-cast polyacrylamide gel (4 - 20 % TruPAGE™ Precast Protein Gels, Sigma-Aldrich). Additionally, 4 µL of a protein marker solution (Marker Precision Plus Protein Kaleidoscope Standards; Bio-Rad Laboratories Inc., Hercules, CA, USA) as well as 4 µL of DNA standard (1 kb DNA Ladder, Sigma-Aldrich) were loaded onto the gel in a separate lane each. The gel electrophoresis was run in TEA-tricine-SDS buffer (60 mM triethanolamine (TEA), 40 mM tricine, 0.1 % (w/v) SDS; pH 8.3) at 100 V for 90 min.

For DNA staining (Fig. S1a), the gel was incubated for 30 min in an aqueous solution of 0.01 % (v/v) SYBR® Green I (Sigma-Aldrich) during shaking at room temperature. To prevent the fluorescent dye from bleaching, the gel was kept in the dark during incubation. Images were acquired using a UV transilluminator (Bio-Rad Universal Hood II Gel Documentation System, Bio-Rad). For assessing a putative proteinase activity of the sulfatase used here, sulfatase treated and untreated BSA is tested for hydrolytic cleavage. To stain the proteins (Fig. S1b), the SDS gel was placed into a Coomassie staining solution (0.1 % (w/v) Coomassie R250, 10 % (v/v) glacial acetic acid, 40 % (v/v) methanol) at room temperature for 1 h. After this incubation time, the gel was destained in 10 % (v/v) acetic acid at room temperature overnight while shaking.

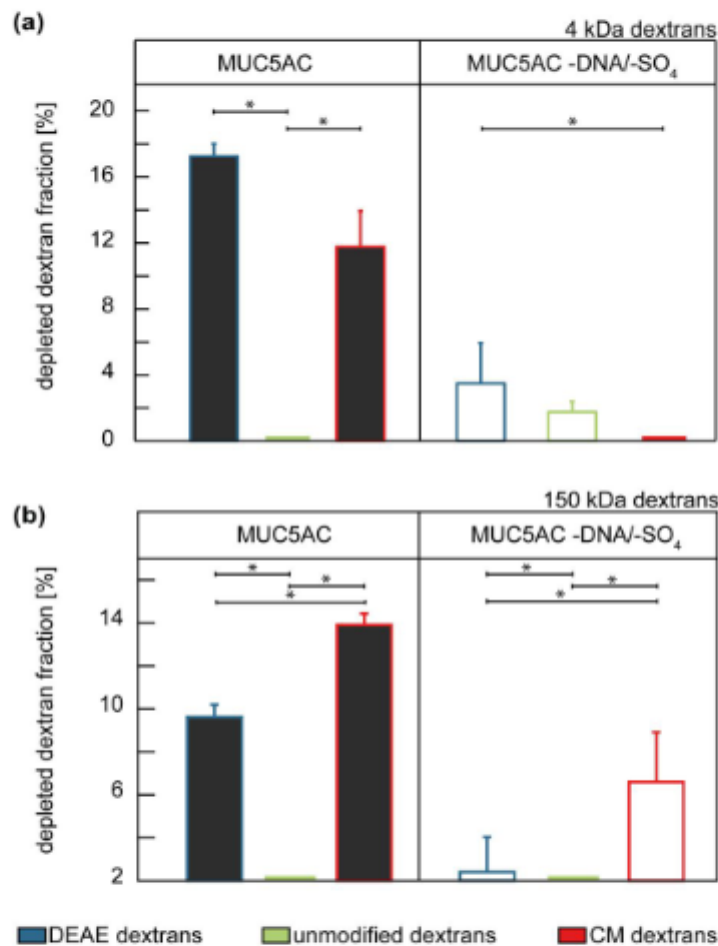


**Figure S1: SDS-PAGE showing the successful removal of mucin-associated DNA (a) and the absence of unspecific proteinase activity of the sulfatase used here (b).** (a) The bright signal indicates the presence of DNA. A bright smear is visible in the lane onto which untreated MUC5AC was loaded, whereas hardly any signal can be detected in the lane onto which the DNase treated mucin sample was loaded. (b) To exclude a possible proteinase activity of the sulfatase used here, this enzyme is tested on the protein BSA. No additional bands indicating an unspecific proteinase activity are found.

## 2. Binding of different molecules to mucins *via* unspecific interactions

### 2.1. Depletion assay conducted with another purification batch of mucins

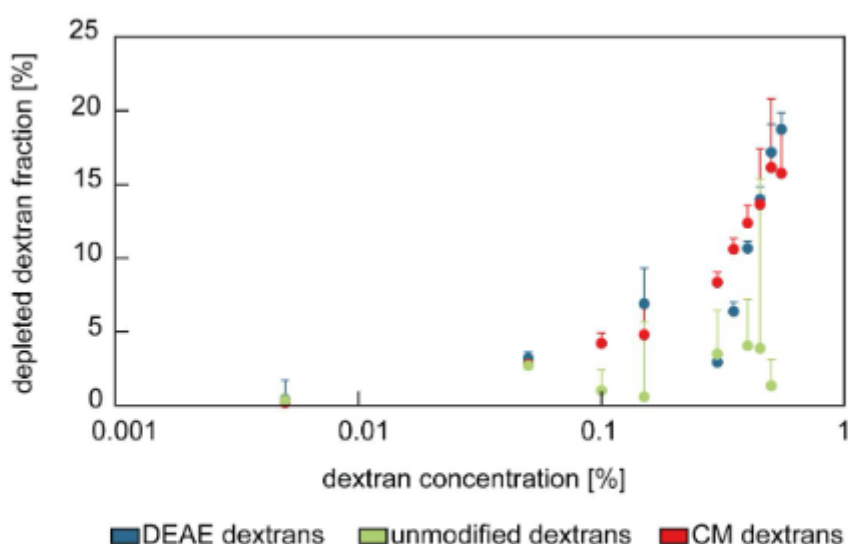
The data shown below depicts an experimental repetition of the depletion tests shown in the first part of the results section of the main paper (Fig. 1); the data shown below was obtained with MUC5AC mucins from another purification batch.



**Figure S2: Depletion assay to assess the binding interaction of native and enzymatically treated mucins with different dextrans.** (a, b) Binding of cationic (blue), neutral (green), and anionic (red) dextrans to adsorbed mucin layers is compared for dextrans with a molecular weight of 4 kDa (a) and 150 kDa (b), respectively. The error bars represent the standard error of the mean as obtained from five individual samples. Asterisks denote statistically significant differences of the dextran samples ( $p \leq 0.05$ ) determined by one-way ANOVA followed by a Tukey post-hoc test for pairwise comparisons.



## 2.2. Depletion assay conducted with different dextran concentrations



**Figure S3: Depletion assay conducted with three different dextran variants at concentrations ranging from 0.005 – 0.5 % (w/v).** A concentration dependency is observed for the binding of cationic (blue) and anionic (red) dextrans to MUC5AC but not for neutral dextrans (green). The fraction of dextrans depleted by the mucins is determined indirectly by quantifying the fraction of dextrans that remained in solution. The error bars represent the standard error of the mean as obtained from three individual samples.

When we probe the binding of anionic, cationic and neutral dextrans to mucins for a dextran concentrations series ranging from 0.005 – 0.5 % (w/v), we find a clear concentration dependency for the binding of cationic and anionic dextrans but not for neutral dextrans (Fig. S3). However, for the high dextran concentrations tested here, the error bars are quite high, which indicates that our depletion assay returns more reproducible results at low dextran concentrations.

The larger variances in the results obtained at higher dextran concentrations can be explained as follows: Binding of dextrans *via* electrostatic attraction changes the local charge state of the mucin molecule thus lowering the propensity of further dextran molecules to bind to the mucin molecule (by establishing repulsive forces between mucin-bound dextrans and free dextrans). This effect can be expected to be especially pronounced at high dextran concentrations when a large number of dextrans has already bound to the mucin molecules. Furthermore, these alterations in the charge state of mucin may induce conformational changes of certain mucin domains or the entire mucin molecule and thus restrict the accessibility of further potential binding sites.

### 2.3 Covalent labelling of different mucin variants with a fluorescence dye and mucin adsorption onto surfaces

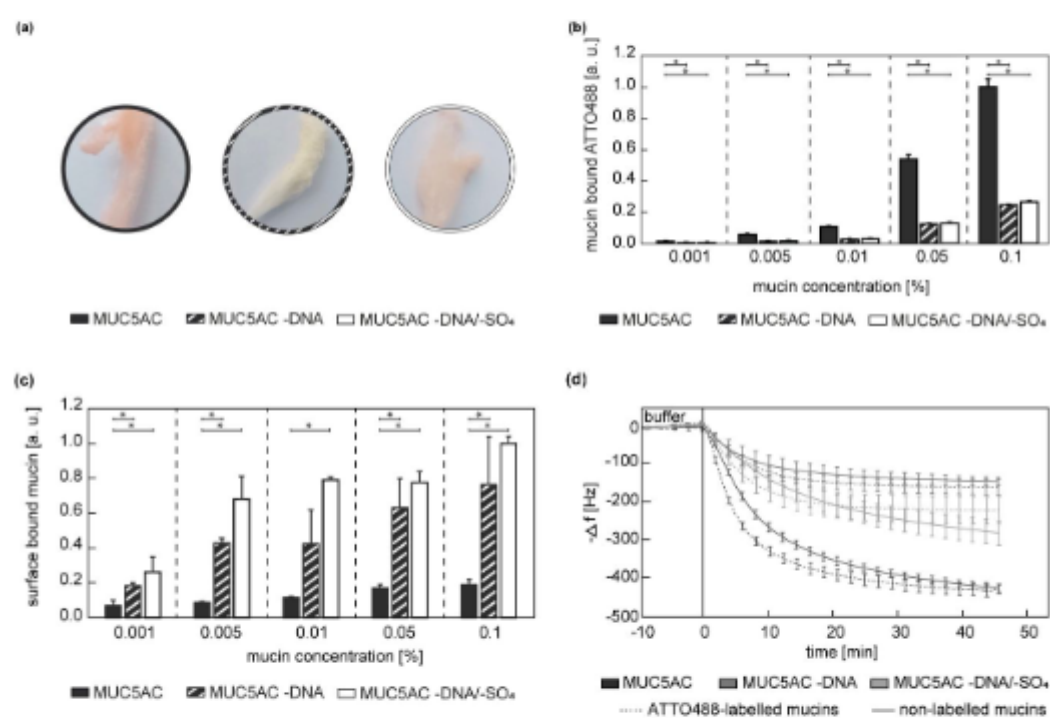
Labelling of three mucin variants was performed as described in the Materials and Methods section of the main text. The color intensity of the lyophilized mucin samples – as assessed by the naked eye (Fig. S4a) - already indicates that the three different mucin samples had different binding affinities towards the fluorophore; the conjugation reaction used for labelling targets free amino groups, which can mainly be found in the termini of the mucin molecule. When we determine the labelling efficiency of the two mucin variants by measuring the fluorescence intensity of aqueous solutions generated from these three mucin variants at different mucin concentrations, we find that native MUC5CA returns a ~5fold higher signal compared to MUC5AC -DNA and MUC5AC -DNA-SO<sub>4</sub> (Fig. S4b). These differences in functionalization efficiency indicate that the accessibility of amine groups in the termini of the enzymatically modified MUC5AC -DNA and MUC5AC -DNA-SO<sub>4</sub> variants are reduced compared to MUC5AC. This finding supports our hypothesis that the elongated conformation of native mucin changes into a more globular structure after enzymatic treatment.

To estimate the number of MUC5AC, MUC5AC -DNA or MUC5AC -DNA/ SO<sub>4</sub> molecules that have adsorbed onto polystyrene surfaces, the fluorescent variants of these mucins were allowed to adsorb onto the bottom of 96-well microtiter plates (which are fabricated from polystyrene); were, we used a set of solutions containing fluorescently labelled mucins in concentrations ranging from 0.001 – 0.1 % (w/v). The fluorescence intensities of such surface attached mucin layers can be correlated with the number of mucin molecules adsorbed after correcting for differences in the fluorophore labelling efficiency (see Fig. S4a,b). With this approach, we found that the MUC5AC -DNA and MUC5AC -DNA-SO<sub>4</sub> variants showed stronger adsorption than the untreated mucin (Fig. S4c). To investigate whether the fluorescent labelling affects the binding of mucins onto hydrophobic surfaces, quartz crystal microbalance with dissipation monitoring (QCM-D; 3T-analytik, Tuttlingen, Germany) measurements (Fig. S4d) are conducted. This technique allows for the detection of adsorbed mass (here: mucin molecules) *via* recording shifts in the resonance frequency of the coated crystal using a commercial software (qCell T Q2 1.9 and qGraph Viewer 1.8; both 3t-analytik).

First, gold coated quartz sensors (3T-analytik) were spin-coated with a thin layer of PDMS as follows: PDMS pre-polymer and cross-linker (Sylgard 184, DowCorning, MI, USA) were mixed in a ratio of 10:1. Then, 10  $\mu$ L of this PDMS premix were added to 1 mL of *n*-hexane, and 100  $\mu$ L of this PDMS/*n*-hexane solution were pipetted onto the middle of the gold-coated chip surface while rotating the chip on a spin-coater (WS-650MZ-23NPPB, Laurell, North Wales, PA, USA). These rotations were conducted first at 1500 rpm for 20 s and then at 3000 rpm for 60 s. After drying the samples at room temperature overnight, measurements were performed

S6

at 30 °C. First, the quartz crystals were rinsed with 20 mM HEPES (pH 7.0) at a flow rate of 100  $\mu\text{L min}^{-1}$  until a stable frequency baseline signal was obtained. For the adsorption of mucin molecules, a 0.01 % (w/v) mucin solution (generated in 20 mM HEPES, pH 7.0) was injected into the test chamber at a flow rate of 100  $\mu\text{L min}^{-1}$  and the resulting frequency shift was monitored for 45 min. For all three mucin variants, we tested both, unlabelled and ATTO488-labelled mucin. In all three cases, no significant differences in the adsorption properties of a labelled and unlabeled mucin were observable. At this point, we emphasize that it is not trivial to compare the results obtained from these QCM-D measurements to the surface attachment tests conducted with fluorescence microscopy. Since QCM-D determines the amount of adsorbed mass, the native mucin induces the strongest signal upon binding onto the PDMS surface.



**Figure S4: ATTO488-labelling of native and enzymatically treated mucins and their relative adsorption efficiency onto hydrophobic surfaces.** The color intensity of the lyophilized mucins (a) and the measured fluorescence signal obtained from mucin solutions (b) is shown for labelled MUC5AC, MUC5AC -DNA and MUC5AC -DNA/-SO<sub>4</sub>. (c) All three mucin variants are dissolved in water at concentrations ranging from 0.001 % to 0.1 % (w/v) and their adsorption onto a polystyrene surface is tested. The signal obtained for MUC5AC -DNA/-SO<sub>4</sub> at the highest mucin concentration tested is set to 1, and all other values are normalized to this value. (d) The adsorption of ATTO488-labelled and unlabelled mucins onto PDMS surfaces is assessed with QCM-D measurements. (b-d) The error bars represent the standard error of mean obtained from three samples. Asterisks (if present) mark significant differences as tested between the mucin samples (b-c) and between the ATTO488-labelled mucin variant and its corresponding, unlabelled mucin (d). For all t-tests a  $p$ -value of  $p \leq 0.05$  was used.

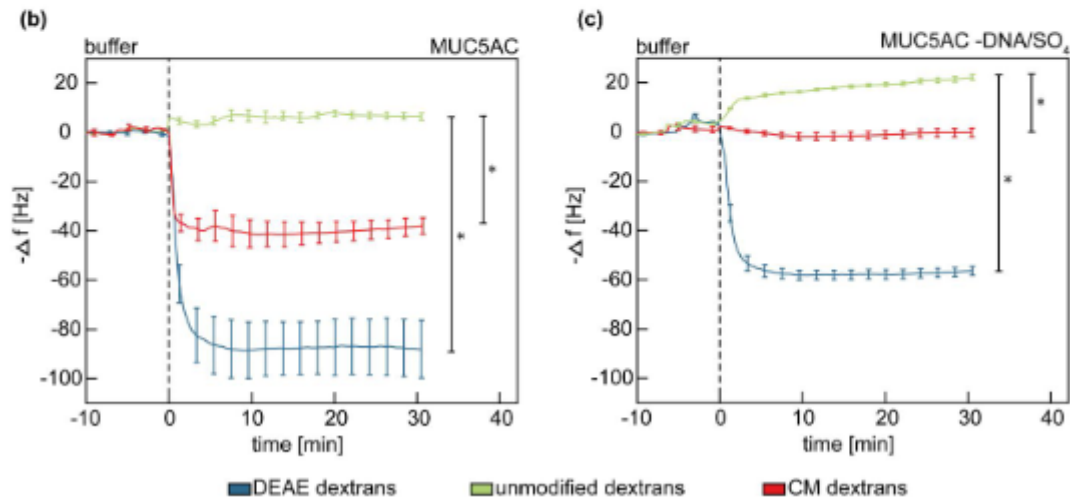
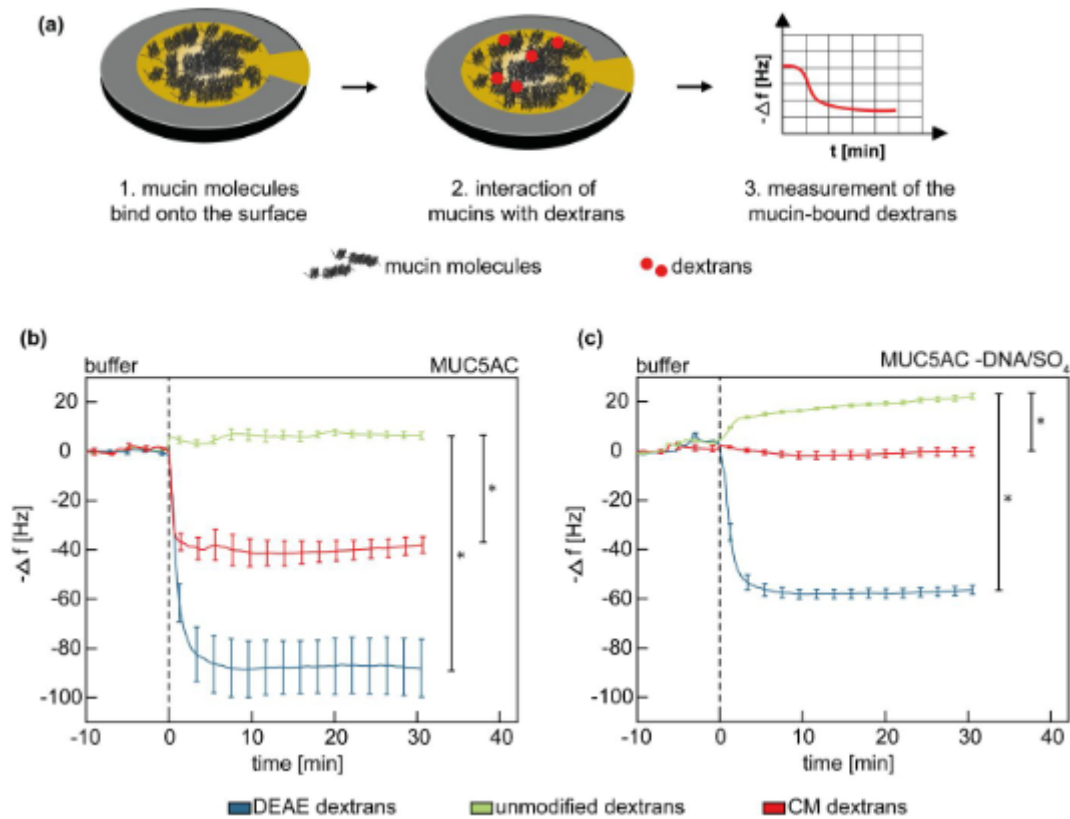
#### 2.4. Investigating the interaction of native and enzymatically modified mucins with dextrans using QCM-D measurements

As test molecules, we selected the 150 kDa dextrans since we receive stronger signals with those larger dextrans in QCM-D. We performed a two-step adsorption assay (Fig. S5a): First, the resulting resonance frequency shift of adsorbed mucin molecules is detected. Then, the subsequent frequency shifts induced by the binding of dextrans to the pre-adsorbed mucins is recorded.

After allowing for mucin adsorption (45 min) onto the PDMS surface as described in 2.3, a rinsing step with HEPES buffer was conducted at a flow rate of  $100 \mu\text{L min}^{-1}$  to remove any unbound mucins. Afterwards, a 0.05 % (w/v) solution of either anionic (CM-modified), cationic (DEAE-modified) or neutral (unmodified) dextrans (all obtained from TdB Consultancy, Uppsala, Sweden) with a molecular weight of 150 kDa each was injected into the chamber, and the resulting frequency shifts were recorded for 30 min. To compensate for the molecular weight differences of the two mucin variants adsorbed onto the surface (see Fig. S4), we here use the frequency shift induced by the adsorption of either mucin variant as a baseline; then, we separately compare the adsorption behavior of the three different dextrans to each mucin variant (Fig. S5b,c).

For intact, untreated MUC5AC we find that cationic dextrans bind strongest, anionic dextrans show intermediate binding, and neutral dextrans appear not to adsorb to the mucin layer at all (Fig. S5b). This result is in full agreement with the outcome of the depletion assay discussed above and in the main text (Fig. S2 and Fig. 1).

For the enzymatically treated MUC5AC -DNA/-SO<sub>2</sub> mucin variant, we find that cationic dextrans bind reasonably well and neutral dextrans do not induce a negative frequency shift as it would be triggered by adsorption to the mucin layer (Fig. S5c). Both of those results agree with the outcome of the depletion tests discussed before. Importantly, when we expose the mucin layer to anionic dextrans, we cannot detect a significant shift in frequency either (Fig. S5c, red curve). Since QCM-D measurements are able to detect even subtle changes in the adsorbed mass, this outcome indicates that almost no anionic dextrans bind to the modified mucin – a finding that is in line with the result obtained from the depletion assay.

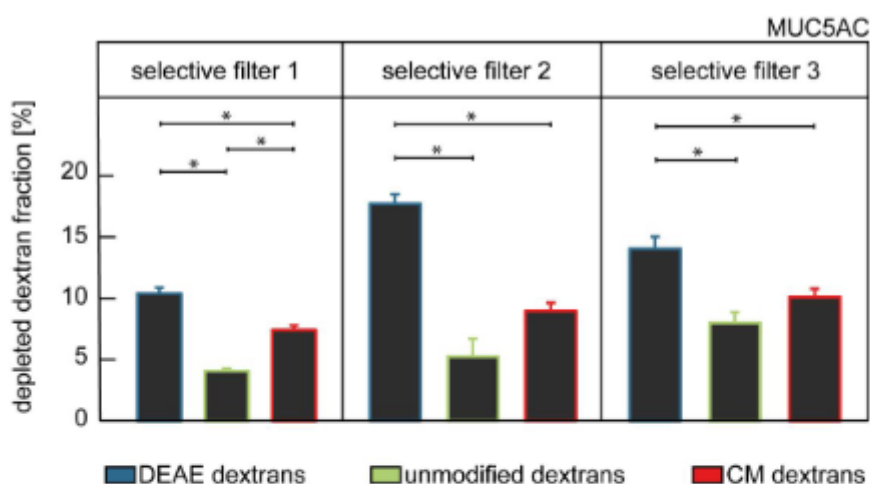


**Figure S5: Binding of different dextrans to mucins which were pre-adsorbed onto hydrophobic PDMS surfaces.** (a) Schematic representation of the adsorption-based affinity assay. In a first step, mucins are adsorbed onto PDMS-coated quartz crystal sensors. When a stable signal is achieved, dextrans are flushed into the measuring cell and the binding of dextrans to the surface-adsorbed mucins is determined from the resulting shift in the resonance frequency of the crystal. Binding of cationic (blue), neutral (green), and anionic (red) dextrans to native mucin (b) and enzymatically treated mucin (c) is compared. The error bars denote the standard error of mean as obtained from three individual measurements. Asterisks mark significant differences ( $p \leq 0.05$ ).

## 2.5. Mucin-functionalized PDMS filters selectively deplete charged dextrans from solution

To support the experimental data obtained with our depletion assay, we conduct molecular depletion tests with dextrans using another experimental adsorption-based platform. A capillary filter system is manufactured from polydimethylsiloxane (PDMS) as described previously.<sup>1</sup> The inner surface of these filters can be functionalized with MUC5AC by flushing a 0.1 % (w/v) MUC5AC (dissolved in 20 mM HEPES buffer (pH 7.0)) solution into the capillaries of the PDMS filters. Then, the mucin molecules are allowed to adsorb onto the capillary surface and, after an incubation time of 2 h, the filter is thoroughly rinsed with HEPES buffer to remove unbound mucin molecules from the capillary system. Dextran solutions containing 0.02 % (w/v) of either cationic, neutral or anionic (FITC-labelled) dextrans (4 kDa) are then pumped through the mucin-functionalized filter at a flow rate of 1 mL min<sup>-1</sup>; for each dextran variant, 1 mL of 'filtered' solution is collected. The fraction of dextrans depleted from solution is determined by measuring the fluorescence intensity of the the solution before and after having passed the filter (see the Materials and Methods section of the main text).

Three different filters were probed for their dextran binding capacity. Whereas in all cases a significant fraction of the cationic dextrans is depleted from the dextran solution, this depletion was always most efficient for cationic dextrans and least efficient for neutral dextrans (Fig. S6).



**Figure S6: Selective removal of dextran molecules by mucin molecules adsorbed to the inner surface of PDMS filters.** The fraction of depleted dextrans is shown for neutral (green), positively (red) and negatively (blue) charged 4 kDa dextrans. The error bars denote the standard error of the mean as obtained from five technical replicates. Asterisks mark significant differences between the dextran groups ( $p \leq 0.05$ ) as obtained by a combination of a one-way ANOVA and Tukey post-hoc tests for pairwise comparisons.

### 3. Modelling the conformation of mucin macromolecules

#### 3.1. Size estimation of the globular VWF domains

The protein sequence of MUC5AC we use in this study has the accession number A0A287ANG4 and was retrieved from the data base UniProtKB (<https://www.uniprot.org>, 09/25/18).

As explained in the main paper, we first segmented the mucin macromolecule into different subunits. For the folded termini of the peptide sequence, we then estimated the radius ( $r$ ) of each VWF domain from the contour length ( $l_c$ ) and the persistence length ( $l_p$ ) of the corresponding peptide sequence according to equation S1:

$$r \approx \frac{1}{\sqrt{6}} * 2l_p \sqrt{\frac{l_c}{2l_p}} \quad (\text{Equation S1})$$

Here, the contour length  $l_c$  of the respective sequence was estimated by multiplying the number of amino acids in this sequence with the typical  $C_\alpha$ -to- $C_\alpha$  distance of an amino acid, the latter of which was approximated as 0.35 nm.<sup>2</sup> The persistence length  $l_p$  was approximated with that of the small globular protein ubiquitin (*i.e.*,  $l_p = 0.39$  nm)<sup>3</sup>.

In the simplified numerical model described below, the whole mucin glycoprotein is assumed to be a continuous linear strand in which the peptide sequence is completely stretched. Therefore, the globular domains, their connecting segments, and the remaining parts of the molecule are all modelled as flexible elements with an approximated cylindrical shape (see 3.3).

#### 3.2. Estimating the charge distribution along the MUC5AC molecule

Since we expected the charge distribution along the whole mucin contour to be highly relevant for the conformation of the glycoprotein, we first asked if assuming a full elementary charge per amino acid would return a similar net charge of the mucin polypeptide as the internet-based charge calculator Prot pi (<https://www.protpi/Calculator/ProteinTool>, 02/03/20, **Table S1**). For a determination of the net charge of each mucin variant at the respective pH value (pH 4.0 or 7.0), a manual calculation is performed by allocating a full elementary charge to single amino acids if the  $pK_a$  value of the amino acid side chains is close to or above the pH level. With this approach, at pH 7.0, the basic amino acids (arg, lys) and the acidic amino acid (asp, glu) are assigned one positive/negative charge each. In contrast, at pH 4.0, the basic amino acids (arg, his, lys) and the acidic amino acid (asp) at pH 4.0 are assigned one positive or negative charge, respectively.

For neutral pH, this approximation matched the Prot pi prediction very well, which is why we kept this charge assignment for this pH level. In contrast, for acidic conditions, we refined our estimation by assigning only half a negative elementary charge to aspartate. This is reasonable since, for this particular amino acid having a  $pK_a$  value close to  $\sim 4.0$ ,<sup>4</sup> full deprotonation is unlikely. Indeed, with this correction, our estimation returns the net charge predicted by Prot pi quite well (see **Table S1**).

**Table S1: Net charge of the whole MUC5AC protein sequence** (without considering any charges corresponding to glycans). The calculations are conducted manually and with the internet-based calculator Prot pi at pH 4.0 and 7.0.

pH	Net charge when assuming full elementary charges/amino acid at both pH conditions	Net charge when assuming full elementary charges for all aa but only half an elementary charge for asp (@pH 4.0)	Net charge according to Prot pi
7.0	- 50	- 50	- 54.2
4.0	+ 167	+ 238.5	+ 233.4

With this refined estimation process, we then calculated the spatial charge distribution for the whole mucin molecule based on the following set of information and assumptions:

1. the amino acid sequence of mucin
2. published information on the amount of negatively charged sialic acids and sulfate groups in the core domain of the protein<sup>5</sup>
3. assuming the amino acid sequence between the 3<sup>rd</sup> and 4<sup>th</sup> VWF-like domain to be strongly glycosylated. This assumption is reasonable since, in this area of the polypeptide chain, there are lots of threonines and serines, which are typical targets for O-glycosylations.<sup>6-7</sup>

Whereas charges established by amino acids in the mucin termini (ID 1-10 and 59-68, **Table S2**) are considered as described above (middle column of **Table S1**), charges corresponding to amino acids in the glycosylated domain are neglected (since we assume those charges to be shielded by the glycans). Instead, all sialic acids and sulfate groups (which we determined to occur in a ratio of 1 : 3.5 based on literature<sup>5</sup>) in this glycosylated region are included into the charge distribution where they are assigned a full negative charge each (element ID 11-58, **Table S2**). The estimation of the spatial distribution of these negative charges is based on experimental data<sup>5</sup> as follows:

Sulfate groups constitute  $\sim 2.1\%$  (w/w) of the molecular weight of MUC5AC. By assuming  $MW_{MUC5AC} \sim 3$  MDa, the corresponding MW of sulfate groups/mucin is  $\sim 63$  kDa. With a

S12



molecular mass of sulfate groups of  $MW_{SO_4} \sim 96$  g/mol, this results in  $\sim 655$  negative charges established by sulfated glycans per mucin. The experimentally determined ratio of sulfate groups to sialic acids residues of 3.5 : 1 then allows us to calculate 187 sialic acids/mucin. In total, this gives  $\sim 842$  negatively charged glycans, which are distributed in the glycosylated core domain of the mucin molecule. Since, in our numerical model, only serines and threonines are assumed to be associated with glycans *via* O-glycosylation, only those amino acids receive negative charges.

With those considerations, the charge distributions shown in **Table S2** are obtained. For enzymatically treated mucins, the contributions of the respective anionic glycans are removed from the charge profile, *i.e.* a net charge of 0 is assigned to the respective amino acid.

**Table S2: Estimated charge distributions for different mucin variants as explained above.** The segments corresponding to the N- and C-terminus are marked in grey, the VWF-domains in black, and the segments of the glycosylated core-domain in white.

element ID	element length [nm]	net charge of the protein sequence considering the sulfated groups and sialic acids				
		MUC5AC (pH 4.0)	MUC5AC (pH 7.0)	MUC5AC -SO <sub>4</sub> (pH 7.0)	MUC5AC -SA (pH 7.0)	MUC5AC -SO <sub>4</sub> /-SA (pH 7.0)
1	25	11.5	8	8	8	8
2	6	-4.5	-8	-8	-8	-8
3	26.5	6	-3	-3	-3	-3
4	26.5	3	-6	-6	-6	-6
5	6	17	-2	-2	-2	-2
6	22.25	4.5	0	0	0	0
7	22.25	2	-2	-2	-2	-2
8	22.25	2.5	-4	-4	-4	-4
9	22.25	3	-1	-1	-1	-1
10	6	14	-4	-4	-4	-4
11	17.5	-5	-5	-1	-4	-6
12	17.5	-1	-1	0	-1	0
13	17.5	-8	-8	-3	-5	-3
14	17.5	-8	-8	-1	-7	-1
15	17.5	-19	-19	-5	-14	4
16	17.5	-9	-9	-3	-6	-5
17	17.5	-4	-4	0	-4	-1
18	17.5	-16	-16	-5	-11	-1
19	17.5	-20	-20	-5	-15	-1
20	17.5	-6	-6	-1	-5	0
21	17.5	-5	-5	-2	-3	-3
22	17.5	-23	-23	-6	-17	0
23	17.5	-8	-8	-2	-6	-2
24	17.5	-1	-1	-1	0	2

S13

25	17.5	-23	-23	-4	-19	0
26	17.5	-36	-36	-6	-30	0
27	17.5	-14	-14	-4	-10	-2
28	17.5	-2	-2	0	-2	0
29	17.5	-23	-23	-7	-16	0
30	17.5	-18	-18	-3	-15	-2
31	17.5	-3	-3	-1	-2	1
32	17.5	-17	-17	-4	-13	0
33	17.5	-31	-31	-6	-25	2
34	17.5	-32	-32	-7	-25	1
35	17.5	-29	-29	-5	-24	0
36	17.5	-33	-33	-8	-25	1
37	17.5	-32	-32	-6	-26	0
38	17.5	-30	-30	-6	-24	0
39	17.5	-30	-30	-5	-25	0
40	17.5	-31	-31	-6	-25	0
41	17.5	-33	-33	-6	-27	1
42	17.5	-30	-30	-5	-25	0
43	17.5	-33	-33	-6	-27	1
44	17.5	-30	-30	-8	-22	0
45	17.5	-23	-23	-6	-17	0
46	17.5	-16	-16	-3	-13	-2
47	17.5	-3	-3	0	-3	0
48	17.5	-12	-12	-4	-8	2
49	17.5	-26	-26	-7	-19	0
50	17.5	-8	-8	-1	-7	0
51	17.5	-2	-2	-1	-1	0
52	17.5	-20	-20	-5	-15	1
53	17.5	-30	-30	-6	-24	0
54	17.5	-23	-23	-6	-17	0
55	17.5	-11	-11	-2	-9	2
56	17.5	-11	-11	-2	-9	1
57	17.5	-8	-8	-2	-6	2
58	10.5	-6	-6	-1	-5	2
59	6	12	-7	-7	-7	-7
60	20	3	-4	-4	-4	-4
61	20	0	-3	-3	-3	-3
62	4	4	-5	-5	-5	-5
63	12	2	-3	-3	-3	-3
64	4	2.5	-4	-4	-4	-4
65	17.75	6	-2	-2	-2	-2
66	17.75	7	4	4	4	4
67	17.75	5.5	0	0	0	0
68	17.75	5.5	-3	-3	-3	-3

S14

### 3.3. Detailed setup of the simulation model and methods

This section presents details of the computational model and methods used in the simulations. The numerical study specifically aims at investigating qualitative differences in the conformation of a mucin filament due to the different line charge distributions described above.

#### 3.3.1. Geometry, material and spatial discretization

The system consists of a single, initially straight filament of length  $L = 1.155 \mu\text{m}$  with a circular cross-section of radius  $R = 7 \text{ nm}$ , which is a simple model for the actual molecular architecture of a mucin filament (see Fig. 2) and yields a slenderness ratio of  $\zeta = 165$ . The structural constitutive parameters for the bending, torsional, axial and shear stiffness are set to  $EI = 2 \times 10^{-4} \text{ pN}\mu\text{m}^2$ ,  $GI_T = 2 \times 10^{-4} \text{ pN}\mu\text{m}^2$ ,  $EA = 2 \times 10^1 \text{ pN}$ , and  $G\bar{A} = 2 \times 10^1 \text{ pN}$ . These values correspond to experimentally determined values for the persistence length  $L_p = EI/k_B T \approx 50 \text{ nm}$ .<sup>8-9</sup> A total of 68 Hermitian Simo-Reissner beam elements (for details of the element formulation see Ref.)<sup>10</sup> are used to discretize the filament in space. This particular discretization is a result of dividing the extended glycosylated domain consisting of 2380 amino acids into 50 amino acids per element and treating the two terminal regions of the filament individually according to the molecular domain structure. The resulting discretization consists of 47 elements with a length of 17.5 nm in the extended glycosylated domain, 1 element for the remaining amino acids in this domain, and 10 elements each for the N- and C-terminal region (see Table S2).

#### 3.3.2. Brownian dynamics and temporal discretization

Thermal excitation and viscous damping of the filament due to the implicitly modeled surrounding fluid are incorporated *via* the micromechanical continuum approach to Brownian dynamics.<sup>11</sup> The thermal energy used to compute the random thermal forces on the filaments is set to  $k_B T = 4 \times 10^{-3} \text{ aJ}$ , *i.e.*, room temperature. The viscous drag forces acting along the filament are computed based on the viscosity  $\eta = 10^{-3} \text{ Pa s}$  of water and individual damping coefficients for translations parallel and perpendicular to the filament axis as well as rotation around the filament axis that follow from the cylindrical shape of the filament. A Backward Euler scheme is used to discretize the problem in time and a base time step size of  $\Delta t = 10^{-3} \text{ s}$  is applied. This is augmented by an adaptive time stepping scheme, in which, however, the stochastic thermal forces are kept constant over an interval of  $\Delta t = 10^{-2} \text{ s}$  each in order to allow the system to converge to the corresponding dynamic equilibrium configuration.

#### 3.3.3. Electrostatic interactions

The electrostatic (self-)interaction of the mucin filament is modeled *via* the so-called section-section interaction potential (SSIP) approach.<sup>12</sup> Here, the applied SSIP law is based

S15

on the Coulomb interaction of two circular cross-sections with homogeneous surface charge. In short, the resulting line load acting on the beam centerline is evaluated in a double numerical integral taking into account all pairs of cross-section slices. The constant prefactor  $C_{\text{elstat}}^{\text{true}} \approx 1.12 \times 10^2 \text{ aJ } \mu\text{m fC}^{-2}$  follows from assuming the dielectric permittivity of water (at room temperature) for the surrounding fluid. In order to not significantly overestimate the effect of charge interactions due to not considering the screening of charges in our model, the actual applied prefactor  $C_{\text{elstat}} = 0.1 \cdot C_{\text{elstat}}^{\text{true}}$  has been reduced by a factor of ten. This overall rather simple model for the charge interactions is still considered to correctly predict significant qualitative changes in the conformation of the filament due to differences in the line charge distributions as analyzed in section 3.2 for different variants of mucin and pH conditions. To obtain the input parameter values for the simulation, the net charge for the specific region of each finite beam element was computed and applied as an element-wise constant line charge density  $\lambda(s)$  along the filament. The complete data set used in the simulation setup for each of the different scenarios to be compared is provided in **Table S2**. To evaluate the mentioned numerical integrals along the filament axis, Gaussian quadrature with five integration points per element is applied.

As a consequence of the electrostatic self-interactions, the filament with an initially straight, stress-free reference configuration defined above will experience locally confined axial tension as well as compression, which is equilibrated in ten additional time steps in the beginning of each simulation during which no thermal forces are applied. This turned out to be crucial for a successful iterative solution of the nonlinear system of equations, because otherwise physical instabilities in form of local buckling was induced by the combination of strong, inverse-distance dependent electrostatic forces and small undulations of the straight fiber axis due to thermal forces.

### 3.3.4. Repulsive steric interactions

Due to the possibly strong attractive electrostatic forces, it is particularly important to account for self-contact of the filament in order to preclude an unphysical interpenetration of distinct parts of the filament, which would also lead to a singularity in the inverse-distance dependent SSIP law. Following the reasoning and conclusions regarding a combination with the SSIP approach from <sup>13</sup>, a so-called penalty contact formulation for beams <sup>14</sup> is applied. The line penalty parameter is set to  $\varepsilon = 10^5 \text{ pN } \mu\text{m}^{-2}$ , which - in combination with a quadratic regularization in the gap value range 0-2 nm - turns out to be sufficiently large to effectively preclude any noticeable penetration in any (dynamic) equilibrium configuration. This is supplemented by the Newton step size control algorithm applied *e.g.* already in <sup>12</sup> in order to preclude also unphysical crossings, *i.e.*, passing of distinct parts of the filament through each

other's volume in between two iterations of the nonlinear solver due to an overly large displacement increment per nonlinear iteration.

### 3.3.5. Boundary conditions

One end of the filament is hinged by means of Dirichlet boundary conditions in order to comply with the experimental setup. Due to a lack of knowledge and control over the fact which end of the filament attaches to the surface in the experiments, the N-terminus is chosen to be pinned in all the simulations, but no noticeable changes in the statistical quantities of interest (see below) are expected if instead the C-terminus was pinned or if the filament was entirely free to move.

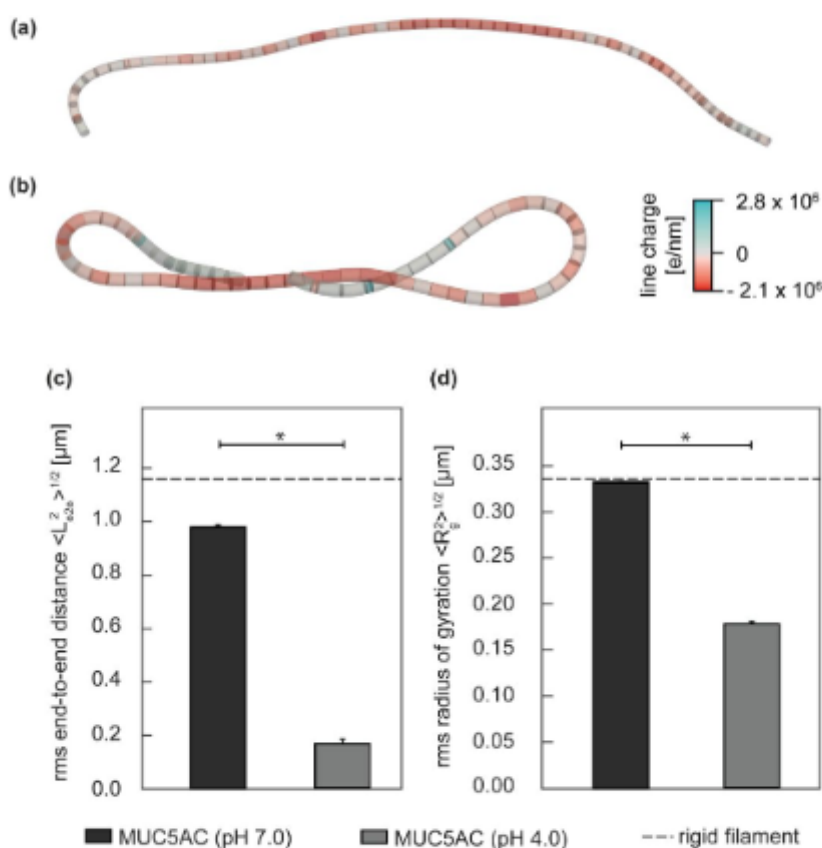
### 3.3.6. Quantities of interest

Since we are interested in the conformation of the filament, we choose the time- and configuration-averaged end-to-end distance  $L_{e2e}$  and radius of gyration  $R_g$  as the quantities of interest to be analyzed in the simulations. To ensure a sufficient sampling of these statistical quantities, the total simulation time was set to  $t_{\text{end}} = 2 \text{ s}$  and five independent, random realizations for each scenario, *i.e.*, set of parameters, have been computed. Note that the radius of gyration is computed in a spatially discrete manner, *i.e.*, the contributions are evaluated at the 69 nodes used for the centerline discretization.

## 4. Simulation results for native MUC5AC at different pH levels and for enzymatically treated mucin variants

### 4.1. Influence of pH changes on the conformation of full, intact mucin

The charge distributions used for this set of simulations are those marked in **Table S2** in orange and green, respectively. At pH 7.0, the mucin molecule exhibits an elongated, stretched conformation (**Fig. S7a**) with an end-to-end distance and radius of gyration close to that of a rigid filament. At an acidic pH of 4.0, the charge pattern of the mucin peptide sequence is changed due to protonation of formerly anionic residues (see above). As a consequence of the ensuing loss of intramolecular repulsion forces, the mucin assumes a more compacted state (**Fig. S7b**). Accordingly, the radius of gyration of the mucin molecule is reduced by ~50% and the end-to-end distance by ~80% compared to neutral pH (**Fig. S7c,d**).

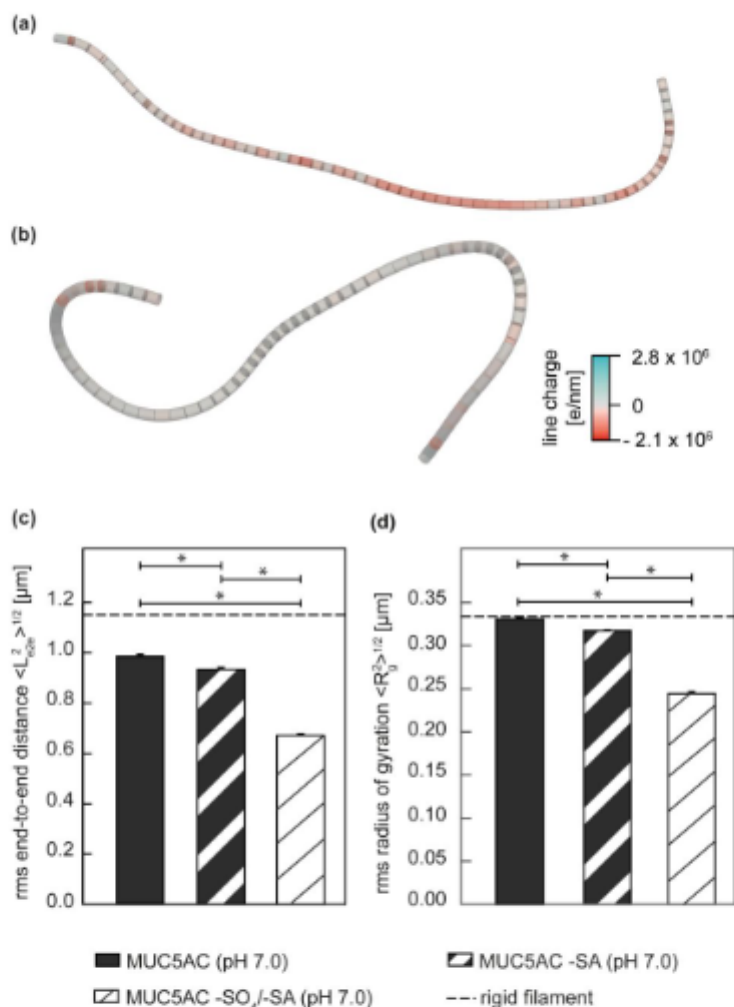


**Figure S7: Numerical simulation results obtained for native, untreated MUC5AC at neutral and acidic pH.** Representative examples of the modelled conformation of native mucin at pH 7.0 and 4.0 are shown in (a) and (b), respectively. The corresponding structural parameters, *i.e.*, the end-to-end distance and the radius of gyration as calculated from the simulated mucins are shown in (c) and (d). The error bars depict the standard error of the mean as obtained from five independent simulation runs. Asterisks mark significant differences between samples as determined with a t-test ( $p \leq 0.05$ ).

S18

## 4.2. Conformational changes of simulated mucins triggered by the removal of anionic glycans

In the next simulation set, the pH is kept constant at 7.0. However, now, untreated MUC5AC is compared to partially deglycosylated variants where either only sialic acid residues or both, sialic acid residues and sulfate groups were removed. The corresponding charge distributions used for these modified mucin variants are listed in the last two columns of **Table S2**.



**Figure S8: Numerical simulation results obtained for native and glycan-reduced mucins.**

Representative examples of the modelled conformation of sialic acid-reduced (MUC5AC-SA), and sialic acid/sulfate-reduced (MUC5AC-SA-SO<sub>4</sub>) mucin at neutral pH are shown in (a) and (b), respectively. The corresponding structural parameters, *i.e.*, the end-to-end distance and the radius of gyration as calculated from the simulated mucins are shown in (c) and (d). The error bars depict to the standard error of the mean as obtained from five independent simulation runs. Asterisks mark significant differences between samples ( $p \leq 0.05$ ); those are tested for by combining a one-way ANOVA and Tukey post-hoc tests for pairwise comparisons conducted afterwards.

When the anionic sialic acid groups are removed from the simulated mucin, the resulting conformational change is only mild (Fig. S8a). This can be rationalized by the fact that, now, the protonation state of the amino acid residues in the protein termini is not affected. Moreover, it was expected that the removal of sialic acids has a weaker influence on the mucin conformation than the removal of sulfate groups (see Fig. 2 in the main text) since the density of sialic acid residues in MUC5AC is 3.5-fold lower than that of sulfate motifs.

Consistent with the argumentation we followed so far, the removal of both, sialic acid residues and sulfate groups leads to a slightly stronger compaction of the mucin molecule (Fig. S8b) than the removal of sulfate groups alone (see Fig. 2 in the main text). Removal of sialic acid residues reduces the end-to-end distance and the radius of gyration of MUC5AC by only ~5% whereas we find a reduction of those parameters by ~30% when both anionic glycans are removed (Fig. S8c,d).

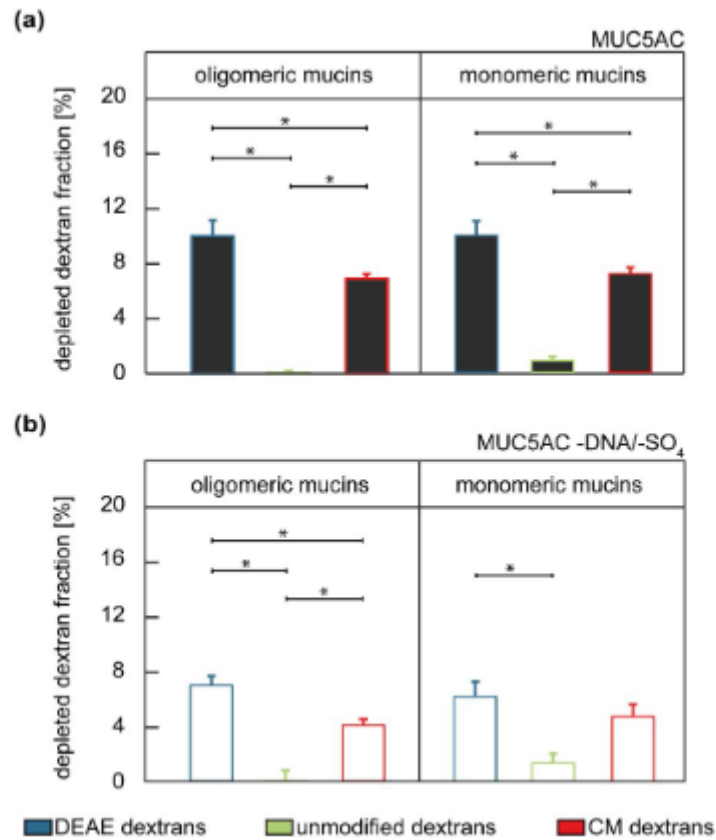
## **5. Interactions of mucins with molecules that bind to mucins *via* unspecific and specific binding interactions**

### **5.1. Influence of reducing agents on the unspecific binding of dextrans**

Physiologically, mucins occur in an oligomeric state rather than in a monomeric state. Since we do not treat our mucins with reducing agents during purification, we assume that our lab-purified mucins consists mostly of oligomers. Since, with our numeric model, we can only simulate monomeric mucin molecules, we here probe differences in the binding of dextrans to native MUC5AC and enzymatically treated MUC5AC -DNA/-SO<sub>4</sub>.

For this purpose, we dissolved both mucin variants in 20 mM HEPES buffer (pH 7.0) either without any further additives or with 10 mM tris(2-carboxyethyl)phosphine (TCEP), which reduces intermolecular (and intramolecular) disulfide bonds. We then coated wells of a 96-well microtiter plate with solutions of these two mucin samples. Indeed, the experimental outcome of our depletion assay is virtually identical for both cases, and no statistically significant differences in dextran binding to reduced (= monomeric) mucin and oligomeric mucin is observed. (Fig. S9).

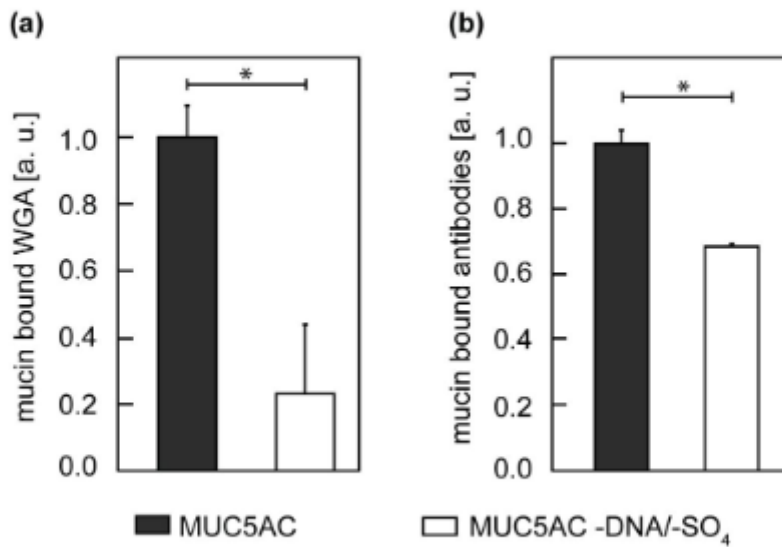




**Figure S9: Dextran depletion assay conducted with monomeric and oligomeric mucin molecules.** The fraction of depleted dextran is shown for neutral (green), positively (blue), and negatively (red) charged 4 kDa dextrans. Experiments are conducted for untreated MUC5AC (a) and MUC5AC -DNA/SO<sub>4</sub> (b), and for oligomeric and monomeric mucin molecules generated from the same mucin purification batch. The error bars represent the standard error of the mean as obtained from five individual samples. Asterisks mark significant differences between dextran samples ( $p \leq 0.05$ ), which are tested with a one-way ANOVA and Tukey post-hoc tests for pairwise comparisons.

## 5.2. Interaction studies between mucin and specifically binding lectins and antibodies

The data shown in Fig. S10 depicts an experimental repetition of the depletion tests described in Fig. 3 of the main text, yet conducted with a different mucin purification batch.



**Figure S10: ELISA test and depletion assay to assess the interaction of native and enzymatically treated mucins with specific binding partners.** WGA (a) and anti-MUC5AC antibodies (b) show a higher binding affinity towards native mucin (MUC5AC) than towards the enzymatically modified mucin variants. The error bars represent the standard error of mean obtained from five samples. Asterisks mark statistically significant differences between samples ( $p \leq 0.05$ ).

## 7. Cited literature

1. Winkeljann, B.; Käs Dorf, B. T.; Boekhoven, J.; Lieleg, O. Macromolecular Coating Enables Tunable Selectivity in a Porous PDMS Matrix. *Macromolecular bioscience* **2018**, *18*, 1700311.
2. Berg, J. M.; Held, A.; Stryer, L.; Lange, C.; Mahlke, K.; Maxam, G.; Seidler, L.; Zellerhoff, N.; Häcker, B.; Jarosch, B., Stryer Biochemie. Springer Berlin Heidelberg: 2015; pp 25-65.
3. Stirnemann, G.; Giganti, D.; Fernandez, J. M.; Berne, B. Elasticity, structure, and relaxation of extended proteins under force. *Proceedings of the National Academy of Sciences* **2013**, *110*, 3847-3852.
4. Horn, F., Biochemie des Menschen: das Lehrbuch für das Medizinstudium. Thieme: 2009; pp 37-49.
5. Marczynski, M.; Balzer, B. N.; Jiang, K.; Lutz, T. M.; Crouzier, T.; Lieleg, O. Charged glycan residues critically contribute to the adsorption and lubricity of mucins. *Colloids and Surfaces B: Biointerfaces* **2019**, 110614.
6. Bansil, R.; Turner, B. S. Mucin structure, aggregation, physiological functions and biomedical applications. *Current opinion in colloid & interface science* **2006**, *11*, 164-170.
7. Gum, J.; Hicks, J.; Toribara, N.; Rothe, E.; Lagace, R.; Kim, Y. The human MUC2 intestinal mucin has cysteine-rich subdomains located both upstream and downstream of its central repetitive region. *Journal of Biological Chemistry* **1992**, *267*, 21375-21383.
8. Shogren, R.; Gerken, T. A.; Jentoft, N. Role of glycosylation on the conformation and chain dimensions of O-linked glycoproteins: light-scattering studies of ovine submaxillary mucin. *Biochemistry* **1989**, *28*, 5525-5536.
9. Round, A. N.; Berry, M.; McMaster, T. J.; Stoll, S.; Gowers, D.; Corfield, A. P.; Miles, M. J. Heterogeneity and Persistence Length in Human Ocular Mucins. *Biophysical Journal* **2002**, *83*, 1661-1670.
10. Meier, C.; Grill, M. J.; Wall, W. A.; Popp, A. Geometrically exact beam elements and smooth contact schemes for the modeling of fiber-based materials and structures. *International Journal of Solids and Structures* **2018**, *154*, 124-146.
11. Cyron, C. J.; Wall, W. A. Numerical method for the simulation of the Brownian dynamics of rod-like microstructures with three-dimensional nonlinear beam elements. *International Journal for Numerical Methods in Engineering* **2012**, *90*, 955-987.
12. Grill, M. J.; Wall, W. A.; Meier, C. A Computational Model for Molecular Interactions Between Curved Slender Fibers Undergoing Large 3D Deformations With a Focus on Electrostatic, van der Waals and Repulsive Steric Forces. *International Journal for Numerical Methods in Engineering* **2020**, *121*, 2285-2330.
13. Grill, M. J.; Meier, C.; Wall, W. A. Investigation of the peeling and pull-off behavior of adhesive elastic fibers via a novel computational beam interaction model. *The Journal of Adhesion* **2019**, 1-30.
14. Meier, C.; Popp, A.; Wall, W. A. A finite element approach for the line-to-line contact interaction of thin beams with arbitrary orientation. *Computer Methods in Applied Mechanics and Engineering* **2016**, *308*, 377-413.

## B.3 Bioinspired dopamine/mucin coatings provide lubricity, wear protection, and cell-repellent properties for medical applications

FULL PAPER



# Bioinspired Dopamine/Mucin Coatings Provide Lubricity, Wear Protection, and Cell-Repellent Properties for Medical Applications

Jian Song, Theresa M. Lutz, Nora Lang, and Oliver Lieleg\*

Even though medical devices have improved a lot over the past decades, there are still issues regarding their anti-biofouling properties and tribological performance, and both aspects contribute to the short- and long-term failure of these devices. Coating these devices with a biocompatible layer that reduces friction, wear, and biofouling at the same time would be a promising strategy to address these issues. Inspired by the adhesion mechanism employed by mussels, here, dopamine is made use of to immobilize lubricious mucin macromolecules onto both manufactured commercial materials and real medical devices. It is shown that purified mucins successfully adsorb onto a dopamine pre-coated substrate, and that this double-layer is stable toward mechanical challenges and storage in aqueous solutions. Moreover, the results indicate that the dopamine/mucin double-layer decreases friction (especially in the boundary lubrication regime), reduces wear damage, and provides anti-biofouling properties. The results obtained in this study show that such dopamine/mucin double-layer coatings can be powerful candidates for improving the surface properties of medical devices such as catheters, stents, and blood vessel substitutes.

## 1. Introduction

Medical devices such as artificial joints, catheters, stents, and blood vessel substitutes, are typically fabricated from synthetic materials and are essential for current medical therapies.<sup>[1]</sup>

Dr. J. Song, T. M. Lutz, Prof. O. Lieleg  
Department of Mechanical Engineering and Munich School of  
Bioengineering  
Technical University of Munich  
85748 Garching, Germany  
E-mail: oliver.lieleg@tum.de

Dr. N. Lang  
Department of Pediatric Cardiology and Congenital Heart Disease,  
German Heart Center Munich  
Technical University of Munich  
80636 Munich, Germany

The ORCID identification number(s) for the author(s) of this article can be found under <https://doi.org/10.1002/adhm.202000831>

© 2020 The Authors. Published by Wiley-VCH GmbH. This is an open access article under the terms of the Creative Commons Attribution-NonCommercial License, which permits use, distribution and reproduction in any medium, provided the original work is properly cited and is not used for commercial purposes.

DOI: 10.1002/adhm.202000831

For those devices to fulfill their envisioned function in the human body, excellent biocompatibility, appropriate mechanical strength, low friction surfaces, as well as high resistance toward wear, corrosion and biofouling are required.<sup>[2]</sup> A main limitation of many implant materials is the cell-adhesive behavior of their surfaces, the ensuing biofouling events and the following inflammation response of the body.<sup>[3]</sup> For instance, neointimal hyperplasia occurs after the placement of metallic stents and polytetrafluoroethylene (PTFE)-based blood vessel substitutes.<sup>[4]</sup> Neointimal proliferation is induced by inflammatory reactions after the placement of the stent or blood vessel substitute followed by proliferation and migration of smooth muscle cells and production of extracellular matrix. As a possible consequence, restenosis sets in and such a closure of the luminal vessel diameter in

the device can be associated with high morbidity and mortality rates.<sup>[5]</sup> Similar issues apply to other medical devices including catheters, where—in addition to eukaryotic colonization events—adhesion of bacteria to the catheter surface aggravates the risk for inflammation.<sup>[6]</sup> Moreover, if the lubricity of a medical device is not good, mechanical shear forces occurring during the implantation process can lead to the transfer of small tissue parts (or single cells) onto the device—and this will speed up the biofouling process.<sup>[7]</sup> Of course, the generation of wear by tribological stress acting on the load-bearing surface of a device can also be a direct reason for both, the short- and long-term failure of certain medical devices.<sup>[8]</sup>

To prevent those issues, coating synthetic materials with a biocompatible layer is a promising strategy.<sup>[9]</sup> One candidate for a biopolymer, which establishes coatings with anti-biofouling, lubricity and wear protection abilities, is the glycoprotein mucin. Mucins are key components of mucosal systems such as the tear fluid, saliva, or stomach mucus and have become popular due to their superior biocompatibility, excellent tribological performance, as well as anti-bacterial and anti-biofouling properties.<sup>[10]</sup> However, mucin-based coatings described in the literature are either based on passive adsorption<sup>[11]</sup> (which works well on polydimethylsiloxane (PDMS)-based surfaces but does not create stable coatings that withstand mechanical shear very well) or involve covalent coupling methods<sup>[12]</sup> (which require polymeric

substrates that can be chemically activated). For metallic surfaces such as steel or PTFE-based materials; however, neither of those two approaches are very promising as there are no appropriate functional groups on those surfaces that were to offer anchoring points for a stable mucin attachment.<sup>[13]</sup> Yet, those materials are frequently used in biomedical applications, which calls for a different coupling strategy to generate stable mucin coatings on them.

Mussels can strongly adhere to almost any material—regardless of its surface roughness. To do so, they produce proteins rich in special tyrosine derivatives called 3,4-dihydroxyphenylalanine (DOPA); DOPA molecules (as well as the chemically related neurotransmitter dopamine) belong to the group of catechols and are present at high concentrations in the tip of the mussel byssus. Catechols such as DOPA or dopamine as well as the self-polymerized variant of the latter, polydopamine, can bind to a broad range of organic and inorganic surfaces.<sup>[14]</sup> This is made possible by the ability of catechols to engage in different molecular interactions with surfaces: examples include complex formation between metal atoms of a metallic surface and the phenolic hydroxyl groups of catechols, hydrophobic interactions and/or  $\pi$ - $\pi$  stacking, electrostatic interactions, and hydrogen bonds.<sup>[15]</sup> The same set of molecular interactions can bind other molecules to an adsorbed dopamine layer. Recently, a simple one-step coating based on dopamine was introduced to immobilize dextran onto various substrates.<sup>[16]</sup> Similarly, with the help of dopamine, polyethylene glycol (PEG, uncharged polymer),<sup>[17]</sup> polyethyleneimine (PEI, polycationic polymer),<sup>[18]</sup> and hyaluronic acid (HA, polyanionic polymer)<sup>[19]</sup> have been deposited onto different surfaces. Thus, using a similar approach might also allow for creating stable but non-covalent mucin coatings on medical devices.

We here develop dopamine/mucin coatings on materials frequently used for medical devices, that is, PDMS, PTFE, and steel substrates, using a simple dip-coating approach. We confirm the successful formation of the double-layer coatings and evaluate the lubricity, wear resistance and cell-repellent properties provided by these dopamine/mucin coatings. By performing cellular adhesion tests with real medical devices, for example, catheters, stents, and blood vessel substitutes, we demonstrate that our approach can also be applied to irregularly shaped, curved objects and as it establishes cell-repellent surfaces on those medical devices as well.

## 2. Results and Discussion

### 2.1. Generating Dopamine/Mucin Double-Layer Coatings by Sequential Adsorption

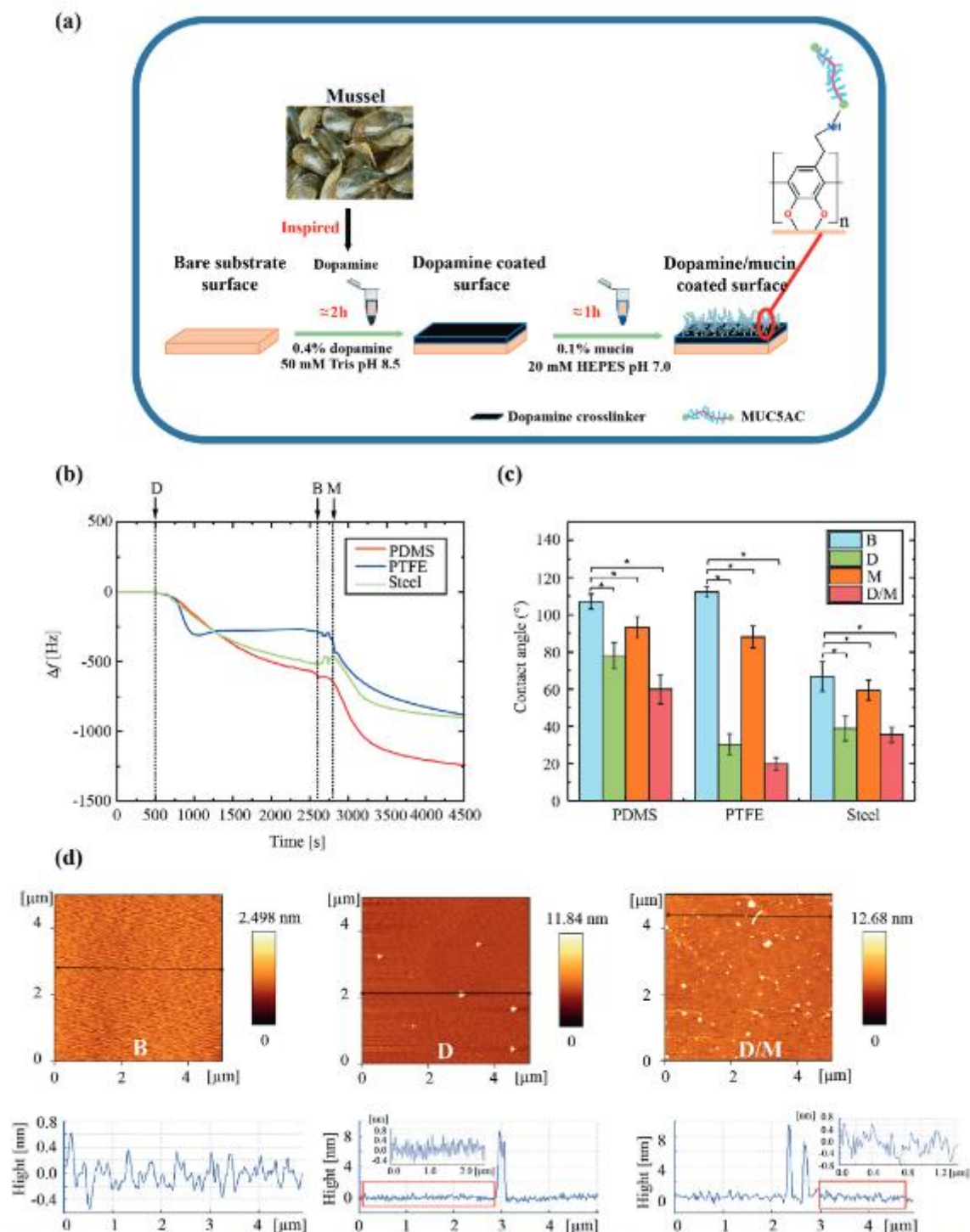
Dopamine spontaneously and firmly adsorbs onto a broad range of surfaces including glass, different metals, and polymers.<sup>[14]</sup> Here, we aim at harnessing this property by utilizing dopamine pre-coatings on different substrates to immobilize mucin glycoproteins. The idea is to conduct a two-step dip-coating procedure, where first dopamine molecules and then mucins self-assemble on the substrate surface thus forming a double-layer by sequential adsorption (Figure 1a). In a first step, we verify the successful formation of such a molecular double-layer by conducting QCM-D (quartz crystal microbalance with dissipation monitor-

ing) measurements with quartz crystals carrying three different surfaces: steel, PTFE, and PDMS surfaces (see Section 4.) are chosen as model substrates as those materials are commonly used for medical devices.<sup>[20]</sup> For all three surfaces, the frequency shift ( $\Delta f$ ) recorded in such QCM-D measurements shows a notable change when a dopamine solution is injected (Figure 1b). This frequency shift is somewhat stronger for the PDMS and steel surfaces than for the PTFE surface; in turn, the adsorption kinetics are faster for dopamine adsorption onto the PTFE substrate. After unbound dopamine is removed by rinsing with buffer, a mucin solution is injected. Also here, in all three cases, we detect a strong decrease in  $\Delta f$ . This indicates, that the mucin macromolecules successfully adsorb onto the pre-coated substrates, and with similar efficiencies for all three substrates.

To verify that the double-layer coatings can also be successfully generated on a macroscopic scale, we next subject cm-sized specimens of all three substrate types to a sequential dip-coating procedure (see Section 4.) and measure the contact angle of each substrate at different steps of the dip-coating process: as a bare substrate, after the first coating layer (dopamine) was applied, and after the top layer (mucin) was added to the dopamine pre-coating. For comparison, we also conduct a single-step coating with mucins, that is, without a dopamine pre-coating. As depicted in Figure 1c, both the dopamine coating and the dopamine/mucin double coating reduces the contact angles of all substrates; we find the strongest effect on the hydrophobic substrates, that is, PDMS and PTFE, but also a noticeable effect on steel. Interestingly, the contact angles obtained with a single-step mucin coating are always higher than those achieved with the other two coatings. This indicates that, whereas mucin can passively adsorb onto a wide range of surfaces, the efficiency of this adsorption process is improved when a dopamine pre-coating is used.<sup>[21]</sup> Moreover, it underscores the results we obtained with QCM-D and demonstrates that a macroscopic dopamine/mucin double coating can be easily developed on very different substrates including hydrophobic PDMS/PTFE and hydrophilic steel.

Having established that the dopamine pre-coating can immobilize mucin glycoproteins on different substrates, we next employ AFM imaging to examine the morphological quality of the coatings at the nanoscale. To obtain images with good quality, we use atomically flat mica as a substrate to carry the coating. As can be seen in Figure 1d, we do not detect any obvious defects. Moreover, with the exception of a few isolated structures in the dopamine/mucin coatings that might indicate local polydopamine or mucin fibers extending from the surface,<sup>[22]</sup> the roughness of the coating is less than 1 nm—also for the dopamine/mucin double-layers. In addition, with fluorescence microscopy using ATTO 594 labeled mucins, we detect a continuous mucin layer on the PDMS samples (Figure S1, Supporting Information), indicating good homogeneity and full surface coverage of the coatings.

Thus, we conclude that the quality of the coatings we developed in this work should be suitable to be used in further experiments. In detail, we aim at probing the lubricity, wear protection abilities, and cell repellent properties and of such dopamine-based coatings on model substrates. Moreover, we will decide if such double-layer coatings are indeed required to obtain the full set of functionalities we envision for a biomedical application. Then,



**Figure 1.** Preparation and characterization of dopamine/mucin double-layers generated by sequential adsorption. a) Samples were immersed into a 0.4% w/v dopamine solution for  $\approx 2$  h and then rinsed thoroughly with Millipore water to remove any unbound dopamine. After this dopamine pre-coating

we will test the correct formation of such a functional coating on exemplary medical devices.

## 2.2. Dopamine/Mucin Coatings Reduce Friction and Wear on PDMS

As we could demonstrate the successful formation of a dopamine/mucin double-layer on different substrates, we next evaluate the tribological properties of the coatings. We first analyze coatings generated on PDMS and use steel as a counterbody to probe the lubricity of the coating using a "poor" lubricant (i.e., simple HEPES buffer).<sup>[21]</sup> With this steel-on-PDMS material combination, one can mimic a hard-on-soft interface as present in several locations of the human body and, accordingly, this particular material combination is commonly used in biotribological studies.<sup>[23]</sup> Moreover, with this set of materials and the rotational tribology setup employed here, we can probe all three lubrication regimes (boundary, mixed, and hydrodynamic lubrication) in detail. To assess the influence of each molecular component used in the double-layer coatings on different lubrication modes, we not only analyze double-layer coatings, but also uncoated (bare) substrates and both, single dopamine and single mucin coatings.

As reported previously,<sup>[10,21]</sup> the tribological properties of a steel-on-PDMS tribo-pairing lubricated with simple buffer are very poor; the very high coefficient of friction (COF)  $\mu$  we measure here in the boundary lubrication and mixed lubrication regime (Figure 2a) underscores this. In part, this bad tribological performance is due to the inability of hydrophobic PDMS to interact well with a water-based lubricant. As demonstrated by the contact angle measurements shown in Figure 1b, a dopamine coating renders a hydrophobic PDMS hydrophilic. Yet, this improvement in PDMS wettability alone is not very efficient in reducing friction: here, only the threshold between mixed lubrication and hydrodynamic lubrication is slightly shifted (Figure 2a). This effect is somewhat stronger for the single mucin coating; however, also here, friction in the boundary lubrication regime is still very high. Only for the double-layer coatings, the COF measured in the boundary lubrication is lowered significantly: here,  $\mu$  is reduced by about one order of magnitude, and this represents decent lubricity suitable for biomedical applications.

In addition to the COF, we also evaluate wear formation on coated and uncoated PDMS. Considering the low wear rate of PDMS in short-time tribological tests, we here use the sensitive 3D surface roughness parameter,  $S_q$ , to compare the post-test surface to untreated samples and to quantify any occurring surface damage.<sup>[10,24]</sup> As displayed in Figure 2b, an uncoated PDMS sample exhibits an ultra-low  $S_q$  value before exposure to tribological stress, and this low  $S_q$  value indicates a very smooth surface texture. After coating with any of the biomolecules tested here,

this roughness parameter is increased by approximately one order of magnitude. With this increased surface roughness, one could expect that the coated surfaces are more prone to wear formation than the uncoated PDMS samples. However, we observe the opposite behavior: Without a protective coating, the  $S_q$  value of a PDMS surface is increased by a factor of  $\approx 10$ , which indeed indicates wear formation; in contrast, with any of the tested coatings, such a pronounced increase in the sample roughness does not occur after tribological treatment.

In a next step, we ask if the dopamine/mucin coatings remain functional after a mechanical challenge. For this purpose, we conduct tribological tests with dopamine/mucin coatings using a higher (but constant) sliding velocity of  $12 \text{ mm s}^{-1}$  and an extended exposure time to tribo-stress of 1 h.<sup>[25]</sup> Interestingly, with this set of parameters, we obtain a nearly constant COF over time (Figure 2c), and the measured value of  $\mu < 0.01$  agrees very well with the results shown in Figure 2a. This indicates that, although the detailed binding mechanism of dopamine to different materials is not fully understood, the stability of the double-layer coatings is very good. Of course, when applied to a medical device inserted into the human body, the dopamine/mucin double-layer will also be challenged by continuous contact with liquid, and this might induce hydrolysis of the biomolecule coating. Thus, we mimic this physiological challenge by incubating a sample set coated with a dopamine/mucin double-layer in a DPBS solution (pH 7.4) for 7 days at RT and comparing the tribological performance of this incubated sample set to samples carrying freshly prepared double-layer coatings. Importantly, both the freshly prepared and the incubated sample set show virtually identical lubricity (Figure 2c,d) in speed-dependent and in time-dependent friction tests. This result is underscored by light microscopy experiments where similar amounts of fluorescently labeled mucins are detected after different incubation times in the DPBS solution (Figure S1, Supporting Information).

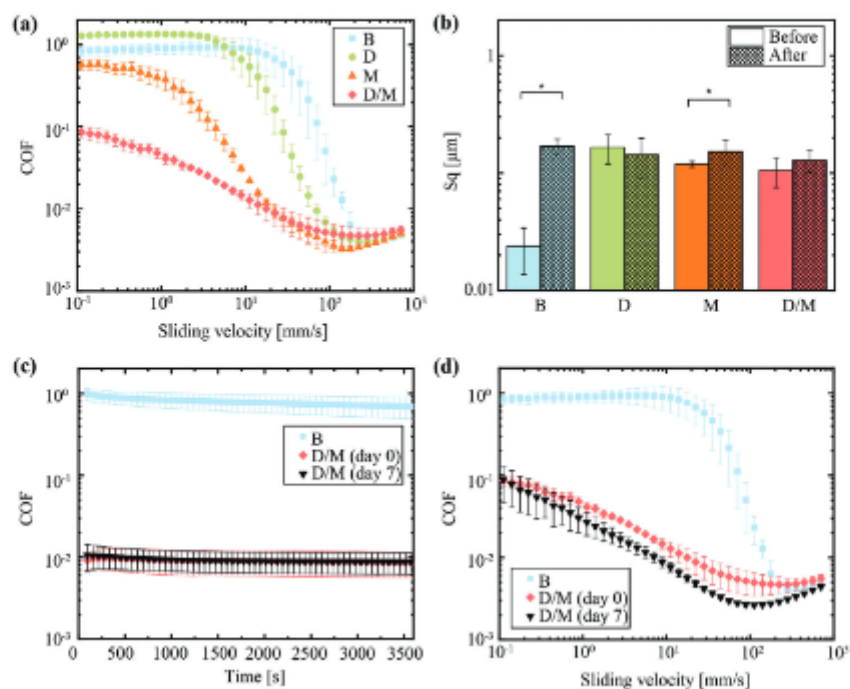
Together, these experiments allow us to conclude that the dopamine-assisted immobilization of mucin on PDMS creates a double-layer that reduces both, friction and wear, and is stable toward mechanical challenge and storage in aqueous environments.

## 2.3. Dopamine/Mucin Coatings Prevent Surface Colonization by Eukaryotic Cells

A key property of dopamine we use here is its ability to create a sticky layer on a substrate, and we can generate dopamine pre-coatings on different inorganic materials, which are typically used in biomedical engineering. However, a sticky surface on medical devices can promote surface colonization with cells which, in turn, can induce thrombus formations and inflammatory responses.<sup>[26]</sup> Mucin coatings generated by simple passive

---

step, the samples were dipped into a 0.1% w/v mucin solution for  $\approx 1$  h, and then thoroughly rinsed again with Millipore water. b) Changes in frequency shift ( $\Delta f$ ) are shown as they occur after sequential exposure of the sensor chips to a dopamine solution followed by rinsing with a mucin solution. The results denote the average as obtained from  $n = 2$  independent measurements. c) Contact angle measurements were conducted on PDMS, PTFE, and steel surfaces. Samples were characterized in their bare state (B) as well as when carrying either a dopamine (D), mucin (M), or dopamine/mucin (D/M) coatings. The error bars denote the standard deviation as obtained from  $n = 6$  independent measurements. Asterisks (\*) indicate statistical significance using a  $p$  value of 0.05. d) Representative AFM images and cross-sectional profiles of mica substrates in their bare state (B) and when carrying a dopamine (D) or dopamine/mucin (D/M) coatings. The black lines in the AFM images denote the location where the cross-sectional profiles have been determined.



**Figure 2.** Tribological properties of dopamine/mucin coatings generated on PDMS. All data shown in this figure was obtained on a steel (ball)-on-PDMS (pins) material pairing using a 20 mM HEPES buffer (pH 7) as a lubricant. a) Stribeck curves as obtained for bare (B) PDMS samples or samples carrying a dopamine (D), mucin (M), or dopamine/mucin (D/M) coatings. b) Surface roughness ( $S_q$ ) of PMDS surfaces carrying different coatings. Values obtained before and after a speed-dependent tribological test are compared. Asterisks (\*) indicate statistically significant differences based on a  $p$  value of 0.05. c) Friction response of bare (B) and dopamine/mucin (D/M) coated samples at a constant sliding velocity of  $12 \text{ mm s}^{-1}$  and d) as a function of the sliding speed. For coated samples, results obtained with freshly prepared (day 0) and stored samples (day 7) are compared. All error bars denote the standard deviation as obtained from  $n = 3$  independent measurements.

adsorption have already been shown to reduce this biofouling problem, but they are not stable enough to provide this property in an application where they are exposed to shear forces. Thus, in a next step, we ask if our stable dopamine/mucin double-layer coatings exhibit suitable anti-biofouling properties.

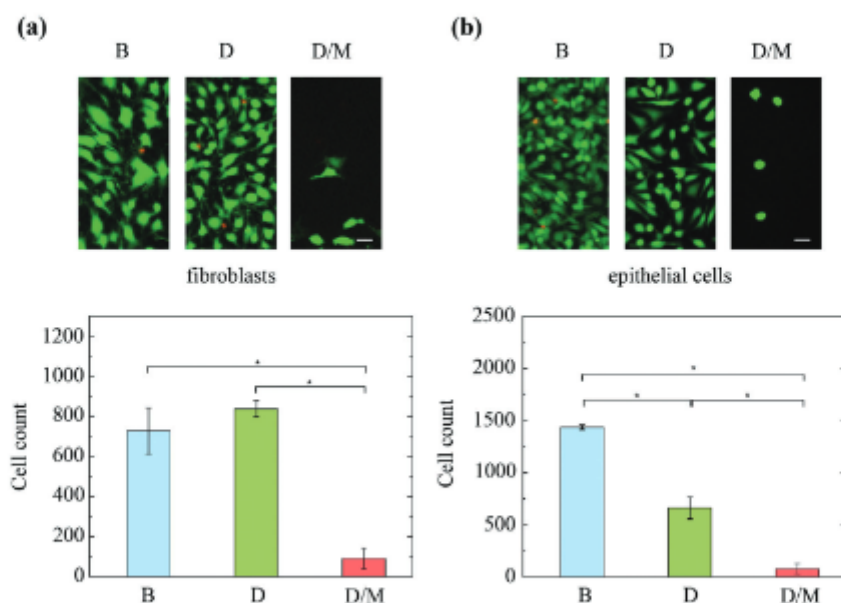
Yet, before we generate the coating on real medical devices, pilot experiments are conducted on a cell-binding surface of a 96 microtiter well plate. With this model surface, we test for putative cytotoxic effects in the presence and absence of the dopamine/mucin coating; we conduct incubation tests with two eukaryotic cell types to ensure that the double-layer coatings we generate indeed provide anti-adhesive properties and reduce unwanted cell colonization (see Section 4 for details). We assess the cell-repellent properties of the dopamine/mucin double-layer by comparing the colonization of commercial tissue culture substrates by fibroblasts (Figure 3a) and epithelial cells (Figure 3b). Indeed, as expected, we find that the double-layer coatings reduce cellular attachment by  $\approx 90\%$  for fibroblasts and by  $\approx 95\%$  for epithelial cells. In addition, fluorescence images obtained for both cell lines show an altered morphology for the samples carrying the double-layer coatings: here, we find mostly cells with round shapes indicating weak adhesion; in contrast, on the uncoated samples, both cell types assume a well-spread, extended morphology as typical for strongly adherent cells. Results from a

viability staining verify that dopamine/mucin-layer is indeed only cell-repellent, but not cytotoxic (Figure S2, Supporting Information). Importantly, on control samples carrying a dopamine coating only, we find a similarly high number of fibroblast cells as on the uncoated samples, and somewhat reduced but still high numbers of epithelial cells. Together with the results obtained from the friction tests discussed above (see Section 2.2.), this shows that a dopamine coating alone is not suitable for an application on medical devices. Thus, further experiments are only conducted with the dopamine/mucin double-layers.

#### 2.4. Dopamine/Mucin Coatings Reduce Wear at High Contact Pressure

So far, we have analyzed the tribological properties of dopamine/mucin coatings on PDMS, a material which is rather resistant to wear formation. In a next step, we ask if dopamine/mucin coatings can also provide wear protection on more sensitive materials and at higher contact pressures. Thus, we next test the wear protection abilities of dopamine/mucin coatings on PTFE, a material that is highly prone to wear damage<sup>[27]</sup>—especially when probed with a hard counter material such as the steel sphere we use here. Since PTFE itself





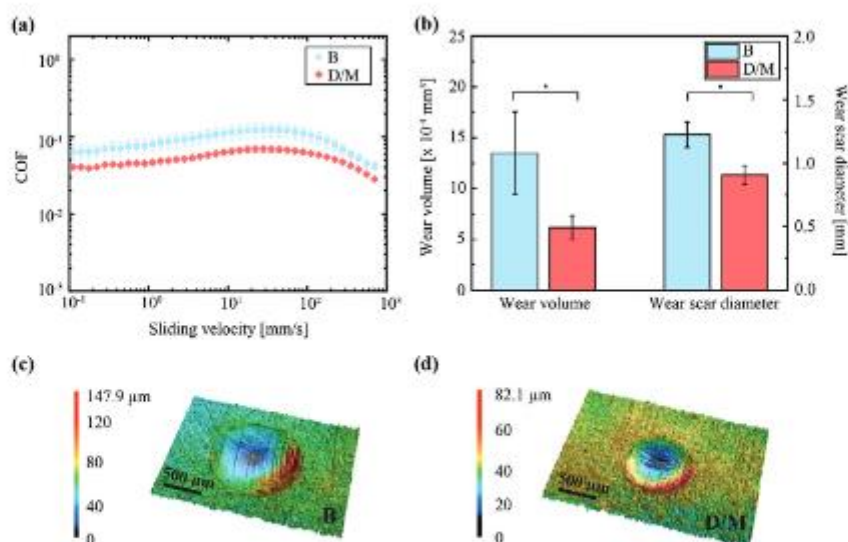
**Figure 3.** Cellular colonization of dopamine and dopamine/mucin coated surfaces. The attachment of a) fibroblasts and b) epithelial cells onto a cell-binding surface without any coating (B, control) as well as with a dopamine (D) and dopamine/mucin (D/M) coatings is compared. The scale bar represents 50  $\mu\text{m}$  and applies to all six images. The error bars represent the standard error of the mean as obtained from analytical triplicates. Asterisks (\*) indicate statistically significant differences based on a  $p$  value of 0.05.

acts as a solid lubricant,<sup>[28]</sup> the COFs obtained with this material pairing (Figure 4a) are lower than the ones obtained on PDMS. Interestingly, also on this substrate, the dopamine/mucin coatings improve the lubricity—albeit only slightly. After tribological testing, we evaluate the material surface using a 3D laser scanning microscope. Representative images of the obtained 3D topographies of both, bare and coated PTFE surfaces, are shown in Figure 4c,d: In both cases, there are some plowing grooves in the center of the wear feature and material pile-up at the edge. This indicates that severe abrasion and plastic deformation occurs during the tribological treatment.<sup>[29]</sup> However, as summarized in Figure 4b, a quantification of those similar images shows that the wear volume of dopamine/mucin coated PTFE samples is reduced by half compared to the uncoated samples. Consistently, also the diameter of the wear scar is reduced by the coating.

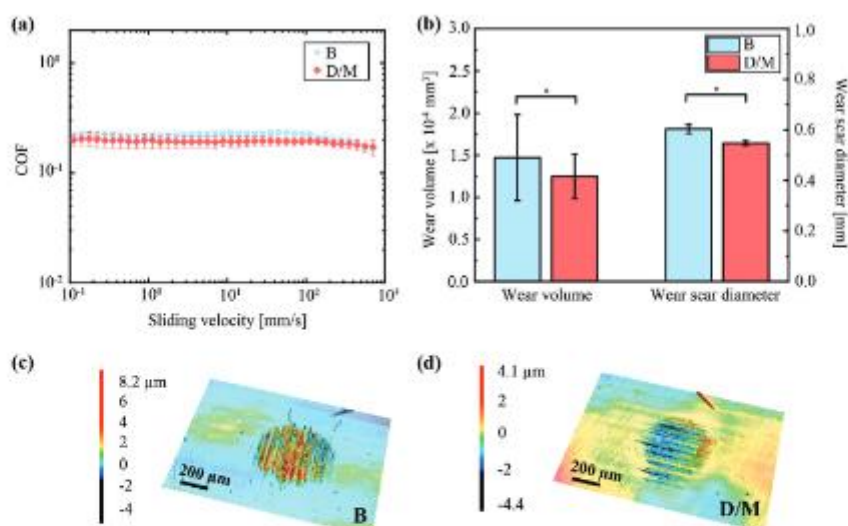
We rationalize this result as follows: First, with the assistance of dopamine, the mucin coating strongly decreases the contact angle of PTFE, shifting its surface properties from hydrophobic to hydrophilic thus improving its interaction with an aqueous lubricant. Moreover, the surface-bound layer of mucin molecules will provide hydration lubrication thus slightly reducing the COF even in the boundary lubrication regime. Furthermore, the macromolecular coating on the PTFE surface will also play a role in supporting/redistributing the applied load, restrict the removal of PTFE material from the surface and therefore protect the surface from severe wear damage.

Importantly, with this steel-on-PTFE material pairing and the measuring parameters chosen here, the resulting contact pressure (according to Hertzian theory) is  $\approx 23$  MPa. This is a simi-

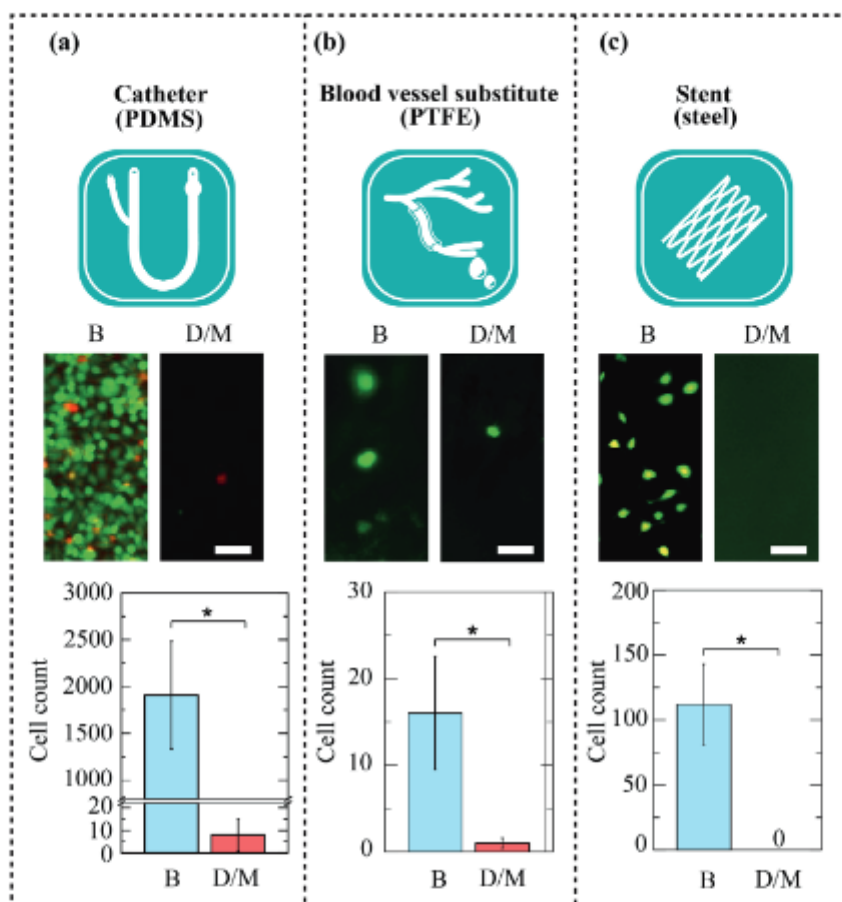
larly high level as what artificial joint prostheses experience under physiological load.<sup>[30]</sup> Thus, the dopamine/mucin coatings might even be able to reduce friction and wear formation in artificial joints. We test this idea by exploring another material combination, that is, coated steel probed with a polyetheretherketone (PEEK) counter body. This choice is motivated by three aspects: first, steel is a material which is widely used in biomedical applications but—compared to hydrophobic polymer materials—only allows for low levels of passive mucin adsorption<sup>[21]</sup>; second, PEEK is often employed as a counter material for biotribological tests<sup>[14,8]</sup>; third, with this particular set of experiments, we aim to mimic highly challenging conditions in the boundary lubrication regime where a high contact pressure is expected to entail asperity-to-asperity contact and thus significant wear formation. In other words, the chances of the coating to provide protective properties are rather low. Indeed, the speed-dependent COFs obtained on bare and coated steel samples are very similar (Figure 5a), and we find clear wear features on both sample variants (Figure 5b,d). The most prominent wear morphology we detected is line-shaped features, which we attribute to abrasive wear caused by local inhomogeneities of the tribo-pairing during every rotation. Overall, owing to the high hardness and elastic modulus of steel, the caused wear volume is approximately an order of magnitude lower than what we found for PTFE surfaces, and the wear diameter is smaller as well. Importantly, when those two wear parameters are compared for coated and uncoated samples, we find a small but significant reduction of both features for the dopamine/mucin coated samples. This result is astonishing given the harsh conditions the material pairing was subjected to. It does, however, underline the great potential the presented



**Figure 4.** Tribological properties of dopamine/mucin coatings generated on PTFE. All data shown in this figure was obtained on a steel (ball)-on-PTFE (pins) material pairing using a 20 mM HEPES buffer (pH 7) as a lubricant. a) Stribeck curves as obtained for bare (B) PTFE samples or samples carrying dopamine/mucin (D/M) coatings. b) Wear volume and wear scar diameter of the PTFE surfaces as calculated after a tribological test. The error bars displayed above denote the standard deviation as obtained from a)  $n = 3$  and b)  $n = 9$  independent measurements, respectively. Asterisks (\*) indicate statistically significant differences based on a  $p$  value of 0.05. c,d) depict example 3D images of a bare PTFE surface c) after tribological measurement as compared to a dopamine/mucin coated PTFE surface d). Please note the different z-scales in c) and d).



**Figure 5.** Tribological properties of dopamine/mucin coatings generated on steel surfaces. All data shown was obtained on a PEEK (ball)-on-steel (pins) material pairing using 20 mM HEPES buffer (pH 7) as a lubricant. a) Stribeck curves as obtained for bare (B) steel samples or samples carrying dopamine/mucin (D/M) coatings. b) Wear volume and wear scar diameter of the steel surfaces as calculated after a tribological test. The error bars displayed above denote the standard deviation as obtained from a)  $n = 3$  and b)  $n = 9$  independent measurements, respectively. Asterisks (\*) indicate statistically significant differences based on a  $p$  value of 0.05. c,d) depict example 3D images of a bare steel surface c) after tribological measurement as compared to a dopamine/mucin coated steel surface d). Please note the different z-scales in c) and d).



**Figure 6.** Epithelial cell colonization of commercial medical devices. The colonization efficiency of HeLa cells seeded onto untreated (B) and dopamine/mucin (D/M) coated catheter a), blood vessel substitute b), and stent c) samples are compared. The scale bar corresponds to 50  $\mu\text{m}$  and applies to all fluorescence images. Error bars represent the standard error of the mean obtained from triplicates, and asterisks denote statistical significance ( $p < 0.05$ ).

dopamine/mucin double-layer holds for protecting an underlying substrate.

### 2.5. Dopamine/Mucin Coatings Establish Cell-Repellent Surfaces on Medical Devices

Having demonstrated that the dopamine/mucin double-layer coatings successfully cover PDMS, steel, and PTFE sample surfaces, provide lubricity and reduce wear formation on all those materials, we now, in a final step, ask if such coatings can also form protective layers on real medical devices made from those materials. The three examples of medical devices we generate our double-layer coatings on are steel-based stents, PDMS-based catheters, and PTFE-based blood vessel substitutes. Since tribology measurements are very difficult to perform with both, highly curved samples such as catheters and fragile objects such as stents, we use cell colonization experiments to assess the func-

tionality of the dopamine/mucin coated device surfaces in comparison to their uncoated counterparts. Indeed, as the three devices we test here can all trigger restenosis *in vivo*, a cell-repellent surface is an important feature for each of them. As a cell line for those experiments, we select epithelial HeLa cells, which are easy to handle and frequently used as model cells in studies characterizing the biocompatibility of both, metallic- and PTFE-based materials.<sup>[31]</sup>

As depicted in Figure 6 and Figure S3, Supporting Information, the three (uncoated) medical devices are colonized by HeLa cells with very different efficiencies: We find the highest density of HeLa cells on the PDMS-based catheter sample and the lowest density on the PTFE-based blood vessel substitute. Indeed, the low number of round cells we detect on blood vessel substitute and stent samples suggests that, here, the cells only weakly interact with the material.<sup>[32]</sup> This could indicate that the manufacturers of the three devices might already have applied some type of surface treatment to reduce the cell-adhesive properties of their

products. Yet, even if such a surface treatment has not been conducted, those findings agree well with previous results from the literature which have reported good cell adhesion on PDMS as well as cell-repellent properties for PTFE.<sup>[12,33]</sup> Anyways, based on the results discussed above (see Section 2.3.), it is possible that a reduction in the cell colonization efficiency can be achieved with our double-layer coatings for all three devices—even for the PTFE-based blood vessel substitute. Indeed, this is what we find: in all three cases, the dopamine/mucin coatings reduce cellular attachment by more than 90%. Together, this shows that all three commercial medical products benefit from our coating and it suggests that the coating could help to reduce adverse reactions such as neointimal proliferation or adhesions. At the same time, it suggests that other anti-biofouling properties reported earlier for passively adsorbed mucin layers or covalent mucin coatings (such as a reduction of bacterial adhesion or protein adsorption) should be provided by the dopamine/mucin coatings as well.<sup>[12,34]</sup> Of course, when applied in a physiological setting, those three devices will encounter site-specific challenges that could affect the functionality of the dopamine/mucin coatings. Thus, it will be a necessary next step in future research to assess the long-term stability and functionality of dopamine/mucin coatings under realistic conditions *in vivo*.

### 3. Conclusion

Inspired by the adhesion of mussels, we here develop dopamine/mucin coatings using a simple two-step dip-coating approach. With this strategy, we introduce an easy and bio-based method to form non-covalent but stable mucin coatings onto both, flat commercial materials and real medical devices alike. Typically, with conventional coating processes, it is very difficult to generate a stable coating on PTFE or steel surfaces.<sup>[35]</sup> With the approach we developed in this study, however, mucin-based coatings are easily possible on PTFE-based blood vessel substitutes and steel-based stents. Our results demonstrate that the dopamine-assisted immobilization of mucin creates a molecular double-layer that decreases friction (especially in the boundary lubrication regime), reduces surface damage, and provides cell-repellent properties. Since dopamine can firmly bind to almost every surface, the double-layer coatings we characterized here have great potential to be applied to other medical devices as well: metal-based artificial heart valves, ceramic-based artificial joints, and polymer-based ocular prostheses, for instance, would benefit from surfaces with low friction, good wear protection, and anti-biofouling properties.

### 4. Experimental Section

**Aqueous Solutions:** HEPES buffer and Tris buffer were prepared by dissolving either 20 mM 4-(2-hydroxyethyl)-1-piperazineethanesulfonic acid (HN78.2, Roth, Karlsruhe, Germany) or 50 mM Tris-(hydroxymethyl)aminomethane (A1379, AppliChem, Darmstadt, Germany) in Millipore water. The final pH values of the HEPES buffer (pH 7.0) and Tris buffer (pH 8.5) solutions used here were adjusted with NaOH or HCl as needed. Solutions containing in-lab purified porcine gastric mucin (see Supporting Information for details of the purification process) were generated at a concentration of 0.1% w/v (=1 mg mL<sup>-1</sup>) in HEPES buffer by incubating lyophilized mucin in HEPES buffer at room temperature

overnight.<sup>[10]</sup> Dopamine hydrochloride (H8502, Sigma, St. Louis, MO, USA) was dissolved at a concentration of 0.4% w/v (=4 mg mL<sup>-1</sup>) in Tris buffer to obtain the polydopamine solution for the coating process described below.<sup>[36]</sup>

**Coating Process:** To investigate the functionality and stability of the dopamine/mucin coatings described here, cylinders made of PDMS, PTFE, or stainless steel were used (see Supporting Information for details). The coatings were prepared by first depositing a dopamine layer on the substrate surface using a dip-coating method (Figure 1a). In detail, the steel, PDMS, or PTFE substrates were immersed into the dopamine solution for ≈2 h and then thoroughly rinsed with Millipore water to remove any unbound dopamine. Afterward, the dopamine pre-coated substrates were placed into the mucin solution, incubated for ≈1 h, and then again thoroughly rinsed with Millipore water. Single dopamine coatings or single mucin coatings were developed for comparison by performing only one incubation step each.

**QCM-D Measurements:** To confirm that the envisioned dopamine/mucin coatings are indeed generated on the substrates tested here, the adsorption behavior of dopamine and mucin on different substrates was studied using a QCM-D with a qcell T-Q2 platform (3T-Analytik, Tuttingen, Germany). For those microscopic adsorption tests, quartz chips with stainless steel, PTFE, and PDMS surfaces were selected (see Supporting Information for details) to ensure comparability to the tests conducted with macroscopic dopamine/mucin coatings. With those different chips, adsorption experiments were conducted as follows: at the beginning of each adsorption test, a pure buffer solution (devoid of dopamine and mucin) was injected at a flow rate of 100 μL min<sup>-1</sup> until a stable baseline was obtained. Then, a dopamine solution was injected at a rate of 100 μL min<sup>-1</sup> for ≈30 min and the change in frequency shift ( $\Delta f$ , Hz) as automatically calculated by the software "qGraph" (3T-Analytik, Tuttingen, Germany) was recorded. After rinsing with a pure buffer solution (flow rate: 1000 μL min<sup>-1</sup>) for ≈2 min, a mucin solution was injected at 100 μL min<sup>-1</sup> for ≈30 min to obtain an adsorption curve.

**Cell Cultivation and Surface Colonization Experiments:** Human epithelial cells (HeLa) were cultured using Minimum Essential Medium Eagle (MEM, M2279, Sigma) supplemented with 10% v/v fetal bovine serum (FBS, F9665, Sigma), a 2 mM L-glutamine solution (Sigma), a 1% v/v non-essential amino acid solution (NEAA, M7145 Sigma), and 1% v/v penicillin/streptomycin (76437, Sigma). Human fibroblast cells (NIH-3T3) were cultured with Dulbecco's Modified Eagle's high glucose Medium (DMEM, D5796, Sigma) supplemented with 10% v/v FBS and 1% v/v penicillin/streptomycin. For both cell types, the environment was adjusted to 37 °C and 5% CO<sub>2</sub> in a humidified atmosphere.

For surface colonization and viability tests, 12 wells of a 96-well plate (M0812-100EA, Sigma) were prepared for each cell type; here, three wells were coated with dopamine and three were coated with dopamine/mucin double-layers as described in Section 2.2. The remaining six wells were left untreated for positive and negative controls. Afterward, all wells were washed three times with sterile Dulbecco's Phosphate Buffered Saline (DPBS, 882104, Sigma). Subsequently, the HeLa and NIH-3T3 cells were seeded into the wells at a concentration of 30 000 cells per well and cultivated in 200 μL medium for 24 h. As a control inducing low cell viability, methanol (MeOH, 4627.1, Roth) was added to a final concentration of 50% v/v 4 h before starting the live/dead analysis. For live/dead staining, the cells were washed with DPBS and 200 μL of DPBS supplemented with 1 μM calcein AM (Invitrogen, Carlsbad, CA, USA) and 2 μM ethidium homodimer 1 (Invitrogen) were added to each well. After 30 min of incubation, fluorescence images of living cells (green color) and dead cells (red color) were recorded using the DMI8 microscope (Leica, Wetzlar, Germany) equipped with a 10x objective (Leica) and a digital camera (Orca Flash 4.0 C11440-22C, Hamamatsu, Japan).

Very similar cell colonization experiments were conducted with HeLa cells seeded onto commercial medical devices: stent (steel, AS-21XXL, Andramed, Reutlingen, Germany), blood vessel substitute (PTFE, Steris, USA), and catheter (PDMS, U400, MediTone Medical, Fellbach, Germany) samples were coated with a dopamine/mucin double-layer. The cell-repellent properties of the dopamine/mucin coatings were assessed with fluorescence microscopy as described above.

**Tribological Tests:** The tribological experiments were performed at 21 °C using the rotational tribology unit (T-PTD 200, Anton Paar, Graz, Austria) of a commercial shear rheometer (MCR 302, Anton Paar) as described before.<sup>[37]</sup> The tribological properties, that is, lubricity and wear resistance, of the coatings were evaluated on different substrates. As counter-parts for these tribological tests, commercial spheres made from either stainless steel (1.4404, Kugel Pompel, Vienna, Austria) or PEEK (Vitrex 450G, Yuwei, Nanjing, China) with a diameter of 12.7 mm were used as received. Further polishing was not necessary as both sphere types showed low roughness (i.e.,  $Sq_{\text{steel}} < 200$  nm,  $Sq_{\text{PEEK}} < 500$  nm) when analyzed with a laser scanning microscope (VK-X1100, Keyence, Osaka, Japan). The lower samples in the tribological measuring configuration carried the coatings were mounted into a sample holder, and coatings were generated in situ. Then, the coated samples were first washed with ultrapure water before 600  $\mu\text{L}$  of a lubricant solution was applied onto the three pions to ensure full coverage with liquid. For measurements, the normal load was chosen to be 6 N. With this load, the average contact pressure can be estimated based on Hertz contact theory with the following equations:

$$p = \frac{2}{3} p_{\text{max}} = \frac{2}{3\pi} \cdot \sqrt[3]{\frac{6 \cdot f_n \cdot \text{per pin} \cdot E^2}{R^2}} \quad (1)$$

$$\frac{1}{E^*} = \frac{1 - \nu_1^2}{E_1} + \frac{1 - \nu_2^2}{E_2} \quad (2)$$

with the Young's moduli and Poisson's ratios displayed in Table S1, Supporting Information. With this approach, an average contact pressure of  $\approx 0.3$  MPa for the steel-on-PDMS pairing,  $\approx 23$  MPa for steel-on-PTFE pairing, and  $\approx 44$  MPa for the PEEK-on-steel pairing was obtained. To explore as many lubrication regimes as possible, the sliding velocity was varied from  $10^{-1}$  to  $10^3$  mm  $\text{s}^{-1}$ . For each condition, three independent experiments were carried out using a fresh set of pins for each measurement.

The durability of the dopamine/mucin coatings were evaluated on PDMS samples as follows: First, dopamine/mucin coated samples were exposed to UV-light for 1 h for sterilization<sup>[21]</sup> and then stored in a commercial DPBS solution (pH 7.4, Lonza, Verviers, Belgium) at room temperature for 7 days. Those storage conditions were chosen to mimic conditions that implanted materials/medical devices experience within the human body. Afterward, the tribological properties were probed using the same tribology unit as above using steel spheres as counter bodies. Here, the sliding velocity was first varied from  $10^{-1}$  to  $10^3$  mm  $\text{s}^{-1}$  and then set to a constant value of 12 mm  $\text{s}^{-1}$  for 1 h.

**Surface Characterization:** The wetting behavior of the coated samples was evaluated by calculating the static contact angle (CA). In brief, a 10  $\mu\text{L}$  drop of Millipore water was pipetted onto the sample surface, and a transversal image of the liquid–solid interface was acquired using a high-resolution camera (Point Gray Research, Richmond, Canada). Then, the CA was determined using the drop-snake analysis tool, a plug-in for the software "ImageJ" (v 1.8.0, NIH, Bethesda, MD, USA). For each condition, at least three independent measurements were carried out.

The surface topography of the samples was investigated using a 3D laser scanning microscope (VK-X1100, Keyence, Osaka, Japan). From the obtained topographical images, the surface roughness,  $Sq$  (root mean square height) was calculated using the software "MultiFile Analyzer" (Keyence, Osaka, Japan). Owing to the ultralow wear rate of PDMS in short-time tribological lab experiments,<sup>[10]</sup> only the wear rates (wear volume and diameter of wear scar) of PTFE and steel samples were evaluated.

The morphological characterization of the samples at the nanoscale was performed using a NanoWizard II atomic force microscope (AFM, JPK Instruments, Berlin, Germany). Samples were probed in air using an OMCL-AC160TS-R3 cantilever (Olympus, Tokyo, Japan). Before imaging, the AFM was allowed to thermally equilibrate for 30 min. A 20  $\mu\text{L}$  drop of the tested sample solution was pipetted onto a freshly cleaved mica slide (dimensions: 1 mm  $\times$  1 mm), incubated for 10 min, then rinsed with Millipore water and finally dried with compressed nitrogen gas. Im-

ages were acquired in tapping mode at room temperature over an area of  $5 \mu\text{m} \times 5 \mu\text{m}$ . From the obtained topographical images, representative cross-sectional profiles were analyzed using the SPM Image Processing software (v.3.3.20, JPK).

**Statistical Analysis:** To evaluate the significant differences between two samples, independent two-sample  $t$ -test was performed.<sup>[12]</sup> Prior to statistical analysis, the normal distribution of the results was verified with the Shapiro–Wilk test, and the homogeneity of variances was measured using the F-test. For non-normal distributed variances, the Wilcoxon–Mann–Whitney-test was used. Student's  $t$ -tests were applied for normal distributed homogenous variances, whereas a Welch's  $t$ -test was performed for unequal variances. The software "Origin" (OriginPro 2020, OriginLab Corp., Northampton, MA, USA) was used to conduct all statistical tests. For  $p$ -values  $< 0.05$ , differences were considered to be statistically significant, and significant differences between tested groups are marked with an asterisk in all graphs.

## Supporting Information

Supporting Information is available from the Wiley Online Library or from the author.

## Acknowledgements

The authors thank Matthias Marczynski for assistance with the mucin purification and Benjamin Winkeljann for help regarding the sample preparation. This project received funding from the European Union's Horizon 2020 research and innovation programme under the Marie Skłodowska-Curie Grant Agreement No 754462.

Open access funding enabled and organized by Projekt DEAL.

## Conflict of Interest

The authors declare no conflict of interest.

## Author Contributions

J.S. and T.M.L. contributed equally to this work. J.S. and O.L. designed the study. J.S. and T.M.L. performed the experiments and analyzed data. N.L. contributed medical materials. All authors contributed to the discussion of the data, wrote the manuscript, and gave approval to the final version of the manuscript.

## Keywords

anti-biofouling, friction, implants, molecular double-layers, wear protection

Received: May 16, 2020

Revised: August 9, 2020

Published online:

- [1] a) C. R. Arciola, D. Campoccia, L. Montanaro, *Nat. Rev. Microbiol.* **2018**, *16*, 397; b) J. Song, Z. Liao, H. Shi, D. Xiang, Y. Liu, W. Liu, Z. Peng, *Tribol. Lett.* **2017**, *65*, 150; c) A. J. T. Teo, A. Mishra, I. Park, Y.-J. Kim, W.-T. Park, Y.-J. Yoon, *ACS Biomater. Sci. Eng.* **2016**, *2*, 454; d) S. M. Kurtz, J. N. Devine, *Biomaterials* **2007**, *28*, 4845; e) A. Girotti, D. Orbanic, A. Ibáñez-Fonseca, C. Gonzalez-Obeso, J. C. Rodríguez-Cabello, *Adv. Healthcare Mater.* **2015**, *4*, 2423.

- [2] A. M. Hussein, S. A. Mohammed, N. Al-Aqeeli, *Materials* **2015**, *8*, 2749.
- [3] a) J. L. Harding, M. M. Reynolds, *Trends Biotechnol.* **2014**, *32*, 140; b) B. Cao, Q. Tang, L. Li, J. Humble, H. Wu, L. Liu, G. Cheng, *Adv. Healthcare Mater.* **2013**, *2*, 1096.
- [4] a) R. A. Byrne, M. Joner, F. Alfonso, A. Kastrati, *Nat. Rev. Cardiol.* **2014**, *11*, 13; b) P. Roy-Chaudhury, B. S. Kelly, M. A. Miller, A. Reaves, J. Armstrong, N. Nanayakkara, S. C. Heffelfinger, *Kidney Int.* **2001**, *59*, 2325.
- [5] D. Buccheri, D. Piraino, G. Andolina, B. Cortese, *J. Thorac. Dis.* **2016**, *8*, E1150.
- [6] C. P. McCoy, N. J. Irwin, L. Donnelly, D. S. Jones, J. G. Hardy, L. Carson, *Int. J. Pharm.* **2018**, *535*, 420.
- [7] M. T. Barford Jessica, Y. Hu, K. Anson, R. M. Coates Anthony, *J. Urol.* **2008**, *180*, 1522.
- [8] J. Song, Y. Liu, Z. Liao, S. Wang, R. Tyagi, W. Liu, *Mater. Sci. Eng., C* **2016**, *69*, 985.
- [9] V. Yesilyurt, O. Veishe, J. C. Doloff, J. Li, S. Bose, X. Xie, A. R. Bader, M. Chen, M. J. Webber, A. J. Vegas, R. Langer, D. G. Anderson, *Adv. Healthcare Mater.* **2017**, *6*, 1601091.
- [10] a) J. M. Coles, D. P. Chang, S. Zauscher, *Curr. Opin. Colloid Interface Sci.* **2010**, *15*, 406; b) O. Svensson, T. Arnebrant, *Curr. Opin. Colloid Interface Sci.* **2010**, *15*, 395; c) B. Winkeljann, K. Boettcher, B. N. Balzer, O. Lieleg, *Adv. Mater. Interfaces* **2017**, *4*, 1700186; d) T. Sandberg, M. Karlsson Ott, J. Carlsson, A. Feiler, K. D. Caldwell, *J. Biomed. Mater. Res., Part A* **2009**, *91A*, 773; e) N. Nikogeorgos, P. Efler, A. B. Kayimazer, S. Lee, *Soft Matter* **2015**, *11*, 489; f) B. Winkeljann, P.-M. A. Leipold, O. Lieleg, *Adv. Mater. Interfaces* **2019**, *6*, 1900366; g) S. K. Linden, P. Sutton, N. G. Karlsson, V. Korolik, M. A. McGuckin, *Mucosal Immunol.* **2008**, *1*, 183.
- [11] a) R. R. Janairo, Y. Zhu, T. Chen, S. Li, *Tissue Eng., Part A* **2013**, *20*, 285; b) I. A. Bushnak, F. H. Labeed, R. P. Sear, J. L. Keddie, *Biofouling* **2010**, *26*, 387.
- [12] B. Winkeljann, M. G. Bauer, M. Marczynski, T. Rauh, S. A. Sieber, O. Lieleg, *Adv. Mater. Interfaces* **2020**, *7*, 1902069.
- [13] a) E. Faure, P. Lecomte, S. Lenoir, C. Vreuls, C. Van De Weerd, C. Archambeau, J. Marcial, C. Jérôme, A.-S. Duwez, C. Decrembleur, *J. Mater. Chem.* **2011**, *21*, 7901; b) S. Kruss, T. Wolfram, R. Martin, S. Neubauer, H. Kessler, J. P. Spatz, *Adv. Mater.* **2010**, *22*, 5499.
- [14] H. Lee, S. M. Dellatore, W. M. Miller, P. B. Messersmith, *Science* **2007**, *318*, 426.
- [15] W.-Z. Qiu, H.-C. Yang, Z.-K. Xu, *Adv. Colloid Interface Sci.* **2018**, *256*, 111.
- [16] Y. Liu, C.-P. Chang, T. Sun, *Langmuir* **2014**, *30*, 3118.
- [17] Y. Zhang, B. Thingholm, K. N. Goldie, B. Ogaki, B. Stadler, *Langmuir* **2012**, *28*, 17585.
- [18] Q. Fu, X. Li, Q. Zhang, F. Yang, W. Wei, Z. Xia, *J. Chromatogr. A* **2015**, *1416*, 94.
- [19] R. Huang, X. Liu, H. Ye, R. Su, W. Qi, L. Wang, Z. He, *Langmuir* **2015**, *31*, 12061.
- [20] a) N. S. Manam, W. S. W. Harun, D. N. A. Shri, S. A. C. Ghani, T. Kurniawan, M. H. Ismail, M. H. I. Ibrahim, *J. Alloys Compd.* **2017**, *701*, 698; b) M. M. M. Bilek, *Appl. Surf. Sci.* **2014**, *310*, 3; c) C. Diaz Blanco, A. Orner, R. Dimitrov, A. Navarro, E. Mendoza, T. Tzanov, *ACS Appl. Mater. Interfaces* **2014**, *6*, 11385; d) C. Kimna, B. Winkeljann, J. Song, O. Lieleg, *Adv. Mater. Interfaces* **2020**, 202000735, unpublished, <https://doi.org/10.1002/admi.202000735>.
- [21] J. Song, B. Winkeljann, O. Lieleg, *ACS Appl. Bio Mater.* **2019**, *2*, 3448.
- [22] M. Marczynski, B. N. Balzer, K. Jiang, T. M. Lutz, T. Crouzier, O. Lieleg, *Colloids Surf., B* **2020**, *187*, 110614.
- [23] A. Sarkar, E. M. Krop, *Curr. Opin. Food Sci.* **2019**, *27*, 64.
- [24] K. Boettcher, B. Winkeljann, T. A. Schmidt, O. Lieleg, *Bioribology* **2017**, *12*, 43.
- [25] J. Song, Z. Liao, S. Wang, Y. Liu, W. Liu, R. Tyagi, *J. Mater. Eng. Perform.* **2016**, *25*, 116.
- [26] T. Goda, T. Konno, M. Takai, K. Ishihara, *Colloids Surf., B* **2007**, *54*, 67.
- [27] S. Affatato, A. Ruggiero, M. Merola, *Composites, Part B* **2015**, *83*, 276.
- [28] T. W. Scharf, S. V. Prasad, *J. Mater. Sci.* **2013**, *48*, 511.
- [29] J. Song, H. Shi, Z. Liao, S. Wang, Y. Liu, W. Liu, Z. Peng, *Polymers* **2018**, *10*, 142.
- [30] G. Lewis, *Bio-Med. Mater. Eng.* **1998**, *8*, 91.
- [31] a) K. C. Chaw, M. Manimaran, F. E. H. Tay, S. Swaminathan, *Microwav. Res.* **2006**, *72*, 153; b) B. Joddar, A. Albayrak, J. Kang, M. Nishihara, H. Abe, Y. Ito, *Acta Biomater.* **2013**, *9*, 6753.
- [32] T. Crouzier, H. Jang, J. Ahn, R. Stocker, K. Ribbeck, *Biomacromolecules* **2013**, *14*, 3010.
- [33] a) B. J. Klenkler, D. Dwivedi, J. A. West-Mays, H. Sheardown, *J. Biomed. Mater. Res., Part A* **2010**, *93A*, 1043; b) R. Sipehia, G. Martucci, M. Barbarosie, C. Wu, *Biomater., Artif. Cells, Immobilization Biotechnol.* **1993**, *21*, 455; c) M. Crombez, P. Chevallier, R. C. Gaudreault, E. Petitclerc, D. Mantovani, G. Laroche, *Biomaterials* **2005**, *26*, 7402.
- [34] G. Petrou, T. Crouzier, *Biomater. Sci.* **2018**, *6*, 2282.
- [35] J. Song, B. Winkeljann, O. Lieleg, *Adv. Mater. Interfaces* **2020**, 2000850, unpublished, <https://doi.org/10.1002/admi.202000850>
- [36] a) S. Kasemset, A. Lee, D. J. Miller, B. D. Freeman, M. M. Sharma, *J. Membr. Sci.* **2013**, *425–426*, 208; b) F. Ponzio, P. Payamyar, A. Schneider, M. Winterhalter, J. Bour, F. Addiego, M.-P. Krafft, J. Hemmerle, V. Ball, *J. Phys. Chem. Lett.* **2014**, *5*, 3436.
- [37] K. Boettcher, S. Grumbain, U. Winkler, J. Nachtsheim, O. Lieleg, *Rev. Sci. Instrum.* **2014**, *85*, 093903.

### **B.3.1 Supplementary information for: Bioinspired dopamine/mucin coatings provide lubricity, wear protection, and cell-repellent properties for medical applications**

© 2020 Wiley-VCH GmbH

**ADVANCED  
HEALTHCARE  
MATERIALS**

#### **Supporting Information**

*for Adv. Healthcare Mater.*, DOI: 10.1002/adhm.202000831

**Bioinspired Dopamine/Mucin Coatings Provide Lubricity,  
Wear Protection, and Cell-Repellent Properties for Medical  
Applications**

Jian Song, Theresa M. Lutz, Nora Lang, and Oliver Lieleg\*

Supporting Information

**Bioinspired Dopamine/Mucin Coatings Provide Lubricity, Wear Protection and Cell-Repellent Properties for Medical Applications**

*Jian Song, Theresa M. Lutz, Nora Lang, Oliver Lieleg\**

Dr. J. Song, T. M. Lutz, Prof. O. Lieleg  
Department of Mechanical Engineering and Munich School of Bioengineering,  
Technical University of Munich, Garching 85748, Germany.  
E-mail: oliver.lieleg@tum.de

Dr. N. Lang  
Department of Paediatric Cardiology and Congenital Heart Disease, German Heart Centre,  
Munich 80636, Germany.



## 1. Mucin Purification

Mucin purification was conducted as described previously.<sup>[1]</sup> In short, food debris in fresh porcine stomachs was washed off with tap water. Afterwards, crude mucus was obtained by manually scraping the surface of the gastric tissue with spoons. The collected mucus was then pooled, diluted 5-fold in PBS buffer (10 mM, pH = 7.4) and stirred overnight for solubilization. Lipid contaminants and cellular debris were removed from this homogenized mucus via two centrifugation steps (first at 8300 x *g* and 4 °C for 30 min; second at 15000 x *g* and 4 °C for 45 min) and a final ultracentrifugation step (150000 x *g* at 4 °C for 1 h). Then, the mucin glycoproteins were separated from other molecules by size exclusion chromatography using an ÄKTA purifier system (GE Healthcare, Chicago, IL, USA) and an XK50/100 column packed with Sepharose 6FF. Subsequently, the mucin fractions were pooled, dialyzed against ultrapure water, and concentrated by cross-flow filtration. Finally, the concentrated mucins were lyophilized and stored at -80 °C before further use.

## 2. Substrate Preparation

PTFE and steel pins (1.4404) were manufactured in an internal workshop from commercially available bars; PDMS pins were produced manually: In brief, PDMS prepolymer and cross-linker (Sylgard 184, Dow Corning, Midland, MI, USA) were mixed in a ratio of 10:1. Then, the mixture was placed into a vacuum chamber for 1 hour to remove air bubbles. Afterwards, the solution was poured into a steel mold and cured at 80 °C for 4 h. All cylindrical substrates were cleaned in an ultrasonic bath using a 70 % (v/v) ethanol (Roth) solution prior to coating.

The mechanical properties of the three materials used as substrates in this study are compiled in **Table S1**:

**Table S1.** Young's moduli and Poisson's ratios of the materials used in this study.

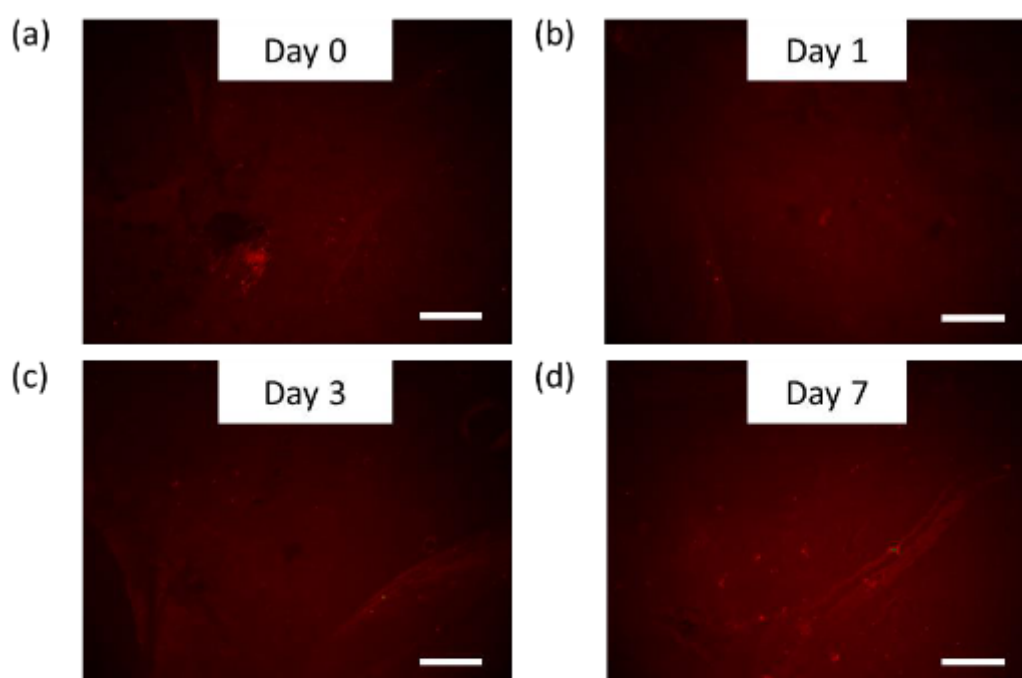
	Steel <sup>[2]</sup>	PTFE <sup>[3]</sup>	PDMS <sup>[4]</sup>	PEEK <sup>[5]</sup>
Young's modulus	210 GPa	1.5 GPa	2 MPa	3.6 GPa
Poisson's ratio	0.30	0.41	0.49	0.388

### 3. Preparation of Coated Chips for QCM-D

QCM-D-chips with steel (1.4404) or gold surfaces were obtained from 3T-Analytik. To generate chips with a thin PDMS layer, gold sensor QCM-D-chips were coated with a thin PDMS film as follows: First, the PDMS prepolymer and cross-linker were mixed in a ratio of 10:1. Next, the mixture was diluted in *n*-hexane to obtain a 1 % (v/v) polymer solution. Afterwards, a bare gold sensor chip was placed into the center of a spin coating device (WS-400B-6NPP/LITE, Laurell, North Wales, USA), and 100  $\mu$ L of the prepared PDMS-*n*-hexane mixture was pipetted onto the gold chip. Then, the spin coater was set into rotation – first at 1500 rpm for 20 s and then at 3000 rpm for 60 s. The PDMS-coated chips were cured at 80 °C for 4 h. PTFE coated QCM-D-Chips were produced in a very similar way, but using a commercial PTFE spray (72247, Nigrin, MTS Group, Rülzheim, Germany) instead of a PDMS solution.

#### 4. Stability of Dopamine/Mucin Coatings after Storage

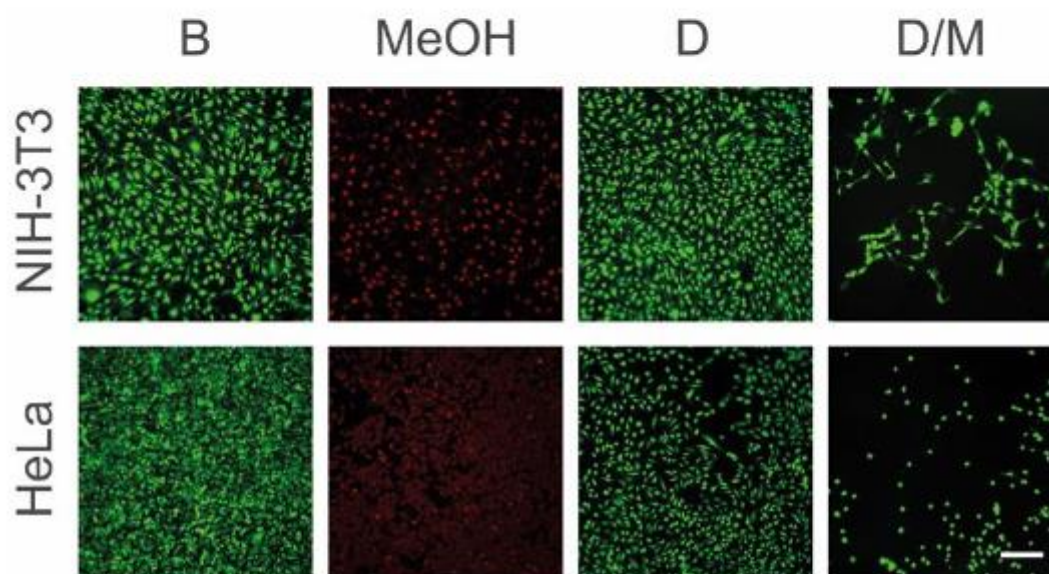
The stability of dopamine/mucin coatings was evaluated using PDMS samples as substrates. First, the mucin was labeled with the dye ATTO 594 (ATTO-TEC, Siegen, Germany) as described previously <sup>[1b]</sup>. Then, the PDMS samples were coated with dopamine/mucin and incubated in a commercial Dulbecco's phosphate buffered saline (DPBS; pH 7.4, Lonza, Verviers, Belgium) solution in the dark at room temperature for 0, 1, 3, and 7 days, respectively. Afterwards, fluorescence images (**Figure S1**) were obtained with on Axioskop 2 MAT mot microscope (Zeiss, Oberkochen, Germany) equipped with a 5x objective (Zeiss) using a digital camera (Orca-R2 C10600, Hamamatsu, Japan) and the image acquisition software HCLImageLive (Hamamatsu).



**Figure S1.** Fluorescence images of dopamine/mucin coatings generated on PDMS samples after different storage times. At all time points investigated (a-d), the fluorescence images show a continuous mucin layer on the PDMS samples. The scale bar corresponds to 1 mm and applies to all images.

### 5. Cellular Colonization Tests on Dopamine and Dopamine/Mucin Coated Surfaces

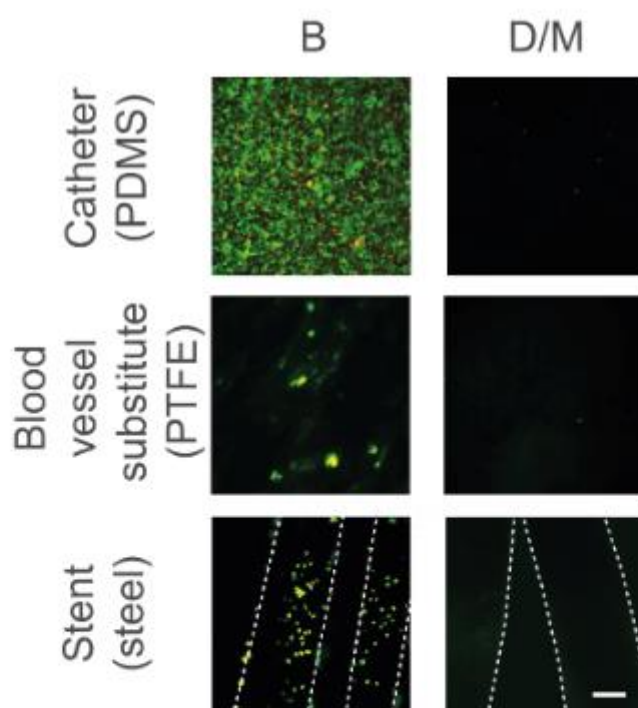
The images shown below (Figure S2) represent a larger view of the microscopy images obtained for the cell adhesion and colonization experiments described in Figure 3 of the main text.



**Figure S2.** Cellular colonization of dopamine and dopamine/mucin coated surfaces. The attachment of fibroblasts (NIH-3T3) and epithelial cells (HeLa) onto a cell-binding surface without any coating (B) as well as with a dopamine (D) and dopamine/mucin (D/M) coating is compared. A cell-binding surface without any coating but incubate with methanol (MeOH) is used as control representing conditions that induce low cell viability. The scale bar corresponds to 50  $\mu\text{m}$  and applies to all images.

## 6. Cellular Colonization Tests on Biomedical Devices

**Figure S3** depicts cell attachment experiments conducted with HeLa cells as described in **Figure 6** in the main text. The images shown here demonstrate that, if uncoated, the whole surface of the PDMS-based catheter is covered with epithelial cells. In comparison, the dopamine/mucin coated catheter surface shows hardly any cell attachment. For stent and PTFE samples, this difference between coated and uncoated samples is less pronounced; most likely, this indicates that the commercial devices already come with an anti-adhesive surface coating. However, also for those samples, the cell-repellant behaviour is noticeably increased by the dopamine/mucin double-layer coatings: in the presence of the double-layer coatings, there are virtually no attached cells visible for the metallic (steel-based) stent sample, and the blood vessel substitute (made from PTFE) shows only very few local cell attachment events.



**Figure S3.** *Epithelial cell colonization of commercial biomedical devices.* Fluorescence images of HeLa cells seeded onto untreated (B) and dopamine/mucin (D/M) coated catheter, blood vessel substitute, and stent samples are compared. For the stent sample, the outline of the metallic parts are indicated by the white dashed lines. The scale bar corresponds to 50  $\mu\text{m}$  and applies to all images.

**7. Cited Literature**

- [1] a) J. Celli, B. Gregor, B. Turner, N. H. Afdhal, R. Bansil, S. Erramilli, *Biomacromolecules* **2005**, *6*, 1329; b) V. J. Schömig, B. T. Käs Dorf, C. Scholz, K. Bidmon, O. Lieleg, S. Berensmeier, *RSC Advances* **2016**, *6*, 44932.
- [2] A. Nayebi, R. El Abdi, O. Bartier, G. Mauvoisin, *Mechanics of Materials* **2002**, *34*, 243.
- [3] P. J. Rae, D. M. Dattelbaum, *Polymer* **2004**, *45*, 7615.
- [4] I. D. Johnston, D. K. McCluskey, C. K. L. Tan, M. C. Tracey, *Journal of Micromechanics and Microengineering* **2014**, *24*, 035017.
- [5] J. Song, D. Xiang, S. Wang, Z. Liao, J. Lu, Y. Liu, W. Liu, Z. Peng, *Tribology International* **2018**, *122*, 218.

## B.4 DNA strands trigger the intracellular release of drugs from mucin-based nanocarriers

# DNA Strands Trigger the Intracellular Release of Drugs from Mucin-Based Nanocarriers

Ceren Kimna, Theresa Monika Lutz, Hongji Yan, Jian Song, Thomas Crouzier, and Oliver Lieleg\*

Cite This: *ACS Nano* 2021, 15, 2350–2362

Read Online

ACCESS |

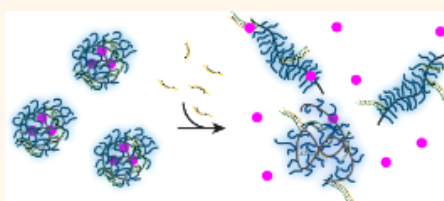
Metrics & More

Article Recommendations

Supporting Information

**ABSTRACT:** Gaining control over the delivery of therapeutics to a specific disease site is still very challenging. However, especially when cytotoxic drugs such as chemotherapeutics are used, the importance of a control mechanism that can differentiate “sick” target cells from the surrounding healthy tissue is pivotal. Here, we designed a nanoparticle-based drug delivery process, which releases an active agent only in the presence of a specific trigger DNA sequence. With this strategy, we are able to initiate the release of therapeutics into the cytosol with high efficiency. Furthermore, we demonstrate how an endogenous marker (e.g., a specific miRNA sequence) that is overexpressed in the initial phases of certain cancer types can be used as a stimulus to autonomously initiate intracellular drug release—and only in cells where this pathophysiological marker is present. We expect that this precisely controlled delivery mechanism can facilitate the design of site-specific treatments for such diseases, where an overexpression of signature oligonucleotide sequences has been identified.

**KEYWORDS:** antibiotics, doxorubicin, drug delivery, nanoparticles, DNA nanotechnology



The COVID-19 pandemic reminds us that treating intracellular infections can be quite difficult. This situation applies not only to viral infections but also to those induced by certain bacteria such as *Listeria monocytogenes* or *Pseudomonas aeruginosa* (which mainly target macrophages and epithelial cells).<sup>1,2</sup> In all of those cases, the pathogens hide inside the host cells, where they are protected from drugs applied via systemic routes. For similar reasons, cancer therapy is problematic, as well. Also here, a drug needs to reach the cell cytosol and accumulate there to take effect, and several barriers need to be overcome by a drug delivery vehicle to achieve this. Moreover, in all of those cases, typical drug administration approaches to deliver the pharmaceutical to both healthy and diseased cells alike, and this is the main reason for the occurrence of unwanted side effects.<sup>3</sup>

Smart delivery mechanisms have been proposed as a strategy to overcome these problems. They aim at initiating drug release only in response to pathophysiological stimuli by making use of biochemical irregularities specifically found in the diseased region.<sup>4</sup> To achieve this goal, complex strategies were developed that employ changes in intracellular pH,<sup>5,6</sup> enzyme levels,<sup>7,8</sup> or redox conditions<sup>9,10</sup> as release triggers. Of course, the main challenge all of those approaches have to deal with is identifying a suitable trigger that satisfies two demands: first, it needs to be highly specific for the particular disease (to ensure that healthy cells remain unaffected); second, it has to

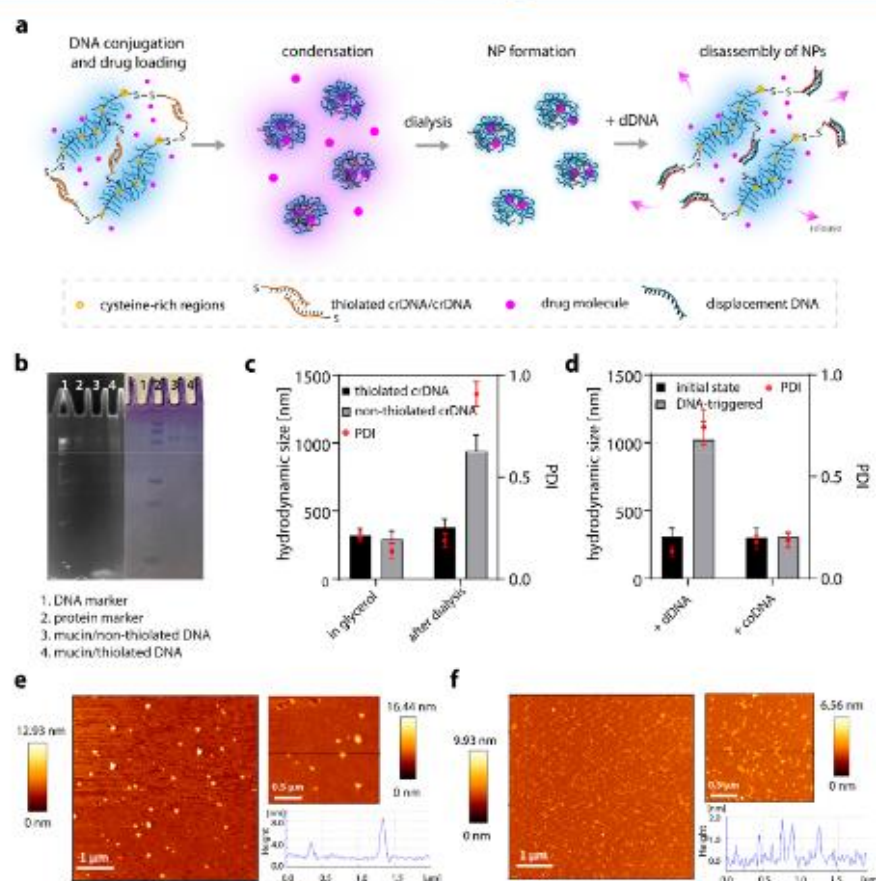
guarantee the delivery of sufficiently high drug doses to the target cells so that therapeutic drug levels are obtained.

In the human body, DNA is a molecule that binds to its partners with extremely high specificity. Consequently, synthetic DNA oligonucleotides making use of these specific and tunable binding properties have emerged as powerful building blocks for a variety of nanomaterial designs.<sup>11–13</sup> Also, oligonucleotides have been used as smart control tools to regulate the liberation of nanoparticles (NPs),<sup>14–16</sup> to enable gene editing<sup>17</sup> and regulation,<sup>18,19</sup> as templates for the diagnosis of RNA/DNA-based pathological disfunctions,<sup>20,21</sup> and as a trigger that allows for spatiotemporal control over the initiation of drug release events from synthetic vehicles.<sup>22–24</sup>

Of course, drugs can be encapsulated not only into vesicles but also into (bio)polymer-based nanoparticles, and many examples can be found in the literature.<sup>25</sup> In this study, mucins are chosen as example biopolymers as their biochemical complexity allows for various functionalizations of the biomacromolecule and offers good binding of both anionic and cationic cargos.<sup>26</sup> Moreover, mucins have been used as

Received: May 14, 2020  
Accepted: August 7, 2020  
Published: August 7, 2020





**Figure 1.** Mucin nanoparticles are generated by condensation with glycerol and can be reversibly stabilized by cross-linking with self-complementary DNA strands. (a) Schematic representation of the mucin condensation process into NPs followed by a DNA-mediated NP disassembly. (b) Electrophoretic separation of SYBR-Safe-stained DNA/mucin mixtures demonstrates that thiolated DNA is trapped in the gel pockets together with mucins, whereas nonthiolated DNA is not. (c) Only thiolated crDNA creates stable mucin NPs after removal of glycerol. (d) On-demand opening of mucin NPs is possible with the addition of dDNA, which destabilizes the condensed mucins through favorable base pairing. A random DNA sequence (control DNA = coDNA) does not induce such an opening of crDNA-stabilized mucin NPs. The reported hydrodynamic sizes represent the intensity average of >95% of counts. Data shown in (c,d) represent mean values, and error bars denote the standard deviation as obtained from  $n = 5$  independent samples. (e,f) Representative atomic force microscopy height images and cross-sectional profiles of the crDNA/mucin-based NPs before (e) and after (f) dDNA-triggered reconfiguration.

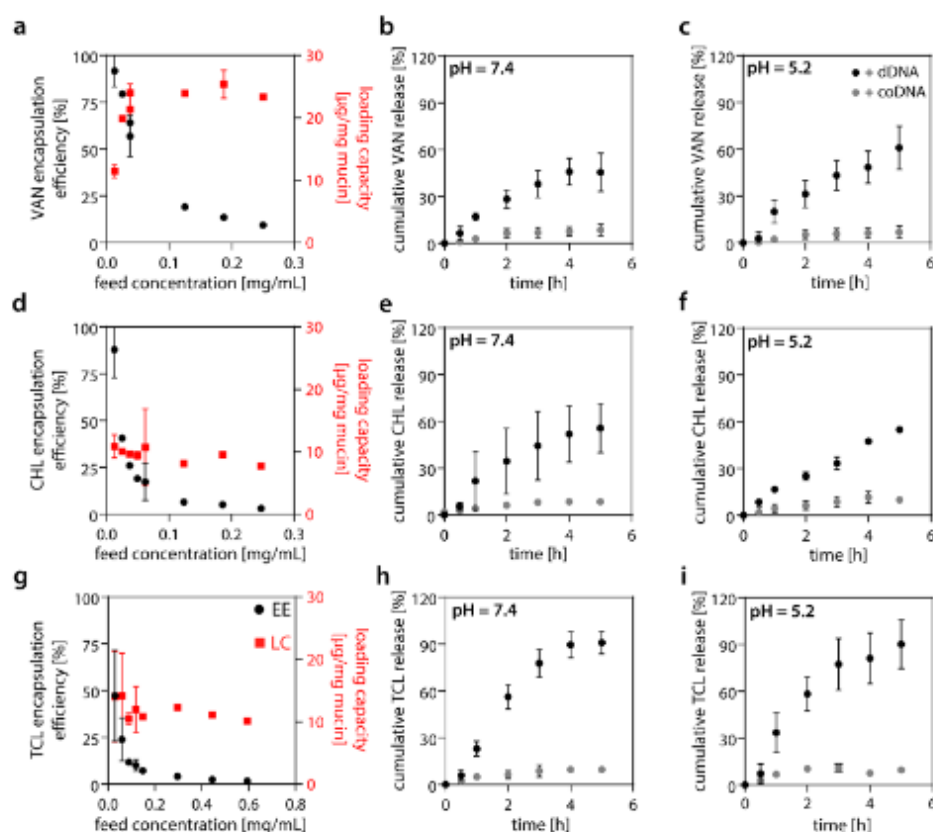
building blocks for functional coatings<sup>27</sup> or hydrogels,<sup>26</sup> and they show little to no immune reaction when inserted into mammals.<sup>28</sup>

Inspired by the great potential mucins hold for biomedical applications and the high specificity and excellent reproducibility of DNA nanotechnology, we present here DNA-cross-linked mucin nanoparticles that offer control over the release of their cargo through a conformational change triggered by DNA displacement. We form mucin nanoparticles through reversible condensation, which only occurs in the presence of the correct trigger DNA. As the design of the stabilizing DNA sequences used for NP cross-linking can be tuned, it is possible to achieve both a controlled drug release triggered by externally supplied synthetic DNA strands and by existing cellular oligonucleotides (such as miRNA) alike.

## RESULTS AND DISCUSSION

**Nanoparticle Preparation and Characterization.** It was demonstrated before that mucin glycoproteins (Figure S1) can be condensed by exposing solubilized mucin molecules to glycerol.<sup>29</sup> However, for a controlled drug delivery application, a transient NP stabilization strategy is required, which can be reversed on demand. Therefore, we modify the previous approach using synthetic self-complementary DNA sequences (cross-linker DNA, crDNA) for mucin cross-linking (Figure 1a). To covalently attach those oligonucleotides to mucins, a thiol modification at the 5' end of the crDNA is used; this allows for spontaneous covalent binding of the crDNA strands to cysteine groups of the mucin glycoprotein.<sup>30</sup> To verify successful crDNA binding to mucins, mucin/DNA mixtures are loaded onto a sodium dodecyl sulfate polyacrylamide gel electrophoresis (SDS-PAGE) to visualize both DNA and proteins (Figure 1b). DNA staining shows that the thiol





**Figure 2.** Encapsulation efficiency, loading capacity, and cumulative release profiles of mucin-based NPs at pH 7.4 and 5.2. Three different antibiotics are compared: vancomycin (a–c), chloramphenicol (d–f), and tetracycline hydrochloride (g–i). Data represent mean values, and error bars denote the standard deviation as obtained from  $n = 3$  independent samples. All curves shown have reached a plateau after  $\sim 5$  h, which is why data obtained at later time points are not depicted. If error bars are not visible, they are smaller than the symbol size.

functionalization is indeed necessary to attach the crDNA to mucin: only here, the crDNA is retained in the gel pocket where the mucin proteins are trapped. In contrast, nonthiolated DNA (which has the same sequence) is separated from mucins and quickly travels across the gel. Furthermore, a periodic acid–Schiff staining suggests that the other protein bands we detect in the gel are likely to be caused by protein contaminations originating from the in-lab purification process (Figure S2). We estimate the number of cysteines that are, in principle, available for disulfide bond formation in a single mucin molecule to be 98; experimentally, we find that  $\sim 13$  crDNA molecules can be attached per mucin (Figure S3).

Importantly, the crDNA sequence is designed such that it contains a partially self-complementary region, and this region is supposed to create intermolecular or intramolecular mucin cross-links, the latter of which are needed to stabilize the mucin-based NPs after removal of glycerol. However, as this self-complementary region is a rather small (8 bp) sequence, a fully complementary displacement DNA (dDNA) strand should bind to the crDNA strands with higher affinity and thus displace its original crDNA binding partner (the crDNA/dDNA pairing over the crDNA/crDNA pairing). Previously, we showed that this strand displacement is highly specific.<sup>15</sup> Therefore, we expect the DNA-stabilized mucin-based NPs to

be stable after glycerol removal but to open up when a suitable trigger is introduced, that is, when dDNA is added to the NP solution (Figure 1a).

We test this idea by determining the size of mucin-based NPs *via* dynamic light scattering (DLS) at different conditions, that is, with thiolated crDNA (which targets cysteines on mucin glycoproteins) and nonthiolated (nonbinding) crDNA, followed by triggering with complementary (dDNA) or mismatching control DNA (coDNA; this sequence was designed such that it does not show a significant binding affinity to crDNA). After condensation with glycerol, we determine similar size ranges (250–330 nm) for NPs independent of whether mucin-binding (*i.e.*, thiol-functionalized) crDNA or nonbinding DNA (nonthiolated crDNA) is used (Figure 1c). This result is expected as the addition of glycerol to a mucin solution has been shown to be sufficient to condense mucins into nanoparticles<sup>29</sup>—a stabilization with DNA is not required for this step. However, when we dialyze the NPs against 150 mM NaCl, only NPs stabilized with thiolated crDNA remain condensed; the low polydispersity index (PDI) of 0.17 we determine for those samples shows that this holds true for the whole mucin NP population. In contrast, NPs created with nonthiolated DNA lose their condensed structure after dialysis, as indicated by the strong

increase in the average mucin “particle” size ( $\sim 950$  nm) and the concomitant increase in the PDI.

We next test if the mucin-based NPs can be opened in a controlled fashion, that is, when a suitable trigger is introduced (Figure 1d). Indeed, we can observe this when monitoring changes in the hydrodynamic size of the NPs upon exposure to dDNA: now, the size of the mucin “NPs” is increased to values in the micron scale ( $\sim 1000$  nm, PDI = 0.80). This suggests that the condensation of mucin into NPs is reversed; that is, the mucin molecules return into their original, elongated state (Table S1). We verify this result by visualizing the morphology of mucin-based NPs both in the absence and presence of dDNA using atomic force microscopy (AFM, Figure 1e,f). Also, this technique demonstrates a drastic morphological difference: without the DNA trigger, we find round, particle-like structures; in the presence of dDNA, we detect irregularly shaped, elongated objects. Cross-sectional profiles obtained from the AFM images suggest that the diameter of the condensed mucin-based NPs is  $\sim 200$  nm. Considering that AFM imaging was conducted with dried mucin objects, those values are in agreement with the results obtained here from DLS measurements and previous findings.<sup>29,31</sup>

Together, those experiments demonstrate that the mucin condensation step is efficiently reversed once the stabilizing crDNA cross-links are opened by the dDNA strands. Control experiments, where a “wrong” DNA sequence (coDNA) is added to the crDNA-stabilized NPs underscore the specific binding of the dDNA strands: in the presence of coDNA, the NPs remain condensed. Together, these results show that an on-demand decondensation of crDNA-stabilized NPs is possible—but only if correctly designed DNA sequences are used for mucin cross-linking and unlinking.

In addition to their ability to open up on demand, it is important that the NPs do not do so spontaneously over time (e.g., driven by thermal forces or by uncontrolled degradation). Using the same methodology, we also confirm that the stability of the mucin NPs in different physiological conditions is preserved over  $\sim 2$  weeks (Figure S4 and Table S2).

**DNA-Mediated Drug Release from Mucin-Based NPs.** So far, we conducted all tests with “ghost” NPs that were not loaded with drugs. In the next step, we test the loading and release of three antibiotics to NPs that differ in terms of their net charge at pH 7.4: tetracycline hydrochloride (TCL, negatively charged),<sup>32</sup> chloramphenicol (CHL, neutral), and vancomycin hydrochloride (VAN, positively charged).<sup>33</sup> Overall, we observe a good drug loading capacity, which is highest for the cationic VAN ( $\sim 25$   $\mu\text{g}/\text{mg}$  mucin), intermediate for the anionic TCL ( $\sim 10$ – $12$   $\mu\text{g}/\text{mg}$  mucin), and a bit lower for the neutral CHL ( $7$ – $10$   $\mu\text{g}/\text{mg}$  mucin). These results directly imply that charged drug molecules can interact with the mucin biopolymer via electrostatic forces,<sup>26,34</sup> and this idea is fully consistent with the molecular architecture of the mucin glycoprotein that carries not only anionic residues but also (albeit fewer) cationic residues in the terminal regions (Figure S1). Thus, binding of cationic molecules is preferred, but the binding of anionic molecules is still possible.<sup>34</sup> For all three antibiotics, mucin-based NPs show decreasing encapsulation efficiency with increasing drug feed. Also, this finding supports the idea that drug loading into mucin-based NPs is facilitated by attractive electrostatic forces which promote drug binding to mucin. Thus, for further experiments, NPs with a high drug payload (i.e., feed concentrations of  $c_{\text{VAN}} = 0.025$  mg/mL,  $c_{\text{TCL}}$

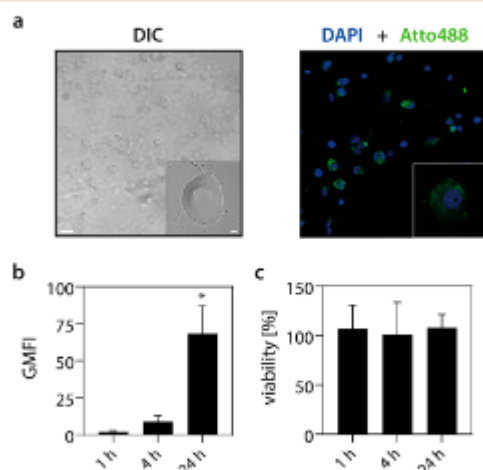
$= 0.06$  mg/mL, and  $c_{\text{CHL}} = 0.025$  mg/mL) are chosen to quantify the release behavior of the entrapped drugs.

As depicted in Figure 2, we obtain good release efficiencies ( $\sim 50$ – $90\%$ ) for all three antibiotics—provided that the correct trigger DNA (dDNA) is added. In control groups, where a “wrong” DNA sequence (coDNA) is added, the cumulative drug release is low ( $<10\%$ ) for all conditions and quite stable during the time span of the experiment. We assume that the observed low level of untriggered release is due to minor amounts of inefficiently encapsulated drug molecules, which unbind spontaneously from the NPs due to thermal fluctuations. In the presence of the trigger DNA, however, the stabilizing crDNA/crDNA cross-links are opened by the formation of a thermodynamically favorable dDNA/crDNA complex. Importantly, we obtain virtually identical results when the release experiments are conducted at pH 5.2. From an application point of view, this robustness of the trigger mechanism suggests that our approach may also be useful for different drug delivery targets. For instance, chemotherapeutic drug carriers could benefit from the mechanism presented here without being negatively affected by the acidic tumor environment (pH  $\sim 6.4$ – $7.0$ ).

Interestingly, the net charge of the loaded drugs is also an important factor affecting the drug release profiles from the NPs. For example, TCL shows a release efficiency higher than that of both VAN and CHL (Figure 2b,c). This is somewhat counterintuitive considering that the neutral CHL and the anionic TCL showed comparable loading capacities. When the incubation temperature of the NPs is increased to levels above the melting temperature of the stabilizing crDNA cross-links, we observe the additional release of CHL and VAN but not of TCL (Figure S5). Above, we have argued that cationic groups on the mucin glycoprotein may support negatively charged TCL binding to the mucin-based NPs through electrostatic forces. Indeed, the loading capacity of NPs generated in solutions supplemented with different salt concentration supports this notion (Figure S6). Following the same line of argument, one would expect those electrostatic binding forces to hamper the release of TCL rather than promoting it. However, it is crucial to realize that the internal charge state of mucin-based NPs at the point of triggered release is different compared to the situation before release was initiated: now, dDNA strands are bound to the mucins which increase the local density of anionic motifs in the mucin-based NPs. We speculate that this local increase in internal negative charges might be responsible for the unexpectedly better release efficiency of TCL from NPs compared to that of CHL. However, although the overall negative charge of mucin glycoprotein is important for the entrapment of molecules into NPs, unspecific binding interactions may also contribute.<sup>35</sup>

**Cellular Uptake of Mucin Nanoparticles.** Having verified that our NPs can be successfully loaded with different drugs and that a controlled release from the NPs can be efficiently triggered with suitable DNA strands, we next ask if the mucin-based NPs can be taken up by cells efficiently. This is an important question as intracellular infections such as those induced by *Listeria monocytogenes* or *Pseudomonas aeruginosa* are difficult to treat. They lead to severe diseases such as listeriosis, pneumonia, endocarditis, and meningitis by mainly targeting macrophages and epithelial cells.<sup>1,2</sup> In these cases, the bacterial pathogens hide in the macrophages where they are protected from systemic antibiotic administration, and persistent infection of macrophages can lead to further

spreading of the infection and/or infection recurrence.<sup>36</sup> We test for the successful uptake of (fluorescently labeled) mucin-based NPs by THP1-derived type 0 (M0) macrophages using confocal imaging and fluorescence-activated cell sorting (FACS) (Figure 3a,b).



**Figure 3.** Uptake of mucin-based NPs and their *in vitro* viability assessed with THP1-derived macrophages type 0 (M0). (a) Differential interference contrast and fluorescent confocal laser scanning microscope images demonstrate the successful uptake of mucin-based NPs (green) by macrophages after 24 h of incubation. Cell nuclei are stained with DAPI (blue). The scale bars represent 20 μm (overview image) and 4 μm (inset). (b) Comparison of the geometric mean fluorescence intensity of macrophages incubated with mucin-based NPs for 1, 4, and 24 h, as obtained by FACS measurements. (c) Viability of THP1-derived type 0 (M0) macrophages after 1, 4, and 24 h of incubation with mucin-based NPs. Data shown in (b,c) represent mean values, and error bars denote the standard deviation as obtained from  $n = 6$  independent samples.

In the FACS experiments, the fluorescence signal arising from membrane-bound NPs is quenched with Trypan Blue, which allows us to accurately determine the signal of internalized NPs. Indeed, confocal images show many fluorescent particles that are colocalized with the macrophages, and the FACS data obtained at increasing intervals of incubation time verify successful uptake of NPs into the cytosol. Moreover, NPs did not show any cytotoxic effect on the macrophages within the incubation period (Figure 3c). Of course, this result was expected as macrophages can actively ingest particles and macromolecules of different sizes and surface properties *via* various pathways.<sup>37</sup> NP uptake is, however, not that easily possible for other cell types, and intracellular bacteria can also infect nonphagocytic cells such as epithelial cells or fibroblasts. Thus, in a next step, we test the uptake efficiency of NPs by HeLa cells. When we evaluate the uptake of fluorescently labeled mucin-based NPs into HeLa cells with FACS, we detect only a slight increase in the fluorescence signal over time, which is not significant (Figure 4a).

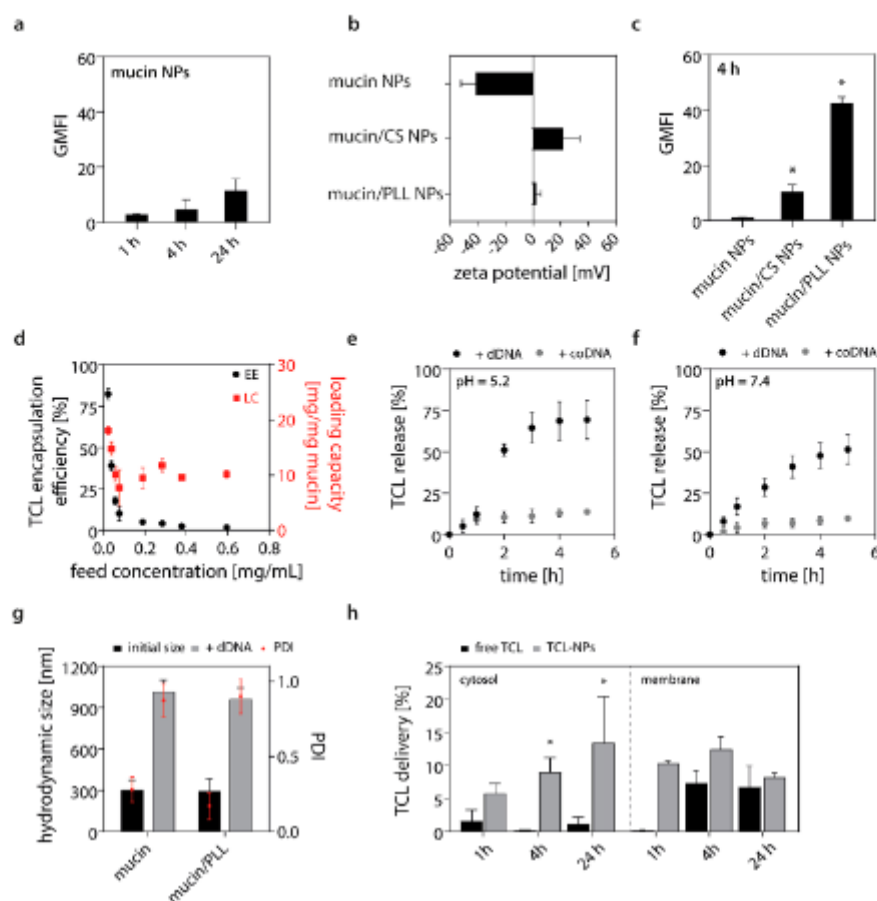
One possible explanation for this result could be the NPs do not interact strongly enough with the cellular membrane: in their present form, the mucin-based NPs have a strongly negative  $\zeta$ -potential of  $-41.5 \pm 10.7$  mV (Figure 4b), which is

likely to give rise to electrostatic repulsion forces between the NPs and anionic components of the glycocalyx on the cellular membrane.<sup>38</sup> Indeed, previous studies have already shown that the  $\zeta$ -potential of nanoparticles is a crucial parameter that affects NP–cell interactions.<sup>39,40</sup> To overcome this problem, in a next step, we aim at changing the surface properties of the mucin-based NPs by coating them with cationic macromolecules. In brief, we subject NPs to a second condensation step where we add either PLL or chitosan to the NP-forming solution (see Materials and Methods). With this modification step, we obtain a strong shift of the formerly negative  $\zeta$ -potential of the mucins NPs into the positive regime (+2.3 and +21.7 mV for PLL- and CS-coated NPs, respectively, Figure 4b). Moreover, coating the NPs with cationic polymers alters the minimum dDNA required to initiate opening of the NPs and, subsequently, drug release. The slightly positive surface charge of PLL-coated NPs may facilitate dDNA/crDNA interactions by “guiding” the negatively charged dDNA to the NPs, therefore reducing the amount of dDNA required to trigger the structural change. However, CS-coated NPs have a strongly positive  $\zeta$ -potential and thus are likely to establish strong electrostatic interactions with DNA; thus, they require larger dDNA concentrations to obtain an efficient drug release (Figure S7).

Control experiments show that neither of those two coatings induces any perceivable cytotoxic effects to HeLa or NIH/3T3 cells (Figure S8)—an unwanted side effect that has been reported before for some cationic NPs.<sup>41,42</sup> More importantly, cellular uptake experiments conducted with those modified mucin-based NPs show successful internalization: after an incubation time of 4 h, both modifications give rise to a significantly improved NP uptake compared to that with unmodified NPs (Figure 4c and Figure S9). Interestingly, there is a slight influence of the NP charge density on the cellular internalization profiles obtained with PLL- and CS-coated NPs: We speculate that a slightly positive surface charge as brought about by the PLL coat is sufficiently high to aid the NPs to the cellular membrane but low enough to prevent permanent trapping of those NPs at the cell membrane, thus improving their internalization compared to that with CS-coated NPs. As we obtained the highest uptake efficiency with the PLL modification, all further experiments were conducted with mucin/PLL NPs.

**Intracellular Drug Release from Mucin-Based NPs.** As described above, the additional PLL modification ensures that mucin-based NPs are efficiently taken up by HeLa cells (Figure S10). However, as this coating might have rendered the NPs more stable, it is a next important step to verify that the triggered drug release from the NPs still operates as planned. Indeed, the TCL loading capacity and release profiles obtained from PLL-modified mucin NPs (Figure 4d–f) *in vitro* are very similar to those obtained for unmodified mucin-based NPs. These results underscore once more the robustness of the DNA-based release mechanism. Also, DLS measurements agree with this assessment: the addition of dDNA triggers the opening of PLL-modified mucin NPs with virtually identical efficiency as for uncoated NPs (Figure 4g).

To assess the intracellular TCL delivery efficiency of PLL-modified NPs, we next compare the uptake of free TCL to the uptake of NP-loaded TCL using incubation conditions with HeLa cells where both variants of drug formulation contain an identical TCL concentration of 5 mM. This feed concentration was chosen as it represents the half-maximal inhibitory

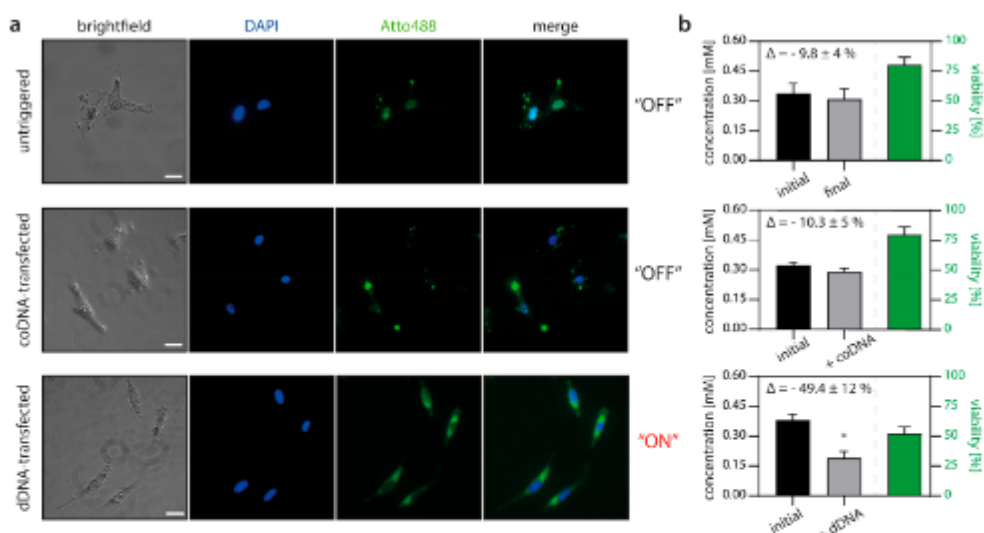


**Figure 4.** Uptake of mucin NPs by HeLa cells and their functionality after surface modification. (a) Geometric mean fluorescence intensity (GMFI) obtained by FACS evaluation of HeLa cells incubated with fluorescently labeled mucin NPs for 1, 4, and 24 h ( $n = 6$ ). (b)  $\zeta$ -Potential measurements of unmodified and modified (chitosan and PLL-coated) mucin NPs conducted at pH 7.4 ( $n = 5$ ). (c) GMFI obtained by FACS evaluation of HeLa cells incubated with unmodified and modified (chitosan and PLL-coated) NPs for 4 h ( $n = 6$ ). (d–f) TCL encapsulation efficiency, loading capacity (d) and cumulative release profiles of PLL-coated mucin NPs at pH 5.2 (e) and 7.4 (f) ( $n = 3$ ). (g) Light scattering measurements indicating a DNA-triggered conformational change (=opening) of unmodified and PLL-modified NPs ( $n = 5$ ). (h) TCL quantification in cytosol and membrane fractions of HeLa cells 1, 4, and 24 h of incubation with NPs (at a fixed TCL concentration of 5 mM,  $n = 6$ ). Data represent mean values, and error bars denote the standard deviation.

concentration of TCL ( $IC_{50}$ ), which ensures that the applied TCL does not induce cytotoxic effects (Figure S11). When we determine the accumulation of TCL in cytosolic and membrane-associated fractions of HeLa cells over time (Figure 4h), we find comparable amounts of TCL for both delivery variants. However, there were much higher cytosolic TCL concentrations for TCL delivered *via* NPs: Here, after an incubation time of 24 h, the TCL dose delivered into the cytosol is  $\sim 12$  times higher than the uptake of free TCL. Importantly, this delivered dose represents a drug concentration that exceeds the subtherapeutic levels (*i.e.*, that is higher than corresponding MIC values) for various bacterial species including *Staphylococcus* spp., some *Streptococcus* groups, and *P. aeruginosa*.<sup>43,44</sup> Therefore, these findings show that mucin-based NPs can concentrate the drug in the cells and act as efficient vectors to overcome the diffusion-related rapid clearance of drugs from the extracellular environment.

Although we could already show that the mucin-based NPs can successfully transport therapeutics across the cellular

membrane, the cytosol microenvironment with its multitude of ongoing complex biochemical reactions could negatively affect the DNA-triggered release of drugs from the NPs. Therefore, we next attempt a triggered, on-demand conformational change of NPs (and an ensuing intracellular drug release) in HeLa cells. For those tests, we load the NPs with a fluorescent dye (Atto488) instead of an antibiotic to visualize the cargo in the cell cytoplasm. HeLa cells, which have successfully internalized such mucin-based NPs, exhibit small fluorescent dots representing Atto488-loaded NPs (Figure 5, top row). When we transfect those HeLa cells with the trigger sequence (*i.e.*, dDNA; see Materials and Methods), we find that the fluorescent cargo distributes across the cytoplasm (Figure 5, bottom row). In contrast, when a control DNA sequence (=coDNA; see above; Figure 5, middle row) is transfected to the cells, the fluorophore is still visible in localized spots, indicating that the cargo remains trapped in the NPs. This observation agrees well with the above-mentioned results,



**Figure 5.** Spatial distribution of the NP cargo after successful uptake of mucin NPs by HeLa cells. (a) Representative fluorescence microscopy images of HeLa cells incubated with Atto488-loaded mucin/PLL NPs (green). The cell nuclei are stained with DAPI (blue). Three conditions are compared: without transfection of DNA strands (“untriggered”) and with transfection of either coDNA (wrong trigger) or dDNA (correct trigger). The scale bars represent 25  $\mu\text{m}$  and apply to all images. (b) TCI concentration in cytosol fractions of nontransfected, coDNA-, and dDNA-transfected HeLa cells before (black) and after (gray bars) dialysis. The insets show the relative reduction in the cytosolic TCI concentration after dialysis of the cell lysates, which indicates the amount of drug liberated from the NPs ( $n = 6$ ). The right y-axis (green bars) represent the *in vitro* viability of HeLa cells after exposure to DOX-loaded mucin NPs at different trigger conditions ( $n = 9$ ). Data shown represent mean values, and error bars denote the standard deviation.

where only the correct DNA key triggered NP dispersal and—as a consequence—drug release.

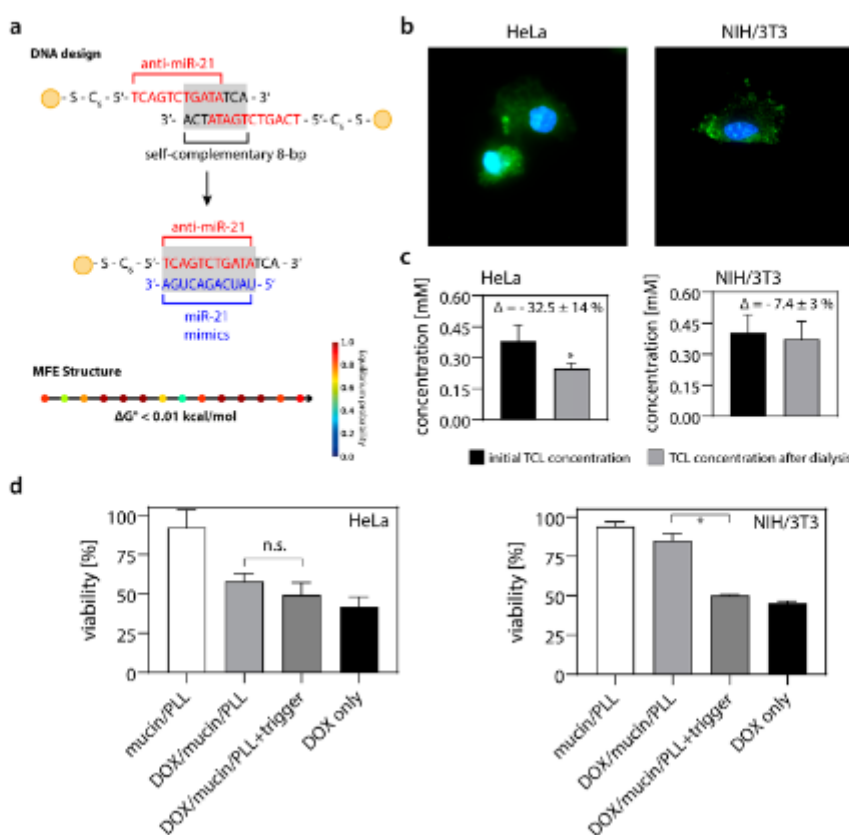
To quantify this observation, we repeat this experiment but, this time, load the NPs with TCI and collect the cytosolic fractions of the three different HeLa cell populations after NP uptake and (if applicable) DNA transfection. In all three cases, we find similar total concentrations of intracellular TCI of 0.30–0.45 mM. However, it is not possible to directly differentiate free TCI from NP-entrapped TCI with a simple spectroscopic analysis. Thus, in a next step, we subject the three cytosolic samples to a dialysis step to deplete liberated TCI from them (while retaining the mucin-based NPs together with their remaining cargo). After 2 days of dialysis, we observe a significant decrease in TCI for cells that were transfected with the dDNA—but not for the other two populations. This finding demonstrates that the dDNA-transfected cells indeed contain free (=liberated) TCI molecules, which is consistent with our observation from optical microscopy. From those tests, we conclude that the DNA-based drug release strategy is also applicable in the subcellular microenvironment, and that the mechanism is not compromised by cytoplasmic components such as oligonucleotides, signal molecules, or metabolic waste products.

To assess the level of control our system allows, we prepare a new set of PLL-coated NPs; however, this time, the NPs are loaded with doxorubicin (DOX), a cytotoxic drug molecule used in chemotherapy. *In vitro* tests with those DOX-loaded NPs agree very well with the results presented for antibiotics above and underscore that on-demand release from the mucin NPs operates with high reliability (Figure S12). Next, we test whether untriggered drug release from the mucin NPs occurs in the cytosol using the same three conditions as described above: untriggered, coDNA-transfected, and dDNA-trans-

fected cells. The reduced cell viability we obtain in the presence of the correct trigger shows that a controlled DOX release is possible in the cytosol, as well (Figure 5b, green bars). On the contrary, no cytotoxic effects are observed in the absence of the correct dDNA trigger. This finding is a clear indication that passive drug leakage from the NPs is negligible.

**Autonomous Drug Release Triggered by Intracellular MicroRNA.** With the DNA design used so far, the mucin-based NPs can successfully release their cargo molecules inside cells; however, for this to happen, cell transfection with the correct trigger DNA (dDNA) is required. Now, in a final step, we aim at modifying our mechanism such that cellular oligonucleotides trigger drug release autonomously. Moreover, our goal is to engineer the mucin-based NPs such that this autonomous release only occurs in particular cell types. If successful, this modified mechanism would be a beneficial tool for many therapies, especially for those where cytotoxic drugs are supposed to reach selected cells only (e.g., a delivery of chemotherapeutics for the inhibition of tumor growth).

Here, we choose a specific microRNA (miRNA) sequence, as miRNA overexpression is a marker for the initiation phase of several human diseases (e.g., cancer, viral infections, and cardiovascular diseases).<sup>45</sup> In particular, we selected miR-21—an oncogenic miRNA overexpressed in many tumors.<sup>46,47</sup> Accordingly, the DNA mechanism designed here is re-engineered with a new sequence design, so that miR-21 can be used as an endogenous trigger to open up mucin-based NPs cross-linked with “anti-miR-21” strands (Figure 6a). The new single-stranded cross-linker DNA contains 14 bp, including a self-complementary 8 bp domain. Eleven base pairs in this sequence are complementary to miR-21, which is why the construct is referred to as “anti-miR-21”. When NPs cross-linked with these anti-miR-21 strands are delivered to cells that



**Figure 6.** Autonomous liberation of mucin NP cargo in the presence of a cell-specific endogenous trigger. (a) Molecular design and selective base-pairing DNA sequences designed for autonomous drug release triggered by cellular miRNA 21. The estimated minimum free energy for the cross-linker “anti-miR-21” sequence shows no secondary structures at 37 °C. Bases are colored according to their probability of being in equilibrium. (b) Representative fluorescence microscopy images of HeLa and NIH/3T3 cells after successful NP uptake. (c) TCL concentration in cytosol fractions of cells before (black bars) and after dialysis (gray bars) ( $n = 6$ ). The insets show the relative reduction in the cytosolic TCL concentration after dialysis of the cell lysates, which indicates the amount of drug liberated from the NPs. (d) *In vitro* viability of HeLa and NIH/3T3 cell lines after being exposed to the DOX-loaded, autonomously opening NPs for 24 h ( $n = 9$ ). Data represent mean values, and error bars denote the standard deviation.

overexpress miR-21, the cellular miR-21 strands are expected to bind competitively (and with a higher affinity) to the cross-linker anti-miR-21 sequence, thereby opening the mucin-based NPs and triggering drug release from them.

As two cellular model systems where we expect different experimental outcomes due to differences in their miR-21 expression levels,<sup>48,49</sup> we choose HeLa cells (high miR-21 expression: target group; see Figure S13) and NIH/3T3 cells (low miR-21 expression: control group). Also, for this set of experiments, we first load the mucin-based NPs with a fluorescent dye and image the cells after incubation with the dye-loaded NPs. Importantly, whereas both cell lines internalize the mucin-based NPs with high efficiency, the NPs remain condensed in NIH/3T3 cells, as illustrated by the localized, spot-like fluorescent signals obtained from them (Figure 6b, right). In contrast, in HeLa cells, the fluorescent “cargo” is spread across the whole cell volume (Figure 6b, left), which is a good indication for successfully triggered NP dispersal.

Also here, we can quantify this impression by repeating this experiment with TCL-loaded NPs and analyzing cell lysates as described above. After dialysis of the cell lysates, we find a significant reduction of TCL for HeLa cells (Figure 6c, left)

but not for NIH/3T3 cells (Figure 6c, right). Again, this suggests that only the cytosol of HeLa cells contains free TCL, which was successfully depleted by the dialysis procedure. Together with the images obtained from light microscopy, these results show that an autonomous drug liberation based on existing cellular oligonucleotides only occurs for the HeLa cells, which is what we set out to achieve. A series of control experiments, where either miR-21 mimics or control (random) DNA strands are transfected to both HeLa and NIH/3T3 cells underscore the results presented so far and verify that the on-demand release achieved with the new cross-linker construct is highly specific, as well (Figure S14).

In the last step, DOX-loaded NPs are prepared using the miR-21-responsive DNA design and tested with the two cell lines as described above (Figure 6d). When HeLa cells are incubated with DOX-loaded NPs, their viability is reduced to ~50%, regardless of whether an external trigger was provided (and to similar levels as when free DOX is delivered to the cells). This result supports our notion that cellular overexpression of miR-21 is sufficient to open mucin NPs and to release their cargo. Importantly, for NIH/3T3 cells, where the cellular level of miR-21 is significantly lower, it is necessary to

provide an external trigger to achieve a reduced cell viability resulting from DOX release from NPs. Together, these results show that mucin NPs can release their payloads in specific (predetermined) cells, whereas nontargeted (*i.e.*, healthy) cells are protected from unwanted drug delivery. Moreover, those findings highlight the specificity and robustness of the drug delivery mechanism developed here.

Antisense oligonucleotides as we use them here have been successfully employed in other drug carrier systems before; examples include polymer-,<sup>50</sup> DNA-,<sup>21</sup> and silica-based templates<sup>24</sup> as well as metal organic frameworks.<sup>51</sup> However, although DNA templates can be patterned with peptides or aptamers to be specifically taken up by target cells, it is important to note that scaling up such constructs to obtain a delivery of therapeutic drug levels would require tens of milligrams of DNA per dose, and this is not economically viable.<sup>52</sup> Rigid inorganic systems that embed DNA as a pore-locking material or that are loaded with an antisense cargo possess other disadvantages: they cannot overcome certain biological barriers, lack colloidal stability, and exhibit dose-dependent cytotoxicity.<sup>53</sup> On the other hand, a polymer-based drug carrier itself does not allow for such a sensitive control over delivery. Here, owing to the biochemical multifunctionality of mucin, we combine the advantages brought about by a biopolymer-based and thus highly biocompatible carrier with the high specificity and tunability of DNA nanotechnology. By engineering NPs from mucin glycoproteins, a broad variety of drugs can be entrapped with high loading capacities, and this should include even hydrophobic drugs.<sup>26</sup> This aspect highlights the outstanding potential that those particular nanocarriers hold for a broad range of pharmacological applications. Additionally, once the mucin NPs have completed their task, the remaining mucin residues can be processed by cell-secreted enzymes, thus leaving only biological byproducts that would also occur otherwise as a result of physiological processes.

## CONCLUSION

Here, we present DNA-cross-linked mucin nanoparticles that undergo a conformational change in the presence of a suitable DNA trigger. These NPs can be loaded with different drugs and with a high encapsulation efficiency; moreover, they show impressive stability toward changes in pH levels and enzymatic attack. With an additional coating, these NPs can be internalized by both phagocytic and nonphagocytic cells. Then, drug release within the cell can be achieved either by transfecting the correct trigger DNA or by re-engineering the NP-stabilizing cross-linker DNA such that cellular miRNA automatically initiates NP dispersal.

This strategy presented here holds great potential for engineering disease-specific drug carriers. For example, autonomous, cell-specific drug release could be combined with cell-specific NP uptake, the latter of which could be achieved by combining the DNA-based release mechanisms with another modification of the NP surface, such as the addition of specific receptors such as cell-specific aptamers or cyclic peptides. Moreover, other cell-specific oligonucleotides (mRNA, siRNA) could be incorporated into such carrier designs to trigger the cytosolic opening of drug-loaded mucin NPs as we introduce them here. Then, other pathophysiological conditions such as undesired overexpression of oligonucleotides (as it occurs during hepatitis C infection,

myocardial infarction, and metabolic diseases)<sup>54</sup> could be used for cell-specific drug release.

## MATERIALS AND METHODS

**SDS-PAGE.** Polyacrylamide gel electrophoresis was employed to demonstrate binding between mucins and thiolated DNA (which is referred to as crDNA in this article, as this DNA sequence is used to stabilize the mucin nanoparticles by cross-linking). As a control, a similar DNA sequence but without thiol modification was used. As a preparatory step prior to gel electrophoresis, 100 mM crDNA was incubated in the presence of 500 mM dithiothreitol (DTT) and 0.5 mM tris(2-carboxyethyl)phosphine hydrochloride (Carl Roth, Karlsruhe, Germany) at room temperature (RT) for 2 h. Then, purified mucin was added to the DNA solution to a final mucin concentration of 0.1 mg/mL and incubated overnight (see Supporting Information for mucin purification). The next day, 6× sample loading buffer (Sigma-Aldrich, Schnellendorf, Germany) was added, and the samples were loaded onto mini-PROTEAN Tris-borate-EDTA (TBE) precast gels (BIO-RAD, Munich, Germany). Electrophoresis was performed at 100 V in 0.5× TBE buffer (pH 8.0) containing 5 mM DTT. DNA staining was conducted by incubating the gel with an SYBR Safe solution (Sigma-Aldrich) in 0.5× TBE buffer for 1 h, and pictures were recorded on a Molecular Imager Gel Doc XR system (BIO-RAD, Munich, Germany). Protein bands were visualized by staining the gel with a Coomassie staining solution overnight, and gel imaging was conducted after destaining the gel with a 10% acetic acid solution.

**Preparation of DNA-Stabilized Mucin Nanoparticles.** The synthetic DNA sequences designed to cross-link mucin-based NPs (=crDNA) and to trigger NP dispersal (=ddDNA) are modified variants of the sequences presented previously by Nowald *et al.*<sup>15</sup> To obtain NP variants that respond to a cellular miRNA trigger, a second set of DNA sequences is designed. The detailed sequences of all synthetic DNA strands used in this study are listed in the Tables S3 and S4. All synthetic DNA sequences were obtained from Integrated DNA Technologies (IDT, Munich, Germany). To prepare cross-linked mucin-based NPs, lyophilized crDNA, or anti-miR-21 strands (which were obtained stabilized in their oxidized form) were first incubated in a 100 mM DTT solution (dissolved in 180 mM phosphate buffer, pH 8) for 1 h to reduce their disulfide bridges. Then, the protection groups and DTT were removed with a Sephadex G-25 column (NAP-25 Sephadex G-25, GE Healthcare, Freiburg, Germany) equilibrated with 180 mM phosphate buffer. The concentration of this manually purified DNA was then adjusted to 100 μM using a NanoDrop-1000 spectral photometer (Thermo Fischer Scientific, Ulm, Germany). Mucin–DNA mixtures (with crDNA and ddDNA) were lyophilized and analyzed with Fourier transform infrared spectroscopy (Vertex 70 FTIR, Bruker, Germany) in the wavelength range of 4000 to 700 cm<sup>-1</sup> (Figure S15).

To prepare DNA-stabilized mucin nanoparticles, a one-step mucin condensation process was used as described in Yan *et al.*<sup>29</sup> but with slight modifications. In brief, lyophilized mucin was UV-sterilized for 2 h, dissolved at a concentration of 10 mg/mL in ddH<sub>2</sub>O, and stirred at 4 °C overnight. Then, prior to mixing the cross-linker DNA with a mucin solution, the reducing agent, tris(2-carboxyethyl)phosphine, was added at a concentration of 100 μM to the DNA solutions and incubated at RT for 1 h. After overnight incubation of mucin and crDNA, the mixture was added to a 30% (v/v) glycerol solution and vortexed for 30 s to form condensed mucin nanoparticles. After this step, a final mucin concentration of 1 mg/mL was obtained. To remove glycerol and unbound crDNA, the mixture was finally transferred to dialysis tubes (Spectrum Spectra/Por Float-A-Lyzer G2, MWCO = 300 kDa, Roth) and dialyzed in ddH<sub>2</sub>O containing 150 mM NaCl at 4 °C and 350 rpm overnight.

**Coating and Physical Characterization of DNA-Stabilized Mucin Nanoparticles.** To coat the mucin-based NPs with a cationic polymer, the DNA-stabilized mucin-based NPs were subjected to a second condensation step. Here, a 30% (v/v) glycerol solution containing either chitosan (chitosan 95/20, Heppe Medical Chitosan,

Halle, Germany) or poly(L-lysine) (PLL, Sigma-Aldrich) was added to the mucin NP/glycerol mixture (to a final chitosan or PLL concentration of 0.05 mg/mL) and then mixed on a vortex mixer for 30 s. Then, the mixture was dialyzed against a 150 mM NaCl solution to remove glycerol and excess chitosan and PLL.

The  $\zeta$ -potential and hydrodynamic size of mucin-based NPs were determined with a Nano ZS Zetasizer (Malvern Instruments, Herrenberg, Germany) at a backscatter angle of 173°. For the stability and degradation studies shown in the Supporting Information, NP suspensions ( $c_{\text{mucin}} = 0.5$  mg/mL) were incubated in phosphate-buffered saline (PBS) (pH 5.2 or 7.4), a trypsin solution (0.5 mg/mL), or DNaseI solution (25 ng/mL or 0.05 mg/mL) at 37 °C. Light scattering measurements were performed at distinct time points (i.e., 1, 5, 7, and 14 days) after initiation of the respective incubation process.

As an additional method (to ensure that the morphological changes of mucin NPs triggered by dDNA addition we determine from measuring the hydrodynamic sizes of the mucin NPs using DLS), we image the mucin NPs before and after dDNA addition by a NanoWizard II atomic force microscope (JPK Instruments, Berlin, Germany) using an OMCL-AC160TS-R3 cantilever (Olympus, Tokyo, Japan) in air tapping mode at RT. Before imaging, the AFM was thermally equilibrated for 30 min. A 20  $\mu$ L drop of the sample solution was pipetted onto a freshly cleaved mica slide, incubated for 5 min, and then rinsed with ddH<sub>2</sub>O and dried with compressed air. From the obtained height images, representative cross-sectional profiles were analyzed using the SPM image processing software (v.3.3.20, JPK). As the mucin NPs are now examined in their dry state, the absolute values obtained with this technique will differ from the numbers we obtain with DLS.

**Drug Loading into Mucin-Based NPs and DNA-Triggered Drug Release.** In this study, the three antibiotics tetracycline hydrochloride (TCL), chloramphenicol (CHL), and vancomycin hydrochloride (VAN) (all obtained from AppliChem, Darmstadt, Germany) and doxorubicin hydrochloride (Sigma-Aldrich, Schnell-dorf, Germany), a drug used in cancer chemotherapy, were used as model drugs. To load these drugs into mucin-based NPs, the different drugs were added to a mucin solution at different feed concentrations (the different concentration ranges tested were chosen according to differences in drug solubility and were 0.03–0.60 mg/mL for TCL, 0.01–0.25 mg/mL for CHL, 0.01–0.25 mg/mL for VAN, 0.008–0.0910 mg/mL for DOX) prior to DNA stabilization, and NPs were created by condensation with glycerol as described above. Then, the drug-loaded NPs were disintegrated by heating to 75 °C to determine the drug encapsulation efficiency and loading capacity. This temperature level was selected as it is high enough to exceed the melting temperature of the crDNA/crDNA complex, thus forcing the stabilizing crDNA/crDNA hybridization to open up. The released drug amount was quantified by measuring the absorbance of the drug molecules at 280 nm (for CHL and VAN), 360 nm (for TCL), and 450 nm (for DOX) with a spectrophotometer (specord 210, Analytikjena, Jena, Germany); absorbance values were converted into concentrations based on linear calibration standard curves (Figure S16). Then, the encapsulation efficiency and the drug loading capacity of mucin-based NPs were determined according to the following equations:

$$\begin{aligned} \text{encapsulation efficiency (\%)} &= \frac{\text{amount of drug entrapped in mucin NPs (mg)}}{\text{amount of initial drug feed (mg)}} \times 100 \\ \text{loading capacity} \left( \frac{\mu\text{g drug}}{\text{mg mucin}} \right) &= \frac{\text{amount of drug entrapped in mucin NPs (\mu\text{g})}}{\text{amount of mucin (mg)}} \end{aligned}$$

To determine the efficiency of the DNA-triggered drug release from mucin-based NPs, 5 mL of a suspension of drug-loaded NPs ( $c_{\text{mucin}} = 1$  mg/mL) was placed in dialysis tubings (Spectrum Spectra/Por

Float-A-Lyzer, Roth, Germany, MWCO = 100 kDa) and immersed into 50 mL of PBS at 37 °C and 350 rpm. Depending on the experiment, the pH in this PBS solution was adjusted to either pH 7.4 (representing standard cytoplasmic conditions) or pH 5.2 (representing endosomal conditions). The release of drugs from the NPs was then initiated by adding 50  $\mu$ L of a 100 mM dDNA solution into the dialysis tubes. With this added amount, the molar ratio of dDNA and crDNA was roughly 1. At selected time intervals, 500  $\mu$ L of the buffer was removed (and characterized) and replaced with the same amount of the fresh buffer. All release measurements were performed as triplicates of independently prepared samples.

**Cell Culture.** Human monocytes (THP1) were obtained from ATCC and cultured in RPMI-1640 medium (Gibco, Sigma-Aldrich, Sweden) supplemented with 10% (v/v) fetal bovine serum (FBS; Sigma-Aldrich) and penicillin/streptomycin (P/S, 100 U/mL). Cells were split at a ratio of 1/5 as soon as the cell density reached  $1 \times 10^6$  cells/mL. To differentiate cells into macrophage type 0, the culture medium was supplemented with 150 nM phorbol 12-myristate 13-acetate (PMA, Sigma-Aldrich), and the THP1 cells were maintained in this medium for 72 h; afterward, the cells were incubated in a complete cell culture medium without PMA for 24 h. To confirm the differentiation of THP1, the expected change in cell morphology change was verified under a bright-field microscope, and the typical macrophage markers CD36 (2.5  $\mu$ g per  $1 \times 10^6$  cells in 100  $\mu$ L; cat. no. 108418, BioLegend) and CD71 (2.5  $\mu$ g per  $1 \times 10^6$  cells in 100  $\mu$ L; cat. no. 108418, BioLegend) were evaluated by fluorescence-activated cell sorting (Gallios flow cytometer, Beckman Coulter) and analyzed with Kaluza software (Beckman Coulter, USA).

Human epithelial cells (HeLa) were cultured with minimum essential medium (MEM; Sigma-Aldrich) containing 10% (v/v) FBS, 2 mM L-glutamine solution (Sigma-Aldrich), and 1% (v/v) non-essential amino acid solution (Sigma-Aldrich). Human fibroblast cells (NIH-3T3) were cultured with Dulbecco's modified Eagle medium (Sigma-Aldrich) supplemented with 10% (v/v) FBS. Those two cell lines were incubated at 37 °C in a humidified atmosphere and 5% CO<sub>2</sub>.

**Uptake of NPs by Macrophages and Epithelial Cells.** Prior to macrophage uptake experiments, fluorescently labeled mucin-based NPs were dialyzed against RPMI-1640 medium (see Supporting Information for fluorescence labeling of mucins). The obtained NP solution was reconstituted in an equal volume of RPMI-1640 medium containing 20% FBS and P/S (200 U/mL). Differentiated THP1-M0 cells were seeded onto a 96-well ultralow and tissue culture plate (Corning Inc., NY, USA). After 1 day of cultivation, cells were incubated with a complete medium containing NPs for 1, 4, and 24 h. Then, the internalization of NPs was determined with FACS analysis (Gallios flow cytometer, Beckman Coulter). Prior to FACS analysis, the cell pellets were resuspended in 500  $\mu$ L of 1 $\times$  PBS containing 0.04% (v/v) of a Trypan Blue solution and incubated for 1 min (this is done to quench the fluorescent signal of NPs adsorbed to the cell membrane). Next, the cellular uptake was visualized on a confocal laser scanning microscope using ZEN 2011 software (Carl Zeiss AG, Germany). Image analysis were performed using ImageJ.

For NP uptake experiments with HeLa cells, those cells were cultivated in a 6-well microtiter plate (Corning Inc., NY, USA) at a concentration of 200,000 cells/well for 24 h (2 mL/well). Afterward, 1/4 of the medium was replaced with a NP dispersion supplemented with 10% FBS and 1% P/S. In predetermined time intervals (i.e., 1, 4, and 24 h), cells were washed twice with PBS, detached by trypsinization, and centrifuged at 500g for 5 min (Eppendorf Centrifuge 5804R, rotor A-4-44, Hamburg, Germany). The fluorescence signal was measured with FACS (BD FACS Calibur OS X, BD Biosciences, San Jose, CA) using a 488 nm argon-ion laser (15 mW). Ten thousand events per sample were recorded at a slow-to-medium detection rate and connected to Cell Quest software (BD Biosciences). All data were further analyzed with Flowing software version 2.5.1 (Turku Centre for Biotechnology, University of Turku, Finland).

**Determination of Intracellular Accumulation and Retention of TCL.** HeLa cells were seeded into a 12-well microtiter plate



(200,000 cells/well), covered with 1 mL of media (MEM) per well, and incubated for 24 h. Afterward, either a TCL solution or TCL-loaded NPs ( $c_{\text{TCL}} = 5 \text{ mM}$ ) were added to cell-containing wells (by substituting 1/4 of the culture medium with 250  $\mu\text{L}$  of sample solution per well). After different periods of incubation, the cells were washed three times with cold PBS, detached from the wells with trypsinization, and centrifuged at 600g and 4 °C for 10 min. Then, the obtained cell pellets were resuspended in 100  $\mu\text{L}$  of lysis buffer containing 20 mM HEPES, 10 mM KCl, 2 mM  $\text{MgCl}_2$ , 1 mM EDTA, and 1 mM EGTA (pH 7.2). After incubation on ice for 15 min, the samples were centrifuged at 20,800g at 4 °C for 45 min. The supernatants (=cytosol fractions) were collected separately, and the remaining pellets were washed with PBS and centrifuged (again at 20,800g and 4 °C, now for 10 min), and the created supernatants were discarded. The remaining pellets (i.e., the membrane fractions of the lysate) were dissolved in lysis buffer. Both the cytosol and the membrane fractions obtained with this procedure were then transferred into 96-well microtiter plates, and their TCL content was determined spectrophotometrically as described above.

**Intracellular Drug Release.** HeLa cells were seeded into a  $\mu$ -slide 8-well ibidiTreat plate (ibidi GmbH, Gräfelfing, Germany; 6000 cells/well), covered with 200  $\mu\text{L}$  of media, and incubated for 24 h. Then, 1/4 of the culture medium (=50  $\mu\text{L}$ ) was replaced with a "drug"-loaded mucin-NP dispersion.

For a visualization of the successful intracellular release of their cargo, the NPs were loaded with a fluorescent dye (Atto488,  $\lambda_{\text{exc}} = 500 \text{ nm}$ ,  $\epsilon_{\text{max}} = 9.0 \times 10^4 \text{ M}^{-1} \text{ cm}^{-1}$ ,  $\lambda_{\text{em}} = 520 \text{ nm}$ , ATTO-TEC GmbH, Siegen, Germany) instead of a drug. Then, after the cells were incubated with the dye-loaded NPs for 4 h, triggered DNA oligonucleotides were transfected to the cells using jetPRIME (Polyplus transfection, Illkirch, France). After 24 h of incubation, the culture media were removed, and the cells were washed with PBS and then fixed in 4% formalin (v/v). The cell nuclei were stained with 4,6-diamino-2-phenylindole (DAPI; 300 nM in PBS). Images were acquired with an inverted light microscope (DMI8 Leica, Leica, Wetzlar, Germany) using a 63 $\times$  lens (PL Fluotar 63 $\times$ /0.70, Leica) and a digital camera (Orca Flash 4.0 C11440, Hamamatsu, Japan). Cell nuclei were detected with an LED 405 filter cube (ex. = 375–435, DC = 455, em. = 450–490, Leica), and dye-loaded NPs were detected with a fluorescein isothiocyanate filter cube (ex. = 460–500, DC = 505, em. = 592–668, Leica). The exposure times were optimized for each filter set, and then identical settings were used for all images acquired with a certain filter set.

A quantitative assessment of the intracellular liberation of cargo from mucin NPs was conducted with TCL-loaded NPs. Briefly, cells were incubated with TCL-loaded NPs and then transfected with the trigger DNA strands as described above. After 24 h of incubation, cytosol fractions were collected by lysis as described above, and their TCL content was determined spectrophotometrically. Afterward, those cytosolic fractions were dialyzed against a 150 mM NaCl solution at 4 °C overnight (Spectrum Spectra/Por Float-A-Lyzer G2, MWCO = 300 kDa, Roth), and the remaining TCL amount in dialysis tubes was quantified. Then, the difference in the TCL concentration was calculated and used to quantify the fraction of TCL that remained in "untriggered" (=still closed) mucin NPs.

Also for the autonomous (miRNA-triggered) drug liberation from mucin NPs in cells, the success of this approach was both visualized and quantified with the methods described above. However, here, a second set of DNA oligonucleotides (containing an anti-miR-21 sequence) was designed for mucin NP cross-linking as described above. As target cells being able to open those NPs with miRNA-21 strands, we selected HeLa cells (which overexpress this particular miRNA variant); as a control group, the NIH/3T3 cell line was used. In addition, as the release event from mucin NPs was supposed to occur autonomously, the transfection step was omitted.

**Statistical Analysis.** The software GraphPad Prism (Prism 8, San Diego, CA, USA) was used to perform all statistical analyses. Prior to each statistical analysis, the normal distribution of the measured values was confirmed with a Shapiro-Wilk test. The homogeneity of variances was assessed with an F-test. For non-normal distributions,

the Wilcoxon–Mann–Whitney test was used. A Student's *t*-test was performed for normally distributed populations with homogeneous variances, whereas a Welch's *t*-test was used in case of unequal variances. As a level for significance, a *p* value of <0.05 was chosen, and significant differences were marked with an asterisk where applicable.

## ASSOCIATED CONTENT

### Supporting Information

The Supporting Information is available free of charge at <https://pubs.acs.org/doi/10.1021/acsnano.0c04035>.

Mucin purification and modification with DNA; characterization of mucin-based NPs; drug loading and release profiles; *in vitro* cell experiments with mucin NPs; preparation of DOX-loaded mucin NPs for autonomous drug release in target cells; autonomous drug release triggered by intracellular microRNA; FT-IR analysis; calibration curves; DNA sequences (PDF)

## AUTHOR INFORMATION

### Corresponding Author

Oliver Lieleg – Department of Mechanical Engineering and Munich School of Bioengineering, Technical University of Munich, 85748 Garching, Germany; [orcid.org/0000-0002-6874-7456](https://orcid.org/0000-0002-6874-7456); Phone: +49 89 289 10952; Email: [oliver.lieleg@tum.de](mailto:oliver.lieleg@tum.de); Fax: +49 89 289 10801

### Authors

Ceren Kimna – Department of Mechanical Engineering and Munich School of Bioengineering, Technical University of Munich, 85748 Garching, Germany; [orcid.org/0000-0003-2283-4295](https://orcid.org/0000-0003-2283-4295)

Theresa Monika Lutz – Department of Mechanical Engineering and Munich School of Bioengineering, Technical University of Munich, 85748 Garching, Germany

Hongji Yan – Division of Glycoscience, Department of Chemistry, School of Engineering Sciences in Chemistry, Biotechnology and Health, KTH Royal Institute of Technology, 106 91 Stockholm, Sweden; [orcid.org/0000-0001-7257-5522](https://orcid.org/0000-0001-7257-5522)

Jian Song – Department of Mechanical Engineering and Munich School of Bioengineering, Technical University of Munich, 85748 Garching, Germany

Thomas Crouzier – Division of Glycoscience, Department of Chemistry, School of Engineering Sciences in Chemistry, Biotechnology and Health, KTH Royal Institute of Technology, 106 91 Stockholm, Sweden; [orcid.org/0000-0002-1981-3736](https://orcid.org/0000-0002-1981-3736)

Complete contact information is available at: <https://pubs.acs.org/doi/10.1021/acsnano.0c04035>

### Author Contributions

The study was designed by C.K. and O.L. T.M.L. conducted the cell cultivation, cytotoxicity, and lysis experiments. H.Y. and T.C. designed the macrophage uptake studies, and H.Y. performed confocal, FACS, and cytotoxicity measurements with macrophages. J.S. conducted the AFM experiments. C.K. performed all other experiments and analyzed the data. The manuscript was written by the contribution of all authors.

### Notes

The authors declare no competing financial interest.

## ACKNOWLEDGMENTS

The authors thank Stephan Fehn for assistance with the preliminary FACS experiments, and Rouven Arnold for help with the RT-PCR test.

## REFERENCES

- (1) Del Porto, P.; Cifani, N.; Guarnieri, S.; Di Domenico, E. G.; Mariggio, M. A.; Spadaro, F.; Guglietta, S.; Anile, M.; Venuta, F.; Quattrucci, S.; Ascenzioni, F. Dysfunctional CFTR Alters the Bactericidal Activity of Human Macrophages against *Pseudomonas Aeruginosa*. *PLoS One* **2011**, *6*, No. e19970.
- (2) Schmiedl, A.; Kerber-Momot, T.; Munder, A.; Pabst, R.; Tschernig, T. Bacterial Distribution in Lung Parenchyma Early after Pulmonary Infection with *Pseudomonas Aeruginosa*. *Cell Tissue Res.* **2010**, *342*, 67–73.
- (3) Rosenblum, D.; Joshi, N.; Tao, W.; Karp, J. M.; Peer, D. Progress and Challenges towards Targeted Delivery of Cancer Therapeutics. *Nat. Commun.* **2018**, *9*, 1410.
- (4) Lu, Y.; Aimetti, A. A.; Langer, R.; Gu, Z. Bioresponsive Materials. *Nat. Rev. Mater.* **2017**, *2*, 16075.
- (5) Zhang, Q.; Lu, L.; Zhang, L.; Shi, K.; Cun, X.; Yang, Y.; Liu, Y.; Gao, H.; He, Q. Dual-Functionalized Liposomal Delivery System for Solid Tumors Based on RGD and a pH-Responsive Antimicrobial Peptide. *Sci. Rep.* **2016**, *6*, 19800.
- (6) Ramirez-Garcia, P. D.; Retamal, J. S.; Shenoy, P.; Imlach, W.; Sykes, M.; Truong, N.; Constandil, L.; Pellissier, T.; Nowell, C. J.; Khor, S. Y.; Layani, L. M.; Lumb, C.; Poole, D. P.; Lieu, T.; Stewart, G. D.; Mai, Q. N.; Jensen, D. D.; Latorre, R.; Scheff, N. N.; Schmidt, B. L.; Quinn, J. F.; Whittaker, M. R.; Veldhuis, N. A.; Davis, T. P.; Bunnett, N. W. A pH-Responsive Nanoparticle Targets the Neurokinin 1 Receptor in Endosomes to Prevent Chronic Pain. *Nat. Nanotechnol.* **2019**, *14*, 1150–1159.
- (7) Lang, T.; Dong, X.; Zheng, Z.; Liu, Y.; Wang, G.; Yin, Q.; Li, Y. Tumor Microenvironment-Responsive Docetaxel-Loaded Micelle Combats Metastatic Breast Cancer. *Sci. Bull.* **2019**, *64*, 91–100.
- (8) Cao, M.; Lu, S.; Wang, N.; Xu, H.; Cox, H.; Li, R.; Waigh, T.; Han, Y.; Wang, Y.; Lu, J. R. Enzyme-Triggered Morphological Transition of Peptide Nanostructures for Tumor-Targeted Drug Delivery and Enhanced Cancer Therapy. *ACS Appl. Mater. Interfaces* **2019**, *11*, 16357–16366.
- (9) Chen, D.; Zhang, G.; Li, R.; Guan, M.; Wang, X.; Zou, T.; Zhang, Y.; Wang, C.; Shu, C.; Hong, H.; Wan, L.-J. Biodegradable, Hydrogen Peroxide, and Glutathione Dual Responsive Nanoparticles for Potential Programmable Paclitaxel Release. *J. Am. Chem. Soc.* **2018**, *140*, 7373–7376.
- (10) Luo, Z.; Hu, Y.; Cai, K.; Ding, X.; Zhang, Q.; Li, M.; Ma, X.; Zhang, B.; Zeng, Y.; Li, P.; Li, J.; Liu, J.; Zhao, Y. Intracellular Redox-Activated Anticancer Drug Delivery by Functionalized Hollow Mesoporous Silica Nanoreservoirs with Tumor Specificity. *Biomaterials* **2014**, *35*, 7951–7962.
- (11) Bathe, M.; Rothmund, P. W. DNA Nanotechnology: A Foundation for Programmable Nanoscale Materials. *MRS Bull.* **2017**, *42*, 882–888.
- (12) Sedlmayer, F.; Aubel, D.; Fussenegger, M. Synthetic Gene Circuits for the Detection, Elimination and Prevention of Disease. *Nat. Biomed. Eng.* **2018**, *2*, 399–415.
- (13) Wamhoff, E. C.; Banal, J. L.; Bricker, W. P.; Shepherd, T. R.; Parsons, M. F.; Veneziano, R.; Stone, M. B.; Jun, H.; Wang, X.; Bathe, M. Programming Structured DNA Assemblies to Probe Biophysical Processes. *Annu. Rev. Biophys.* **2019**, *48*, 395–419.
- (14) Kimna, C.; Liele, O. Engineering an Orchestrated Release Avalanche from Hydrogels Using DNA-Nanotechnology. *J. Controlled Release* **2019**, *304*, 19–28.
- (15) Nowald, C.; Käsrdorf, B.; Liele, O. Controlled Nanoparticle Release from a Hydrogel by DNA-Mediated Particle Disaggregation. *J. Controlled Release* **2017**, *246*, 71–78.
- (16) Diaz, J. A.; Gibbs-Davis, J. M. Sharpening the Thermal Release of DNA from Nanoparticles: Towards a Sequential Release Strategy. *Small* **2013**, *9*, 2862–2871.
- (17) Hendel, A.; Bak, R. O.; Clark, J. T.; Kennedy, A. B.; Ryan, D. E.; Roy, S.; Steinfeld, L.; Lunstad, B. D.; Kaiser, R. J.; Wilkens, A. B.; Bacchetta, R.; Tsalenko, A.; Dellinger, D.; Bruhn, L.; Porteus, M. H. Chemically Modified Guide RNAs Enhance CRISPR-Cas Genome Editing in Human Primary Cells. *Nat. Biotechnol.* **2015**, *33*, 985–989.
- (18) Feldmann, D. P.; Cheng, Y.; Kandil, R.; Xie, Y.; Mohammadi, M.; Harz, H.; Sharma, A.; Peeler, D. J.; Moszczynska, A.; Leonhardt, H.; Pun, S. H.; Merkel, O. M. *In Vitro* and *In Vivo* Delivery of siRNA via Viper Polymer System to Lung Cells. *J. Controlled Release* **2018**, *276*, 50–58.
- (19) Raemdonck, K.; Naeye, B.; Buyens, K.; Vandenbroucke, R. E.; Høget, A.; Demeester, J.; De Smedt, S. C. Biodegradable Dextran Nanogels for RNA Interference: Focusing on Endosomal Escape and Intracellular siRNA Delivery. *Adv. Funct. Mater.* **2009**, *19*, 1406–1415.
- (20) Domljanovic, I.; Carstens, A.; Okholm, A.; Kjems, J.; Nielsen, C. T.; Heegaard, N. H.; Astakhova, K. Complexes of DNA with Fluorescent Dyes Are Effective Reagents for Detection of Auto-immune Antibodies. *Sci. Rep.* **2017**, *7*, 1925.
- (21) Wang, D.; Fu, Y.; Yan, J.; Zhao, B.; Dai, B.; Chao, J.; Liu, H.; He, D.; Zhang, Y.; Fan, C.; Song, S. Molecular Logic Gates on DNA Origami Nanostructures for microRNA Diagnostics. *Anal. Chem.* **2014**, *86*, 1932–1936.
- (22) Li, S.; Jiang, Q.; Liu, S.; Zhang, Y.; Tian, Y.; Song, C.; Wang, J.; Zou, Y.; Anderson, G. J.; Han, J.-Y.; Chang, Y.; Liu, Y.; Zhang, C.; Chen, L.; Zhou, G.; Nie, G.; Yan, H.; Ding, B.; Zhao, Y. A DNA Nanorobot Functions as a Cancer Therapeutic in Response to a Molecular Trigger *In Vivo*. *Nat. Biotechnol.* **2018**, *36*, 258.
- (23) Douglas, S. M.; Bachelet, I.; Church, G. M. A Logic-Gated Nanorobot for Targeted Transport of Molecular Payloads. *Science* **2012**, *335*, 831–834.
- (24) Zhang, P.; Cheng, F.; Zhou, R.; Cao, J.; Li, J.; Burda, C.; Min, Q.; Zhu, J. J. DNA - Hybrid - Gated Multifunctional Mesoporous Silica Nanocarriers for Dual - Targeted and microRNA - Responsive Controlled Drug Delivery. *Angew. Chem., Int. Ed.* **2014**, *53*, 2371–2375.
- (25) Nitta, S. K.; Numata, K. Biopolymer-Based Nanoparticles for Drug/Gene Delivery and Tissue Engineering. *Int. J. Mol. Sci.* **2013**, *14*, 1629–1654.
- (26) Duffy, C. V.; David, L.; Crouzier, T. Covalently-Crosslinked Mucin Biopolymer Hydrogels for Sustained Drug Delivery. *Acta Biomater.* **2015**, *20*, 51–59.
- (27) Song, J.; Winkeljann, B.; Liele, O. Biopolymer - Based Coatings: Promising Strategies to Improve the Biocompatibility and Functionality of Materials Used in Biomedical Engineering. *Adv. Mater. Interfaces* **2020**, 2000850.
- (28) Yan, H.; Seignez, C.; Hjorth, M.; Winkeljann, B.; Blakeley, M.; Liele, O.; Phillipson, M.; Crouzier, T. Immune - Informed Mucin Hydrogels Evade Fibrotic Foreign Body Response *In Vivo*. *Adv. Funct. Mater.* **2019**, *29*, 1902581.
- (29) Yan, H.; Chircov, C.; Zhong, X.; Winkeljann, B.; Dobryden, I.; Nilsson, H. E.; Liele, O.; Claesson, P. M.; Hedberg, Y.; Crouzier, T. Reversible Condensation of Mucins into Nanoparticles. *Langmuir* **2018**, *34*, 13615–13625.
- (30) Islam, M. A.; Firdous, J.; Choi, Y. J.; Yun, C. H.; Cho, C. S. Design and Application of Chitosan Microspheres as Oral and Nasal Vaccine Carriers: An Updated Review. *Int. J. Nanomed.* **2012**, *7*, 6077.
- (31) Marczyński, M.; Balzer, B. N.; Jiang, K.; Lutz, T. M.; Crouzier, T.; Liele, O. Charged Glycan Residues Critically Contribute to the Adsorption and Lubricity of Mucins. *Colloids Surf., B* **2020**, *187*, 110614.
- (32) Chang, P. H.; Jiang, W. T.; Li, Z.; Jean, J. S.; Kuo, C. Y. Antibiotic Tetracycline in the Environments - a Review. *Res. Rev.: J. Pharm. Anal.* **2015**, *4*, 86–111.

- (33) Johnson, J. L.; Yalkowsky, S. H. Reformulation of a New Vancomycin Analog: An Example of the Importance of Buffer Species and Strength. *AAPS PharmSciTech* **2006**, *7*, E33–E37.
- (34) Marczyński, M.; Käs Dorf, B. T.; Altaner, B.; Wenzler, A.; Gerland, U.; Liele, O. Transient Binding Promotes Molecule Penetration into Mucin Hydrogels by Enhancing Molecular Partitioning. *Biomater. Sci.* **2018**, *6*, 3373–3387.
- (35) Liele, O.; Ribbeck, K. Biological Hydrogels as Selective Diffusion Barriers. *Trends Cell Biol.* **2011**, *21*, 543–551.
- (36) Proctor, R. A.; Von Eiff, C.; Kahl, B. C.; Becker, K.; McNamara, P.; Herrmann, M.; Peters, G. Small Colony Variants: A Pathogenic Form of Bacteria That Facilitates Persistent and Recurrent Infections. *Nat. Rev. Microbiol.* **2006**, *4*, 295.
- (37) Foroozandeh, P.; Aziz, A. A. Insight into Cellular Uptake and Intracellular Trafficking of Nanoparticles. *Nanoscale Res. Lett.* **2018**, *13*, 339.
- (38) Weiss, L. The Cell Periphery. *International Review of Cytology*; Elsevier: London, 1969; Vol. 26, pp 63–105.
- (39) He, C.; Hu, Y.; Yin, L.; Tang, C.; Yin, C. Effects of Particle Size and Surface Charge on Cellular Uptake and Biodistribution of Polymeric Nanoparticles. *Biomaterials* **2010**, *31*, 3657–3666.
- (40) Dante, S.; Petrelli, A.; Petrini, E. M.; Marotta, R.; Maccione, A.; Alabastri, A.; Quarta, A.; De Donato, F.; Ravasenga, T.; Sathya, A.; Cingolani, R.; Proietti Zaccaria, R.; Berdondini, L.; Barberis, A.; Pellegrino, T. Selective Targeting of Neurons with Inorganic Nanoparticles: Revealing the Crucial Role of Nanoparticle Surface Charge. *ACS Nano* **2017**, *11*, 6630–6640.
- (41) Dawson, K. A.; Salvati, A.; Lynch, I. Nanotoxicology: Nanoparticles Reconstruct Lipids. *Nat. Nanotechnol.* **2009**, *4*, 84.
- (42) Patil, S.; Sandberg, A.; Heckert, E.; Self, W.; Seal, S. Protein Adsorption and Cellular Uptake of Cerium Oxide Nanoparticles as a Function of Zeta Potential. *Biomaterials* **2007**, *28*, 4600–4607.
- (43) The European Committee on Antimicrobial Susceptibility Testing. Breakpoint Tables for Interpretation of MICs and Zone Diameters, [http://www.eucast.org/clinical\\_breakpoints/](http://www.eucast.org/clinical_breakpoints/) (accessed 2020-05-07).
- (44) Li, X. Z.; Livermore, D. M.; Nikaido, H. Role of Efflux Pump (S) in Intrinsic Resistance of *Pseudomonas Aeruginosa*: Resistance to Tetracycline, Chloramphenicol, and Norfloxacin. *Antimicrob. Agents Chemother.* **1994**, *38*, 1732–1741.
- (45) Garzon, R.; Calin, G. A.; Croce, C. M. microRNAs in Cancer. *Annu. Rev. Med.* **2009**, *60*, 167–179.
- (46) Pan, X.; Wang, Z. X.; Wang, R. microRNA-21: A Novel Therapeutic Target in Human Cancer. *Cancer Biol. Ther.* **2010**, *10*, 1224–1232.
- (47) Si, M.; Zhu, S.; Wu, H.; Lu, Z.; Wu, F.; Mo, Y. mir-21-Mediated Tumor Growth. *Oncogene* **2007**, *26*, 2799.
- (48) Neilson, J. R.; Zheng, G. X.; Burge, C. B.; Sharp, P. A. Dynamic Regulation of miRNA Expression in Ordered Stages of Cellular Development. *Genes Dev.* **2007**, *21*, 578–589.
- (49) Zhang, P.; He, Z.; Wang, C.; Chen, J.; Zhao, J.; Zhu, X.; Li, C. Z.; Min, Q.; Zhu, J. J. *In Situ* Amplification of Intracellular microRNA with MNzyme Nanodevices for Multiplexed Imaging, Logic Operation, and Controlled Drug Release. *ACS Nano* **2015**, *9*, 789–798.
- (50) Deng, X.; Cao, M.; Zhang, J.; Hu, K.; Yin, Z.; Zhou, Z.; Xiao, X.; Yang, Y.; Sheng, W.; Wu, Y.; Zeng, Y. Hyaluronic Acid-Chitosan Nanoparticles for Co-Delivery of mir-34a and Doxorubicin in Therapy against Triple Negative Breast Cancer. *Biomaterials* **2014**, *35*, 4333–4344.
- (51) Zhang, P.; Yue, L.; Vázquez-González, M.; Zhou, Z.; Chen, W.-H.; Sohn, Y. S.; Nechushtai, R.; Willner, I. microRNA-Guided Selective Release of Loads from Micro/Nano Carriers Using Auxiliary Constitutional Dynamic Networks. *ACS Nano* **2020**, *14*, 1482–1491.
- (52) Messaoudi, S.; Greschner, A. A.; Gauthier, M. A. Progress toward Absorption, Distribution, Metabolism, Elimination, and Toxicity of DNA Nanostructures. *Adv. Ther.* **2019**, *2*, 1900144.
- (53) Lin, Y.-S.; Hurley, K. R.; Haynes, C. I. Critical Considerations in the Biomedical Use of Mesoporous Silica Nanoparticles. *J. Phys. Chem. Lett.* **2012**, *3*, 364–374.
- (54) Christopher, A. F.; Kaur, R. P.; Kaur, G.; Kaur, A.; Gupta, V.; Bansal, P. microRNA Therapeutics: Discovering Novel Targets and Developing Specific Therapy. *Perspect. Clin. Res.* **2016**, *7*, 68.

## **B.4.1 Supplementary information for: DNA strands trigger the intracellular release of drugs from mucin-based nanocarriers**

Supplemental information

for

### **DNA Strands Trigger the Intracellular Release of Drugs from Mucin-Based Nanocarriers**

*Ceren Kimna<sup>1</sup>, Theresa Monika Lutz<sup>1</sup>, Hongji Yan<sup>2</sup>, Jian Song<sup>1</sup>, Thomas Crouzier<sup>2</sup>, and  
Oliver Lieleg<sup>\*1</sup>*

<sup>1</sup>Department of Mechanical Engineering and Munich School of Bioengineering, Technical University of Munich, Boltzmannstraße 11, 85748 Garching, Germany

<sup>2</sup>Division of Glycoscience, Department of Chemistry, School of Engineering Sciences in Chemistry, Biotechnology and Health, KTH Royal Institute of Technology, AlbaNova University Center, 106 91 Stockholm, Sweden

\* Corresponding author

Prof. Dr. Oliver Lieleg

Department of Mechanical Engineering and Munich School of Bioengineering,  
Technical University of Munich,

Boltzmannstraße 11, 85748 Garching, Germany

e-mail: [oliver.lieleg@tum.de](mailto:oliver.lieleg@tum.de),

phone: +49 89 289 10952, fax: + 49 89 289 10801

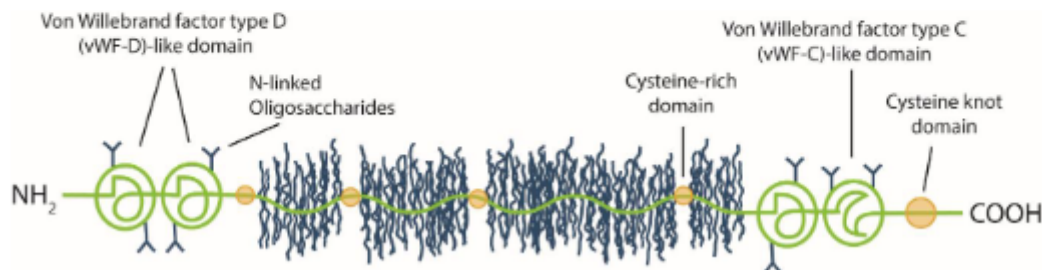
## 1. Mucin purification and modification with DNA

### 1.1. Mucin purification

Porcine gastric mucin MUC5AC was purified manually as described previously.<sup>1</sup> In brief, gastric mucus was obtained from gently rinsed pig stomachs by manual scraping the surface of the gastric tissue. The collected mucus was diluted 5-fold in a sodium phosphate buffer (10 mM, pH = 7.0) containing 170 mM NaCl and 0.04 % (w/v) sodium azide (Carl Roth, Karlsruhe, Germany) and stirred at 4 °C overnight. Cellular debris was removed *via* two centrifugation steps (first run: 8300 g at 4 °C for 30 min; second run: 15000g at 4 °C for 45 min), and a final ultracentrifugation step (150000 g at 4 °C for 1 h). Subsequently, the mucins were purified by size exclusion chromatography using an ÄKTA purifier system (GE Healthcare, Munich, Germany) and an XK50/100 column packed with Sepharose 6FF. The obtained mucin fractions were pooled, dialyzed against ultrapure water, and concentrated by cross-flow filtration. The concentrates were then lyophilized and stored at -80 °C until further use. With this purification procedure, highly functional mucin is obtained; however, our mucin samples also contain small amounts of protein impurities as well as mucin-associated DNA.

### 1.2. Mucin structure

The mucin is a large glycoprotein. Its terminal ends are partially folded, whereas the central region is extended due to their highly glycosylation. These glycans constitute about two-thirds of the molar mass of the molecule. Some of these carbohydrates contain negatively charged sulfate groups and sialic acids, which render the mucin molecule overall polyanionic (**Fig. S1**).



**Figure S1: Schematic representation of the mucin structure.**

In the main paper, to investigate the reversibility of the condensation process, which creates nanoparticles from mucin macromolecules, the size of condensed mucins is investigated in different states (*i.e.*, condensed and subjected to different pH levels, enzymatic environments, or triggered) by dynamic light scattering (DLS). For comparison, we here show similar size DLS measurements (**Table S1**) conducted with mucins from a freshly prepared solution (without any condensation agent). Therefore, freeze-dried mucin was solubilized in ddH<sub>2</sub>O (0.1 mg/mL) and then analyzed as in the main paper.

**Table S1:** DLS results obtained for a freshly prepared mucin solution (0.1 mg/mL)

	Intensity-average hydrodynamic size [nm]	Area [%]	Polydispersity Index (PDI)
Peak 1	1523	87.2	0.74
Peak 2	25.22	12.8	

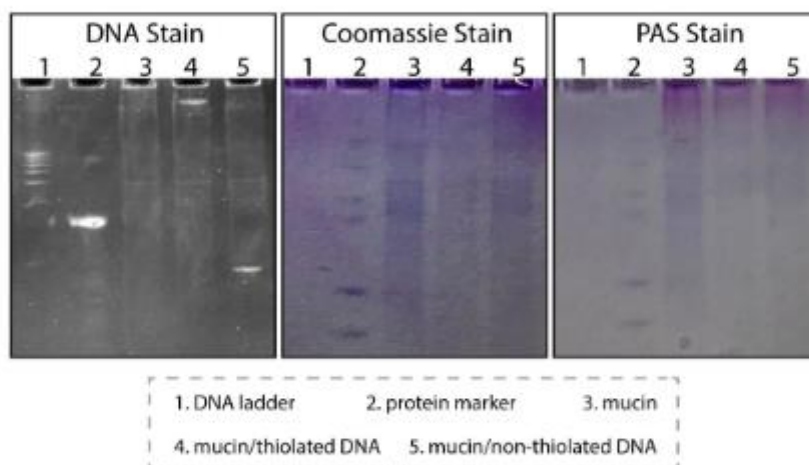
### 1.3. Fluorescence labeling of mucin

A carboxy modified ATTO dye (Atto488, ATTO-TEC GmbH, Siegen, Germany) was conjugated to mucin *via* carbodiimide chemistry. In brief, 5 mM EDC and 5 mM sulfo-NHS were added to the dye solution ( $C_{\text{ATTO}} = 1.0$  mg/mL in MES buffer (10 mM, pH = 5)) and incubated at room temperature in a light excluded environment for 3 h. This extended incubation time ensured that the remaining free EDC was hydrolyzed before mucin was added to avoid crosslinking of the mucin molecules. In parallel, 40 mg of purified MUC5AC was dissolved in 19 mL PBS (10 mM, pH = 7). Then, the solutions were thoroughly mixed and again allowed to react at RT for 3 h. To remove unbound dye molecules, the mixture was dialyzed against ultrapure water for 2 days (molecular weight cut-off = 300 kDa). The labeled mucins were then lyophilized and stored at - 80 °C until further use.

### 1.4. Verifying the specificity of DNA/mucin interactions

For the detection of mucin glycoproteins, SDS gels were stained with a PAS (periodic acid/Schiff solution) set. In brief, after DNA and Coomassie staining, the gel was placed into an 0.5 % periodic acid solution (Carl Roth, Germany) and incubated for 7 min while shaking at RT. Afterwards, the gel was rinsed with distilled water and carefully transferred into 100 mL of Schiff's reagent (Carl Roth, Germany). After incubation for 15 min, the gel was rinsed

with tap water and then imaged. Here, mucin was stained in a light pink color as shown in the bands of columns 3, 4 and 5 (**Fig. S2**).



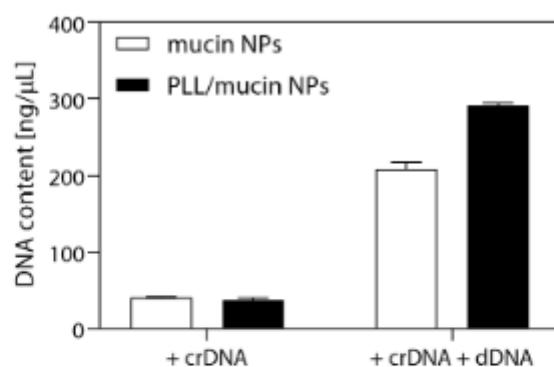
**Figure S2: Electrophoretic separation of triple-stained mucin and DNA/mucin mixtures.** The same gel is imaged after DNA, Coomassie and PAS staining to show DNA, protein and glycoprotein (= mucin) components, respectively.

## 2. Characterization of mucin-based NPs

### 2.1 Determining the amount of crDNA conjugated to mucin and the amount of dDNA needed for triggering NP dispersal

First, mucin was solubilized at a concentration of 1 mg/mL and incubated with the crDNA strands. Then, unmodified and PLL-coated mucin NPs were prepared as described in the main text. Unbound crDNA molecules were removed by dialyzing the samples against ddH<sub>2</sub>O for 2 days. Afterwards, the DNA content of the mucin-NP samples was measured spectrophotometrically (Nanodrop-1000, Thermo Fischer Scientific, Ulm, Germany).

Since the manually purified is associated with DNA (content ~ 5 ng/μL), this value was subtracted from those obtained from crDNA conjugated mucin samples ( $C_{\text{crDNA}} = \sim 40 \text{ ng}/\mu\text{L}$ , **Fig. S3**). With this approach, we determined that ~13 crDNA molecules can bind to a single mucin molecule. With the same strategy, we found that the PLL coating did not affect the crDNA content; this was expected since the crDNA conjugation was performed prior to PLL coating.



**Figure S3: single-stranded DNA content of mucin and PLL/mucin NPs after crosslinking and dDNA incorporation.** Data shown represent mean values, error bars denote the standard deviation as obtained from  $n = 3$  independent samples.

The protein sequence of MUC5AC (the mucin molecule used in this study) was retrieved from the database UniProtKB (<https://www.uniprot.org>, 25th September 2018, Accession number: A0A287ANG4). From this sequence, we can estimate that a single mucin molecule comprises 270 cysteine; however, 109 of them are located in the glycosylated region of the glycoprotein, where they are unlikely to interact with the crDNA strands due to a combination of electrostatic repulsion and steric effects. The remaining cysteines are located in the terminal regions ( $91 + 70 = 161$  in total) of the mucin macromolecule; however, also there, not all of them are accessible for disulfide bond formation (due to the presence of folded polypeptide strands in the vWF-C-like and vWF-D-like domains). By excluding these domains, we conclude that  $\sim 98$  cysteines from the mucin polypeptide backbone could be accessible in total. With this value, we can calculate the minimal conjugation efficiency of mucin/crDNA to be 13 DNA/98 cysteines (which corresponds to  $\sim 13\%$ ).

Next, the trigger DNA (dDNA) was added to the crDNA-crosslinked mucin NPs, and excessive dDNA (that did not interact with the mucin NPs) was removed by dialysis. After 2 days of dialysis, the DNA concentration of the samples was determined as described above. With this approach, we measure  $\sim 75 \pm 4$  dDNA molecules bound per mucin molecule, which corresponds to 12 dDNA strands per crDNA/crDNA complex. For the PLL-coated mucin NPs, the corresponding value was found to be higher, *i.e.*,  $\sim 21 \pm 1$  dDNA strands per crDNA/crDNA cross-link. We interpret this finding such that electrostatic attraction forces



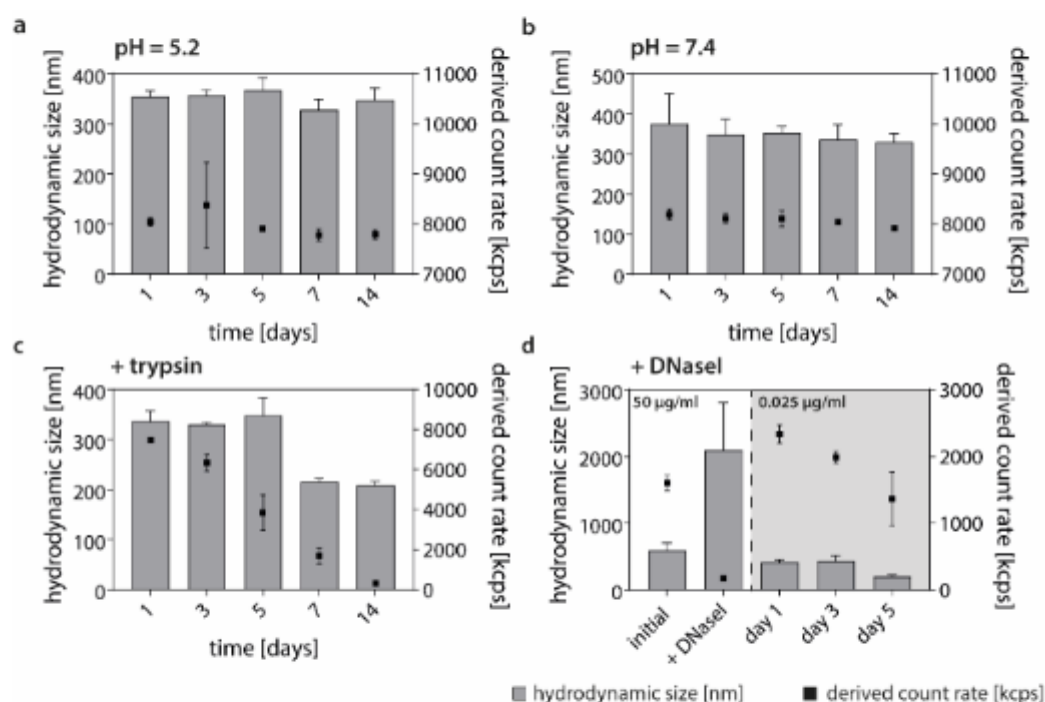
between the cationic coating of the NPs and the negatively charged DNA trap dDNA strands on the NP surface.

## **2.2. Stability of mucin-based NPs**

We analyzed the stability of DNA-cross-linked mucin NPs when subjected to different buffer conditions that mimic distinct, physiologically relevant challenges. In this particular set of experiments, we tracked two parameters describing the mucin NP population: the average NP size and the derived count rate, the latter of which is a function of the number of intact NPs. First, we incubated the DNA-stabilized mucin-based NPs at two different pH levels, *i.e.*, at 7.4 and 5.2. Those values were chosen as they represent cytoplasmic and endosomal pH levels, respectively. Importantly, we found that even after extended incubation for 14 days at 37°C, the mucin-based NPs maintained their condensed configuration and the derived count rate remained virtually constant as well (**Fig. S4a,b**). At the same time, the polydispersity index (PDI) of the NPs showed only little variation (**Table S2**), which indicates moderately homogeneous size distributions and the presence of only a few aggregates.<sup>2</sup> Of course, in an intracellular environment, the mucin-based NPs will also be exposed to enzymatic attack. Since the NPs are formed from a proteinous component (mucin), we challenged the DNA-stabilized mucin-based NPs with trypsin. After NP exposure to this enzyme, we observed a slow decrease in the derived count rate over time (**Fig. S4c**). At the same time, the size of the mucin-based NPs remained relatively constant during the first 5 days and then started to decrease as well. This suggests that the mucin-based NPs are somewhat vulnerable towards enzymatic digestion with trypsin. Previously, we demonstrated that a trypsin treatment of mucins mainly removes the terminal domains of the glycoprotein but leaves the glycosylated central region of mucins largely intact.<sup>3</sup> With this information in mind, both the decrease in the count rate and average size of mucin-based NPs can be interpreted as gradual enzymatic digestion of the NPs. This slow degradation is probably initiated at the termini of the mucin glycoproteins. However, the protease seems not to be able to easily attack mucin/mucin cross-links established *via* crDNA linked to cysteine residues of the mucin backbone.

Those DNA cross-links should, however, be degradable by DNaseI, since this enzyme can attack the DNA backbone by catalyzing the hydrolytic cleavage of phosphodiester linkages (**Fig. S4d**). Indeed, when the mucin-based NPs were exposed to a high concentration of this

enzyme (50 µg/mL, grey shaded area), we found a clear response of the NPs: after only 4 h of incubation, we observe a rapid size increase. However, whereas this proves once more that it is indeed the DNA-based cross-links that stabilize the mucin-based NPs, this DNaseI concentration is much higher than the average levels present in human serum (which are in the range of 3–24 µg/mL).<sup>4</sup> Interestingly, when incubated with a physiological DNaseI concentration (0.025 µg/mL), the mucin-based NPs particles were relatively stable over time: we only detected with a slight size reduction after 3 days, which was accompanied by a moderate decrease in the derived count rate. This suggests that the risk of rapid NP degradation in the bloodstream environment is relatively low.



**Figure S4: Stability of mucin-based NPs at different pH levels and in the presence of enzymes.** **a,b**, Hydrodynamic size measurements of mucin-based NPs at pH = 7.4 (**a**) and 5.2 (**b**). **c,d** Degradation behavior of mucin-based NPs in the presence of trypsin (**c**), and DNase I at two concentrations (**d**). Data shown represents mean values, error bars denote the standard deviation as obtained from  $n = 5$  independent samples.

**Table S2: PDI values of mucin NPs that were incubated at different conditions for up to 14 days.**

incubation condition	PDI value				
	Day 1	Day 3	Day 5	Day 7	Day 14
pH = 7.4	0.15	0.17	0.21	0.35	0.24

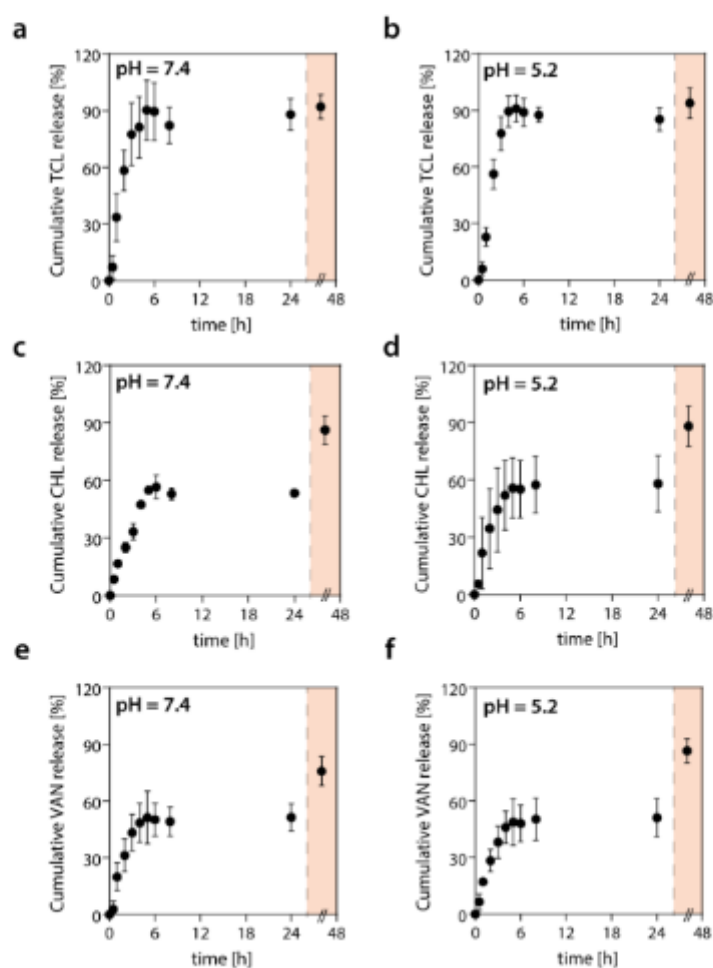
pH = 5.2	0.10	0.13	0.12	0.17	0.16
trypsin	0.18	0.19	0.32	0.41	0.48
DNase I (0.025 µg/mL)	0.19	0.26	0.61	-	-
DNase I (50 µg/mL)	0.21	0.81*	-	-	-

\* data was taken after 4 h

### 3. Drug loading and release profiles

#### 3.1 Drug release including a terminal drug release event triggered by heating

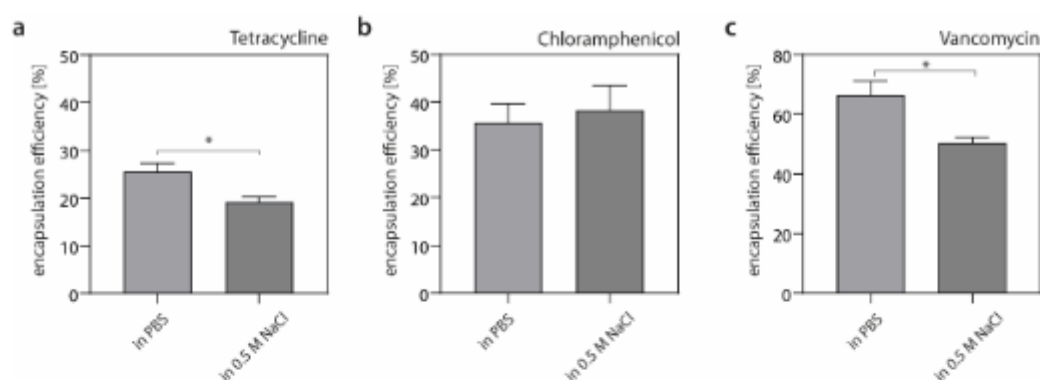
After drug release from the mucin NPs was completed, *i.e.*, when a plateau in the release profiles was reached after ~24 h, the NP suspensions were heated up to 75 °C (which exceeds the melting temperature of the crDNA/crDNA hybridizations) and the final drug concentration was quantified (**Fig. S5**).



**Figure S5: Extended drug release profiles.** The data points after the dashed line (red area) show the drug amount detected after subjecting the NPs to a heating step (75°C). The data shown represents mean values, error bars denote the standard deviation as obtained from  $n = 3$  independent samples.

### 3.2 Encapsulation efficiency of mucin NPs prepared at different salt concentrations

To check whether the charge state of the drugs is a relevant factor for determining their loading capacity into mucin NPs, we prepared drug loaded NPs in both, physiological buffer (containing 154 mM NaCl) and buffer supplemented with 0.5 M NaCl. After dialysis in the corresponding buffers, the drug entrapment efficiency was determined for both cases as described in the main text. Indeed, at the higher salt content, we observed a decrease in the encapsulation efficiency of both, positively and negatively charged drugs (**Fig. S6**). In contrast, no significant change occurred for the uncharged drug. Therefore, those results suggest that electrostatic interactions between drug molecules and mucin contribute to the loading capacity of the generated NPs.

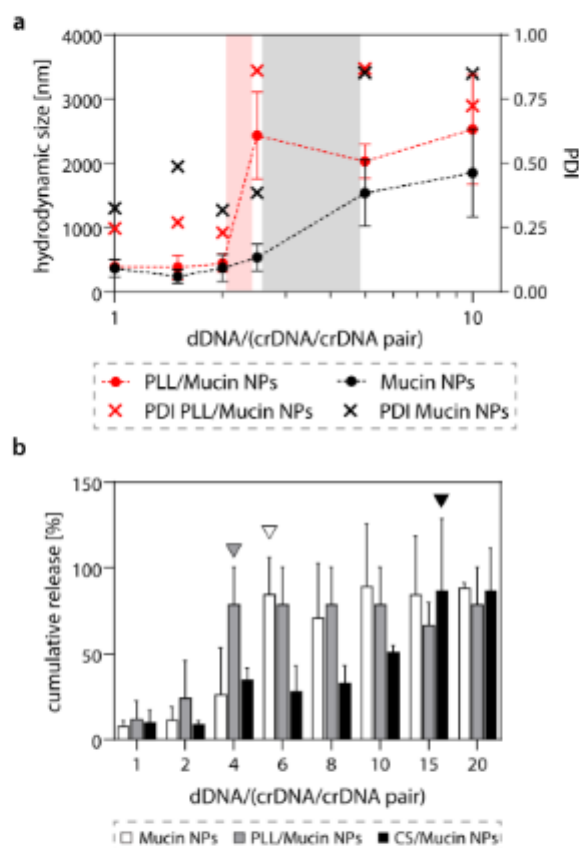


**Figure S6: Tetracycline (a), Chloramphenicol (b) and Vancomycin (c) encapsulation efficiency of mucin NPs in different salt conditions.** The data shown represents mean values, error bars denote the standard deviation as obtained from  $n = 5$  independent samples.

### 3.3 Determining the minimal dDNA concentration required for triggering drug release from mucin NPs

Ideally, each dDNA molecule could open a crDNA/crDNA pair. However, we experimentally determined above (**Fig. S3**) that, at the concentrations used here, ~12 dDNA strands per crDNA/crDNA are required.

To determine the minimum dDNA concentration needed to initiate the conformational change of mucin NPs into elongated objects, we exposed PLL-coated and uncoated mucin NPs to a serially diluted dDNA solution, where the ratio (number of dDNA strands/number of crDNA/crDNA complexes) was adjusted from 0.1 to 10. Then, the samples were characterized in terms of their hydrodynamic size and PDI (Fig. S7).



**Figure S7: a, Light scattering measurements of mucin NPs under a dDNA gradient showing the threshold dDNA concentration required to force the particulate structure to unfold. b, Cumulative drug release from mucin NPs (unmodified, PLL and CS-coated).** Triangles show the minimum number of dDNA required to obtain an efficient drug release.

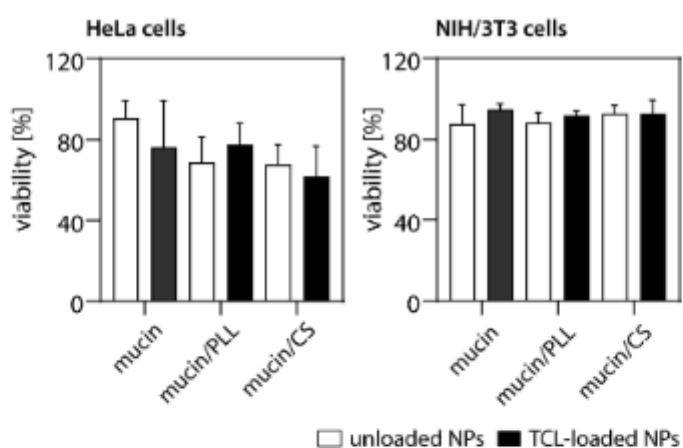
After conducting those DLS experiments, three variants of TCL-loaded NPs (unmodified, CS-coated, and PLL-coated) were prepared, and drug release was triggered from these samples by adding different concentrations of dDNA strands (1–20 dDNA molecules per crDNA/crDNA cross-link). The obtained cumulative drug release was quantified after 6 h of incubation at RT.

PLL-coated NPs required a lower amount of dDNA strands to obtain a cumulative release of at least 50% than uncoated mucin-based NPs. In contrast, CS-coated NPs required a larger concentration of dDNA (*i.e.*, 15 dDNA strands per crDNA/crDNA crosslink) to obtain a similarly high level of drug release as for the other two mucin NP variants. This finding can be explained by the strong electrostatic interactions occurring between the polycationic CS coating and the negatively charged DNA strands.

#### 4. *In vitro* cell experiments with mucin NPs

##### 4.1. *In vitro* cytotoxicity of mucin NPs

The viability of HeLa, NIH/3T3 and THP-1 derived macrophage type 0 after incubation with different mucin NPs (see main text) was evaluated with a WST-1 assay. Cells incubated with only cell culture medium were used as a negative control (NC). First, cells from three separate well plates ( $5 \times 10^3$  cells/well of a 96-well plate) were incubated with NPs. After incubating cells with NPs for predetermined time periods (1, 4 and 24 h for macrophages; 24 h for HeLa and NIH/3T3 cells). The medium was replaced with a WST-1 solution (10% v/v in each incubation medium). After an incubation time of 30 min, the absorbance of the medium at 450 nm was measured with a plate reader (Victor3, Perkin Elmer, Rodgau, Germany). The cellular viability was calculated by normalizing the absorbance value of NP-treated cells to that obtained for the NC (**Fig. S8** for HeLa and NIH/3T3 cells, **Fig. 3c** for macrophages).

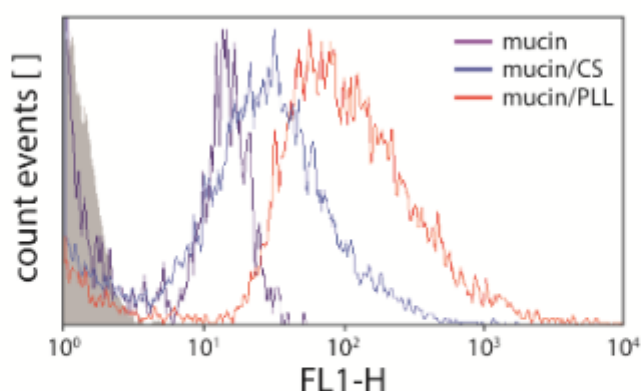


**Figure S8:** *In vitro* viability of HeLa and NIH/3T3 cells incubated with mucin NPs for 24 h. Data shown represents mean values, error bars denote the standard deviation as obtained from  $n=9$  independent samples.

##### 4.2. NP internalization verified by FACS

NPs used for FACS experiments were made from fluorescently-labeled mucins. All FACS measurements were performed in the presence of Trypan Blue (TB) to quench the fluorescence signal arising from NPs bound to the cell membrane. A remarkable increase in

the fluorescence intensity was observed for the HeLa cells incubated with surface-modified NPs. This demonstrates the successful cellular uptake of those NPs (**Fig. S9**).



**Figure S9: FACS examination.** FACS examination of HeLa cells incubated with three different mucin NP variants for 4 h: unmodified mucin NPs, CS-coated mucin NPs and PLL-coated mucin NPs. The grey area represents the control cell population which was not incubated with any mucin NPs.

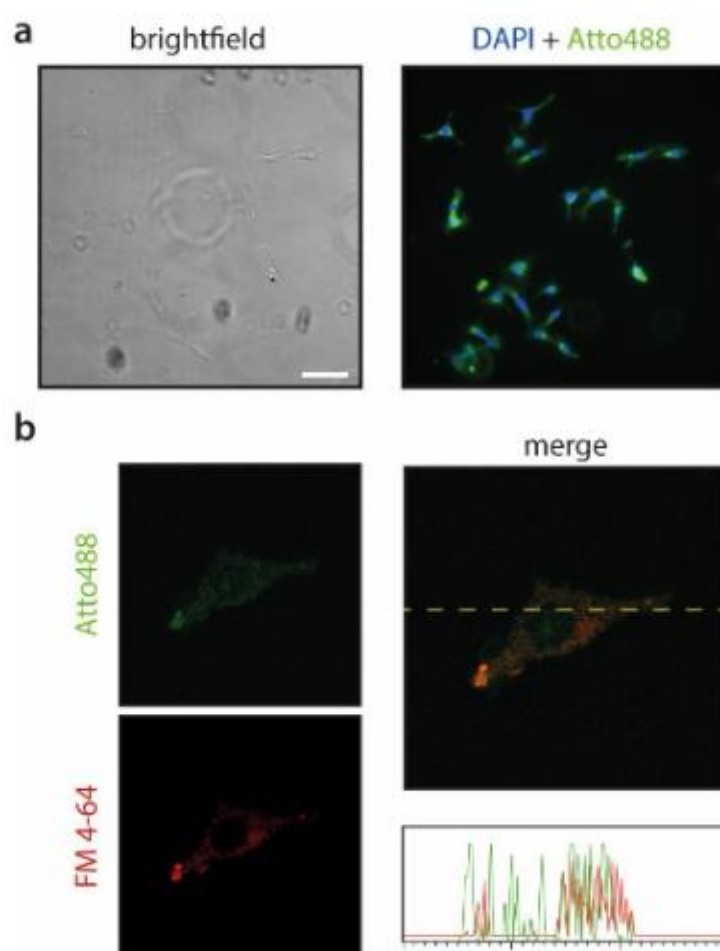
#### 4.3. Fluorescence microscopy and CLSM imaging

NPs used for fluorescence and CLSM imaging were made from fluorescently labeled mucins. HeLa cells were seeded at a density of 6,000 cells/well into a  $\mu$ -Slide 8-well ibidiTreat plate (ibidi GmbH, Gräfelfing, Germany), covered with 200  $\mu$ L MEM medium (supplemented with 10% v/v FBS, 2 mM L-glutamine and 1% v/v non-essential amino acid solution) and incubated for 24 h. Then, one-fourth of the culture medium (i.e., 50  $\mu$ L) was replaced with a mucin NP solution, and the NPs were allowed to interact with the cells for 4 h. Then, the cells were washed twice with DPBS and fixed with 4% formalin. 4,6-diamino-2-phenylindole (DAPI, Sigma Aldrich; 300 nM in PBS) was used for nucleus staining. The images shown in **Fig. S10a** were acquired on a DMI8 Leica microscope (Leica, Wetzlar, Germany) using a 20 $\times$  lens (PL Fluotar 20 $\times$ /0.70, Leica) and a digital camera (Orca Flash 4.0 C11440, Hamamatsu, Japan).

A putative colocalization of NPs and cellular endosomes was tested with CLSM. After 24 h of cell cultivation, one-fourth of the medium (i.e., 50  $\mu$ L) was replaced with the mucin NP solution containing 1  $\mu$ L of endosome marker (FM 4-64; Invitrogen T13320, 10  $\mu$ g/mL in ddH<sub>2</sub>O), and the cells were further incubated for additional 24 h. Next, the cells were washed twice with DPBS, fixed with 4% formalin. Confocal imaging was performed on a Leica TCS



SP5 II setup (Leica, Wetzlar, Germany) comprising a DMI6000 microscope corpus (Leica) and a 40x oil immersion objective (HCX PL APO; NA = 1.25, Leica). An argon laser (a laser power of 40 % was selected) was used to excite fluorescence from the atto488-labeled mucin NPs at 488 nm, while the endosomes were detected at wavelengths between 590 – 750 nm. High-resolution images of the cells were analyzed with the software ImageJ (Fiji). The green fluorescent spots in **Fig. S10b** represent mucin NPs that were able to escape endosomes, whereas signals obtained from NPs trapped in endosomes overlap with the endosomal marker and thus give a yellow/orange color when the images are merged. We speculate that this good result is, at least in part, due to the cationic surface of the PLL-coated mucin NPs.<sup>3</sup>



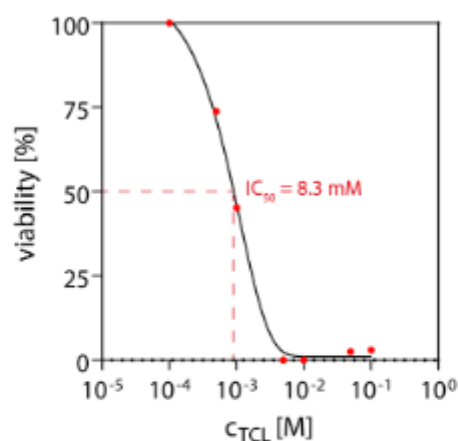
**Figure S10: Localization of fluorescently labeled mucin/PLL NPs in HeLa cells.** **a**, Fluorescence microscopy images of HeLa cells incubated with NPs (green) for 24 h. Cell nuclei were stained with DAPI (blue). The scale bar shown in (a) represents 20  $\mu$ m and applies to (b) as well. **b**, CLSM image of a HeLa cell where endosomes

are stained with FM4-64 (red) and the NPs are stained with Atto488 (green). The profile in the lower right corner denotes the fluorescence intensity variations measured along the yellow dashed line; the red line represents the location of endosomes and the green line represents mucin NPs.

#### 4.4. $IC_{50}$ value determination for TCL

The half-maximal inhibitory concentration of TCL ( $IC_{50}$ ) was assessed with a water-soluble tetrazolium (WST-1) assay (Sigma Aldrich). In brief, TCL solutions ( $c = 0.1 - 100$  mM) were incubated with HeLa cells ( $5 \times 10^3$  cells/well of a 96-well plate) for 24 h and the medium in the wells was replaced with a solution containing 20  $\mu$ L WST-1 per 1 mL medium. After 30 min of incubation, the absorption of the medium was measured at an excitation wavelength of 450 nm (Victor3 plate reader, Perkin Elmer, Rodgau, Germany).

Then, the cell viability was calculated by normalizing the absorbance value obtained for drug-treated HeLa cells to that obtained for the negative control (where cells were only incubated with cell culture medium). The cell viability was then plotted against the concentration of the initial drug feed, and the half-maximal growth inhibition ( $IC_{50}$ ) was determined to be 8.4 mM, *i.e.*, where the cells showed 50% viability (**Fig. S11**).

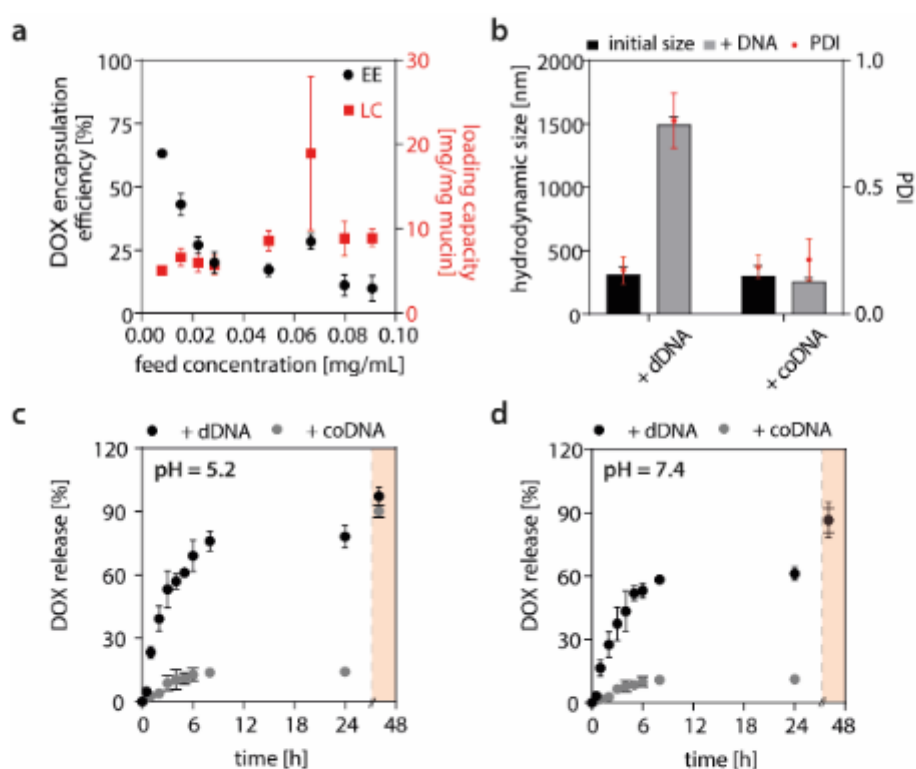


**Figure S11: Concentration-dependent cytotoxicity of TCL towards HeLa cells.** The TCL concentration corresponding to the viability of HeLa cells of 50% is then selected as the  $IC_{50}$  value of TCL.

## 5. Preparation of DOX-loaded mucin NPs for autonomous drug release in target cells

Prior to *in vitro* cell culture experiments, DOX-loaded nanoparticles were characterized in terms of drug encapsulation and loading capacity, on-demand configurational change and release profiles at pH = 5.2 and 7.4 (**Fig. S12**). First, drug loading experiments were carried out as described in the Methods section in a DOX feed range of 0.01 – 0.09 mg/mL (**Fig. S12a**). The on-demand reconfiguration of the DOX-loaded NPs was determined by measuring the change in their hydrodynamic size after addition of a dDNA (**Fig. S12b**). In these experiments, coDNA was used as a control.

To determine the release profiles at pH = 5.2 and 7.4, 5 mL of DOX-NP suspensions were placed in dialysis tubes and the release is initiated by adding 50  $\mu$ L of a 100 mM dDNA solution (**Fig. S12c,d**). Next, the DOX content of the NPs were determined.



**Figure S12:** **a**, DOX encapsulation efficiency and loading capacity of mucin NPs (n = 3). **b**, On-demand opening of DOX-loaded mucin NPs (n = 5) is not possible with the addition of a random control DNA (coDNA), but a trigger DNA (dDNA). **c**, **d**, The cumulative release profiles of DOX-loaded mucin-based NPs (n = 3) at pH = 5.2 (**c**) and 7.4 (**d**). The data points after the dashed line (red area) show the drug amount detected after subjecting the NPs to a heating step (75°C). The data shown represents mean values, error bars denote the standard deviation.

## 6. Autonomous drug release triggered by intracellular microRNA

### 6.1. Real time-PCR

Expected differences in miR-21 expression levels were confirmed for the two cell lines used in this study, i.e., HeLa (target cells) and NIH/3T3 (control cells), with RT-PCR. First, HeLa and NIH/3T3 cells were cultured to reach approximately 95 % confluency as described in the Methods section. The total RNA content of the cells was extracted (GeneJet RNA Purification Kit, Thermo Fisher), and the RNA concentration was determined using a Nanodrop spectrophotometer. 2000 ng of total RNA was reverse-transcribed into cDNA by using High-Capacity cDNA Reverse Transcription Kit (Thermo Fisher) combined with miR-21 and U6 stem-loop primers. Both stem-loop RT primers were designed according to the method developed by Chen et al.<sup>6</sup>

5'-GTCGTATCCAGTGCAGGGTCCGAGGTATTTCGCACTGGATACGACTCAACA-3'

(miR-21 stem-loop)

5'-GTCGTATCCAGTGCAGGGTCCGAGGTATTTCGCACTGGATACGACAAAATA-3'

(U6 stem-loop)

Following cDNA synthesis, RT-PCR was performed using primers designed in the studies by Xu et al. and Zhang et al.:<sup>7,8</sup>

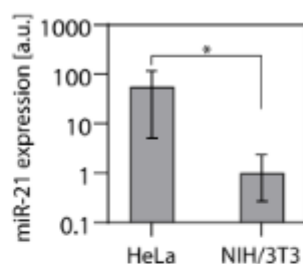
5'-CTCGCTTCGGCAGCACA-3' (forward U6)

5'-AACGCTTCACGAATTTGCGT-3' (reverse U6)

5'-GCCCCTAGCTTATCAGACTGATG-3' (forward miR-21)

5'-CAGTGCAGGGTCCGAGGT-3' (reverse miR-21)

RT-PCR was carried out using the PowerUp SYBR Green Master Mix (Applied Biosystems, Thermo Fisher, Waltham, MA, USA) in a StepOnePlus Real-Time PCR System (Thermo Fisher). Amplification signals were observed between the cycles 15 and 35. U6 was used as an internal control to normalize the miRNA-21 levels.

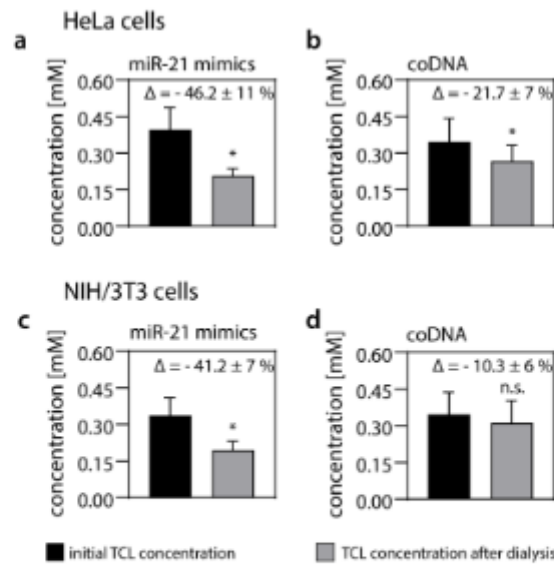


**Figure S13: Quantitative real-time PCR analysis of miR-21 in HeLa and NIH/3T3 cells.** Data shown represent mean values, error bars denote the standard deviation as obtained from  $n = 3$  technical replicates.

## 6.2. Intracellular drug release experiments

A series of control experiments were performed to verify that the release of TCL from mucin NPs is highly specific, i.e., that it is only triggered by the correct DNA-base pairing. First, TCL-loaded NPs were incubated with HeLa or NIH/3T3 cells for 4 h as described in the main paper (See “Intracellular drug release” in the Methods section). Next, cells were transfected with either miR-21 mimics (i.e., trigger strand) or coDNA. To quantify the amount of liberated TCL, cytosol fractions of cell lysates were collected as described in the main text, and their TCL content was determined spectrophotometrically (**Fig. S14**, black bars). Then, those cytosol fractions were subjected to a dialysis step (see main text), and the remaining TCL amount was determined (**Fig. S14**, grey bars). With this procedure, a significant reduction in the TCL amount was achieved for HeLa as well as NIH/3T3 cells transfected with miR-21 mimics; this shows that, here, free (= liberated) TCL was present in the cytosol. In contrast, no significant reduction was observed for the control group of NIH/3T3 cells, where coDNA was transfected (**Fig. S14, d**).

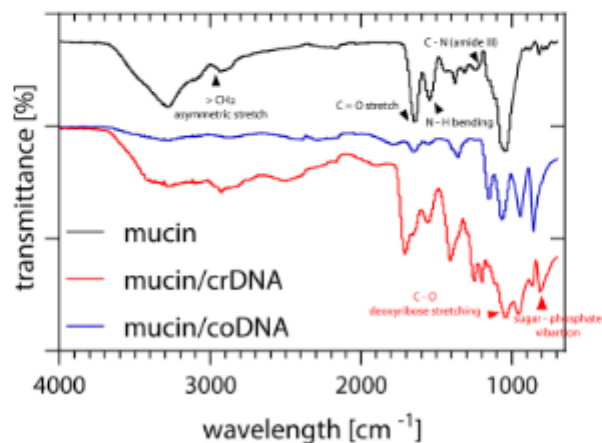
Importantly, for HeLa cells, which produce miR-21 strands, our results indicated the successful release of TCL from the mucin NPs even without transfection of the correct trigger DNA strands (**Fig. S14, b**) – albeit with lower efficiency than when the miR-21 mimics are supplied externally. This agrees with our assumption that cytosolic miR-21 strands produced by the HeLa cell line should be sufficient to open the mucin NPs. At the same time, it shows that this autonomous liberation of TCL from mucin NPs is – at least to some extent – cell-specific.



**Figure S14: TCL concentration in the cytosol fractions of HeLa and NIH/3T3 cells, respectively, before (black bars) and after dialysis (grey bars).** Cells are transfected with either miR-21 mimics or coDNA, as defined on top of each graph. Insets show the percentage of TCL concentration reduction in the cytosols achieved by cytosol dialysis and indicates the liberated drug amount. Data shown represent mean values, error bars denote the standard deviation as obtained from  $n = 6$  independent samples.

## 7. Fourier-transform infrared spectroscopy (FT-IR)

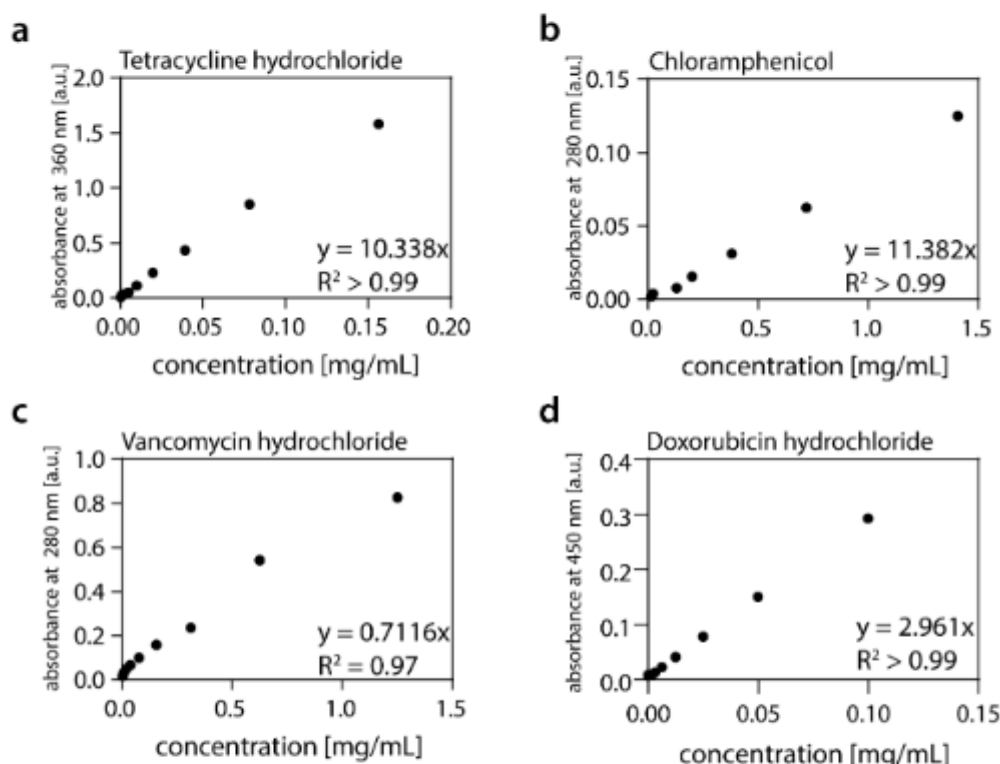
Mucin/DNA mixtures were prepared as described in the main text and pre-frozen at  $-20\text{ }^{\circ}\text{C}$ . Next, the samples were lyophilized for 1 day and analyzed with Fourier Transform Infrared Spectroscopy (FT-IR, Vertex 70 FTIR, Bruker, Germany) in the wavelength range of  $4000$  to  $700\text{ cm}^{-1}$ .



**Figure S15: FT-IR diagram of mucin, mucin/crDNA and mucin/coDNA**

## 8. Calibration curves

Standard curves for the three drug solutions shown (**Figure S16**) were obtained by measuring the absorbances of serially diluted drug solutions (at 280 nm for CHL and VAN, at 360 nm for TCL and at 450 nm for DOX, respectively) with a spectrophotometer (specord 210, Analytikjena, Jena, Germany). In the concentration range tested here, a linear relation between the absorbance values and the drug concentration holds.



**Figure S16: Standard curves.** **a**, Tetracycline hydrochloride (TCL) **b**, chloramphenicol (CHL) **c**, vancomycin hydrochloride (VAN) and **d**, Doxorubicin standard curves which relate the absorbance of the respective drug solution and with the drug concentration.

## 9. DNA sequences

For the synthetic DNA sequences used in this study, the energy needed to fully break the structures formed with either crDNA, or antimir-21 ( $\Delta G$ ) was calculated by considering the longest stretch of complementary bases. Also, oligonucleotides used as crosslinkers were tested with the NUPACK software to ensure that they do not form any secondary structures<sup>9</sup>. The minimum free energy of the structures was calculated using nearest-neighbor empirical

parameters for oligonucleotides at 37 °C and in the presence of 5 mM Mg<sup>2+</sup> and 150 mM Na<sup>+</sup>.

**Table S3** and **Table S4** list the molecular design of the sequences and their properties such as dimerization energy, melting temperature, the number of hybridized base pairs and modifications.

**Table S3:** Designed oligonucleotide sequences. The table lists their dimerization energy, melting temperature and the possible number of hybridized base pairs when they interact with crDNA strands.

abbreviation	sequence from 5' to 3'	dimerization energy, ΔG (kcal/mol)	melting temperature (°C)	# of hybridized base pairs	modification at the 5' end
crDNA	AAAAGAAGCAAAGACAACCCGGGTAA	-18.57	60.6	8	thiol
dDNA	TTACCCGGGTTGTCTTTGCTTC	-43.99	75.3	22	-
coDNA	AATGAGCACAAACAGAAACGAAG	-3.61	N/A	2	-

**Table S4:** Designed oligonucleotide sequences for the HeLa-cell specific release experiments. The table lists their dimerization energy, melting temperature and the possible number of hybridized base pairs when they interact with antimir-21 strands.

abbreviation	sequence from 5' to 3'	dimerization energy, ΔG (kcal/mol)	melting temperature (°C)	# of hybridized base pairs	modification at the 5' end
antimir-21	TCAGTCTGATATCA	-10.97	48.2	8	thiol
miR-21 mimics	TATCAGACTGA	-15.61	39.0	11	-
coDNA-2	GGAATCCAAGTG	-1.95	N/A	2	-

## References

- Schömig, V. J.; Käsdorf, B. T.; Scholz, C.; Bidmon, K.; Lileg, O.; Berensmeier, S. An Optimized Purification Process for Porcine Gastric Mucin with Preservation of Its Native Functional Properties. *RSC Adv.* **2016**, *6*, 44932-44943.
- Gaumet, M.; Vargas, A.; Gurny, R.; Delie, F. Nanoparticles for Drug Delivery: The Need for Precision in Reporting Particle Size Parameters. *Eur. J. Pharm. Biopharm.* **2008**, *69*, 1-9.
- Käsdorf, B. T.; Weber, F.; Petrou, G.; Srivastava, V.; Crouzier, T.; Lileg, O. Mucin-Inspired Lubrication on Hydrophobic Surfaces. *Biomacromolecules* **2017**, *18*, 2454-2462.
- Macanovic, M.; Lachmann, P. Measurement of Deoxyribonuclease I (DNase) in the Serum and Urine of Systemic Lupus Erythematosus (SLE) - Prone NZB/NZW Mice by a New Radial Enzyme Diffusion Assay. *Clin. Exp. Immunol.* **1997**, *108*, 220-226.
- Kircheis, R.; Kichler, A.; Wallner, G.; Kurs, M.; Ogris, M.; Felzmann, T.; Buchberger, M.; Wagner, E. Coupling of Cell-Binding Ligands to Polyethylenimine for Targeted Gene Delivery. *Gene Ther.* **1997**, *4*, 409-418.
- Chen, C.; Ridzon, D. A.; Broomer, A. J.; Zhou, Z.; Lee, D. H.; Nguyen, J. T.; Barbisin, M.; Xu, N. L.; Mahuvakar, V. R.; Andersen, M. R. Real-Time Quantification of microRNAs by Stem - Loop RT - PCR. *Nucleic Acids Res.* **2005**, *33*, e179.
- Xu, X. M.; Qian, J. C.; Deng, Z. L.; Cai, Z.; Tang, T.; Wang, P.; Zhang, K. H.; Cai, J.-P. Expression of Mir-21, Mir-31, Mir-96 and Mir-135b Is Correlated with the Clinical Parameters of Colorectal Cancer. *Oncol. Lett.* **2012**, *4*, 339-345.



8. Zhang, P.; He, Z.; Wang, C.; Chen, J.; Zhao, J.; Zhu, X.; Li, C.-Z.; Min, Q.; Zhu, J.-J. *In Situ* Amplification of Intracellular microRNA with MNzyme Nanodevices for Multiplexed Imaging, Logic Operation, and Controlled Drug Release. *ACS Nano* **2015**, *9*, 789-798.
9. Zadeh, J. N.; Steenberg, C. D.; Bois, J. S.; Wolfe, B. R.; Pierce, M. B.; Khan, A. R.; Dirks, R. M.; Pierce, N. A. Nupack: Analysis and Design of Nucleic Acid Systems. *J. Comput. Chem.* **2011**, *32*, 170-173.

## B.5 A stable mucin based nanoparticle system for the co-delivery of hydrophobic and hydrophilic drugs

International Journal of Biological Macromolecules 215 (2022) 102–112



Contents lists available at ScienceDirect

International Journal of Biological Macromolecules

journal homepage: [www.elsevier.com/locate/ijbiomac](http://www.elsevier.com/locate/ijbiomac)



### A pH-stable, mucin based nanoparticle system for the co-delivery of hydrophobic and hydrophilic drugs

Theresa M. Lutz, Ceren Kimna, Oliver Lieleg<sup>\*</sup>

School of Engineering and Design, Department of Materials Engineering, Technical University of Munich, Boltzmannstraße 15, 85748 Garching, Germany  
Center for Protein Assemblies, Munich Institute of Biomedical Engineering, Technical University of Munich, Ernst-Otto-Fischer Str. 8, 85748 Garching, Germany

#### ARTICLE INFO

**Keywords:**  
Glycoprotein  
Hexperidin  
β-Carotene  
Swelling

#### ABSTRACT

Biopolymer-based drug carriers are commonly used for the development of safe delivery systems. However, biopolymer-based systems are often highly sensitive to the acidic pH levels in the stomach and release most of their cargo before they have reached their point of destination. Such premature drug release combined with the resulting high dose requirements is not cost-efficient and comes with the risk of unwanted side effects on non-target tissues/organs. This problem can be mitigated by the mucin-based drug carriers developed here, which exhibit good stability at acidic pH levels as proven by dynamic light scattering and enzymatic degradation tests with pepsin. In addition, the mucin-based particles can deliver hydrophobic and hydrophilic drugs simultaneously, which is demonstrated both with experiments performed under *in vitro* sink conditions and with drug transport tests involving eukaryotic cells as targets. As photo-induced cross-links covalently stabilize these particles, they can release their payload over time in a sustained manner. The drug carrier system introduced here combines good stability with high drug encapsulation efficiency and very good biocompatibility and thus may be valuable for a broad spectrum of applications in biological settings.

#### 1. Introduction

For their delivery, drugs are often embedded into carrier objects made from natural or synthetic sources [1,2]. Indeed, a broad range of drug delivery systems has been developed from synthetic polymers, some of which are biodegradable, whereas others are not [3]. Although biological and bio-derived polymers are typically well biodegradable and biocompatible, they are used less frequently than precisely tailored, synthetic polymeric carrier systems. A few examples of biomacromolecules (typically polysaccharides and proteins) employed as matrix components for drug carrier systems include chitosan, hyaluronic acid, agarose, dextran, gelatine, albumin, and collagen [4]. In either case, a key task of the carrier material is to provide properties that match the selected field of application: on the one hand, when applied to the human body, the carrier needs to be stable enough to resist uncontrolled degradation (which would result in premature drug release); on the other hand, the carrier matrix determines the release kinetics of the drug [5,6].

To achieve these two goals, there are various options of how to encapsulate a pharmaceutical compound into a carrier matrix: typical carriers used for drug encapsulation include polymer-based micro- or

nanoparticles [7], micelles [8], liposomes [9], hydrogel matrices [10], dendrimer-based particles [11], carbon nanotubes [12] and macromolecular coatings [13]. For a carrier system to efficiently transport drugs, it can be helpful if the matrix material interacts with the drug molecules by unspecific or specific binding. Of course, a compromise is needed between strong binding (which is helpful for drug loading) and weak binding (which is helpful for drug release). In addition to finding the right balance here, it is also challenging to transport both hydrophobic and hydrophilic drugs with the same carrier system.

Such a co-loading of polar and non-polar molecules is possible for particles of complex composition, such as particles comprising a mixture of hydrophilic and hydrophobic polymers [14], synthetic amphiphilic polymers [15,16], or mixtures of proteins/(bio-)polymers [17–19]. However, few versatile drug carrier systems are made from only one, naturally occurring biomacromolecule that achieves a similarly efficient co-loading of hydrophobic and hydrophilic molecules [20]. However, such a one-component, bio-derived system would be more practical and might also offer better biocompatibility than synthetic drug carriers. Albumin particles are a very promising candidate for this multi-faceted problem, but also those carriers come with limitations: this particulate system is only stable in a pH range from 4 to 9 [21,22]; thus, when

<sup>\*</sup> Corresponding author at: Technical University of Munich, Center for Protein Assemblies (CPA), Ernst-Otto-Fischer Straße 8, 85747 Garching, Germany.  
E-mail address: [oliver.lieleg@tum.de](mailto:oliver.lieleg@tum.de) (O. Lieleg).

<https://doi.org/10.1016/j.ijbiomac.2022.06.081>

Received 28 April 2022; Received in revised form 7 June 2022; Accepted 11 June 2022

Available online 17 June 2022

0141-8130/© 2022 Elsevier B.V. All rights reserved.

applied orally, the stability of albumin-based systems in the harsh acidic environment of the stomach is low [23,24].

Here, mucin glycoproteins, which constitute the fundamental structural and functional components of mucus, might be a suitable alternative. Mucins occur on the gastric and intestinal epithelium [25] and form stable gels – especially in the stomach. To maintain their functionality, these biomacromolecules have to cope with harsh pH conditions and need to resist enzymatic digestion [26]. Indeed, purified gastric mucins are remarkably stable – not only towards chemical challenges such as strong pH alterations and enzymatic attack but also towards thermal and physical sterilization methods [27]. In addition, the complex biochemical architecture of mucin glycoproteins can be beneficial when designing a versatile drug carrier system. Mucins are intrinsically amphiphilic: Their hydrophilic, strongly glycosylated core domain is flanked by two hydrophobic termini, and this might allow mucins to interact with both polar and non-polar drugs [28].

Moreover – depending on the pH level – mucins can be expected to be polyanionic and polycationic at the same time. The first property is established by anionic sulfate groups and sialic acid residues located in the strongly glycosylated core domain of the glycoprotein; the second property originates from non-glycosylated amino acids located in the termini of the polypeptide chain [29]. The detailed (calculated) distribution of the polarities and charges along the polypeptide chain of a MUCSAC molecule is shown in [30]. Indeed, mucin-based carrier objects such as DNA-crosslinked nanoparticles or ionically cross-linked coatings have been developed recently and served as suitable carrier matrices for selected molecules such as doxorubicin or different antibiotics [13,31]. However, co-loading of molecules with different polarities into mucin-based carrier particles has not been achieved yet.

Here, we introduce covalently stabilized particles generated from lab-purified porcine gastric mucins. Those mucin particles can be loaded with hydrophobic and hydrophilic antioxidants and efficiently transport molecules with different polarities into cells. Owing to the covalent cross-links keeping the mucins in a compacted particle configuration, these mucin particles are stable across a broad pH range. Moreover, the agglomeration of the mucin particles in an acidic environment temporarily protects them from rapid enzymatic degradation by pepsin. Finally, particle swelling gives rise to release kinetics that enables continuous cargo liberation over time. Thus, those biopolymer-based, non-toxic particles are excellent candidates for a drug carrier system that can be administered via the gastrointestinal tract.

## 2. Materials and methods

Unless stated otherwise, all chemicals used here were obtained from Carl Roth (Karlsruhe, Germany).

### 2.1. Mucin purification and functionalization with methacrylic anhydride

Porcine gastric mucins were purified as described in Schömig et al. [32]; this procedure is briefly outlined in the supplement (see supplement, section 1). For functionalization of the lab-purified mucins with methacrylic anhydride (MA;  $MW_{MA} = 154$  Da, Sigma Aldrich, St. Louis, USA), we followed procedures introduced by Duffy et al. [28] and Oläret et al. [33] with a few modifications. First, the mucins were dissolved at  $10 \text{ mg mL}^{-1}$  (w/v) in ultrapure water. Afterward, the solution was cooled on ice and titrated with 5 M sodium hydroxide (NaOH) until a pH value of 8.0 was reached. This pH value ensures optimal reaction conditions between the MA and amino/hydroxyl groups of mucins. Then, the mucin solution was mixed with a 94 % methacrylic anhydride solution ( $8.47 \times 10^{-4}$  mL methacrylic anhydride per mg mucin), and the mixture was gently stirred on ice. Here, using a larger batch of mucin (in the gram range) allowed for handling well-manageable quantities of methacrylic anhydride and enables us to employ the same batch of methacrylated mucin throughout the whole study. During the methacrylation step, the pH value of the solution was maintained at 8.0 for

24 h. Unbound MA was separated from the mucin-MA conjugates by centrifugation ( $4300 \times g$  for 10 min at  $4^\circ\text{C}$ ) and size exclusion chromatography (ÄKTA purifier system; GE Healthcare, Chicago, IL, USA) using an XK50/100 column packed with Sepharose 6FF. The collected fractions were lyophilized and stored at  $-80^\circ\text{C}$ .

### 2.2. Fabrication of photo-crosslinked mucin-particles

To prepare condensed mucin-particles, 1 % (w/v) mucin-MA was rehydrated in distilled water and mixed with 100 % glycerol in a 1:4 ratio under a strong stirring [34]. Then,  $12.5 \mu\text{L}$  of the radical photoinitiator 2-hydroxy-4'-(2-hydroxyethoxy)-2-methylpropiophenone (Irgacure 2959; Sigma Aldrich;  $200 \text{ mg mL}^{-1}$  in 70 % (v/v) ethanol) was added to 1.25 mL of the prepared mucin-MA/glycerol solution. After thorough mixing, the mucin-MA particles were covalently stabilized by photo-crosslinking the methacryloyl groups (UV treatment:  $365 \text{ nm}$ ,  $-10 \text{ mW cm}^{-2}$ ; M365L2, Thorlabs GmbH, Lübeck, Germany) for 15 min. The generated mucin particles were centrifuged at  $20,817 \times g$  for 10 min to remove the remaining glycerol. The particles generated with this method are very well soluble in aqueous solutions (without the need of adding any detergent) and thus were resuspended in either  $\text{ddH}_2\text{O}$ , aqueous buffer, or cell culture medium for further experiments.

### 2.3. Rheological experiments

To assess the viscoelastic properties of mucin-MA and mucin solutions/gels before and after UV exposure, a commercial shear rheometer (MCR 302, Anton Paar GmbH, Graz, Austria) equipped with a plate-plate geometry (25 mm) was employed using a plate separation of  $300 \mu\text{m}$ . UV-induced gelation was followed at a probing frequency of 1 Hz using a torque-controlled protocol ( $M = 5 \mu\text{Nm}$ ). The storage ( $G'$ ) and loss moduli ( $G''$ ) of the samples were recorded at  $20^\circ\text{C}$  for 25 min using a sampling rate of  $2 \text{ min}^{-1}$ . For those tests,  $150 \mu\text{L}$  of a sample solution was pipetted onto a transparent bottom plate (P-PTD200/GL, Anton Paar). The measurement was started; after 5 min, UV exposure (365 nm) was initiated to crosslink the mucin-MA molecules.

### 2.4. Indirect verification of successful mucin-methacrylation by fluorophore conjugation

Mucin-MA and mucin ( $1 \text{ mg mL}^{-1}$  each) were prepared in  $\text{ddH}_2\text{O}$  and mixed with  $1 \text{ mg mL}^{-1}$  fluorescein *o*-acrylate (Sigma Aldrich; dissolution ratio of 1:9 in 70 % EtOH: $\text{ddH}_2\text{O}$ ). The idea was to show that the mucin modification allows the mucin-MA molecule to react further with other acrylate groups (which are offered by the fluorescein conjugate). The mucins were dialyzed after adding the photoinitiator and subsequent UV irradiation (Spectrum™ Spectra/Por®7 Pre-treated RC Tubing, Roth, Germany MWCO: 50 kDa) against  $\text{ddH}_2\text{O}$  for 5 days to remove unbound fluorescein *o*-acrylate; then, the mucins were lyophilized. Successful fluorescent labeling of the mucins was verified as follows: The mucin solutions ( $1 \text{ mg mL}^{-1}$ ) were transferred into wells of a 96-well microtiter plate ( $100 \mu\text{L}$  per well), and the fluorescence signal was measured using a scanning multi-well spectrophotometer (Fluoroskan Ascent L, Thermo Fisher Scientific, Waltham, MA, USA; Ex/Em = 485/538 nm). To convert the determined values into binding capacities of the fluorescent dye towards the mucins, a standard curve was obtained for the fluorescein *o*-acrylate dye (see supplement Fig. S1).

### 2.5. Scanning electron microscopy (SEM)

The microarchitecture of mucin gels was analyzed using SEM (JBOL-JSM-6060LV, Jeol, Echting, Germany). For this purpose, cured mucin gel samples ( $\emptyset = 8 \text{ mm}$ ) were dehydrated by incubation in 50 %, 70 %, 80 %, and 100 % ethanol for 30 min each. After an additional incubation step in 100 % ethanol overnight, the samples were dried at the critical point, sputtered with a thin gold layer ( $\sim 10 \text{ nm}$ ) by a MED 020 super

device (BAL-TEC, Balzers, Liechtenstein) in a saturated argon atmosphere, and then imaged with SEM using an acceleration voltage of 8 kV. Images were recorded at  $\times 1000$  and  $\times 5000$  magnification.

## 2.6. Colloidal properties of UV-crosslinked mucin particles

The hydrodynamic size of photo-crosslinked mucin particles was characterized using dynamic light scattering (DLS). Furthermore, the particle stability was assessed with this technique by incubating mucin particles in biologically relevant fluids at different pH levels (at 37 °C). To do so, simulated body fluid (SGF; containing 80  $\mu\text{M}$  sodium taurocholate, 20  $\mu\text{M}$  lecithin, and 34.2 mM NaCl; pH = 1.6) [35] and simulated intestinal fluid (SIF; containing 3 mM sodium taurocholate, 0.2 mM lecithin, 19.12 mM maleic acid, 68.62 mM NaCl, and 34.8 mM NaOH; pH = 6.5) [35] were prepared. The samples were analyzed on a Litesizer 500 (Anton Paar, Graz, Austria) equipped with a 35 mW laser diode ( $\lambda = 658$  nm). All measurements were performed at  $(25.0 \pm 0.1)$  °C in automatic mode. Measurement points were acquired after sample incubation for 0.5 h, 1 h, 2 h, 3 h, 5 h, 7 h, 10 h, 24 h, 48 h, 72 h under static conditions at 37 °C (and at 4 °C for the control) and evaluated by analyzing the number-weighted size distribution over the time.

Furthermore, to determine the zeta potential of the generated particles at different conditions, the photo-crosslinked mucin particles were dispersed at a concentration of 12.5  $\mu\text{g mL}^{-1}$  in either 10 mM HEPES buffer (pH = 7.0) or SGF (here, to avoid damage to the zeta potential cuvette, the pH value was set to pH = 2.5 instead of 1.6), and placed into capillary cuvettes (Omega cuvette, Anton Paar). A subset of those prepared mucin particles was additionally incubated with either albumin or lysozyme (Sigma Aldrich) at room temperature overnight (using mucin: albumin or mucin: lysozyme ratio of 1:1). Then, the zeta potential of the particles was quantified via electrophoretic light scattering (ELS) using the Smoluchowski approximation of the Henry equation.

## 2.7. Enzymatic degradation tests

To obtain detectable mucin particle degradation products upon enzymatic treatment, the mucin particles were labeled with fluorescein *o*-acrylate. For this purpose, mucin particles were formed as described above; however, the mucins were dissolved together with the fluorescent dye (1 mg mL<sup>-1</sup> fluorescein *o*-acrylate per 10 mg mL<sup>-1</sup> mucin solution). After the centrifugation step, the mucin particles were resuspended directly in the buffer containing the respective test enzyme: 10 mM sodium phosphate buffer supplemented with 170 mM NaCl was prepared and supplemented with trypsin (trypsin (Sigma Aldrich): mucin ratio of 1:20; pH 8.0); the second test was conducted in 10 mM HCl containing pepsin (pepsin (Sigma Aldrich): 1 mg mL<sup>-1</sup>, pH = 3.0). Then, 100  $\mu\text{L}$  of the prepared fluorescently labeled mucin particles were pipetted into a trans-well insert (cellQART PET translucent, MWCO: 0.4  $\mu\text{m}$ ; Sabeu GmbH, Northeim, Germany) of a standard 24-well plate and incubated at 37 °C. Here, mucin degradation products (but not intact mucins) could pass the membrane and be collected in the reservoir (containing 500  $\mu\text{L}$  of the corresponding buffer) located below. After 0.5 h, 1 h, 2 h, 3 h, 5 h, 7 h, 10 h, and 24 h, 200  $\mu\text{L}$  of the reservoir solution were substituted with fresh buffer, and the fluorescent signal of the collected solution was measured (Ex/Em = 485/538; Fluoroskan Ascent).

## 2.8. Atomic force microscope (AFM)

To determine the size of the UV-crosslinked mucin particles in a dry state, images were acquired using a NanoWizard II APM (JPK Instruments, Berlin, Germany), using air tapping mode, and an OMCL-AC160TS-R3 cantilever (Olympus, Tokyo, Japan). First, 10  $\mu\text{L}$  of the mucin particle dispersion was pipetted onto a glass slide and allowed to air dry at room temperature for 5 d. After 30 min of thermal equilibration of the device (at room temperature), height images were

recorded (line rate: 1 Hz). Representative cross-sectional profiles were evaluated with the image processing software SPM (v.3.3.20, JPK).

## 2.9. Drug encapsulation efficiency of mucin particles

The particles were prepared as described in the section 'Fabrication of photo-crosslinked mucin-particles'; however, the required antioxidants/fluorescent dyes were added to the mucin solution before particle formation was initiated. Owing to the short particle stabilization time (15 min of UV irradiation) and the rapid separation of glycerol and unbound cargo from the generated mucin particles by centrifugation (10 min), a premature release of the encapsulated payload was avoided. The encapsulation efficiency of different molecules into mucin particles was quantified spectrophotometrically. The range of tested molecules includes hydrophobic/hydrophilic antioxidants: hesperidin (Sigma Aldrich) and  $\beta$ -carotene (Sigma Aldrich); hydrophobic/hydrophilic dyes: ATTO495 and ATTO532 (ATTO-TEC, Siegen, Germany). For an overview of the physicochemical characteristics of those molecules, please refer to Table S1 (see supplement). In brief, 100  $\mu\text{L}$  of cargo-loaded mucin particles (feed concentrations of cargo molecules per 10 mg mL<sup>-1</sup> mucin solution: 5 mg  $\beta$ -carotene, 1.25 mg hesperidin, 78.1 ng ATTO532, 39.0 ng ATTO495) were placed on top of a trans-well insert (cellQART PET translucent, MWCO: 0.4  $\mu\text{m}$ ; Sabeu GmbH, Northeim, Germany) that the inner dimensions fit the reservoirs of a 24-well plate. Each reservoir contained 500  $\mu\text{L}$  of a receiving solution (SIF, SGF) into which molecules released from the mucin particles can migrate by diffusing across the insert membrane. After different time points (for antioxidants: 1 h, 2 h, 3 h, 4 h, 5 h, 6 h, 10 h, 24 h; for dyes: 1 h, 4 h, 6 h, 24 h), 200  $\mu\text{L}$  of this receiving solution was collected from the reservoir and replaced by a fresh buffer. The content of antioxidants in these collected samples was indirectly determined using a FRAP assay (see below), whereas the dye content in each sample was directly quantified by measuring the fluorescence signal of the carboxy-modified ATTO495 (Ex/Em = 485/510 nm; Fluoroskan Ascent) and amine-modified ATTO532 (Ex/Em = 540/590; Fluoroskan Ascent) fluorophore. Standard curves converted the obtained emission intensity values into concentrations (see supplement Fig. S1).

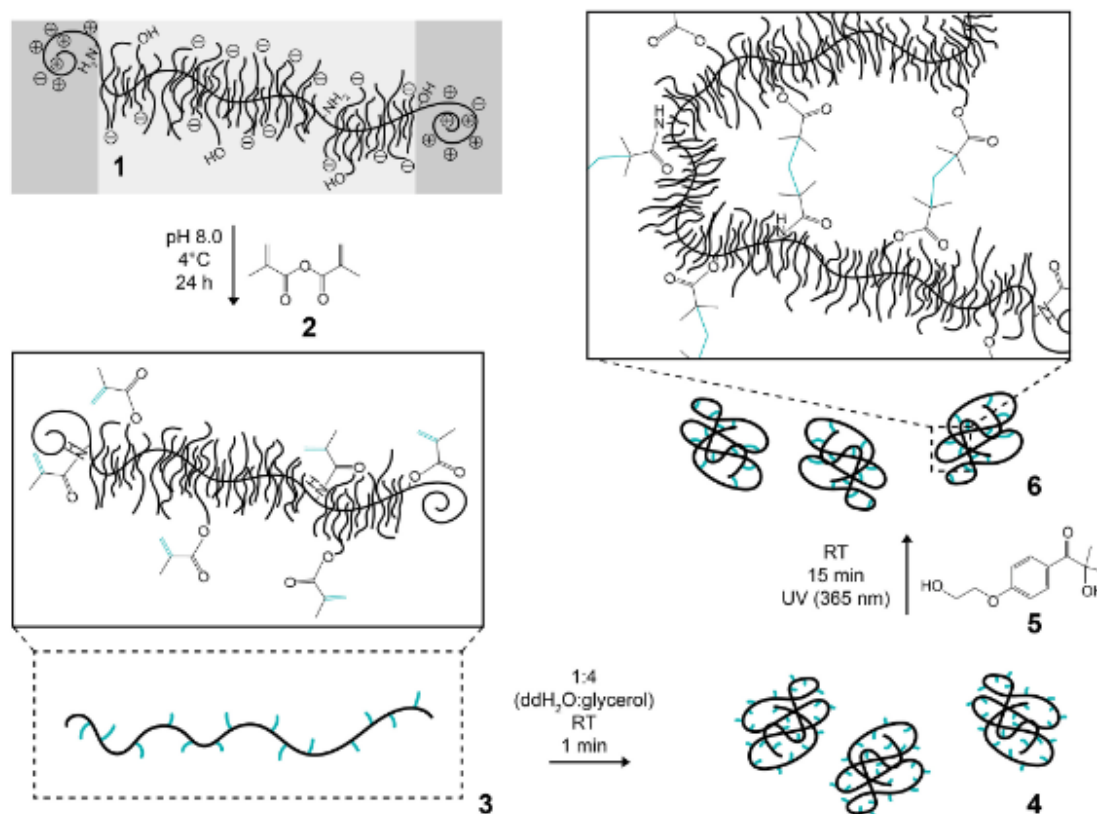
Then, encapsulation efficiency (EE) and drug loading capacity (DL) values were calculated as follows:

$$EE (\%) = \frac{\text{mass of cargo molecules in the particles}}{\text{mass of cargo molecules in the feed solution}} \times 100 \quad (1)$$

$$DL = \frac{\text{mass of cargo molecules in the particles}}{\text{mass of mucin particles}} \quad (2)$$

## 2.10. Ferric reducing antioxidant power (FRAP) assay

The  $\beta$ -carotene and hesperidin activity of drug-loaded (feed concentrations per 10 mg mL<sup>-1</sup> mucin solution: 5 mg  $\beta$ -carotene, 1.25 mg hesperidin) mucin particles was determined by measuring the ability of the antioxidant molecules to reduce the ferric-tripyridyltriazine complex into the ferrous-tripyridyltriazine complex; this assay was conducted as described previously [36], albeit with minor modifications. In brief, the activity of the hydrophobic/hydrophilic antioxidants was determined using FRAP, i.e., a reagent containing 300 mM acetate buffer (pH 3.6), 20 mM FeCl<sub>3</sub>, and 10 mM 2,4,6-tripyridyl-s-triazine (Sigma Aldrich) prepared in 40 mM HCl (mixed in a volume ratio of 10:1:1). The  $\beta$ -carotene or hesperidin samples were mixed with the FRAP reagent in a 1:6 ratio (v/v), the samples were vortexed at room temperature for 6 min, centrifuged (106  $\times g$  for 30 s), and then measured at 595 nm using a spectrophotometric plate reader (SpectraMax ABS Plus, Molecular Devices, San José, USA). Ethanol (for  $\beta$ -carotene) or ddH<sub>2</sub>O (for hesperidin) solutions were used as a reference. Their absorbance at the test wavelength was subtracted from all measurements conducted with molecule-loaded samples. The obtained results were converted into antioxidant



**Fig. 1.** Schematic representation of the mucin functionalisation and stabilisation process leading to stable particles. First, hydroxyl- and amino groups of mucin glycoproteins (1; the hydrophobic mucin termini are shaded in dark grey, the hydrophilic core domain in light grey; symbols indicate areas with anionic (○) and cationic charges (⊕)) are functionalized with methacrylic anhydride (2) resulting in mucin-MA molecules (3). Then, these mucin-MA molecules are condensed in glycerol (4) to obtain spherical particles. Finally, the mucin-MA particles are covalently crosslinked with the help of the photoinitiator Irgacure 2959 (5); upon UV exposure, stable particles are formed via a radicalization reaction (6).

concentrations using a regression equation (see supplement Fig. S1), prepared by determining FRAP values of serially diluted  $\beta$ -carotene and hesperidin solutions, respectively.

## 2.11. Particle uptake and cargo transport tests into cells

### 2.11.1. Cell cultivation

As of model cell lines, human epithelial cells (HeLa) and NIH 3T3 fibroblasts were used. HeLa cells were cultivated in Minimum Essential Medium Eagle (MEM; Sigma Aldrich) supplemented with 10 % (v/v) fetal bovine serum (FBS; Sigma Aldrich), 2 mM L-glutamine solution (Sigma Aldrich), 1 % (v/v) non-essential amino acid solution (NEAA; Sigma Aldrich) and 1 % penicillin/streptomycin (Sigma Aldrich). Fibroblasts (NIH 3T3) were cultivated in Dulbecco's Eagle's high glucose Medium (DMEM, Sigma Aldrich) supplemented with 10 % FBS and 1 % penicillin/streptomycin. Both cell lines were incubated at 37 °C and 5 % CO<sub>2</sub> in a humidified atmosphere.

### 2.11.2. Flow cytometry

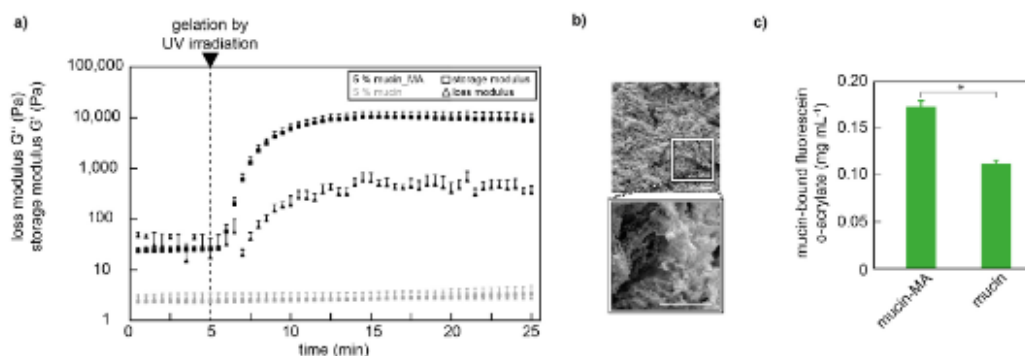
For these experiments, 6-well microtiter well plates were seeded with HeLa or NIH 3T3 cells (200,000 cells per well) and incubated at 37 °C for 24 h before use. Three different experiments were conducted using a flow cytometer: First, the uptake of fluorescent mucin particles (prepared as described in the section 'enzymatic degradation tests') was determined at different time points (1 h, 4 h, 24 h). Here, control

samples were incubated without adding mucin particles. Second, the cells were incubated with the prepared mucin particles at 37 °C or 4 °C for 2 h. In the third test, cell incubation with the mucin particles was conducted at 37 °C for 2 h; however, the cells were pre-incubated (1 h) with one of the following inhibitors: 7  $\mu\text{g mL}^{-1}$  chlorpromazine (Sigma Aldrich), 1  $\mu\text{g mL}^{-1}$  filipin (Sigma Aldrich), or 50  $\mu\text{M}$  amiloride (Sigma Aldrich). After this inhibitor incubation step, the cells were washed with D-PBS and then the particles were added. As control groups, cell samples without inhibitor pre-incubation were used.

After all incubation steps were concluded, the cells were washed three times with 1 mL D PBS and they were detached from the wells by adding 200  $\mu\text{L}$  of 0.25 % (w/v) trypsin/EDTA (1 mL medium was used to stop the trypsin activity after 3 min). The collected cells were centrifuged at 600  $\times g$  for 5 min, resuspended in D-PBS, and the supernatant was discarded. Then, the cell pellet was dissolved in 500  $\mu\text{L}$  D-PBS and the fluorescence signal of the cell population was measured using FACS (BD FACS Calibur OS X, BD Biosciences, San Jose, CA) equipped with an Ex/Em = 488/530 nm argon-ion laser (15 mW). 10,000 events/sample were collected and recorded at medium to high detection rates; the results were analyzed using the software Cell Quest (BD Biosciences).

### 2.11.3. Cargo transport tests

For cargo transport experiments, the wells of a  $\mu$ -Slide 8-well ibidi-Treat plate (ibidi GmbH, Gräfelfing, Germany) were first incubated with 5000 cells (either HeLa or NIH 3T3) per well for 24 h and covered with



**Fig. 2.** Rheological experiments and fluorescence labeling tests of mucin glycoproteins to demonstrate the formation of intra- and intermolecular crosslinks. (a) After UV curing, a mucin-MA solution forms a gel-like network dominated by elastic properties. In contrast, unmodified mucin molecules remain in the state of a viscoelastic solution. Error bars represent the standard deviation as obtained from three replicates. (b) After UV exposure, SEM images of methacrylated mucin samples indicate the presence of a finely reticulated 3D material (scale bar: 5  $\mu\text{m}$ ). (c) Surface-adsorbed methacrylated mucin molecules show stronger interactions with fluorescein *o*-erythrate molecules than unmodified mucins. Error bars represent the standard deviation as obtained from five replicates. Asterisks mark statistically significant differences ( $p \leq 0.05$ ) as determined with an unpaired Welch's *t*-test.

200  $\mu\text{L}$  of the respective cell medium. The next day, the medium was replaced by a fresh medium containing mucin particles, loaded with both carboxy-modified ATTO dyes (mucin concentration: 0.125  $\text{mg mL}^{-1}$ ; ATTO dye concentration:  $5 \times 10^{-4}$   $\text{mg mL}^{-1}$  of the hydrophobic ATTO495 dye and the hydrophilic ATTO532 dye, respectively). After different time points (0.5 h, 1 h, 2 h, 3 h, 4 h, 5 h, 6 h, 10 h, and 24 h), the cells were washed three times with Dulbecco's Phosphate Buffered Saline (D-PBS, Sigma Aldrich) and fixed with 4 % (v/v) formalin dissolved in D-PBS (pH 7.3). After this fixation step, the cell nuclei were stained with 4,6-diamino-2-phenylindole (DAPI (Sigma Aldrich); 300 nM in D-PBS) for 10 min. Then, the DAPI solution was replaced with D-PBS, and the cells were imaged on a Leica DMi8 microscope (Leica, Wetzlar, Germany) equipped with a 63 $\times$  objective (Leica, HC PL FLUOTAR, 63 $\times$ /0.70 CORR PH2) and a digital camera (Orca Flash 4.0 C11440–22C, Hamamatsu, Japan). The acquired images were edited with the Fiji ImageJ (public domain, version 1.53c, June 2020) software.

The corrected total cell fluorescence (CTCF) for each channel was then calculated according to the following formula:

$$\text{CTCF} = \text{integrated density} - (\text{area}_{\text{cell}} \times \text{mean fluorescence of background}) \quad (3)$$

For the calculation of the CTCF, nine eukaryotic cells were evaluated (originating from  $\geq 3$  images). As a control group, the same experiments were conducted with a concentration of free ATTO dye of  $5 \times 10^{-4}$   $\text{mg mL}^{-1}$ ; this corresponds to the concentration of this dye offered in the encapsulated form in the same set of experiments.

### 2.12. Statistical analysis

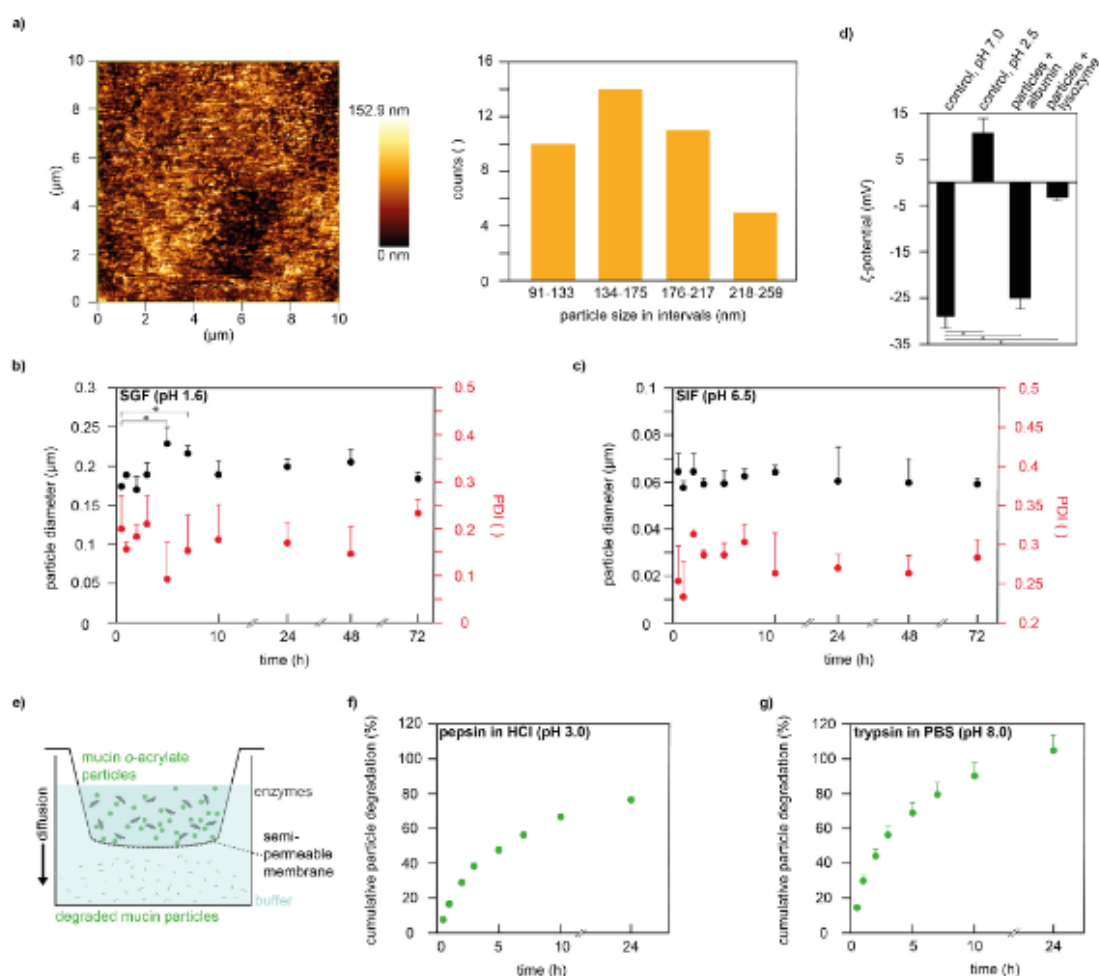
The software GraphPad Prism (Prism 8, San Diego, CA, USA) was used to apply a Shapiro-Wilk test to the data to test for normal distribution. To conduct pairwise comparisons, a standard *t*-test was applied for equal variances; for unequal variances, an unpaired Welch's *t*-test was used. A Dunnett's T3 multiple comparisons test (non-normal distributed/unequal variances) or a one-way ANOVA/Tukey post-hoc test (normal distribution/equal variances) was applied for multiple comparisons within a group. For all tests, the threshold for significance was set to a *p*-value of  $p \leq 0.05$ .

## 3. Results and discussion

### 3.1. Mucin particles are stabilized via UV-driven crosslinking

To create stable mucin-based nanoparticles (Fig. 1), our strategy is as follows: first, the mucin glycoproteins are functionalized with methacrylic anhydride (MA) [28,33]. With this procedure, the amino- and hydroxyl groups of the protein backbone and the hydroxyl groups of the mucin-bound carbohydrates (located in the core domain of the polypeptide chain) are modified. Then, in the next step, the methacryloyl mucins are mixed with glycerol to create particles: As shown previously, at the water-glycerol interface, the overall structure of solubilized mucin macromolecules changes from an extended chain configuration into a compact, globular morphology [34], and we expect a similar behavior for methacryloyl mucins.

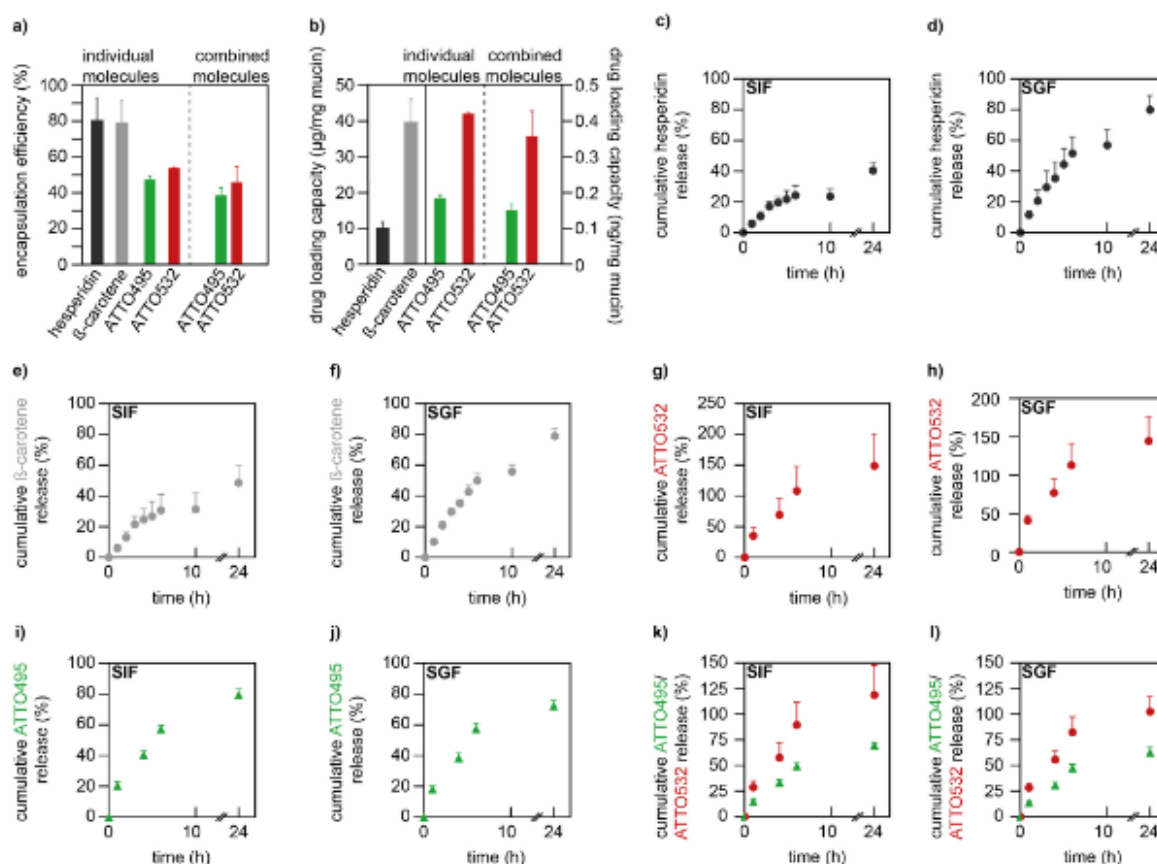
For stabilization, the mucin particles are exposed to UV light, which triggers a radical-based reaction of the methacrylated groups; this should result in the formation of intra- and intermolecular covalent bonds, which are supposed to stabilize the structure of mucin particles upon glycerol removal as required for successful drug loading of the mucin-based carriers. To determine a UV irradiation time that is sufficient to form stable mucin particles during this process, we follow the viscoelastic properties of mucin solutions reconstituted from the same methacryloyl mucins; here, gelation (i.e., a transition from a viscoelastic solution dominated by viscous properties into a viscoelastic solid dominated by elastic properties) is expected to occur upon exposure of the conjugated mucins to UV light. Indeed, this behavior is observed for the methacrylated mucins, which form a gel with a shear modulus of  $\sim 10$  kPa; such gel formation, however, is absent for unmodified mucins (Fig. 2a), which underlines the efficient formation of photo-induced crosslinks between conjugated mucins. We do, however, find indications for low levels of spontaneous inter-mucin crosslinks in the conjugated mucin sample: here (before UV exposure), the viscoelastic moduli are  $\sim 10$  fold higher than for the unmodified mucin sample. However, only after UV illumination of the methacryloyl mucin sample, a proper gel with pronounced elastic properties is obtained (see supplement Fig. S2). In addition, SEM images (Fig. 2b) demonstrate the formation of an interconnected 3D material after UV exposure, which agrees with our rheological assessment. Moreover, as the shear stiffness of the methacrylated mucin sample reaches a plateau  $\sim 10$  min after UV illumination was initiated, we conclude that a similar UV exposure time should be sufficient to allow for efficient crosslinking of the mucin macromolecules in their nanoparticle state.



**Fig. 3.** AFM images and DLS measurements show successful particle formation and demonstrate the good stability of the mucin particles. (a) An exemplary AFM image visualizes an ensemble of dried, UV-crosslinked mucin particles adsorbed to a glass slide. From this image, the height profile of individual particles is determined (top curve), which results in a size distribution (bottom bar plot) covering a range from 0.1  $\mu\text{m}$  to 0.3  $\mu\text{m}$ . (b)–(c): Size changes of the mucin particles over time. Here, the mucin particles were stored either in SGF (b) or SIF (c) buffer. Then, the diameter of the particles and the polydisperse index (PDI) of the particle population were followed over 72 h. (d) The zeta potential of the mucin particles is assessed in 10 mM HEPES buffer and SGF. A subset of particles was incubated with albumin or lysozyme before determining the zeta potential at neutral pH (i.e., in 10 mM HEPES buffer). (e) Schematic representation of the enzymatic degradation assay using trans-well inserts. (f)–(g): Enzymatic treatment of fluorescently labeled mucin particles with pepsin (in 10 mM HCl, pH 3.0; f) or trypsin (in PBS buffer, pH 8.0; g). The error bars represent the standard deviation from three (hydrodynamic size, PDI, degradation experiments) and ten ( $\zeta$ -potential measurements) replicates, respectively. The zeta potential and DLS measurements results were statistically analyzed using one-way ANOVA/Dunnett's T3 multiple comparisons test (zeta potential) or one-way ANOVA/Tukey post-hoc multiple comparison tests (DLS) using a significance threshold of  $p \leq 0.05$ .

In addition to this rheology-based verification of successful mucin modification, we also attempt a more direct approach to confirm the presence of the methacrylate groups on the mucins. As mucin glycoproteins are large molecules with many functional groups, conventional detection techniques such as mass spectroscopy (MS) or nuclear magnetic resonance (NMR) fail to assess the degree of mucin methacrylation. Thus, we incubate untreated and methacryloyl mucins with an acrylated fluorescein variant and, after UV treatment and dialysis, detect the tagged mucin molecules by fluorescence microscopy. Here, the rationale is that, with this particular dye, the efficient formation of fluorescent mucins requires mucin-bound acrylate groups (see Methods). And indeed, we find stronger fluorescent signals for the methacrylated mucins than for unmodified mucins (Fig. 2c).

Having confirmed that mucin methacrylation was successful and enabled UV-inducible crosslinking reactions between mucins, we next prepare mucin particles by glycerol-driven compaction and UV irradiation. With this process, mucin particles with diameters of 0.06–0.3  $\mu\text{m}$  are generated as determined from AFM images (Fig. 3a) and dynamic light scattering (Fig. 3b–c), respectively. As for mucin particles stabilized with DNA-based crosslinks [31], the size measurements reported here return similar results. However, preparing those particles in a SIP medium (pH 6.5) leads to the formation of somewhat smaller particles than particle preparation in SGF (pH 1.6). This result indicates that the particles might form small aggregates at acidic pH values. Given the moderately positive  $\zeta$ -potential of  $(10.6 \pm 3.2)$  mV we measure for the mucin particles at acidic pH (Fig. 3d), it is reasonable to assume that



**Fig. 4.** Encapsulation efficiency, drug loading capacity, and cumulative release profiles of antioxidants and ATTO dyes into and from UV-crosslinked mucin particles. (a) Encapsulation efficiencies and (b) drug loading capacities of different antioxidants and ATTO dyes when loaded into mucin particles individually or in combination. Release profiles of hesperidin (c, d) and  $\beta$ -carotene (e, f) as well as ATTO532 (g, h), ATTO495 (i, j), and ATTO/ATTO (k, l) combinations in fluids mimicking intestinal (SIF) and stomach (SGF) conditions. Error bars represent the standard deviation as obtained from three independent samples. If no error bars are visible, they are comparable to the symbol size.

there are inter-particle repulsion forces keeping the nanoparticles apart. However, in acidic environments, the mucin glycoprotein can be expected to carry both, cationic and anionic residues [29], and this could facilitate particle aggregation. In contrast, at neutral pH (where the  $\zeta$ -potential of the particles is  $-29.0 \pm 2.6$  mV), the mucins should be mostly anionic [29] thus creating stable, single particles (Fig. 3d).

For applications in the oral delivery of pharmaceuticals across the gastrointestinal tract, where a certain level of robustness towards degradation in the stomach by enzymes is required, such particle aggregates could be advantageous as the effective surface area available for enzymatic attack is reduced. Here, especially the long residence time in the stomach (which typically is around 3 h [37,38]) needs to be considered as unwanted particle degradation would entail premature cargo release. However, we find that, when incubated in simulated gastric fluid (SGF), the mucin particles are remarkably stable (Fig. 3b and f): In the absence of pepsin, the polydispersity index (PDI) of the particle ensemble remains below 0.3, and we do not detect a significant reduction in particle size within 24 h of incubation. In the presence of pepsin (Fig. 3f), the level of particle degradation after 3 h is only  $(38 \pm 1)$  %, which supports the notion that the majority of the particles will reach the intestinal tract. This finding can be rationalized by the high glycosylation density of mucins, which – compared to other proteins – increases their stability towards proteolytic degradation [29]. In

addition, the presence of particle aggregates at acidic pH (see above) might improve their stability since these compact structures may reduce pepsin activity by restricting its access. At approximately neutral pH (as present in simulated intestinal fluid, SIF), the stability of the mucin particles is very good as well (Fig. 3c): here, we do not detect any significant alterations in the particle ensemble size during the whole observation time of 72 h either. In contrast, when the mucin particles are incubated with trypsin at a slightly alkaline pH (where the intestinal protease trypsin has its highest activity), the particles are efficiently degraded after 10 h (Fig. 3g). This result can be advantageous for the application envisioned here: encapsulated drugs can be expected to be transported to the intestine and are also likely to be actively liberated from their carriers by enzymatic break-down.

In addition to their good stability, the mucin particles also come with surface properties that should be favorable for cellular uptake. Similar to mucin nanoparticles stabilized with synthetic DNA strands [31], the UV-crosslinked particles generated here have anionic properties at neutral pH, and those anionic surface properties are maintained when the particles are incubated with anionic (e.g., albumin) or even cationic (e.g., lysozyme) proteins (Fig. 3d). This binding propensity of mucin particles towards proteins is similar to that of elongated mucins [39] but should be unproblematic when the particles travel through the gastrointestinal tract as they help preventing strong particle aggregation. In fact, a more



neutral  $\zeta$ -potential could even improve the cellular uptake of the particles at their final target site.

### 3.2. Mucin particles can be loaded with hydrophobic and hydrophilic cargoes

Since the mucin particles are stable at different pH conditions as they occur in the stomach and the intestine, we next probe the drug loading capabilities of those particles. In detail, we aim at incorporating hydrophilic and hydrophobic molecules into the particles (see supplement Table S1 for an overview of the tested cargo molecules), which we assume to interact with the mucin carrier material in different ways: As the two hydrophobic termini of the mucin glycoprotein are spatially well separated from each other by the hydrophilic core domain, polar drugs should be able to bind to the glycosylated core domain of mucin, whereas non-polar drugs are likely to bind to the termini of mucin. Owing to this complex architecture of mucins, the particles generated from this glycoprotein should enable encapsulation of both, polar and non-polar drugs. To test this expectation, we first select antioxidants for drug loading tests (Fig. 4). Antioxidants have a positive effect on the body as they scavenge excessive reactive oxygen species (ROS) that can trigger inflammation [40] and cause diseases such as cystic fibrosis, chronic obstructive pulmonary diseases [41], and Crohn's disease [42]. We choose a polar and a non-polar antioxidant variant for our experiments, i.e., hesperidin and  $\beta$ -carotene [43,44]; at the pH levels studied here, those two molecules should be uncharged. For both molecules, we obtain very good encapsulation efficiency (EE) values of 80 %–90 % (Fig. 4a, see supplement Table S2). Those values are similar to the EEs achieved for hesperidin in lipid nanoparticles [45] and PLGA-chitosan particles [46], as well as for  $\beta$ -carotene in zein-based particles [47].

Importantly, we can load both molecules into the same particle species, demonstrating the great versatility of such mucin-based carriers. To some extent, the drug loading capacity (DL) of the mucin carrier system can be improved by increasing the feed concentration; however, this reduces the EE (see supplement Fig. S3a–b). The ability of mucin particles to host polar and non-polar cargo molecules with similar efficiency agrees with the structure of the mucin glycoprotein: as mentioned above, the long, hydrophilic, glycosylated central region and the hydrophobic termini of the mucin are spatially separated and constitute the most likely binding partners for hydrophilic and hydrophobic drug molecules, respectively. As the mucin glycans carry many anionic residues, it is not surprising that anionic antioxidants such as ascorbic acid (see supplement Table S1, Fig. S3e, and h) cannot be loaded into mucin particles very well.

When analyzing the release behavior of the encapsulated hesperidin and  $\beta$ -carotene cargoes, we find that it takes 10 h until most of the release process is completed (Fig. 4c–d/ Fig. 4e–f). After this period, the cumulative release of hesperidin is –23 % (in SIF) and –57 % (in SGF); for  $\beta$ -carotene, we determine –31 % (SIF) and –56 % (SGF); those release values, however, still increase over the course of the next 14 h. When considering the envisioned application of our mucin particles as gastrointestinal drug carriers, this is a promising result: the particles can be expected to remain in the stomach for an average period of only 3 h, and then they should move on to the intestinal tract (it should take ~20 h until they reach the colon [36]). Thus, the largest proportion of the loaded drugs should be liberated in the intestine. Interestingly, we find higher release efficiencies at acidic pH, which holds for both antioxidants.

To gain further insight into the dominating release mechanism driving the liberation of the antioxidants, we apply five different mathematical models to the release data – namely zero-order and first-order release kinetics as well as Higuchi, Hixson-Crowell, and Korsmeyer-Peppas models (see supplement Fig. S4). Based on the correlation coefficients obtained from fitting those models to the different release curves, the non-linear Korsmeyer-Peppas model turns out to be best suited to describe the experimental data throughout the whole

experimental time frame ( $R^2 > 0.97$ ). The Korsmeyer-Peppas model describes a release of molecules that is governed by buffer/water diffusion into the polymeric matrix or a carrier, swelling of the matrix, and its dissolution [48] – and this picture agrees with the high-water binding capacity of mucins [49] and the strong swelling propensity of cross-linked mucin gels [50]. In other words, the mucin-based particles can be expected to swell in an aqueous environment; however, owing to the covalent cross-links introduced by the methacrylate procedure, the particles are not disintegrated but rather become more porous over time, and this facilitates the (non-Fickian) diffusive release ( $n > 1$ ) of their payload [51]. At this point, we would like to mention that the release process of antioxidants from the mucin particles is more efficient at acidic pH than at neutral pH. This could be due to pH-dependent differences in the swelling behavior of the mucin particles: At acidic conditions, the mucin carries both cationic and anionic residues (whereas the cationic groups can be expected to be deprotonated at neutral pH). Thus, those additional charged moieties might induce stronger swelling and, therefore, more efficient release in SGF than in SIF.

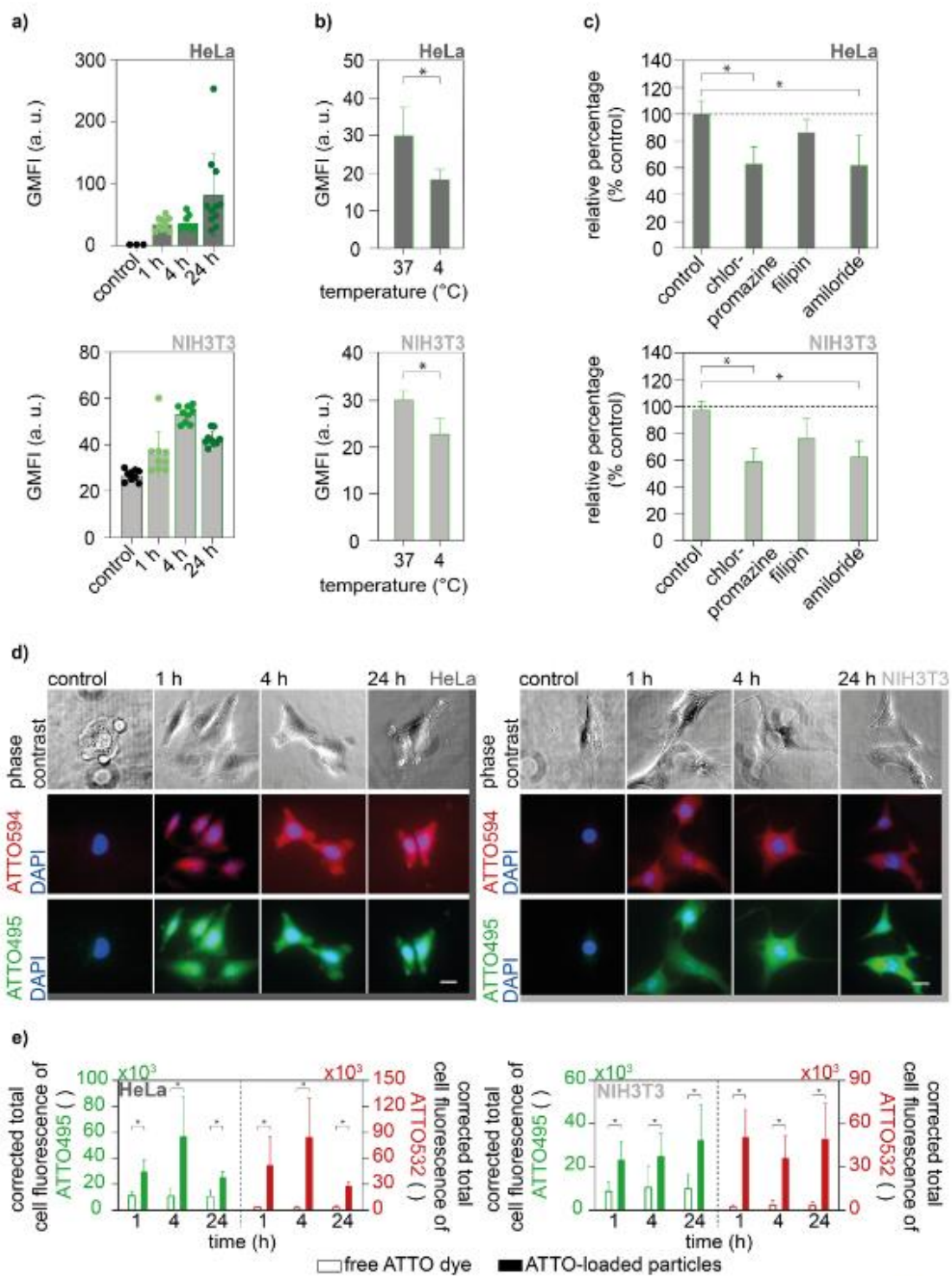
So far, we could show that two antioxidants with different polarities ( $\beta$ -carotene and hesperidin) can be loaded into the same particle species. However, investigating their simultaneous co-loading was not possible as their detection requires an indirect PRAP assay which cannot differentiate between the two molecules. To motivate that such a simultaneous loading is possible, we switch to model molecules that can be separately detected more easily: fluorophores. Also here, we select a pair of molecules with different polarities while avoiding negative net charges (see above; as the mucins are strongly polyanionic, loading anionic molecules into mucin particles is very difficult, see supplement Fig. S3).

First, we determine the EE of two modified ATTO dyes (ATTO495: hydrophobic; ATTO532: hydrophilic) when loaded into the mucin particles – either separately or in combination. In either case, we obtain decent EEs in 35 %–70 % and comparable DL values (Fig. 4a–b see supplement Fig. S3h). In other words, co-loading of two molecules with different polarities into the same mucin particle is indeed possible – and with similar efficiencies as when the molecules are loaded individually. Control experiments on the particle diameter of the dye-loaded mucin particles are compiled in Fig. S5 and demonstrate that the geometric properties of the particles are relatively independent of the loaded cargo. Consistently, the release behavior of the two dye molecules is similar for single-cargo loading (Fig. 4g–j) and co-loading (Fig. 4k–l).

In summary, we conclude that both polar and non-polar cargo molecules can be loaded into the mucin particles – provided that they are not anionic. An explanation can be offered by the high negative charge density located in the glycosylated central region of the mucin glycoprotein. Whereas this feature provides multiple binding sites for cationic molecules [29], it creates strong electrostatic repulsive forces for anionic molecules, thus rendering their binding less likely. Even though there are also a few cationic binding sites on the unglycosylated termini of the mucin protein [29], to which anionic molecules can bind, the compacted configuration of the mucins achieved in the particle state will bring both (weak) attractive and (strong) repulsive electrostatic forces into close proximity, thus preventing efficient loading of anionic cargoes.

Cellular uptake of mucin particles and delivery of their cargo into eukaryotic cells.

Having demonstrated that the mucin particles successfully encapsulate and release hydrophobic and hydrophilic drugs, we next ask if mucin particles can be internalized by cells and if drug-loaded mucin particles can successfully transport their cargo into cells. Based on previous results, which had shown that surface-bound, elongated mucins repel eukaryotic cells [39,52], one might draw the conclusion that strong repulsive forces acting between the negatively charged mucin core domain and components of the cell membrane might prevent mucin particles from being efficient drug delivery vehicles. And indeed, other mucin particles stabilized with DNA-crosslinks had to be functionalized with a cationic coat to achieve decent cellular uptake rates [31].



(caption on next page)

**Fig. 5. Cellular uptake of mucin particles and encapsulated/free ATTO dyes.** (a) FACS data shows how the uptake of fluorescent mucin particles by HeLa (top) and NIH 3T3 (bottom) cells increases over time. (b) For both cell lines, particle uptake is dependent on the incubation temperature. (c) Cellular uptake of mucin particles in the presence of different inhibitors. Data shown in (a)–(c) represents average values from  $n \geq 5$  samples per condition. The error bars represent the standard error of the mean, and statistically significant differences are marked by asterisks (one-way ANOVA/Dunnett's T3 multiple comparisons test ( $p \leq 0.05$ )). (d) Phase-contrast and fluorescence microscope images of HeLa cells (left) and NIH 3T3 cells (right) incubated with ATTO495/532-loaded mucin particles. The scale bar denotes 20  $\mu\text{m}$  and applies to all images. (e) From such fluorescence images, the fluorescence intensity of both ATTO dye variants is calculated using Image J. Cells incubated with free (unencapsulated) dyes serve as control groups. Data shown represent average values from  $n = 9$  analyzed cells; the error bars denote the standard deviation. Statistically significant differences are marked by asterisks and were determined by an unpaired Welch's *t*-test ( $p \leq 0.05$ ).

However, the situation might be different here.

Biocompatibility tests conducted with HeLa and NIH 3T3 cells demonstrate that our mucin particles have hardly any inhibitory effect on the cellular viability; we only find a somewhat reduced cell viability (which is still around 80 %) for NIH 3T3 cells when they are exposed to concentrated mucin particles ( $\geq 0.25 \text{ mg mucin mL}^{-1}$ , see supplement Fig. S6). Here, nutrition transport to the cells is probably restricted by a gel-like layer of aggregated mucin particles covering the top of the cells. At a particle concentration of  $0.125 \text{ mg mucin mL}^{-1}$ , we find excellent viability for both cell lines, i.e., similar values as for control cells incubated in the same 96-well plate. Thus, cellular uptake and drug transport tests with cells are conducted with this particle concentration.

To quantify the accumulation of mucin particles in the cytosol, cells are incubated with fluorescent particles and then analyzed using a flow cytometer; for both cell types, we find good particle uptake over time (Fig. 5a). Interestingly, the geometric mean fluorescence intensity (GMFI) detected for HeLa cells after 24 h of nanoparticle incubation is  $\sim 2$  times higher than the value determined for NIH 3T3 cells. For the second cell line, an increase in GMFI is detected until 4 h, followed by a slight reduction at 24 h. The latter might be explainable by a release of fluorescent degradation products of the mucin particles from the cytosol.

Furthermore, to gain a better understanding of the microscopic mechanisms driving nanoparticle uptake, the influence of a temperature block on nanoparticle internalization is investigated (Fig. 5b). After 2 h of incubation with nanoparticles, uptake of mucin particles at  $4^\circ\text{C}$  is significantly reduced by  $\sim 35\%$  for HeLa and by  $\sim 25\%$  for NIH 3T3 cells when compared to results obtained for incubation at  $37^\circ\text{C}$ . At  $4^\circ\text{C}$ , the particles should still be able to bind to the cell surface; however, their uptake is limited [53]. During the later steps of the experiment (e.g., during the washing process and trypsin-mediated cell harvesting), the temperature is increased again, which allows certain temperature-driven pathways (e.g., clathrin-mediated uptake) to function again. This might explain why the reduction in uptake efficiency we observe upon applying this temperature block is only moderate.

In the last step, to identify relevant uptake mechanisms contributing to the internalization of mucin nanoparticles, cells are pre-incubated with endocytic inhibitors (i.e., chlorpromazine, filipin, or, amiloride), which can specifically block certain uptake pathways (Fig. 5c). After 2 h of incubation with (fluorescent) mucin particles, both cell types show a significantly reduced particle uptake for chlorpromazine as well as for amiloride treatment compared to the control condition (no inhibitor). Chlorpromazine inhibits clathrin-mediated endocytosis, whereas amiloride (a specific inhibitor of the  $\text{Na}^+/\text{H}^+$  exchange [54]) inhibits uptake by macropinocytosis. Both uptake mechanisms allow for the internalization of objects with sizes up to  $\sim 200 \text{ nm}$  (clathrin) [55,56] or up to  $1\text{--}5 \mu\text{m}$  (macropinocytosis) [57], which agrees with the size range of the mucin particles created here. In contrast, treating the cells with filipin (which inhibits cellular uptake via caveolae) does not lead to a significant change, as this mechanism only allows for the uptake of objects with sizes up to  $50\text{--}80 \text{ nm}$ .

To evaluate the putative success of cargo transport into cells, we co-load the mucin particles with the two ATTO dyes (ATTO532 and ATTO495). Then, the cells are incubated with the dye-loaded particles, and after different time points, the particle uptake process is stopped by fixing the cells. The cells are imaged by fluorescence microscopy (Fig. 5d). As an analysis of the obtained fluorescence images shows

(Fig. 5e), the number of dyes taken up by cells is more prominent when the dyes are encapsulated into mucin carrier particles. In control groups, where free, unencapsulated dyes were offered at the same concentration, the corresponding fluorescent signals were significantly lower for each time point tested and for both, HeLa and NIH 3T3 fibroblast cells (Fig. 5e; see supplement Fig. S7). This finding agrees with results reported elsewhere, where the cellular uptake of free molecules (i.e., doxorubicin and curcumin) was about half as efficient as their uptake in encapsulated form, i.e., when loaded into LipoNiosome-particles [58]. Moreover, lysis tests with the second set of cells incubated with ATTO-loaded mucin particles confirm that the number of molecules arriving in the cytosol increases over time – for both dye variants and cell lines (see supplement Fig. S8). In other words, those tests confirm that the mucin particles can serve as efficient transport vehicles for both hydrophobic and hydrophilic molecules into eukaryotic cells.

#### 4. Conclusion

Here, a single biological macromolecule, i.e., the glycoprotein mucin, is used to create stable particles that can be loaded with hydrophilic and hydrophobic molecules and enable delivery of their cargo into the cytosol. Owing to UV-induced cross-links stabilizing the mucin particles and weak particle aggregate formation at acidic pH, the mucin particles resist degradation by the gastric protease pepsin reasonably well. However, the intestinal protease trypsin entails an efficient degradation of the mucin-based carriers. By combining molecular co-delivery of two drugs with a continuous release of such drugs over time, those mucin-based particles could be very beneficial for transporting pharmaceuticals to the intestines while preventing premature drug liberation in the stomach. Such stable and versatile drug carriers made from biopolymers could hold the potential for a broad range of applications, e.g., as components of nasal/inhalation sprays [59,60] or to alleviate chronic diseases of the intestinal region such as Crohn's disease [61]. For the latter, the oxidative stress induced by such ROS is suspected to be responsible for tissue inflammation and the ensuing fibrosis [62]. Thus, antioxidants transported into the intestinal region should be helpful to mitigate the increased occurrence of reactive oxygen species, thus alleviating the symptoms of such chronic diseases [63].

#### CRedit authorship contribution statement

Theresa M. Lutz: Conceptualization, Methodology, Investigation, Data curation, Writing, Visualization.

Ceren Kimnas: Conceptualization, Methodology, Formal analysis, Data curation, Writing.

Oliver Liele: Conceptualization, Methodology, Resources, Writing, Supervision, Funding acquisition.

#### Declaration of competing interest

There are no conflicts of interest to declare.

#### Acknowledgments

This project was funded by the Munich Multiscale Biofabrication Network. The authors thank Tobias Fuhrmann for assistance with the mucin purification and Dr. Benjamin Winkeljann for assistance with the

rheology experiments.

## Appendix A. Supplementary data

Supplementary data to this article can be found online at <https://doi.org/10.1016/j.ijbiomac.2022.06.061>.

## References

- M.-F. Li, et al., The formation of zinc-chitosan complex coacervated particles: relationship to encapsulation and controlled release properties, *Int. J. Biol. Macromol.* 116 (2018) 1232–1239.
- B. Vaidya, et al., Cyclodextrin modified chitosan loaded PLGA nanoparticles for improved therapeutic efficacy against non-small cell lung cancer, *Int. J. Biol. Macromol.* 122 (2019) 338–347.
- E. Fournier, et al., Biocompatibility of implantable synthetic polymeric drug carriers: focus on brain biocompatibility, *Biomaterials* 24 (19) (2003) 3311–3331.
- H. Idreza, et al., A review of biodegradable natural polymer-based nanoparticles for drug delivery applications, *Nanomaterials* 10 (10) (2020) 1970.
- C. Le Tien, et al., N-acylated chitosan: hydrophobic matrices for controlled drug release, *J. Control. Release* 93 (1) (2003) 1–13.
- A. Bernkop-Schnürch, S. Scholler, R.G. Biebel, Development of controlled drug release systems based on thiolated polymers, *J. Control. Release* 66 (1) (2000) 39–48.
- S.Y. Fam, et al., Stealth coating of nanoparticles in drug-delivery systems, *Nanomaterials* 10 (4) (2020) 787.
- M. Ghezzi, et al., Polymeric micelles in drug delivery: an insight of the techniques for their characterization and assessment in biorelevant conditions, *J. Control. Release* 332 (2021) 312–336.
- V.P. Torchilin, Recent advances with liposomes as pharmaceutical carriers, *Nat. Rev. Drug Discov.* 4 (2) (2005) 145–160.
- N. Hoang, S.M. Nimjee, Central nervous system drug delivery after ischemic or hemorrhagic stroke, *Nerv. Syst. Drug Deliv.* (2019) 473–500.
- S. Karimi, H. Namazi, Simple preparation of maltose-functionalized dendrimer/graphene quantum dots as a pH-sensitive biocompatible carrier for targeted delivery of doxorubicin, *Int. J. Biol. Macromol.* 156 (2020) 648–659.
- A.S. Skwarcecki, M.G. Nowak, J. Milewska, Synthetic strategies in construction of organic macromolecular carrier-drug conjugates, *Org. Biomol. Chem.* 18 (30) (2020) 5764–5783.
- C. Kimna, et al., Smart biopolymer-based multi-layers enable consecutive drug release events on demand, *Adv. Mater. Interfaces* 7 (19) (2020) 2000735.
- H. Nic, et al., Core/shell microspheres via coaxial electrohydrodynamic atomization for sequential and parallel release of drugs, *J. Biomed. Mater. Res. A* 95 (3) (2010) 709–716.
- X. Xiong, K. Tam, L. Gan, Release kinetics of hydrophobic and hydrophilic model drugs from pluronic F127/poly (lactic acid) nanoparticles, *J. Control. Release* 103 (1) (2005) 73–82.
- H. Wang, et al., Enhanced anti-tumor efficacy by co-delivery of doxorubicin and paclitaxel with amphiphilic methoxy PEG-PLGA copolymer nanoparticles, *Biomaterials* 32 (32) (2011) 8281–8290.
- B.B. Mandal, S. Kundu, Self-assembled silk sericin/polyoxamer nanoparticles as nanocarriers of hydrophobic and hydrophilic drugs for targeted delivery, *Nanotechnology* 20 (35) (2009), 355101.
- O.G. Jones, E.A. Decker, D.J. McClements, Formation of biopolymer particles by thermal treatment of  $\beta$ -lactoglobulin-pectin complexes, *Food Hydrocoll.* 23 (5) (2009) 1312–1321.
- S. Fathollahipour, et al., Electrospinning of PVA/chitosan nanocomposite nanofibers containing gelatin nanoparticles as a dual drug delivery system, *J. Biomed. Mater. Res. A* 103 (12) (2015) 3852–3862.
- A.O. Elzoghby, W.M. Samy, N.A. Elgindy, Dextrin-based nanocarriers as promising drug and gene delivery systems, *J. Control. Release* 161 (1) (2012) 38–49.
- H. Kouchakzadeh, M.S. Safavi, S.A. Shojasadati, Efficient delivery of therapeutic agents by using targeted albumin nanoparticles, *Adv. Protein Chem. Struct. Biol.* 98 (2015) 121–143.
- A. Parodi, et al., Albumin nanovectors in cancer therapy and imaging, *Biomolecules* 9 (6) (2019) 218.
- L. Palani Kumar, et al., pH-responsive high stability polymeric nanoparticles for targeted delivery of anticancer therapeutics, *Commun. Biol.* 3 (1) (2020) 1–17.
- H. Shi, et al., Human serum albumin conjugated nanoparticles for pH and redox-responsive delivery of a prodrug of cisplatin, *Chemistry—A European Journal* 21 (46) (2015) 16547–16554.
- S.K. Lai, Y.-Y. Wang, J. Hanes, Mucus-penetrating nanoparticles for drug and gene delivery to mucosal tissues, *Adv. Drug Deliv. Rev.* 61 (2) (2009) 158–171.
- D. Walker, et al., Enzymatically active biomimetic micropropellers for the penetration of mucus gels, *Sci. Adv.* 1 (11) (2015), e1500501.
- C.A. Rickert, et al., Several sterilization strategies maintain the functionality of mucin glycoproteins, *Macromol. Biosci.* 20 (7) (2020) 2000090.
- C.V. Duffy, L. David, T. Crouzier, Covalently-crosslinked mucin biopolymer hydrogels for sustained drug delivery, *Acta Biomater.* 20 (2015) 51–59.
- T.M. Lutz, et al., Repulsive backbone-backbone interactions modulate access to specific and unspecific binding sites on surface-bound mucins, *Langmuir* 36 (43) (2020) 12973–12982.
- B.T. Käscher, et al., Mucin-inspired lubrication on hydrophobic surfaces, *Biomacromolecules* 18 (8) (2017) 2454–2462.
- C. Kimna, et al., DNA strands trigger the intracellular release of drugs from mucin-based nanocarriers, *ACS Nano* 15 (2) (2020) 2350–2362.
- V.J. Schömig, et al., An optimized purification process for porcine gastric mucin with preservation of its native functional properties, *RSC Adv.* 6 (50) (2016) 44932–44943.
- E. Oläret, et al., Double-cross-linked networks based on methacryloyl mucin, *Polymers* 13 (11) (2021) 1706.
- H. Yan, et al., Reversible condensation of mucins into nanoparticles, *Langmuir* 34 (45) (2018) 13615–13625.
- M.R. Marques, R. Loebenberg, M. Almkuknazi, Simulated biological fluids with possible application in dissolution testing, *Dissolution Technol.* 18 (3) (2011) 15–28.
- L. Müller, K. Theile, V. Böhm, In vitro antioxidant activity of tocopherols and tocotrienols and comparison of vitamin E concentration and lipophilic antioxidant capacity in human plasma, *Mol. Nutr. Food Res.* 54 (5) (2010) 731–742.
- F.J. Varum, H.A. Merchant, A.W. Bazit, Oral modified-release formulations in motion: the relationship between gastrointestinal transit and drug absorption, *Int. J. Pharm.* 395 (1–2) (2010) 26–36.
- S.S. Davis, Formulation strategies for absorption windows, *Drug Discov. Today* 10 (4) (2005) 249–257.
- B. Winkeljans, et al., Covalent mucin coatings form stable anti-biofouling layers on a broad range of medical polymer materials, *Adv. Mater. Interfaces* 7 (4) (2020), 1902069.
- E. Nur, et al., Oxidative stress in sickle cell disease; pathophysiology and potential implications for disease management, *Am. J. Hematol.* 86 (6) (2011) 484–489.
- I.-T. Lee, C.-M. Yang, Role of NADPH oxidase/ROS in pro-inflammatory mediators-induced airway and pulmonary diseases, *Biochem. Pharmacol.* 84 (5) (2012) 581–590.
- E. Alkhamy-Cozmic, et al., Oxidative stress in the pathogenesis of crohn's disease and the interconnection with immunological response, microbiota, external environmental factors, and epigenetics, *Antioxidants* 10 (1) (2021) 64.
- S.A. van Acker, et al., Influence of iron chelation on the antioxidant activity of flavonoids, *Biochem. Pharmacol.* 56 (8) (1998) 935–943.
- K.-H. Chang, et al., Lipophilic antioxidants in neurodegenerative diseases, *Clin. Chim. Acta* 485 (2018) 79–87.
- S. Saad, et al., Improved cardioprotective effects of hesperidin solid lipid nanoparticles prepared by supercritical antisolvent technology, *Colloids Surf. B: Biointerfaces* 187 (2020), 110628.
- H. Jin, et al., Nasal delivery of hesperidin/chitosan nanoparticles suppresses cytokine storm syndrome in a mouse model of acute lung injury, *Front. Pharmacol.* (2021) 1786.
- L. Mahalakshmi, et al., Micro-and nano-encapsulation of  $\beta$ -carotene in zein protein: size-dependent release and absorption behavior, *Food Funct.* 11 (2) (2020) 1647–1660.
- J. Supramaniam, et al., Magnetic nanocellulose alginate hydrogel beads as potential drug delivery system, *Int. J. Biol. Macromol.* 118 (2018) 640–648.
- T. Crouzier, et al., Modulating mucin hydration and lubrication by deglycosylation and polyethylene glycol binding, *Adv. Mater. Interfaces* 2 (18) (2015), 1500308.
- J.S. Brand, et al., Covalently crosslinked pig gastric mucin hydrogels prepared by radical-based chain-growth and thiol-ene mechanisms, *Macromol. Biosci.* 22 (2021), 2100274.
- S. Yang, C. Washington, Drug release from microparticulate systems, in: *Microencapsulation: Methods and Industrial Applications*, Taylor & Francis Group, New York, 2006.
- J. Song, et al., Bioinspired Dopamine/Mucin coatings provide lubricity, wear protection, and cell-repellent properties for medical applications, *Adv. Healthc. Mater.* 10 (4) (2021) 2000831.
- L.I. FitzGerald, A.P. Johnston, It's what's on the inside that counts: techniques for investigating the uptake and recycling of nanoparticles and proteins in cells, *J. Colloid Interface Sci.* 587 (2021) 64–78.
- J.J. Kennick, A.P. Johnston, R.G. Parton, Key principles and methods for studying the endocytosis of biological and nanoparticle therapeutics, *Nat. Nanotechnol.* 16 (3) (2021) 266–276.
- J. Rejman, et al., Size-dependent internalization of particles via the pathways of clathrin- and caveolae-mediated endocytosis, *Biochem. J.* 377 (1) (2004) 159–169.
- A. Panariti, G. Miscrocchi, I. Rivalta, The effect of nanoparticle uptake on cellular behavior: disrupting or enabling functions? *Nanotechnol. Sci. Appl.* 5 (2012) 87.
- H. Hillaireau, P. Couvreur, Nanocarriers' entry into the cell: relevance to drug delivery, *Cell. Mol. Life Sci.* 66 (17) (2009) 2873–2896.
- S. Naderinezhad, G. Amoebdiny, F. Maghirlaee, Co-delivery of hydrophilic and hydrophobic anticancer drugs using biocompatible pH-sensitive lipid-based nanocarriers for multidrug-resistant cancers, *RSC Adv.* 7 (48) (2017) 30008–30019.
- H. Calmet, et al., Nasal sprayed particle deposition in a human nasal cavity under different inhalation conditions, *PloS one* 14 (9) (2019), e0221330.
- F. Liverini, F. Buttini, O.S. Usmani, 100 years of drug delivery to the lungs, in: *Concepts and Principles of Pharmacology*, 2019, pp. 143–159.
- S. Hua, et al., Advances in oral nano-delivery systems for colon targeted drug delivery in inflammatory bowel disease: selective targeting to diseased versus healthy tissue, *Nanomedicine* 11 (5) (2015) 1117–1132.
- M.A. Alsaighbi, Concepts of oxidative stress and antioxidant defense in Crohn's disease, *World J. Gastroenterol.* 19 (39) (2013) 6540.
- E.B. Kurutas, The importance of antioxidants which play the role in cellular response against oxidative/nitrosative stress: current state, *Nutr. J.* 15 (1) (2015) 1–22.

**B.5.1 Supplementary information for: A stable mucin based nanoparticle system for the co-delivery of hydrophobic and hydrophilic drugs**

Supplementary Material

for

A pH-stable, mucin based nanoparticle system for the  
co-delivery of hydrophobic and hydrophilic drugs

Theresa M. Lutz<sup>1,2</sup>, Ceren Kimna<sup>1,2</sup>, and Oliver Lieleg<sup>1,2</sup>#

<sup>1</sup> School of Engineering and Design, Department of Materials Engineering,  
Technical University of Munich, Boltzmannstraße 15, 85748 Garching, Germany

<sup>2</sup> Center for Protein Assemblies and Munich Institute of Biomedical Engineering,  
Technical University of Munich, Ernst-Otto-Fischer Str. 8, 85748 Garching, Germany

# corresponding author:

Prof. Dr. Oliver Lieleg

Technical University of Munich, Center for Protein Assemblies (CPA)

Ernst-Otto-Fischer Straße 8, 85747, Garching, Germany

e-mail: [oliver.lieleg@tum.de](mailto:oliver.lieleg@tum.de),

phone: +49 89 289 10952, fax: + 49 89 289 10801

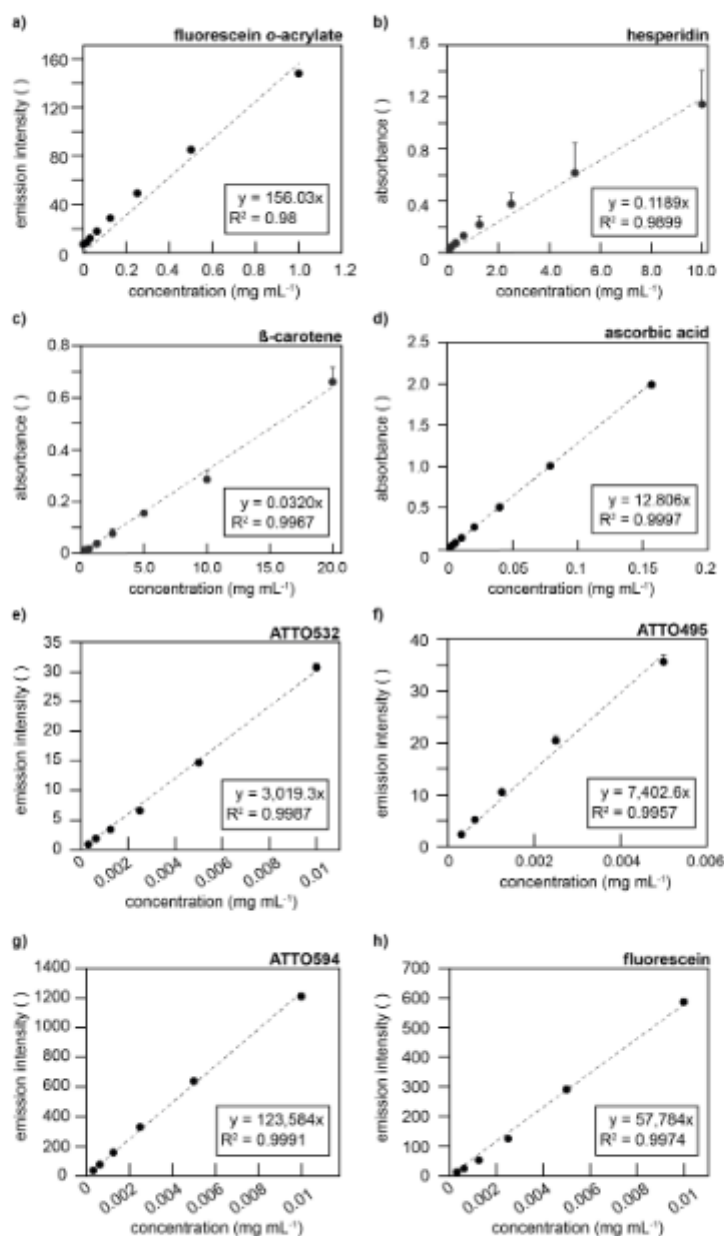
ORCID: TL (0000-0002-5072-3931); CK (0000-0003-2283-4295); OL (0000-0002-6874-7456)

## 1. Mucin purification

Porcine gastric mucins were purified as described in Schömig et al. [1]. In brief, the mucus was manually scraped off from the mucosal surface of pig stomachs. Afterwards, the mucus was mixed with 10 mM sodium phosphate buffer (pH 7.0; supplemented with 170 mM NaCl and 0.04% (w/v) NaN<sub>3</sub>) in a ratio of 1:5. The solution was homogenized at 4°C overnight, cellular debris was removed by two centrifugation steps (first, at 8300 *x g* and 4°C for 30 min; second, at 15000 *x g* and 4°C for 45 min) and one ultracentrifugation step (at 150000 *x g* and 4°C for 1 h). The mucin glycoproteins in the remaining supernatant were separated from smaller particles by size exclusion chromatography (ÄKTA purifier system) using a XK50/100 column filled with Sepharose 6FF. The collected fractions were dialyzed against ddH<sub>2</sub>O and concentrated by cross-flow filtration (equipped with a membrane with a MWCO of 100 kDa; GE Healthcare). After a final lyophilization step, the obtained protein stocks were stored at -80°C until further use.

## 2. Standard curves

The standard curves shown below were used to calculate the number of fluorescently labelled groups on the mucins (fluorescein (*o*-acrylate)), as well as the encapsulation efficiency and time dependent release of antioxidants (hesperidin,  $\beta$ -carotene, ascorbic acid) and fluorescent dyes (ATTO495, ATTO532, ATTO594, fluorescein) into/from mucin particles (Fig. S1).



**Figure S1: Standard curves for different molecules.** The absorbance/emission behavior of different molecules is determined in dilution series to (a) assess the availability of methacrylate groups grafted onto mucins or (b-h) to determine the encapsulation efficiency/loading capacity of cargo molecules into mucin particles (or their release behavior from the mucin particles). Error bars represent the standard deviation as obtained from three individual samples each.

### 3. Physico-chemical properties of antioxidants and fluorescent dyes

To describe the physicochemical properties of the molecules used in this study as putative cargoes in more detail, **Table S1** compiles information on these molecules, e.g., their molecular weight, charge, and solubility. For the last property, the partition coefficient (logP) is an important factor: typically,  $\log P > 0$  indicates hydrophobic molecules, whereas  $\log P < 0$  defines hydrophilic molecules [2].

**Table S1: Properties of selected antioxidants and fluorescent dyes.** The properties listed in the table include the manufacturer, molecular weight, charge profile and hydrophobicity/hydrophilicity of the individual antioxidants/dyes used for the drug encapsulation experiments as well as the determined encapsulation efficiency in UV-crosslinked mucin particles. N.A. = not applicable. N.D. = not determined/information not available.

Molecule	Manufacturer	Molecular weight [g mol <sup>-1</sup> ]	Net charge <sup>#</sup> @ pH=7.4	pK <sub>s</sub>	Partition coefficient (logP)
β-carotene	Sigma Aldrich (C9750)	537	neutral	N.A.	15 [3]
hesperidin	Sigma Aldrich (H5254)	611	neutral	pK = 7.15 [4]	-0.26 [4]
ascorbic acid	Carl Roth (3525.1)	176	anionic	pK <sub>1</sub> = 4.1 pK <sub>2</sub> = 11.6 [5]	-1.64 [6]
ATTO 495 carboxy	ATTO-TEC (AD 495-21)	452	cationic	N.D.	-0.81 [7] homepage ATTO-TEC: soluble in polar solvents*
ATTO 594 carboxy	ATTO-TEC (AD 594-21)	1137	anionic	N.D.	N.D. homepage ATTO-TEC: soluble in polar solvents*
fluorescein	Sigma Aldrich (F6377)	376	anionic	pK <sub>1</sub> = 3.14 pK <sub>2</sub> = 4.04 pK <sub>3</sub> = 6.28 [8]	0.61 [9]
ATTO 532 amine	ATTO-TEC (AD 532-91)	916	cationic	N.D.	-6.48 [10] homepage ATTO-TEC: soluble in polar solvents*

# according to the structural formula shown by the manufacturer

\* <https://www.atto-tec.com>: The product is soluble in polar solvents, e.g., dimethylformamide (DMF), dimethylsulfoxide (DMSO), or acetonitrile. However, due to their inherent reactivity, NHS-esters and maleimides must be well protected from OH-containing solvents like ethanol and, in particular, water.

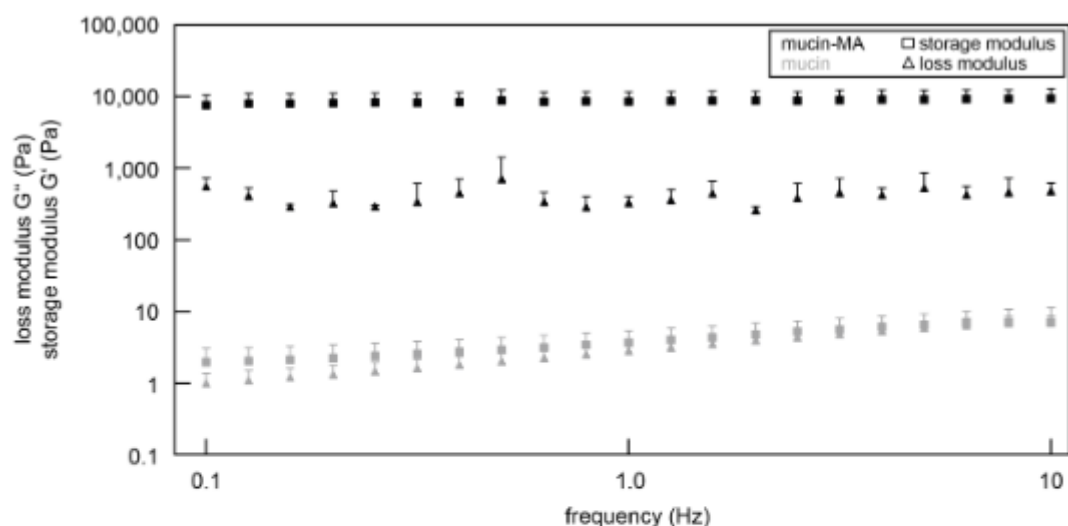


However, when attempting to categorize these molecules in terms of polarity, we not only take their partitioning coefficient into account; we also consider information from the manufacturer regarding what solvent to use when solubilizing these molecules. In addition, we also rate the molecular architecture of the molecules: if several aliphatic groups or aromatic rings are present, which carry no or hardly any polar functional groups, we consider this a strong indication for hydrophobic properties.

Based on this set information, we rate the following molecules as (rather) hydrophobic:  $\beta$ -carotene, ATTO495, and fluorescein; in contrast, we rate the following molecules as (rather) hydrophilic: hesperidin, ascorbic acid, ATTO594, and ATTO532.

#### 4. Rheological experiments

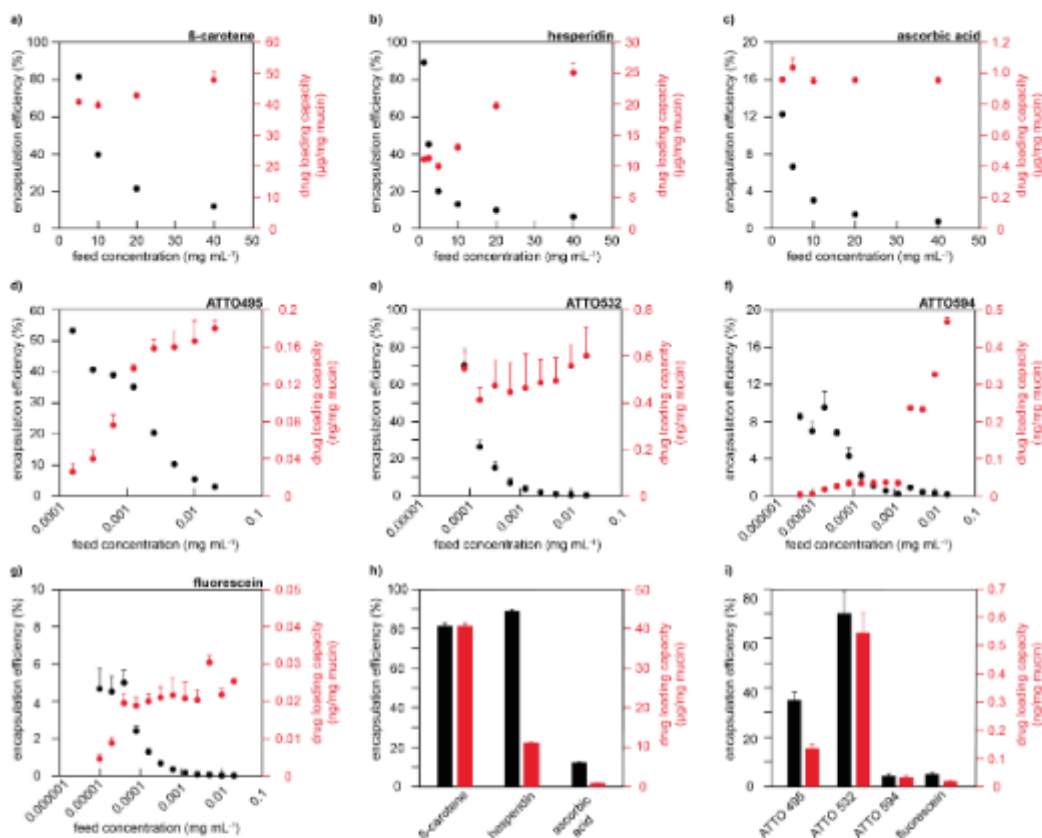
The frequency spectra shown below confirm that the viscoelastic properties of both, gels assembled from unmodified and mucin-MA glycoproteins, are quite independent from the applied shear frequency. Thus, characterizing both systems by the storage and loss modulus determined at an intermediate frequency of 1 Hz (as done in **Figure 2a** of the main text) is a valid approach (**Fig. S2**).



**Figure S2: Rheology characterization of hydrogels assembled from unmodified mucin glycoproteins and photo-crosslinked mucin-MA macromolecules, respectively.** Both gels are all dominated by elastic properties ( $G' > G''$ ) and both viscoelastic moduli show only a weak dependency on the applied shear frequency. The error bars represent the standard deviation as obtained from three individual samples.

## 5. Encapsulation efficiencies and loading capacities of mucin particles

To find the optimal conditions for loading the mucin particles with cargo molecules, dilution series with different concentrations of antioxidant/fluorescent dye molecules were prepared. Then, for each concentration, the encapsulation efficiency (EE) and drug loading (DL) capacity was determined as shown in Figure S3.



**Figure S3: Encapsulation efficiency and drug loading capacity of mucin particles loaded with different antioxidants or fluorescent dyes.** Three antioxidants (a:  $\beta$ -carotene; b: hesperidin; c: ascorbic acid) and four fluorescent dyes (d: ATTO495; e: ATTO532; f: ATTO594; g: fluorescein) are compared as cargoes for mucin particles. For the drug release experiments shown in the main paper, the respective cargo concentration was chosen as depicted in (h) and (i), *i.e.*, as a compromise that provides good loading capacity and encapsulation efficiency at the same time. The error bars represent the standard deviation as obtained from three individual samples.

Based on those pre-tests, release experiments were conducted (as shown in the main text) using the feed concentrations compiled in **Table S2**.

**Table S2:** Feed concentrations as well as the corresponding encapsulation efficiencies (EE) and drug loading capacities (DL) of the different cargo molecules as used for the drug release experiments shown in the main text.

Cargo molecule	Feed concentration	EE [%]	DL
$\beta$ -carotene	5 mg/mL	81 $\pm$ 1	(40.7 $\pm$ 0.7) $\mu$ g/mg mucin
hesperidin	1.25 mg/mL	89 $\pm$ 1	(11.1 $\pm$ 0.1) $\mu$ g/mg mucin
ATTO495	39 ng/mL	35 $\pm$ 3	(0.14 $\pm$ 0.01) ng/mg mucin
ATTO532	78 ng/mL	70 $\pm$ 9	(0.55 $\pm$ 0.07) ng/mg mucin

## 6. Mathematical models to describe the obtained drug release profiles

To identify the microscopic mechanism that mainly drives cargo liberation from the mucin particles, different kinetic models (e.g., zero order, first order, Higuchi, Hixson-Crowell and Korsmeyer-Peppas models) were fitted to the release data shown in Figure 4 of the main text. In the equations describing those different models (S1-S5), the following parameters occur: time ( $t$ ); mass of released drug at time point zero ( $W_0$ ), at time  $t$  ( $W_t$ ) and at equilibrium ( $W_\infty$ ); characteristic release constant of the system ( $k_i$ ); diffusion exponent ( $n$ ).

Zero-order kinetic model	$(W_t - W_0) = k_0 * t$	(Equation S1)
--------------------------	-------------------------	---------------

First-order kinetic model	$\ln\left(\frac{W_\infty}{W_t}\right) = k_1 * t$	(Equation S2)
---------------------------	--	---------------

Higuchi kinetic model	$W_t = k_2 * t^{\frac{1}{2}}$	(Equation S3)
-----------------------	-------------------------------	---------------

Hixson-Crowell kinetic model	$W_0^{\frac{1}{3}} - W_t^{\frac{1}{3}} = k_3 * t$	(Equation S4)
------------------------------	---	---------------

Korsmeyer-Peppas kinetic model	$\frac{W_t}{W_\infty} = k_4 * n^t$	(Equation S5)
--------------------------------	------------------------------------	---------------

When trying to fit those different models to the experimental release data obtained with hesperidin and  $\beta$ -carotene, we find that the Korsmeyer-Peppas model fits best (Fig. S4). Here, we obtain  $R^2$  values larger than 0.97 for each of the four data sets. As this model contains another parameter that can be determined from an optimized fit (i.e., the diffusion exponent 'n'). By doing so, we find  $n > 1$  for both cargo molecules and both buffer conditions. In agreement with one of the key assumptions of this model, this result suggests that drug release from the mucin particles is mainly driven by particle swelling [11].

a)

zero order

antioxidant	buffer	R <sup>2</sup>	k <sub>0</sub>
hesperidin	SIF	0.7422	2.4141
hesperidin	SGF	0.8855	5.8395
β-carotene	SIF	0.7811	3.2310
β-carotene	SGF	0.8867	5.7333

b)

first order

antioxidant	buffer	R <sup>2</sup>	k <sub>1</sub>
hesperidin	SIF	0.7576	-0.0122
hesperidin	SGF	0.9327	-0.0386
β-carotene	SIF	0.8063	-0.0172
β-carotene	SGF	0.9369	-0.0374

c)

Higuchi

antioxidant	buffer	R <sup>2</sup>	k <sub>2</sub>
hesperidin	SIF	0.9105	8.8153
hesperidin	SGF	0.9587	20.0320
β-carotene	SIF	0.9225	11.5770
β-carotene	SGF	0.9606	19.6730

d)

Hixson-Crowell

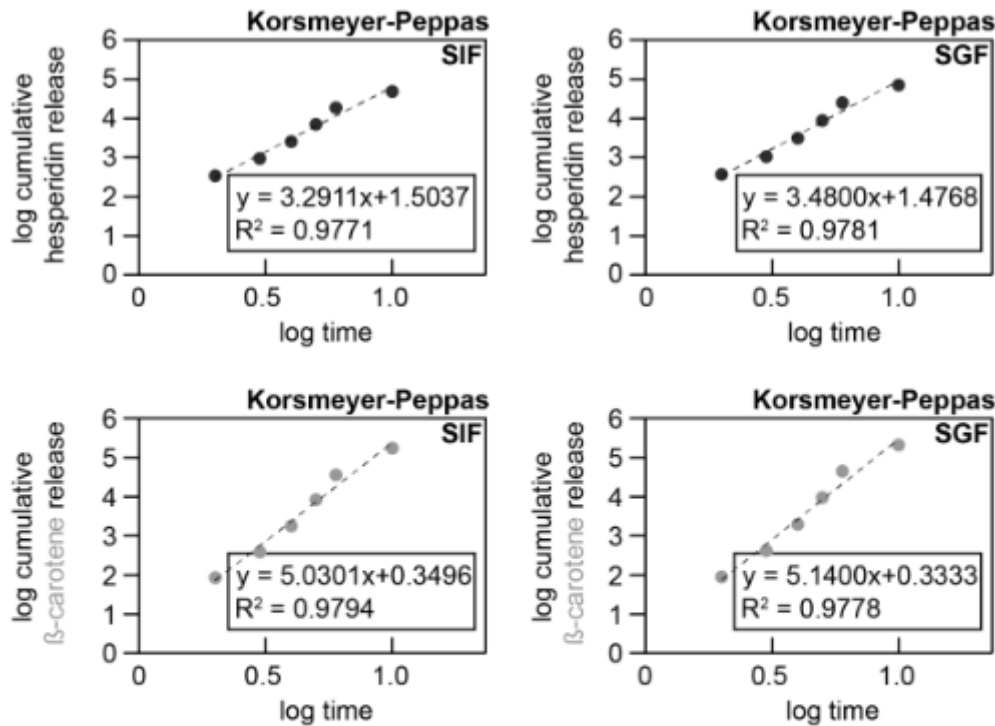
antioxidant	buffer	R <sup>2</sup>	k <sub>3</sub>
hesperidin	SIF	0.7524	0.0413
hesperidin	SGF	0.9192	0.1189
β-carotene	SIF	0.7980	0.0571
β-carotene	SGF	0.9222	0.1157

e)

Korsmeyer-Peppas

antioxidant	buffer	R <sup>2</sup>	k <sub>4</sub>	n
hesperidin	SIF	0.9771	0.1849	3.2911
hesperidin	SGF	0.9781	0.1693	3.4800
β-carotene	SIF	0.9794	-0.4564	5.0301
β-carotene	SGF	0.9778	-0.4772	5.1400

f)

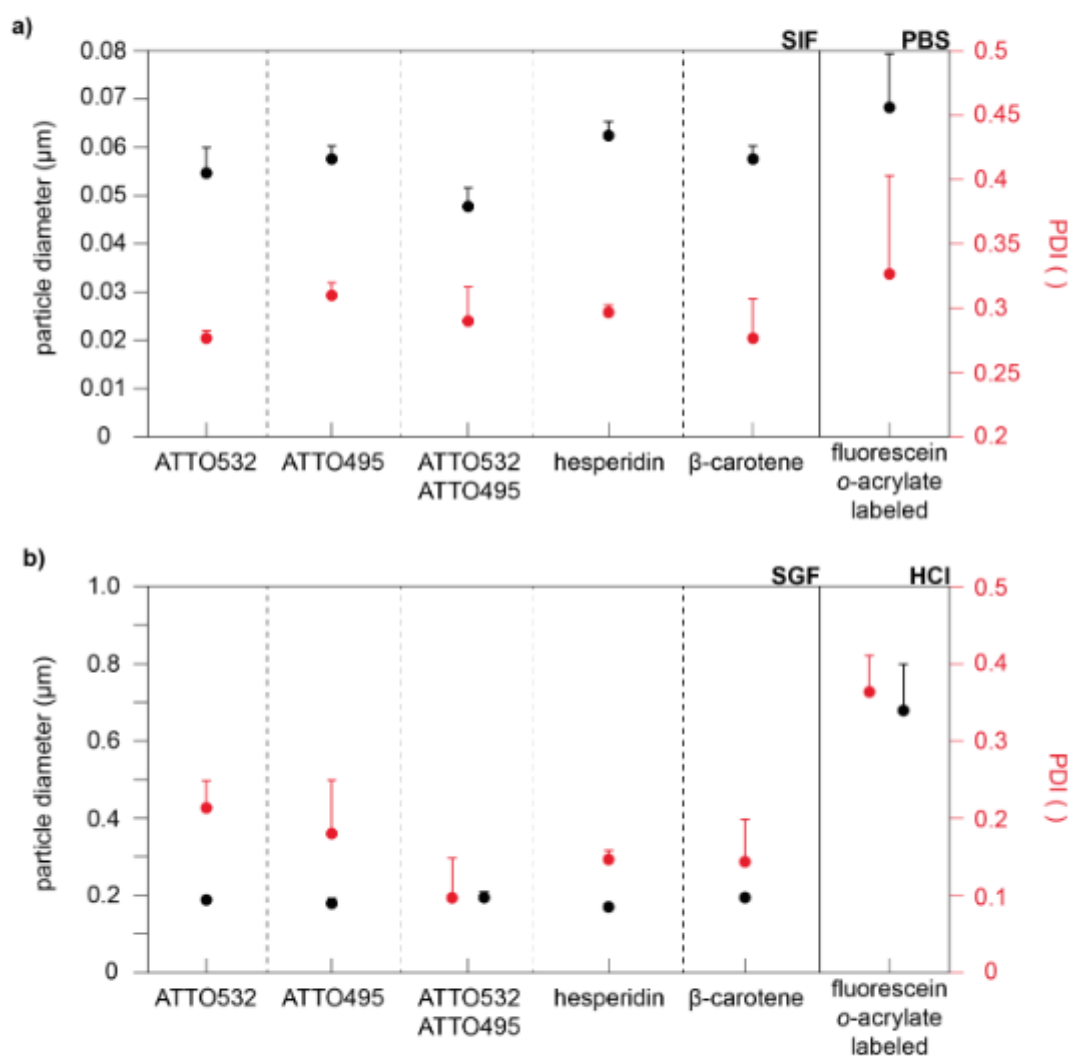


**Figure S4: Suitability of different release models for describing the kinetics of cargo release from mucin particles.** The tested release models include the zero order (a), first order (b), Higuchi (c), Hixson-Crowell (d) and Korsmeyer-Peppas (e) release models. (f) The Korsmeyer-Peppas-model describes the experimental data best.

9

## 7. Additional light scattering data on mucin-particles

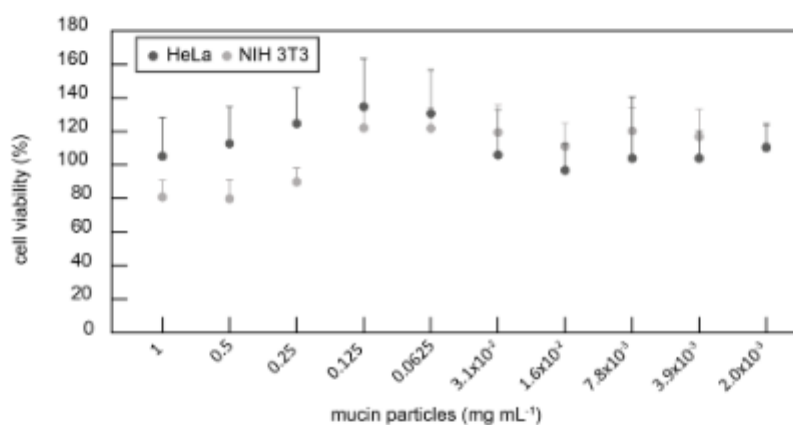
The data shown in Figure S5 demonstrates that the average size of the particle population (as well as its PDI) remains very similar when the mucin particles are loaded with molecular cargoes (ATTO532, ATTO495, hesperidin,  $\beta$ -carotene control) and then incubated in simulated intestinal fluid (Fig. S5a) or simulated gastric fluid (Fig. S5b). In addition, fluorescein *o*-acrylate labeled mucin particles incubated in 10 mM PBS (pH 8.0) exhibit very similar size and PDI values as well; only incubation in 10 mM HCl (pH 3.0) gives rise to slightly increased size and PDI values.



**Figure S5: Light scattering data obtained for different mucin particles.** (a,b) Average particle size and polydispersity index (PDI) of mucin particles loaded with a molecular cargo (ATTO532 and/or ATTO495, hesperidin,  $\beta$ -carotene) after incubation in simulated intestinal fluid (a) or in simulated gastric fluid (b). In addition, data on fluorescently labelled mucin particles incubate in 10 mM PBS (a) or 10 mM HCl (b) is shown as well. The error bars represent the standard deviation as obtained from three individual samples.

## 8. Water-soluble tetrazolium (WST-1) assay to assess putative cytotoxic effects of mucin particles

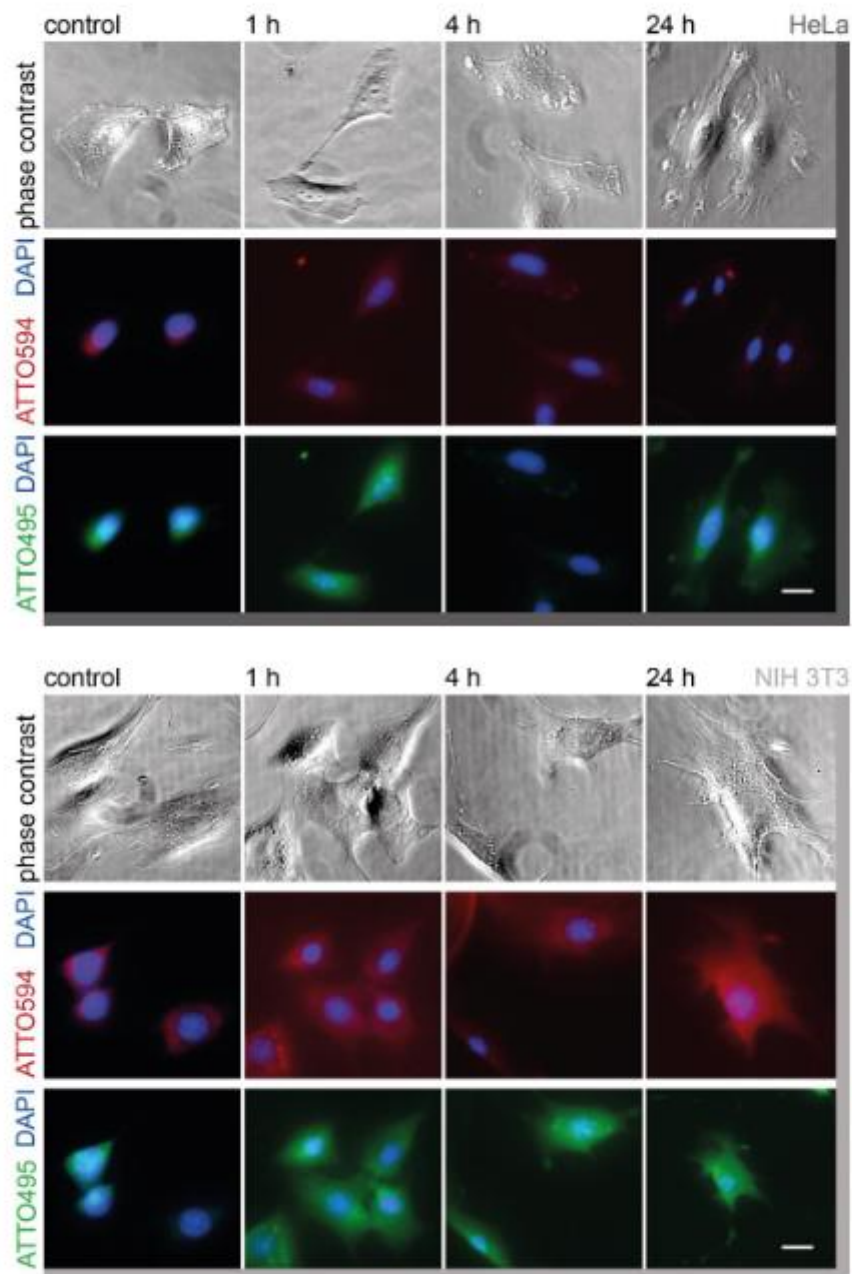
To determine if the mucin particles have any negative influence on cell viability, mucin particle solutions (with mucin concentrations ranging from 1 to  $2.0 \times 10^{-3}$  mg mL<sup>-1</sup>) were prepared in the corresponding cell culture media. Then, HeLa and NIH 3T3 cells (each were seeded at a density of 5,000 cells per well into a 96-well microtiter plate) were incubated with those particle solutions for 24 h at 37°. On the next day, the media was discarded, the cells were washed three times with D-PBS, and then incubated with the corresponding media containing 2 % of a WST-1 solution for 2 h. Then, the supernatant was removed and its absorption behavior was determined at an excitation wavelength of 450 nm (SpectraMax ABS Plus). The viability values depicted in **Figure S6** were then calculated as relative numbers using the result obtained for a group of control cells (which received particle-free media) for normalization.



**Figure S6:** Effect of cargo-free mucin particles on the viability of HeLa and NIH 3T3 cells, respectively. Data shown represents average values from test conducted with the same cell batch but using three independent sets of cells each. The error bars denote the standard error of the mean.

### 9. Additional information on the transport studies of ATTO dye-loaded mucin particles into eukaryotic cells

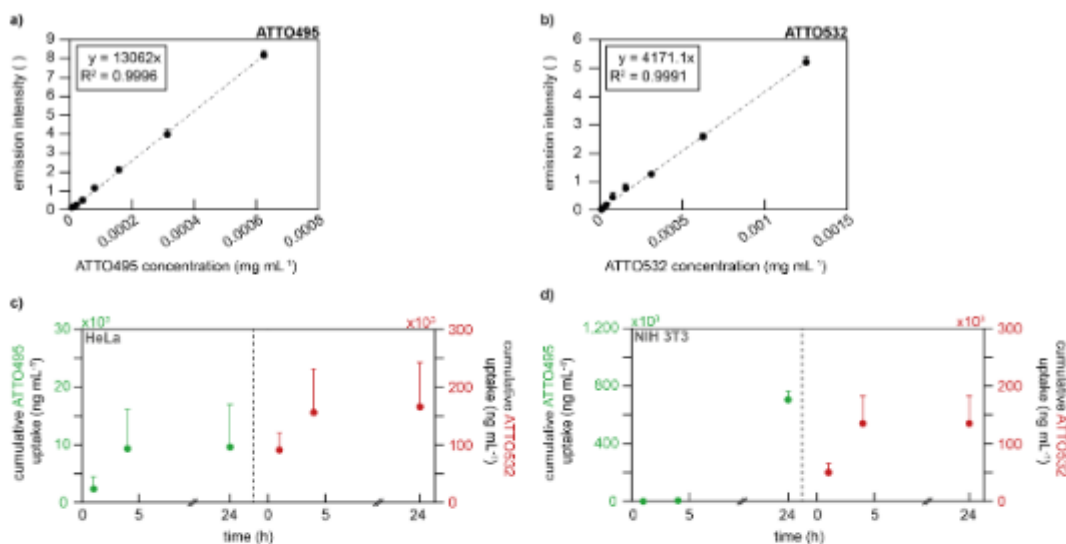
Figure S7 compiles example images of cells incubated with free ATTO molecules. Those (and additional, but very similar) fluorescence images were analyzed to calculate the data shown as open bars in Figure 6d of the main text.



**Figure S7:** Phase contrast and fluorescence microscope images of HeLa cells (upper panel) and NIH 3T3 cells (lower panel) incubated with free (= unencapsulated) ATTO495 and ATTO594 dye molecules, respectively. The scale bars represent 20  $\mu\text{m}$  and applies to all images in this figure.



In addition to analyzing fluorescence microscopy images of cells incubated with cargo-loaded mucin particles, also cell lysis experiments were conducted to determine the amount of dye cargo transported into the cytosol. Here, cells were seeded into wells of a 12-well microtiter plate (200,000 cells/well) and incubated with 0.5 mL of the respective culture medium at 37°C for 24 h [12]. Afterwards, the medium was replaced with fresh medium containing ATTO-loaded mucin particles. After an incubation time of 1 h, 4 h and 24 h, the cells were washed three times with D-PBS and collected from the microtiter plate by scraping. The collected cells were then centrifuged at 600 x g and 4°C for 10 min, and the supernatant was discarded. The cell pellets were resuspended in lysis buffer (20 mM HEPES, 10 mM KCl, 2 mM MgCl<sub>2</sub>, 1 mM EDTA, and 1 mM EGTA (pH = 7.2)), incubated on ice for 15 min, centrifuged at 20,800 x g at 4°C for 45 min, and the obtained supernatants (cytosolic fractions) were collected. The concentration of either ATTO dye in the cytosolic fractions obtained with this procedure was then quantified via fluorescence measurements (ATTO495: Ex/Em = 485/510 nm; ATTO532: Ex/Em = 540/590; Fluoroskan Ascent). To determine the ATTO dye concentrations in those cell lysis tests, additional standard curves were obtained to cover the low-concentration range of ATTO dyes we obtained in those lysis experiments (Fig. S8).



**Figure S8: Standard curves of ATTO dyes (a, b) as used for the cell lysis tests with HeLa (c) and NIH3T3 cells (d).** Error bars represent the standard deviation as obtained from three individual samples.


The results obtained from those cell lysis experiments are depicted in Figure S8. Similar to the results obtained from quantifying the fluorescence microscopy images, also here, we find that the amount of dyes arriving in the cells increases over time.


## References

1. Schömig, V.J., et al., *An optimized purification process for porcine gastric mucin with preservation of its native functional properties*. RSC advances, 2016. **6**(50): p. 44932-44943.
2. Roda, A., et al., *Bile acid structure-activity relationship: evaluation of bile acid lipophilicity using 1-octanol/water partition coefficient and reverse phase HPLC*. Journal of lipid research, 1990. **31**(8): p. 1433-1443.
3. Pham-Hoang, B.N., et al., *Strategies to improve carotene entry into cells of Yarrowia lipolytica in a goal of encapsulation*. Journal of Food Engineering, 2018. **224**: p. 88-94.
4. Váňová, J., et al., *Determination of distribution constants of antioxidants by electrokinetic chromatography*. Cogent Chemistry, 2017. **3**(1): p. 1385173.
5. Zuo, R., et al., *Determination of creatinine, uric and ascorbic acid in bovine milk and orange juice by hydrophilic interaction HPLC*. Food chemistry, 2015. **182**: p. 242-245.
6. Pepe, D., et al., *Decylglucoside-based microemulsions for cutaneous localization of lycopene and ascorbic acid*. International journal of pharmaceutics, 2012. **434**(1-2): p. 420-428.
7. Janiesch, J.-W., et al., *Key factors for stable retention of fluorophores and labeled biomolecules in droplet-based microfluidics*. Analytical chemistry, 2015. **87**(4): p. 2063-2067.
8. Zhang, X.-F., et al., *Prototropic equilibria, tautomerization and electronic absorption properties of dibenzofluorescein in aqueous solution related to its capability as a fluorescence probe*. Photochemical & Photobiological Sciences, 2008. **7**(9): p. 1079-1084.
9. Baba, K., et al., *A method for enhancing the ocular penetration of eye drops using nanoparticles of hydrolyzable dye*. Journal of controlled release, 2011. **153**(3): p. 278-287.
10. Hughes, L.D., R.J. Rawle, and S.G. Boxer, *Choose your label wisely: water-soluble fluorophores often interact with lipid bilayers*. PloS one, 2014. **9**(2): p. e87649.
11. Oucif, A., et al., *Poly (hydroxyethyl methacrylate-co-hydroxyethyl acrylate) soft contact lenses for acetazolamide release*. Polymer Bulletin, 2021: p. 1-20.
12. Kimna, C., et al., *DNA strands trigger the intracellular release of drugs from mucin-based nanocarriers*. ACS nano, 2020. **15**(2): p. 2350-2362.

## C. Licences for publications

### C.1 Bio-based and bio-inspired adhesives from animals and plants for biomedical applications

Home Help ▾ Live Chat Sign in Create Account



Bio-based and bio-inspired adhesives from animals and plants for biomedical applications

Author: Theresa M. Lutz,Ceren Kimna,Angela Casini,Oliver Lieleg

Publication: Materials Today Bio

Publisher: Elsevier

Date: January 2022

© 2022 The Authors. Published by Elsevier Ltd.

#### Journal Author Rights

Please note that, as the author of this Elsevier article, you retain the right to include it in a thesis or dissertation, provided it is not published commercially. Permission is not required, but please ensure that you reference the journal as the original source. For more information on this and on your other retained rights, please visit: <https://www.elsevier.com/about/our-business/policies/copyright#Author-rights>

BACK

CLOSE WINDOW

© 2023 Copyright - All Rights Reserved | [Copyright Clearance Center, Inc.](#) | [Privacy statement](#) | [Data Security and Privacy](#)  
| [For California Residents](#) | [Terms and Conditions](#)Comments? We would like to hear from you. E-mail us at [customercare@copyright.com](mailto:customercare@copyright.com)

## Author rights

The below table explains the rights that authors have when they publish with Elsevier, for authors who choose to publish either open access or subscription. These apply to the corresponding author and all co-authors.

Author rights in Elsevier's proprietary journals	Published open access	Published subscription
Retain patent and trademark rights	√	√
Retain the rights to use their research data freely without any restriction	√	√
Receive proper attribution and credit for their published work	√	√
Re-use their own material in new works without permission or payment (with full acknowledgement of the original article): 1. Extend an article to book length 2. Include an article in a subsequent compilation of their own work 3. Re-use portions, excerpts, and their own figures or tables in other works.	√	√
Use and share their works for scholarly purposes (with full acknowledgement of the original article): 1. In their own classroom teaching. Electronic and physical distribution of copies is permitted 2. If an author is speaking at a conference, they can present the article and distribute copies to the attendees 3. Distribute the article, including by email, to their students and to research colleagues who they know for their personal use 4. Share and publicize the article via Share Links, which offers 50 days' free access for anyone, without signup or registration 5. Include in a thesis or dissertation (provided this is not published commercially) 6. Share copies of their article privately as part of an invitation-only work group on commercial sites with which the publisher has a hosting agreement	√	√
Publicly share the preprint on any website or repository at any time.	√	√
Publicly share the accepted manuscript on non-commercial sites	√	√ using a CC BY-NC-ND license and usually only after an embargo period (see <a href="#">Sharing Policy</a> for more information)
Publicly share the final published article	√ in line with the author's choice of end user license	x
Retain copyright	√	x

## C.2 Repulsive backbone-backbone interactions modulate access to specific and unspecific binding sites on surface-bound mucins



### Repulsive Backbone-Backbone Interactions Modulate Access to Specific and Unspecific Binding Sites on Surface-Bound Mucins

Author: Theresa M. Lutz, Matthias Marczynski, Maximilian J. Grill, et al

Publication: Langmuir

Publisher: American Chemical Society

Date: Nov 1, 2020

Copyright © 2020, American Chemical Society

#### PERMISSION/LICENSE IS GRANTED FOR YOUR ORDER AT NO CHARGE

This type of permission/license, instead of the standard Terms and Conditions, is sent to you because no fee is being charged for your order. Please note the following:

- Permission is granted for your request in both print and electronic formats, and translations.
- If figures and/or tables were requested, they may be adapted or used in part.
- Please print this page for your records and send a copy of it to your publisher/graduate school.
- Appropriate credit for the requested material should be given as follows: "Reprinted (adapted) with permission from {COMPLETE REFERENCE CITATION}. Copyright {YEAR} American Chemical Society." Insert appropriate information in place of the capitalized words.
- One-time permission is granted only for the use specified in your RightsLink request. No additional uses are granted (such as derivative works or other editions). For any uses, please submit a new request.

If credit is given to another source for the material you requested from RightsLink, permission must be obtained from that source.

### C.3 Bioinspired dopamine/mucin coatings provide lubricity, wear protection, and cell-repellent properties for medical applications



- Home
- Help ▾
- Live Chat
- Sign in
- Create Account



#### Bioinspired Dopamine/Mucin Coatings Provide Lubricity, Wear Protection, and Cell-Repellent Properties for Medical Applications

Author: Oliver Lieleg, Nora Lang, Theresa M. Lutz, et al

Publication: Advanced Healthcare Materials

Publisher: John Wiley and Sons

Date: Sep 17, 2020

© 2020 The Authors. Published by Wiley-VCH GmbH

#### Quick Price Estimate

##### Content Delivery:

A copy of this content may be purchased following completion of your permissions order.  
High Res Image files - please contact Wiley

I would like to... ?	reuse in a dissertation/thesis ▾	Will you be translating? ?	No ▾
Requestor Type ?	Author of this Wiley article ▾	Select your currency	EUR - € ▾
Format ?	Print and electronic ▾	Quick Price	0.00 EUR
Portion ?	Full article ▾		

JOHN WILEY AND SONS LICENSE  
TERMS AND CONDITIONS

Jan 24, 2023

---

---

This Agreement between Theresa Lutz ("You") and John Wiley and Sons ("John Wiley and Sons") consists of your license details and the terms and conditions provided by John Wiley and Sons and Copyright Clearance Center.

License Number 5475241147191

License date Jan 24, 2023

Licensed Content  
Publisher John Wiley and Sons

Licensed Content  
Publication Advanced Healthcare Materials

Licensed Content Title Bioinspired Dopamine/Mucin Coatings Provide Lubricity, Wear  
Protection, and Cell-Repellent Properties for Medical Applications

Licensed Content  
Author Oliver Lieleg, Nora Lang, Theresa M. Lutz, et al

Licensed Content  
Date Sep 17, 2020

Licensed Content  
Volume 10

Licensed Content  
Issue 4

Licensed Content  
Pages 11

Type of use Dissertation/Thesis

Requestor type Author of this Wiley article

Format Print and electronic

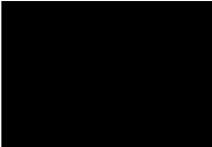
Portion Full article

Will you be translating? No

Title phd thesis of Theresa Monika Lutz

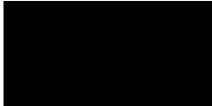
Institution name Technical University of Munich

Expected presentation date Jun 2023

Requestor Location Theresa Lutz  


Publisher Tax ID EU826007151

Billing Type Invoice

Billing Address Theresa Lutz  


Total 0.00 EUR

Terms and Conditions

**TERMS AND CONDITIONS**

This copyrighted material is owned by or exclusively licensed to John Wiley & Sons, Inc. or one of its group companies (each a "Wiley Company") or handled on behalf of a society with which a Wiley Company has exclusive publishing rights in relation to a particular work (collectively "WILEY"). By clicking "accept" in connection with completing this licensing transaction, you agree that the following terms and conditions apply to this transaction (along with the billing and payment terms and conditions established by the Copyright Clearance Center Inc., ("CCC's Billing and Payment terms and conditions"), at the time that you opened your RightsLink account (these are available at any time at <http://myaccount.copyright.com>).



## Terms and Conditions

- The materials you have requested permission to reproduce or reuse (the "Wiley Materials") are protected by copyright.
- You are hereby granted a personal, non-exclusive, non-sub licensable (on a stand-alone basis), non-transferable, worldwide, limited license to reproduce the Wiley Materials for the purpose specified in the licensing process. This license, and any CONTENT (PDF or image file) purchased as part of your order, is for a one-time use only and limited to any maximum distribution number specified in the license. The first instance of republication or reuse granted by this license must be completed within two years of the date of the grant of this license (although copies prepared before the end date may be distributed thereafter). The Wiley Materials shall not be used in any other manner or for any other purpose, beyond what is granted in the license. Permission is granted subject to an appropriate acknowledgement given to the author, title of the material/book/journal and the publisher. You shall also duplicate the copyright notice that appears in the Wiley publication in your use of the Wiley Material. Permission is also granted on the understanding that nowhere in the text is a previously published source acknowledged for all or part of this Wiley Material. Any third party content is expressly excluded from this permission.
- With respect to the Wiley Materials, all rights are reserved. Except as expressly granted by the terms of the license, no part of the Wiley Materials may be copied, modified, adapted (except for minor reformatting required by the new Publication), translated, reproduced, transferred or distributed, in any form or by any means, and no derivative works may be made based on the Wiley Materials without the prior permission of the respective copyright owner. For STM Signatory Publishers clearing permission under the terms of the [STM Permissions Guidelines](#) only, the terms of the license are extended to include subsequent editions and for editions in other languages, provided such editions are for the work as a whole in situ and does not involve the separate exploitation of the permitted figures or extracts. You may not alter, remove or suppress in any manner any copyright, trademark or other notices displayed by the Wiley Materials. You may not license, rent, sell, loan, lease, pledge, offer as security, transfer or assign the Wiley Materials on a stand-alone basis, or any of the rights granted to you hereunder to any other person.
- The Wiley Materials and all of the intellectual property rights therein shall at all times remain the exclusive property of John Wiley & Sons Inc, the Wiley Companies, or their respective licensors, and your interest therein is only that of having possession of and the right to reproduce the Wiley Materials pursuant to Section 2 herein during the continuance of this Agreement. You agree that you own no right, title or interest in or to the Wiley Materials or any of the intellectual property rights therein. You shall have no rights hereunder other than the license as provided for above in Section 2. No right, license or interest to any trademark, trade name, service mark or other branding ("Marks") of WILEY or its licensors is granted hereunder, and you agree that you shall not assert any such right, license or interest with respect thereto
- NEITHER WILEY NOR ITS LICENSORS MAKES ANY WARRANTY OR REPRESENTATION OF ANY KIND TO YOU OR ANY THIRD PARTY, EXPRESS, IMPLIED OR STATUTORY, WITH RESPECT TO THE MATERIALS OR THE ACCURACY OF ANY INFORMATION CONTAINED IN THE MATERIALS, INCLUDING, WITHOUT LIMITATION, ANY IMPLIED WARRANTY OF MERCHANTABILITY, ACCURACY, SATISFACTORY QUALITY, FITNESS FOR A PARTICULAR PURPOSE, USABILITY, INTEGRATION OR NON-INFRINGEMENT AND ALL SUCH WARRANTIES ARE HEREBY EXCLUDED BY WILEY AND ITS LICENSORS AND WAIVED BY YOU.

- WILEY shall have the right to terminate this Agreement immediately upon breach of this Agreement by you.
- You shall indemnify, defend and hold harmless WILEY, its Licensors and their respective directors, officers, agents and employees, from and against any actual or threatened claims, demands, causes of action or proceedings arising from any breach of this Agreement by you.
- IN NO EVENT SHALL WILEY OR ITS LICENSORS BE LIABLE TO YOU OR ANY OTHER PARTY OR ANY OTHER PERSON OR ENTITY FOR ANY SPECIAL, CONSEQUENTIAL, INCIDENTAL, INDIRECT, EXEMPLARY OR PUNITIVE DAMAGES, HOWEVER CAUSED, ARISING OUT OF OR IN CONNECTION WITH THE DOWNLOADING, PROVISIONING, VIEWING OR USE OF THE MATERIALS REGARDLESS OF THE FORM OF ACTION, WHETHER FOR BREACH OF CONTRACT, BREACH OF WARRANTY, TORT, NEGLIGENCE, INFRINGEMENT OR OTHERWISE (INCLUDING, WITHOUT LIMITATION, DAMAGES BASED ON LOSS OF PROFITS, DATA, FILES, USE, BUSINESS OPPORTUNITY OR CLAIMS OF THIRD PARTIES), AND WHETHER OR NOT THE PARTY HAS BEEN ADVISED OF THE POSSIBILITY OF SUCH DAMAGES. THIS LIMITATION SHALL APPLY NOTWITHSTANDING ANY FAILURE OF ESSENTIAL PURPOSE OF ANY LIMITED REMEDY PROVIDED HEREIN.
- Should any provision of this Agreement be held by a court of competent jurisdiction to be illegal, invalid, or unenforceable, that provision shall be deemed amended to achieve as nearly as possible the same economic effect as the original provision, and the legality, validity and enforceability of the remaining provisions of this Agreement shall not be affected or impaired thereby.
- The failure of either party to enforce any term or condition of this Agreement shall not constitute a waiver of either party's right to enforce each and every term and condition of this Agreement. No breach under this agreement shall be deemed waived or excused by either party unless such waiver or consent is in writing signed by the party granting such waiver or consent. The waiver by or consent of a party to a breach of any provision of this Agreement shall not operate or be construed as a waiver of or consent to any other or subsequent breach by such other party.
- This Agreement may not be assigned (including by operation of law or otherwise) by you without WILEY's prior written consent.
- Any fee required for this permission shall be non-refundable after thirty (30) days from receipt by the CCC.
- These terms and conditions together with CCC's Billing and Payment terms and conditions (which are incorporated herein) form the entire agreement between you and WILEY concerning this licensing transaction and (in the absence of fraud) supersedes all prior agreements and representations of the parties, oral or written. This Agreement may not be amended except in writing signed by both parties. This Agreement shall be binding upon and inure to the benefit of the parties' successors, legal representatives, and authorized assigns.
- In the event of any conflict between your obligations established by these terms and conditions and those established by CCC's Billing and Payment terms and conditions, these terms and conditions shall prevail.

- WILEY expressly reserves all rights not specifically granted in the combination of (i) the license details provided by you and accepted in the course of this licensing transaction, (ii) these terms and conditions and (iii) CCC's Billing and Payment terms and conditions.
- This Agreement will be void if the Type of Use, Format, Circulation, or Requestor Type was misrepresented during the licensing process.
- This Agreement shall be governed by and construed in accordance with the laws of the State of New York, USA, without regards to such state's conflict of law rules. Any legal action, suit or proceeding arising out of or relating to these Terms and Conditions or the breach thereof shall be instituted in a court of competent jurisdiction in New York County in the State of New York in the United States of America and each party hereby consents and submits to the personal jurisdiction of such court, waives any objection to venue in such court and consents to service of process by registered or certified mail, return receipt requested, at the last known address of such party.

#### WILEY OPEN ACCESS TERMS AND CONDITIONS

Wiley Publishes Open Access Articles in fully Open Access Journals and in Subscription journals offering Online Open. Although most of the fully Open Access journals publish open access articles under the terms of the Creative Commons Attribution (CC BY) License only, the subscription journals and a few of the Open Access Journals offer a choice of Creative Commons Licenses. The license type is clearly identified on the article.

##### The Creative Commons Attribution License

The [Creative Commons Attribution License \(CC-BY\)](#) allows users to copy, distribute and transmit an article, adapt the article and make commercial use of the article. The CC-BY license permits commercial and non-

##### Creative Commons Attribution Non-Commercial License

The [Creative Commons Attribution Non-Commercial \(CC-BY-NC\) License](#) permits use, distribution and reproduction in any medium, provided the original work is properly cited and is not used for commercial purposes.(see below)

##### Creative Commons Attribution-Non-Commercial-NoDerivs License

The [Creative Commons Attribution Non-Commercial-NoDerivs License \(CC-BY-NC-ND\)](#) permits use, distribution and reproduction in any medium, provided the original work is properly cited, is not used for commercial purposes and no modifications or adaptations are made. (see below)

##### Use by commercial "for-profit" organizations

Use of Wiley Open Access articles for commercial, promotional, or marketing purposes requires further explicit permission from Wiley and will be subject to a fee.

Further details can be found on Wiley Online Library  
<http://olabout.wiley.com/WileyCDA/Section/id-410895.html>

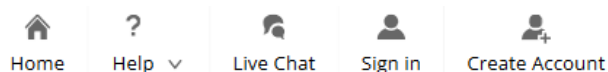
##### Other Terms and Conditions:

v1.10 Last updated September 2015

Questions? [customercare@copyright.com](mailto:customercare@copyright.com) or +1-855-239-3415 (toll free in the US) or +1-978-646-2777.

---

## C.4 DNA strands trigger the intracellular release of drugs from mucin-based nanocarriers



### DNA Strands Trigger the Intracellular Release of Drugs from Mucin-Based Nanocarriers



Author: Ceren Kimna, Theresa Monika Lutz, Hongji Yan, et al

Publication: ACS Nano

Publisher: American Chemical Society

Date: Feb 1, 2021

Copyright © 2021, American Chemical Society

#### PERMISSION/LICENSE IS GRANTED FOR YOUR ORDER AT NO CHARGE

This type of permission/license, instead of the standard Terms and Conditions, is sent to you because no fee is being charged for your order. Please note the following:

- Permission is granted for your request in both print and electronic formats, and translations.
- If figures and/or tables were requested, they may be adapted or used in part.
- Please print this page for your records and send a copy of it to your publisher/graduate school.
- Appropriate credit for the requested material should be given as follows: "Reprinted (adapted) with permission from {COMPLETE REFERENCE CITATION}. Copyright {YEAR} American Chemical Society." Insert appropriate information in place of the capitalized words.
- One-time permission is granted only for the use specified in your RightsLink request. No additional uses are granted (such as derivative works or other editions). For any uses, please submit a new request.

If credit is given to another source for the material you requested from RightsLink, permission must be obtained from that source.

## C.5 A stable mucin based nanoparticle system for the co-delivery of hydrophobic and hydrophilic drugs



RightsLink

Home

Help ▾

Live Chat

Sign in

Create Account



### A pH-stable, mucin based nanoparticle system for the co-delivery of hydrophobic and hydrophilic drugs

Author: Theresa M. Lutz, Ceren Kimna, Oliver Lieleg

Publication: International Journal of Biological Macromolecules

Publisher: Elsevier

Date: 31 August 2022

© 2022 Elsevier B.V. All rights reserved.

#### Journal Author Rights

Please note that, as the author of this Elsevier article, you retain the right to include it in a thesis or dissertation, provided it is not published commercially. Permission is not required, but please ensure that you reference the journal as the original source. For more information on this and on your other retained rights, please visit: <https://www.elsevier.com/about/our-business/policies/copyright#Author-rights>

BACK

CLOSE WINDOW

## Author rights

The below table explains the rights that authors have when they publish with Elsevier, for authors who choose to publish either open access or subscription. These apply to the corresponding author and all co-authors.

Author rights in Elsevier's proprietary journals	Published open access	Published subscription
Retain patent and trademark rights	√	√
Retain the rights to use their research data freely without any restriction	√	√
Receive proper attribution and credit for their published work	√	√
Re-use their own material in new works without permission or payment (with full acknowledgement of the original article): 1. Extend an article to book length 2. Include an article in a subsequent compilation of their own work 3. Re-use portions, excerpts, and their own figures or tables in other works.	√	√
Use and share their works for scholarly purposes (with full acknowledgement of the original article): 1. In their own classroom teaching. Electronic and physical distribution of copies is permitted 2. If an author is speaking at a conference, they can present the article and distribute copies to the attendees 3. Distribute the article, including by email, to their students and to research colleagues who they know for their personal use 4. Share and publicize the article via Share Links, which offers 50 days' free access for anyone, without signup or registration 5. Include in a thesis or dissertation (provided this is not published commercially) 6. Share copies of their article privately as part of an invitation-only work group on commercial sites with which the publisher has a hosting agreement	√	√
Publicly share the preprint on any website or repository at any time.	√	√
Publicly share the accepted manuscript on non-commercial sites	√	√ using a CC BY-NC-ND license and usually only after an embargo period (see <a href="#">Sharing Policy</a> for more information)
Publicly share the final published article	√ in line with the author's choice of end user license	x
Retain copyright	√	x

## D. Full list of publications

### D.1 Peer-reviewed

- 1 C. A. Rickert, **T. M. Lutz**, M. Marczynski, *Several sterilization strategies maintain the functionality of mucin glycoproteins*, *Macromolecular Bioscience*, 2020
- 2 C. Kimna, **T. M. Lutz**, H. Yan, J. Song, T. Crouzier, O. Lieleg, *DNA strands trigger the intracellular release of drugs from mucin-based nanocarriers*, *ACS Nano*, 2020
- 3 J. Song, **T. M. Lutz**, N. Lang, O. Lieleg, *Bioinspired dopamine/mucin coatings provide lubricity, wear protection, and cell-repellent properties for medical applications*, *Advanced Healthcare Materials*, 2020
- 4 **T. M. Lutz**, M. Marczynski, M. Grill, W. A. Wall, O. Lieleg, *Repulsive backbone-backbone interactions modulate access to specific and unspecific binding sites on surface-bound mucins*, *Langmuir*, 2020
- 5 M. G. Bauer, R. Reithmeir, **T. M. Lutz**, *Wetting behavior and stability of surface-modified polyurethane materials*, *Plasma Processes and Polymers*, 2021
- 6 L. Tebcharani, C. Wanzke, **T. M. Lutz**, J. Rodon-Fores, O. Lieleg, J. Boekhoven, *Emulsions of hydrolyzable oils for the zero-order release of hydrophobic drugs*, *Journal of Controlled Release*, 2021
- 7 **T. M. Lutz**, C. Kimna, Angela Casini, O. Lieleg, *Bio-based and bio-inspired adhesives from animals and plants for biomedical applications*, *Materials Today Bio*, 2022
- 8 C. Kimna, M. G. Bauer, **T. M. Lutz**, S. Mansi, E. Akyuz, Z. Doganyigit, P. Karakol, P. Mela, O. Lieleg, *Multifunctional 'Janus' films combine broad-range tissue adhesion with guided drug release*, *Advanced Functional Materials*, 2022
- 9 **T. M. Lutz**, C. Kimna, O. Lieleg, *A pH-stable mucin-based nanoparticle system for the co-delivery of hydrophobic and hydrophilic drugs*, *International Journal of Biological Macromolecules*, 2022
- 10 M. Marczynski, **T. M. Lutz**, R. Schlatterer, M. Henkel, B. Balzer, O. Lieleg, *Contamination with black carbon nanoparticles alters the selective permeability of mucin hydrogels: Implications for molecular transport across mucosal barriers*, *ACS Applied Nano Materials*, 2022

## D.2 Not peer-reviewed yet

### Paper

- 1 *Crosslinking strategy modulates the mechanical properties of mucin nanoparticles and the governing cellular uptake mechanisms*, unpublished

### Book chapter

- 1 C. Kimna, **T. M. Lutz**, O. Lieleg, *Fabrication and characterization of mucin nanoparticles for drug delivery applications*, *Mucins – Methods and Protocols*, edited by Akihiko Kameyama (submitted to Springer Nature)



## E. Bibliography

1. Xiong, G., et al., *Fast-curing mussel-inspired adhesive Derived from vegetable oil*. ACS Applied Bio Materials, 2021. **4**(2): p. 1360-1368.
2. Song, J., et al., *Bioinspired Dopamine/Mucin Coatings Provide Lubricity, Wear Protection, and Cell-Repellent Properties for Medical Applications*. Advanced Healthcare Materials, 2021. **10**(4): p. 2000831.
3. Marczynski, M., et al., *Charged glycan residues critically contribute to the adsorption and lubricity of mucins*. Colloids and Surfaces B: Biointerfaces, 2020. **187**: p. 110614.
4. Ushida, K. and T. Murata, *Materials science and engineering of mucin: a new aspect of mucin chemistry*. Studies in Natural Products Chemistry, 2013. **39**: p. 115-159.
5. Assmann, A., et al., *A highly adhesive and naturally derived sealant*. Biomaterials, 2017. **140**: p. 115-127.
6. Yaman, A., *Alternative methods of terminal sterilization for biologically active macromolecules*. Current Opinion in Drug Discovery & Development, 2001. **4**(6): p. 760-763.
7. Funatsu, K., et al., *Impact of ethylene oxide sterilization of polymer-based prefilled syringes on chemical degradation of a model therapeutic protein during storage*. Journal of Pharmaceutical Sciences, 2019. **108**(1): p. 770-774.
8. Rickert, C.A., et al., *Several sterilization strategies maintain the functionality of mucin glycoproteins*. Macromolecular Bioscience, 2020. **20**(7): p. 2000090.
9. Bekard, I.B., et al., *The effects of shear flow on protein structure and function*. Biopolymers, 2011. **95**(11): p. 733-745.
10. Yuk, H., et al., *Dry double-sided tape for adhesion of wet tissues and devices*. Nature, 2019. **575**(7781): p. 169-174.
11. Zhou, G. and T. Groth, *Host responses to biomaterials and anti-inflammatory design—a brief review*. Macromolecular Bioscience, 2018. **18**(8): p. 1800112.
12. Horejs, C., *Preventing fibrotic encapsulation*. Nature Reviews. Materials, 2021. **6**(7): p. 554-554.
13. Pakshir, P., et al., *Controlled release of low-molecular weight, polymer-free corticosteroid coatings suppresses fibrotic encapsulation of implanted medical devices*. Biomaterials, 2022: p. 121586.
14. Javitt, G., et al., *Assembly mechanism of mucin and von Willebrand factor polymers*. Cell, 2020. **183**(3): p. 717-729. e16.
15. Schömig, V.J., et al., *An optimized purification process for porcine gastric mucin with preservation of its native functional properties*. RSC advances, 2016. **6**(50): p. 44932-44943.
16. Marczynski, M., et al., *An improved, filtration-based process to purify functional mucins from mucosal tissues with high yields*. Separation and Purification Technology, 2022. **294**: p. 121209.
17. Duffy, C.V., L. David, and T. Crouzier, *Covalently-crosslinked mucin biopolymer hydrogels for sustained drug delivery*. Acta biomaterialia, 2015. **20**: p. 51-59.
18. Olăreț, E., et al., *Double-Cross-Linked Networks Based on Methacryloyl Mucin*. Polymers, 2021. **13**(11): p. 1706.
19. Kimna, C., et al., *DNA strands trigger the intracellular release of drugs from mucin-based nanocarriers*. ACS nano, 2020. **15**(2): p. 2350-2362.
20. Olsen, J.V., S.-E. Ong, and M. Mann, *Trypsin cleaves exclusively C-terminal to arginine and lysine residues*. Molecular & cellular proteomics, 2004. **3**(6): p. 608-614.
21. Polzonetti, V., et al., *Modulatory effect of oleuropein on digestive enzymes*, in *Olives and Olive Oil in Health and Disease Prevention*. 2010, Elsevier. p. 1327-1333.
22. Aloy, A., *Chirurgische Intensivmedizin: Kompendium für die Praxis*. Springer, 2007, ISBN 978-3-211-29679-0, S. 295.
23. Kilpatrick, D.C., *Animal lectins: a historical introduction and overview*. Biochimica et Biophysica Acta (BBA)-General Subjects, 2002. **1572**(2-3): p. 187-197.
24. Schwefel, D., et al., *Structural basis of multivalent binding to wheat germ agglutinin*. Journal of the American Chemical Society, 2010. **132**(25): p. 8704-8719.

25. Gilboa-Garber, N., [32] *Pseudomonas aeruginosa lectins*, in *Methods in enzymology*. 1982, Elsevier. p. 378-385.
26. del Carmen Portillo-Téllez, M., et al., *Folding and homodimerization of wheat germ agglutinin*. *Biophysical journal*, 2011. **101**(6): p. 1423-1431.
27. Peters, B.P., et al., *Interaction of wheat germ agglutinin with sialic acid*. *Biochemistry*, 1979. **18**(24): p. 5505-5511.
28. Ma, H. and R. O'Kennedy, *The structure of natural and recombinant antibodies*. *Peptide Antibodies*, 2015: p. 7-11.
29. Bara, J., et al., *Gastric M1 mucin, an early oncofetal marker of colon carcinogenesis, is encoded by the MUC5AC gene*. *International journal of cancer*, 1998. **75**(5): p. 767-773.
30. Day, W.A., et al., *Covalently deposited dyes: a new chromogen paradigm that facilitates analysis of multiple biomarkers in situ*. *Laboratory Investigation*, 2017. **97**(1): p. 104-113.
31. Müller, L., K. Theile, and V. Böhm, *In vitro antioxidant activity of tocopherols and tocotrienols and comparison of vitamin E concentration and lipophilic antioxidant capacity in human plasma*. *Molecular nutrition & food research*, 2010. **54**(5): p. 731-742.
32. Hecht, H. and S. Srebnik, *Structural characterization of sodium alginate and calcium alginate*. *Biomacromolecules*, 2016. **17**(6): p. 2160-2167.
33. Brus, J., et al., *Structure and dynamics of alginate gels cross-linked by polyvalent ions probed via solid state NMR spectroscopy*. *Biomacromolecules*, 2017. **18**(8): p. 2478-2488.
34. Kuo, C.K. and P.X. Ma, *Ionicly crosslinked alginate hydrogels as scaffolds for tissue engineering: Part 1. Structure, gelation rate and mechanical properties*. *Biomaterials*, 2001. **22**(6): p. 511-521.
35. Batista, P.S.P., et al., *Alginate: Pharmaceutical and medical applications, in Extracellular Sugar-Based Biopolymers Matrices*. 2019, Springer. p. 649-691.
36. Kuver, R. and S.P. Lee, *Calcium binding to biliary mucins is dependent on sodium ion concentration: relevance to cystic fibrosis*. *Biochemical and biophysical research communications*, 2004. **314**(2): p. 330-334.
37. Forstner, J. and G. Forstner, *Effects of calcium on intestinal mucin: implications for cystic fibrosis*. *Pediatric Research*, 1976. **10**(6): p. 609-613.
38. Dey, P., *Diagnostic Flow Cytometry in Cytology*. Springer, 2021, ISBN 9789811626555, Chapter 1-2.
39. Berne, B.J. and R. Pecora, *Dynamic light scattering: with applications to chemistry, biology, and physics*. 2000: Courier Corporation.
40. Doane, T.L., et al., *Nanoparticle  $\zeta$ -potentials*. *Accounts of chemical research*, 2012. **45**(3): p. 317-326.
41. Austin, J., et al., *Routine, ensemble characterisation of electrophoretic mobility in high and saturated ionic dispersions*. *Scientific reports*, 2020. **10**(1): p. 1-12.
42. Lowry, G.V., et al., *Guidance to improve the scientific value of zeta-potential measurements in nanoEHS*. *Environmental Science: Nano*, 2016. **3**(5): p. 953-965.
43. Bowen, R. and N. Hilal, *Atomic force microscopy in process engineering: An introduction to AFM for improved processes and products*. 2009: Butterworth-Heinemann.
44. Mezger, T., *Das Rheologie-Handbuch: Für Anwender von Rotationsund Oszillations-Rheometern*. Vincentz Verlag, 2000. Vincentz, Hannover.
45. Lutz, T.M., et al., *Bio-based and bio-inspired adhesives from animals and plants for biomedical applications*. *Materials Today Bio*, 2022: p. 100203.
46. Lutz, T.M., et al., *Repulsive backbone-backbone interactions modulate access to specific and unspecific binding sites on Surface-Bound mucins*. *Langmuir*, 2020. **36**(43): p. 12973-12982.
47. Marczyński, M., et al., *Transient binding promotes molecule penetration into mucin hydrogels by enhancing molecular partitioning*. *Biomaterials science*, 2018. **6**(12): p. 3373-3387.

48. Käsdorf, B.T., et al., *Mucin-inspired lubrication on hydrophobic surfaces*. Biomacromolecules, 2017. **18**(8): p. 2454-2462.
49. Winkeljann, B., et al., *Covalent Mucin Coatings Form Stable Anti-Biofouling Layers on a Broad Range of Medical Polymer Materials*. Advanced Materials Interfaces, 2020. **7**(4): p. 1902069.
50. Coles, J.M., D.P. Chang, and S. Zauscher, *Molecular mechanisms of aqueous boundary lubrication by mucinous glycoproteins*. Current Opinion in Colloid & Interface Science, 2010. **15**(6): p. 406-416.
51. Bansil, R. and B.S. Turner, *Mucin structure, aggregation, physiological functions and biomedical applications*. Current opinion in colloid & interface science, 2006. **11**(2-3): p. 164-170.
52. Corfield, A.P., et al., *Ocular mucins: purification, metabolism and functions*. Progress in Retinal and Eye Research, 1997. **16**(4): p. 627-656.
53. Linden, S., et al., *Mucins in the mucosal barrier to infection*. Mucosal immunology, 2008. **1**(3): p. 183-197.
54. Allen, A., D.A. Hutton, and J.P. Pearson, *The MUC2 gene product: a human intestinal mucin*. The international journal of biochemistry & cell biology, 1998. **30**(7): p. 797-801.
55. Lieleg, O., et al., *Mucin biopolymers as broad-spectrum antiviral agents*. Biomacromolecules, 2012. **13**(6): p. 1724-1732.
56. Crouzier, T., et al., *Modulating mucin hydration and lubrication by deglycosylation and polyethylene glycol binding*. Advanced Materials Interfaces, 2015. **2**(18): p. 1500308.
57. Marczynski, M., et al., *Structural alterations of mucins are associated with losses in functionality*. Biomacromolecules, 2021. **22**(4): p. 1600-1613.
58. Lu, W., E.P. Lillehoj, and K.C. Kim, *Effects of dexamethasone on Muc5ac mucin production by primary airway goblet cells*. American Journal of Physiology-Lung Cellular and Molecular Physiology, 2005. **288**(1): p. L52-L60.
59. Birchenough, G.M., et al., *New developments in goblet cell mucus secretion and function*. Mucosal immunology, 2015. **8**(4): p. 712-719.
60. Yan, H., et al., *Reversible condensation of mucins into nanoparticles*. Langmuir, 2018. **34**(45): p. 13615-13625.
61. Bautista-Sánchez, D., et al., *The promising role of miR-21 as a cancer biomarker and its importance in RNA-based therapeutics*. Molecular Therapy-Nucleic Acids, 2020. **20**: p. 409-420.
62. Lutz, T.M., C. Kimna, and O. Lieleg, *A pH-stable, mucin based nanoparticle system for the co-delivery of hydrophobic and hydrophilic drugs*. International Journal of Biological Macromolecules, 2022. **215**: p. 102-112.
63. Marczynski, M., C. Kimna, and O. Lieleg, *Purified mucins in drug delivery research*. Advanced Drug Delivery Reviews, 2021. **178**: p. 113845.
64. Foroozandeh, P. and A.A. Aziz, *Insight into cellular uptake and intracellular trafficking of nanoparticles*. Nanoscale research letters, 2018. **13**(1): p. 1-12.
65. Liu, W., et al., *Stress-induced mucus secretion and its composition by a combination of proteomics and metabolomics of the jellyfish Aurelia coerulea*. Marine drugs, 2018. **16**(9): p. 341.
66. Chaudhary, G., et al., *Concentration-independent mechanics and structure of hagfish slime*. Acta biomaterialia, 2018. **79**: p. 123-134.
67. Ewoldt, R.H., T.M. Winegard, and D.S. Fudge, *Non-linear viscoelasticity of hagfish slime*. International Journal of Non-Linear Mechanics, 2011. **46**(4): p. 627-636.
68. Joseph, C., Y. Togawa, and N. Shindo, *Bacterial and viral infections associated with influenza*. Influenza and other respiratory viruses, 2013. **7**: p. 105-113.
69. Chillappagari, S., et al., *Altered protease and antiprotease balance during a COPD exacerbation contributes to mucus obstruction*. Respiratory Research, 2015. **16**(1): p. 1-9.
70. Hedstrom, L., *Serine protease mechanism and specificity*. Chemical reviews, 2002. **102**(12): p. 4501-4524.

71. Buccheri, D., et al., *Understanding and managing in-stent restenosis: a review of clinical data, from pathogenesis to treatment*. Journal of thoracic disease, 2016. **8**(10): p. E1150.
72. Newby, A.C. and A.B. Zaltsman, *Molecular mechanisms in intimal hyperplasia*. The Journal of pathology, 2000. **190**(3): p. 300-309.
73. Matsushashi, Y., et al., *Real-time visualization of thrombus formation at the interface between connectors and tubes in medical devices by using optical coherence tomography*. Plos one, 2017. **12**(12): p. e0188729.
74. Simpson, F.C., et al., *Collagen analogs with phosphorylcholine are inflammation-suppressing scaffolds for corneal regeneration from alkali burns in mini-pigs*. Communications biology, 2021. **4**(1): p. 608.
75. Patil, S.D., F. Papadimitrakopoulos, and D.J. Burgess, *Concurrent delivery of dexamethasone and VEGF for localized inflammation control and angiogenesis*. Journal of controlled release, 2007. **117**(1): p. 68-79.
76. Weiss, L., *The cell periphery*. International review of cytology, 1969. **26**: p. 63-105.
77. Sun, S., et al., *Specificity and mechanism of action of alpha-helical membrane-active peptides interacting with model and biological membranes by single-molecule force spectroscopy*. Scientific reports, 2016. **6**(1): p. 1-10.
78. Rascol, E., J.-M. Devoisselle, and J. Chopineau, *The relevance of membrane models to understand nanoparticles–cell membrane interactions*. Nanoscale, 2016. **8**(9): p. 4780-4798.
79. Barile, F.A., *Principles of Toxicology Testing*, Taylor & Francis, 2013, ISBN 9781842145289, chapter 3.
80. Takao, S. and H. Shinchi, *Pancreaticogastrostomy: a pancreas-transfixing method with duct-to-mucosa anastomosis (with video)*. Journal of Hepato-biliary-pancreatic Sciences, 2012. **19**(2): p. 131-134.
81. Kanza Aziz, C.L.W. and A.A. Javed, *Operative Complications and Their Management Following Resection*. Surgery for Pancreatic and Periapillary Cancer: Principles and Practice, 2018: p. 227.
82. Walker, D., et al., *Enzymatically active biomimetic micropropellers for the penetration of mucin gels*. Science Advances, 2015. **1**(11): p. e1500501.
83. Li, L., et al., *A microfluidic in vitro system for the quantitative study of the stomach mucus barrier function*. Lab on a Chip, 2012. **12**(20): p. 4071-4079.
84. Cui, W., J. Li, and G. Decher, *Self-assembled smart nanocarriers for targeted drug delivery*. Advanced Materials, 2016. **28**(6): p. 1302-1311.
85. Zhang, W., et al., *Mitochondria-specific drug release and reactive oxygen species burst induced by polyprodrug nanoreactors can enhance chemotherapy*. Nature communications, 2019. **10**(1): p. 1-14.
86. Wang, S., et al., *Tumor-specific drug release and reactive oxygen species generation for cancer chemo/chemodynamic combination therapy*. Advanced Science, 2019. **6**(5): p. 1801986.
87. Dehghani, E., M. Salami-Kalajahi, and H. Roghani-Mamaqani, *Simultaneous two drugs release from Janus particles prepared via polymerization-induced phase separation approach*. Colloids and Surfaces B: Biointerfaces, 2018. **170**: p. 85-91.
88. Wang, T., et al., *Potential application of functional porous TiO<sub>2</sub> nanoparticles in light-controlled drug release and targeted drug delivery*. Acta biomaterialia, 2015. **13**: p. 354-363.
89. Park, C., et al., *Controlled release of guest molecules from mesoporous silica particles based on a pH-responsive polypseudorotaxane motif*. Angewandte Chemie International Edition, 2007. **46**(9): p. 1455-1457.
90. Yang, L., et al., *Bio-inspired lubricant drug delivery particles for the treatment of osteoarthritis*. Nanoscale, 2020. **12**(32): p. 17093-17102.
91. Dey, S., et al., *DNA origami*. Nature Reviews Methods Primers, 2021. **1**(1): p. 1-24.
92. Tebcharani, L., et al., *Emulsions of hydrolyzable oils for the zero-order release of hydrophobic drugs*. Journal of Controlled Release, 2021. **339**: p. 498-505.

93. Fischer, V. and M. Haffner-Luntzer. *Interaction between bone and immune cells: Implications for postmenopausal osteoporosis*. in *Seminars in cell & developmental biology*. 2022. Elsevier.
94. Liu, C., et al., *Effects of combined calcium and vitamin D supplementation on osteoporosis in postmenopausal women: a systematic review and meta-analysis of randomized controlled trials*. *Food & function*, 2020. **11**(12): p. 10817-10827.
95. Ornelas-Soto, N., et al., *Enhancing internalization of silica particles in myocardial cells through surface modification*. *Materials Science and Engineering: C*, 2017. **79**: p. 831-840.
96. Sacanna, S. and D.J. Pine, *Shape-anisotropic colloids: Building blocks for complex assemblies*. *Current opinion in colloid & interface science*, 2011. **16**(2): p. 96-105.
97. Tang, L., et al., *Self-Assembly Mechanism of Complex Corrugated Particles*. *Journal of the American Chemical Society*, 2021. **143**(47): p. 19655-19667.
98. Lakshmanan, I., et al., *MUC5AC interactions with integrin  $\beta$ 4 enhances the migration of lung cancer cells through FAK signaling*. *Oncogene*, 2016. **35**(31): p. 4112-4121.
99. Yamanoi, K. and J. Nakayama, *Reduced  $\alpha$ GlcNAc glycosylation on gastric gland mucin is a biomarker of malignant potential for gastric cancer, Barrett's adenocarcinoma, and pancreatic cancer*. *Histochemistry and Cell Biology*, 2018. **149**(6): p. 569-575.
100. Yang, J., *Identification of novel biomarkers, MUC5AC, MUC1, KRT7, GAPDH, CD44 for gastric cancer*. *Medical Oncology*, 2020. **37**(5): p. 1-10.
101. Lee, H.K., et al., *Expression of mucins (MUC1, MUC2, MUC5AC and MUC6) in ALK-positive lung cancer: Comparison with EGFR-mutated lung cancer*. *Pathology-Research and Practice*, 2019. **215**(3): p. 459-465.
102. Kufe, D.W., *Mucins in cancer: function, prognosis and therapy*. *Nature Reviews Cancer*, 2009. **9**(12): p. 874-885.
103. Ruprai, H., et al., *Porous chitosan adhesives with L-DOPA for enhanced photochemical tissue bonding*. *Acta Biomaterialia*, 2020. **101**: p. 314-326.
104. Zhou, D., et al., *Dopamine-modified hyaluronic acid hydrogel adhesives with fast-forming and high tissue adhesion*. *ACS applied materials & interfaces*, 2020. **12**(16): p. 18225-18234.
105. Gowda, A.H., et al., *Design of tunable gelatin-dopamine based bioadhesives*. *International Journal of Biological Macromolecules*, 2020. **164**: p. 1384-1391.
106. Liu, H., et al., *A dopamine-functionalized aqueous-based silk protein hydrogel bioadhesive for biomedical wound closure*. *New Journal of Chemistry*, 2020. **44**(3): p. 884-891.
107. Kimna, C., et al., *Multifunctional "Janus-Type" Bilayer Films Combine Broad-Range Tissue Adhesion with Guided Drug Release*. *Advanced Functional Materials*, 2022: p. 2105721.
108. Le, N.X.T. and N.Y. Lee, *Chitosan-polydopamine hydrogel complex: a novel green adhesion agent for reversibly bonding thermoplastic microdevice and its application for cell-friendly microfluidic 3D cell culture*. *Lab on a Chip*, 2020. **20**(19): p. 3524-3534.
109. Pham, T.-N., et al., *In situ formation of silver nanoparticles-contained gelatin-PEG-dopamine hydrogels via enzymatic cross-linking reaction for improved antibacterial activities*. *International journal of biological macromolecules*, 2020. **146**: p. 1050-1059.
110. Zhu, W., et al., *A novel DOPA-albumin based tissue adhesive for internal medical applications*. *Biomaterials*, 2017. **147**: p. 99-115.
111. Murphy, C.M., M.G. Haugh, and F.J. O'brien, *The effect of mean pore size on cell attachment, proliferation and migration in collagen-glycosaminoglycan scaffolds for bone tissue engineering*. *Biomaterials*, 2010. **31**(3): p. 461-466.
112. Oladapo, B.I., S. Zahedi, and A. Adeoye, *3D printing of bone scaffolds with hybrid biomaterials*. *Composites Part B: Engineering*, 2019. **158**: p. 428-436.
113. Ghouse, S., et al., *The design and in vivo testing of a locally stiffness-matched porous scaffold*. *Applied materials today*, 2019. **15**: p. 377-388.

114. Barik, D., K. Kundu, and M. Dash, *Montmorillonite stabilized chitosan-co-mucin hydrogel for tissue engineering applications*. RSC advances, 2021. **11**(48): p. 30329-30342.
115. Barik, D., et al., *Polymer-Protein Hybrid Network Involving Mucin: A Mineralized Biomimetic Template for Bone Tissue Engineering*. Macromolecular Bioscience, 2021. **21**(6): p. 2000381.
116. Gurtner, G.C., et al., *Wound repair and regeneration*. Nature, 2008. **453**(7193): p. 314-321.
117. Adikwu, M., J. Okafor, and E. Ibezim, *Evaluation of a Mucin-Honey formulation for Healing in Full Thickness Experimental Wounds in Rats*. Journal of Pharmaceutical Research, 2012. **11**(2): p. 49-55.
118. Allaw, M., et al., *Innovative strategies to treat skin wounds with mangiferin: fabrication of transfersomes modified with glycols and mucin*. Nanomedicine, 2020. **15**(17): p. 1671-1685.
119. Vinogradov, S.V., T.K. Bronich, and A.V. Kabanov, *Nanosized cationic hydrogels for drug delivery: preparation, properties and interactions with cells*. Advanced drug delivery reviews, 2002. **54**(1): p. 135-147.
120. Lotito, V. and T. Zambelli, *Playing with sizes and shapes of colloidal particles via dry etching methods*. Advances in Colloid and Interface Science, 2022. **299**: p. 102538.
121. Wang, J., et al., *More effective nanomedicines through particle design*. small, 2011. **7**(14): p. 1919-1931.
122. Brown, T.D., et al., *Effect of Nanoparticle Composition, Size, Shape, and Stiffness on Penetration Across the Blood-Brain Barrier*. ACS Biomaterials Science & Engineering, 2020. **6**(9): p. 4916-4928.
123. Wang, S., et al., *Penetration of nanoparticles across a lipid bilayer: effects of particle stiffness and surface hydrophobicity*. Nanoscale, 2019. **11**(9): p. 4025-4034.
124. Li, M., Z. Gao, and J. Cui, *Modulation of Colloidal Particle Stiffness for the Exploration of Bio-Nano Interactions*. Langmuir, 2022.
125. Swanson, J.A., *Shaping cups into phagosomes and macropinosomes*. Nature reviews Molecular cell biology, 2008. **9**(8): p. 639-649.
126. Danhier, F., et al., *PLGA-based nanoparticles: an overview of biomedical applications*. Journal of controlled release, 2012. **161**(2): p. 505-522.
127. Locatelli, E. and M. Comes Franchini, *Biodegradable PLGA-b-PEG polymeric nanoparticles: synthesis, properties, and nanomedical applications as drug delivery system*. Journal of Nanoparticle Research, 2012. **14**(12): p. 1-17.
128. Jain, A.K. and S. Thareja, *In vitro and in vivo characterization of pharmaceutical nanocarriers used for drug delivery*. Artificial cells, nanomedicine, and biotechnology, 2019. **47**(1): p. 524-539.
129. Champion, J.A., Y.K. Katare, and S. Mitragotri, *Particle shape: a new design parameter for micro-and nanoscale drug delivery carriers*. Journal of controlled release, 2007. **121**(1-2): p. 3-9.
130. Beck-Broichsitter, M., et al., *Characterization of novel spray-dried polymeric particles for controlled pulmonary drug delivery*. Journal of controlled release, 2012. **158**(2): p. 329-335.
131. Butnarasu, C., et al., *Mucosomes: Intrinsically Mucoadhesive Glycosylated Mucin Nanoparticles as Multi-Drug Delivery Platform*. Advanced Healthcare Materials, 2022. **11**(15): p. 2200340.
132. Phan, H.T. and A.J. Haes, *What does nanoparticle stability mean?* The Journal of Physical Chemistry C, 2019. **123**(27): p. 16495-16507.
133. Hoshino, Y., H. Lee, and Y. Miura, *Interaction between synthetic particles and biomacromolecules: fundamental study of nonspecific interaction and design of nanoparticles that recognize target molecules*. Polymer Journal, 2014. **46**(9): p. 537-545.
134. Kimna, C., et al., *Biopolymer-based nanoparticles with tunable mucoadhesivity efficiently deliver therapeutics across the corneal barrier*. Materials Science and Engineering: C, 2021. **121**: p. 111890.

135. Rezgui, R., et al., *Precise quantification of cellular uptake of cell-penetrating peptides using fluorescence-activated cell sorting and fluorescence correlation spectroscopy*. *Biochimica et Biophysica Acta (BBA)-Biomembranes*, 2016. **1858**(7): p. 1499-1506.
136. Bridgewater, R.E., C.H. Streuli, and P.T. Caswell, *Extracellular matrix promotes clathrin-dependent endocytosis of prolactin and STAT5 activation in differentiating mammary epithelial cells*. *Scientific reports*, 2017. **7**(1): p. 1-10.
137. FitzGerald, L.I. and A.P. Johnston, *It's what's on the inside that counts: Techniques for investigating the uptake and recycling of nanoparticles and proteins in cells*. *Journal of Colloid and Interface Science*, 2021. **587**: p. 64-78.
138. Dutta, D. and J.G. Donaldson, *Search for inhibitors of endocytosis: Intended specificity and unintended consequences*. *Cellular logistics*, 2012. **2**(4): p. 203-208.
139. Brandenberger, C., et al., *Quantitative evaluation of cellular uptake and trafficking of plain and polyethylene glycol-coated gold nanoparticles*. *Small*, 2010. **6**(15): p. 1669-1678.
140. Rejman, J., et al., *Size-dependent internalization of particles via the pathways of clathrin-and caveolae-mediated endocytosis*. *Biochemical journal*, 2004. **377**(1): p. 159-169.
141. Panariti, A., G. Miserocchi, and I. Rivolta, *The effect of nanoparticle uptake on cellular behavior: disrupting or enabling functions?* *Nanotechnology, science and applications*, 2012. **5**: p. 87.
142. Wang, Z., et al., *Size and dynamics of caveolae studied using nanoparticles in living endothelial cells*. *ACS nano*, 2009. **3**(12): p. 4110-4116.
143. Hillaireau, H. and P. Couvreur, *Nanocarriers' entry into the cell: relevance to drug delivery*. *Cellular and molecular life sciences*, 2009. **66**(17): p. 2873-2896.
144. Smith, S.A., et al., *The endosomal escape of nanoparticles: toward more efficient cellular delivery*. *Bioconjugate chemistry*, 2018. **30**(2): p. 263-272.
145. Chen, J., et al., *Metal-phenolic coatings as a platform to trigger endosomal escape of nanoparticles*. *ACS nano*, 2019. **13**(10): p. 11653-11664.
146. Goldshtein, M., et al., *Mechanisms of cellular uptake and endosomal escape of calcium-siRNA nanocomplexes*. *International journal of pharmaceutics*, 2016. **515**(1-2): p. 46-56.
147. Guo, P., et al., *Nanoparticle elasticity directs tumor uptake*. *Nature communications*, 2018. **9**(1): p. 1-9.

## **F. Acknowledgements**

Ein großer Dank gilt allen, die mich während meiner gesamten Promotionszeit unterstützt haben und maßgeblich dazu beigetragen haben, dass meine eingereichte Dissertation in dieser Art und Weise zustande gekommen ist.

Natürlich möchte ich mich an dieser Stelle zunächst bei Prof. Dr. Oliver Lieleg bedanken, der mir die Möglichkeit eingeräumt hat, dass ich als Biochemikerin an einem eher physikalisch begründeten Lehrstuhl arbeiten durfte. Vielen Dank auch für die Bereitstellung der abwechslungsreichen Themen und die Verantwortung, die ich für meine Projekte übernehmen durfte. Des Weiteren möchte ich mich für die gute Betreuung, die Unterstützung durch fachliche Diskussionen und konstruktive Ratschläge, und das Korrigieren einiger Manuskripte während meiner Promotionszeit bedanken.

Außerdem herzlichsten Dank an die Mitglieder der Prüfungskommission für die Umsetzung der Prüfungsvorgaben im Rahmen des Protokolls.

Natürlich gebührt auch ein großer Dank an alle KollaborationspartnerInnen – Prof. Dr. Thomas Crouzier, Dr. Hongji Yan, Dr. Nora Lang, Prof. Dr. Wolfgang A. Wall, Dr. Maximilian Grill, Prof. Dr. Job Boekhoven, Laura Tebcharani, Dr. Caren Wanzke, Dr. Jennifer Rodon-Fores, Prof. Dr. Angela Casini, Prof. Dr. Petra Mela, Salma Mansi, Dr. Enes Akyuz, Prof. Dr. Zuleyha Doganyigit, Prof. Dr. Percin Karakol, Dr. Bizan Balzer und Rebecca Schlatterer – und den KollegInnen aus dem Arbeitskreis Lieleg – Dr. Ceren Kimna, Dr. Benjamin Winkeljann, Prof. Dr. Jian Song, Dr. Matthias Marczynski, Dr. Martin Kretschmer, Dr. Marvin Ertelt, Maria Bauer, Carolin Rickert, Di Fan, Ufuk Gürer, Bernardo Miller Naranjo – für eine langjährige und erfolgreiche Zusammenarbeit. Darüber hinaus möchte ich mich noch bei den Studentinnen Defne Gövem und Rosa Reithmeir für Ihre Mitarbeit bedanken, bei Iris König-Decker für administrative Unterstützung und bei den zahlreichen technischen AssistentInnen – Tobias Fuhrmann, Mona Wolff, Katja Bäuml, Gabriele Chmel und Karin Vogt – die das eine oder andere Mal mit Verbrauchsmaterial ausgeholfen haben.

Zu guter Letzt möchte ich mich noch bei meinen Eltern bedanken, die mir diesen zweiten Bildungsweg ermöglicht haben. Sie standen immer hinter mir, haben mich immer unterstützt und waren auch dann für mich da, wenn es im Leben nicht alles so gelaufen ist wie es eigentlich sein sollte.